8-24-2016 12:00 AM

Development of Novel Anode Materials for Lithium Ion Batteries

Mike A. Nieradko
The University of Western Ontario

Supervisor
Oleg A Semenikhin
The University of Western Ontario

Graduate Program in Chemistry
A thesis submitted in partial fulfillment of the requirements for the degree in Doctor of Philosophy

Abstract

This thesis focuses on the development of new anodes for Li ion batteries. Aluminium has been long considered as a promising anode material for Li ion batteries because of its low cost, abundance, and low toxicity. Aluminium undergoes alloying with lithium through intermetallic LiAl formation which offers a relatively high theoretical capacity of 993 mAh/g compared to 372 mAh/g for graphite that is currently the principal anode material in commercial Li ion batteries. However, despite intensive research, all aluminium-based anodes tested so far suffered from rapid capacity fading and failure within the first few cycles. Furthermore, there is insufficient understanding of the mechanisms of such capacity fading and the lack of ideas how to overcome this problem.

In this work, we were able to demonstrate that the problems that have been plaguing Al anodes are not insurmountable and can be solved by judicious selection of the anode materials, their conditioning and treatment, as well as battery design. An important difference from all other studies is that we propose and justify the use of an electrochemical approach to formation of the LiAl nanostructure directly on the bulk anode surface, as opposed to the usual methods tested in the literature that involve application of various kinds of nanoparticles, nanowires, as well as thin evaporated or sputtered films. Using the approach developed in this work, we were able to fabricate and test battery prototypes with Al anodes, $LiFePO_4$ cathodes and solid polymer electrolyte that showed sustained performance for more than 400 cycles over a wide range of charge-discharge rates with high output voltage of 2.6 – 2.8 V and over 90% coulombic efficiency without any failure or capacity fading.

Keywords

aluminum anode, lithium-ion battery, solid polymer electrolyte, carbon nitride, poly(ethylene oxide), electrochemistry

Co-Authorship Statement

All of the experimental work was carried out by Mike Nieradko under the direction and supervision of Dr. Oleg Semenikhin except where noted below. All of the chapters in this thesis were originally written, edited, and revised by Mike Nieradko under the supervision of Dr. Oleg Semenikhin who was actively involved in all steps through the entire process.

Chapter 4.6: H.Y. Nie. carried out TOF-SIMS depth profiling experiments

Acknowledgments

I would like to thank my supervisor, Dr. Oleg Semenikhin for his expert guidance over the past four years. He was instrumental in helping me navigate through the often complicated course of this work and to bring it together into the final form you see here. I would also like to give special thanks to my graduate co-worker Ladan Eskandarian for the many fruitful discussions we had in developing these anodic materials into a practical solid state battery prototype design.

Table of Contents

List of Tables

List of Figures

Symbols and Acronyms

A	Surface Area
CNx	Carbon Nitride
C_{dl}	Double Layer Capacitance
CEr	Counter Electrode
CE	Coulombic Efficiency
CPE	Constant Phase Element
CV	Cyclic Voltammogram
Cyc	Cycles
EC	Ethylene Carbonate
EDX	Energy Dispersive X-ray
EMC	Ethylmethyl Carbonate
DEC	Diethyl Carbonate
e^-	electron
E	Potential
E^o	Standard Potential
ΔE_{ohm}	Voltage Drop
eV	Electron Volt
ΔG	Gibbs Free Energy
DMC	Dimethyl Carbonate
F	Faraday Constant
I	Current
M_w	Molecular Weight
NMP	1-methyl-2-pyrrolidinone
PC	Propylene Carbonate
PEO	Poly(Ethylene Oxide)
PVDF	Poly(Vinylidene Fluoride)
R	Resistance
R_{ct}	Charge Transfer Resistance
R_e	Electrolyte Resistance
RE	Reference Electrode
RT	Room Temperature
ρ	Electric (Specific) Resistivity
SEM	Scanning Electron Microscopy
SEI	Solid Electrolyte Interphase
SPE	Solid Polymer electrolyte
TEM	Transmission Electron Microscopy
TOF-SIMS	Time-of-Flight Secondary Ion Mass Spectrometry
WEr	Working Electrode
wt.%	Weight Percent
XRD	X-ray Diffraction
Z_{ct}	Charge Transfer Impedance

Chapter 1

1 Introduction

1.1 Motivation for this Work

The current global energy economy largely operates based on fossil fuels which presents several challenges going into the future. Of particular concern is the ever growing demand for non-renewable oil sources, and the impact of greenhouse gas emissions such as CO_2 on climate change. These factors have increased demand for alternative and preferably renewable energy sources including solar, wind, hydroelectric and geo-thermal power. These renewable energy sources are largely intermittent in nature because of their weather dependence. Furthermore peak electricity demand times during the day may not reconcile with peak generation times and vice versa. In urban centers the issue of CO_2 emissions and consequent air pollution may only be solved by replacing internal combustion engines with ideally zero-emission vehicles such as electric or hybrid electric vehicles. Therefore the goal of an energy-sustainable energy economy that also retains the freedom of personal transportation cannot be achieved without tackling the problem of energy-storage technology, specifically batteries. This battery technology must be rechargeable, efficient, portable and offer high capacity and long cycle life.

Lithium ion batteries (LIBs) have emerged as the dominant form of portable rechargeable energy storage technology both for electronics and in the development of electric cars [1]. They offer an unmatchable combination of high energy and power density among batteries because of certain fundamental advantages over other battery chemistries. Firstly, Li has the most negative reduction potential of any element, allowing Li based batteries to have the highest possible cell voltage. Also, Li is the third lightest element and has one of the smallest ionic radii of any single charged ion. These factors allow Li-based batteries to have high gravimetric (mAh/g) and volumetric (mAh/cm^3) capacity and power density. Finally, although multivalent cations such as Pb^{2+}/Pb^{4+} in lead-acid

batteries allow for higher charge capacity per ion, the additional charge significantly reduces their mobility. This is an important consideration given that the rate-limiting factor for battery performance is typically ionic transport in the solid electrodes.

A conventional Li-ion battery is typically composed of a carbonaceous anode (generally graphite), a carbonate-based organic electrolyte with a Li-containing salt (e.g. $LiPF_6$) and a Li-containing transition metal oxide cathode (for instance, $LiFePO_4$) [2]. Li ions are intercalated and deintercalated between graphite and $LiFePO_4$ through the electrolyte during the charge and discharge stages. While LIBs have become the battery of choice for many applications they are often also the limiting factor. Specifically LIBs often make up a large portion of the mass and volume of portable electronics which limits their available energy, and thus requires frequent recharging. Ultimately these limitations and the battery performance come down to the electrode materials of the anode and the cathode. In the anode chemistry graphite presents several disadvantages [3]. These include poor mechanical properties, incompatibility with some common electrolyte solvents (e.g. propylene carbonate) and most importantly a poor gravimetric capacity of 372 mAh/g due to their requiring 6 carbon atoms to contain 1 lithium ion. With the demand for safe Li-ion batteries exhibiting high power, large capacity and high rate capability ever increasing, intensive research has been carried out worldwide to find alternative anode materials to replace the currently used graphite.

In 1971 Dey demonstrated that Li metal can electrochemically alloy with certain other metals at room temperature in an organic electrolyte electrochemical cell [4]. Over the past few decades these "metal-alloying" electrode materials have comprised a great deal of the research into alternative high capacity anodes for LIBs [3,5]. The greatest literature focus has been on anodes comprised of silicon (Si), silicon oxide (SiO_x), tin (Sn) or tin oxides (SnO_x). Unlike graphitic materials these anodes undergo lithiation through lithium-metal intermetallic alloy phase formation. These metals and metal oxides offer high theoretical capacities due to the relatively large stoiochiometric ratio of Li that they can commonly accommodate. For example the highest order Si and Sn alloys offer theoretical capacities of 3579 mAh/g for $Li_{15}Si_4$ and 960 mAh/g for $Li_{17}Sn_4$. However

this advantage of metal-alloying anode materials is offset by two big drawbacks. Firstly there are large volumetric expansions during intermetallic phase formation ($Li_{15}Si_4$ = 676%, $Li_{17}Sn_4$ = 323%) compared to LiC_6 formation (~ 6%) in graphite anodes. This can cause active materials to crack and fracture, eventually losing complete electrical contact. It can also cause significant destruction of the protective solid-electrolyte interphase (SEI) layer present on the anode, resulting in continuous electrolyte decomposition, loss of lithium availability and increasing cell impedance. The second issue is the poor mobility of Li during the alloying and de-alloying processes relative to the intercalation/deintercalation processes that occur with Li in graphite anodes. As a result these metal-alloying anode materials generally suffer from a large irreversible capacity in the first cycle, low rate capability (charge/discharge rate) and limited cycle lifetime.

Development of these metal-alloying anode materials to make them practically feasible for LIBs has largely focused on the use of nanoscale architectures [3,5]. Nanostructured electrodes such as nanowires, nanoparticles and amorphous thin films can compensate for slow electron and Li ion transport typical of alloying materials by decreasing electron and Li ion diffusion lengths, enabling higher rate performance and higher capacity utilization. Nanoscale dimensions can additionally prevent the build-up of internal stresses during the volume expansion and contraction of intermetallic phase formation/dissolution, which would otherwise lead to the formation and propagation of cracks within these high-capacity active materials [6]. Another successful strategy commonly employed in tandem with nanostructures is compositing with graphitic materials, using a hierarchical arrangement such as encapsulation of the alloying material particles within a carbon shell [3]. This approach combines the low volumetric expansion and good conductivity of graphitic materials to maintain continuous electrical contact, while still allowing adequate void space and short diffusion paths for the alloying material. Even considering these promising developments, metal-alloying anodes that demonstrate high mass loading with high (> 800 mAh/cm^3) volumetric capacity and long cycle life (1000+ cycles) in an actual full Li-ion battery cell have yet to be demonstrated at the time of this writing.

Since 2001 aluminium (Al) has also emerged as another potential alternative anode to graphite in LIBs because of its low cost, abundance, and low toxicity [7-10]. Like Si and Sn it undergoes alloying with lithium through intermetallic LiAl formation which offers a relatively high theoretical capacity of 993 mAh/g compared to graphite. Higher intermetallic phases such as Al_2Li_3 and Al_4Li_9 with theoretical capacities of 1490 and 2234 mAh/g respectively are also known. An additional advantage of Al over Si and Sn is the high conductivity of Al. Since it also undergoes lithiation through lithium-metal alloying reactivity the development of Al anodes in the literature has also entirely focused on the use of nanostructures. However, unlike its Si and Sn counterparts Al anodes have generally performed poorly. Multiple studies of just the active nanostructured material (nanowires, thin films, etc.) typically reveal rapid capacity loss with complete loss of electrical contact, sometimes after just a few cycles [7-10]. Attempts to improve the performance of nanostructured Al anodes by compositing with carbon through mechanical or gas-phase methods have shown some success over the years relative to Al itself [11-13]. More elaborate architectures such as yolk-shell Al composited with TiO_2 have also recently emerged showing improved capacity and cycle life [14].

The explanation for the continued poor performance of nanostructured Al anodes largely remains unresolved and under great debate in the literature. Typically the reason that is given is pulverization of active materials during alloying/de-alloying because this process has been well documented in Si and Sn anodes over the years [3,5]. Evidence for severe cracking and fracture as being the primary failure mechanism for nanowire Al anodes was confirmed by in-situ transmission electron microscopy (TEM) [9]. Prior to this important study the work of earlier groups made similar assumptions to explain the rapid capacity loss they observed in Al [7,8]. However to date other research groups remain unconvinced and instead assert that it is the slow Li transport during LiAl phase formation and dissolution that is the main culprit for poor performance [15]. This phenomenon termed "lithium trapping" results in detectable quantities of lithium remaining in the bulk of the Al anode even after prolonged delithiation [15-17]. Convoluting all of these discussions further is the role of the oxide (alumina) layer that

can be present natively on Al or made thicker synthetically. Some groups assert that the oxide layer is largely irrelevant in lithiation-delithiation by merely acting as an ionic conducting pathway for lithium and in this regard the thickness does not matter [15]. However the same studies that demonstrated pulverization of nanostructured Al anodes showed that the oxide can be beneficial because it is lithiated into a mechanically robust layer that prevents the onset of anode failure [9]. Overall the common approaches used to tackle the issues of metal-alloying anodes have shown limited success with Al anodes, suggesting that the advantages conferred by nanostructures do not necessarily carry over to this material. As a result Al has been severely underutilized and largely neglected in high capacity anode research compared to its Si and Sn counterparts.

1.2 Scope of this Thesis

The continued poor performance of nanostructured Al anodes prepared in traditional way suggests that bulk Al metal anodes may be a promising alternative. Bulk Al metal offers many advantages relative to nanostructures including ease of preparation, wide availability, low cost, minimal environmental impact, good conductivity and mechanical robustness. Furthermore, due to its high conductivity, Al is already widely used in Li batteries as a material for current collectors. Furthermore, Al is well-known for its ability to form nanostructured and very robust coatings upon electrochemical treatment. Electrochemical anodizing of Al is known for almost 100 years and is extremely widely used in the industry. Therefore, we wanted to investigate if the electrochemical formation of the LiAl phase can be also used to nanostructure the surface of bulk Al anodes and produce stable and efficient anodes for Li ion batteries. This approach differs fundamentally from the usual method of introducing nanosize structures employed in battery technology whereby the nanoparticles are prepared separately and then applied to the electrode surface with the use of various conducting fillers and binders. In our approach presented in this thesis, we grow the nanostructure directly on the surface of solid Al anodes without the need of any additional binders or conductive fillers.

In order to be able to prepare a mechanically stable intermetallic phase and prevent pulverization, the effect of mechanical properties of the bulk Al material on lithiation-delithiation and intermetallic phase formation must be considered. There are a wide variety of commercial methods available to process and manufacture aluminium that can include hardening and softening methods or alloying with elements in the molten state. Overall these various methods can produce a wide variety of mechanical properties in the resulting bulk Al material. The role of the surface oxide in Al anodes is clearly under significant debate in the literature, whether it is beneficial, detrimental or largely irrelevant towards cycling performance. Therefore this issue also requires investigation. The compositing of carbon with nanostructured Al has received limited attention in the literature but appears promising. The compositing of nitrogen-doped carbon has been utilized with Si and Sn anodes and should prove fruitful with Al anodes but has not yet been investigated to our knowledge. In this regard reactive magnetron sputtering offers a convenient highly configurable method for compositing nitrogen-doped carbon with bulk Al materials.

All of these above effects are first investigated carefully in a liquid half-cell three-electrode environment, where we can isolate and study coated and uncoated Al anodes to determine the reasons why they may perform poorly. The arguments presented by the literature are considered to explain our results including pulverization of active materials, lithium trapping and a possible detrimental effect from the surface oxide. To demonstrate the practical usefulness of our findings these same coated and uncoated Al anodes are then tested in an optimized solid-state battery design utilizing a solid polymer electrolyte and transition metal oxide cathode under prolonged cycling at a variety of charging-discharging rates.

Chapter 2 provides a brief overview of the operating principles of a conventional lithium ion battery followed by specific details of the electrochemistry involving graphite, Si, Sn and Al anodes. Brief details are also provided regarding the cathodic and solid polymer electrolyte materials used in this work. The properties of carbon nitride (CNx) prepared using reactive magnetron sputtering are examined and a summary of their preparation and

the influence of the bonding and structure on the electronic properties is provided. Several anode samples in this work were further characterized by time-of-flight secondary ion mass spectrometry (TOF-SIMS). Since TOF-SIMS is a more specialized surface analysis technique not commonly employed in the literature we also provide some background on its application to these materials.

Chapter 3 describes the experimental setup used in this work as well as specific parameters involved in anode preparation, CNx deposition, cell assembly, together with the electrochemical and surface characterization parameters used in the experiments performed in chapter 4. Also included are descriptions of the electrochemical techniques and methodology used to characterize anode materials.

In Ch. 4.1 we investigate lithiation-delithiation in a liquid half-cell environment of a commercial Al 1100 material from Goodfellow (GF Al) that had been strain-hardened. The anode surfaces were prepared with varying degrees of surface oxide remaining. In all cases increased oxide content impaired the reversibility of GF Al due to increasing diffusion-limited losses in the discharge peak and also produced increased heterogeneity in the morphology of the formed LiAl intermetallic phase. Under continuous cycling a GF Al anode with the surface oxide removed displayed a relatively stable charge/discharge response over time with a few plateau potential jumps and minimal change in coulombic efficiency. However surface analysis did reveal systematic large scale cracking of the porous morphology.

Ch. 4.2 describes similar half-cell experiments with a different commercial Al 1100 material from McMaster-Carr (MC Al) that had been softened by thermal annealing processing. The electrochemistry revealed evidence of increased volume change associated with intermetallic phase formation leading to poorer initial reversibility at all current densities investigated relative to GF Al materials. This effect was further exacerbated with an MC Al anode that was prepared with the native surface oxide intact. In the surface analysis MC Al materials displayed increased heterogeneity and cracking of the porous morphology. Under continuous cycling an MC Al anode with the surface

oxide remaining exhibited a severely unstable charge/discharge response over time relative to GF Al, with numerous plateau potential jumps, significant degradation of coulombic efficiency and a heterogeneous multilayer porous structure.

In Ch. 4.3 we perform half-cell testing with a commercial Al 2024 material Duraluminum (Dural) that was precipitation hardened by alloying with copper and magnesium. The Dural offered improved mechanical toughness relative to GF Al and MC Al leading to a more stable charge/discharge response over time and a homogenous intact porous structure. However this benefit was strongly counterbalanced by impaired reversibility and conductivity at all current densities investigated as well as increased diffusion-limited losses in the discharge process.

In Ch. 4.4 and 4.5 we characterize the effect of CNx coating on the performance and properties of GF Al and Dural anodes, as well as the effect of annealing and varying CNx nitrogen content. Various sandwich structures using sputtered Al layer on Al and Cu substrates were also investigated. CNx coatings were shown to assist initially in volume change containment upon lithiation-delithiation and formation of a stable LiAl intermetallic phase; however, the effect was transient and the performance was still insufficient. Soft sputtered Al layers showed very poor performance thus highlighting the ineffectiveness of using traditional nanostructures for Al anodes.

Ch. 4.6 describes the results of more in-depth studies of several investigated systems using time-of-flight secondary ion mass spectrometry (TOF-SIMS). TOF-SIMS turned out to be instrumental in revealing the mechanism of formation of nanostructured LiAl interphase on the Al surface.

Ch. 4.7 describes the results for a series of coated and uncoated anodes that were characterized in an optimized solid-state battery prototype with solid polymer electrolyte. With a bare GF Al anode we observed a stable charge/discharge response with continuous cycling across a variety of current densities prior to eventual battery failure. CNx coatings were shown to be instrumental in cycling to even higher current densities

while maintaining good reversibility. Overall, using battery prototypes with solid polymer electrolyte allowed us to achieve much better performance than in liquid cells. The best prototype was able to withstand more than 400 charge-discharge cycles with current densities up to 0.65 mA/cm^2 without failure.

Chapter 5 discusses the results obtained in chapter 4. Ch. 5.1 begins with an examination of the mechanism during the early stages of lithiation-delithiation and the growth of the porous structure at the anode surface. The role of surface oxide is also discussed and it is concluded that in both GF Al and MC Al the surface oxide is irreversibly lithiated early during the cycling resulting in a significant detrimental impact towards reversibility. However, this effect largely becomes insignificant over time with the formation of a relatively thick LiAl phase on the surface. Specific attention is then focused on the failure mechanisms of pulverization of active materials and lithium trapping within the anode bulk during half-cell experiments. Ch. 5.2 discusses how the mechanisms from section 5.1 are altered in the context of differing mechanical properties of GF Al, MC Al and Dural. Here we conclude that the softened mechanical properties of MC Al are detrimental towards reversibility and mechanical stability of bulk Al anodes under continuous cycling because they produce a more severe strain response in the material in regards to the internal stresses generated by lithiation-delithiation. The strain-hardening processing of GF Al offers a good compromise of improved mechanical toughness over MC Al without introducing inert alloying elements such as Cu in Dural that are detrimental both towards reversibility and conductivity. The effect of CNx thin film coatings on the lithiation-delithiation of bulk Al anodes is considered in 5.3. Here we conclude that the CNx film can provide volume change containment for intermetallic phase formation as well as improved conductivity with both effects enhanced by thermal annealing of the anode and increased nitrogen content in the film. However these benefits cannot be fully realized without the additional scaffolding effect provided by solid polymer electrolyte in the solid-state battery design.

1.3 References

1. Nitta, N.; Wu, F.; Lee, J.T.; Yushin, G., *Materials Today*, **2015**, *18*, 5, 252-264.
2. Scrosati, B.; Garche, J., *Journal of Power Sources*, **2010**, *195*, 2419-2430.
3. Nitta, N.; Yushin, G., *Part. Part. Syst. Charact.* **2014**, *31*, 317-336.
4. Dey, A.N., *Journal of the Electrochemical Society*, **1971**, *118*, 1547-1549.
5. Park, C.M.; Kim, J.H.; Sohn, H.J., *Chem. Soc. Rev.* **2010**, *39*, 3115-3141.
6. Mukhopadhyay, A.; Sheldon, B.W., *Progress in Materials Science*, **2014,** *63*, 58-116.
7. Hamon, Y.; Brousse, T.; Jousse, F.; Topart, P.; Buvat, P.; Schleich, D.M., *Journal of Power Sources*, **2001,** *97-98*, 185-187.
8. Au, M.; McWhorter, S.; Ajo, H.; Adams, T.; Zhao, Y.; Gibbs, J., *Journal of Power Sources*, **2010**, *195*, 3333-3337.
9. Liu, Y.; Hudak, N.S.; Huber, D.L.; Limmer, S.J.; Sullivan, J.P.; Huang, J.Y., *Nano Lett.* **2011**, *11*, 4188-4194.
10. Sharma, S.K.; Kim, M.S.; Kim, D.Y.; Yu, J.S., *Electrochimica Acta*, **2013**, *87*, 872-879.
11. Chen, Z.; Qian, J.; Ai, X.; Cao, Y.; Yang, H., *Electrochimica Acta*, **2009**, *54*, 4118-4122.
12. Park, J.H.; Hudaya, C.; Kim, A.Y.; Rhee, D.K.; Yeo, S.J.; Choi, W.; Yoo, P.J.; Lee, J.K., *Chem. Commun.,* **2014**, *50*, 2837.
13. Huang, Y.; Lin, X.; Pan, Q.; Li, Q.; Zhang, X.; Yan, Z.; Wu, X.; He, Z.; Wang, H., *Electrochimica Acta*, **2016,** *193*, 253-260.
14. Li, Sa.; Niu, J.; Zhao, Y.C.; So, K.P.; Wang, C.; Wang, C.A.; Li, J., *Nature Communications*, **2015**, *6*, 1-7.
15. Oltean, G.; Tai, C.W.; Edstrom, K.; Nyholm, L., *Journal of Power Sources*, **2014**, *269*, 266-273.
16. Owen, J.R.; Maskell, W.C.; Steele, B.C.H., *Solid State Ionics*, **1984,** *13*, 329-334.
17. Liu, D.X.; Co, A.C., *J. Am. Chem. Soc.,* **2016**, *138*, 231-238.

Chapter 2

2 Background

2.1 Intercalation of Lithium Ions and Lithium-Ion Batteries

A lithium ion battery is typically composed of a carbonaceous anode, a carbonate-based organic electrolyte with a Li-containing salt dissolved, and a Li metal oxide cathode. Both electrodes are capable of having lithium ions insert into them through intercalation. In order to charge the battery, the positive lithium ions move from cathode to anode. When discharging, the ions move in reverse. As the positive lithium ions migrate away from the anode, the lithium-containing compound is reduced, releasing electrons. The electrolyte serves as a reservoir of Li ions for intercalation. Lithium ion batteries are considered secondary rechargeable batteries and are distinct from the first generation primary lithium batteries which utilize lithium metal as an anode material and are non-rechargeable.

Traditionally a high-capacity lithium ion battery is made from a lithium cobalt oxide ($LiCoO_2$) cathode and a graphite (C) anode [1]. Both electrodes are produced from active (Li ion storing) powders mixed with a small content (3–5 wt%) of a polymer binder (mostly polyvinylidene fluoride, PVDF) and a small amount (1–5 wt%) of conductive carbon additives (mostly carbon black) and casted on both sides of metal current collector foils (Al foil for cathode and Cu foil for anode). A typical thickness for the finished electrode layer ranges from 60 to 100 μm on each side of a foil. In a battery, the electrodes are separated with a porous electrically insulated membrane with a typical thickness of 15–25 μm. Organic carbonate solvents are used as a polar aprotic conductive pathway for lithium ions between electrodes. A combination of linear and cyclic carbonates in the form of 1:1 ethylene carbonate (EC) to dimethyl carbonate (DMC) is typically used because it offers an ideal mixture of high ionic conductivity and low viscosity for transport of lithium salt ions ($LiPF_6$ or $LiClO_4$). A schematic of a

commercial lithium ion battery involving a carbon anode and a transition metal oxide cathode is shown in **Fig. 2-1-1** [2], with the processes of deintercalation at the anode and intercalation at the cathode.

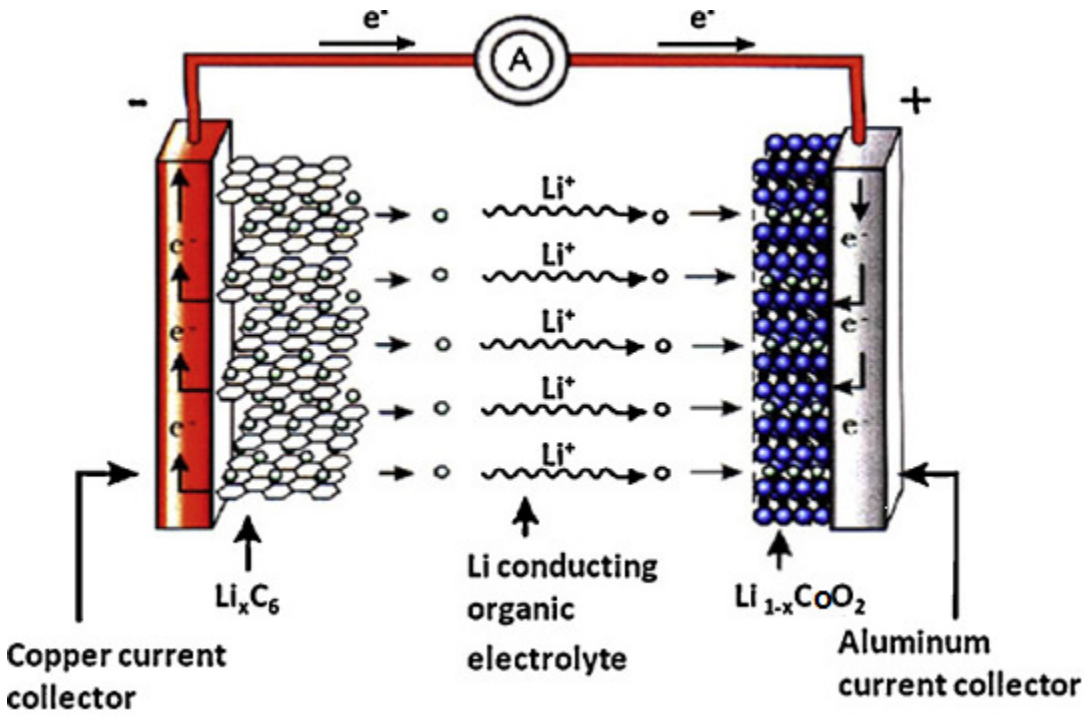

Figure 2-1-1: Schematic of a common lithium ion battery with graphite anode and $LiCoO_2$ cathode, from ref. 2.

Before we continue it is important to clarify some terminology from the literature. In lithium ion batteries the main parameter of interest for electrode material performance is typically "capacity" [1]. This term generally refers to specific capacity, gravimetric capacity or mass capacity denoting charge per unit mass (mAh/g). This value is often cited because it can be calculated easily with reasonable accuracy and is important for weight-sensitive applications. The mass in this term is only the mass of active material of the particular electrode, not including additional mass for example from binders or collector foils. In many applications it is important for an electrode material to show good performance at a sufficiently high mass loading. In this case another term is specified, the

"volumetric capacity" or charge per unit volume (mAh/cm^3) which can be calculated from the specific capacity, mass loading and the thickness of the electrode active material. Since each electrode undergoes both charge then discharge there are capacities associated with both processes, and they may differ significantly. The ratio of the capacities for the two processes in a particular cycle is termed the "coulombic efficiency" and is expressed in percent.

2.2 Graphite and Metal Anodes in Lithium-Ion Batteries

Historically, the most commercially successful electrode chemistry for lithium ion batteries has been intercalation-type electrodes. For the anode this would be various graphitic materials. Intercalation electrodes are capable of providing rapid Li ion transport by having Li conductive 1D paths or 2D planes within relatively large individual particles (commonly > 5 μm diameter in anode particles) [1]. This nature of Li insertion and extraction offers the advantage of low-volume expansion on lithiation-delithiation resulting in good mechanical and electrochemical stability of intercalation electrodes.

In graphite anodes the mechanism of Li ion insertion (intercalation) occurs between the graphite sheets with 6 carbon atoms containing one Li ion. Based on the common Li ion battery shown previously in **Fig. 2-1-1** the electrode chemistry can be described in eq. 1, where $LiMO_2$ represents a generic transition metal lithium oxide cathode [2]:

$$yC+LiMO_2 \leftrightarrow Li_xC_y + Li(1-x)MO_2,\ x \sim 0.5,\ y= 6 \qquad (1)$$

This process for LiC_6 formation offers a minimal volume expansion of approximately 6% [3]. The low volume changes in the graphite anode particles are particularly advantageous because of the need to maintain a low strain within a solid electrolyte interphase (SEI) layer. The SEI layer is formed in the first cycle at both anodic and cathodic material surfaces prior to initial Li ion intercalation, and involves irreversible partial reduction and decomposition of the electrolyte. Ideally this process is confined to

the first charging of the electrode. Otherwise electrolyte solvent-permeable defects may form and continuously grow upon electrolyte reduction at a low anode potential, irreversibly consuming Li from the cell and reducing its capacity with cycling.

While intercalation anodes such as graphite have been very successful commercially and steadily improved throughout the years they still suffer from several disadvantages [1]. Firstly the graphitic material has poor mechanical properties; it is brittle and prone to breaking easily. Secondly it is susceptible to exfoliation in certain battery solvents such as propylene carbonate, which limits the choice of electrolytes. Finally the most important limitation of graphite anodes is that the LiC_6 formation noted above only offers a relatively low theoretical mass capacity of 372 mAh/g [1], due to the requirement of 6 carbon atoms to contain one Li ion. Since the demand for safe Li-ion batteries exhibiting high power, large capacity, and high rate capability is ever increasing, research has been carried out worldwide to find new electrode materials to replace the currently used materials. By using higher capacity active materials and designing a structure/material that reduces the need for a separator membrane, binders, conductive additives, or current collectors, the overall battery energy density can be increased.

Various alternatives have been proposed for anodic materials in the form of metals, metal oxides, and metal nitrides across the periodic table [1]. These fall into the category of either 'alloy-type' or 'conversion-type' active materials and in general can offer much higher theoretical capacity than intercalation electrodes such as graphite. The former group consists of electrodes capable of electrochemically alloying with lithium, and often have high mass capacity due to the relatively large stoichiometric ratio of Li that such active materials can commonly accommodate. The most heavily studied 'metal-alloying' anode materials have been in group IV, particularly those based on Si and SnO_2 [4].

The electrochemical reactions of lithium with silicon at elevated temperatures follow the equilibrium Li-Si binary phase diagram, forming intermetallic compounds such as $Li_{12}Si_7$ Li_7Si_3, $Li_{13}Si_4$ and $Li_{22}Si_5$, showing distinct voltage plateaus for each two-phase region [4]. However at room temperature charging of a Si anode there are only two phases

observed with the final stoichiometry being $Li_{15}Si_4$ and the lithiation proceeding through a solid-state amorphization mechanism (Eqs. 2,3). The final alloy $Li_{15}Si_4$ offers an impressive theoretical mass capacity of 3579 mAh/g which has been the prime motivator in pushing the development of Si anode materials.

During charging of Si anode:

$$Si\ (crystalline) + xLi^+ + xe^- \rightarrow Li_xSi\ (amorphous) + (3.75 - x)\ Li^+ + (3.75 - x)\ e^- \rightarrow Li_{15}Si_4\ (crystalline) \quad (2)$$

During discharge of Si anode:

$$Li_{15}Si_4\ (crystalline) \rightarrow Si\ (amorphous) + yLi^+ + ye^- + Li_{15}Si_4\ (residual) \quad (3)$$

Electrochemical lithiation of Sn at elevated temperatures proceeds through seven different Li-Sn crystallographic phases within the Li-Sn phase diagram: Li_2Sn_5, LiSn, Li_7Sn_3, Li_5Sn_2, $Li_{13}Sn_5$, Li_7Sn_2 and $Li_{17}Sn_4$ [4]. Very early in Sn anode development SnO_2 was suggested to be a superior alternative material, because of the lithium oxide (Li_2O) formed "gluing" or holding the Sn grains together [1]. The basic reaction mechanism of SnO_2-based materials at room temperature is shown in eq. 4 with the first step involving reduction of the oxide [4].

$$SnO_2 + 4Li^+ + 4e^- \rightarrow Sn + 2Li_2O + 4.25Li^+ + 4.25e^- \rightarrow Li_{4.25}Sn + 2Li_2O \quad (4)$$

The final form of $Li_{4.25}Sn$ is equivalent to $Li_{17}Sn_4$ and results in a theoretical mass capacity of 960 mAh/g. This is significantly lower than the theoretical maximum of 3579 mAh/g for Si. However Sn is still considered an attractive anode material due to its volumetric capacity of about 2000 mAh/cm^3 which is comparable to Si.

While Si and SnO_2 anodic materials may offer very high theoretical mass or volumetric capacities they suffer from severe irreversible capacity loss during the discharge of the first cycle. This behaviour is due to the extreme volumetric expansions of 676% and 323% for the highest order $Li_{15}Si_4$ and $Li_{17}Sn_4$ alloys respectively relative to the

unlithiated materials [3]. This results in severe mechanical degradation in the form of cracking and pulverization of active materials eventually causing complete loss of electrical contact. Therefore for the development of Si and Sn based materials the literature focus has been on nanostructured anodes [4]. Nanostructured electrodes such as powders and nanowires can compensate for slow electron and Li ion transport in the active material by decreasing electron and Li ion diffusion length. Most importantly they offer large surface areas to accommodate the necessary extreme volume changes. These architectures can be further improved by compositing the active material with a relatively inactive material. The most common choice here are various carbon-based composites with graphite, carbon nanotubes, amorphous carbon or graphene. The low volumetric expansion of carbon offers a buffering component against cracking and pulverization of the metal-alloying active material. Additionally the carbon content improves conductivity through continuous electrical contact between Si or Sn particles while preventing their aggregation in the nanoscale architecture. Overall the dramatically improved performance and stability at nanoscale dimensions is a key feature of Si and Sn anodic materials for lithium-ion batteries.

2.3 Background of Aluminum Anodes

2.3.1 Structure and Properties of Aluminum

Aluminum in its elemental state is a silvery-white, soft, non-magnetic, ductile metal. Its key features include very low density and excellent corrosion resistance due to rapid formation of a passive native oxide layer (Al_2O_3) with thickness of a few nanometers. Aluminum adopts a face-centered cubic crystal structure shown in **Fig. 2-3-1**. Pure bulk Al metal has relatively poor mechanical properties which can be improved through a variety of processing methods. Typically this processing involves a variety of cold-working methods such as strain-hardening to increase material hardness [5-6]. The strain-hardening method multiplies the number of dislocations compared to the initial unworked bulk Al material and entangles them through dislocation-dislocation interactions. This effectively results in plastic deformation being relatively more difficult to perform than the initial unworked bulk material. Alternatively a range of thermal annealing methods can be used to create the opposite effect [7]. The thermal annealing treatment annihilates a significant portion of the dislocations present originally. However the dislocations that remain have higher mobility and the processed material has coarser grain boundaries. This effectively results in a softer material with plastic deformation being relatively easier to perform than the unworked material. Overall there are a plethora of processing techniques available and thus commercial bulk Al materials can possess a wide variety of mechanical properties.

Another way to improve the mechanical properties of Al and also mitigate the issue of its high reactivity in the elemental state is to alloy Al with other metals. The most common alloying elements employed are typically copper, zinc, magnesium, manganese and silicon. Another class of alloys that has become important particularly in the aerospace industry is lithium-aluminum alloys, due to the weight advantage provided by the extremely low density of lithium. In general each 1 wt% of lithium results in a density reduction of 3% in the resulting alloy relative to aluminum itself. This lighter density is

made possible through the substitution of Al atoms by Li atoms in the FCC lattice. Therefore lithium-aluminum alloys may be considered as substitutional alloys as opposed to interstitial alloys such as lithium-silicon where lithium occupies the interstitial vacancies in the lattice. Shown in **Table 2-3-1** are some relevant properties of aluminum as well as lithium for comparison.

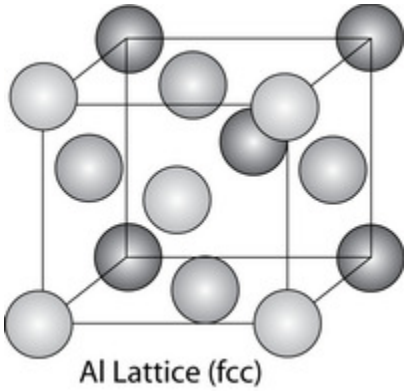

Figure 2-3-1: Face-centered cubic crystal structure of Al

Element	Al	Li
Density (g/cm^3)	2.70	0.535
Melting Point (^oC)	660.32	180.54
Atomic Radius, empirical (pm)	125	145
Crystal Structure	FCC	BCC
Lattice Parameter (pm)	404.95	351.25
Space Group	Fm_3m	lm_3m

Table 2-3-1: Properties of elemental aluminum and lithium

2.3.2 Properties of Lithium-Aluminum Intermetallics

Historically alloys between lithium and metals including aluminum were produced thermally by heating them together at high temperatures beyond the melting point [8]. Then in 1971 Dey showed that electrochemical alloying of metallic lithium with various metal electrodes can occur spontaneously with high coulombic efficiency at room temperature, in organic carbonate electrolytes containing lithium salts [9]. The alloying was observed in several materials including Sn and Al with the resulting intermetallic phase crystal structures and stoichiometry being consistent with alloys produced thermally. Another important result was the absence of alloying in other materials such as stainless steel and most importantly Cu. Therefore these latter unreactive materials would eventually become the common current collector materials in both primary and secondary lithium batteries. Since Dey's important study aluminum has been extensively studied as a possible anode to replace metallic lithium in primary lithium batteries due to its low cost, wide availability, high conductivity, mechanical stability and low environmental impact [3].

Shown in **Fig. 2-3-2** is the Al-Li binary phase diagram with the crystal structure data of the intermetallic phases summarized in **Table 2-3-2** [10]. The term 'L' denotes the liquid phase near the melting point of aluminum at 660 ^{o}C.

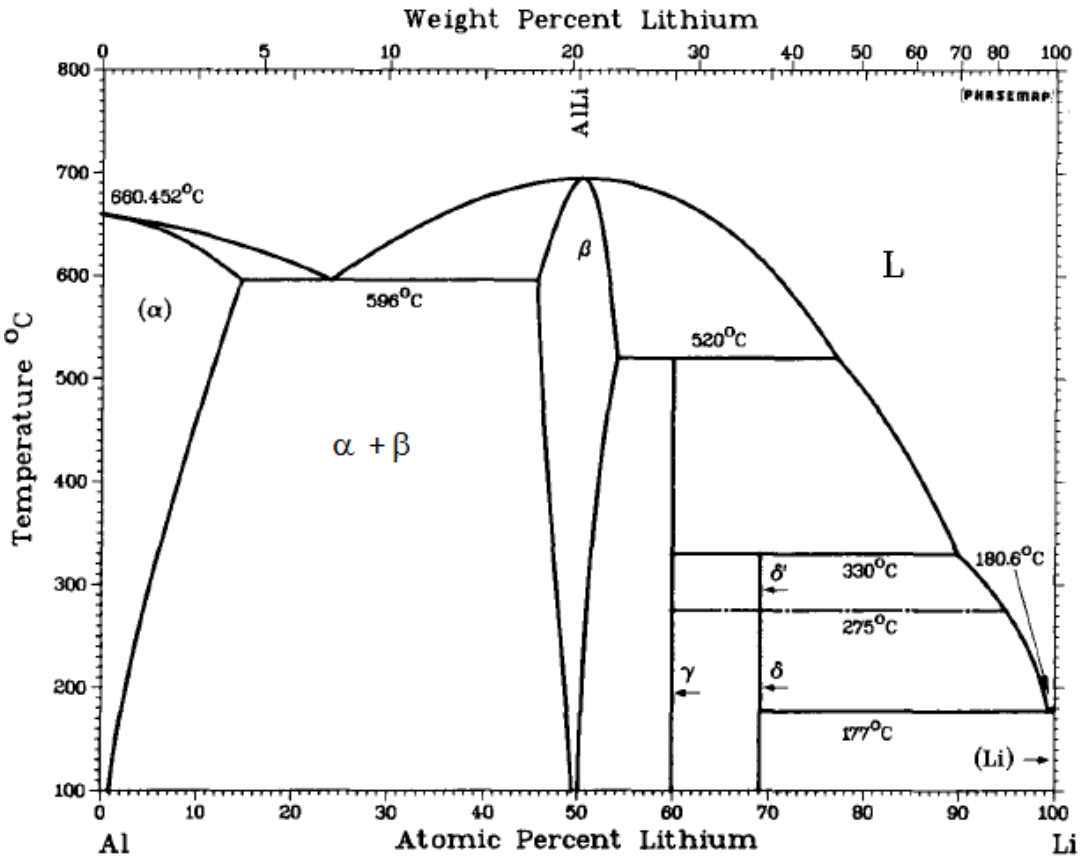

Figure 2-3-2: Binary Al-Li Phase Diagram, from ref. 10.

Phase	Alternate notation	Approximate composition(a), at.% Li	Space group	Tempera-ture, °C	Lattice parameters, nm a	b	c
(Al)	α	0-15	$Fm3m$	<660.5	0.40495(b)	···	···
AlLi	β	45-55	$Fd3m$	<700	0.637(c)	···	···
Al_2Li_3	γ	60-61	$R\bar{3}m$	<520	0.4508	···	1.426
Al_4Li_9	δ	69.2	$C2/m$	275-330	1.91551(5)	0.54288(1)	0.44988(1)
Al_4Li_9	δ′	69.2	···	<275	···	···	···
(Li)	···	100	$Im3m$	<180.6	···	···	···

(a) From the phase diagram. (b) At 0 at.% Li. (c) At 50 at.% Li.

Table 2-3-2: Al-Li crystal structure data, from ref. 10.

Overall there are three possible lithium-aluminum alloys of LiAl, Al_2Li_3 and Al_4Li_9 denoted as α/β, γ and σ respectively in the diagram. To illustrate the electrochemical alloying behaviour of Al-Li at room temperature, **Fig. 2-3-3** shows a plot of the lithium electrochemical potential (in eV) versus the mole fraction of lithium in the lithium/aluminum system [11]. Overlaid near the top of the graph are charge and discharge curves for formation and dissolution of intermetallic phases on an Al foil electrode from an organic carbonate electrolyte with a lithium salt. From this figure we observe that the higher order Al_2Li_3 and Al_4Li_9 phases (γ and σ) are absent near room temperature. Therefore the LiAl phase remains and may actually comprise two different phases, α or β depending on the lithium concentration within the Al host. There is actually a relatively wide concentration range between 5% and 45% mole fraction of lithium where both α and β LiAl phases exist together at room temperature, near the equilibrium potential of 0.38V versus lithium metal electrode.

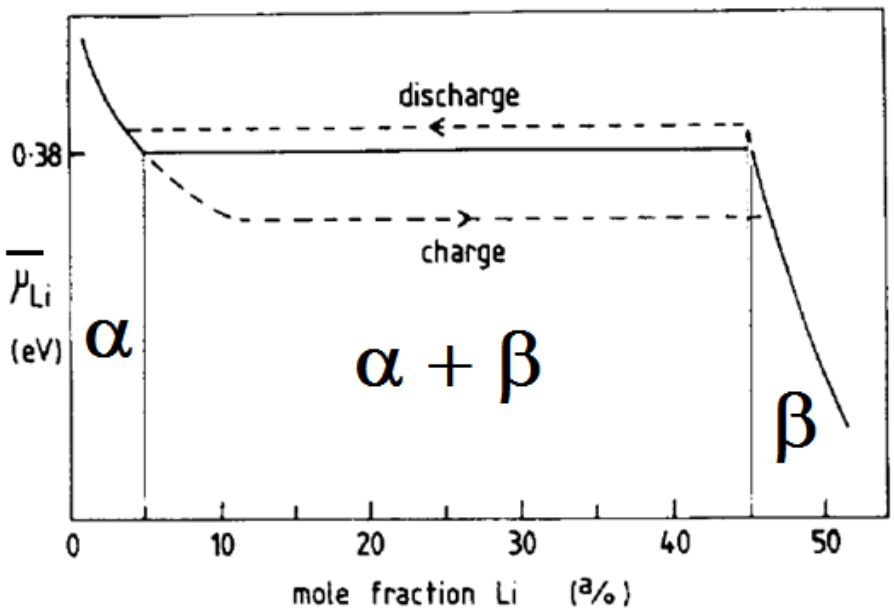

Figure 2-3-3: Electrochemical potential of Li as a function of mole fraction in Li/Al, from ref. 11.

According to **Table 2-3-2** the α and β LiAl phases have their own distinct lattice parameters [10]. The α phase at low concentration can be considered as a 'substitutional solid solution' of lithium in a face-centered cubic Al lattice with structure similar to **Fig. 2-3-1** (a = 0.405 nm), and diffusion of solute Li atoms occurring through the movement of dislocations [12]. Supersaturation of the α phase results in the β phase which has a NaTl-type crystal structure (a = 0.637 nm) shown in **Fig. 2-3-4** with space group Fd3m [13]. This Zintl phase structure can be considered as a diamond-like lattice of Al (blue spheres) with Li (black spheres) occupying the vacancies in the lattice. The increase in lattice parameter here for β-LiAl is directly responsible for the volumetric expansion of Al upon lithiation. The electrochemical interconversion between α and β LiAl phases at room temperature described in this section will be important in describing the mechanism of lithiation-delithiation for Al anodes in lithium-ion (secondary) batteries.

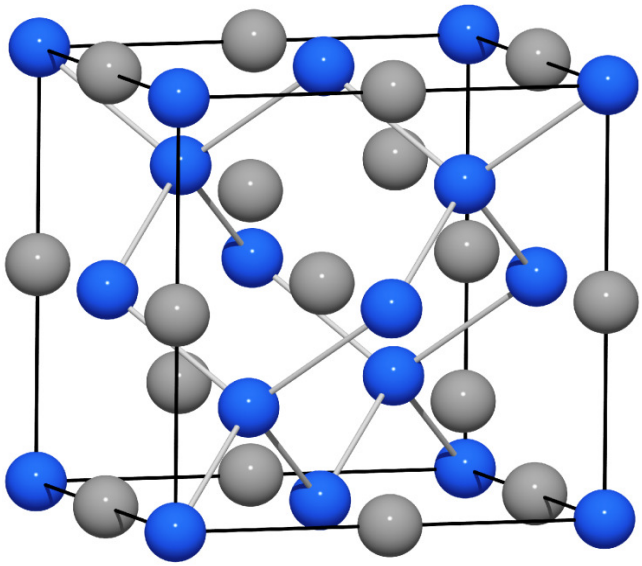

Figure 2-3-4: Atomic arrangement of a NaTl-type crystal structure for β-LiAl intermetallic phase

2.3.3 Electrochemistry of Aluminum Anodes in Lithium-Ion Batteries

With the continued investigation of aluminum anodes for lithium (primary) batteries interest eventually grew for using this material to replace carbon in lithium ion (secondary) batteries. Based on the stoichiometry and the low atomic weight of Al the LiAl, Al_2Li_3 and Al_4Li_9 alloys offer theoretical mass capacities of 993, 1490 and 2234 mAh/g respectively. Therefore the maximum theoretical lithium uptake for an aluminum electrode is 2.25 Li atoms per Al atom. This value is below the 4.25 or 3.75 Li atoms for each Sn or Si atom possible in the highest order $Li_{17}Sn_4$ and $Li_{15}Si_4$ alloys at room temperature [4]. However as described in Ch. 2.2 both Sn and Si intermetallic alloy formation suffer from severe volumetric expansions of 676% and 323% respectively for the highest order alloys which causes rapid irreversible capacity loss as anode materials [3]. Studies of Al anodes in lithium ion batteries over the past 15 years have revealed that only the lowest order (LiAl) alloy phase is formed during lithiation-delithiation in aprotic polar carbonate solvents at room temperature [14-24]. This is consistent with the absence of higher order lithium-aluminum alloys at room temperature in primary lithium batteries discussed in Ch. 2.3.2. The structural determination of the intermetallic phase in Al anodes is typically made after galvanic cycling through X-ray diffraction (XRD).

While this lowest order intermetallic alloy only allows for an uptake of one Li atom per Al atom it still offers a good theoretical mass capacity of 993 mAh/g compared to the value of 372 mAh/g for graphite. Furthermore the volumetric expansion for LiAl alloy formation is only 97% [3], which is considerably less than for the higher order Si and Sn based alloys described above. The formation and dissolution of LiAl is a single alloy transition unlike the stepwise pathway for formation of higher order Si intermetallic alloys. Therefore the charge-discharge curves for Al anodes are characterized by wide and flat charge/discharge plateaus. This is an important requirement for steady power output of anodic materials in lithium ion batteries.

Recently the mechanism of lithiation in Al anodes has been investigated both in crystalline bulk materials and semi-crystalline nanostructures. For bulk Al materials Liu et al. have studied the mechanism of lithiation in thin Al foil, shown in **Fig. 2-3-5** [25]. This figure is only a schematic representation of the processes and certain details such as solid-electrolyte interphase (SEI) formation and volume changes of the Al host material have been omitted. First the lithium ions arrive at the electrode surface (panel a). Lithiation of Al then proceeds through an initial nucleation of an α-LiAl solid solution in the electrode surface (panels b,c). This process is accompanied by a lattice contraction in the Al host through rearrangement of domains. As the Li concentration in the Al matrix increases towards supersaturation a crystalline phase of β-LiAl begins to nucleate and grow within the solid solution of α-LiAl (panel d). This process is accompanied by a lattice expansion in the Al host. Therefore a two-phase equilibrium between α and β phases of LiAl is established, leading to the lithiation potential plateau. As lithiation continues additional Li will diffuse into the bulk of the anode as a progressively deeper front of α-LiAl, while additional α-LiAl crystallizes into β-LiAl closer to the anode surface (panel e inset). This electrochemical lithiation of Al through a solid-solution mediated pathway leading to crystallization is fundamentally different from the amorphization pathway described previously for other metal-alloying anode materials such as Si and SnO_2 [4]. Physically the creation and movement of these LiAl phases is based on the mobility of dislocations within the Al host. Huang et al. revealed that initial nucleation of intermetallic phases in metal-alloying anodes occurs at surface sites with high density of mobile dislocations [26]. The accompanying lattice contractions and expansions of lithiation proceed through movement of these dislocations, creating a dislocation-induced stress (DIS) that is localized to the surface of the material during initial lithiation [27]. As lithiation continues (time increases) and the diffusion front moves deeper these dislocations will progressively move towards the interior of the anode bulk. As a result the DIS will decrease at the surface and increase in the bulk, eventually reaching a steady state.

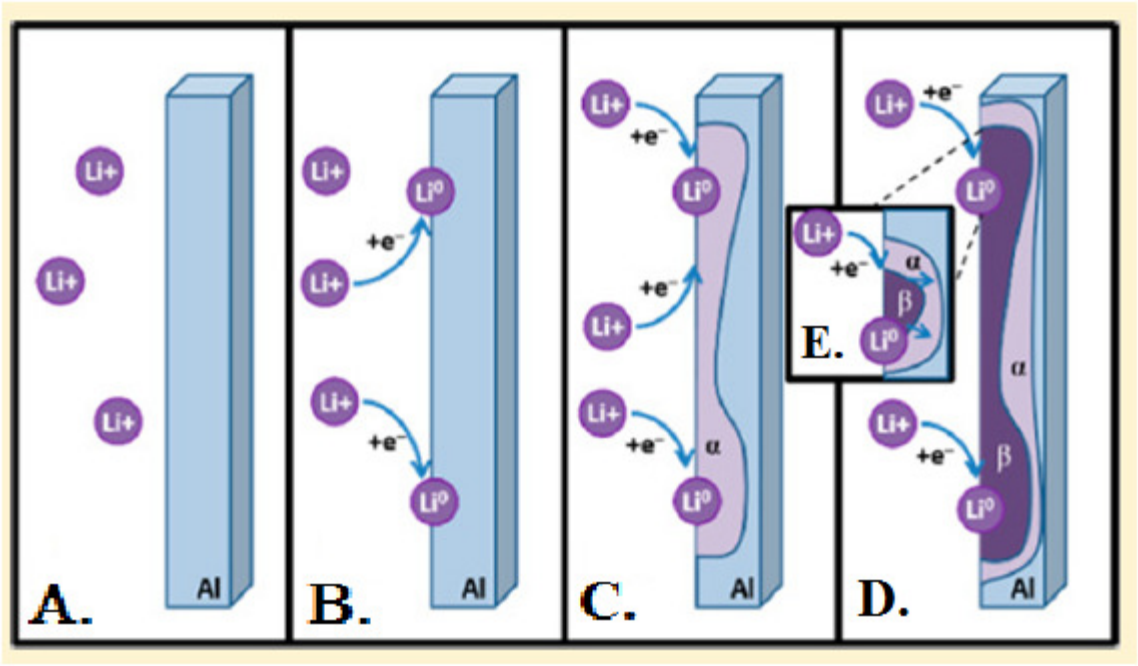

Figure 2-3-5: Schematic of lithiation mechanism in a crystalline thin Al foil anode, from ref. 25.

A common choice for nanostructured anode materials is thin semi-crystalline films prepared on hard substrates through electron-beam deposition or thermal evaporation. Recently Leenheer et al. utilized in-situ transmission electron microscopy (TEM) to investigate the mechanism of lithiation in a 50 nm Al thin film prepared through electron-beam deposition on silicon nitride substrate [28]. Initially there were isolated nucleation events at the anode surface involving formation of α-LiAl solid solution, followed by crystallized growth into the β-LiAl phase. However continued nucleation and growth of intermetallic phases did not proceed through a surface-to-interior lithiation front mechanism described above for bulk Al materials (**Fig. 2-3-5**). Beyond the initial nucleation and growth events the continued formation of intermetallic phase instead propagated laterally across the anode surface. Additional nucleation events were only observed to occur at the boundary between lithiated and unlithiated material rather than continuing at previously isolated unreactive regions. The propagation of the lateral lithiation fronts was highly non-uniform with different sub-regions of the anode lithiating at very different rates. In contrast in-situ TEM of thin Si anodes in the same study revealed lithiation fronts that spread uniformly across the anode surface. The difference

in lithiation behavior between these two materials was again ascribed to the phase growth dependence in Al anodes on crystallization into β-LiAl. In comparison lithiation of Si occurs through a solid-state amorphization mechanism as described previously in Ch. 2.2. A comparative schematic of the surface-to-interior lithiation front mechanism versus that of lateral lithiation front propagation for bulk versus thin film Al anodes is shown in **Fig. 2-3-6**.

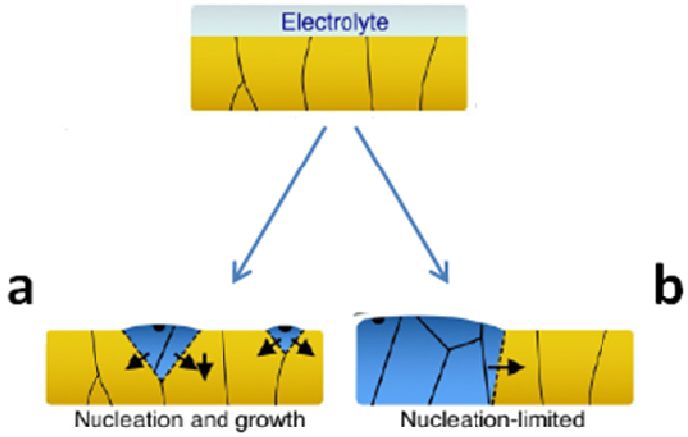

Figure 2-3-6: Schematic of lithiation mechanisms and lithiated phase front progression (a) Surface-to-interior lithiated phase front progression characteristic of bulk Al anodes, (b) Lateral phase front propagation characteristic of nanostructured thin film Al anodes. Lines denote grain boundaries and half-circles denote nucleation points, from ref. 28.

Like Si and Sn based materials the focus on nanostructures has entirely driven the development to improve the performance of Al anodes because it is also a metal-alloying anode, and the volumetric expansion of 97% for LiAl formation is still relatively large compared to the small value of 6% for LiC_6 formation in graphite anodes [3]. Therefore it is assumed that Al nanostructured anodes such as amorphous thin films, powders and nanowires will offer the same advantages relative to bulk Al anodes described previously for Si and Sn nanostructures, particularly in the accommodation of volume changes.

However in the literature nanostructured Al anodes have consistently shown high capacity initially with rapid capacity loss observed after a few cycles [14-24].

Currently there is significant debate in the literature concerning the dominant capacity loss mechanisms responsible for the continuing poor performance of Al nanostructured anodes. Firstly the volumetric expansion and contraction of intermetallic alloy formation and dissolution can impair stability of the solid-electrolyte interphase (SEI) layer present on the anode surface [29]. The SEI layer is formed initially from partial irreversible reduction and decomposition of the electrolyte. In graphitic anodic materials the volumetric expansion for lithiation is low at around 6% [3], resulting in minimal growth or change of the SEI layer beyond the first cycle. In Al like in other metal-alloying anodes such as Si the much larger volume changes can partially destroy the SEI layer present upon delithiation [29]. With continued expansion and contraction of cycling this will expose fresh Al material for continuous formation of thick SEI layers, causing significant permanent loss of lithium from the electrolyte. Secondly there is the pulverization of the active LiAl material [14, 19], which is considered by many to be the dominant failure mechanism in Al nanostructures because it is consistently observed in Li-Si and Li-Sn intermetallic alloy active materials. The progression of pulverization in Al anodes has been intensely studied through in-situ TEM of Al nanowires (NW) during repeated lithiation-delithiation cycles, shown in the series of images in **Fig. 2-3-7** [19]. Fig. (a) shows a schematic illustration of the in-situ experimental setup. Fig (b) shows a pristine Al NW with diameter of 40 nm contacted with the Li_2O/Li electrode to form an electrochemical device. Fig. (c) then shows the Al NW after the first lithiation with volume expansion observed in both radial and longitudinal directions. Progressing to the first delithiation stage (d) voids are formed indicated by red and yellow arrows. Continued delithiation in (e) enlarges these voids and forms new ones, indicated in blue arrows. After the second lithiation (f) the voids shrink and are partially healed. Switching back to the second delithiation in (g) increases the number and size of the voids. These trends continue until the NW is finally pulverized into nanoparticles (l, m), causing complete loss of electrical contact within the LiAl active material as well as to the supporting substrate.

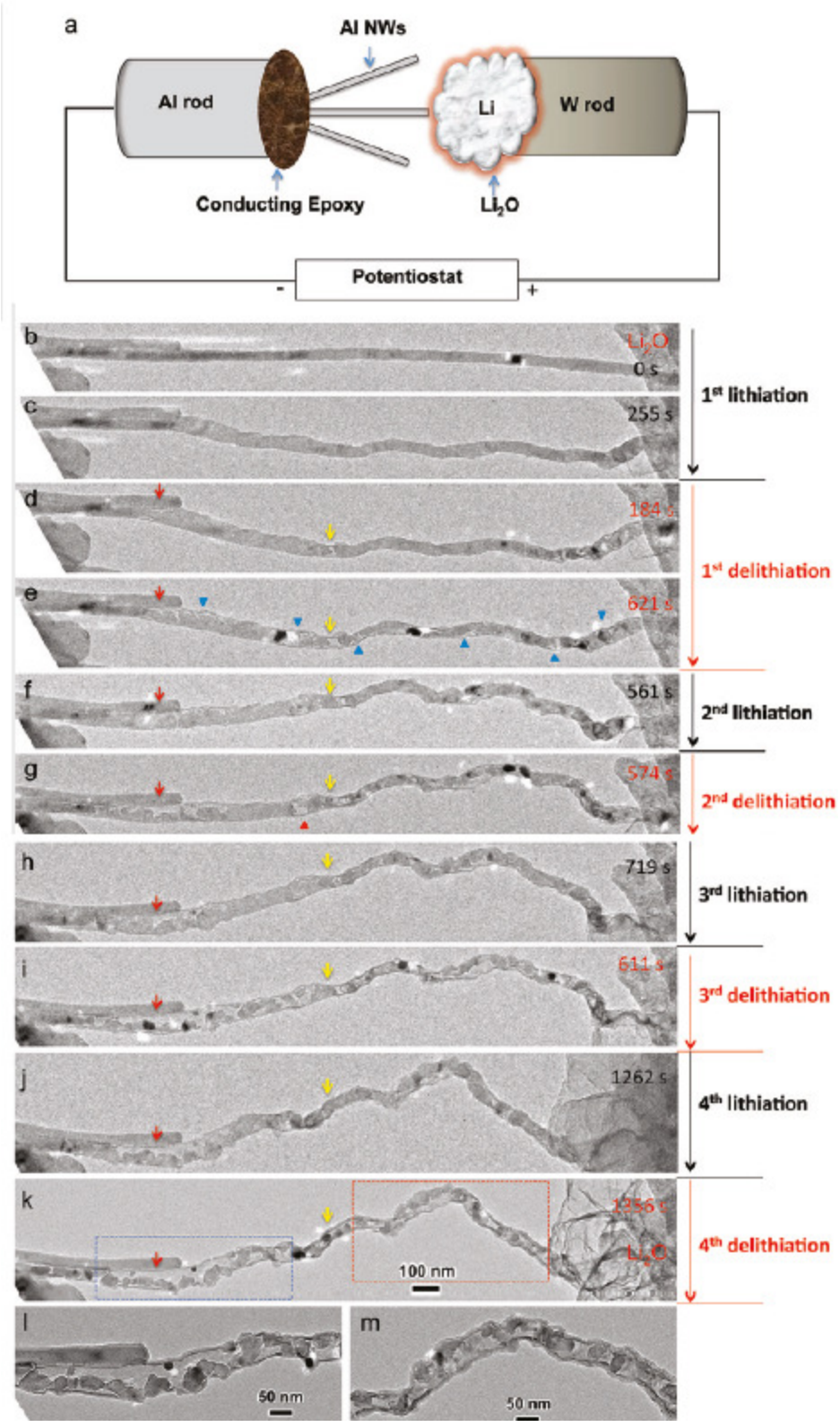

Figure 2-3-7: Pulverization of a single aluminum NW upon electrochemical cycling, from ref. 19.

Another body of literature has emerged claiming that the dominant capacity loss mechanism is instead "lithium trapping", due to diffusion-limited Li transport in Al [24]. Like in Si anodes Al suffers from poor mass transport kinetics associated with the breaking and forming of chemical bonds upon electrochemical alloying of Li with Al. As described previously lithiation-delithiation of Al occurs through a mechanism of two LiAl phases (α and β) based on the lithium concentration available within the host matrix. The reported diffusion coefficients of Li within α-LiAl and β-LiAl phases vary significantly but are around 10^{-11} cm^2/s and 10^{-9} cm^2/s respectively [24]. These values are relatively slow compared to the diffusion coefficient of 10^{-7} cm^2/s for Li in LiC_6 in a graphite anode [1]. Practically speaking, the impaired Li transport in LiAl would limit the discharge rate and thus the power density. Three decades ago Owen et al. proposed a model to explain lithium trapping shown in **Fig. 2-3-8** in terms of the charge and discharge processes [11]. For simplicity the volumetric changes of alloy formation and dissolution have not been included in the figure. Additionally it is assumed that the surface oxide layer plays no part in lithiation-delithiation and therefore merely acts as an ion conducting pathway to the Al core. The graphs in the bottom half show the Li concentration versus distance into the anode.

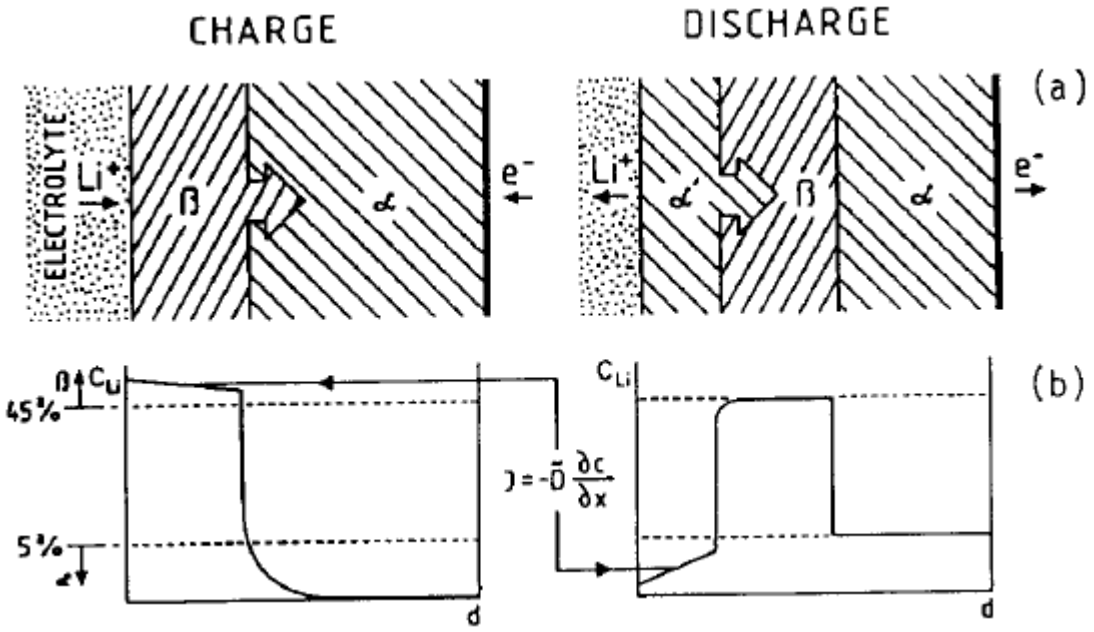

Figure 2-3-8: Owen's model for lithium trapping in charge/discharge processes of Al anodes, from ref. 11.

Initially the α-LiAl phase nucleates on the Al surface. As lithiation continues the α-LiAl phase will progress into the Al bulk, while near the electrode surface the increasing Li concentration will convert α-LiAl phase to β-LiAl. Upon applying the opposite current delithiation (oxidation) will begin from the LiAl/alumina interface, regenerating the Al from its surface and then progressing inwards. Therefore the recovery of lithium back into the electrolyte first happens at the electrode surface. Due to the differing diffusion coefficients of the two phases this gives rise to a lithium-rich β–LiAl layer trapped between two lithium deficient α-LiAl layers. Additionally the lithium that is now trapped can diffuse towards the surface or deeper into the Al bulk. Experimentally the phenomenon of lithium trapping has been shown by observing lithium present in Al electrodes even after the de-alloying step [25]. Considering diffusion is time dependent this capacity loss mechanism can become progressively worse with additional cycling. However recent evidence shows that it may be possible to circumvent this issue by minimizing the time during which the Al electrode is maintained at oxidizing potentials, because it allows less time for the trapped lithium to diffuse further into the Al bulk [24]. This is performed experimentally by cycling the Al electrode to a lower anodic (oxidizing) potential limit during delithiation.

Finally for Al anodes there is the point of contention regarding the influence of surface alumina layer on cycling performance and failure mechanisms. In other active electrode materials for lithium ion batteries such as $LiCoO_2$, $LiMn_2O_4$ and MoO_3 it is widely reported that the presence of an alumina layer can improve the durability and rate capability of the electrode during lithiation/delithiation [30-33]. However the underlying mechanisms of the alumina layer on these materials and Al anodes are well not understood in the literature. In Sn-based systems the surface oxide (SnO_2) present natively on the anode is typically reduced first at a potential considerably higher before lithiation begins [4]. For Al anodes some studies assert that the oxide merely acts as an inert ion conducting pathway for lithium towards the Al core [24], as demonstrated above in the Owen's model. These studies show that changing the alumina thickness does not noticeably affect the electrochemical performance. Other studies show that the alumina is first irreversibly lithiated into a super-hard Li-O-Al layer [19], similar to lithiation of

SiO_2 that occurs in Si anodes [34]. This process occurs first prior to lithiation of the Al core. The resulting Li-O-Al layer has poor electrical conductivity compared to the original alumina layer, and is therefore considered a source of permanent capacity loss. However the Li-O-Al layer acts to contain the pulverization of electroactive materials, by enlarging through elastic and plastic deformation to act as a solid electrolyte with exceptional mechanical robustness and ion conduction. Shown in **Fig. 2-3-9** are in-situ TEM images and EELS maps of a pristine Al nanowire anode with a native 4 nm oxide layer that was lithiated into a thicker 5 nm Li-O-Al layer [19].

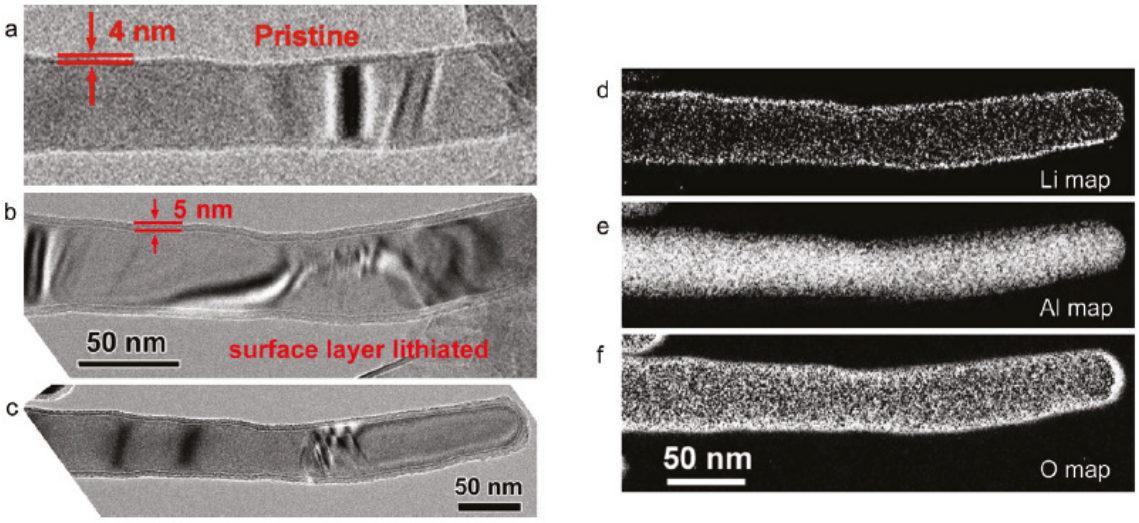

Figure 2-3-9: Evolution of the surface Al_2O_3 layer to the Li-O-Al layer. (a) Pristine Al nanowire with 4 nm native Al_2O_3 layer, (b) Lithiation of the surface layer, whose thickness was increased to 5 nm, (c) The Al nanowire with the lithiated surface layer, (d-f) EELS maps of Li, Al, O respectively, indicating that the surface Al_2O_3 layer had evolved to Li-O-Al after lithiation, from ref. 19.

The continuing poor performance for lithiation-delithiation of Al nanostructured anodes suggests that the alternative of bulk Al anodes may be preferable. Bulk Al materials offer advantages of ease of preparation, mechanical robustness and improved conductivity over nanostructures. For this purpose it is important to consider the processing methods used

to manufacture commercial bulk aluminum. As described in Ch. 2.3.1 there are a wide variety of processing techniques available to modify the mechanical properties of bulk Al metal through mechanical, thermal or alloying methods. Therefore commercial bulk Al metal can offer a wide variety of mechanical properties.

As described previously the mechanism of lithiation-delithiation in metal-alloying anode materials such as Al depends on the density and mobility of dislocations within the host [25-27]. One would expect the processing methods on bulk Al materials will determine the arrangement and mobility of dislocations within the host [5-7], which will affect the relative ease of plastic deformation of the resulting LiAl alloy. Therefore one should expect that the resulting mechanical properties of bulk Al materials should influence these various lattice contractions and expansions for nucleation and growth of intermetallic phases. As an anode in lithium-ion batteries these properties will in turn affect the material's response to the volume changes of lithiation-delithiation, and ultimately electrode degradation and failure [35]. Additionally these mechanical properties should affect the properties of any surface oxide present on the Al material. The influence of mechanical properties and the surface oxide of Al materials on lithiation-delithiation, specifically capacity loss mechanisms such as solid-electrolyte interphase (SEI) formation, surface oxide lithiation/reduction, pulverization of active materials and mass transport limitations of Li in the bulk material (lithium trapping) are key issues that will be investigated in this thesis work beginning in Ch. 4.1.

2.4 Cathode Materials

The cathode of a battery is the positive electrode which gains electrons from the external circuit and is reduced during the electrochemical reaction. The cathode materials in a rechargeable lithium ion battery must meet several crucial requirements to be successfully used [36]. In particular the material should contain a readily reducible/oxidizable element; for example, a transition metal such as Fe; the material should react with lithium ions in a reversible manner, very rapidly both on insertion and removal, and have these processes occur at high positive potentials. A lithium ion cell should be assembled in the discharge state. Therefore, the cathode must act as a source of lithium which requires the use of air-stable lithiated intercalation compounds to facilitate the cell assembly. The properties of an ideal cathode material for lithium-ion batteries include readily reversible reactions, little bonding and structural modification during the charge-discharge process [37].

The common cathode material choice for lithium-ion batteries are intercalation-type compounds, specifically lithiated transition metal oxides. An intercalation compound interacts with cations and electrons from external sources, forming a new compound in which the structural elements of the initial compound are maintained. Lithium ions act as guest species that can be inserted in the host lattice during discharge and extracted from the host with little structural modification [38].

Recently, transition metal phosphates such as olivine $LiFePO_4$ and other lithium transition-metal phosphates, have been demonstrated as possible candidates for cathode materials [39]. The most common cathode materials are summarized in **Table 2-4-1** [40].

cathode	$LiFePO_4$	$LiFePO_4$ +5%C	$LiMn_2O_4$	$LiCoO_2$
Density/g cm^{-3}	3.60	3.48	4.31	5.10
Potential/V	3.50	3.50	4.05	3.90
Specific capacity /mAh g^{-1}	169	159	148	274
Specific energy /Wh g^{-1}	0.59	0.56	0.56	0.98

Table 2-4-1: Electrochemical parameters of several cathode materials, from ref. 40.

Olivine $LiFePO_4$ in particular is an attractive cathode material that will be used in the battery prototypes of this thesis work because of its low cost, ease of preparation and perceived thermodynamic and kinetic stability. The crystal structure of olivine $LiFePO_4$ is shown in **Fig. 2-4-2** [41].

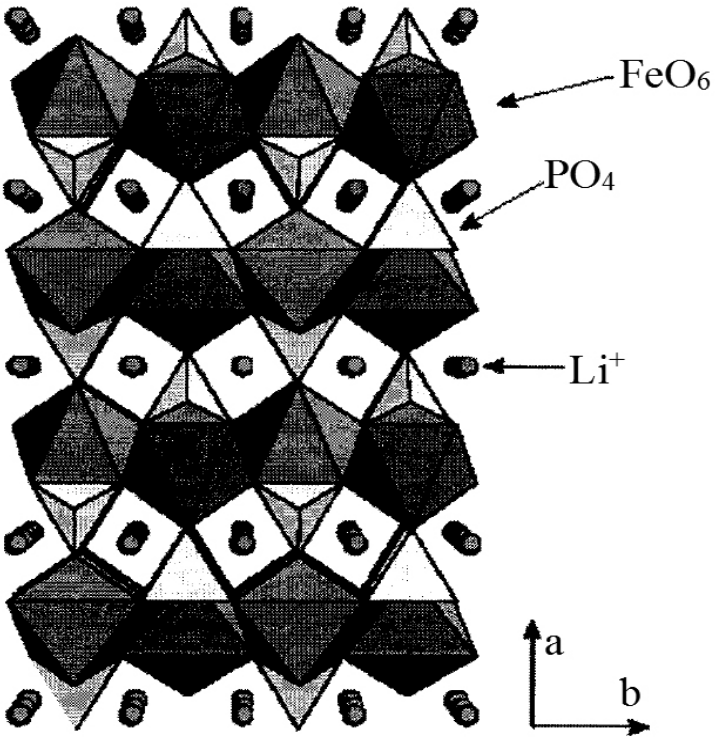

Figure 2-4-2: The crystal structure of olivine $LiFePO_4$, from ref. 41.

2.5 Solid Polymer Electrolytes

Conventional Li-ion batteries use liquid electrolytes containing a lithium salt such as $LiPF_6$ or $LiClO_4$ dissolved in a mixture of organic alkyl carbonate solvents that are liquid at room temperature, like ethylene (EC), dimethyl (DMC), diethyl (DEC) and ethylmethyl (EMC) carbonate to yield high ionic and electronic conductivity. These solvents are high vapor pressure, toxic, and flammable liquids that require expensive and heavy stainless steel hermetic seals to prevent leakage. These requirements add to the packaging cost and lower the energy density (volumetric capacity, mAh/cm^3) of the battery, as well as limiting the design of thin flexible shapes and sizes. Furthermore, many of these organic solvents have undesirable high reactivity towards electrodes, such as propylene carbonate towards graphite anodes [42].

Solid polymer electrolytes have emerged as an alternative to liquid electrolytes, offering high ionic conductivity, wide electrochemical window, and high stability at both electrodes. Solid polymer electrolytes (SPEs) are formed by incorporating lithium salts into polymer matrices and casting them into thin films. There are several possible advantages with the solid polymer electrolyte compared to conventional liquid ones [43]. Most importantly the SPE can function as a mechanically rigid separator in a cell, isolating the negative and positive electrodes from each other and preventing the cathode reaction products from diffusing to the anode side to create a short circuit. Additionally it solves the issue of electrolyte leakage, while at the same time enabling the battery to have high energy density, easy processability, good cycle life and flexible geometry. Compared to liquid electrolytes, solid polymer electrolytes show lower ionic conductivities and lower lithium-ion transport numbers (<0.3), but they are less reactive towards electrodes [44-45].

Over the past two decades, poly(ethylene oxide) (PEO) has emerged as the major polymer host matrix used in SPEs for Li-ion batteries. PEO features a high dielectric constant, strong lithium ion solvating ability and a glass transition temperature well below zero (around -60°C), [46-50]. Solid polymer electrolytes solely consisting of PEO

and a lithium salt generally have poor ionic conductivity (>10^{-4} S/cm) at the near ambient operating temperatures desired for Li-ion battery applications, primarily due to the high degree of crystallinity in PEO (60-70%). The conduction of PEO-based solid polymer electrolytes occurs through lithium ion hopping along the polymer chain assisted by the ether oxygen, and typically this process takes place in the amorphous region along with the long range segmental motion of the polymer chains [51-52].

Therefore in PEO-based SPEs the design goal is to suppress the PEO crystallinity in order to maximize the mobile phase for ion conduction. One strategy involves blending high molecular weight PEO with polymers having a high glass transition temperature, such as polystyrene [53], poly(methyl methacrylates [54] and poly(vinyl acetate) [55]. This combines the mechanical strength from one component and the conductivity from the other component. The second approach, that will be instead employed in the battery tests of this thesis work, is through the addition of ceramic nanoparticles such as TiO_2, SiO_2 and Al_2O_3. These nanoparticles impede the PEO recrystallization process, as well as to provide specific conducting pathway along PEO-ceramic interface and stabilize the lithium interface more efficiently. Furthermore these nanoparticles can compensate for and even improve the mechanical strength of solid polymer electrolyte lost due to a decrease in the degree of crystallization [45, 50, 56-60]. Therefore these ceramic fillers can allow for a solid polymer electrolyte that offers high ionic conductivity, while at the same time being mechanically rigid to suppress and control the intermetallic LiAl phase growth at the anode during battery tests.

2.6 Carbon Nitride (CNx)

The two most common allotropes of carbon are diamond and graphite. Amorphous carbon may contain various proportions of either of these forms. On one end is "diamond-like" tetrahedral amorphous carbon (ta-C) which consists of 80-85% sp^3 bonding. The presence of sp^2 sites in ta-C introduces π- π^* states which decreases the band gap relative to diamond but still remains as an insulating material. In contrast to ta-C is "graphitic" amorphous carbon (a-C) which consists of 95% sp^2 bonding. In this sp^2-rich material the presence of sp^3 sites breaks up the graphitic network resulting in disordered graphitic islands 15 to 20 Å in diameter. This creates a band gap unlike graphite itself resulting in semi-metallic conductivity [61]. Nitrogen can be incorporated into sp^2 hybridized amorphous carbon (a-C) to create amorphous carbon nitride thin films (a-CNx). The addition of a small amount of nitrogen into these materials can further increase the electronic conductivity through the introduction of more π and π^* states. Significant nitrogen content allows for cross-linking which further breaks up the graphitic network. This creates a more open structure with superior mechanical properties and increased band gap relative to amorphous graphite. Therefore these materials are converted from a highly conductive semi-metal (a-C) to a semiconductor material (a-CNx) due to structural modification [62]. A schematic of a-CNx structure is shown in **Fig. 2-6-1** [63].

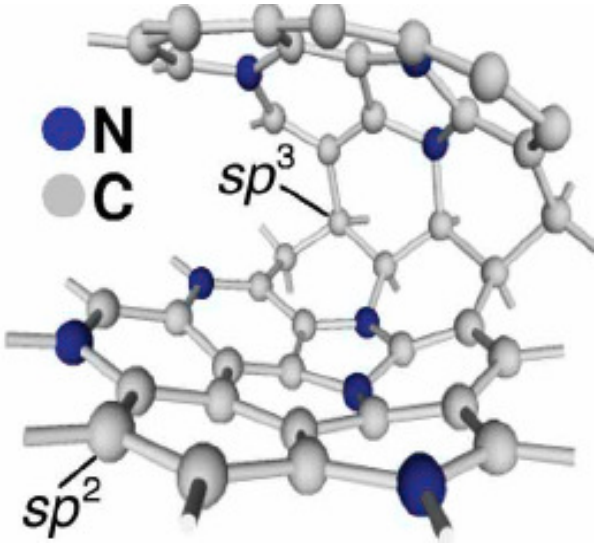

Figure 2-6-1: Proposed structure of nitrogen-doped amorphous carbon (a-CNx) combines sp^2 and sp^3 carbon atoms. From ref. 63.

The deposition of carbon nitrides can be realized using a variety of deposition techniques resulting in a wide number of different possible sp^3, sp^2 and sp bonding configurations in these materials, shown in **Fig. 2-6-2** [64-66]. The numbers in red indicate the number of valence electrons within the occupied levels, with the notation "N π" denoting occupied or un-occupied non-bonding levels localized on the nitrogen. Overall these bonding arrangements can be described as n-type doping, insulating or intrinsic semiconducting. The first two bonding modes (a) and (b) are diamond-like and therefore insulating, with the extra electron in the π* of (b) allowing for n-type doping. Bonding modes (c), (e) and (f) are pyridinic, pyrrolic and olefinic respectively and will be intrinsic semiconductors relative to graphite even though they have more π- π* states. Bonding modes (d) and (g) involves substitution of graphitic carbons by nitrogen, with the extra electron in π* resulting in an n-type semiconductor relative to graphite. Finally the nitrile bonding mode (g) has a shorter bond length than C=N resulting in a relatively insulating band gap compared to modes (c) to (g). In general nitrogen incorporation into ta-C to create ta-CNx will have bonding modes predominantly (a) and (b), while a-CNx created from amorphous graphite will consist primarily of bonding modes (c) to (h).

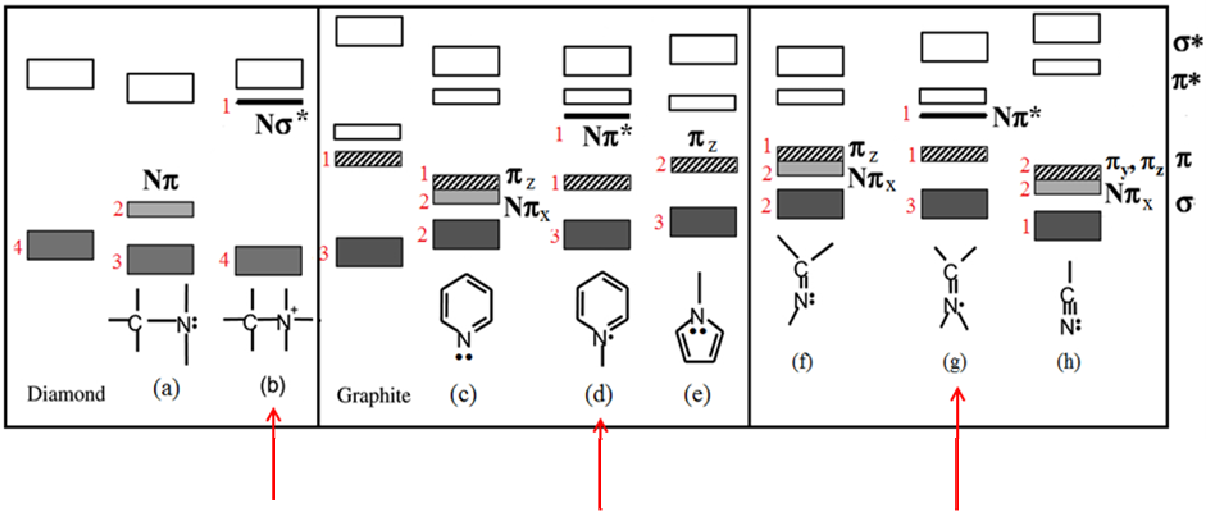

Figure 2-6-2: Different possible bonding arrangements in carbon nitride and their relative band gaps. Numbers in red indicate number of electrons in occupied levels. The letter "N" denotes occupied or unoccupied non-bonding levels localized on the nitrogen. Red arrows indicate n-type doping configurations. Modified from ref. 66.

2.6.1 Carbon Nitride Thin Film Deposition

For the amorphous carbon nitride coatings in this work we want good electrical conductivity as well as good ionic conductivity through favourable Li ion penetration to the metal-film interface. Therefore we want to target the graphitic carbon nitride coatings rich in sp^2 functional groups (a-CNx) as opposed to the insulating properties of the diamond-like tetrahedral carbon nitride coatings (ta-CNx). A variety of deposition methods are available to prepare amorphous carbon nitride coatings. In general high-energy methods such as vacuum cathodic arc deposition favor the formation of insulating ta-CNx over a-CNx [67]. Direct current (DC) and radio frequency (RF) magnetron sputtering (MS) are two well developed low-energy deposition techniques that offer a wide variety of amorphous sp^2-rich CNx thin film materials [67]. Magnetron sputtering is a physical vapor deposition technique in which momentum transfer of positively charged ions ejects matter from a target material towards a substrate where deposition occurs. **Fig. 2-6-3** shows the sputter deposition of a graphite target using an Ar gas source. The graphite target is held at a negative bias (typically hundreds of volts) relative to the

substrate and vacuum chamber, which are grounded. Argon gas is introduced into the vacuum chamber leading to a fraction of argon atoms being positively ionized, and forming a plasma in the presence of the strong electric field between the target and substrate. Due to the large negative target bias, positively charged ions are accelerated towards the target, collide with it, and eject some of the material by ion bombardment. The resulting collision ejects carbon upwards by momentum transfer towards the substrate where it is deposited to create a thin film. A magnetron placed behind the target focuses the charged plasma near the target surface, increasing ion bombardment and sputter deposition rate. Use of nitrogen as a second component of the plasma allows for reaction of ionized nitrogen species in the plasma with the carbon material ejected from the target to generate carbon nitride thin films. Magnetron sputtering through both RF and DC power supplies allows for high throughput production of conductors and semiconductors. Overall this makes it a very attractive technique for developing carbon nitride thin film materials with tunable electrochemical properties based on a wide variety of deposition parameters. For preparation of CNx thin film in this thesis work we have utilized a custom-build RFMS deposition system shown in **Fig. 2-6-4.**

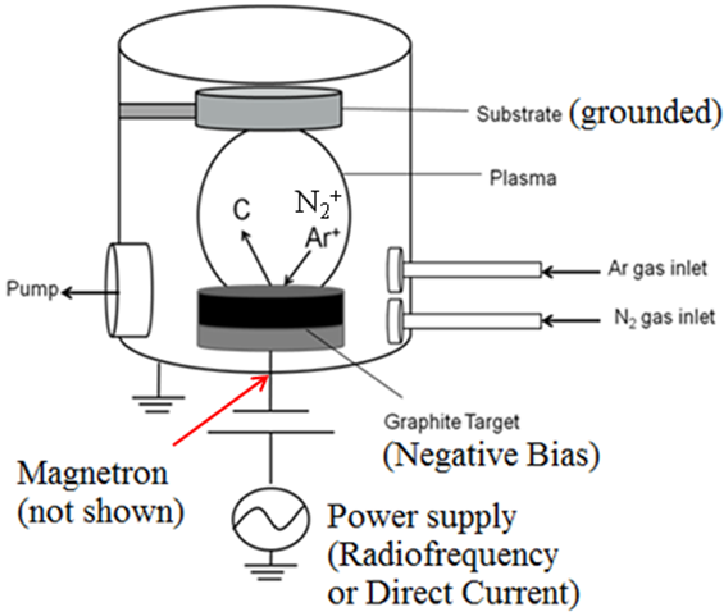

Figure 2-6-3: Schematic of the magnetron sputtering process

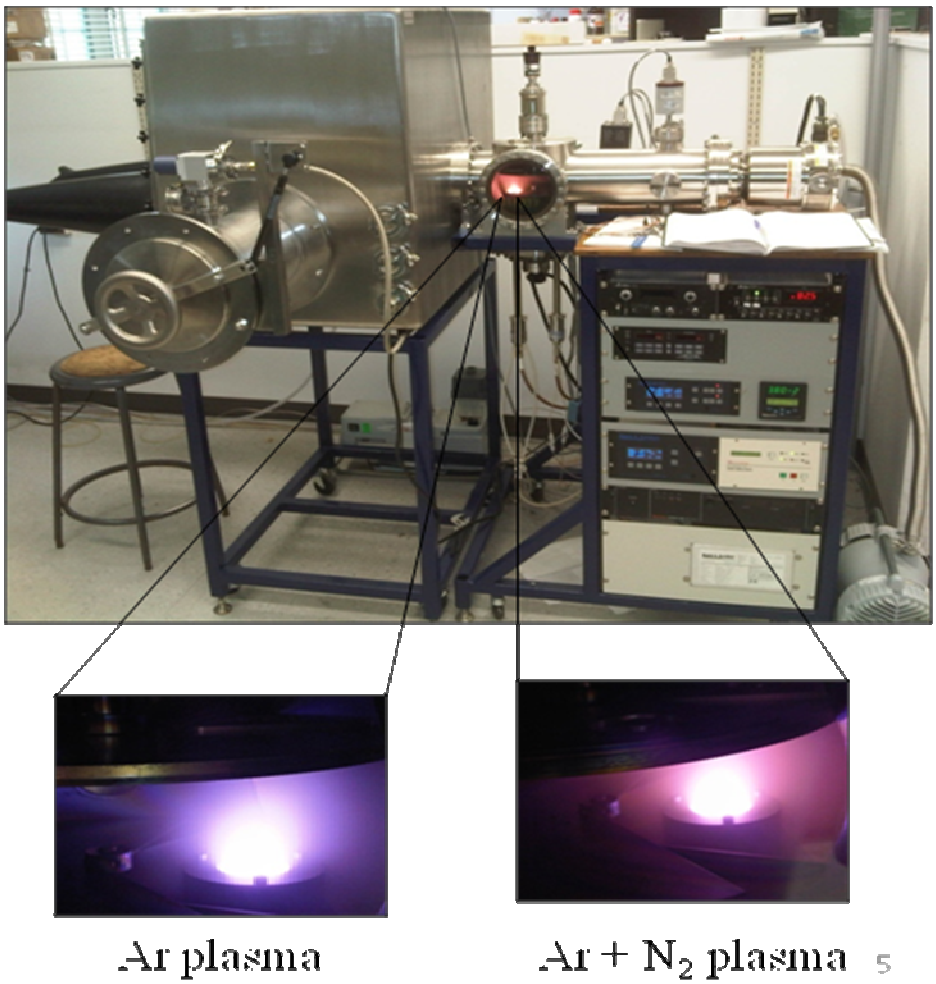

Figure 2-6-4: Custom-built vacuum system for radiofrequency magnetron sputtering deposition of CNx films.

The structure and bonding of vacuum sputtered carbon nitride prepared through RFMS are highly dependent upon the plasma composition which can be controlled through a variety of tunable deposition parameters including deposition power, target bias, nitrogen partial pressure, target to substrate separation, substrate temperature or bias and total plasma (chamber) pressure [68]. In practice the three deposition parameters that are typically varied are deposition power, total chamber pressure and the nitrogen partial pressure.

Increasing the deposition power in DCMS and RFMS results in increased kinetic energy for bombarding species. This increases the mean free path decreasing the number of collisions for reactivity in forming CN containing species in the plasma. Additionally the high kinetic energy of bombarding species at the growing film surface decreases nitrogen content in the film, through preferential chemical re-sputtering of nitrogen. There is a linear dependence of film thickness on the magnetron power [69]. Based on these effects a higher deposition power in general will create a CNx film with increased thickness, lower nitrogen content, higher conductivity and increased intrinsic film stress through increased film disorder. In practice high power films deposited at 100 W in DCMS are well known for rapid delamination in solution. Furthermore this problem is exacerbated when the film is prepared at high nitrogen contents (over 50% N_2 in plasma) [70].

Increasing the total deposition pressures such as 3-5 Pa increases the nitrogen content in the film through an increased likelihood of nitrogen reacting with carbon at the target as well as decreasing the mean free path of the ejected CN species from the target [68]. The decreased kinetic energy of incident species will promote further reaction before impact, and limit the chemical re-sputtering of nitrogen in the film. Freshly deposited amorphous carbon nitride films are highly disordered and possess a significant intrinsic stress. This stress arises from a combination of tensile stress from the deposition technique and nitrogen incorporation as well as compressive stress from gaseous moisture and oxygen inclusions in the film [71]. A high deposition pressure will increase the formation of more chain-terminating C≡N (nitrile) bonds in order to relieve the elevated internal film stress [72]. The resulting CNx film will be less dense and therefore more disordered, which may negatively impact the film adhesion in solution.

Incorporation of nitrogen into amorphous carbon thin films modifies the film structure and bonding, leading to changes in the π and π^* states as well as their distribution [73]. At low nitrogen partial pressures below 5% there is mostly olefinic and graphitic substitution by nitrogen, leading to the introduction of more π and π^* states and an increase in conductivity. Increased nitrogen partial pressure in the plasma increases the pyrdinic and pyrrolic bonding as well as the formation of more C≡N terminating groups.

This further nitrogen incorporation significantly alters the properties of CNx films deposited through RFMS. Firstly there is increased film thickness causing both increased tensile and compressive stress [74]. Secondly the formation of more nitrile groups leads to decreased film density and increased porosity through the reduction of connectivity for the amorphous carbon network. This structural modification is similar to that described earlier for elevated deposition pressures [72]. Overall as the nitrogen content in the film is further increased there is a transition from the semi-metallic conductivity of graphite to the semiconducting behavior of nitrogen rich carbon nitride [75].

Over time, CNx films deposited through RFMS undergo further structural and morphological modification through film relaxation [74]. This process can be accelerated through post-deposition thermal annealing to change film properties and bonding configurations [76]. At temperatures up to 200 ^{o}C the stress relief predominantly arises from the combination of decreased nitrile content and the conversion of N-C sp^3 to N=C sp^2 bonding. At higher annealing temperatures above 200 ^{o}C there is a dissociation of N=Csp^2 bonding and recombination of C=Csp^2 bonding together with further reduced nitrile content, leading to continued film relaxation.

In this thesis work we were interested in relatively thick CNx films with strong adhesion to the substrate that would not degrade early in our electrochemical tests. As described previously CNx film deposited at high magnetron powers of 100 to 150 W rapidly delaminate in solution. However a relatively low magnetron power of 25 W would likely require an excessively long deposition time to produce a CNx film of adequate thickness for our electrochemical tests. This could lead to overheating of the vacuum pumping system leading to shortened equipment lifetime. Therefore a compromise of 50 W was chosen for the magnetron power. Increasing the total deposition pressure allows for increased nitrogen content in the film, but at a cost of increased disorder which may negatively impact the film adhesion in solution. Therefore a total deposition pressure of 1 Pa was selected. We were interested in films with significant nitrogen content since these films were expected to possess a more open structure favourable for Li ion penetration due to increased pyridinic and nitrile functional groups [77]. They should also possess

superior mechanical properties (hardness) due to increased cross-linking [62]. From preliminary tests prior to this thesis work we determined that a nitrogen partial pressure of 75% in the plasma offered metal-CNx materials with good film stability in solution as well as reversibility of lithiation-delithiation at relatively high current densities. For comparison metal-CNx materials with a lower nitrogen plasma content of 25% are also investigated in Ch. 4.4 and 4.7. Thermal annealing of metal-CNx materials at relatively mild temperatures of 150 to 300 ^{o}C may offer improved film stability as well as adhesion through increased reactivity of the deposited CN species with the substrate. The resulting effect on reversibility of lithiation-delithiation relative to non-annealed materials in both liquid half-cell and solid-state battery electrochemical experiments is investigated in Ch. 4.4, 4.5 and 4.7.

2.7 Time-Of-Flight Secondary Ion Mass Spectrometry (TOF-SIMS)

Time of flight secondary-ion mass spectrometry (TOF-SIMS) involves the bombardment of a solid or liquid surface using pulses of energetic primary ions from an ion gun [78]. Sample surfaces must be stable under UHV conditions ~ 10^{-6} to 10^{-9} bar. The resulting high-energy collision cascade causes an ejection of a large number of sputtered (secondary) particles. These are predominantly electrons; neutral species, atoms, and molecules; with a small fraction consisting of secondary atomic and cluster ions. Therefore secondary ion mass spectrometry is the measurement of mass to charge ratio of these secondary ions emitted by primary ion bombardment.

Primary ion sources come in three types: 1) ions of gaseous elements (Ar^+, Xe^+, O_2^+, etc.) generated with duoplasmatrons or electron ionization, 2) surface ionization source to generate Cs^+ through vaporization and ionization in a porous tungsten plug, and 3) liquid-metal-ion guns (LMIG). In LMIG, tungsten tips are wetted by metals or metal alloys such as gallium and bismuth. Application of a high voltage produces an intense electrical field at the tip resulting in evaporation of positive primary ions [79]. These can then be focused by a series of optics into a primary ion beam with spot sizes ~ 100 nm to 1 μm. LMIG also possess the advantage that they can be pulsed with very narrow pulse width ~ 10 ns. This pulse can then be compressed into a smaller pulse width using a bunching unit before it is allowed to strike the sample surface. Such procedures also apply to generating polyatomic ions such as Bi_3^+ [80-81] and Au_3^+ [82]. A mass filter is applied to the primary ion stream to separate polyatomic particles from the atomic ones.

Samples are treated as a grid using a well-defined raster pattern depending on the number of pixels desired and the raster scan area (e.g. 128 x 128 pixels in a 128 x 128 μm^2 area). Therefore each pixel of the raster receives a single pulse of primary ions, generating a complete mass spectrum. Due to the parallel detection nature of TOF analyzers, the entire

mass spectrum can be simultaneously acquired at one secondary ion polarity (positive or negative). The m/z ratio of secondary ions is based on measuring the time required for emitted ions to reach the detector inside the flight tube of the spectrometer.

As described above, the primary ion gun is operated in short pulses (pulse width ~ 10 ns) resulting in a complete mass spectrum for each pixel. As the primary ions strike the sample surface a low-energy electron "floodgun" (10 to 1000 eV) is used to neutralize the resulting sample charging. This electron gun can be pulsed such that the electrons irradiate the sample surface between pulses of primary ions. Secondary ions emitted by this primary ion pulse bombardment are then post accelerated (extracted) by a fixed voltage into the TOF tube. This accelerates all secondary ions to a common potential energy and therefore approximately the same kinetic energy upon entering the TOF tube. The kinetic energy will be proportional to the velocity squared, with velocity inversely proportional to the time of flight. Assuming singly charged ions (z=1) the resulting m/z ratio of a secondary ion will therefore be directly proportional to the time of flight squared. Ions of lighter mass will reach the detector in shorter time than heavier ions. The reflectron positioned after the flight tube serves to provide energy focusing for ions of the same mass leaving the flight tube by means of a retarding electric field. This reduction in kinetic energy spread enhances mass resolution. Modern TOF analyzers typically achieve high mass resolution of $M/\Delta M > 10000$, allowing the possibility to distinguish between several ions at the same nominal mass [83]. Secondary ions are detected as they impact a multi-channel plate (MCP) at the end of the flight tube. **Fig. 2-7-1** shows the schematics of a TOF-SIMS instrument

The general SIMS Equation for any emitted species is shown in Equation 5 [84].

$$I_m = I_p * Y_m * \alpha_m * f_m * C_m \qquad (5)$$

where $\mathbf{I_m}$ is the secondary ion current of species m (positive or negative), $\mathbf{I_p}$ is the primary ion pulsed current, $\mathbf{Y_m}$ is the sputter yield, $\alpha_\mathbf{m}$ is the ionization probability, $\mathbf{f_m}$ is the instrumental transmission factor and $\mathbf{C_m}$ is the fractional concentration of species **m** in

the surface. Sputter yield deals with the total number of sputtered particles of species m for each incident ion. The ionization probability is the chance that a sputtered species m will become ionized as it leaves the surface. For practical purposes the secondary ion yield is of more use. It is defined as the number of secondary ions detected per projectile impact.

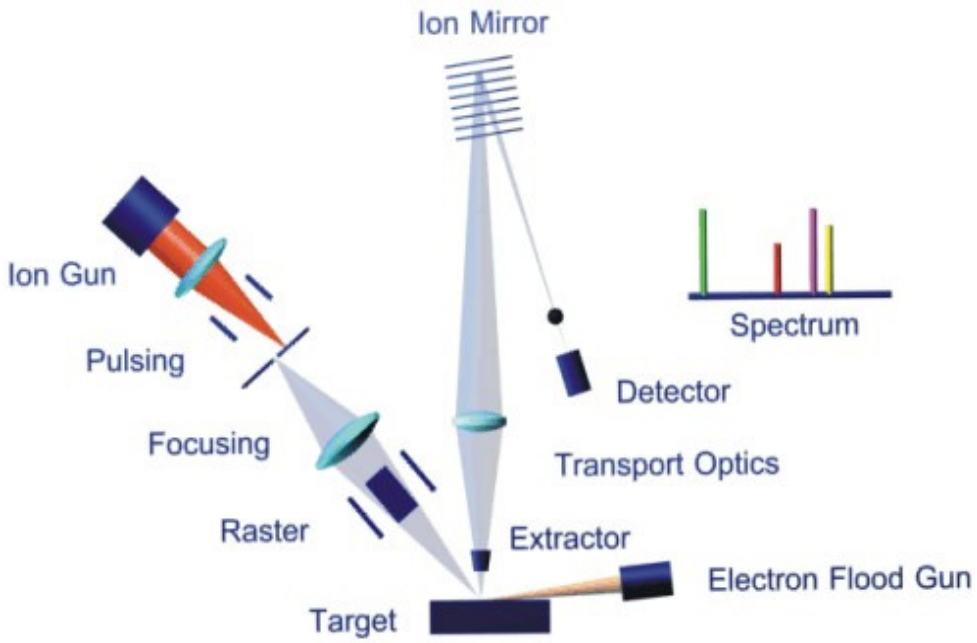

Figure 2-7-1: Schematic of a TOF-SIMS instrument.

The sputter yield of secondary particles will depend on the size of the collision cascade induced by primary ion bombardment. This cascade is directly dependent on primary ion mass, energy, angle of incidence and sample characteristics. Sputtering of materials is a damaging process involving the removal of elements, structural fragments and molecular species. Every molecule that is impacted will be destroyed. This will occur whether the entire molecule is desorbed or only a small piece such as a carbon or hydrocarbon fragment is removed. Ionization of sputtered particles is different for molecular (parent-like) ions compared to fragment ions although the emission process for both is highly collisional. Characteristic large molecular ions can be formed by Bronsted acid-base

(proton transfer) reactions as well as various cationization and anionization mechanisms. Ionization of fragment particles is thought to be largely induced by collisions, either directly with the primary particle or with fast recoil atoms near the impact site [85]. Ionization mechanisms to form secondary ions are strongly influenced by electron exchange processes between the departing species and the surface. As a result the electronic state of the surface is of critical importance for ion yields. This “matrix effect” can be clearly seen by secondary ion emission from a pure metal compared to that of the metal oxide. The former will yield primarily positive elemental and cluster ions while the latter will yield negative metal oxide (Me_mO_n) cluster ions. This is due to the negative charge of oxygen in the lattice, which will cause predominantly negative secondary ion emission if it is a major component of the cluster [86].

TOF-SIMS is an inherently destructive form of analysis because it requires consumption of the sample material [83]. Emission of secondary ions due to primary ion bombardment requires the creation of a disturbed or perturbed region of "damage" on the sample surface [87]. An incoming primary ion may strike an unaffected area or it may strike one of these damaged areas. In "static" SIMS the probability is very low ($P<<1$) that secondary ion emission will occur from these pre-bombarded (damaged) areas. Therefore when the surface is probed by the primary ion beam, all of the atoms or molecules of the surface are likely in their original condition because all prior probing events are too far away to affect them. The total number of primary ions that strike the surface is considered the primary ion dose (PID) and will be dependent on the operational parameters of the primary ion source. On a per unit area basis this is defined as the primary ion dose density (PIDD). The static limit is defined as the highest PIDD that can be used for obtaining molecular information without significantly damaging the surface [88]. Primary ion impact events are remote from each other such that the analyzed surface resembles its original pristine state. Experimentally this means that at the static limit there must be no more than a 10% drop in the initial intensity of the ion fragment being analyzed, with higher static limits for fragments with lower mass.

The goal of static SIMS is to maximize the secondary ion yields of important analyte signals while using the lowest possible primary ion beam current. These yields are dependent on 1) the composition, bonding and surface properties of sample material, 2) the composition, mass and ionization probability of a particular secondary ion, and 3) the primary ion parameters such as mass, kinetic energy and angle of incidence. The optimization of these yields has been the driving force for development of cluster primary ion sources such as SF_5^+, Bi_3^+, Au_n^+ and C_{60}^+ [89]. With increased primary ion mass the ion penetration and energy transfer during the collision cascade will become increasingly more shallow. Fragmentation of the cluster upon impact will result in multiple cooperative low-energy cascades localized at the sample surface. This "soft-ionization" source will therefore predominantly enhance the ion yields of higher mass species critical to SIMS analysis of both organic and inorganic samples. However it will also increase the yield of fragment ions because the cluster inevitably induces more surface disruption.

2.6.1 Dual-beam depth profiling

SIMS analysis beyond the static limit is known as dynamic SIMS. This high primary ion dose method is used to obtain depth profiles of secondary ions that may be characteristic of surface, bulk and interfacial layers [89]. Cluster primary ions such as Bi_3^+ mostly deposit their kinetic energy at a shallow depth resulting in high surface sensitivity and enhancement of high mass secondary ion yields. However this means that the resulting sputtering rate (sample erosion in terms of depth) is very slow. Therefore it is beneficial to employ an additional low energy monoatomic primary ion source as a "sputter" or "etching" beam. This dual-beam depth profiling mode allows for the combined benefits of enhanced higher mass secondary ion yields from the cluster primary ion "analysis" beam, and enhanced sputtering rate of the material studied from the atomic primary ion "sputter" beam [90]. In this mode the low-energy sputter beam is initially pulsed at a large area of the sample. This is followed by a pulse of the high-energy analysis cluster beam at a smaller sub-section of the area created by the sputter beam. Only the secondary ions generated by the analysis cluster beam are collected at the detector. These alternating

pulses of analysis and sputter beams are continued until the desired layer of the sample is reached.

The choice of sputtering and analysis beams has significant effects on the resulting depth profiles. They can exacerbate matrix effects at the surface of a sample, amplify back-reflection effects due to projectile-deposited energy at hard substrate/organic interfaces, cause varying degrees of sample damage, mixing of layers and changes in secondary ion signals. In this work we wished to focus on negative polarity secondary ions to see characteristic nitrogen and oxygen containing species, because such ions with electronegative atoms typically appear in the negative spectrum. Analysis of these negative species would allow us to characterize carbon nitride (CNx) layers, oxides, electrolyte, interfaces, etc. Therefore we chose Cs^+ as a low-energy sputtering source and cluster Bi_3^+ as the high-energy analysis source [91-93]. The use of a Bi_3^+ cluster ion analysis beam minimizes sample damage leading to high intensities of characteristic high mass fragments. This benefit is crucial for characterizing the carbon nitride thin films employed in this work. Higher mass C_x^-, C_xN^-, $C_xN_y^-$ fragments should arise solely from this nitrogen-substituted graphitic polymer, as opposed to simpler fragments such as C_2^- and CN^- which significantly overlap with atmospheric surface contamination species in the TOF-SIMS chamber. The use of Cs^+ as the sputter source increases negative secondary ion yield due to Cs^+ implantation into the surface resulting in a change of the work function of the surface under investigation [93].

Recently TOF-SIMS depth profiling has been applied to study electrode processes at Si anodes during lithiation/delithiation [29] such as composition of the SEI layer, and lithiation/reduction of the surface oxide layer. These are parasitic processes that may influence anode efficiency, degradation and failure. In addition to tracking lithium, TOF-SIMS allows one to visualize the distribution of representative metal, oxide and electrolyte species at the surface as well as throughout the bulk of the cycled material. For Al this technique has so far been restricted to this metal's role as a positive electrode current collector with a passivated surface, not as an electroactive anode material in a lithium ion battery [94-96]. Additionally those studies with Al did not utilize depth

profiling or cluster primary ions in the sample analysis and were restricted to the positive ion mode. To date there have only been a few TOF-SIMS studies of carbon nitride thin films prepared through magnetron sputtering [97-99]. However these studies either did not perform depth profiling, or simply ignored the behaviour of higher mass CN fragments. Furthermore the CNx materials investigated were not utilized in any form of charge storage.

2.8 References

1. Nitta, N.; Yushin, G., *Part. Part. Syst. Charac.,*. **2014**, *31*, 317-336.
2. Scrosati, B.; Garche, J., *Journal of Power Sources*, **2010**, *195*, 2419-2430.
3. Fauteux, D.; Koksbang, R., *Journal of Applied Electrochemistry,* **1993**, *23*, 1-10.
4. Park, C.M.; Kim, J.H.; Sohn, H.J., *Chem. Soc. Rev.,* **2010**, *39*, 3115-3141.
5. Nes, E., *Progress in Materials Science*, **1998**, *41*, 129-193.
6. Van Den Beukel, A.; Kocks, U.F., *Acta Metall.,* **1982,** *30,* 1027-1034.
7. Van Den Beukel, A., *Acta Metall.,* **1980**, *28*, 965-969.
8. Hansen, M.; Anderko, K., *Constitution of Binary Alloys*, McGraw-Hill: New York, 1958.
9. Dey, A.N., *Journal of the Electrochemical Society*, **1971**, *118*, 1547-1549.
10. McAlister A.J., *Bulleting of Alloy Phase Diagrams,* **1982,** *3*, 177-183.
11. Owen, J.R.; Maskell, W.C.; Steele, B.C.H., *Solid State Ionics*, **1984,** *13*, 329-334.
12. Evans, J.T., *Scripta Metallurgica*, **1987,** *21*, 1435-1438.
13. Kishio, K.; Brittain, J.O., *J. Phys. Chem. Solids.,* **1979,** *40,* 933-940.
14. Hamon, Y.; Brousse, T.; Jousse, F.; Topart, P.; Buvat, P.; Schleich, D.M., *Journal of Power Sources*, **2001,** *97-98*, 185-187.
15. Lindsay, M.J.; Wang, G.X.; Liu, H.K., *Journal of Power Sources*, **2003,** *119-121*, 84-87.
16. Lei, X.; Wang, C.; Yi, Z.; Liang, Y.; Sun, J., *Journal of Alloys and Compounds*, **2007,** *429,* 311-315.
17. Au, M.; McWhorter, S.; Ajo, H.; Adams, T.; Zhao, Y.; Gibbs, J., *Journal of Power Sources*, **2010**, *195*, 3333-3337.

18. Hudak, N.S.; Huber, D.L., *ECS Transactions,* **2011,** *33(24),* 1-13.
19. Liu, Y.; Hudak, N.S.; Huber, D.L.; Limmer, S.J.; Sullivan, J.P.; Huang, J.Y., *Nano Lett.* **2011**, *11*, 4188-4194.
20. Hudak, N.S.; Huber, D.L., *Journal of the Electrochemical Society,* **2012,** *159(5)*, A688-A695.
21. Kuksenko, S.P., *Russian Journal of Electrochemistry,* **2013,** *49,* 67-75.
22. Sharma, S.K.; Kim, M.S.; Kim, D.Y.; Yu, J.S., *Electrochimica Acta*, **2013**, *87*, 872-879.
23. Leite, M.S.; Ruzmetov, D.; Li, Z.; Bendersky, L.A.; Bartelt, N.C.; Kolmakov, A.; Talin, A.A., *Journal of Materials Chemistry A*, **2014,** *2*, 20552.
24. Oltean, G.; Tai, C.W.; Edstrom, K.; Nyholm, L., *Journal of Power Sources*, **2014**, *269*, 266-273.
25. Liu, D.X.; Co, A.C., *J. Am. Chem. Soc.,* **2016**, *138*, 231-238.
26. Liu, X.H.; Huang, J.Y., *Energy Environ. Sci.,* **2011,** *4,* 3844.
27. Zhu, J.; Zhou, J.; Chen, B.; Liu, Z.; Liu, T., *J. Solid State Electrochem.,* **2016**, *20*, 37-46.
28. Leenheer, A.J.; Jungjohann, K.L.; Zavadil, K.R.; Harris, C.T., *ACS Nano*, **2016,** *10,* 5670-5678.
29. Schroder, K.W.; Dylla, A.G.; Harris, S.J.; Webb, L.J.; Stevenson, K.J., *ACS Appl. Mater. Interfaces*, **2014,** *6,* 21510-21524.
30. Li, C.; Zhang, H.; Fu, L.; Liu, H.; Wu, Y.; Rahm, E.; Holze, R.; Wu, H., *Electrochim. Acta*, **2006**, *51 (19)*, 3872–3883.
31. Riley, L. A.; Cavanagh, A. S.; George, S. M.; Jung, Y. S.; Yan, Y.; Lee, S.-H.; Dillon, A. C., *ChemPhysChem*, **2010**, *11 (10)*, 2124–2130.
32. Kim, Y. J.; Kim, H.; Kim, B.; Ahn, D.; Lee, J.-G.; Kim, T.-J.; Son, D.; Cho, J.; Kim, Y.-W.; Park, B., *Chem. Mater.,* **2003**, *15 (7)*, 1505–1511.
33. Scott, I. D.; Jung, Y. S.; Cavanagh, A. S.; Yan, Y.; Dillon, A. C.; George, S. M.; Lee, S.-H., *Nano Lett.*, **2011**, *11 (2)*, 414–418.
34. Sim, S.; Oh, P.; Park, S.; Cho, J., *Adv. Mater.,* **2013,** *25,* 4498-4503.
35. Mukhopadhyay, A.; Sheldon, B.W., *Progress in Materials Science*, **2014,** *63*, 58-116.

36. Whittingham, M. S., *Chemical Reviews*, **2004**, *104, 10*, 4271-4302.
37. Linden, D. R., *Handbook of Batteries*. Third ed.; McGraw-Hill: New York, 2001.
38. Tarascon, J. M.; Armand, M., *Nature*, **2001**, *414, 6861*, 359-367.
39. Kudryavtsev, E. N.; Sibiryakov, R. V.; Agafonov, D. V.; Naraev, V. N.; Bobyl, A. V., *Russian Journal of Applied Chemistry*, **2012**, *85, 6*, 879-882.
40. Dunn, J., James, C, Gaines, LL, Gallagher, K, Dai, Q, Kelly, JC *Material and Energy Flows in the Production of Cathode and Anode Materials for Lithium Ion Batteries*; ANL/ESD-14/10 Rev.; Argonne National Laboratory: Argonne, IL USA, 2015.
41. Yuan, L.-X.; Wang, Z.-H.; Zhang, W.-X.; Hu, X.-L.; Chen, J.-T.; Huang, Y.-H.; Goodenough, J. B., *Energy & Environmental Science*, **2011**, *4, 2*, 269-284.
42. Baril, D.; Michot, C.; Armand, M., *Solid State Ionics*, **1997**, *94, 1*, 35-47.
43. Fergus, J. W., *Journal of Power Sources*, **2010**, *195, 15*, 4554-4569.
44. Armand, M., *Solid State Ionics*, **1994**, *69, 3*, 309-319.
45. Croce, F.; Appetecchi, G. B.; Persi, L.; Scrosati, B., *Nature*, **1998**, *394, 6692*, 456-458.
46. Armand, M., *Solid State Ionics*, **1983**, *9*, 745-754.
47. Armand, M. B., *Annual Review of Materials Science*, **1986**, *16, 1*, 245-261.
48. Armand, M., *Advanced Materials*, **1990**, *2, 6-7*, 278-286.
49. Hickner, M. A., *Materials Today*, **2010**, *13, 5*, 34-41.
50. Di Noto, V.; Lavina, S.; Giffin, G. A.; Negro, E.; Scrosati, B., *Electrochimica Acta*, **2011**, *57*, 4-13.
51. Bailey Jr, F. E.; Koleske, J. V., Chapter 6 - *PROPERTIES OF POLY(ETHYLENE OXIDE). In Poly (ethylene Oxide)*, Academic Press 1976; pp 105-149.
52. Berthier, C.; Gorecki, W.; Minier, M.; Armand, M. B.; Chabagno, J. M.; Rigaud, P., *Solid State Ionics*, **1983**, *11, 1*, 91-95.
53. Gray, F. M.; Vincent, C. A.; Kent, M., *Solid State Ionics*, **1988**, *28*, 936-940.
54. Morita, M.; Ishikawa, M.; Matsuda, Y., *Journal of Alloys and Compounds*, **1997**, *250, 1–2*, 524-527.
55. Stevens, J. R.; Such, K.; Cho, N.; Wieczorek, W., *Solar Energy Materials and Solar Cells*, **1995**, *39, 2*, 223-237.

56. Baskaran, R.; Selvasekarapandian, S.; Kuwata, N.; Kawamura, J.; Hattori, T., *Journal of Physics and Chemistry of Solids*, **2007**, *68, 3*, 407-412.
57. Bruce, P. G.; Scrosati, B.; Tarascon, J. M., *Angewandte Chemie (International ed. in English)*, **2008**, *47, 16*, 2930-46.
58. Quartarone, E.; Mustarelli, P., *Chemical Society Reviews*, **2011**, *40, 5*, 2525-2540.
59. Croce, F.; Persi, L.; Ronci, F.; Scrosati, B., *Solid State Ionics*, **2000**, *135, 1–4*, 47-52.
60. Croce, F.; Curini, R.; Martinelli, A.; Persi, L.; Ronci, F, *The Journal of Physical Chemistry B*, **1999**, *103, 48*, 10632-10638.
61. Robertson, J.; O'Reilly, E.P., *Physical Review B*, **1987,** *35, 6,* 2946-2957.
62. Alibart, F.; Durand-Drouhin, O.; Debiemme-Chouvy, C.; Benlahsen, M., *Solid State Communications,* **2008,** *145,* 392-396.
63. L. Hultman, J. Neidhardt, N. Hellgren, H. Sjostrom, J.E. Sundgren, *MRS Bull. 28* (**2003**) 1941.
64. Muhl, S.; Mendez, J.M. *Diamond and Related Materials,* **1999,** *8,* 1809-1830.
65. Robertson, J.; Davis, C., *Diamond and Related Materials,* **1995,** *4,* 441-444.
66. Rodil, S.E.; Muhl, S., *Diamond and Related Materials,* **2004,** *13,* 1521-1531.
67. Muhl, S.; Mendez, J.M. *Diamond and Related Materials,* **1999,** *8,* 1809-1830.
68. Kaltofen, R.; Sebald, T.; Weise, G., *Thin Solid Films,* **1996,** *290-291,* 112-119.
69. Byers, J.C.; Billon, F.; Debiemme-Chouvy, C.; Deslouis, C.; Pailleret, A.; Semenikhin, O.A. *Acs Applied Materials & Interfaces,* **2012**, *4*, 4579.
70. Peponas, S.; Guedda, M.; Benlahsen, M., *Solid State Communciations,* **2008,** *146*, 78-82.
71. Alibart, F.; Durand Drouhin, O., *Applied Surface Science,* **2008,** *254,* 5564-5568.
72. Durand-Drouhin, O.; Benlahsen, M., *Solid State Communications,* **2004,** *131,* 425-429.
73. Lazar, G.; Clin, M.; Charvet, S., *Diamond and Related Materials*, **2003,** *12,* 201-207.
74. Peponas, S.; Benlahsen, M.; Guedda, M., *J. Appl. Phys.,* **2009,** *106,* 013525.

75. Mubumbila, N. ; Tessier, P.Y.; Angleraud, B.; Turban, G., *Surface and Coatings Technology,* **2002,** *151-152,* 175-179.
76. Lejeune, M.; Benlahsen, M., *Diamond and Related Materials,* **2008,** *17,* 29-35.
77. Li, Z.; Wu, G.; Deng, S., *Chemical Engineering Journal,* **2016,** *283*, 1435-1442.
78. J.C. Vickerman and D. Briggs. *TOF-SIMS Surface Analysis by Mass Spectrometry*, IM Publications, Chichester, UK, 2001.
79. J.C. Vickerman, A. Brown, N.M. Reed (Eds), *Secondary Ion Mass Spectrometry, Principles and Applications*, Oxford University Press, 1989.
80. F. Kollmer, *Appl. Surf. Sci*. **2004,** *153*, 231-232.
81. D. Touboul, F. Kollmer, E. Niehuis, A. Brunelle, O. Laprevote, *J Am Soc Mass Spectrom.*, **2005**, *16,* 1608.
82. M. Benguerba, A. Brunelle, S. Della-Negra, J. Depauw, H. Joret, Y. Le Beyec, M.G. Blain, *Nucl. Instrum. Meth. B,* **1991,** *8,* 62.
83. A. Benninghoven, *Angew. Chem. Intl. Ed. Engl.*, **1994,** *33*, 1034.
84. J.C. Vickerman, A. Brown, N.M. Reed (Eds), *Secondary Ion Mass Spectrometry, Principles and Applications*, Oxford University Press, 1989.
85. J. Sunner, *Org. Mass Spectrom.*, **1993,** *28*, 805.
86. O. Ganschow, L. Wiedmann, A. Benninghoven in *Secondary Ion Mass Spectrometry SIMS II*, Springer-Verlag, New York, 1979, p.263
87. A. Benninghoven, F.G. Rudenauer, H.W. Werner. *Secondary Ion Mass Spectrometry*, John Wiley and Sons, New York, 1987, p. 671.
88. B. Hagenhoff, *Mikrochim. Acta.*, **2000,** *132*, 259.
89. Mahoney, C., *Mass Spectrometry Reviews*, **2010,** *29,* 247-293.
90-91. Brison, J.; Muramoto, S.; Castner, D.G., *J. Phys. Chem. C,* **2010,** *114,* 5565-5573.
92. Seah, M.P.; Green, F.M.; Gilmore, I.S., *J. Phys. Chem. C,* **2010,** *114,* 5351-5359.
93. Gnaser, H., *Physical Review B*, **2001,** *63*, 045415.
94. Myung, S.T.; Sasaki, Y., *Electrochimica Acta*, **2009,** *55,* 288-297.
95. Myung, S.T.; Natsui, H., *Journal of Power Sources,* **2010,** *195,* 8297-8301.
96. Myung, S.T.; Yashiro, H., *Journal of Power Sources,* **2014,** *271,* 167-173.
97. Huang, L.; Hung, Y.; Chang, S., *IEEE Transactions on Magnetics,* **1997,** *33,* 4551-4559.

98. Lopez, S.; Dunlop, H.M.; Benmalek, M., *Surface and Interface Analysis,* **1997,** *25,* 827-835.

99. Neuhaeuser, M.; Hilgers, H., *Diamond and Related Materials,* **2000,** *9,* 1500-1505.

Chapter 3

3 Materials and Methods

3.1 Materials

Aluminum 1100 alloy foil was obtained from two sources: Goodfellow, 99%, half-hard, 0.3 mm thickness and McMaster-Carr, 99%, soft, 0.5 mm thickness. Aluminum 2024 alloy (Dural) foil was obtained from McMaster-Carr: 93% Al, heat-treated, 0.5 mm thickness. Copper foil was obtained from Goodfellow: 99.9%, half-hard, 0.3 mm thickness. All substrates were cut into discs of 14 mm diameter before any further preparation. Silver (99.9%, 0.5 mm dia., half-hard) and platinum (99.95%, 0.5 mm dia., annealed) wires for lithium half-cells were obtained from Alfa-Aesar. Carbon (graphite) target (99.999%, 2 in. dia., 0.125 in. thick) for magnetron sputtering was obtained from Goodfellow. $LiFePO_4$ nanoparticles (97%, <5 um dia.), $LiPF_6$ (99.99%, battery grade), polyvinylidene fluoride (avg. MW 275000) and polyethylene oxide (avg. MW 4 million) were obtained from Aldrich. "Super P" conductive carbon black (99%) was obtained from Alfa Aesar. TiO_2 nanoparticles (99%, 15 nm dia.) were obtained from "Nanostructured and Amorphous Materials" (Los Alamos, New Mexico, USA). Propylene carbonate (99.7%, anhydrous) and 1-methyl-2-pyrrolidinone (99.5%) were obtained from Aldrich. Acetonitrile, potassium hydroxide, hydrochloric acid and ethanol were obtained from Caledon. Ultra-pure argon and nitrogen gases for radiofrequency magnetron sputtering deposition were obtained from Praxair. All materials were used without further purification with the exception of polyethylene oxide, which was first dried at 50 ^{o}C under vacuum for 4 hours.

3.2 Aluminum Alloy Material Properties

We investigated the influence of mechanical properties of aluminum on the cycling performance of bulk aluminum anodes in Li-ion batteries, using three different commercially available aluminum materials. These materials are considered "wrought" alloys. Therefore they are initially cast as ingots and then rolled into sheets prior to any additional processing.

Firstly, the McMaster-Carr aluminum is considered an 1100 alloy, with 99% Al content and the remainder primarily as Fe + Si impurities. It is a "soft-annealed" alloy with a temper designation of "dead soft, O". For this processing method the aluminum is thermally annealed at 450-550 ^{o}C and then cooled after being rolled into sheets. Considering that the melting point of pure Al is 660 ^{o}C at 1 bar (standard conditions) this processing creates a softer material afterwards with coarser grain boundaries. The end result is that plastic deformation is relatively easier to perform compared to the initial unworked 1100 alloy sheet. Secondly, the Goodfellow aluminum is also considered an 1100 alloy with similar composition. It is a "strain-hardened" alloy with a temper designation of "half-hard, H14". "Half-hard" is a degree of cold-working ranging from "quarter hard" to "fully hard". This strain hardening processing method entangles the dislocations that were present initially in the aluminum. The end result is that plastic deformation is relatively more difficult to perform compared to the initial unworked 1100 alloy sheet. Finally, the Dural is considered a 2024 alloy, with 93% Al content, 4-5% Cu, 1-2% Mg and the remainder an assortment of impurities. It is a "heat-treated" alloy with a temper designation "T3". The aluminum is melted initially and mixed with alloying elements in the molten state. The mixture is quenched, cold-worked and finally naturally aged to a stabilized state. The copper content primarily precipitates at the grain boundaries during this process, considered as "precipitation hardening". The end result is that plastic deformation is significantly more difficult compared to any 1100 alloy material.

Additionally in Ch. 4.5 a copper substrate (Goodfellow) with 99.9% Cu content and half-hard temper was utilized for deposition of composite anode samples.

3.3 Anode Sample Properties and Electrochemical Characterization Summary

A variety of anode samples were prepared on aluminum, Dural and copper substrates and characterized electrochemically either in liquid 3-electrode half cells or in a prototype solid-state 2-electrode battery cell. The various sample properties and electrochemical characterizations are summarized in **Tables 3-3-1 to 3-3-7** below, along with the respective sub-chapters of chapter 4 where the results may be found. The remainder of this chapter will describe all details of sample preparation and characterization according to this labeling scheme.

Table 3-3-1: Goodfellow Al (GF Al) anodes and their testing procedure in liquid half-cells in Ch. 4.1.

Sample Code	**GF1**	**GF2**	**GF3**	**GF4**	**GF5**
Substrate	GF Al	GF Al	GF Al	GF Al	GF Al
Polishing	yes	yes	yes	no	yes
Etching	yes	no	yes	no	yes
Drying	vac. des. RT	vac. des. RT	moist oven 90 ^{o}C	vac. des. RT	vac. des. RT
Experiment	4x8	4x8	4x8	4x8	Failure
CV Vertices (V)	0.35, 2.2	0.22, 2.1	0.21, 2.1	0.25, 2.1	-
Galvanic Cycle Upper/Lower Pot. Limits (V)	2.77 -0.43	2.62 -0.58	2.61 -0.59	2.65 -0.55	2.64 -1.36

Table 3-3-2: McMaster-Carr Al (MC Al) anodes and their testing procedure in liquid half-cells in Ch. 4.2.

Sample Code	**MC1**	**MC2**	**MC3**
Substrate	MC Al	MC Al	MC Al
Polishing	yes	no	no
Etching	yes	no	no
Drying	vac. des. RT	vac. des. RT	vac. des. RT
Experiment	4x8	4x8	Failure
CV Vertices (V)	0.24, 2.1	0.23, 2.1	-
Galvanic Cycle Upper/Lower Potential Limits (V)	2.64, -0.56	2.63, -0.57	2.67, -1.33

Table 3-3-3: Duraluminum (Dural) anodes and their testing procedure for liquid half-cells in Ch. 4.3.

Sample Code	**DU1**	**DU2**
Substrate	Dural	Dural
Polishing	yes	yes
Etching	yes	yes
Drying	vac. des. RT	vac. des. RT
Experiment	4x8	Failure
CV Vertices (V)	0.13, 2.2	-
Galvanic Cycle Upper/Lower Potential Limits (V)	2.73, -0.47	2.68, -1.32

Table 3-3-4: Al-CNx and Dural-CNx anodes and their testing procedure for liquid half-cells in Ch. 4.4

Sample Code	**AC1**	**AC2**	**AC3**	**DC1**	**DC3**	**DC2**	**DC4**
Substrate	GF Al	GF Al	GF Al	Dural	Dural	Dural	Dural
CNx N_2 plasma (%)	75	75	75	75	75	25	25
CNx Thickness (nm)	75	75	75	75	75	75	75
Annealing	no	2 hours 150 ^oC	no	no	no	no	no
Experiment	4x8	4x8	Failure	4x8	Failure	4x8	Failure
CV Vertices (V)	0.14 1.5	0.14 1.5	-	0.13 2.2	-	0.11 2.2	-
Galvanic Cycle Upper/Lower Potential Limits (V)	2.54 -0.26	3.1 -0.2	2.55 -1.45	2.73 -0.47	2.76 -1.24	2.71 -0.49	2.52 -1.48

Table 3-3-5: Composite anodes with Goodfellow Al (GF Al) substrate and their testing procedure for liquid half-cells in Ch. 4.5.

Sample Code	**ACM2**	**ACM3**	**ACM1**
Substrate	GF Al	GF Al	GF Al
Al thickness (nm)	25	25	25
CNx N_2 plasma (%)	75	75	-
CNx Thickness (nm)	75	75	-
Annealing	no	2 h 150 ^oC	no
Experiment	4x8	4x8	4x8
CV Vertices (V)	0.19 2.1	0.13 2.0	0.28 2.2
Galvanic Cycle Upper/Lower Potential Limits (V)	2.59 -0.21	2.53 -0.37	2.68 -0.32

Table 3-3-6: Composite anodes with copper substrate and their testing procedure for liquid half-cells in Ch. 4.5.

Sample Code	**CM1**	**CM2**	**CM3**	**CM4**
Substrate	Cu	Cu	Cu	Cu
First CNx N_2 plasma (%)	-	-	75	75
First CNx Thickness (nm)	-	-	75	25
Al thickness (nm)	25	25	25	75
Second CNx N_2 plasma (%)	75	75	75	75
Second CNx Thickness (nm)	75	75	75	50
Annealing	no	2 h 150 ^{o}C	no	no
Experiment	4x8	4x8	4x8	4x8
CV Vertices (V)	0.15 2.1	0.16 2.1	0.26 2.2	0.22 2.3
Galvanic Cycle Upper/Lower Potential Limits (V)	3.05 -0.25	3.06 -0.24	3.16 -0.14	3.32 -0.68

Table 3-3-7: Battery anodes with Goodfellow Al (GF Al) substrate and their testing procedure for battery prototypes in Ch. 4.7.

Sample Code	**BAT1**	**BAT2**	**BAT3**	**BAT4**	**BAT5**	**BAT6**
Substrate	GF Al	GF Al	GF Al	GF Al	GF Al	GF Al
CNx layer	-	75% N_2 75 nm	75% N_2 75 nm	25% N_2 75 nm	75% N_2 75 nm	75% N_2 75 nm
Annealing	no	no	2 h 300 ^oC	no	no	no
Cyc. @ 0.016 mA/cm^2	-	-	-	-	8	8
Cyc. @ 0.033 mA/cm^2	8	8	8	8	8	-
Cyc. @ 0.065 mA/cm^2	100	200	200	200	100	-
Cyc. @ 0.13 mA/cm^2	100	200	200	200	100	-
Cyc. @ 0.32 mA/cm^2	400	200	200	200	50	-
Cyc. @ 0.46 mA/cm^2	-	-	-	-	50	-
Cyc. @ 0.59 mA/cm^2	-	-	-	-	50	-
Cyc. @ 0.65 mA/cm^2	-	-	-	-	50	-

3.4 Aluminum and Copper Substrate Preparation

Electrodes were first polished by hand with coarse (1200) grit sandpaper, fine (4000 grit) sandpaper and finally rotary polishing. Aluminum 1100 electrodes were sonicated in detergent + milliQ water, etched in 1 M potassium hydroxide solution and sonicated in ethanol for 15 minutes each. For Dural and copper electrodes the potassium hydroxide

etching step was replaced by 1 M hydrochloric acid for 15 minutes. The substrates were dried using argon gas and placed under vacuum in a desiccator before further use.

For chapters 4.1 and 4.2 both types of aluminum 1100 alloy were also prepared with varying degrees of surface oxide remaining, to investigate its effect on electrochemical performance. Specifically in Ch. 4.1 sample GF1 was polished, etched and then dried in a desiccator under vacuum, while sample GF2 had the etching step omitted. Sample GF3 was polished, etched, wet with water and then dried in an oven under air at 90 ^{o}C. Finally sample GF4 had both polishing and etching steps omitted. These preparations for Ch. 4.1 materials were summarized previously in Table 3.1. For Ch. 4.2 sample MC1 was polished, etched and then dried in a desiccator under vacuum, while sample MC2 had both polishing and etching steps omitted.

All other substrates prepared in this work, starting from chapter 4.3 onwards were prepared with the surface oxide removed through both polishing and etching steps followed by drying under vacuum in a desiccator to minimize oxide regrowth.

3.5 Vacuum deposition of carbon nitride

Aluminum, copper or Dural substrates were placed in a stainless steel holder with 0.3mm deep circular grooves. A mask plate with 10.7 mm holes was screwed into place on top of the holder. This holder was loaded into a nitrogen-filled glovebox. Through a load-lock system the substrate holder is then introduced into a custom built vacuum deposition system used for radiofrequency magnetron sputtering of carbonaceous materials as well as aluminum. In this work the target to substrate distance was 7 cm. The substrate temperature was not controlled and it is known that the substrate temperature would not be expected to exceed 100^{o}C for the deposition powers used in this work. Depending on the plasma composition the target was negatively biased at 100 to 200V. Ultrahigh purity argon and nitrogen gas were used as gas sources. A 5 cm diameter carbon target was used as a carbon source. The total chamber pressure for all CNx depositions was 7.5 mTorr (1

Pa) with a magnetron power of 50 W. The partial pressure of nitrogen was varied by adjusting the rates of mass flow of nitrogen gas and argon gas as expressed in equation 1:

$$\%\,N_2 = \frac{\text{Flow Rate of } N_2}{\text{Flow Rate of } N_2 + \text{Flow Rate of Ar}} \text{ X } 100\ \% \qquad (1)$$

The flow rate, measured in standard cubic centimeters per minute, was controlled using a mass flow controller (MKS Type 1179A). In this thesis work plasma compositions of 75% or 25% N_2 were used for the CNx layers. Initially the chamber was pumped down to a base pressure of $1*10^{-6}$ Torr through a combination of rotary and turbomolecular pump. Then a high pressure (3 Pa) 50% N_2 plasma was used to clean (pre-sputter) the chamber and carbon graphite target of contaminants for 15 minutes. During this cleaning procedure the substrate holder was blocked by a rotating mask plate. After turning off the plasma and gas flows the chamber was once again pumped down to a base pressure below $1*10^{-6}$ Torr. Finally the mask plate was rotated away above the carbon target to expose the substrate after the plasma parameters were set for deposition. To achieve the desired thickness of CNx layers, the deposition rates for 25% and 75% N_2 plasmas were 2.78 and 3.75 nm/min respectively. Deposition of thin aluminum films was performed similarly, using a 2.5 cm diameter aluminum target as the aluminum source. In this case deposition was performed in a pure Ar plasma at a magnetron power of 50 W, total pressure of 15 mTorr (2 Pa) and a deposition rate of 5 nm/min.

3.6 Post-Deposition Thermal Annealing of Vacuum Sputtered Materials

Certain vacuum sputtered materials were annealed using a custom-built oven with independent control of the temperature above and below the substrate to allow uniform heating. The oven was located inside a nitrogen-filled glovebox that was directly attached to the vacuum deposition system to ensure samples were not exposed to the atmosphere prior or during annealing. The films were annealed at 150 ^{o}C for 2 hours, removed from

the oven and allowed to cool to room temperature in the glovebox for several hours. Alternatively, for high temperature annealing the material was instead annealed using a quartz-tube oven under nitrogen gas at 300 ^{o}C for 2 hours.

3.7 Lithium Half-Cell Assembly and Testing

Three-electrode lithium half-cells were assembled in glass cells in an argon-filled glovebox with < 1 ppm H_2O and O_2 content. The cells consisted of a working electrode (anode sample), platinum wire counter electrode and silver wire pseudo-reference electrode. A Teflon gasket with 5 mm inner diameter was placed over the working electrode, resulting in an exposed area of 0.196 cm^2. The purpose of this gasket was to allow for surface analysis of uncycled material after cycling of the exposed area was complete. The electrolyte solution was 0.1M $LiPF_6$ in propylene carbonate with a volume of 10 mL. To improve stability and consistency, between measurements the silver reference electrode was stored in a solution of supporting electrolyte of the same concentration as during measurements. All potentials were measured with respect to this reference electrode. This reference potential was controlled after each experiment via the ferrocene/ferrocinium redox couple and was re-calculated vs. a Li^+/Li electrode, as is common practice in this field. All quoted potentials in this work are therefore relative to Li^+/Li. Cyclic voltammetry and galvanostatic cycling were performed on the cells at room temperature with a PAR 273A potentiostat/galvanostat and Corrware software.

Two types of electrochemistry experiments were performed in half-cells. In the first type of experiment the working electrode was initially charged potentiodynamically to a potential of +1.5V or +2V vs. Li^+/Li. This was followed by a cyclic voltammogram from the right vertex potential to the left vertex potential and back to the right vertex potential at a scan rate of 1 mV/s for 3 scans. Afterwards, galvanic cycling was performed at four different current densities of 0.13, 0.25, 0.5 and 1 mA/cm^2 for 8 cycles each. These experiments will henceforth be referred to as "4x8" experiments. Alternatively, "failure" experiments were performed by cycling immediately at a higher current density of 0.5

mA/cm^2 for a varied number of cycles, without initial conditioning from a cyclic voltammogram. This experiment was designed to monitor the anode degradation over time, and to the test the practical applicability of continuous operation over hundreds of cycles. Vertex potentials for CVs and upper/lower potential limits for galvanic cycles can be found in **Tables 3-3-1 to 3-3-7** described previously. For both types of half-cell experiments charge and discharge steps were set at a maximum of 1000 seconds each.

After electrochemical measurements all anodes were removed from the cell and immediately rinsed with acetonitrile to remove excess $LiPF_6$ and propylene carbonate. Samples were then stored in a desiccator under vacuum until surface analysis was performed. In all cases the cycling data was analyzed using Corrview software to determine potentials of charge and discharge plateaus, and then fitted to determine the coulombic efficiencies of both the main discharge plateaus and diffusion-limited portions.

3.8 Cathode Preparation

For anode samples in chapter 4.7 tested in a two-electrode battery coin cell prototype, a complementary cathode material was prepared outside the glovebox under ambient conditions based on the literature procedure [1]:

6 wt. % polyvinylidene fluoride (PVDF) binder was dissolved in N-methyl-2-pyrrolidinone (NMP). 85 wt.% active material ($LiFePO_4$) and 5 wt. % "super P" conductive carbon black were ground and mixed together in a mortar and pestle, followed by mixing in a vortex apparatus for 10 min. The dissolved NMP-binder mixture was added to the ground $LiFePO_4$-C mixture, such that the binder constitutes 10 wt. % of the total weight of the final mixture. The above mixture was vortexed at maximum rpm for about 30 minutes. If needed, more NMP was added in order to obtain slurry of required consistency. The final slurry was magnetically stirred at 300 rpm for 24 hours. The following day this slurry was spin coated on the polished and etched copper substrate at

300 rpm under N_2 gas. At this rotation speed the slurry uniformly spreads on the copper disc. The resulting cathode was dried under vacuum in a desiccator at 90°C overnight. The cathode was placed between two weighing papers to protect the coating and pressed under a load of approximately 5 tons using a hydraulic press. The cathodes were then transferred into an argon-filled glove box (H_2O and O_2 < 1 ppm) and stored there before spin-coating of the prepared solid polymer electrolyte mixture.

3.9 Preparation and Spin-Coating of Solid Polymer Electrolyte (SPE)

For battery tests a solid polymer electrolyte was prepared using acetonitrile, poly(ethylene oxide) (PEO), $LiPF_6$ and TiO_2 inside an argon-filled glovebox according to modification of the following literature procedure [2]:

Commercial anatase TiO_2 nanoparticles were dried at 50 ^oC under vacuum for 4 hours. 1 M solution of $LiPF_6$ in acetonitrile was prepared and stirred at RT for 2 hours. TiO_2 nanoparticles (10 wt. %) were ground in a mortar and pestle, and then added to the above solution. The resulting slurry was then ultrasonically agitated for 30 min at RT. This procedure was to avoid both agglomeration of TiO_2 nanoparticles and to remove gas bubbles present in the solution, which could significantly affect the spin coating process. Then the slurry was stirred for an additional 2 hours at RT. PEO was added to the mixture at a [O]:[Li] ratio of 12:1 for PEO monomer:$LiPF_6$ and stirred at RT for 20 hours. The resulting slurry was spin coated at 150 rpm on both anode and cathode. The resulting polymer-coated anode and cathode were left to evaporate at room temperature under argon gas for 8 hr to remove the acetonitrile. Then the coated samples were dried under vacuum in a desiccator at 50 ^oC for 8 hours, at which point they are ready to be used in battery coin cell assembly.

3.10 Lithium-Ion Battery Cell Assembly and Testing

For the results of chapter 4.7 a two-electrode electrochemical cell design was developed in-house and is shown in **Fig. 3-1**. In this cell the anode is considered as both the counter electrode (CEr) and reference electrode (RE), and the cathode is the working electrode (WEr). The anode and cathode are separated by the solid polymer electrolyte (SPE) layer. The cell design is a Teflon cup with inner diameter of 14 mm and depth of 10 mm. A copper metal rod inserted through the base serves as the current collector for the cathode, and a copper spring through the lid as the collector for the anode. The assembly and testing of the cell was performed inside an argon-filled glovebox according to the following procedure:

A polymer-coated cathode was placed face up inside the bottom of the Teflon cell and connected as the working electrode. To ensure swelling of the SPE layer, a micropipette was used to dispense 100 μL of propylene carbonate onto the polymer-coated cathode. Then the polymer-coated anode was placed face down on top. The spring-loaded cap for the Teflon cell was then tightened to complete assembly. A wire welded to the copper spring was connected as both counter and reference electrodes. Finally, the cell was allowed to stabilize for 2 hours before commencing galvanic cycling, to ensure proper wetting of the polymer electrolyte by the propylene carbonate. Cell testing was performed using a Princeton Applied Research Potentiostat/Galvanostat Model 263A and Corrware software. The galvanostatic charge-discharge cycles were conducted at multiple current densities for varying numbers of cycles. The details may be found in **Table 3-3-7**. The charge/discharge time limits were set at 500 seconds each for all battery samples, with the exception of sample BAT5 in which the time limits were 1000, 1000, 500, 500, 250, 200, 150 and 100 seconds respectively. For all experiments the upper and lower potential limits were +5V and 0V respectively. Exposed sample diameter was 14 mm for both anode and cathode electrodes resulting an electrode area of 1.54 cm^2.

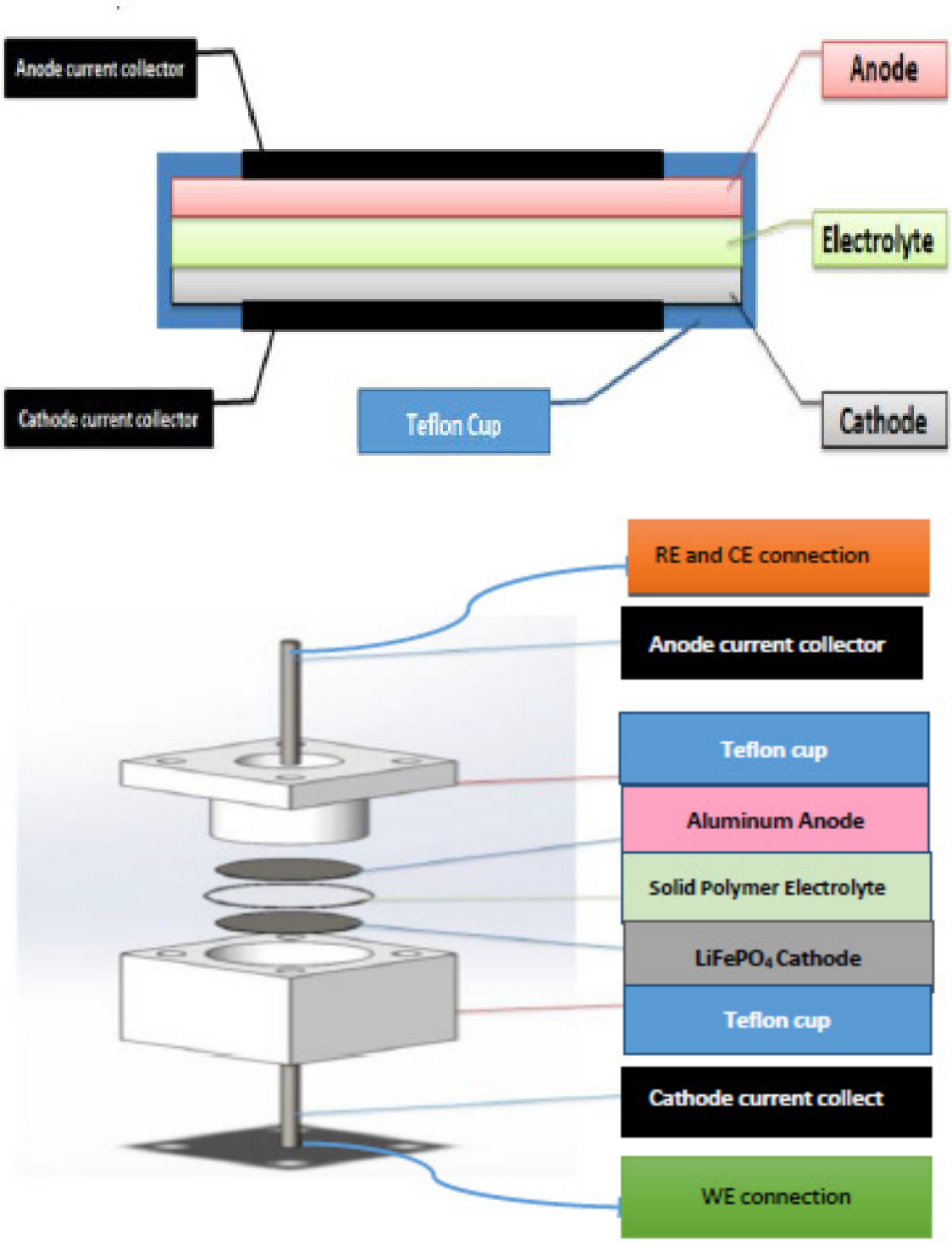

Figure 3-1: Schematic cross-section structure of a lithium-ion battery coin cell with solid polymer electrolyte

3.11 Scanning Electron Microscopy (SEM)

After electrochemical measurements the morphology of each anode sample was investigated by scanning electron microscopy (SEM) using a Zeiss LEO 1540 XB scanning electron microscope. All images were collected at an electron column voltage of 1 kV, with possible magnifications of 100, 1000, 5000, 10000 and 25000 if surface charging was not excessive.

3.12 Energy-Dispersive X-ray (EDX) Spectroscopy

Energy dispersive x-ray (EDX) analysis was performed with the attached Oxford Instruments X-sight detector. All EDX spectra were collected at 7 kV electron column voltage, acquisition time of 50 seconds and 1000x magnification and analyzed in INCA software.

3.13 Time-Of-Flight Secondary Ion Mass Spectrometry (TOF-SIMS) Depth Profiling

TOF-SIMS analysis was performed on certain anode samples after electrochemical measurements using an ION-TOF (GmbH) TOF-SIMS IV spectrometer operating in the dual-beam profiling mode. The instrument was equipped with a 25 keV Bi_3^+ cluster primary ion beam with a pulse width < 2 ns (target current ~ 1 pA) as the analysis gun with a 3 keV Cs^+ primary ion beam (target current ~ 16 nA) as the sputter gun, both angled at 45^o incidence. The sputter gun was pulsed for 1 second at an area of 150 µm x 150 µm with a pause of 500 ms, until activation of the analysis gun to generate secondary ions from a 75 µm x 75 µm analysis area within this sputter crater. This process was repeated for a total sputter time of 400-700 seconds and 250-350 seconds within the cycled and uncycled areas respectively. The secondary ions were extracted by an electric field (2 kV), mass separated and detected via a reflectron-type time-of-flight analyzer. Due to the typical suppression of positive ion yields by the Cs^+ sputtering beam, only

secondary ions of negative polarity were collected. For each scan with the analysis gun, mass spectra were collected from a raster of 128x128 pixels. A pulsed low energy (18 eV) electron floodgun was used to neutralize sample charging. The base pressure of the analytical chamber was around $1*10^{-8}$ mbar. Data acquisition and analysis of spectra, images and depth profiles was performed in IonSpec and IonImage v 4.1 software (ION-TOF). Negative ion spectra calibration was performed with H^- and C^- peaks. Structure attributions or assignments of ion peaks were made according to the instrument resolution ($M/\Delta M$ = 6000 at m/z 429), accuracy and valence rule. Identification of secondary ion series such as Al_x^- and C_xN^- was confirmed by observing their co-localization in the images acquired throughout profiling.

3.14 Surface Profilometry

After removal from the TOF-SIMS instrument chamber the samples were immediately subjected to surface profilometry using a KLA Tencor P-10 surface profiler. The stylus was operated with an applied force of 30 mg (30 μN) across a distance of 7000 μm corresponding to a line scan of gasket area to the cycled area and across to the opposite gasket area.

3.15 Electrochemistry Techniques and Methodology used in Lithium-Ion Battery Research

3.15.1 Cyclic Voltammetry

Cyclic voltammograms (CVs) can be used to characterize the redox processes occurring in both anodic and cathodic materials during lithiation-delithiation in lithium ion batteries (LIB) [3-6]. Typically a CV is performed in a liquid half-cell electrochemical setup where the electrode of interest can be isolated as the working electrode and there is a separate cell compartment with a reference electrode. In this 3-electrode cell both counter and reference electrodes for LIB electrode research are typically lithium metal foils or

wires. However other materials are possible too such as platinum and silver wires used for counter and reference electrodes respectively in this thesis work. Regardless of the reference electrode used it is possible to measure the formal potential of a known redox system such as the ferrocene/ferrocenium couple relative to the same reference system, and then convert the potential scale to the Li^+/Li potential scale common for Li battery research in the literature. Isolating the electrode of interest as a working electrode in a 3 electrode half cell with a liquid electrolyte ensures that the redox processes observed in the CV are strictly occurring at the working electrode. Therefore the potentials that are measured are not affected by changes occurring at the reference electrode, because the reference electrode does not take part in any electrochemical reactions.

In a CV the system first typically sits at its open-circuit potential (OCP). Optionally it may then first be charged potentiodynamically to an anodic potential well above the region where any cathodic processes are expected to occur at the working electrode surface. Then a potential is applied between the working-counter electrode couple to "sweep" the system to more negative potentials. This produces cathodic currents associated with reduction processes occurring at the working electrode, and the potential sweep continues until a designated left vertex is reached in the CV. Then the system is swept in the reverse direction to more positive potentials. This produces anodic currents associated with oxidation processes occurring at the working electrode until a designated right vertex is reached in the CV. This forward and reverse potential sweeping of the system can be repeated to observe how redox features in the CV change with repeated scanning.

In LIB research the redox processes observed in the CV depend on the anode system. For example with the most common choice being graphitic materials the reduction processes are typically lithium ion intercalation (lithiation) between the graphite sheets, with the corresponding oxidation process being lithium ion deintercalation (delithiation) back into the electrolyte solution. In metal or metal-oxide anode systems such as Si, SnO_2 and Al the processes of lithiation-delithiation occur through electrochemical metal-alloying and de-alloying reactions to form intermetallic compounds of various stoichiometry. In

addition to onset potentials and peaks associated with redox processes there are features of a CV that may be indicative of other important processes such as the relative degree of volume change during lithiation-delithiation and the formation of solid electrolyte interphase (SEI) layer at the electrode surface. Considering the focus of this thesis work is Al anodes we describe here the typical CV features involved with lithiation-delithiation of a commercially available Al 1100 alloy (99% Al) in an electrolyte of 0.1M $LiPF_6$ in propylene carbonate. The features of typical Al anode CVs shown here will be referred to frequently in the half-cell results presented in Ch. 4.1 to 4.5.

Shown in **Fig. 3-2** are the features of a typical CV of a bulk Al anode recorded between approximately 0.25V and 2V at a scan rate of 1 mV/sec for 3 scans. The bolded numbers in the figure denote the first, second and third scans respectively. All potentials are quoted relative to the Li^+/Li potential scale. The CV is begun by sweeping in the cathodic direction starting from 2.0V. Initially we see a small increase in the cathodic current below 2V due to initial formation of the SEI layer. The SEI formation involves irreversible partial reduction and decomposition of the electrolyte and any traces of moisture that may be present [7]. Continued sweeping in the cathodic direction results in the onset of lithiation around 0.4V to 0.5V and is associated with a sharp increase in current. This corresponds to onset of Li^+ reduction to yield a LiAl alloy (i.e. $Li^+ + e^- + Al \rightarrow LiAl$), which has a standard potential of +0.4V vs. Li^+/Li [5-6].

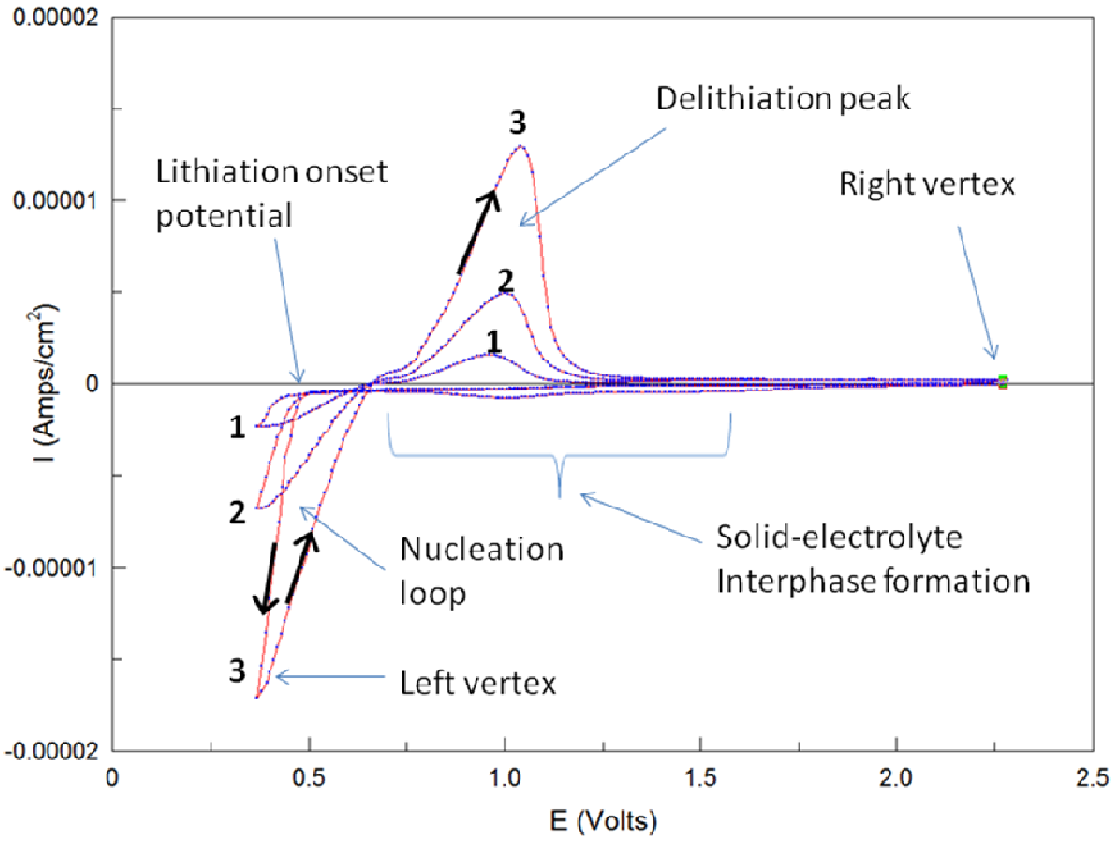

Figure 3-2: Features of a typical cyclic voltammogram (CV) for lithiation-delithiation of a bulk Al anode. Numbers indicate first, second and third scans respectively with each scan commencing at the right vertex potential. Black arrows indicate the scan direction.

The slope that follows the lithiation onset potential will be related to the degree of volume change in the anode. Following the onset the lithiation process continues in the CV until it is terminated by the left vertex. The chosen potential for the left vertex is significantly more positive than 0V to prevent possible deposition of lithium metal at the anode. Sweeping back in the anodic direction is characterized by a so-called 'nucleation loop' in the scan. This behaviour is associated with formation of the new LiAl intermetallic phase [5]. The intermetallic alloy phase formed has a higher surface area due to the associated volume change, 97% for LiAl [8]. Therefore the current of the reverse scan is higher than on the direct scan. Also, the kinetics of the lithiation may

differ on lithiated and non-lithiated substrates. The area enclosed by the loop is proportional to the volume changes associated with the intermetallic phase formation. Continued sweeping in the anodic direction will result in a large broad oxidation peak at 0.9V to 1.0V, which corresponds to oxidation and delithiation of the LiAl alloy (i.e. LiAl $\rightarrow Li^+ + Al + e^-$) [5-6]. The difference between the onset potential and this peak potential may be considered as a measure of the electrochemical irreversibility of the lithiation/delithiation processes, and is commonly termed the 'overvoltage'.

Further CV scans will alter each of these respective features described above. The formation of SEI will continue although in progressively smaller amounts. This suggests that some portion of the SEI layer is destroyed on the delithiation part of the scan, due to the volume changes of alloying/de-alloying anodes [7] or other processes. As fresh Al material is exposed this will result in more SEI formation in additional scans. In general the cathodic currents following the lithiation onset potential and anodic currents of the delithiation peak will become progressively larger, also resulting in an enlargement of the loop. These features should be attributed to continuing formation of the new intermetallic LiAl phase and progressively increasing surface area of the anode associated with this process. This indicates that repeated lithiation-delithiation cycles give rise to continuing growth of the new phase at the electrode surface. This will also contribute to continuing SEI formation.

3.15.2 Galvanic Cycling

Galvanic cycles (chronopotentiograms) are practically useful for simulating the real charge/discharge behavior of battery materials. The cycles involve a current being applied to a system while the potential is monitored. The current is applied until a particular limit of charge or potential is reached, at which point it is stopped or the reverse current is applied. In this work Al anodes are cycled both in a 3-electrode liquid half-cell as well as in a 2-electrode battery prototype using a solid polymer electrolyte (SPE) and a $LiFePO_4$ cathode. To illustrate the features of galvanic cycles for Al anodes and their meaning let us first consider again the 3-electrode liquid half-cell. Shown in

Fig. 3-3 are the characteristic features of a galvanic cycle for an Al anode at a current density of 0.25 mA/cm^2.

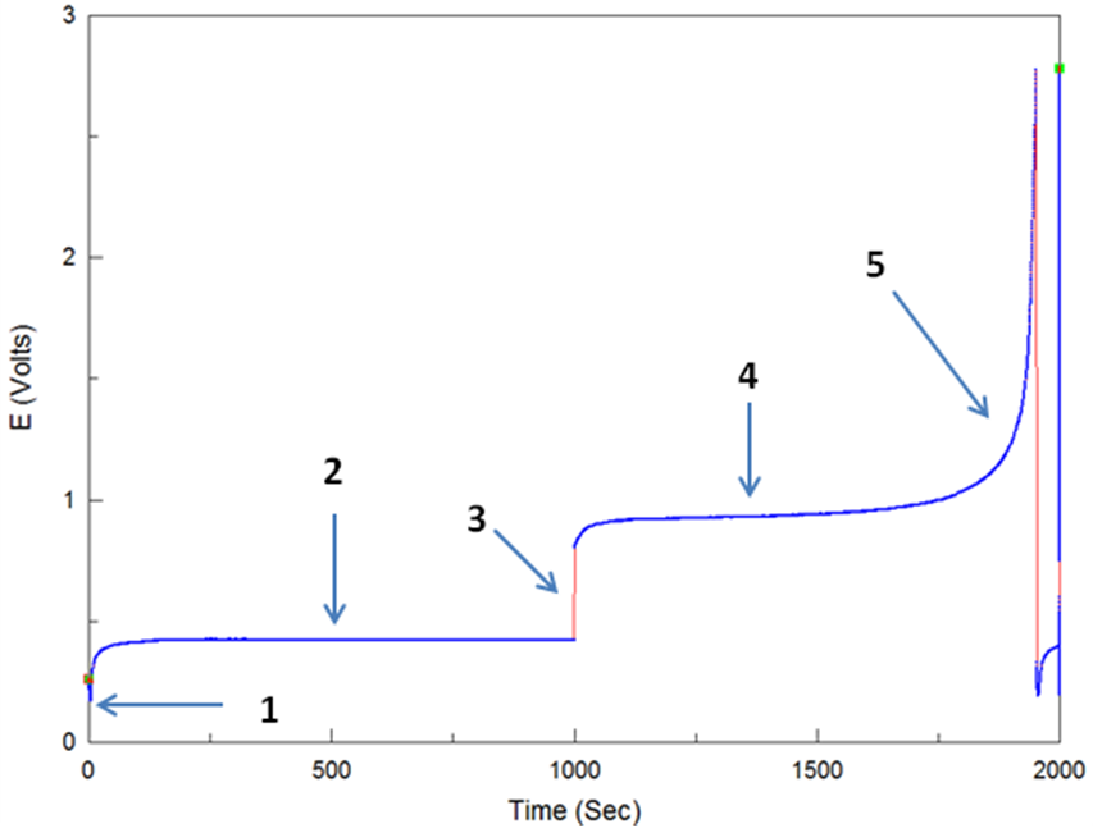

Figure 3-3: Typical galvanic cycle for lithiation-delithiation of an Al anode in a 3-electrode half-cell. Numbers indicate the features of interest: (1) potential overshot (2) charge plateau (3) IR drop (4) discharge plateau (5) discharge tail.

Overall the shape of the potential response in a galvanic cycle (chronopotentiogram) can be rationalized by considering the concentration changes of the redox species of interest as a function of time. In the case of Al anodes this would involve the reversible electron transfer reaction 'Al + Li^+ + e^- <--> LiAl'. Charging of the anode corresponds to reduction (lithiation) in the forward direction of this equation with discharging corresponding to oxidation (delithiation) in the opposite direction. Before applying the current, there is no LiAl formed yet and the initial potential is determined by some other equilibria.

The current to charge the anode is applied first, producing a potential minimum (**1**). This potential overshot is associated with the formation of a new electroactive phase at the anode surface. For Al anodes this would be initial formation of the intermetallic LiAl phase at the Al surface [5-6]. This minimum is followed by a single long and flat charging plateau **(2)** that corresponds to the continuing formation of the intermetallic phase at the surface of the phase formed earlier. A plateau is formed because an equilibrium is set up between the intermetallic LiAl phase and Li ions in the electrolyte solution, which allows the electrode potential to be described by the Nernst equation (2):

$$E = E^0 + \frac{RT}{nF} \ln \frac{[Li^+]}{[LiAl]} \qquad (2)$$

Since the concentration of Li ions in the solution should stay constant, and the activity of a solid LiAl phase is unity, the electrode potential should also stay constant once the equilibrium is established. Deviations from this Nernstian potential may be observed only if the equilibrium conditions at the electrode are violated such as due to slow electrode kinetics. For the charge plateau such a deviation would be represented by some degree of downward drift of the potential. Generally speaking, even if there are some other concurrent processes, the electrode potential will still be determined by the electrochemical equilibrium with the highest exchange current density. Therefore the appearance of multiple charge (or discharge) plateaus in a galvanic cycle will correspond to multiple redox processes, and only one redox process will occur at a time at or around its equilibrium potential (when overvoltages are taken into account), until it finishes and then the cell potential will move on until it encounters the next process. The duration of the plateau for each respective redox process will be proportional to the amount of charge and the amount of electroactive material present. Here for lithiation of Al anodes there is only a single reduction process (LiAl formation) and it is a bulk material so there is no limitation by the amount of the electroactive material. Therefore, only a single charging plateau is observed and charging continues until it is terminated by a pre-defined time constraint.

Upon switching the current direction, the cell potential exhibits an instantaneous jump **(3)** caused by non-zero resistance of the electrolyte (IR drop). The significance of this feature will be discussed in the next section. This jump is followed by a long flat discharge plateau **(4)** governed by the same Nernstian type equilibrium between the intermetallic LiAl phase and Li ions in the solution described above for the charging portion, plus the overvoltage, which provides the necessary driving force to extract the Li ions. As delithiation continues, the lithium concentration progressively decreases resulting in a steady reversion of intermetallic LiAl phase within the host matrix to delithiated Al (6). However, the potential stays approximately constant as long as there is still some LiAl phase left. As we progress further the potential begins to rapidly increase reflecting the depletion of the LiAl phase (**5**). This indicates the end of the main discharge plateau. Fitting the linear portion of the discharge plateau (**4**) and dividing by the total charging time allows for calculation of the coulombic efficiency (CE), which represents the ratio of the delithiation and lithiation charges and describes the reversibility of lithiation-delithiation. The cycle terminates when the electrode potential reaches a preset limiting value, which in this case was +2.7 V. There may be also additional processes that are associated with different equilibria or kinetics and thus they appear as separate plateaus. They will be described as appropriate in the corresponding sections.

For Al anodes in a 2-electrode battery prototype setup with a solid polymer electrolyte and $LiFePO_4$ cathode the cycle behaviour will be quite different, shown in **Fig. 3-4**. The anode plays the role of both the reference and counter electrodes in this system and therefore the cell voltage will be the difference of the potentials between anode and cathode. However, since we intentionally fabricated the cathodes in such a way so that $LiFePO_4$ is in a huge excess as compared to the amount of LiAl phase formed, we consider that the cathode potential remains constant throughout all experiments and the changes in the cell voltage are related to the processes at the anode. Again there is initially a potential overshot for initial formation of new LiAl phase (**1**), followed by a 'charging plateau' (**2**) involving lithiation of the anode and delithiation of the cathode. After the instantaneous potential jump of the IR drop (**3**) there is a 'discharging plateau' (**4**) involving delithiation of the anode and lithiation of the cathode. As this process is

exhausted the cell potential sharply decreases towards the preset limiting value of 0V that indicates full discharge. Similar to the half-cells the linear portion of the 'discharging plateau' may be divided by the total time of the charging portion to determine the coulombic efficiency of the cycle.

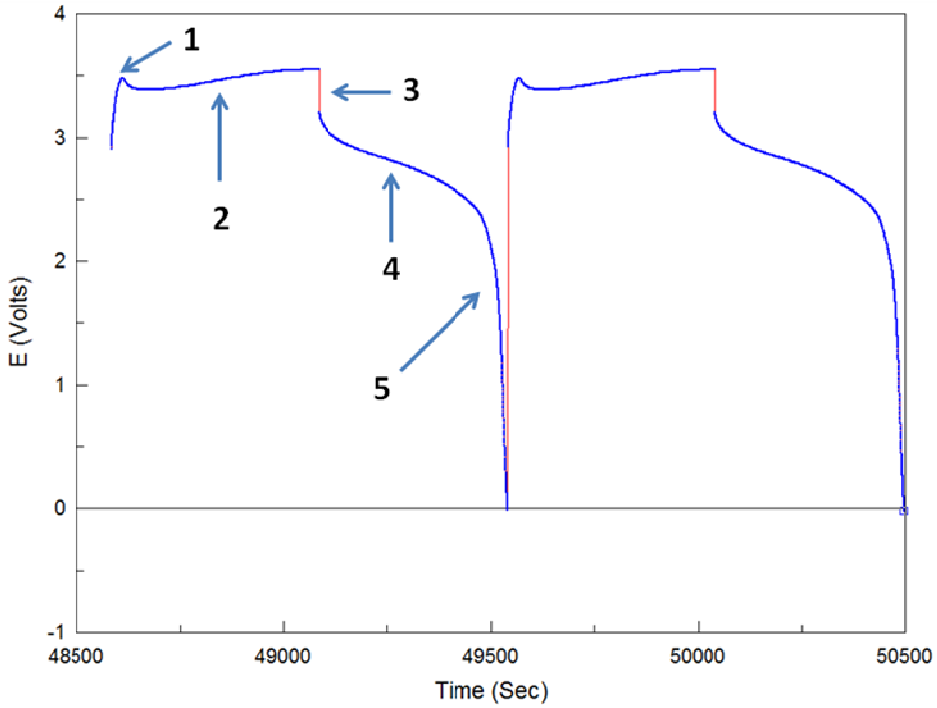

Figure 3-4: Typical galvanic cycles for lithiation-delithiation in a 2-electrode battery prototype setup with a solid polymer electrolyte, conductive $LiFePO_4$ cathode and a bulk Al anode at a current density of 0.065 mA/cm^2. Numbers indicate the features of interest: (1) potential overshot (2) anode lithiation and cathode delithiation plateau (3) IR drop (4) anode delithiation and cathode lithiation plateau (5) discharge tail.

Unlike in the half-cells the charge/discharge plateaus are clearly not flat here for the battery and instead show some upward/downward drifting in potentials respectively. Therefore there is some deviation from the Nernstian equilibrium potentials. The LiAl phase formation and dissolution on Al anodes occurs during charging and discharging portions of the battery cycle respectively. Therefore a change in battery cycle features implies a kinetic, resistance or mechanical (from SPE) limitation against LiAl phase

formation and dissolution, which causes deviation from the equilibrium potential in charging and discharging portions of the cycle respectively.

3.15.3 Determination of the IR drop from galvanic cycles

The Randles circuit is one of the simplest and most common equivalent circuit models. It includes a bulk electrolyte resistance, a double layer capacitor or a constant phase element (CPE) in case of developed interfaces, and a polarization or a charge-transfer resistance. The Randles circuit can be used as a good general approach to model the various phenomena going on at the interface of the anode in lithium ion battery. It describes the electrochemical process of charge transfer for one electrode in an electrolyte, such as the Al anode (working electrode) in the 3-electrode half-cell. **Fig. 3-5** shows the Randles circuit with the electrolyte resistance R_e, the charge transfer resistance R_{ct}, in parallel with the double layer capacitance C_{dl}. In more advanced models, the simple charge-transfer resistance can be replaced with complex charge-transfer impedance Z_{ct} or even more complex circuits; however, the most important fact for us is that these circuit elements will always be in parallel with the double-layer capacitance of the electrode.

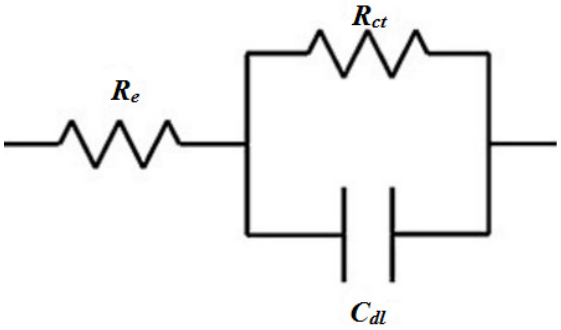

Figure 3-5: The typical Randles circuit for a working electrode in a half-cell.

In the 2-electrode Li-ion battery prototype, the current flows between the anode: Al and cathode: $LiFePO_4$ through an ionically conducting electrolyte. Therefore, the equivalent circuit of the cell must be modified as shown in **Figure 3-6** to include the impedances of

the anode and the cathode, both with their corresponding double-layer capacitances, as well as the resistance of electrolyte in series with the two electrodes.

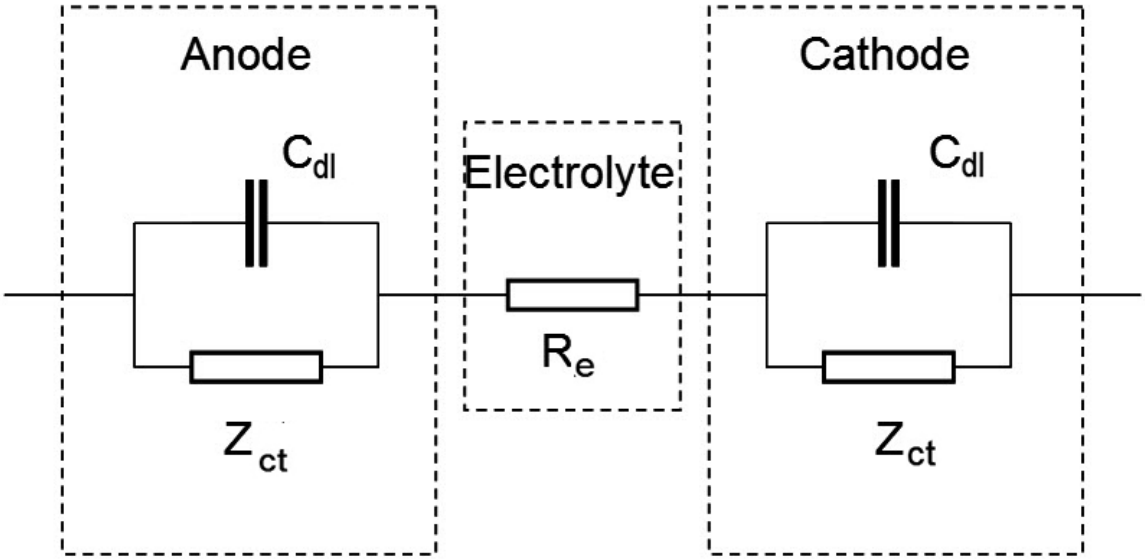

Figure 3-6: The equivalent circuit for battery prototypes.

When current is flowing in an electrochemical cell, there is an IR voltage drop (potential difference) between the working (WEr) and counter (CEr) electrodes. In the half-cell this effect is balanced by the presence of the reference electrode (RE) so that only a portion of the electrolyte resistance is actually measured at the working electrode. In the battery prototypes, there is no separate reference electrode and the IR voltage drop occurs between the $LiFePO_4$ cathode (WEr) and Al anode (CEr). This voltage drop is related to the electrolyte resistance R_e and the magnitude of the current I according to Ohm's law:

$$\Delta E_{ohmic} = I * R_e \qquad (3)$$

where ΔE_{ohmic} is the ohmic drop or IR drop, and R_e is the ohmic resistance of the electrolyte. The IR drop is inversely proportional to the electrolyte conductivity. The lower the conductivity of the electrolyte, the higher the ohmic resistance and therefore the higher the IR drop [9].

The IR drop and thus the value of R_e can be determined using so-called current interrupt method. In this method, the current in the electrochemical cell is abruptly changed. However, since the voltages at capacitances in the equivalent circuit of **Fig. 3-6** cannot change instantaneously, the electrode impedances Z_{ct} are short-circuited at the time of the current interrupt and the only change in the voltage across the cell is associated with the potential drop at the electrolyte resistance $I \cdot R_e$. In our galvanic cycles, the current changes from +I to –I; hence; $\Delta I=2I$ and R_e can be expressed with equation 4:

$$R_e = \frac{\Delta E}{2I} \qquad (4)$$

Therefore, using this approach, we can determine the resistivity (R_e) of our solid polymer electrolytes from the potential jumps when the current direction is switched during galvanic cycles of a battery.

However, if we measure not the instantaneous but steady-state IR drop (steady-state means after fully charging the double-layer capacitances in **Fig. 3-6**; this usually takes several seconds), the resistance will correspond not to R_e but to the sum of R_e and two charge transfer resistances R_{ct} at the anode and the cathode. Again, we assume that for the cathode, R_{ct} is small because of its much higher capacity. Therefore, we will measure this way the sum of the R_e and the R_{ct} at the anode. In this work, we mainly are interested not in instantaneous but steady state IR drop that can be obtained from the separation between the charging and discharging plateaus. The plateau separation and the charge transfer resistance have the same meaning of the degree of irreversibility of the charging and discharging processes, but the latter is more convenient when comparing the effects at different current densities. We will use both these parameters in our discussion as appropriate.

3.16 References

1. Choi, S.; Kim, T.H.; Lee, J.I., *ChemSusChem*, **2014,** *7,* 3483-3490.
2. Ibrahim, S.; Yassin, M.M., *Ionics,* **2011,** *17,* 399-405.
3. Hamon, Y.; Brousse, T.; Jousse, F.; Topart, P.; Buvat, P.; Schleich, D.M., *Journal of Power Sources*, **2001,** *97-98*, 185-187.
4. Hudak, N.S.; Huber, D.L., *ECS Transactions,* **2011,** *33(24),* 1-13.
5. Oltean, G.; Tai, C.W.; Edstrom, K.; Nyholm, L., *Journal of Power Sources*, **2014**, *269*, 266-273.
6. Liu, D.X.; Co, A.C., *J. Am. Chem. Soc.,* **2016**, *138*, 231-238.
7. Schroder, K.W.; Dylla, A.G.; Harris, S.J.; Webb, L.J.; Stevenson, K.J., *ACS Appl. Mater. Interfaces*, **2014,** *6,* 21510-21524.
8. Fauteux, D.; Koksbang, R., *Journal of Applied Electrochemistry,* **1993**, *23*, 1-10.
9. Macdonald, J. R.; Johnson, W. B., *Fundamentals of Impedance Spectroscopy*. John Wiley & Sons, Inc. 2005; pp 1-26.

Chapter 4

4 Results

4.1 Bare Aluminum Anodes, Al 1100 alloy, Goodfellow, Half-Hard

Summary

To investigate the effects of mechanical properties and the surface oxide on lithiation-delithiation we prepared bare Goodfellow Al (GF Al) (half-hard) anodes with varying degrees of surface oxide removal. The preparation of the four GF Al samples (GF1 to GF4) used in this sub-chapter was described previously in the experimental details of Ch. 3. In particular, sample GF1 had the native surface oxide removed as much as possible by polishing and etching; sample GF2 was polished but not etched with some native oxide remaining; sample GF3 had the native oxide removed but new oxide was formed by thermal oxidation in moist atmosphere; and sample GF4 had its native oxide fully intact. These samples were characterized electrochemically in 4x8 experiments, which begin with a cyclic voltammogram (CV) for three scans, followed by four sets of eight galvanic cycles at progressively higher current densities. In the initial CVs we only observed minor differences in the features with increasing oxide content, primarily in the region of solid-electrolyte interphase (SEI) formation and the overvoltage of lithiation-delithiation. In the galvanic cycles we observed minor differences in the charge-discharge plateau separation, as well as a detrimental impact of the oxide on the charge-discharge reversibility at lower current densities due to more pronounced diffusion-limited losses in the discharge peak. Surface analysis of these samples after electrochemistry revealed increased heterogeneity in the porous intermetallic alloy of GF2 to GF4 with regions of limited reactivity.

An additional sample (GF5) of the same type as GF1 (native oxide removed), which showed the best performance in the 4x8 experiments, was characterized electrochemically in a failure experiment, in which galvanic cycling of the anode begins immediately at a higher current density without initial conditioning through a CV. This cycling was sustained for 140 cycles to observe the anode performance over time. A pronounced degradation of the performance was observed, which manifested itself as potential jumps in the charge/discharge plateaus as well as systematic cracking of the anode surface.

4.1.1 Cyclic Voltammograms, Galvanic Cycles, Calculations

Shown in **Fig. 4-1-1** are the features of a typical CV of a bare GF Al anode recorded between approximately 0.25V and 2V vs. Li^+/Li reference electrode at a scan rate of 1 mV/sec for 3 scans. The bolded numbers in the figure denote the first, second and third scans respectively. The CV is begun by sweeping in the cathodic direction starting from 2.0 V. Initially we see a small increase in the cathodic current below 2V due to initial formation of the SEI layer.

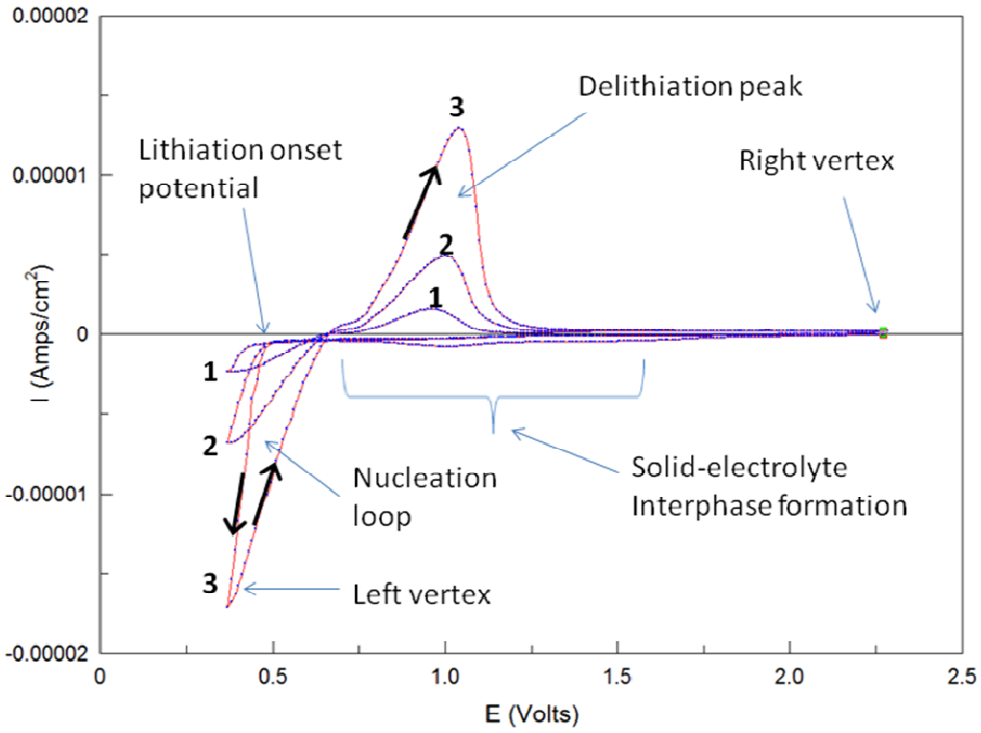

Figure 4-1-1: Typical cyclic voltammogram (CV) for lithiation-delithiation of a GF Al anode. This is sample GF1 which was subjected to polishing and etching in alkaline conditions prior to electrochemical scans. Numbers indicate first, second and third scans respectively with each scan commencing at the right vertex potential. Black arrows indicate the scan direction.

The SEI formation involves irreversible partial reduction and decomposition of the electrolyte and any traces of moisture that may be present [1]. Continued sweeping in the cathodic direction results in the onset of lithiation around 0.4V to 0.5V and is associated with a sharp increase in current. This should correspond to onset of Li^+ reduction to yield a LiAl alloy (i.e. $Li^+ + e^- + Al = LiAl$), which has a standard potential of +0.4V vs. Li^+/Li [1-3]. The slope following the lithiation onset potential will be related to the degree of volume change in the anode. Following the onset the lithiation process continues until the CV scan is terminated at the left vertex. Sweeping back in the anodic direction is characterized by a so-called nucleation loop in the scan. This behaviour is associated with the formation of the new phase [1]. As the intermetallic alloy phase formed has a higher surface area due to the associated volume change, the current of the reverse scan are

higher than on the direct scan. Also, the kinetics of the lithiation may differ on lithiated and non-lithiated substrates. Continued sweeping in the anodic direction results in a large broad oxidation peak at 0.9V to 1.0V, which should correspond to oxidation and delithiation of the LiAl alloy (i.e. $LiAl = Li^+ + Al + e^-$) [1-2]. The difference between the onset potential and this peak potential may be considered as a measure of the electrochemical irreversibility of the lithiation-delithiation processes.

Further CV scans alter each of these respective features described above. One can see that SEI still continues to be formed albeit in progressively smaller amounts. This suggests that some portion of the SEI layer is destroyed on the delithiation part of the scan, due to the volume changes of alloying/de-alloying anodes [5]. As fresh anode material is exposed this will result in more SEI formation in additional scans. The cathodic currents following the lithiation onset potential and anodic currents of the delithiation peak will become progressively larger, also resulting in an enlargement of the loop. These features should be attributed to continuing formation of the new intermetallic phase and progressively increasing surface area of the anode associated with this process. This indicates that repeated lithiation-delithiation cycles give rise to continuing growth of the new phase at the electrode surface.

A number of minor differences are observed in the CV features with increased oxide content. First we consider the partial cathodic scans between 2V and 0.25V (**Fig. 4-1-2**). The bolded numbers **1** to **4** denote the GF1, GF2, GF3 and GF4 samples respectively (no oxide, some oxide, thermal oxide, native oxide). Within this region GF4 (native oxide) shows the smallest cathodic current for the SEI formation, with the largest current observed for GF2. These two samples have a broad SEI formation possibly due to lack of the etching step since the etched GF1 and GF3 samples do instead show a distinct reduction peak observed around 1.0 V. This value is in agreement with the potential range observed for SEI formation on Al nanowires [1]. Additional scanning produces larger amounts of additional SEI formation for GF2 to GF4 relative to GF1 (no oxide). This behaviour suggests that varying degrees of surface oxide retention during anode

preparation of GF Al may promote more SEI formation during lithiation-delithiation as a parasitic loss of lithium.

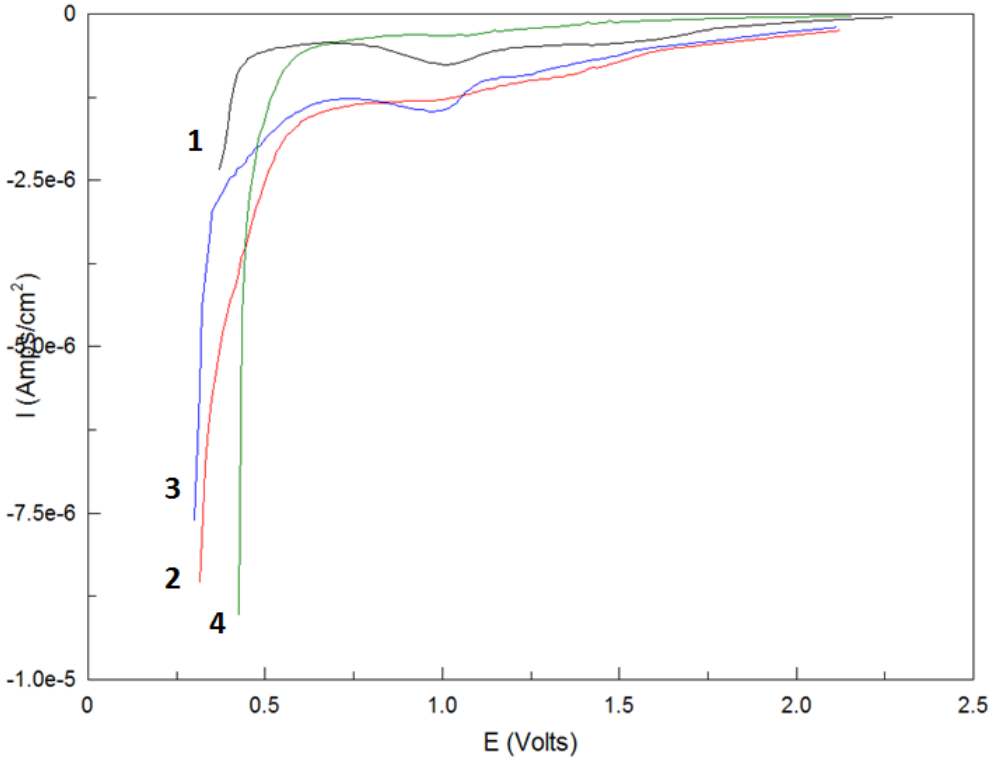

Figure 4-1-2: Initial cyclic voltammograms of four GF Al anodes prepared with varying degrees of surface oxide remaining. Partial cathodic scans from 2V to 0.35V to highlight SEI formation and lithiation onset behaviour. Samples GF1 (oxide removed), GF2 (polished only), GF3 (additional oxide) and GF4 (native oxide) in black (1), red (2), blue (3) and green (4) colors respectively.

Moving on we observe that increased oxide content causes a shift in the lithiation onset potential with a shallower slope afterwards. However, once the cathodic current sharply increases the shapes for all four samples are comparable. Additional scanning will produce an even smaller difference in the onset potentials and overall very similar slopes. This is understandable since the processes after the start of lithiation and especially in the 2nd and subsequent scans occur on a different surface of the LiAl intermetallic phase formed during the scanning.

Next we compare the full CV scans of all samples in **Fig. 4-1-3**. All samples show well defined nucleation loops in the anodic scans with a much smaller loop area observed for GF1 (no oxide). The delithiation peak potential is shifted positively with increased oxide content.

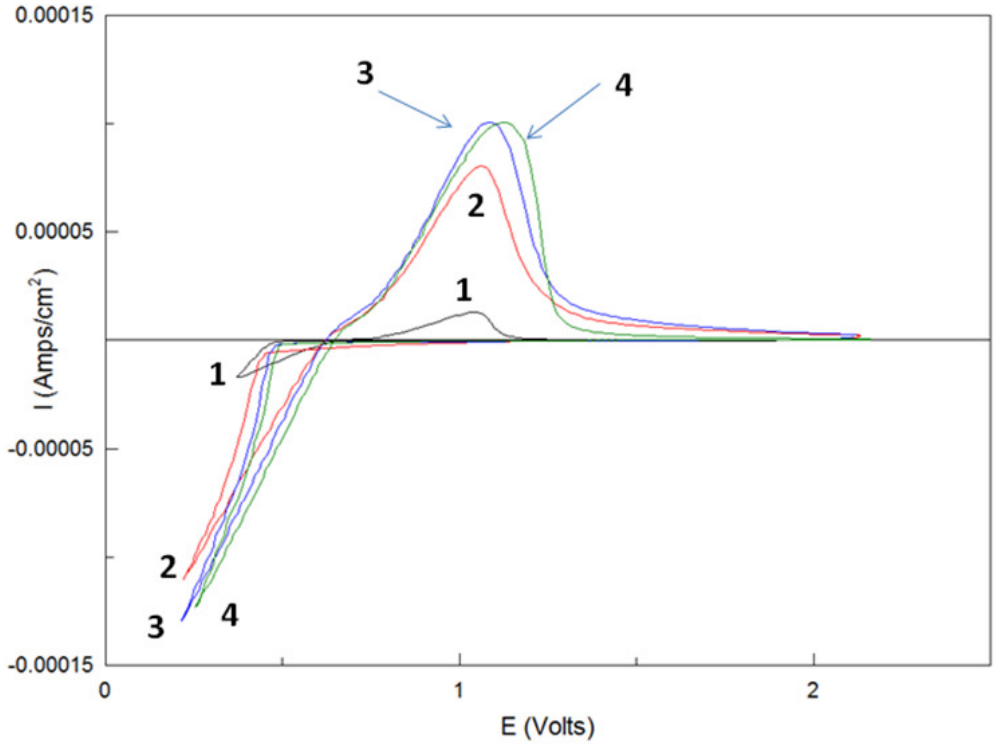

Figure 4-1-3: Initial cyclic voltammograms of four GF Al anodes prepared with varying degrees of surface oxide remaining. Full single scans with samples GF1 (oxide removed), GF2 (polished only), GF3 (additional oxide) and GF4 (native oxide) in black (1), red (2), blue (3) and green (4) colors respectively.

In view of the shifts in lithiation onset potentials discussed earlier, this results in a slightly larger overvoltage for the samples with oxide layers (GF2 to GF4) relative to the sample without oxide (GF1). This suggests that the relative absence of surface oxide is beneficial for lithiation-delithiation. The shift in the delithiation peak potential was most pronounced for the native oxide sample (GF4), whereas the peak symmetry for samples GF1 to GF3 appears fairly similar. This behaviour suggests that it may be more difficult to extract lithium from the intermetallic phase that was formed in the presence of native

surface oxide. The increasing diffusion-limited loss of lithium within the electrode bulk due to increased surface oxide content is a topic that will be explored in more detail in the galvanic cycles.

Shown in **Fig. 4-1-4** are characteristic features of a typical set of half-cell galvanic cycles for a GF Al anode at two current densities of 0.25 mA/cm^2 (black) and 1 mA/cm^2 (red). Initially we observe a potential minimum in the charging portion of the cycle **(1)** due to the potential overshot involved in formation of the intermetallic LiAl phase at the Al surface [2, 6-7]. This minimum is followed by a single long and flat charging plateau **(2)** that corresponds to the continuing formation of the intermetallic phase at the surface of the phase formed earlier. Therefore, the corresponding potential is lower and is governed by the equilibrium between the intermetallic LiAl phase and Li ions in the electrolyte solution in accordance with the Nernst equation [2]. At lower current densities the charging plateau is relatively flat. The fact that the charging potential remains independent of the amount of Li ions reacted at the electrode clearly indicates the formation of the intermetallic phase rather than an intercalation compound or a solid solution. Otherwise the Nernstian potential would be constantly changing in the course of lithiation-delithiation. At higher current densities the plateau potential shifts downwards due to an increased driving force required for lithiation. Moreover, there is an increasing downward trend due to diffusion-limited transport of lithium ions in the Al host that should cause an additional concentration polarization at the electrode.

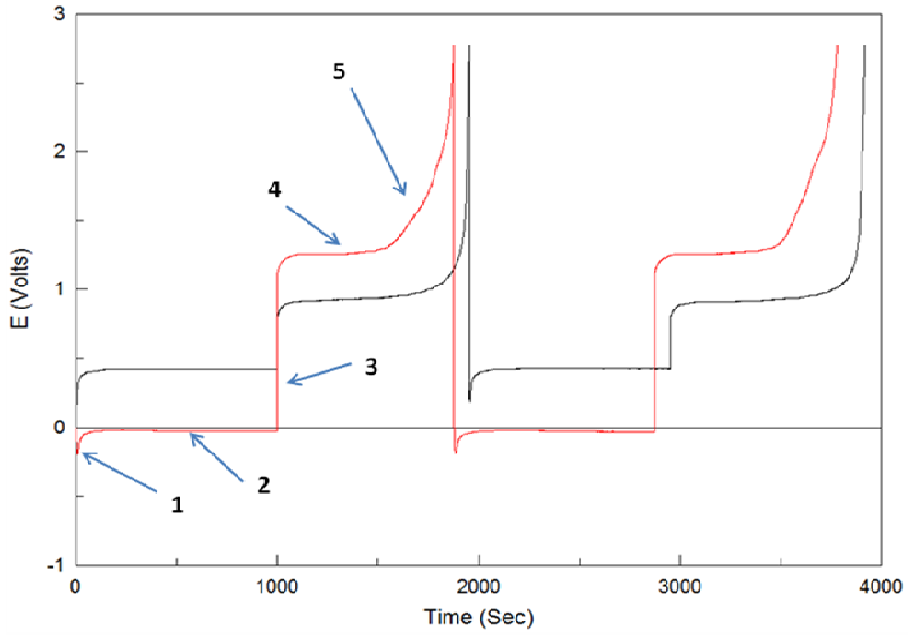

Figure 4-1-4: Typical galvanic cycles for lithiation-delithiation of a bare GF Al anode. This is sample GF1 which was subjected to polishing and etching in alkaline conditions prior to electrochemical scans. Numbers indicate the features of interest: (1) potential overshot (2) charge plateau (3) IR drop (4) discharge plateau (5) discharge tail and diffusion-limited plateaus. Galvanic cycles are shown at current densities of 0.25 and 1 mA/cm^2 in black and red colors respectively

Charging continues until it is terminated by time, at which point the opposite current is applied and the system begins to discharge. Importantly, since we use bulk Al anodes, the charging is never limited by the amount of Al present. At the time of switching the current direction, the cell potential exhibits an instantaneous jump **(3)** caused by non-zero resistance of the electrolyte (IR drop). This jump is followed by a long flat discharge plateau **(4)** governed by the same Nernstian type equilibrium between the intermetallic LiAl phase and Li ions in the solution described above for the charging portion. Similar to the charging plateau, this discharge plateau will shift to higher potentials with increasing current density due to increased driving force required for delithiation. Therefore, the resulting separation between the charge and discharge plateaus will

increase with the current density. This behaviour will be analyzed in more details later; here we just note that the separation between plateaus clearly exceeds the values that could be expected from reversible electrochemical reaction at the electrode even factoring in reasonable values of the IR drop due to electrolyte resistivity. It should be also noted that the IR drop is as seen in **Fig. 4-1-4** extends over several seconds and thus should include contributions from both the electrolyte and charge-transfer resistances (the instantaneous jump due to pure electrolyte resistance is observed in liquid electrolytes over the timescale of milliseconds).

As delithiation continues the lithium concentration progressively decreases resulting in a steady reversion of intermetallic LiAl phase within the host matrix to porous delithiated Al [2]. However, the potential stays approximately constant as long as there is still some LiAl phase left. As we progress further the potential begins to rapidly increase reflecting the depletion of the LiAl phase. This indicates the end of the main discharge plateau. Fitting the linear portion of the discharge plateau (**4**) and dividing by the total charging time allows for calculation of the coulombic efficiency (CE), which represents the ratio of the delithiation and lithiation charges and describes the reversibility of lithiation-delithiation. As the potential further increases there may one or multiple additional changes of inflection corresponding to additional electrochemical processes of a very short duration, typically appearing at higher current densities **(5)**. The cycle terminates when the electrode potential reaches a preset limiting value, which in this case was +2.7 V.

Let us use this approach to analyze the differences that are observed in the galvanic cycles with increasing oxide content. Shown in **Fig. 4-1-5** are the set of galvanic cycles of GF1, GF2, GF3 and GF4 in black, red, blue and green colors respectively at a current density of 0.25 mA/cm^2. In all cases we observe a very stable charging/discharging response. With increased oxide content (GF1 -> GF4) there are small shifts in both charging and discharging potentials. This is consistent with the differing lithiation onset and delithiation peak potentials described in the CVs. Unlike the smaller overvoltage observed in the CV of GF1, here the plateau separation of GF1 at lower current densities

is actually larger than for GF2 to GF4. This discrepancy is likely related to the very low lithiation-delithiation currents in the CV of this sample that were smaller than even the lower cycling current densities here. Therefore unlike samples GF2 to GF4, GF1 did not experience as extensive formation of the LiAl phase before the start of galvanic cycles and so initially featured different surface conditions. However, the main difference between the samples in **Fig. 4-1-5** is that they feature markedly different lengths of the discharge plateaus and thus different coulombic efficiencies. This indicates that the presence and structure of the surface oxide on the Al surface do have an effect on the mechanism and efficiency of the lithiation-delithiation processes.

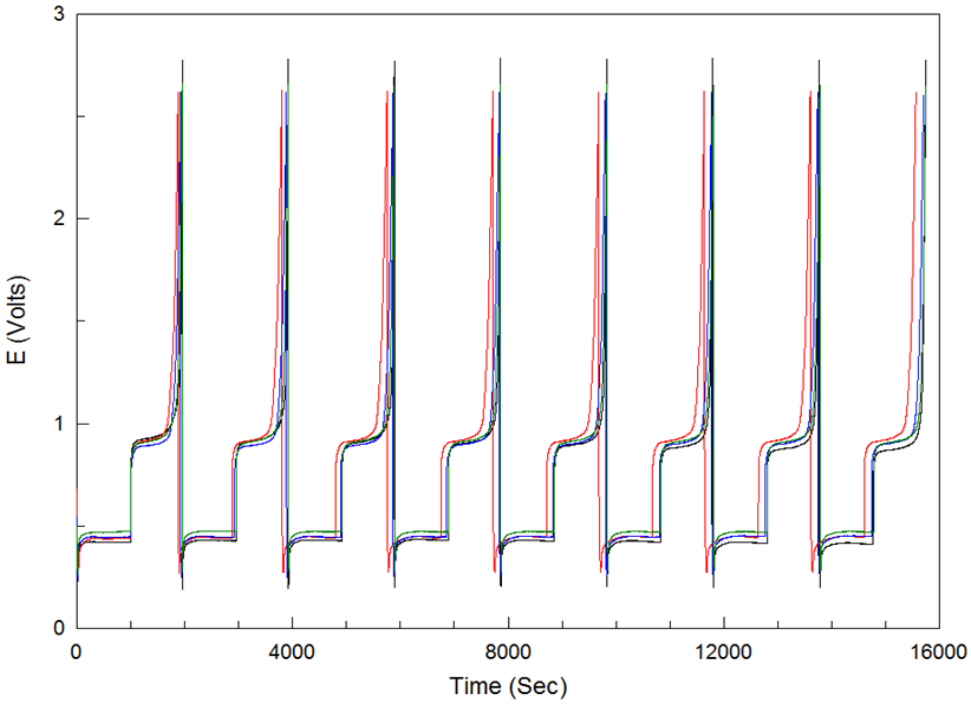

Figure 4-1-5: Galvanic cycles of four GF Al anodes prepared with varying degrees of surface oxide remaining at a current density of 0.25 mA/cm^2. Samples GF1 (oxide removed), GF2 (polished only), GF3 (additional oxide) and GF4 (native oxide) in black, red, blue and green colors respectively.

Shown in **Fig. 4-1-6** are the first (a) and last (b) galvanic cycles for all four samples in this set. One can see that the increased oxide content decreases the duration of the main discharge plateau and thus the coulombic efficiency (CE) **(Fig. 4-1-6 a)**. This effect is most apparent in GF2 and GF3 relative to GF1 with only a small difference observed for GF4. However the differences in CE become less pronounced by the eighth cycle **(Fig. 4-1-6 b)**. The evolution of the coulombic efficiencies with the cycle number is shown in **Fig. 4-1-7** for the four current densities used. One can see that for all current densities the sample with the surface oxide removed (GF1) performed best. The only exception was the highest current density (**Fig. 4-1-7 d)** where all samples performed quite poorly. Even then, the GF1 performance was not worse than that of the other samples. The GF1 sample also showed the smallest variability in the efficiency with cycling except again at the highest current density.

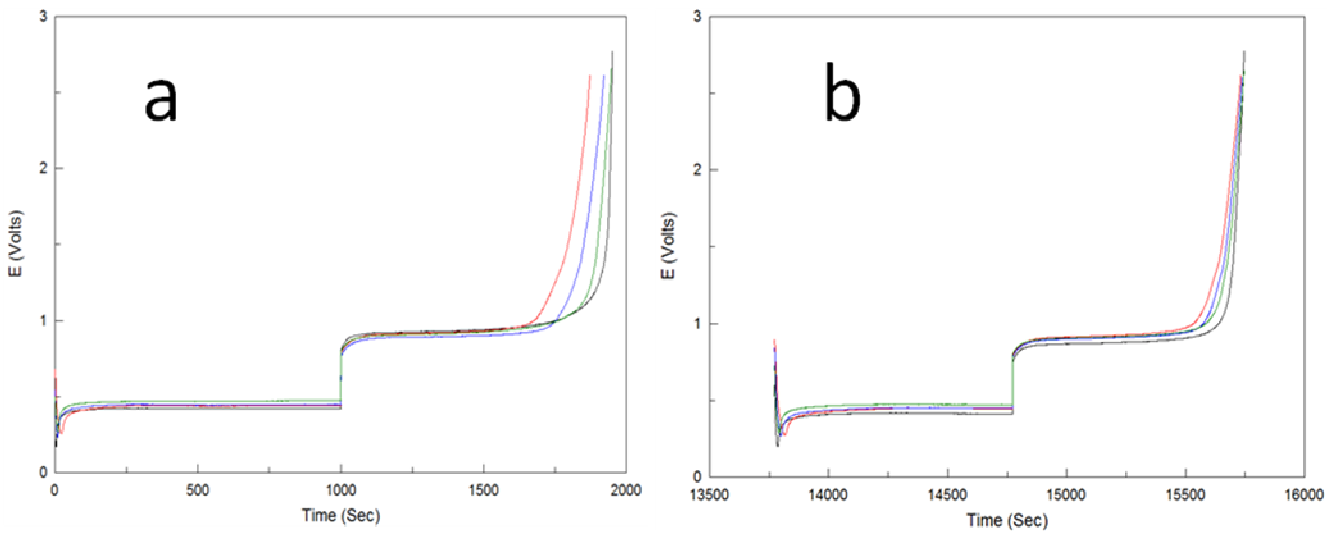

Figure 4-1-6: (a) First and (b) last galvanic cycles of four GF Al anodes prepared with varying degrees of surface oxide remaining at a current density of 0.25 mA/cm^2. Samples GF1 (oxide removed), GF2 (polished only), GF3 (additional oxide) and GF4 (native oxide) in black, red, blue and green respectively. Cycles in the right figure have been offset to overlap the curves on the same time scale.

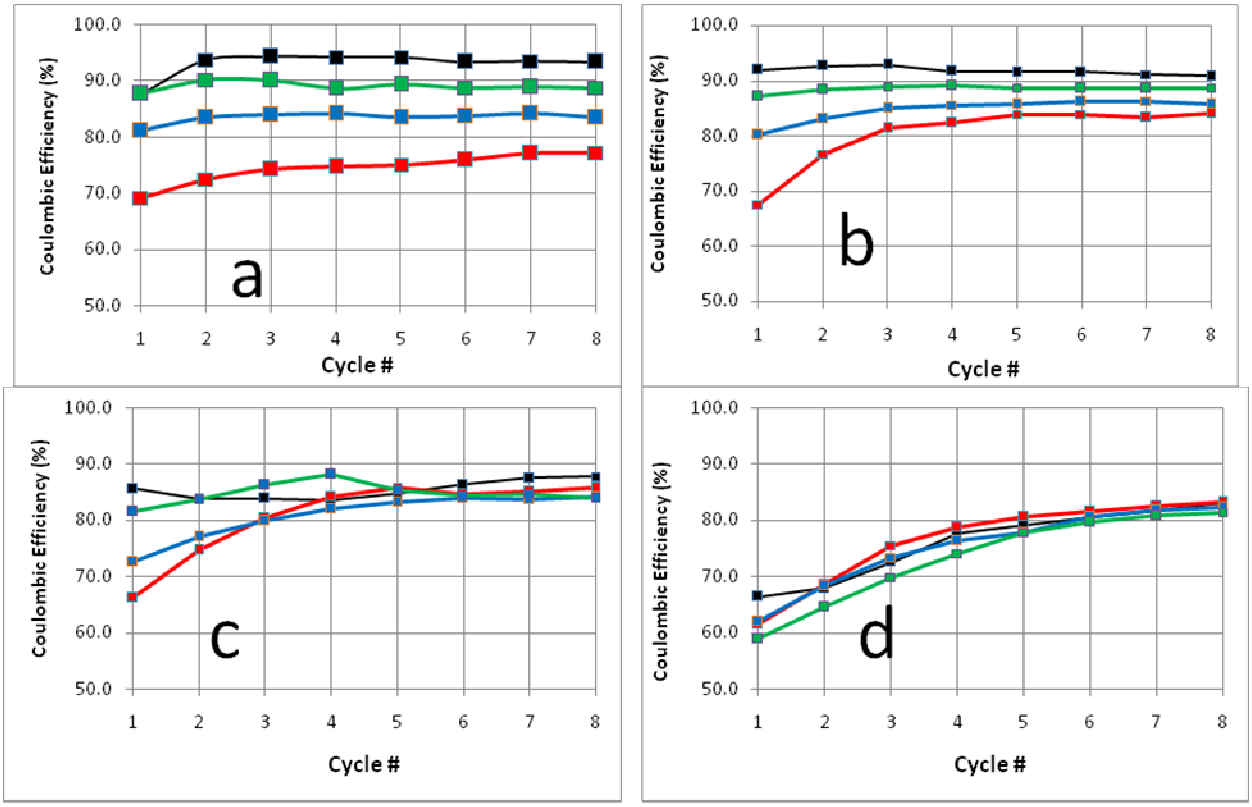

Figure 4-1-7: Coulombic efficiencies of four GF Al anodes prepared with varying degrees of surface oxide remaining at current densities of (a) 0.13 (b) 0.25 (c) 0.5 and (d) 1 mA/cm^2. Samples GF1 (oxide removed), GF2 (polished only), GF3 (additional oxide) and GF4 (native oxide) in black, red, blue and green respectively.

Importantly, the performance of all samples at high current densities markedly improved with cycling. This shows that this limitation can be partially overcome with electrode conditioning whereby a new LiAl phase is constantly made, lithated and delithiated at the electrode surface during repeated charging-discharging cycles, especially, at low current densities. We call this process electroformation and it will be discussed in considerable detail below.

To investigate the stability and cycling ability of the GF Al anode we performed a half-cell failure experiment on a new sample GF5. The sample was prepared in the same way as "oxide-free" sample GF1 described above since that sample showed the best

performance. However, in this experiment no prior electroformation of the LiAl phase was performed using either a CV or galvanic cycles at low current densities. The cycling was commenced directly at a high current density of 0.5 mA/cm^2 for a total of 140 cycles. This current density is equivalent to that of the third set of cycles in the 4x8 experiments.

Shown in **Fig. 4-1-8** is the full set of the corresponding galvanic cycles. One can see that the cycling behaviour is quite non-uniform and shows in particular significant and quite abrupt changes in both charging and discharging potentials (potential jumps). Since little further detail is seen in this figure due to the sheer number of cycles, **Fig. 4-1-9** shows the first two and last two cycles in black and red respectively. Arrows in the red curve indicate that, in addition to the main discharge plateau, secondary and tertiary plateaus appear over time in the discharge portion of the cycle. These plateaus indicate the occurrence of some additional processes that occur at much higher overvoltages as compared to the main delithiation process. The shape of these plateaus are also different: the potential is not constant and changes with time thus indicating that these responses are from a phase that have variable composition and thus whose Nernstian potential changes with the delithiation time. We can tentatively attribute these processes to delithiation of α-LiAl phase, a solid solution of Li in Al, which is known to exist at low Li concentrations even at room temperatures [2]. Therefore, these processes likely represent the very last stages of delithiation. Since the Li concentration in the α-LiAl phase is low (below 10%), these processes require a greater overvoltage and are likely to be diffusion-controlled. α-LiAl is also known to possess a more positive equilibrium potential as compared to β-LiAl [8]. Importantly, these processes are observed only in certain conditions and their occurrence is likely to signify certain structural changes at the electrodes. In order to characterize the performance of the sample, we used two parameters: the separation between the charge plateau and the main discharge plateau and the coulombic efficiency (CE) of the main discharge plateau. The first parameter is plotted in **Fig. 4-1-10**, whereas the CEs of the main as well as the secondary and tertiary discharge plateaus are shown in **Fig. 4-1-11** and **Fig. 4-1-12** respectively for every fifth cycle starting from the first cycle. As in the main discharge plateau the CEs of these additional discharge plateaus were obtained by fitting the respective linear portions and

dividing by the total charging time of 1000 sec. Additionally, the figures also show the data for cycles right before and after the potential jumps observed within the cycle set. We did not observe the secondary diffusion plateau begin to appear until approximately the 25th cycle with the tertiary plateau appearing around the 5th cycle. Therefore both secondary and tertiary efficiencies are absent within these regions of the respective figures.

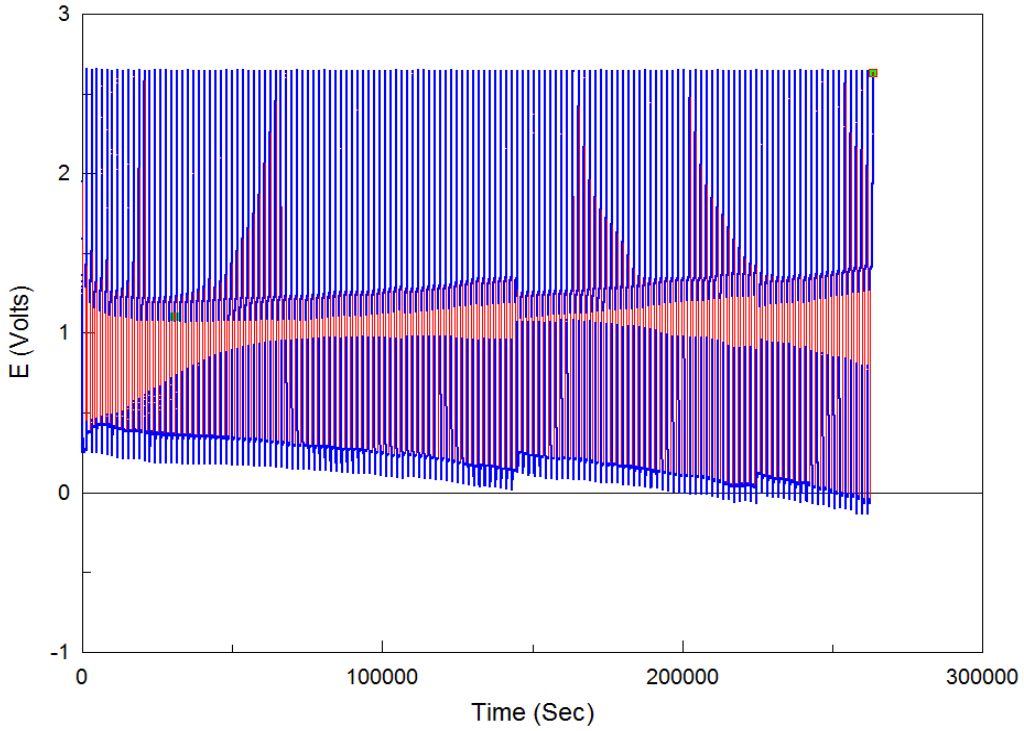

Figure 4-1-8: Full set of galvanic cycles for a bare GF Al anode with oxide removed GF5 subjected to 140 cycles at a current density of 0.5 mA/cm^2 without an initial CV.

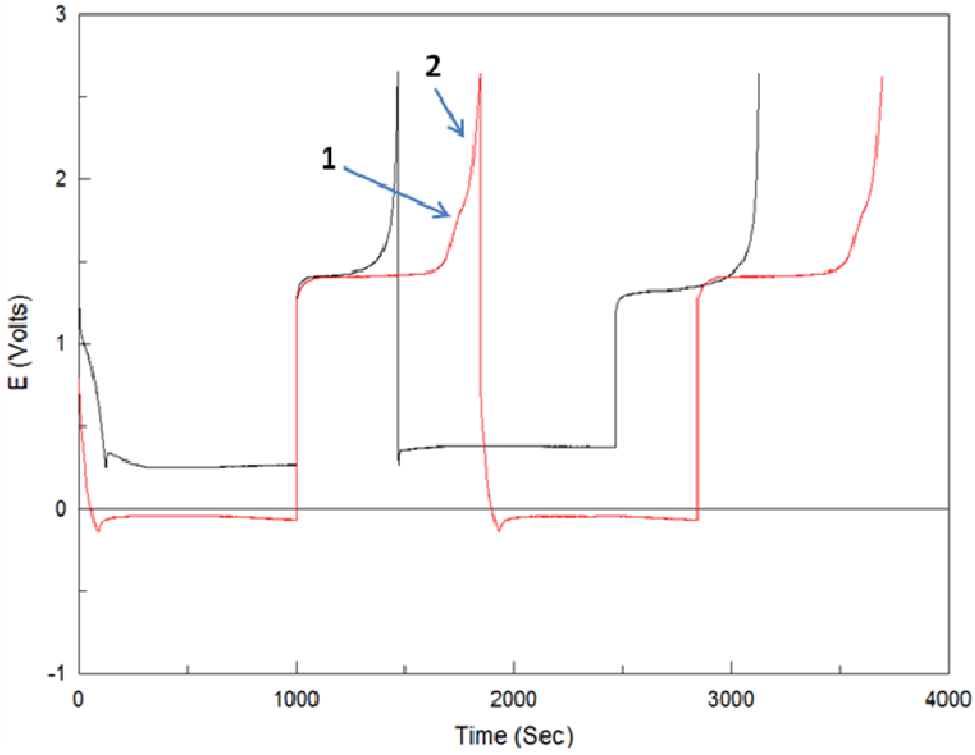

Figure 4-1-9: First two (black) and last two (red) galvanic cycles for a bare GF Al anode with oxide removed GF5 subjected to 140 cycles at a current density of 0.5 mA/cm^2 without an initial CV. Numbers in the red curve denote the secondary and tertiary diffusion-limited plateaus appearing over time. The red curve has been offset to overlap with the time scale of the black curve.

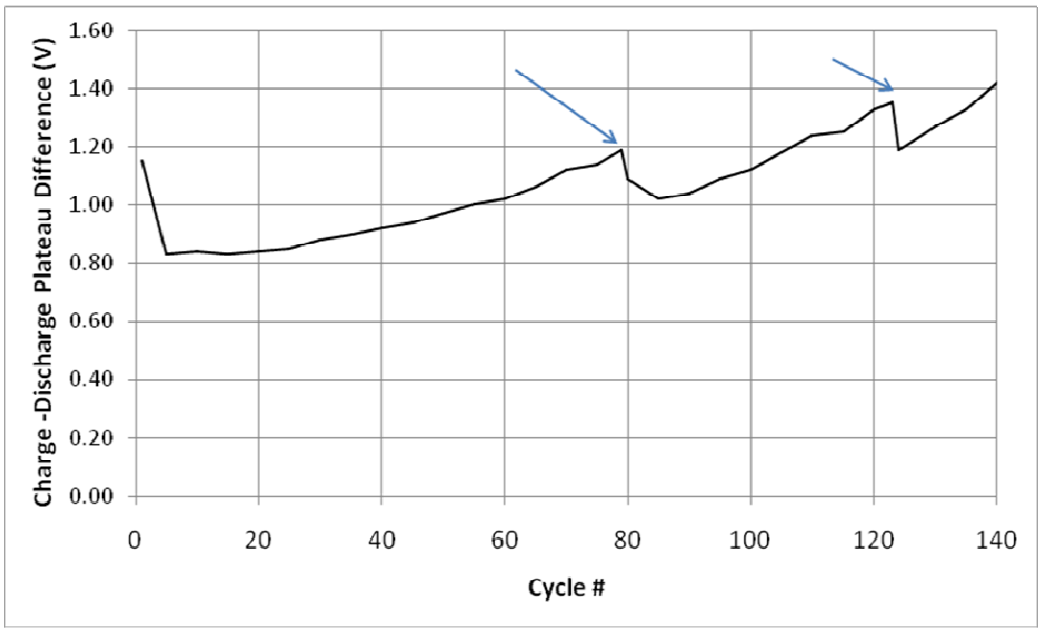

Figure 4-1-10: Charge-Discharge plateau separation for the main discharge plateau in a bare GF Al anode with oxide removed GF5 subjected to 140 cycles at a current density of 0.5 mA/cm^2 without an initial CV. Plateau jump events are indicated with arrows.

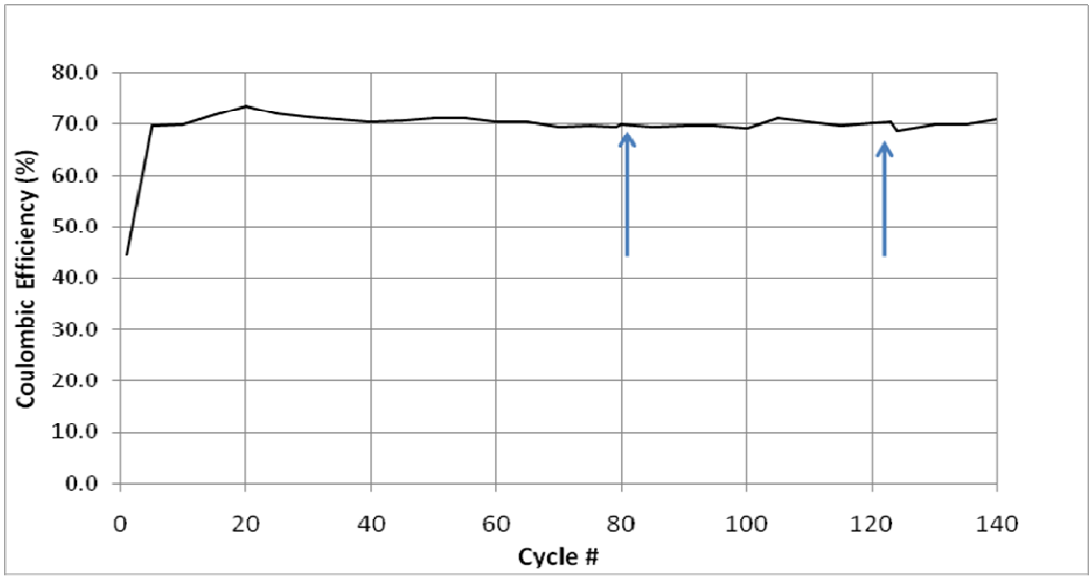

Figure 4-1-11: Coulombic efficiency for the main discharge plateau in a bare GF Al anode with oxide removed GF5 subjected to 140 cycles at a current density of 0.5 mA/cm^2 without an initial CV. Plateau jump events are indicated with arrows.

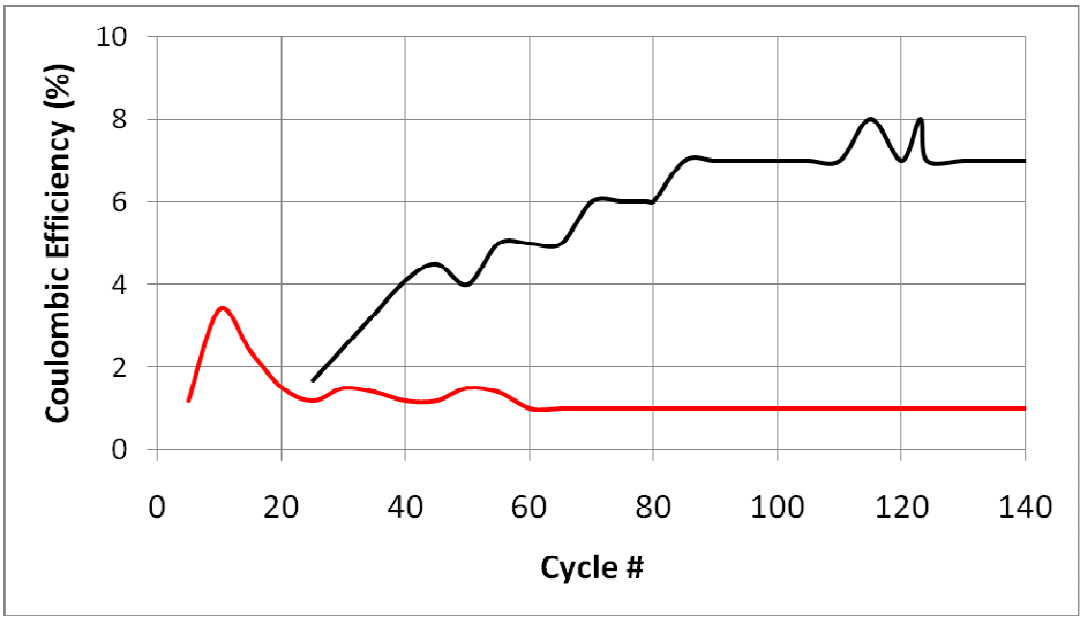

Figure 4-1-12: Coulombic efficiencies for the secondary (black) and tertiary (red) diffusion-limited discharge plateaus in a bare GF Al with oxide removed GF5 subjected to 140 cycles at a current density of 0.5 mA/cm^2 without an initial CV.

The very first cycle shows a distinctly larger plateau separation of 1.15V accompanied by a poor main CE of only 44% (**Fig. 4-1-9 to 4-1-11**). However this rapidly improves by the fifth cycle to a separation of 0.83V and main CE of 70%. These rapid changes are likely due to the initial formation of both the SEI layer and the intermetallic LiAl alloy microstructure at the Al surface. Normally in the 4x8 experiments these processes would occur during the three scans of the initial CV as well as the cycle sets at lower current densities, but those steps are omitted here in this experiment. At the fifth cycle the tertiary diffusion-limited plateau begins to appear above 2.3V with a CE of a few percent (**Fig. 4-1-12**). Up to the 20th cycle the main CE steadily increases to a maximum of 73% with the plateau separation maintaining a minimum value around 0.84V (**Fig. 4-1-10, 4-1-11**). At the 25th cycle and onwards a number of related trends begin to develop. There is the appearance of the secondary diffusion-limited plateau around 1.6V soon after the main plateau, with an initial CE of 2% (**Fig. 4-1-12**). This process steadily grows to a maximum around 7% highlighting the structural changes at the electrode. At the same

time, the main CE steadily decreases to a minimum of around 70%, at which it fluctuates for the remainder of the experiment (**Fig. 4-1-11**). During this time the plateau separation gradually increases accompanied by increased downward curvature in the potential of the charging plateau (**Fig. 4-1-10**). The main discharge plateau shifts positive over time and so do the potentials of the secondary and tertiary plateaus. This again suggests the occurrence of structural changes that affect the overvoltage of the lithiation-delithiation processes. By the 20th cycle the potential of the tertiary plateau reaches the cycle upper potential limit of +2.7V. Therefore the CE of this tertiary process rapidly drops to an insignificant value of around 1% where it remains for the rest of this experiment (**Fig. 4-1-12**).

In the meantime, the plateau separation increases to 1.15V by the 80th cycle. At the 80th cycle there is a noticeable jump in plateau potentials (**Figs. 4-1-8, 4-1-10**). Immediately following the jump the charge plateau is shifted positive and the main discharge plateau shifted negative resulting in a smaller separation of 1.02V (**Fig. 4-1-10**). The overall peak shape and width of the 79th and 81st cycles appeared very similar. In both cases the main CE is around 70% with the secondary and tertiary plateaus remaining around 7% and 1% respectively (**Figs. 4-1-11, 4-1-12**). After the jump the main plateau separation appears to briefly stabilize but soon again begins to increase towards a value of 1.35V (**Fig. 4-1-9**). Approaching the 125th cycle the charge plateau has now shifted below 0V vs. Li+/Li and we observe the second jump (**Figs. 4-1-8, 4-1-10**). Once again the plateau separation resets to a smaller value of 1.19V and immediately begins to increase again with only very minor changes observed in the efficiencies. By the 140th cycle both secondary and tertiary diffusion-limited plateaus are readily evident in the discharge peak shape (**Fig. 4-1-9).**

The origin of these plateau jumps is likely related to systematic large scale cracking and removal of a portion of the intermetallic structure from the surface of the Al anode as the stress of repeated lithiation-delithiation volume changes accumulates. Evidence of this cracking is presented in the SEM images of section 4.1.2. This process is referred to as 'pulverization' of active material in the literature is thought to be the dominant capacity

loss mechanism for Al and other metal-alloying anodes [6]. As mechanical stresses of cracks and voids accumulate there are ever greater driving forces required for lithiation/delithiation until a critical point is reached, the jump where the active material is broken into smaller pieces. The rather small change in plateau potentials here during the jumps accompanied by a minimal change in the main CE may be due to the mechanical stability of the strain-hardened GF Al anode. In contrast Ch. 4.2 will demonstrate how the McMaster-Carr (MC) bulk Al anode softened by full annealing produces a significantly more severe failure mechanism in all respects. The relation of mechanical properties and capacity loss mechanisms in Al anodes will be further discussed in Ch. 5.

4.1.2 SEM images

Shown in **Fig. 4-1-13 a-f** are SEM images of the uncycled (a-b) and cycled areas (c-f) of the bare GF Al anodes GF1 (oxide removed) and GF3 (additional oxide) after being subjected to the 4x8 experiments. The uncycled area of GF1 shows the typical Al etching pattern (**Fig. 4-1-13 a**).

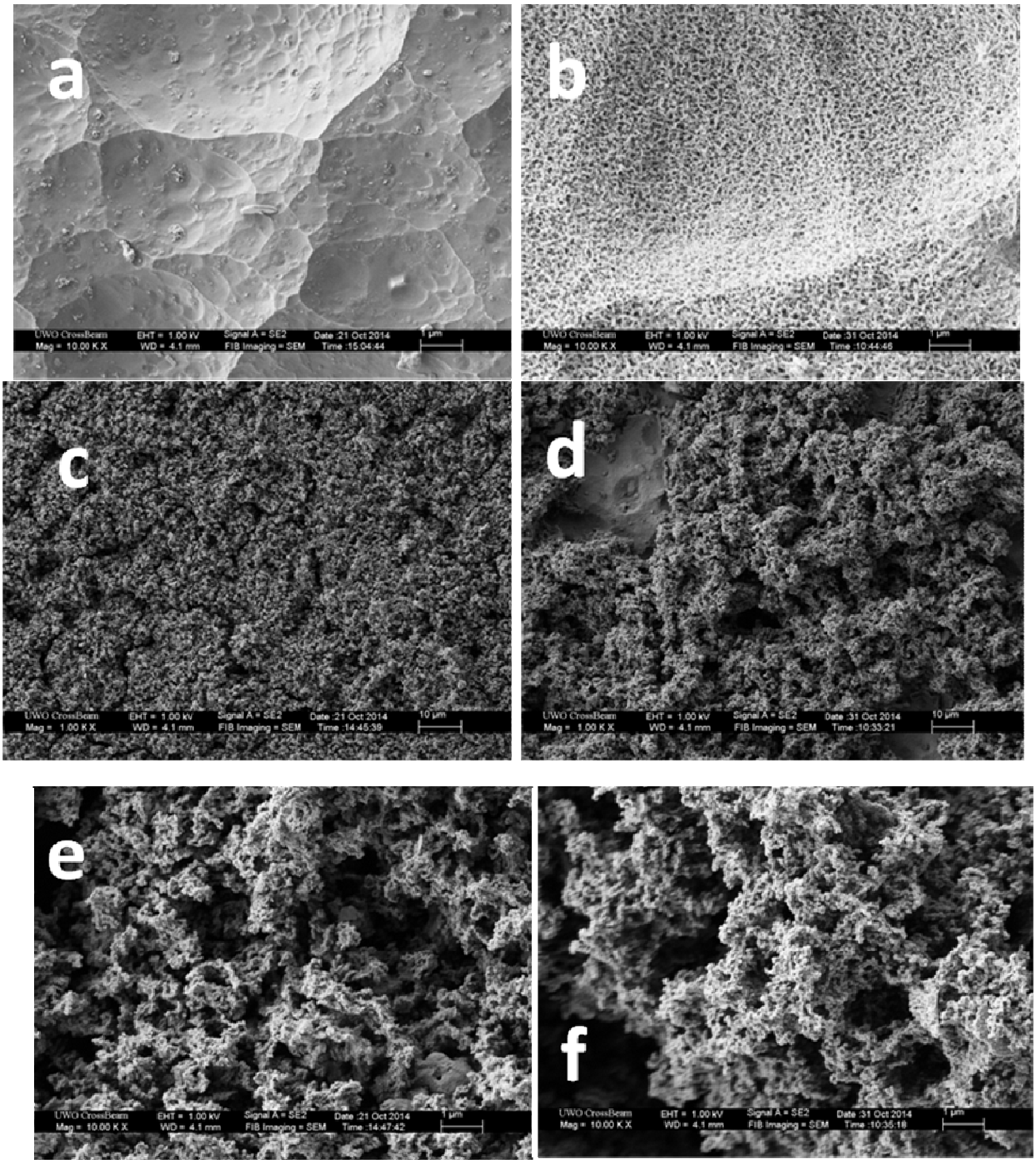

Figure 4-1-13: SEM images of uncycled (a, b) and cycled (c-f) areas for bare GF Al anodes GF1 (oxide removed) (a,c,e) and GF3 (additional oxide) (b,d,f) after being subjected to 4x8 experiments. Magnifications of (a-b) 10000x (c-d) 1000x (e-f) 10000x.

Increased oxide content in GF3 will make this uncycled morphology more rough relative to GF1 (**Fig. 4-1-13 b**), with the omission of both polishing and etching steps in GF4 producing a mostly featureless surface. Within the cycled area of GF1 we observe a fairly homogenous morphology, with a porous structure that should primarily consist of the well known intermetallic LiAl alloy (**Fig. 4-1-13 c, e**). Surveying across the entire cycled area of GF1 did not reveal any unreacted aluminum substrate. With the increased oxide content of GF3 the porous morphology becomes considerably more heterogeneous with larger voids and multiple areas of limited reactivity in terms of intermetallic alloy formation (**Fig. 4-1-13 d, f**).

Shown in **Fig. 4-1-14 a-c** are SEM images of the cycled area of the bare GF Al anode GF5 prepared with full oxide removal and then subjected to 140 cycles at a high current density of 0.5 mA/cm^2 without an initial CV. The electrochemical behaviour of this sample was characterized in **Figs. 4-1-8 to 4-1-12**. One can see large systematic cracking throughout the porous morphology of the cycled area, which should be related to the sudden plateau jumps observed in the galvanic cycles. This is most evident when viewing the lowest magnification image (**Fig. 4-1-14 a**). When looking more closely at higher magnification the fine details of the porous structure itself are quite similar to that observed in GF1 (**Fig. 4-1-14 b-c**). This is reasonable considering both materials were prepared under identical conditions. The morphology in this failure sample GF5 essentially appears to be the porous structure of GF1 broken into several large pieces.

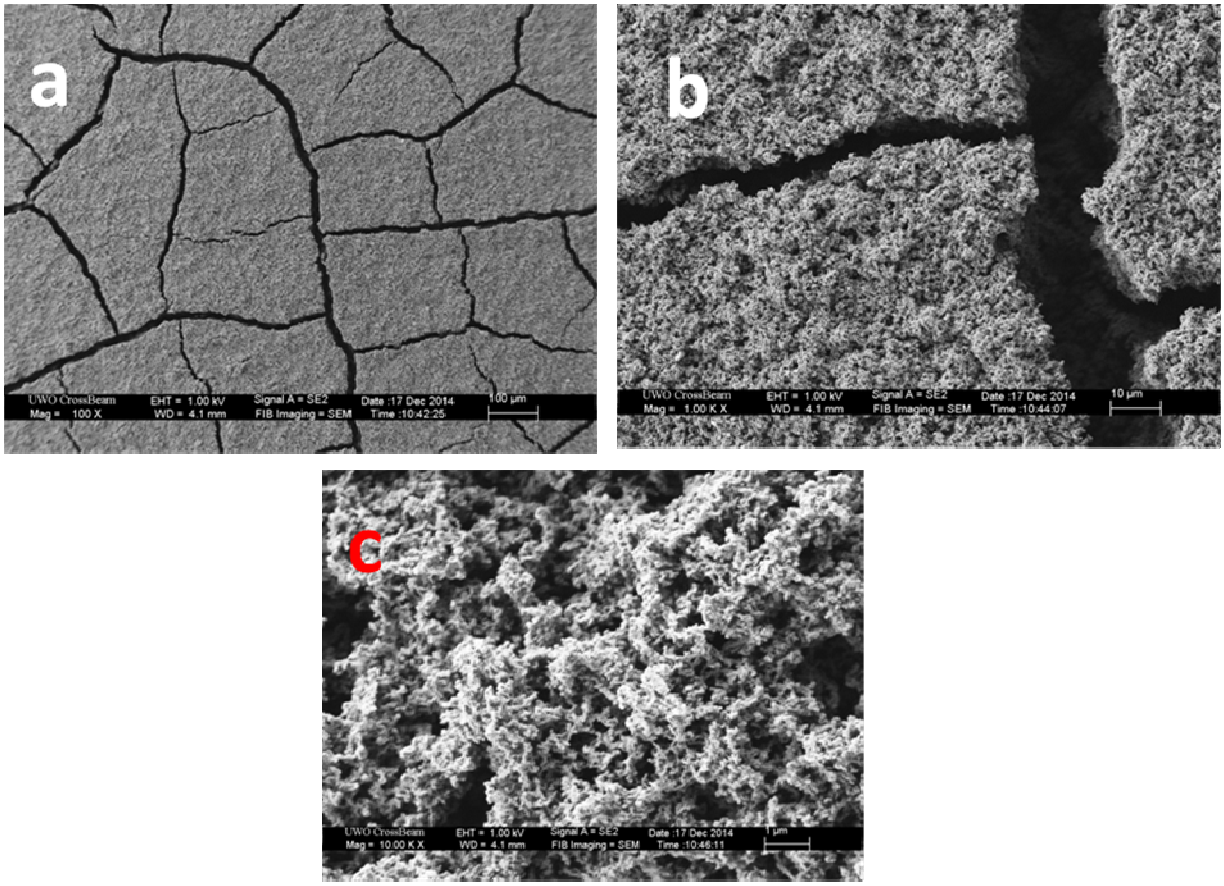

Figure 4-1-14: SEM images of cycled area for bare GF Al anode with oxide removed GF5 subjected to 140 cycles at a current density of 0.5 mA/cm^2 without an initial CV. Magnifications of (a) 100x (b) 1000x (c) 10000x.

4.1.3 EDX Composition Chart

Shown in **Table 4-1-15** is the EDX composition chart in atomic % of the uncycled and cycled areas of the four GF Al anodes GF1 to GF4 after being subjected to the 4x8 experiments as well as the GF Al anode GF5 after being subjected to 140 cycles at a current density of 0.5 mA/cm^2. The predominance of Al within the uncycled areas indicates a mostly unreactive aluminum substrate with surface contamination by the electrolyte (**a,c,e,h,j**).

Table 4-1-15: EDX composition chart of uncycled and cycled areas of four GF Al anodes prepared with varying degrees of surface oxide remaining after being subjected to 4x8 experiments (GF1 to GF4) and GF Al anode without surface oxide after being subjected to 140 cycles at a current density of 0.5 mA/cm^2 (GF5). Spectra were collected at a column voltage of 7 kV for 50 seconds at 1000x magnification.

		Atomic %					
Sample	**Area**	**C**	**O**	**F**	**Al**	**Si**	**P**
GF1	(a)Uncycled	1.65	1.92	0.59	95.67	0.09	0.08
	(b)Porous	8.14	18.29	37.77	34.74	0.28	0.79
GF2	(c) Uncycled	3.01	29.56	0.93	65.34	0.81	0.35
	(d)Porous	6.13	40.29	23.57	29.05	0.15	0.81
GF3	(e) Uncycled	1.05	11.85	1.89	84.71	0.24	0.27
	(f) Porous	5.74	29.90	24.98	38.20	0.25	0.93
	(g) Flat	2.66	20.93	8.54	67.38	0.20	0.31
GF4	(h)Uncycled	2.17	2.49	1.14	93.79	0.15	0.27
	(i)Porous	2.90	20.32	38.13	37.88	0.49	0.27
GF5	(j) Uncycled	1.63	1.83	0.77	95.45	0.29	0.03
	(k)Porous	2.36	9.48	47.33	38.74	1.39	0.69

Carbon and oxygen content should arise from a combination of trace propylene carbonate and residual surface oxide present after the various electrode preparations. Phosphorus and fluorine content should arise from trace $LiPF_6$ salt remaining after rinsing. The small amount of silicon detected in all samples likely originates from a combination of silicon carbide paper used for polishing, and as an impurity commonly found in 1100 aluminum alloys. It is important to note that pure silicon itself is a well-studied anode for lithium ion intercalation [9]. A limitation of the EDX technique is the inability to track lithium content due to the overlap of its low energy x-rays with the baseline peak close to 0 eV. The increased oxide presence in samples GF2 and GF3 will result in significantly higher oxygen content within the uncycled areas relative to GF1 (**c,e**). However the uncycled area of GF4 only shows slightly more oxygen (**h**). The discrepancy here in GF4 may be due to the 7 kV voltage mostly profiling the Al core below the crystalline oxide, compared to the more disordered or amorphous oxide in GF2 and GF3.

The cycled porous areas of GF1 to GF4 show significantly elevated carbon, oxygen and fluorine content (**b,d,f,i**). This is likely due to the presence of intact electrolyte within the intermetallic structure, as well as the products of solvent electroreduction and salt decomposition in the SEI layer [5]. Similar to their uncycled areas the increased oxide presence in samples GF2 to GF4 will result in a higher oxygen content within the cycled porous areas (**d,f,i**). For the partially reactive flat regions of GF3 described in the SEM images (**Fig. 4-1-13 d)** the EDX composition will be intermediate (**g**) between that of the uncycled area (**e**) and the fully reactive porous structure (**f**). When pushed towards failure the GF5 anode will resemble the cycled composition of GF1 but with dramatically higher F:O and F:Al ratios in both counts and percentages (**k**). Considering the $LiPF_6$ salt this fluorine content should predominantly come from the electrolyte. However it is not clear in what form does this elevated fluorine content exist within the systematically cracked intermetallic structure. As described in the CVs of GF1 to GF4 the continued lithiation-delithiation of GF Al will cause some degree of additional SEI formation beyond the first cycle. With sustained cycling in GF5 mechanical stresses will accumulate in the form of cracking. This will continuously cause partial destruction of the SEI present within the structure and expose fresh Al material for more SEI formation. The $LiPF_6$ salt is also

expected to thermally degrade over time into LiF and PF_5 if any trace moisture content is present [10].

4.1.4 References

1. Oltean, G.; Tai, C.W.; Edstrom, K.; Nyholm, L., *Journal of Power Sources*, **2014**, *269*, 266-273.
2. Liu, D.X.; Co, A.C., *J. Am. Chem. Soc.,* **2016**, *138*, 231-238.
3. Maskell, W.C.; Owen, J.R., *J. Electrochem. Soc.,* **1985,** *132,* 1602-1607.
5. Schroder, K.W.; Dylla, A.G.; Harris, S.J.; Webb, L.J.; Stevenson, K.J., *ACS Appl. Mater. Interfaces*, **2014,** *6,* 21510-21524.
6. Liu, Y.; Hudak, N.S.; Huber, D.L.; Limmer, S.J.; Sullivan, J.P.; Huang, J.Y., *Nano Lett.* **2011**, *11*, 4188-4194.
7. Hudak, N.S.; Huber, D.L., *Journal of the Electrochemical Society,* **2012,** *159(5)*, A688-A695.
8. Wen, C.J.; Boukamp, B.A.; Huggins, R.A., *J. Electrochem. Soc.,* **1979,** *126,* 2259.
9. Park, C.M.; Kim, J.H.; Sohn, H.J., *Chem. Soc. Rev.,* **2010**, *39*, 3115-3141.
10. Yang, H.; Zhuang, G., *Journal of Power Sources,* **2006,** *161,* 573-579.

4.2. Bare Aluminum Anodes, Al 1100 alloy, McMaster-Carr, Dead-Soft

Summary

In Ch. 4.1 we investigated the effects of mechanical properties and the surface oxide on lithiation/delithiation using bare Goodfellow Al (GF Al) (half-hard) anodes with and without native surface oxide. As a comparison in this sub-chapter we prepared bare McMaster-Carr Al (MC Al) (dead-soft) anodes both with and without native surface oxide. The preparation of the two MC Al samples (MC1 and MC2) used in this sub-chapter was described previously in the experimental details of Ch. 3. In particular, sample MC1 had the native surface oxide removed as much as possible by polishing and etching while sample MC2 had its native oxide fully intact. These samples were characterized electrochemically in 4x8 experiments, which begin with a cyclic voltammogram (CV) for three scans, followed by four sets of eight galvanic cycles at progressively higher current densities. In the initial CVs we observed several differences in the features of MC Al anodes consistent with increased volume change of intermetallic phase formation relative to GF Al anodes. In the galvanic cycles we observed minor differences in the charge-discharge plateau separation, as well as poor initial reversibility of MC1 at lower current densities which was further exacerbated with increased surface oxide content in MC2. Surface analysis of these two samples after electrochemistry revealed increased heterogeneity in the porous intermetallic alloy structure of MC Al anodes relative to GF Al anodes. An additional sample (MC3) of the same type as MC1 (native oxide intact), which showed the worst performance in the 4x8 experiments, was characterized electrochemically in a failure experiment, in which galvanic cycling of the anode begins immediately at a higher current density without initial conditioning through a CV. This cycling was sustained for 264 cycles to observe the anode performance over time. A significantly pronounced degradation of the performance was observed relative to GF Al anodes, which manifested as numerous potential jumps in the charge/discharge

plateaus, severe degradation of coulombic efficiency as well as a significantly heterogeneous multilayer porous structure.

4.2.1 Cyclic Voltammograms, Galvanic Cycles, Calculations

The typical features of CVs with bare Al anodes were described previously in Ch. 4.1.1. Therefore this section will focus only on differences observed in the CV features of MC Al anodes relative to GF Al anodes. First we consider the partial cathodic scans between 2 V and 0.25 V vs. Li^+/Li reference electrode (**Fig. 4-2-1**). For the purposes of comparison the analogous GF Al anodes GF1 and GF4 from Ch. 4.1 are included. The bolded numbers **1** to **4** denote the GF1, MC1, MC2 and GF4 samples respectively (1 hard, no oxide; 2 soft, no oxide; 3 soft, native oxide; 4 hard, native oxide).

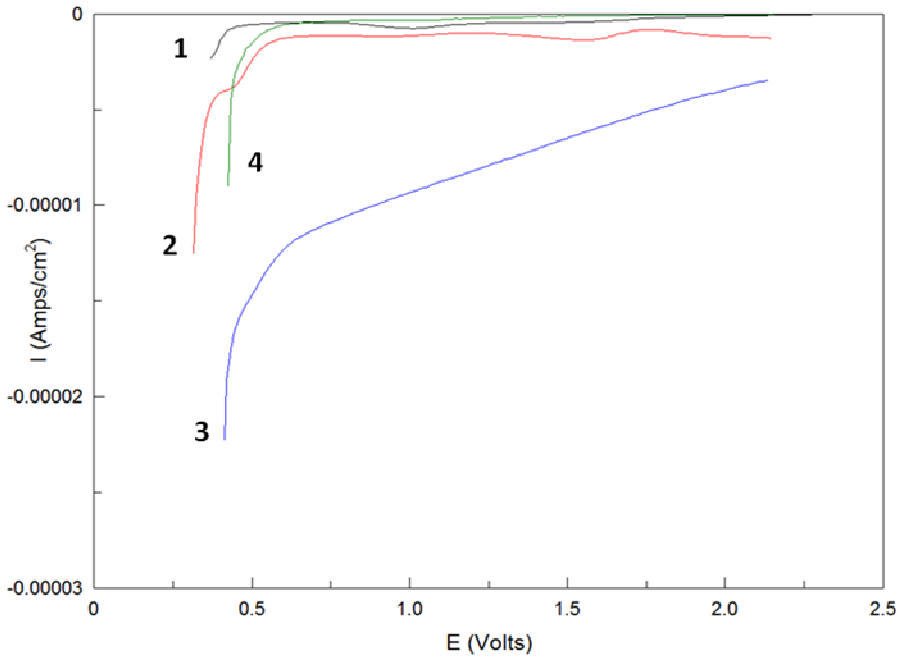

Figure 4-2-1: Initial cyclic voltammograms of two soft MC Al anodes MC1 and MC2 prepared with varying degrees of surface oxide remaining. Comparative half-hard GF Al anodes GF1 and GF4 from Ch. 4.1 are included. Partial cathodic scans from 2V to 0.25V to highlight SEI formation and lithiation onset behaviour. Samples GF1 (half-hard, oxide removed), MC1 (soft, oxide removed), MC2 (soft, native oxide) and GF4 (half-hard, native oxide) are in black (1), red (2), blue (3) and green (4) respectively.

Both MC Al samples show larger cathodic currents for the SEI formation. Sample MC1 (oxide removed) shows a distinct reduction peak around 1.5V. This value is different from the peak of 1.0V in GF Al sample GF1 (oxide removed), which is the typical potential range observed for SEI formation on Al nanowires (1). Similar to what was observed in GF Al with native oxide (GF4) the MC Al anode with native oxide (MC2) shows a broader SEI formation with no apparent peaks and a larger cathodic current. Additional scanning in the CV will produce larger amounts of additional SEI formation for MC1 relative to GF1, with this formation further increased in MC2. Therefore, the SEI formation seems to be enhanced in the following order: half-hard<soft, oxide removed<soft, native oxide. The softening processing of MC Al should allow for a

greater degree of volume change relative to the strain-hardened GF Al, due to greater mobility of dislocations within the Al host (2). This allows for greater SEI formation in MC Al initially. Furthermore, one can expect a greater destruction of SEI in the delithiation scan for soft anodes (see below) leading to increased SEI formation in subsequent scans. Moving on, we observe that MC1 (MC Al, curve 2) shows a double lithiation onset plateau followed by a later onset potential relative to GF1 (GF Al, curve 1). Additionally, the slope following the onset potential is considerably steeper for MC1, which suggests a greater degree of volume change for intermetallic phase formation in the MC Al anode. Increased oxide content in the MC Al (MC2) makes the onset appear earlier, which is consistent with the behaviour observed in the GF Al sample with native oxide (GF4). Additional scanning will produce a consistently later lithiation onset potentials in the CVs and steeper slopes for MC Al anodes relative to GF Al.

Next we compare the full CV scans of all samples in **Fig. 4-2-2**. Both soft MC Al samples show well defined nucleation loops in the anodic scans. The loop size for MC Al in both MC1 and MC2 is considerably larger than GF Al in GF1. Like the steeper onset slope for MC1 and MC2 in **Fig. 4-2-1** this suggests a greater degree of volume change for intermetallic phase formation for MC Al than GF Al. The delithiation peak potential is shifted positively in MC1 (soft) relative to GF1 (half-hard). Considering the later lithiation onset potential observed for MC1 relative to GF1 results in a larger overvoltage for soft MC Al. This is also seen in the larger overvoltage of the soft MC Al sample with native oxide MC2 relative to GF4 (half-hard). The delithiation peak of MC1 appears delayed and slanted towards the right relative to GF1. If the MC Al anode experiences larger volume changes than GF Al we would expect more time would be required for full delithiation. The native oxide version of soft MC Al (MC2) shows an even greater delay in the delithiation peak relative to MC1. This is consistent with half-hard GF Al samples GF4 relative to GF1 and again suggests that it is more difficult to extract lithium ions from the intermetallic phase that was formed in the presence of native surface oxide. At the same time, the formation of the new LiAl phase also requires a larger overvoltage both in hard and soft Al samples. However, the electrochemical performance and in

particular cyclability and reversibility of the lithiation-delithiation processes appeared to be better in samples without surface oxide.

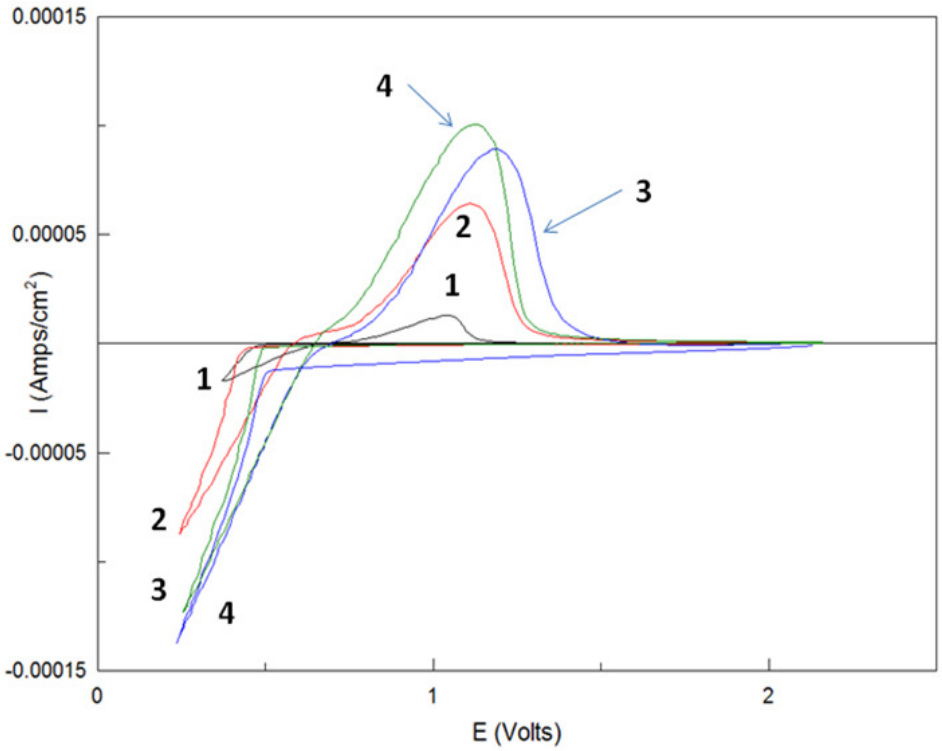

Figure. 4-2-2: Initial cyclic voltammograms of two soft MC Al anodes MC1 and MC2 prepared with varying degrees of surface oxide remaining. Comparative half-hard GF Al anodes GF1 and GF4 from Ch. 4.1 are included. Full single scans with samples GF1 (hard, oxide removed), MC1 (soft, oxide removed), MC2 (soft, native oxide) and GF4 (hard, native oxide) are in black (1), red (2), blue (3) and green (4) colors, respectively.

Shown in **Fig. 4-2-3** are the features of a typical set of galvanic cycles for soft MC Al anode MC1 (oxide removed) at a current density of 0.25 mA/cm^2 in red color, with the comparative cycle set of the half-hard GF Al anode GF1 (oxide removed) in black color. Overall we observe a similar sequence of events (denoted in the numbers **1** to **5**) within the cycle set as described previously for GF Al anodes in Ch. 4.1, with single long and flat plateaus for both charge and discharge portions. There is slightly more curvature following the IR jump of MC1 before the discharge plateau is established as well as

visible sloping observed in this plateau. Both features indicate a greater change in the electrochemical kinetics and thus the overvoltage for MC1. Additionally, there are small differences observed in terms of plateau separation and the reversibility of the discharge plateau which will be discussed further in the next figures.

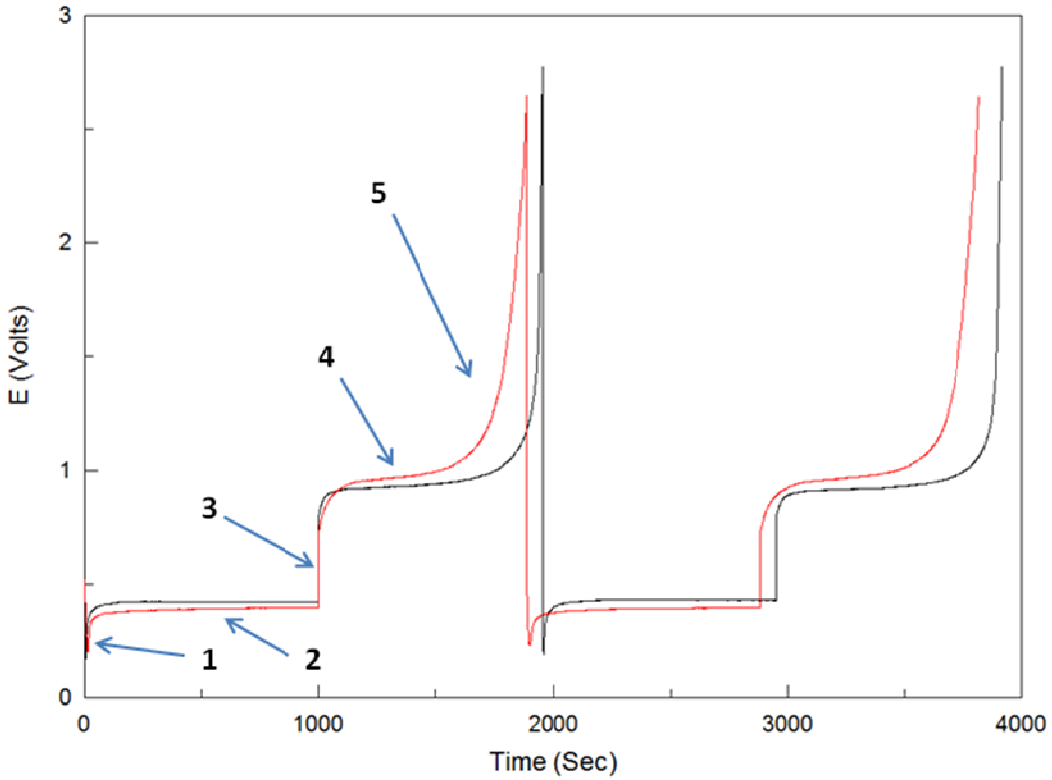

Figure 4-2-3: Typical galvanic cycles for lithiation/delithiation of a soft MC Al anode (red curve). This is sample MC1 which was subjected to polishing and etching in alkaline conditions prior to electrochemical scans. Comparative half-hard GF Al anode GF1 (oxide removed) from Ch. 4.1 is also included (black curve). Numbers indicate the features of interest: (1) potential overshot (2) charge plateau (3) IR drop (4) discharge plateau (5) discharge tail. Galvanic cycles are shown at a current density of 0.25 mA/cm^2.

Shown in **Fig. 4-2-4** are the set of galvanic cycles of soft MC Al anodes MC1 (oxide removed) and MC2 (native oxide) in red and blue colors respectively at a current density of 0.25 mA/cm^2. The comparative cycle sets of the half-hard GF Al anodes GF1 and GF4 are included in black and green colors respectively. In both soft MC Al anodes we

observe a very stable charging/discharging response, even though the reversibility of the discharge plateau is clearly impaired for the MC2 sample with native oxide (blue). Throughout the set MC1 (soft MC Al) has a lower charge plateau potential and larger plateau separation than GF1 (half-hard GF Al), consistent with the later lithiation onset potential and larger overvoltage seen in the CV (**Fig. 4-2-2**). Together these features suggest again that the softened mechanical properties of MC Al allow for a greater degree of volume change for intermetallic phase formation relative to half-hard GF Al.

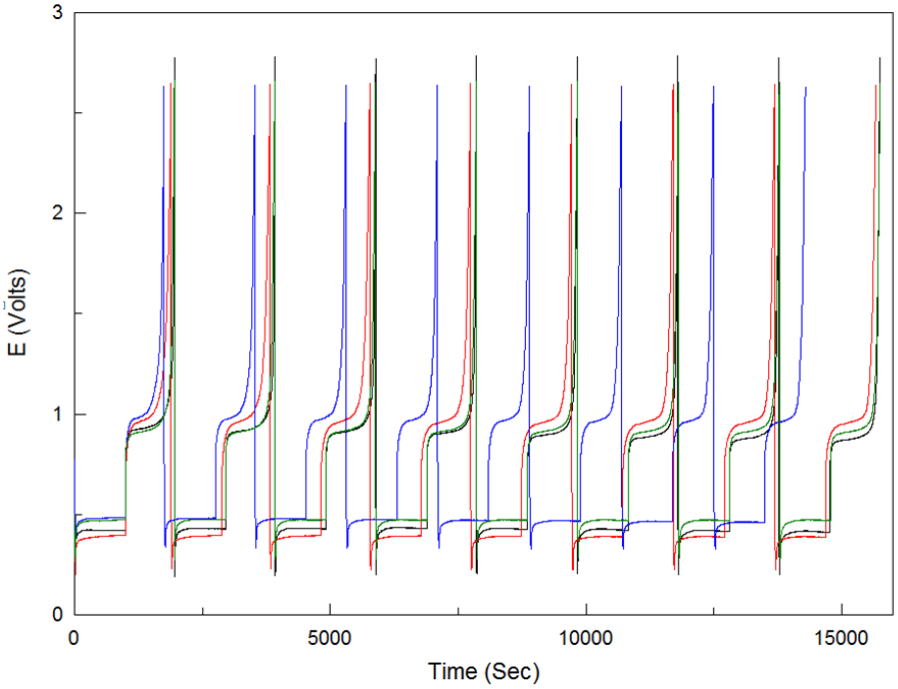

Figure 4-2-4: Galvanic cycles of two soft MC Al anodes MC1 and MC2 prepared with varying degrees of surface oxide remaining at a current density of 0.25 mA/cm^2. Comparative half-hard GF Al anodes GF1 and GF4 from Ch. 4.1 are included. Samples GF1 (hard, oxide removed), MC1 (soft, oxide removed), MC2 (soft, native oxide) and GF4 (hard, native oxide) are in black, red, blue and green colors, respectively.

This trend also appears to carry over to the native oxide versions of the two Al materials with soft MC2 consistently showing a larger plateau separation than half-hard GF4.

Shown in **Fig. 4-2-5** are the first (a) and last (b) galvanic cycles for both MC Al and GF Al samples in this set. One can see that the softened mechanical properties of the MC Al initially decrease quite considerably the duration of the main discharge plateau and thus the coulombic efficiency (CE) relative to half-hard GF Al (**Fig. 4-2-5 a**). This effect is readily apparent in MC1 (soft) compared to GF1 (hard, both oxide removed) and is further amplified in the initial discharge peak shape of MC2 (native oxide). However, the differences in CE for MC1 relative to GF1 become less pronounced by the eighth cycle (**Fig. 4-2-5 b**). Here the end of the discharge appears very similar for MC2 relative to MC1 but the reversibility for MC2 remains poor. The evolution of the coulombic efficiencies with the cycle number is shown in **Fig. 4-2-6** for the four current densities used. We observe that the initial CE of MC1 (soft, red curve) is again poor relative to GF1 (hard, black curve) but significantly improves over time, especially in the third set (**Fig. 4-2-6 c**). The native oxide soft sample MC2 show the worst performance in all cycles except those at the highest current density when all samples perform rather poorly **(Fig. 4-2-6 d)**.

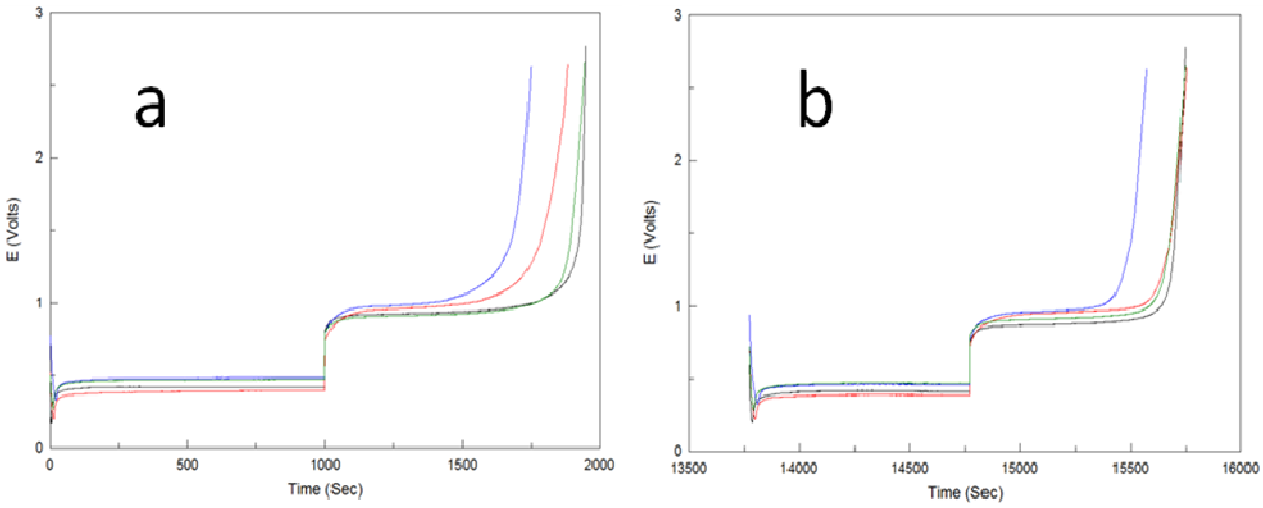

Figure 4-2-5: (a) First and (b) last galvanic cycles of two soft MC Al anodes MC1 and MC2 prepared with varying degrees of surface oxide remaining at a current density of 0.25 mA/cm^2. Comparative half-hard GF Al anodes GF1 and GF4 from Ch. 4.1 are included. Samples GF1 (hard, oxide removed), MC1 (soft, oxide removed), MC2 (soft, native oxide) and GF4 (hard, native oxide) are in black, red, blue and green colors, respectively. Cycles in the right figure have been offset to overlap the curves on the same time scale.

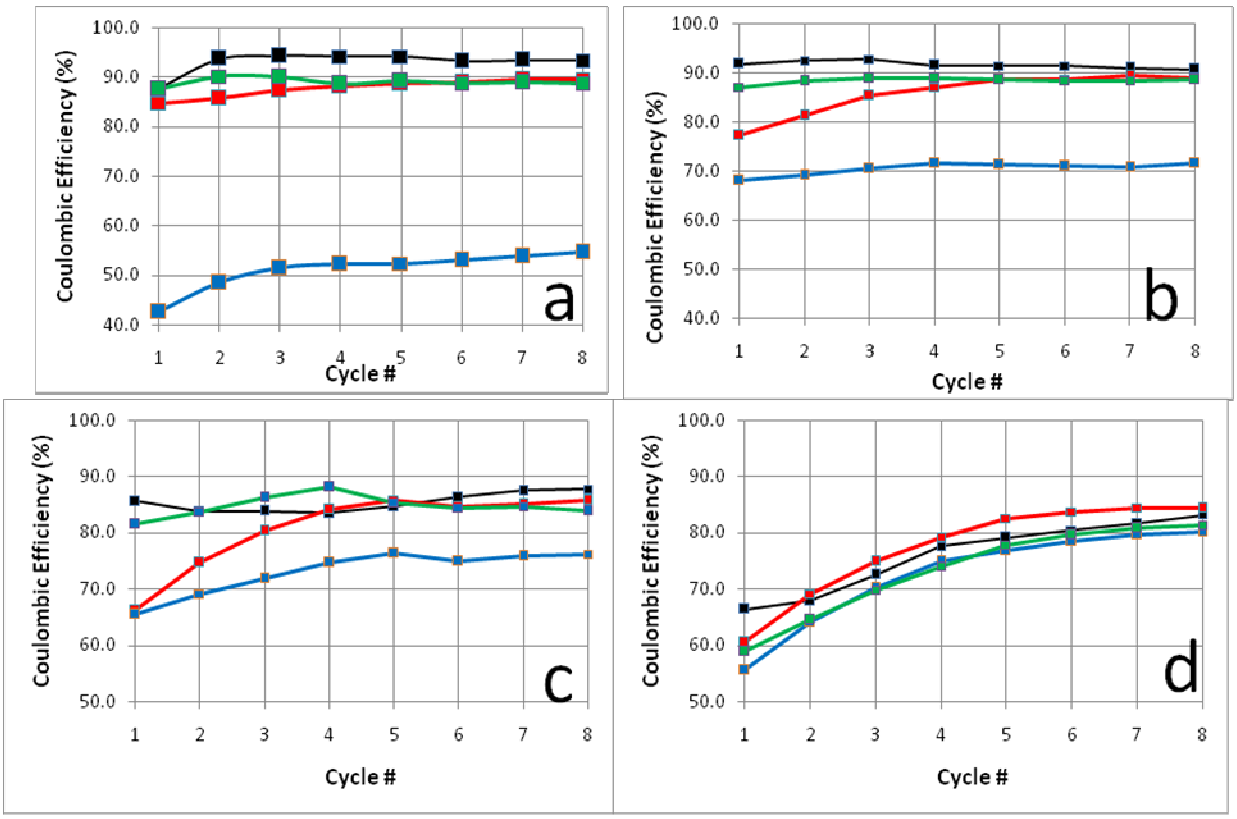

Figure 4-2-6: Coulombic efficiencies of two soft MC Al anodes MC1 and MC2 prepared with varying degrees of surface oxide remaining at current densities of (a) 0.13 (b) 0.25 (c) 0.5 and (d) 1 mA/cm^2. Comparative half-hard GF Al anodes GF1 and GF4 from Ch. 4.1 are included. Samples GF1 (hard, oxide removed), MC1 (soft, oxide removed), MC2 (soft, native oxide) and GF4 (hard, native oxide) are in black, red, blue and green colors, respectively.

Overall these series of 4x8 galvanic cycles suggest that soft MC Al anodes in most cases showed worse performance both in terms of reversibility/coulombic efficiency and plateau separation relative to half-hard GF Al. This may be due to more pronounced volume changes and repeated significant destruction/pulverization of the intermetallic phase during the delithiation scan, which would be consistent with the increased SEI formation observed in the CVs of MC Al anodes **(Fig. 4-2-1)**. This contrast again is likely related to the difference in mechanical properties (hardness) of the two materials.

However some brief conditioning at each current density allows for the formation of a more stable intermetallic phase and improved performance of MC Al by the eighth cycle (**Fig. 4-2-6 a-d**). While the presence of native oxide in MC Al (MC2) clearly has a strong detrimental effect on reversibility, there does appear to be a similar trend of improvement with cycling. There is also a considerable increase in performance with the removal of the oxide both with soft and half-hard Al (cf. MC2 and GF4, MC1 and GF1).

To investigate the stability and cycling ability of the MC Al anodes, we performed a half-cell failure experiment on a new sample MC3. The sample was prepared in the same way as "native oxide" sample MC2 described above. Considering the strong detrimental effect of increased oxide content on the reversibility for MC Al in the 4x8 cycles (**Fig. 4-2-6 a-c**), we wanted to observe a worst-case scenario here of drastic CE changes over time. As in the GF Al anode half-cell failure experiment in Ch. 4.1 no prior electroformation of the LiAl phase was performed using either a CV or galvanic cycles at low current densities. The cycling was commenced immediately at a high current density of 0.5 mA/cm^2 for a total of 264 cycles. This current density is equivalent to that of the third set of cycles in the 4x8 experiments.

Shown in **Fig. 4-2-7** is the full set of the corresponding galvanic cycles. One can see that the cycling behaviour is highly unstable compared to the similar experiment with half-hard GF Al (GF5) (**Fig. 4-1-8**). Here the plateau potential jumps occur with significantly larger amplitude and higher frequency. Before each jump the overvoltages both in the charging and discharging plateaus markedly increase so that the charge potential even drifts well below 0 V vs. Li^+/Li. **Fig. 4-2-8** shows the first two and last two cycles in black and red, respectively. Arrows in the red curve indicate the secondary and tertiary plateaus appearing over time in the discharge portion of the cycle, which were also observed with cycling of GF Al earlier in Ch. 4.1 (**Fig. 4-1-9**) and have been attributed to the diffusion-controlled delithiation of the α-LiAl intermetallic phase. One can see that the sample performance significantly deteriorated with cycling. Not only the reversibility of the charging-discharging processed got significantly lower, but also the overvoltages of the charging-discharging processes increased as well. The first red curve also shows

the instance of a potential jump, as indicated with an arrow. To further characterize the performance of the sample, the separation between the charge plateau and the main discharge plateau is plotted in **Fig. 4-2-9**, together with the coulombic efficiencies of the main as well as the secondary and tertiary discharge plateaus shown in **Fig. 4-2-10** and **Fig. 4-1-11** respectively for every fifth cycle starting from the first cycle. Additionally, the figures also show the data for cycles right before and after the potential jumps observed within the cycle set. We did not observe the secondary diffusion plateau until approximately the 25th cycle. Therefore the secondary process CE is absent within that initial region of **Fig. 4-2-11**. For the sake of comparison, the data from the half-hard GF Al half-cell failure experiment (GF5, oxide-removed) from Ch 4.1 are included in black color in both **Fig. 4-2-9** and **Fig. 4-2-10**, with the new soft MC3 data appearing in blue color.

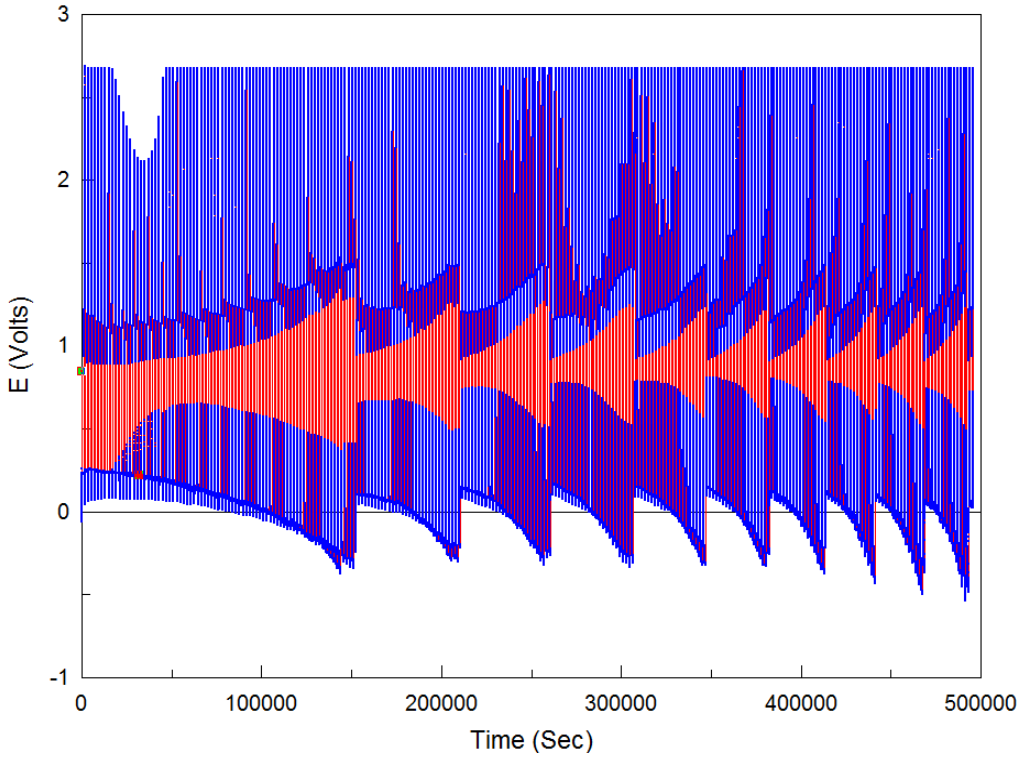

Figure 4-2-7: Full set of galvanic cycles for the MC3 soft MC Al anode with native oxide subjected to 264 cycles at a current density of 0.5 mA/cm^2 without an initial CV.

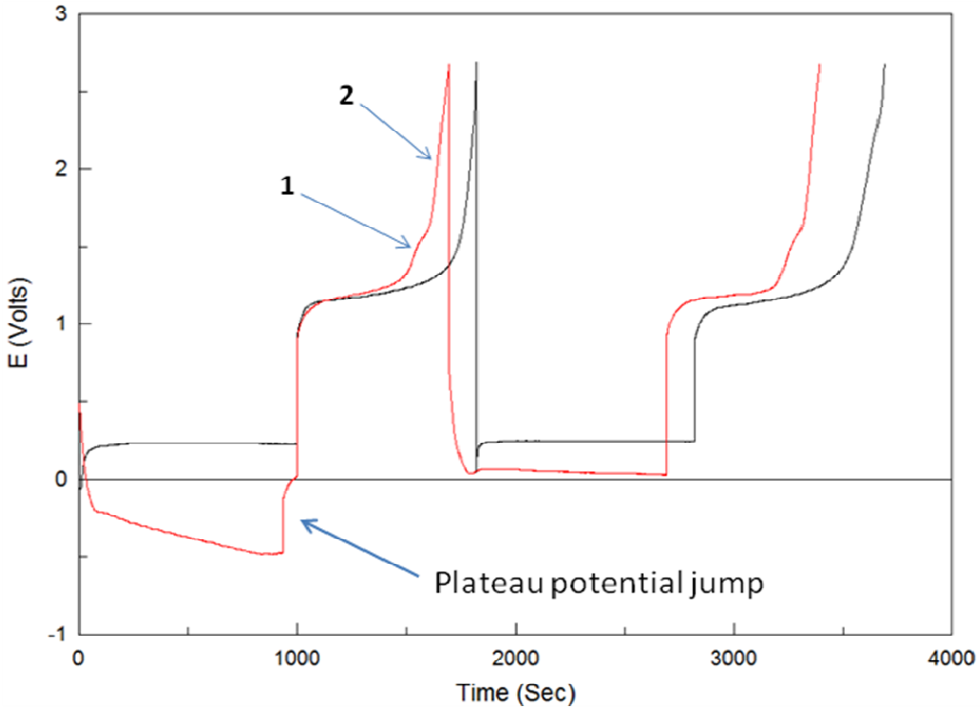

Figure 4-2-8: First two (black) and last two (red) galvanic cycles for the MC3 soft MC Al anode with native oxide subjected to 264 cycles at a current density of 0.5 mA/cm^2 without an initial CV. Numbers in the red curve denote the secondary and tertiary diffusion-limited plateaus. The red curve has been offset to overlap with the time scale of the black curve.

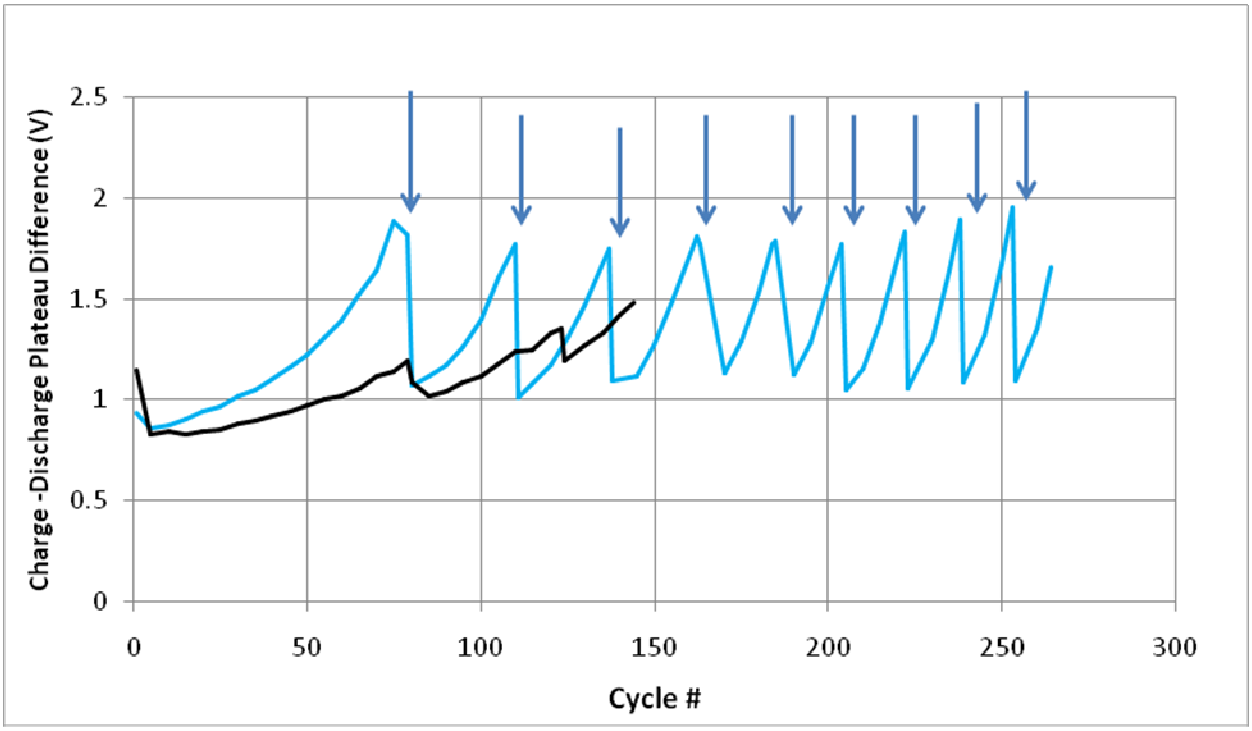

Figure 4-2-9: Charge-Discharge plateau separation (blue curve) for the main discharge plateau for MC3 soft MC Al anode with native oxide subjected to 264 cycles at a current density of 0.5 mA/cm^2 without an initial CV. For comparison, data for half-hard GF5 GF Al anode (oxide removed) from Ch. 4.1 are included in black. Plateau jump events in MC3 are indicated with arrows.

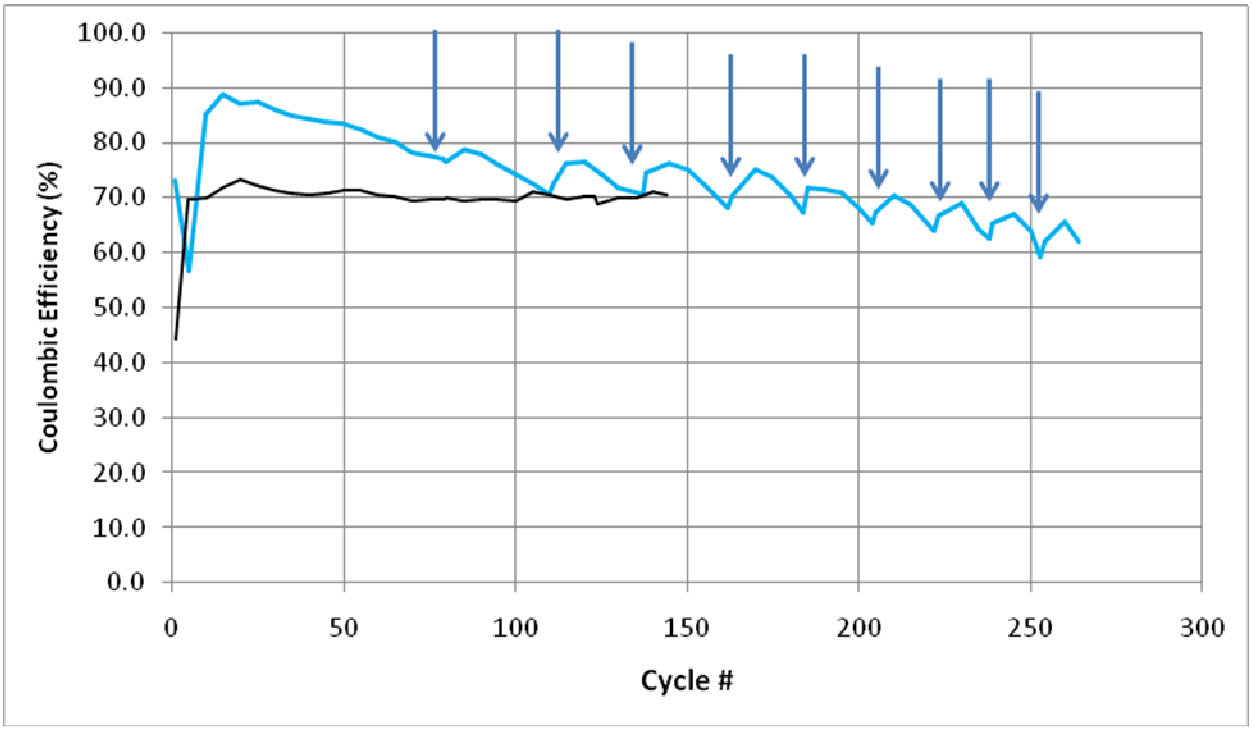

Figure 4-2-10: Coulombic efficiency data for the main discharge plateau (blue curve) for MC3 soft MC Al anode with native oxide subjected to 264 cycles at a current density of 0.5 mA/cm^2 without an initial CV. For comparison, data for half-hard GF5 GF Al anode (oxide removed) from Ch. 4.1 are included in black. Plateau jump events in MC3 are indicated with arrows.

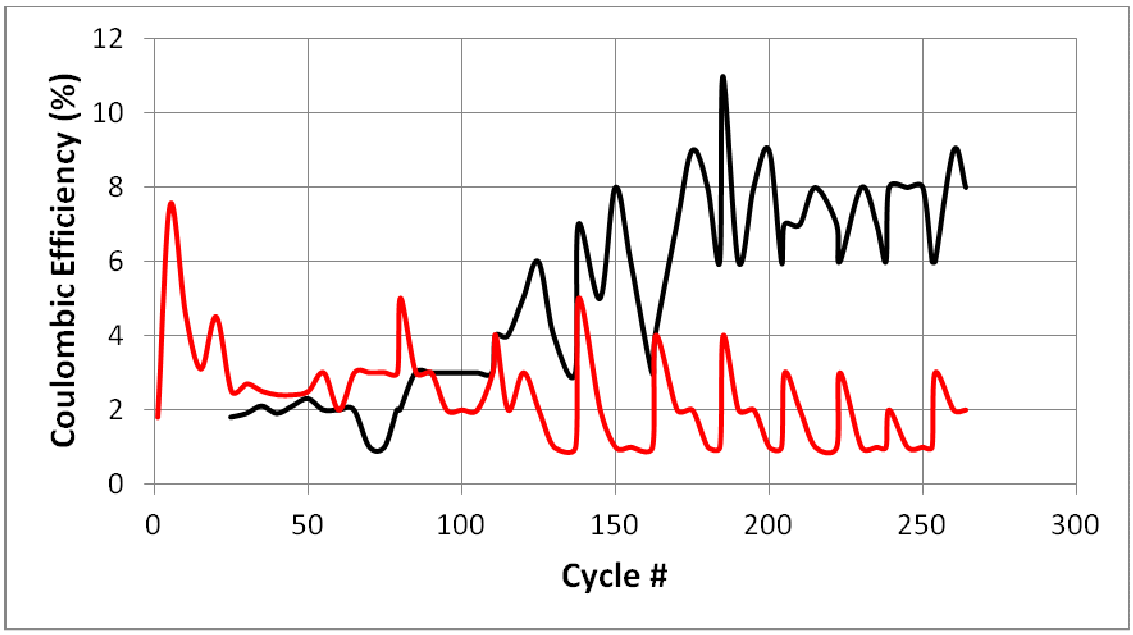

Figure 4-2-11: Coulombic efficiencies for the secondary (black) and tertiary (red) diffusion-limited discharge plateaus for MC3 soft MC Al anode with native oxide subjected to 264 cycles at a current density of 0.5 mA/cm^2 without an initial CV.

The very first cycle for the MC3 MC Al soft sample shows a large plateau separation of 0.935 V with a main CE of 73% (**Fig. 4-2-9, 4-2-10**). Upon closer examination the tertiary plateau has already appeared during discharge with about 2% CE (**Fig. 4-2-8 a**), though it may be difficult to see in the figure presented here. Progressing towards the fifth cycle there is a considerable shortening of the main plateau. This results in the main CE plummeting down to only 57% while the tertiary CE spikes up to a set maximum of 7%, even though the plateau separation decreases to 0.86V at this point (**Fig. 4-2-9, 4-2-10, 4-2-11**). Moving from the 5th to the 10th cycle, we see a sharp reversal of the main CE back up to 85%, partially driven by a drop in the tertiary CE down to 4% (**Fig. 4-2-10, 4-2-11**). Between the 10th and 20th cycles we encounter a very interesting feature (**Fig. 4-2-7**). Rather than being terminated by the upper limit the discharge peak reaches the full time constraint of 1000 s (equivalent to the 1000 s duration of the charging cycle). Therefore, the principal CE reaches a maximum value for the whole set at 89% with a plateau separation around 0.9V (**Fig. 4-2-9, 4-2-10**). This improvement is due to a

longer main plateau rather than a smaller charge associated with the diffusion-controlled processes because the CE of the tertiary plateau stays constant at around 3-4% (**Fig. 4-2-11**). The parallel appearance of a maximum principal CE and a minimum in the main plateau separation in MC3 is consistent with the similar behaviour for half-hard GF5.

Following the 25th cycle, a number of related trends begin to develop (**Fig. 4-2-7**). The secondary diffusion-limited plateau appears around 1.55V soon after the main plateau, with an initial CE of 2% (**Fig. 4-2-11**). This process will steadily grow to a maximum CE of almost 10% by the end of the set highlighting the structural changes at the electrode. This is noticeably higher than the maximum secondary process CE of 7% in half hard GF5 (GF Al), which is likely related to the larger capability for the volume changes due to intermetallic phase formation in MC Al anodes. After the 15th cycle the main CE of soft MC Al MC3 shows a constant steady drop accompanied by a continuous increase in the plateau separation (**Fig. 4-2-9, 4-2-10, 4-2-11**). The trends for diminishing the CE and increasing the separation are considerably faster for the soft MC3 than those observed within the same cycle region for the half-hard GF5. The downward curvature in the charging plateau for MC3 also becomes far more severe as it drifts negative below 0V. The main discharge plateau shifts positive over time and so do the potentials of the secondary and tertiary plateaus. By the 25th cycle the potential of the tertiary plateau reaches the cycle upper potential limit of +2.7V. Therefore the CE of this tertiary process drops to a value of 2-3% where it stays until we encounter the plateau jumps (**Fig. 4-2-11**).

By the 79th cycle the plateau separation for MC3 has increased to 1.82V. At the 80th cycle we observe the first jump in the plateau potentials (**Fig. 4-2-9**). Immediately following the jump the plateau separation resets to a smaller value of 1.08V and the charge plateau itself appears flat again. The principal CE also starts to improve. The diffusion plateau potentials shift downwards after the jump and we observe a local maximum of 5% for the tertiary CE as the process has a longer duration before being terminated by the upper limit (**Fig. 4-2-11**). However, in the other respects, the overall peak shape and width appeared fairly similar before and after the jump. After the jump

the MC3 system appears to briefly stabilize and improve. From the 80th to the 85th cycle the main CE increases to 79% with the plateau separation showing a small change to 1.1V (**Fig. 4-2-9, 4-2-10**). However, this effect is only temporary and soon again the same degradation trends continue. Approaching the 111th cycle the main CE has dropped to 73% and we observe a second plateau jump (**Fig. 4-2-9**). Once again the plateau separation resets to a smaller value of 1.01V and soon begins to increase again by the 115th cycle. As before the system briefly improves with the main CE increasing to 76% by the 120th cycle (**Fig. 4-2-10**). The third jump is then seen in the 138th cycle (**Fig. 4-2-9**). In comparison the GF Al failure anode GF5 only experienced two plateau jumps by the end of 140 cycles with far less severity and a main CE that was relatively unchanged during those events. We encounter six further plateau jumps in the set of 264 cycles for MC3, which become separated by progressively shorter intervals with increased severity in both the CE and plateau separation trends. The result is a set of cycles that look like a Christmas tree shape (**Fig. 4-2-7**). Throughout these plateau jumps the secondary process CE continues to climb while the tertiary contribution continues to show local maxima at each jump (**Fig. 4-2-11**). By the 264th cycle the main CE has dropped down to 62% from a set maximum of 89% with a plateau separation here of almost 1.7V (**Fig. 4-2-9, 4-2-10**).

The origin of these trends is likely to be systematic large scale cracking and removal of portions of the intermetallic structure from the surface of the Al anode as the stress of repeated lithiation/delithiation volume changes accumulates. This process is referred to as 'pulverization' of active material in the literature and is thought to be the dominant capacity loss mechanism for Al and other metal-alloying anodes [3]. As the mechanical stresses of cracks and voids accumulate there are ever greater driving forces required for lithiation/delithiation until a critical point is reached where a portion of the active material with the most accumulated stresses is broken into smaller pieces and removed from the electrode surface. This results in temporary improvements in the anode performance (the jump). Comparison between the MC3 (MC Al, native oxide) and GF5 (GF Al, oxide removed) samples suggests that the pulverization mechanism is far more severe in soft Al anodes. The softened mechanical properties of the MC Al allow for a

greater degree of volume change due to easier intermetallic phase formation relative to harder GF Al, as seen in the increased SEI formation, larger CV overvoltage, larger CV loop and increased cycle plateau separation (**Figs. 4-2-1 to 4-2-4**). At first, this process is favourable as suggested by a superior early performance of soft MC3 (CE of 89% relative to the maximum of 73% in GF5). However, this effect is short lived as the cycling continues and the stresses start to accumulate. In the end these softened mechanical properties exacerbated by the increased surface oxide content likely lead to impaired mechanical stability for MC Al against pulverization. If an MC Al anode prepared without surface oxide was cycled continuously at this current density we would still expect the performance degradation to be more severe than GF5, though the results could be more gradual than for MC3. The relation of the mechanical properties and capacity loss mechanisms in Al anodes will be further discussed in Ch. 5.

4.2.2 SEM images

Shown in **Fig. 4-2-12 a-f** are SEM images of the uncycled (a-b) and cycled areas (c-f) of the soft MC Al anodes MC1 (oxide removed) and MC2 (native oxide) after being subjected to the 4x8 experiments. Sample MC1 prepared with full oxide removal **(Fig. 4-2-12 c+e)** appears to have a cycled porous morphology that is more heterogeneous than the analogous half-hard GF Al anode GF1 (oxide removed) described in Ch. 4.1.2.

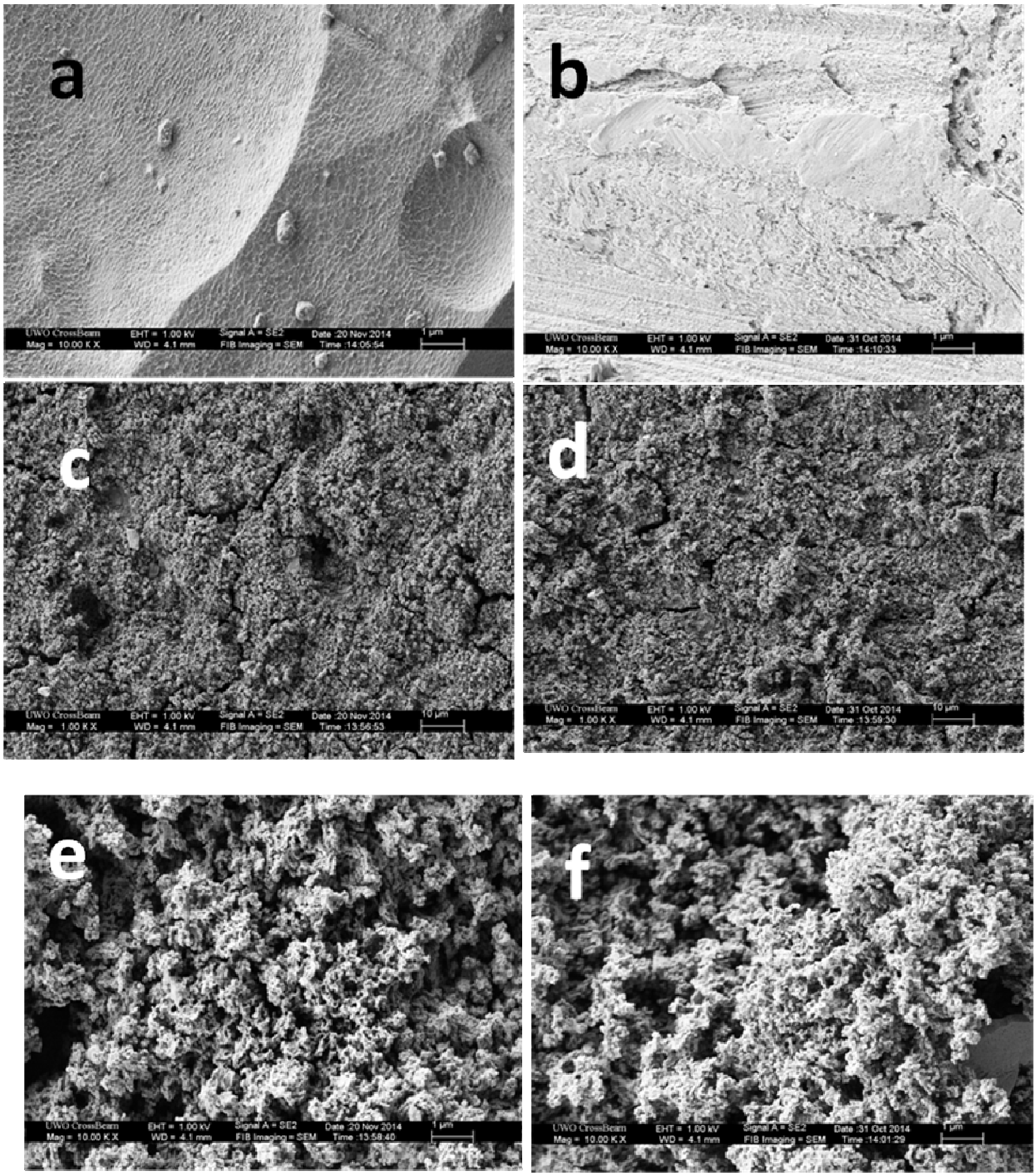

Figure 4-2-12: SEM images of uncycled (a, b) and cycled (c-f) areas for soft MC Al anodes MC1 (oxide removed) (a,c,e) and MC2 (native oxide) (b,d,f) after being subjected to 4x8 experiments. Magnifications of (a-b) 10000x; (c-d) 1000x; (e-f) 10000x.

There are numerous small cracks dispersed around the intermetallic material in this cycled area together with larger void size. Collectively these features reinforce a larger degree of volume change occurring in the soft MC Al anode compared to half-hard GF Al when prepared and cycled under identical conditions. The uncycled area of MC1 reveals the pattern typical for etched surfaces. It shows coarser larger grain sizes consistent with aluminium softened by thermal annealing **(Fig. 4-2-12 a)**. Sample MC2 with the original native oxide retained appears to take this trend even further. The cycled area has increased heterogeneity with even more cracking evident throughout the structure. **(Fig. 4-2-12 d+f)**. As expected the uncycled area is also much rougher than MC1 with no etching pattern visible **(Fig. 4-2-12 b)**.

Cycling the MC3 MC Al anode towards failure creates a multilayered structure with what appears to be a crust **(Fig. 4-2-13 a-c)**. There are long cracks dispersed among this structure with multiple voids of various sizes. This is in sharp contrast to the GF5 GF Al failure sample described in Ch. 4.1.2, which showed a fairly homogenous porous morphology broken into several large pieces. However it is important to note that the MC Al failure sample here was prepared without removal of native oxide. The crust present in this multilayer structure of MC3 may be due to intermetallic debris being released into the electrolyte solution due to pulverization of the active material observed in the galvanic cycles (**Fig. 4-2-7**). We did visually observe that such debris could readily separate from the cycled area into the solution when removing the MC3 anode from the cell after the galvanic cycles were completed.

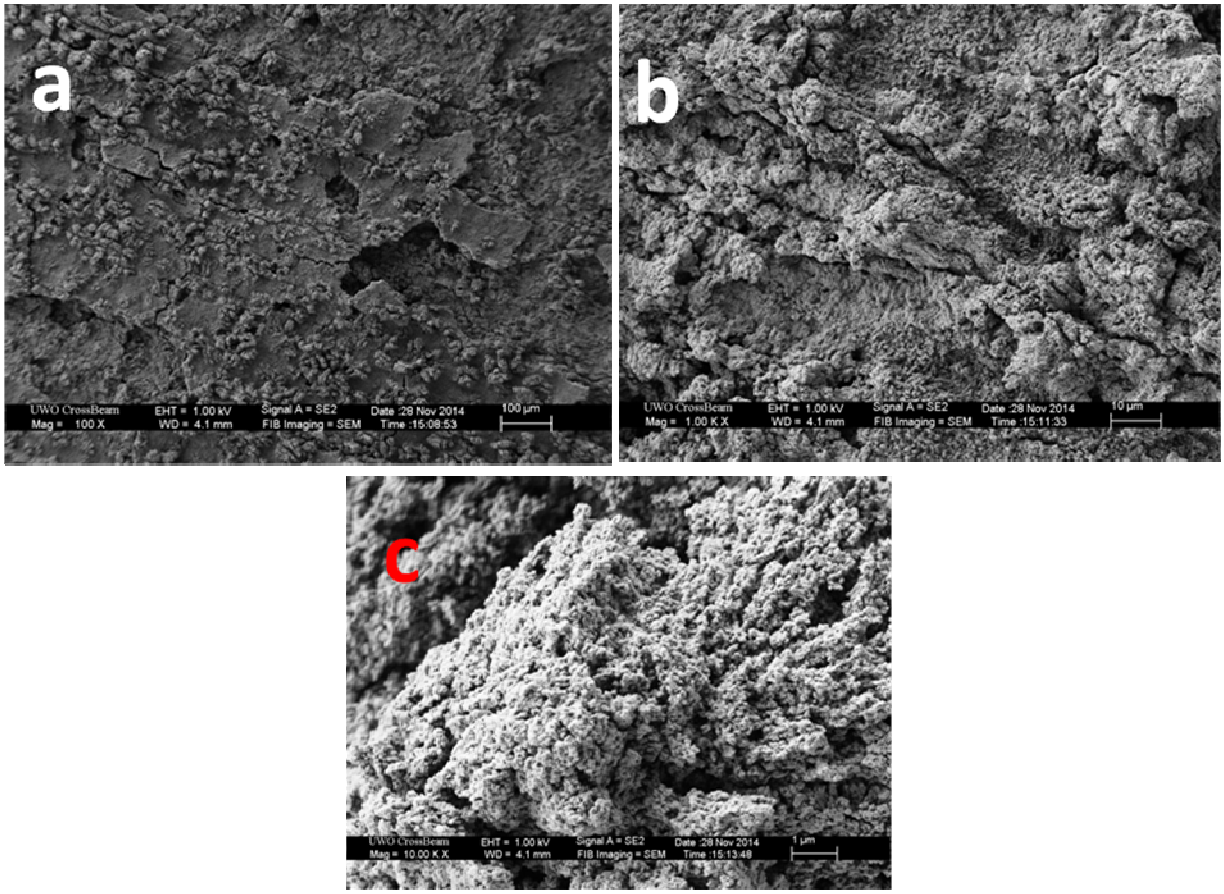

Figure 4-2-13: SEM images of cycled area for soft MC Al anode with native oxide MC3 after being subjected to 264 cycles at a current density of 0.5 mA/cm^2 without an initial CV. Magnifications of (a) 100x (b) 1000x (c) 10000x.

4.2.3 EDX Composition Chart

Shown in **Table 4-2-14** is the EDX composition chart of uncycled and cycled areas of the two soft MC Al anodes MC1 and MC2 after being subjected to the 4x8 experiments as well as the soft MC Al anode MC3 after being subjected to 264 cycles at a current density of 0.5 mA/cm^2. The predominance of Al within the uncycled area indicates unreacted aluminium substrate with surface contamination by the electrolyte (**a,c,e**). Carbon and oxygen content should arise from a combination of trace propylene carbonate

and residual surface oxide present after the various electrode preparations. Trace phosphorus and fluorine contents should arise from $LiPF_6$ salt remaining after rinsing. The small amount of silicon detected in all samples likely originates from a combination of silicon carbide paper used for polishing, and as an impurity commonly found in Al 1100 alloys. Lithium cannot be detected due to the overlap of its low energy X-rays with the baseline peak close to 0 eV. Less than one percent of Mg is detected in the spectra of both MC Al samples (**a,c**). This element was absent in the EDX spectra of all GF Al samples in Ch 4.1.3 (**Fig. 4-1-15**). These are both Al 1100 alloy materials and the Mg here is a trace amount. Therefore the differences observed in the electrochemistry of these two materials should still be based on the mechanical properties. The native oxide presence in sample MC2 results in a similar composition with higher oxygen content within the uncycled area (**c**). Again the minor increase in oxygen content for MC2 should be due to the 7 kV voltage mostly profiling the Al core below the crystalline oxide.

Table 4-2-14: EDX composition chart of uncycled and cycled areas of two MC Al anodes MC1 (oxide removed) and MC2 (native oxide) after being subjected to 4x8 experiments and MC Al anode with native oxide after being subjected to 264 cycles at a current density of 0.5 mA/cm^2 (MC3). Spectra were collected at a column voltage of 7 kV for 50 seconds at 1000x magnification.

		Atomic %						
Sample	**Area**	**C**	**O**	**F**	**Mg**	**Al**	**Si**	**P**
MC1	(a)Uncycled	1.74	1.42	0.32	0.66	95.15	0.68	0.04
	(b)Porous	4.89	32.95	28.54	0.39	32.16	0.42	0.65
MC2	(c) Uncycled	1.93	3.83	0.27	0.63	92.77	0.60	0.03
	(d)Porous	4.94	28.35	25.75	0.37	37.89	2.18	0.51
MC3	(e) Uncycled	1.73	1.18	0.22	0.69	95.54	0.54	0.10
	(f) Porous	2.20	8.62	62.96	0.09	24.06	0.83	1.24

The cycled porous area of MC1 shows significantly elevated carbon, oxygen and fluorine content (**b**). This is likely due to the presence of electrolyte within the intermetallic structure, as well as the products of solvent electroreduction and salt decomposition in the SEI layer (5). The cycled porous area of MC1 shows a nearly identical composition to GF Al sample GF1 described earlier (**d**). When pushed towards failure the MC3 anode resembles the cycled composition of MC1 but with dramatically higher F:O and F:Al ratios in both counts and percentages (**f**). Considering the $LiPF_6$ salt this fluorine content should predominantly come from the electrolyte. However it is not clear in what form does this elevated fluorine content exist within the systematically cracked intermetallic

structure. As described in the CVs of MC1 and MC2 the continued lithiation/delithiation of MC Al will cause some degree of additional SEI formation beyond the first cycle. With sustained cycling in MC3 mechanical stresses will accumulate in the form of cracking. This will continuously cause partial destruction of the SEI present within the structure and expose fresh Al material for more SEI formation. The $LiPF_6$ salt is also expected to thermally degrade over time into LiF and PF_5 if any trace moisture content is present [6].

4.2.4 References

1. Oltean, G.; Tai, C.W.; Edstrom, K.; Nyholm, L., *Journal of Power Sources*, **2014**, *269*, 266-273.
2. Van Den Beukel, A., *Acta Metall.,* **1980**, *28*, 965-969.
3. Liu, Y.; Hudak, N.S.; Huber, D.L.; Limmer, S.J.; Sullivan, J.P.; Huang, J.Y., *Nano Lett.* **2011**, *11*, 4188-4194.
5. Schroder, K.W.; Dylla, A.G.; Harris, S.J.; Webb, L.J.; Stevenson, K.J., *ACS Appl. Mater. Interfaces*, **2014,** *6,* 21510-21524.
6. Yang, H.; Zhuang, G., *Journal of Power Sources,* **2006,** *161,* 573-579.

4.3 Bare Duraluminum (Dural) Anodes, Al 2024 alloy, Heat-Treated

Summary

In Ch. 4.2 we investigated the effects of mechanical properties on lithiation/delithiation behaviour using McMaster-Carr Al (MC Al) (dead-soft) anodes compared to Goodfellow Al (GF Al) (half-hard) anodes. Here in Ch. 4.3 we take the study of the mechanical properties even further by using as an electrode material Duraluminum (Dural) with the native oxide removed. Dural is an Al 2024 alloy with 93% Al, 4-5% Cu and 1-2% Mg content manufactured through heat-treated precipitation hardening. The result is that Dural is considerably harder in terms of plastic deformations than any Al 1100 alloy material including MC and GF Al described in Chapters 4.1 and 4.2. The preparation of the Dural sample (DU1) used in this sub-chapter was described previously in the experimental details of Ch. 3. In particular, sample DU1 had the native surface oxide removed by polishing followed by etching in acidic solution. This sample was characterized electrochemically in a 4x8 experiment, which begins with a cyclic voltammogram (CV) for three scans, followed by four sets of eight galvanic cycles at progressively higher current densities. Overall we observed several features consistent with higher resistance against lithiation/delithiation in Dural, possibly due to the precipitated copper content within the alloy. In the initial CV this behaviour appeared as a larger overvoltage relative to both GF Al and MC Al anodes. In the galvanic cycles this behaviour appeared as a larger plateau separation as well as noticeably poorer coulombic efficiency (CE) at lower current densities. Surface analysis of sample DU1 after electrochemistry revealed increased heterogeneity in the porous intermetallic structure relative to GF Al and MC Al anodes with multiple areas of limited reactivity. An additional sample (DU2) of the same type as DU1 was characterized electrochemically in a failure experiment, in which galvanic cycling of the anode begins immediately at a higher current density without initial conditioning through a CV. This cycling was sustained for 300 cycles to observe the anode performance over time. Severe diffusion-

limited losses of coulombic efficiency (CE) relative to GF Al and MC Al anodes were observed, in an otherwise relatively stable charging/discharging response with few plateau jumps. Surface analysis revealed a fully reactive anode material with no evidence of systematic cracking characteristic of pulverization. The results show that the degradation behaviour observed with MC and GF Al and described in Ch. 4.1 and 4.2 is indeed related to the mechanical properties of materials. However, the presence of Mg and Cu in the Dural alloy seems to be quite detrimental for the lithiation-delithiation processes; therefore, Dural was dismissed as a potential candidate for Al-based anodes for Li-ion batteries.

4.3.1 Cyclic Voltammograms, Galvanic Cycles, Calculations

The typical features of CVs with Al anodes were described previously in Ch. 4.1.1. Therefore, this section will focus only on differences observed in the CV features of Dural anodes relative to half-hard GF Al and soft MC Al anodes. First we consider the partial cathodic scans between 2V and 0.25V vs. Li^+/Li reference electrode (**Fig. 4-2-1**). For the purposes of comparison the data for analogous GF Al and MC Al anodes GF1 and MC1 with the native oxide removed from Ch. 4.1 and 4.2 are included. The bolded numbers **1** to **3** denote the GF1 (hard, oxide removed), MC1 (soft, oxide removed) and DU1 (Dural, oxide removed) samples respectively.

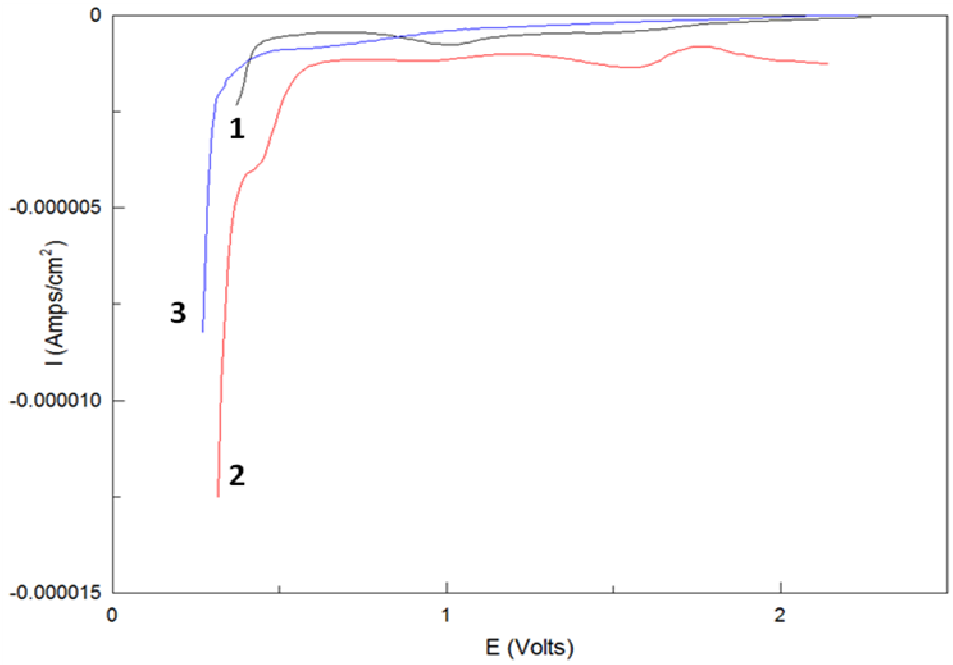

Figure 4-3-1: Initial cyclic voltammogram of Dural anode DU1 prepared with oxide removed (curve 3, blue). Comparative data for half-hard GF1 GF Al (curve 1, black) and soft MC1 MC Al (curve 2, red) anodes from Ch. 4.1 and 4.2 are also included. Partial cathodic scans from 2V to 0.25V to highlight SEI formation and lithiation onset behaviour.

Dural (DU1, blue curve 3) shows a cathodic current for SEI formation that is comparable to half-hard GF Al (GF1, black curve 1) but noticeably less than soft MC Al (MC1, red curve 2). This SEI formation appears broadened with no distinct reduction peaks observed before the onset of lithiation. The absence of reduction peaks in Dural may be related to the alloying Cu and Mg elements. Further CV scans produce additional SEI formation for DU1 that is intermediate between that of GF1 and MC1. Moving on, we observe that Dural (curve 3) shows a significantly later onset relative to both GF Al (curve 1) and MC Al (curve 2). This large difference is likely due to the increased driving force required for lithiation of Dural. As described previously, Cu in Dural primarily precipitates at the grain boundaries where lithiation should begin. Since the Cu content is inert towards lithiation [1], it should increase the resistance of the anode to lithiation of Al and formation of an intermetallic phase. The onset slope of Dural appears similar to MC Al but steeper than GF Al. Further scanning produces consistently later lithiation

onset potentials in the CV for Dural relative to GF Al and MC Al with a slope comparable to MC Al.

Next we compare the full CV scans of all samples in **Fig. 4-3-2**. Dural shows well defined nucleation loops in the anodic scan with the size comparable to soft MC Al.

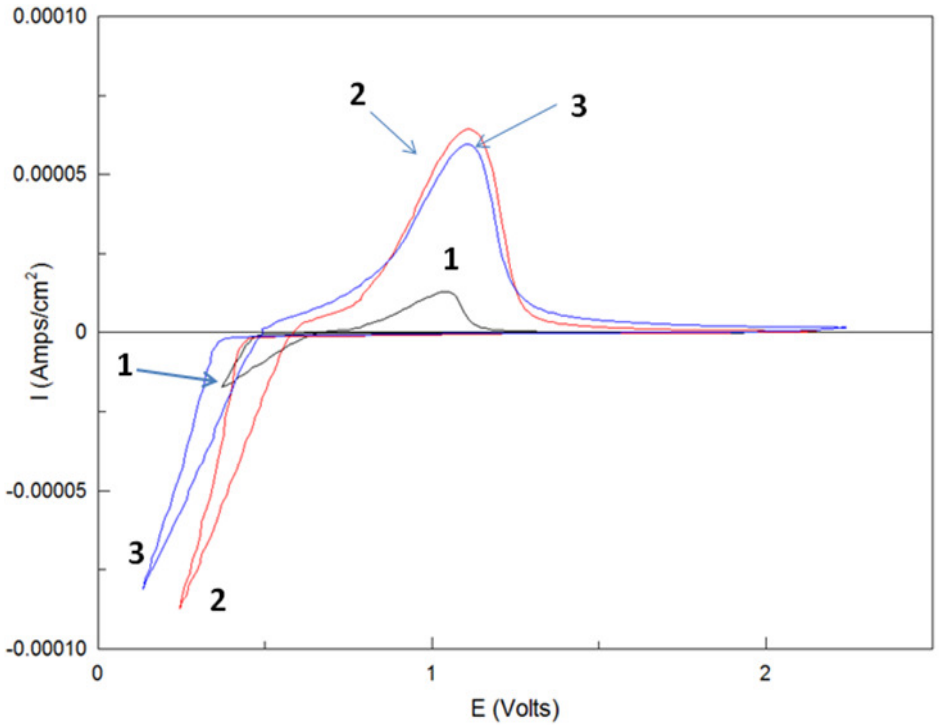

Figure 4-3-2: Initial cyclic voltammogram of Dural anode DU1 (blue, curve 3) prepared with oxide removed. Comparative data for half-hard GF1 GF Al (black, curve 1) and soft MC1 MC Al (red, curve 2) anodes from Ch. 4.1 and 4.2 are also included.

The delithiation peak potential is shifted positively in DU1 (Dural) relative to GF1 (GF Al). This suggests that the overvoltage for the lithiation process is considerably larger for Dural compared to half-hard GF Al. While the delithiation peak potential of DU1 is similar to that for soft MC Al MC1, the MC1 anode still has an earlier lithiation onset

potential. Therefore, Dural has a larger overvoltage relative to soft MC Al as well, although the difference is smaller. As is the case with the lithiation onset potentials, the increased overvoltages here suggest increased resistance against lithiation resulting from inert Cu precipitates at the grain boundaries.

Shown in **Fig. 4-3-3** are the typical features of galvanic cycles for the Dural anode DU1 (blue color) and the half-hard GF Al anode GF1 (black color) at a current density of 0.25 mA/cm^2. Overall we observe a similar sequence of events (denoted in the numbers **1** to **5**) as was described previously in Ch. 4.1 and 4.2. Dural shows increased downward and upward curvature in charge and discharge plateaus respectively, with significantly more curvature also appearing immediately following the IR jump. These features indicate pronounced changes in the electrochemical kinetics with Dural. Additionally, there are considerable differences in terms of plateau separation and the reversibility of the charging-discharging processes, which are presented in detail in the next figures.

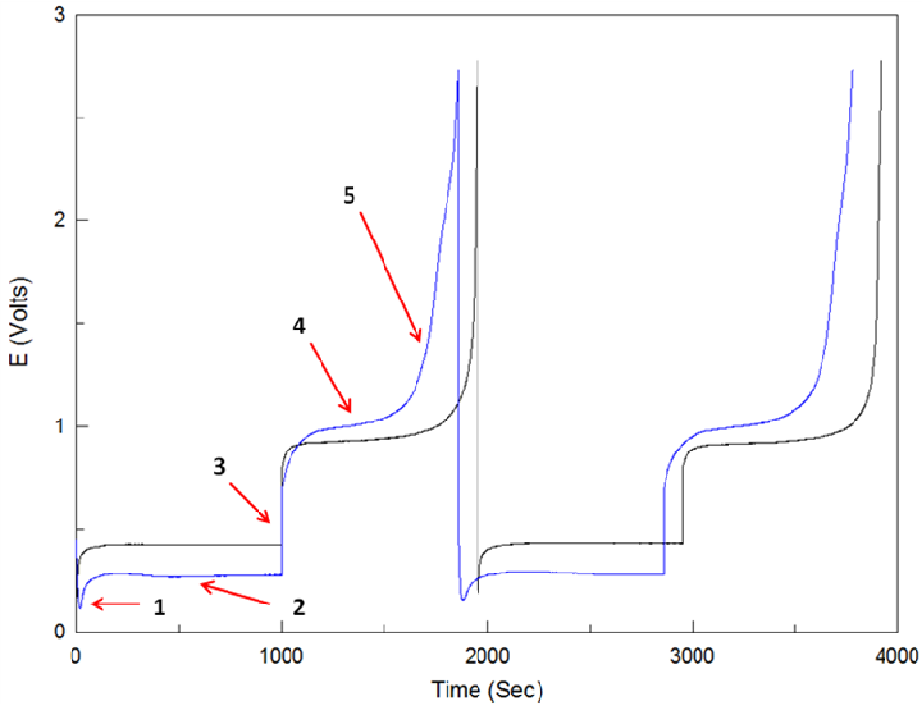

Figure 4-3-3: Typical galvanic cycles for lithiation/delithiation of a Dural anode (blue curve). This is sample DU1 which was subjected to polishing and etching in acidic conditions prior to electrochemical scans. Comparative data for half-hard GF Al anode GF1 from Ch. 4.1 are also included (black curve). Numbers indicate the features of interest: (1) potential overshot (2) charge plateau (3) IR drop (4) discharge plateau (5) discharge tail. Galvanic cycles are shown at a current density of 0.25 mA/cm^2.

Shown in **Fig. 4-3-4** are the set of galvanic cycles for the Dural anode DU1 (blue) at a current density of 0.25 mA/cm^2. The comparative cycle sets of the half-hard GF Al and soft MC Al anodes GF1 and MC1 are included in black and red colors respectively. For Dural, we observe a stable charging/discharging response, even though the reversibility of the main discharge plateau is worse. Throughout the set, Dural has a significantly lower charge plateau potential and much larger plateau separation than both GF1 (half-hard GF Al) and MC1 (soft MC Al), consistent with the later lithiation onset potential and larger overvoltage seen in the CV (**Fig. 4-3-2**). Furthermore, the charge plateau of

DU1 Dural has increasing downward curvature unlike the flat shape of GF1 and MC1. Taken together, these features suggest again that the presence of inert Cu in Dural significantly increases its resistance to lithiation-delithiation as compared to the same processes in Al 1100 materials. This results in increased contribution of diffusion-limited processes, which is clearly seen in the discharge peak shape.

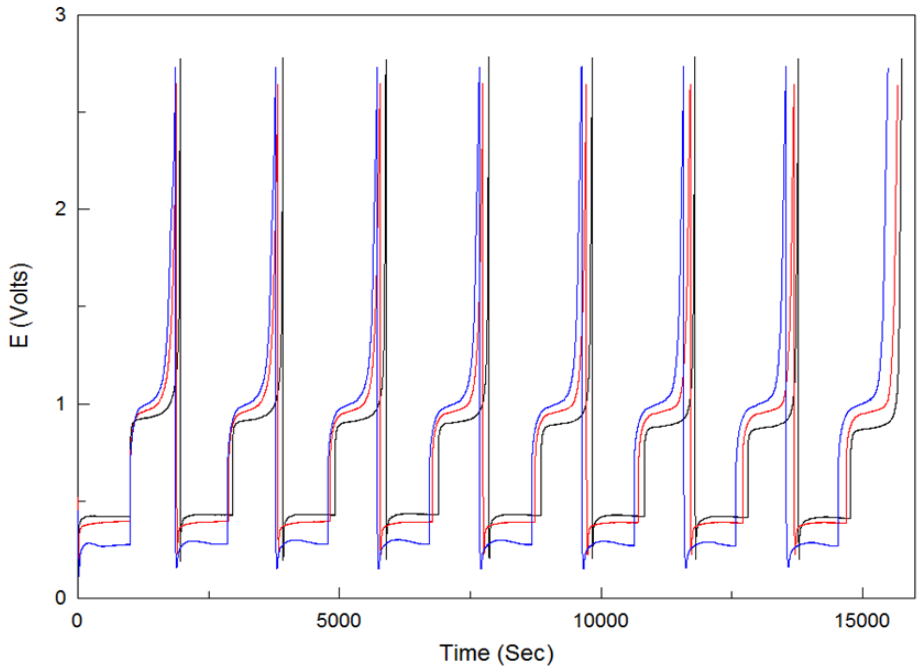

Figure 4-3-4: Galvanic cycles for Dural DU1 anode (blue) prepared with oxide removed at a current density of 0.25 mA/cm^2. Comparative data for half-hard GF1 GF Al (black) and soft MC1 MC Al (red) anodes from Ch. 4.1 and 4.2 are also included.

Shown in **Fig. 4-3-5** is the comparison of the first (a) and last (b) galvanic cycles for these three samples in this set. One can see that the presence of alloying elements in Dural initially decreases significantly the duration of the main discharge plateau and thus the coulombic efficiency (CE) relative to both half-hard GF Al and soft MC Al (**Fig. 4-3-5 a**). The effect is severe enough for the diffusion-limited discharge plateaus (indicated with arrow) to appeared as early as in the second set of cycles in a 4x8 experiment. In

comparison, GF1 (half-hard) and MC1 (soft) samples will not show diffusion-limited discharge plateaus until the third or fourth sets. By the eighth cycle, the discharge peak shapes become comparable but the discharge plateau of DU1 remains shorter (**Fig. 4-3-5 b**). The evolution of the coulombic efficiencies with the cycle number is shown in **Fig. 4-3-6** for the four current densities used. One can see that the CE of DU1 (Dural, blue curve) is the worst among all samples at all current densities except the highest one, where all samples performed rather poorly, but significantly improves over time similar to the trend for MC1 (MC Al, red curve) **(Fig. 4-3-6 c).**

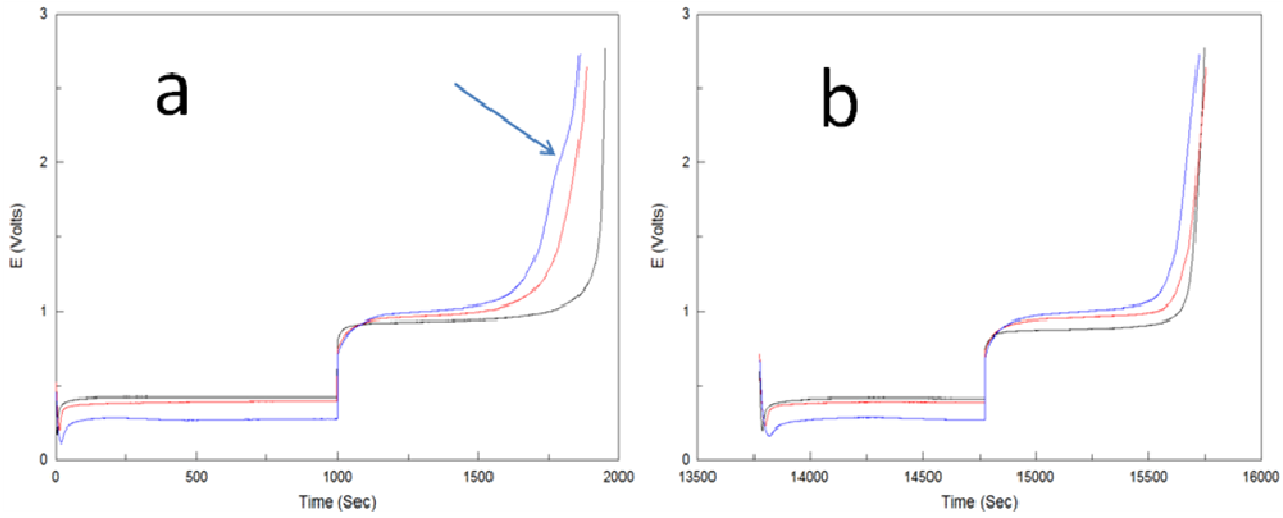

Figure 4-3-5: (a) First and (b) last galvanic cycles of Dural anode DU1 (blue) prepared with oxide removed at a current density of 0.25 mA/cm^2. Comparative data for half-hard GF Al (black) and soft MC Al (red) anodes GF1 and MC1 from Ch. 4.1 and 4.2 are also included. Cycles in the right figure have been offset to overlap the curves on the same time scale. Arrow indicates appearance of diffusion-limited discharge plateau in DU1.

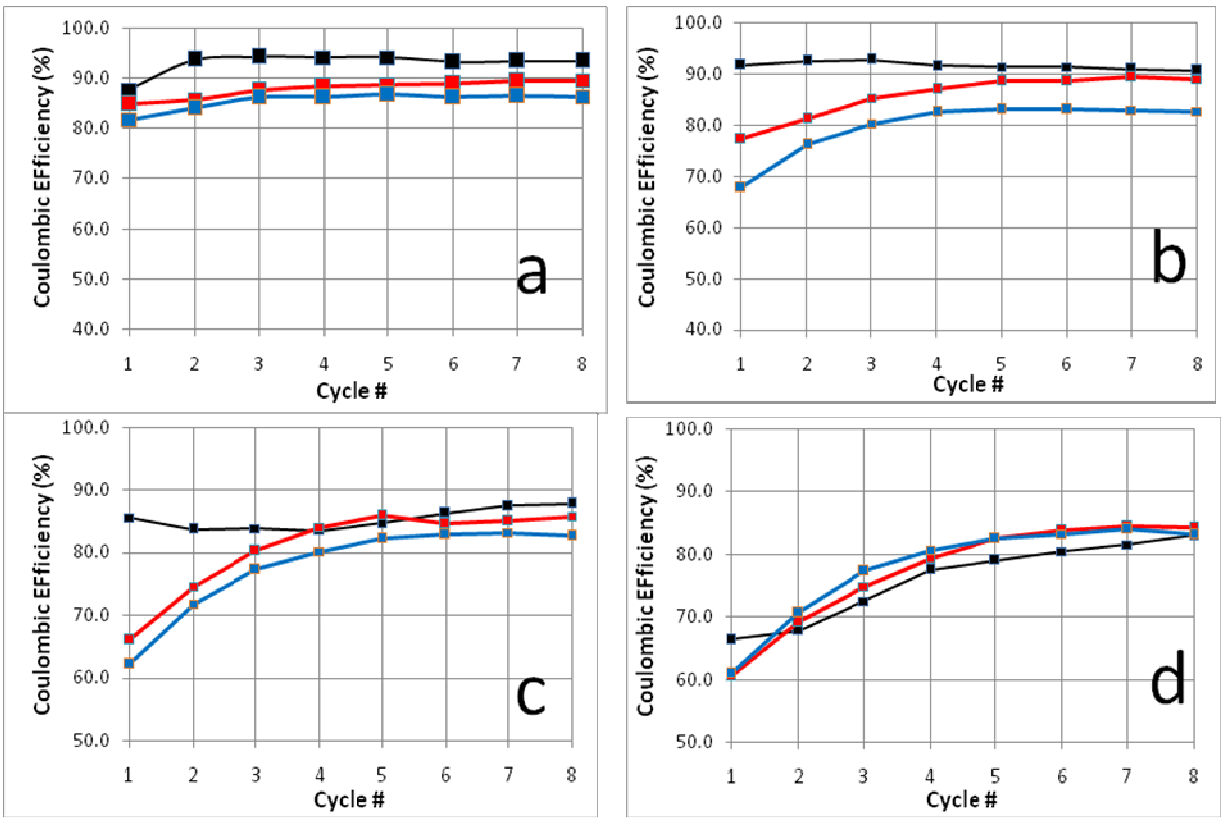

Figure 4-3-6: Coulombic efficiencies for Dural anode DU1 (blue) prepared with oxide removed at current densities of (a) 0.13 (b) 0.25 (c) 0.5 and (d) 1 mA/cm^2. Comparative data for half-hard GF Al (black) and soft MC Al (red) anodes GF1 and MC1 from Ch. 4.1 and 4.2 are also included.

To investigate the stability and cycling ability of the Dural anode, we performed a half-cell failure experiment on a new sample DU2. The sample was prepared in the same way as "oxide removed" sample DU1 used for the 4x8 experiment. We chose an oxide-free preparation for DU2 to have a clear comparison of mechanical stability and lithiation-delithiation behaviour under continuous cycling relative to the oxide-free GF Al failure anode GF5 from Ch 4.1 (**Fig. 4-1-8**). As in the previous half-cell failure experiments described in Ch. 4.1 and 4.2, no prior electroformation of the LiAl phase was performed using either a CV or galvanic cycles at low current densities. The cycling was commenced immediately at a high current density of 0.5 mA/cm^2 for a total of 300

cycles. This current density is equivalent to that of the third set of cycles in the 4x8 experiment.

Shown in **Fig. 4-3-7** is the full set of the corresponding galvanic cycles. One can see that the cycling behaviour is relatively stable compared to half-hard GF Al (**Fig. 4-1-8**) and soft MC Al (**Fig. 4-2-7**) anodes. There is only one plateau potential jump observed early around 120000 sec with the charge plateau potential not drifting below 0V vs. Li^+/Li until much later around 400000 sec. Approaching the 500000 sec region and beyond there is noticeable degradation of cycling stability, possibly indicating the usable limit for cycling of Dural under these conditions. **Fig. 4-3-8** shows the first two and last two cycles in black and red respectively. Arrows in the red curve indicate the secondary and tertiary plateaus appearing over time in the discharge portion of the cycle, which were also observed with cycling of GF Al in Ch. 4.1 (**Fig. 4-1-9**) and MC Al in Ch. 4.2 (**Fig. 4-2-8**), and have been attributed to the diffusion-controlled delithiation of the α-LiAl intermetallic phase. To further characterize the performance of the sample, the separation between the charge plateau and the main discharge plateau is plotted in **Fig. 4-3-9** for every fifth cycle, together with the coulombic efficiencies of the main as well as the secondary and tertiary discharge plateaus shown in **Fig. 4-3-10** and **Fig. 4-3-11**, respectively . Additionally, the figures also show the data for cycles right before and after the potential jumps observed within the cycle set. For DU2 we did not observe the secondary diffusion plateau until approximately the 25th cycle. Therefore the secondary process CE is absent within that region of **Fig. 4-3-11**. For the sake of comparison, the data for the half-hard GF Al half-cell failure experiment (GF5) from Ch. 4.1 and soft MC Al half-cell failure experiment (MC3) from Ch. 4.2 are included in black and blue colors respectively in both **Fig. 4-3-9** and **Fig. 4-3-10**, with the new DU2 (Dural) data in yellow.

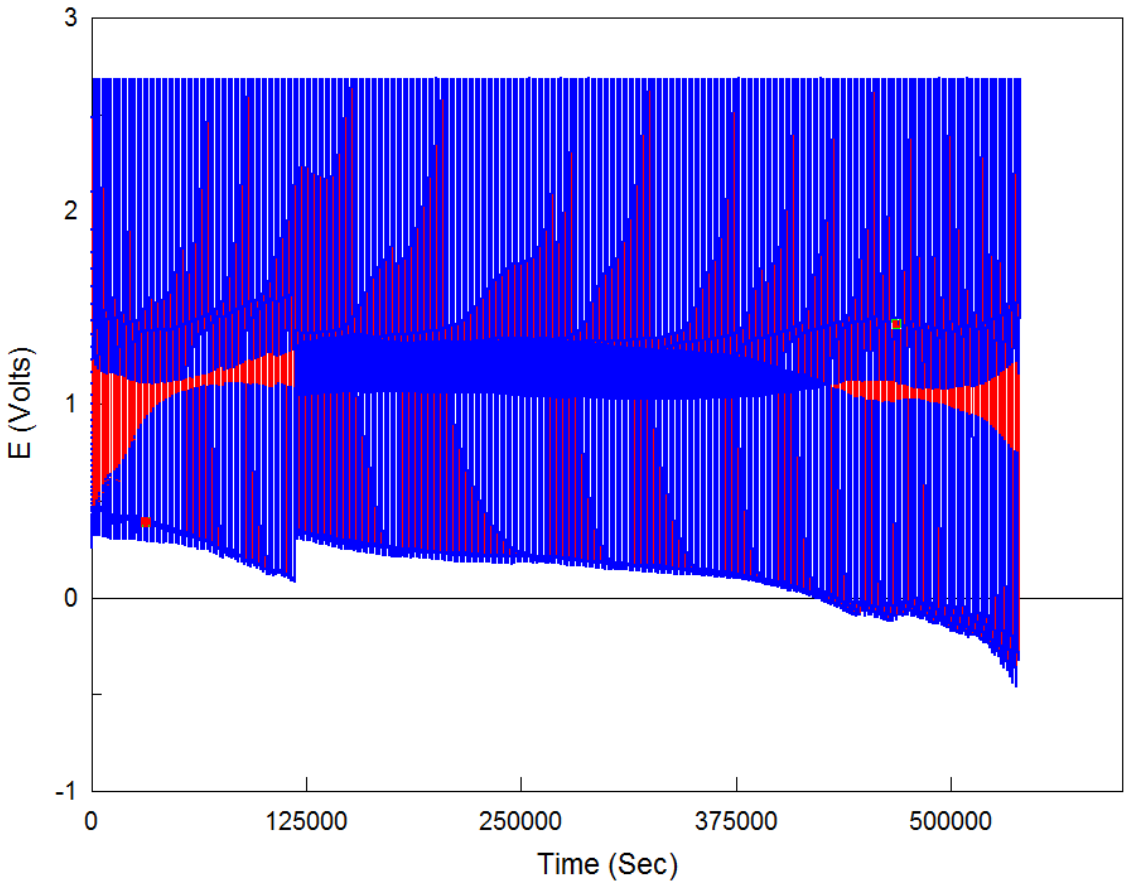

Figure 4-3-7: Full set of galvanic cycles for the DU2 Dural anode prepared with oxide removed and subjected to 300 cycles at a current density of 0.5 mA/cm^2 without an initial CV.

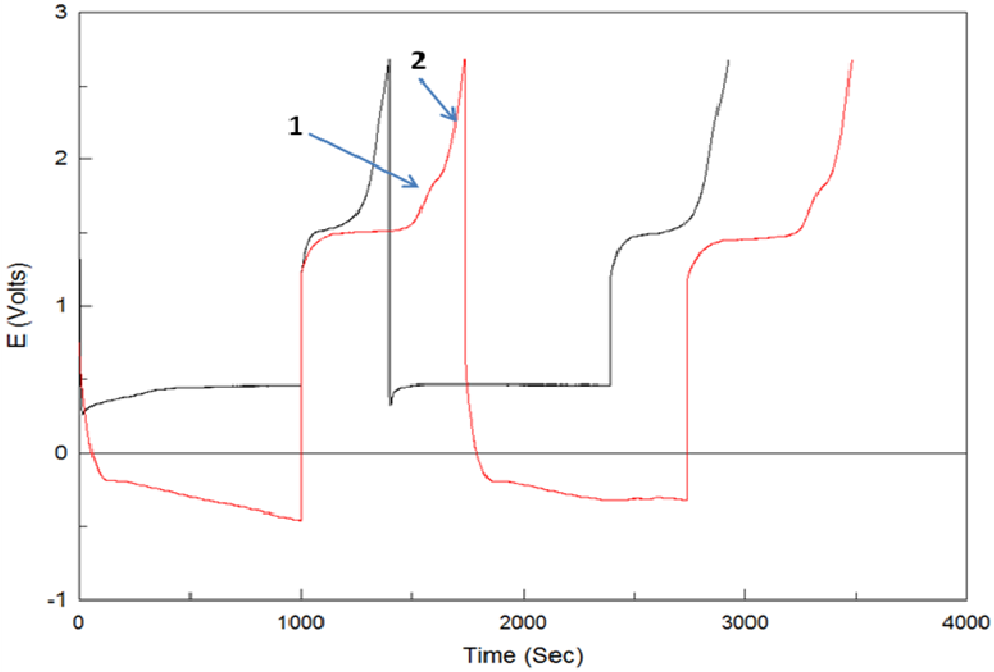

Figure 4-3-8: First two (black) and last two (red) galvanic cycles for the DU2 Dural anode prepared with oxide removed and subjected to 300 cycles at a current density of 0.5 mA/cm^2 without an initial CV. Numbers in the red curve denote the secondary and tertiary diffusion-limited plateaus. The red curve has been offset to overlap with the time scale of the black curve.

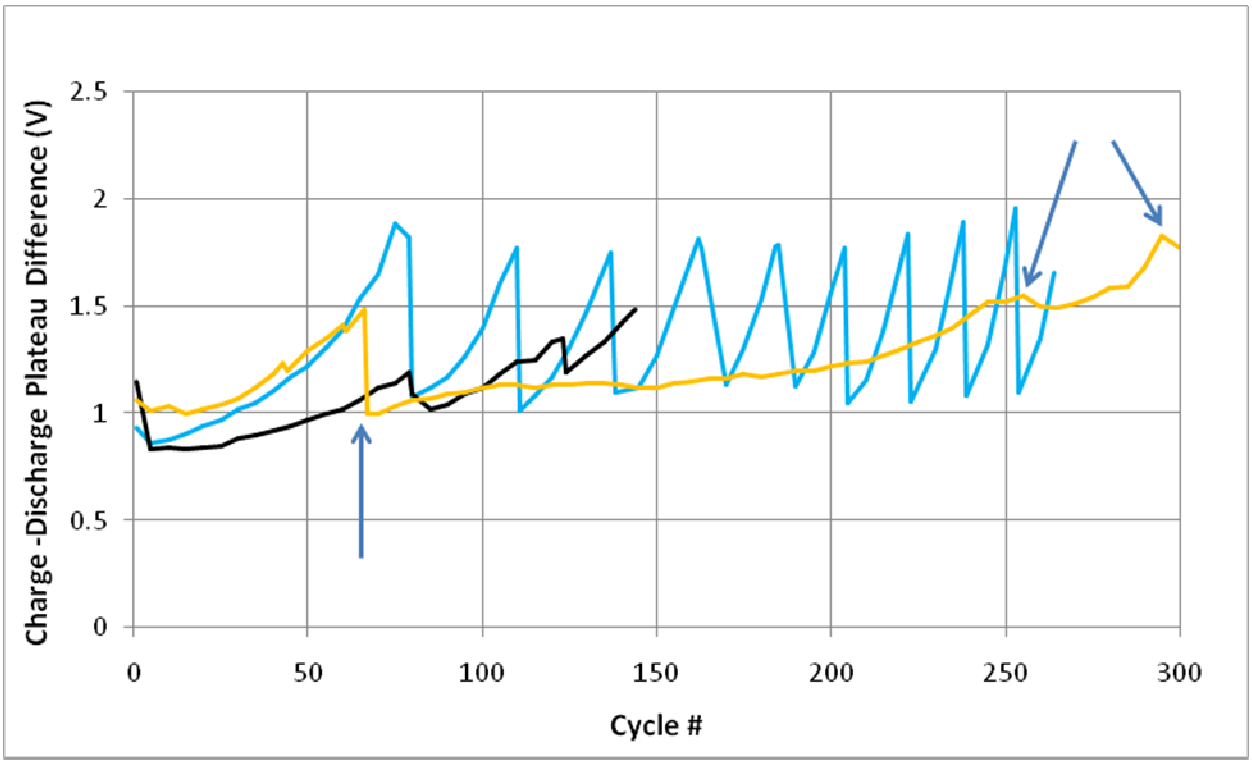

Figure 4-3-9: Charge-Discharge plateau separation (yellow curve) for the main discharge process for DU2 Dural anode prepared with oxide removed and subjected to 300 cycles at a current density of 0.5 mA/cm^2 without an initial CV. For comparison, the data for half-hard GF5 GF Al (black) and soft MC3 MC Al (blue) anodes from Ch. 4.1 and 4.2 are included. The plateau jump events in DU2 are indicated with arrows.

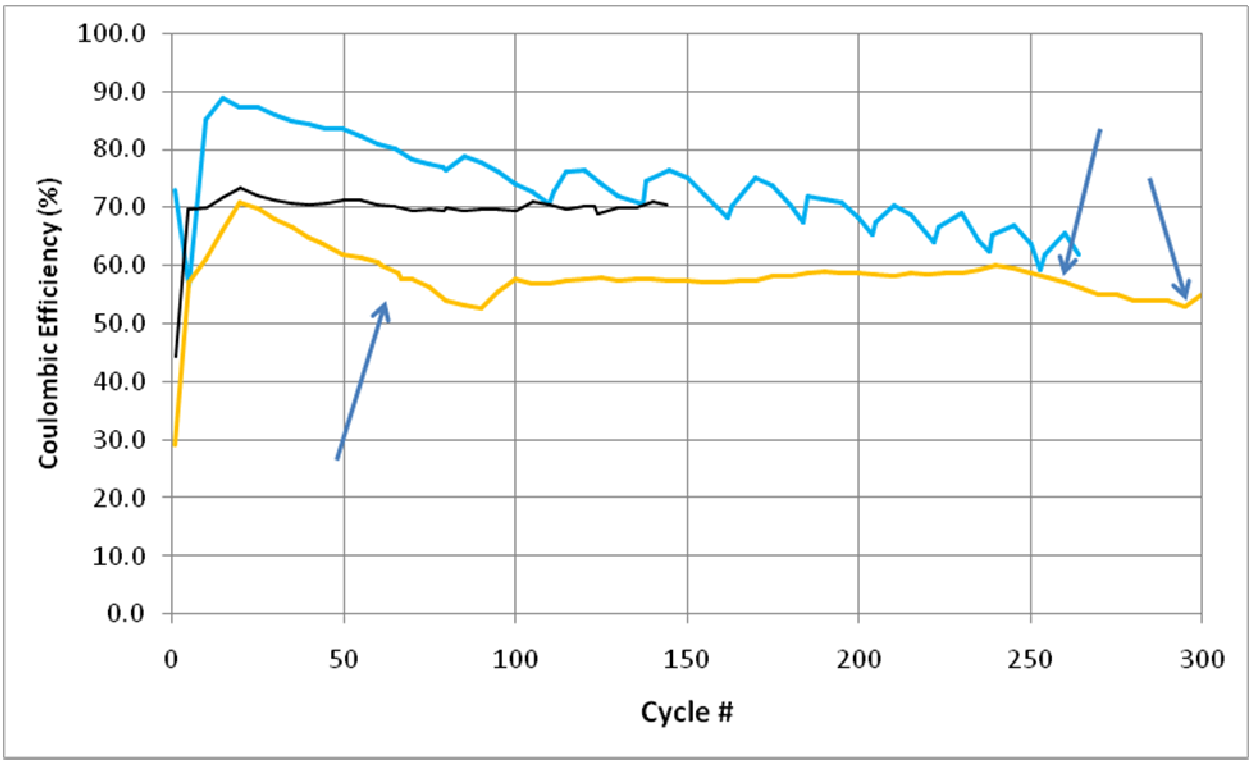

Figure 4-3-10: Coulombic efficiency data for the main discharge plateau (yellow curve) for DU2 Dural anode prepared with oxide removed and subjected to 300 cycles at a current density of 0.5 mA/cm^2 without an initial CV. For comparison, the data for half-hard GF5 GF Al (black) and soft MC3 MC Al (blue) anodes from Ch. 4.1 and 4.2 are included. The plateau jump events in DU2 are indicated with arrows.

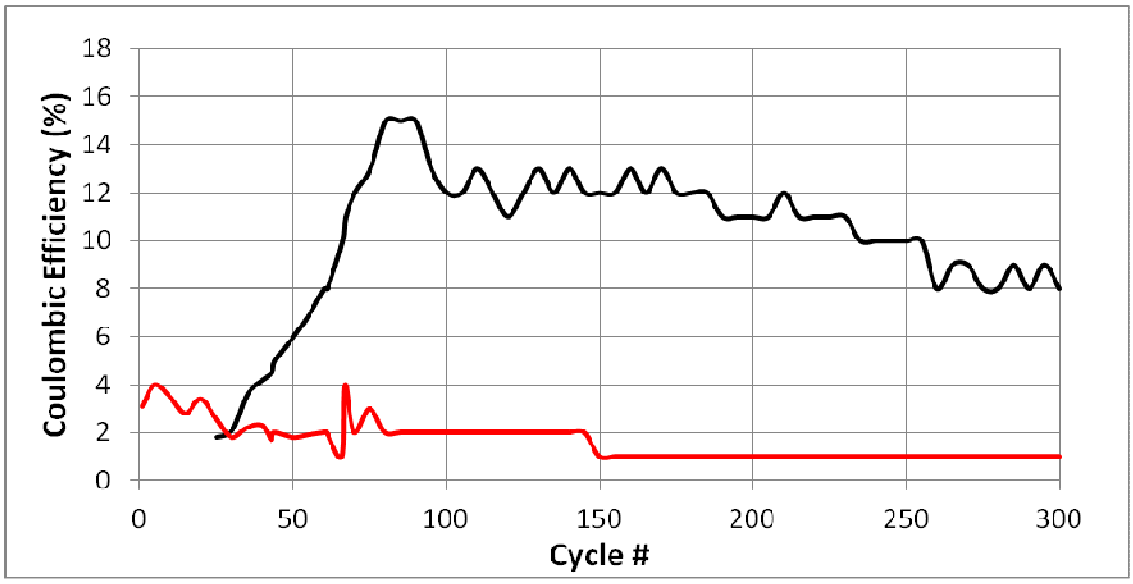

Figure 4-3-11: Coulombic efficiencies for the secondary (black) and tertiary (red) diffusion-limited discharge plateaus for DU2 Dural anode (oxide removed) and subjected to 300 cycles at a current density of 0.5 mA/cm^2 without an initial CV.

The very first cycle for the DU2 Dural sample shows a plateau separation of 1.06V with a main CE of only 29% (**Fig. 4-3-9, 4-3-10**). Upon closer examination the tertiary plateau has already appeared during discharge with about 3% CE (**Fig. 4-3-8 a).** The reversibility of DU2 rapidly improves by the fifth cycle to a separation of 1.01V and main CE of 57% with the tertiary process CE also increasing to 4% (**Fig. 4-3-9, 4-3-10, 4-3-11**). Progressing from the 5th to the 20th cycle, we observe another large improvement in main CE, reaching a maximum for the whole set at 71% with the plateau separation remaining small around 1.02V. This large improvement between the first and 20th cycles is driven by a significant increase in the length of the main plateau rather than that associated with the diffusion-controlled processes. In fact, the tertiary CE remains relatively unchanged around 3% by the 20th cycle (**Fig. 4-3-11**). At the 25th cycle the secondary diffusion-limited plateau appears at 1.74V soon after the main plateau, with an initial CE of 2% (**Fig. 4-3-11**). This diffusion-limited process will steadily grow to a maximum efficiency of 15% by cycle 90. The maximum efficiency of this secondary process is considerably higher than the value of 8% observed in the half-hard GF Al

failure anode (GF5, oxide removed) (**Fig. 4-1-12**). This illustrates again how the reversibility of Dural suffers from the presence of alloying elements like copper, similar to what was observed in the 4x8 experiment (**Fig. 4-3-5, 4-3-6**). It is the presence of this secondary process growing rapidly over time that will directly contribute to the overall poor main CE of Dural DU2. From the 25th cycle onwards, the main CE shows a constant steady drop accompanied by a continuous increase in the plateau separation (**Fig. 4-3-9, 4-3-10**). The downward curvature of the charge plateau becomes progressively more severe but the potential will not go below 0V until the 235th cycle (**Fig. 4-3-7**). The main discharge plateau shifts positive over time and so do the potentials of the secondary and tertiary plateaus. By the 25th cycle the potential of the tertiary plateau reaches the cycle upper potential limit of +2.65V. Therefore the fitted CE of this tertiary process drops to a value of 2% where it stays until we encounter the first plateau jump (**Fig. 4-3-11**).

By the 66th cycle the plateau separation increases to 1.48V with the main CE dropping down to 58% (**Fig. 4-3-9, 4-3-10**). At the 67th cycle we observe the first jump in the plateau potentials. Immediately following the jump the plateau separation resets to a smaller value of 1.00V and the charge plateau itself appears flat again. The diffusion plateau potentials also shift downwards after the jump and we observe a local maximum of 4% for the tertiary CE as the process has a longer duration before being terminated by the upper limit of the potential (**Fig. 4-3-11**). However, in the other respects, the overall peak shape and width appeared fairly similar before and after the jump. After the jump the Dural (DU2) system appears to briefly stabilize in its degradation but does not show the temporary improvements observed after jumps in soft MC Al (MC3) (**Fig. 4-3-10**). From the 67th to the 70th cycle the main CE will remain around 58% with the plateau separation unchanged at 1.00V (**Fig. 4-3-9, 4-3-10**). From the 70th to the 90th cycle the same degradation trends continue. At the 90th cycle we reach the worst cycle of the entire set with a maximum of 15% for the secondary CE and a minimum of 52% for the main CE (**Fig. 4-3-10, 4-3-11**). From the 90th to the 100th cycle the main CE improves to 58% with the secondary CE dropping to 12%. This is unusual given that there is no plateau jump apparent anywhere in this region of the figure for plateau separation (**Fig. 4-3-9**).

From the 100th to the 150th cycle and up to the 250th cycle we encounter an interesting region of stability (**Fig. 4-3-9**). The plateau separation remains at a smaller value around 1.2V and increases very slowly, only accelerating beyond the 200th cycle. The main CE gradually improves to 60% with the secondary efficiency decreasing to 10%, (**Fig. 4-3-10, 4-3-11**). Onwards from the 250th cycle the reversibility begins to degrade again, accompanied by the sharp downward curvature of the charge plateau below 0V (**Fig. 4-3-7**). This degradation is not due to increasing contribution of the secondary process as its CE continues to decrease to 8% (**Fig. 4-3-11**). Even with the plateau separation approaching almost 2V by now the system will not show another noticeable plateau jump until close to the 300th cycle (**Fig. 4-3-9**). Here we see a temporary improvement between the 295th and 300th cycle, which would likely be very brief. If we continued cycling, we would fully expect the plateau separation to increase well above 2V with the main CE dropping below 50%, even though the diffusion-related efficiencies are clearly not increasing anymore.

The origin of these trends is again likely to involve systematic large scale "pulverization" of a portion of the intermetallic structure from the anode surface as the stress of repeated lithiation/delithiation volume changes accumulates [2]. This process has been already discussed in Ch. 4.2. The performance of Dural sample DU2 appears to be intermediate between half-hard GF Al (GF5) and soft MC Al (MC3). The rapid improvements due to initial LiAl electroformation is consistent with the behaviour observed with two other samples. The noticeable degradation immediately afterwards is similar to MC3. Clearly the reversibility of Dural towards lithiation/delithiation is significantly impaired by the presence of alloying elements Cu and Mg in the alloy. This also leads to increased litiation-delithiation and appearance of diffusion-limited delithiation processes. The limited number of plateau jumps and overall cycling stability observed beyond the 100th cycle in DU2 must be related to the improved mechanical properties of Dural, due to the precipitation hardening effect of the Cu and Mg dopants. However, in the end, despite improved mechanical stability and cyclability, the electrochemical performance of Dural was shown to be insufficient for its use in Li ion batteries. The most likely reason is the

inhibiting effect of the alloying elements on the kinetics of lithiation-delithiation processes, as will be further discussed in Ch. 5.

4.3.2 SEM images

Shown in **Fig. 4-3-12** are SEM images of the uncycled area of the Dural anode (DU1) with oxide removed, as well as the reference GF Al (GF1) anode from Ch. 4.1. **Fig. 4-3-13** shows the cycled areas of the same two samples at different magnifications after being subjected to the 4x8 experiments. In sharp contrast to both Al 1100 materials the Dural (DU1) has a cycled area morphology that is significantly more heterogeneous under these 4x8 conditions (**Fig. 4-3-13 c-d**). There are numerous sub-areas of limited reactivity that closely resemble the uncycled substrate (**Fig. 4-3-12 d**). This poor reactivity should be due to the significant copper content which is inert towards lithiation [1].

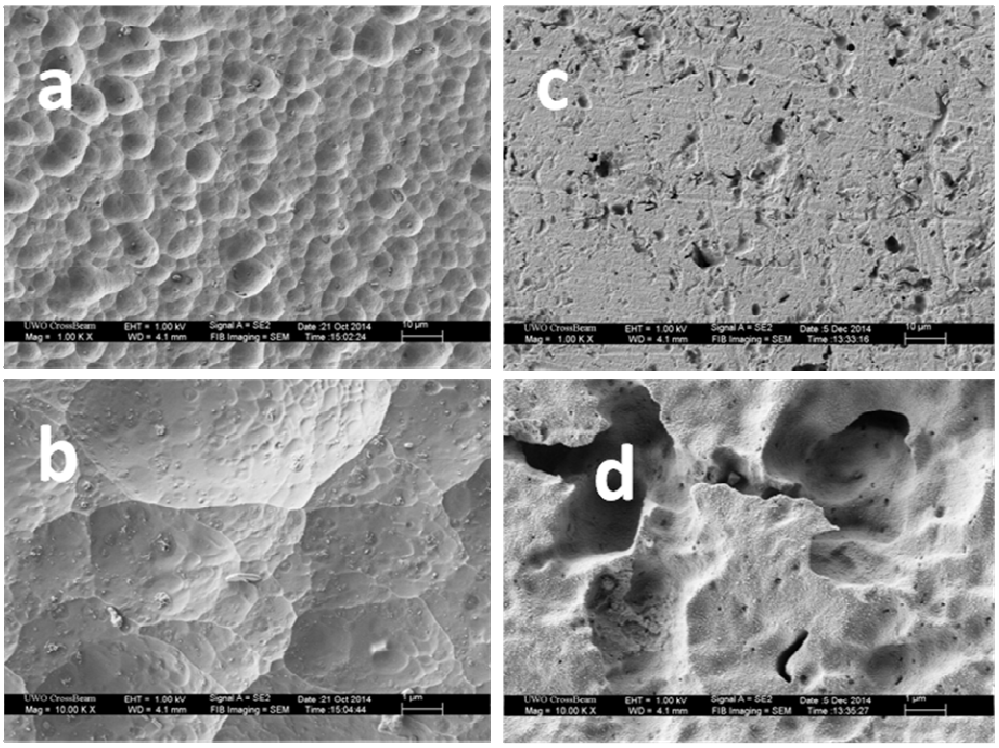

Figure 4-3-12: SEM images of uncycled areas for (a-b) GF Al (GF1) (oxide removed), (c-d) Dural (DU1) (oxide removed) anodes. Magnifications of (a,c) 1000x, (b,d) 10000x.

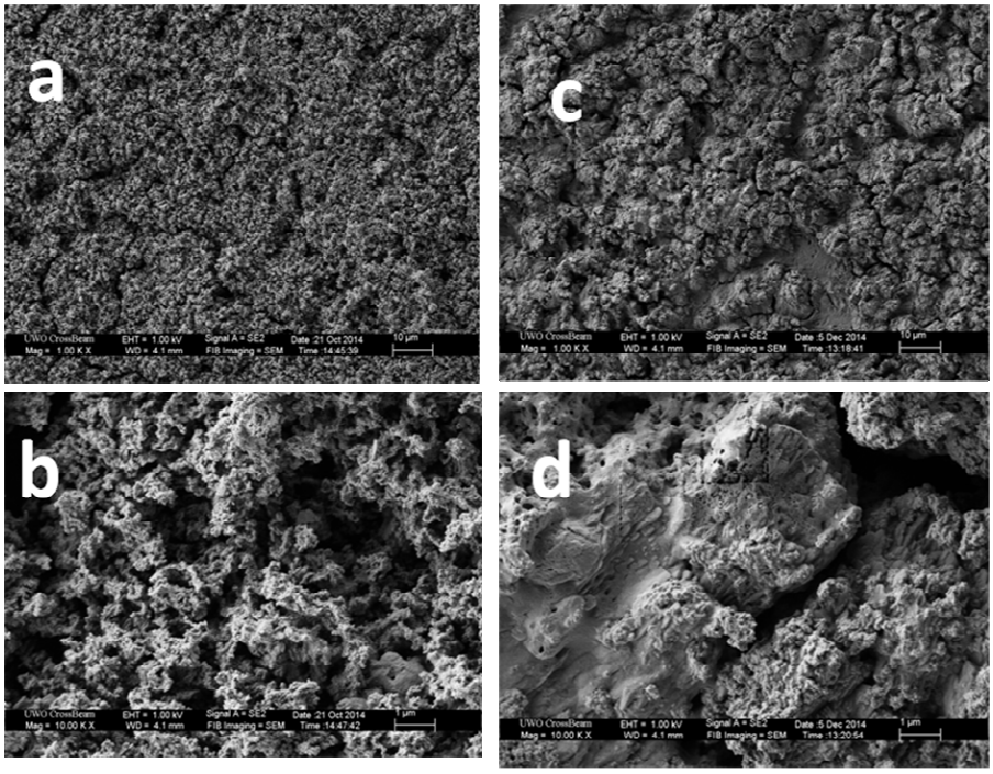

Figure 4-3-13: SEM images of cycled areas from 4x8 experiments for (a-b) GF Al (GF1) (oxide removed), (c-d) Dural (DU1) (oxide removed) anodes. Magnifications of (a,c) 1000x, (b,d) 10000x.

Copper is introduced into Dural during its manufacturing and predominantly precipitate at the grain boundaries, which is also where lithiation will commence. The uncycled area in Dural itself shows a rough pitted etching pattern completely different from those observed in half-hard GF Al and soft MC Al anodes (**Fig. 4-3-12 c-d**). Pushing the DU2 Dural anode towards failure results in a homogenous and globular morphology that appears to be fully reactive compared to the 4x8 version (DU1) (**Fig. 4-3-14 d-e**). Unlike the Al 1100 materials such as GF Al here (**Fig. 4-3-14 a-b**), there are no signs of large systematic cracking or a multilayer crust in the cycled morphology of this anode. Additionally the porous nanostructure is more compact in Dural than GF Al (**Fig. 4-3-14 f**).

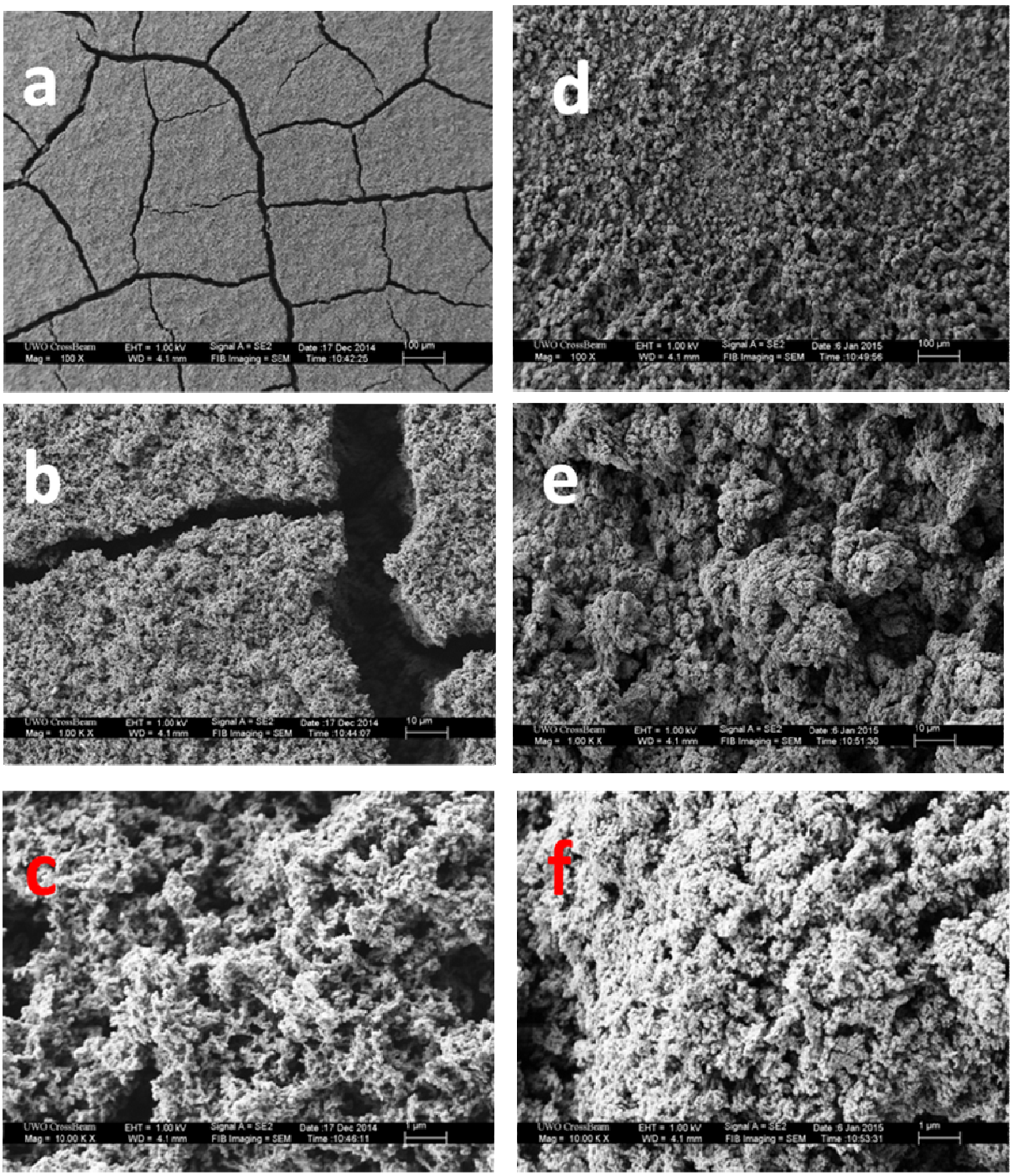

Figure 4-3-14: SEM images of cycled areas for (a-c) GF Al (GF5) (oxide removed), (d-f) Dural (DU2) (oxide removed) anodes subjected to 140 and 300 cycles each respectively at a current density of 0.5 mA/cm^2 without an initial CV. Magnifications of (a,d) 100x, (b,e) 1000x, (c,f) 10000x.

4.3.3 EDX Composition Chart

Shown in **Table 4-3-15** is the EDX composition data for the uncycled as well as cycled porous and cycled flat areas of the Dural DU1 anode with oxide removed after being subjected to the 4x8 experiment. Also shown in the Table are the results for Dural DU2 anode which was subjected to failure experiment for 300 cycles at a current density of 0.5 mA/cm^2. The predominance of Al with small amounts of Cu and Mg within the uncycled area indicates an unreactive Dural substrate with surface contamination by the electrolyte (**a**). Carbon and oxygen content should arise from a combination of trace propylene carbonate and residual surface oxide present after the electrode preparation. The resulting very low oxygen content of a few percent is expected given the polished and etched preparation.

Table 4-3-15: EDX composition chart of uncycled and cycled areas of Dural anode (oxide removed) after being subjected to a 4x8 experiment (DU1), as well as DU2 Dural anode (oxide removed) that was subjected to 300 cycles at a current density of 0.5 mA/cm^2. The spectra were collected at a column voltage of 7 kV for 50 seconds at 1000x magnification.

		Atomic %							
Sample	**Area**	**C**	**O**	**F**	**Mg**	**Al**	**Si**	**P**	**Cu**
DU1	(a)Uncycled	1.68	1.99	0.16	1.06	92.08	0.31		2.72
	(b)Porous	9.08	41.59	23.41	0.30	23.59	0.18	0.74	1.10
	(c) Flat	3.53	7.93	1.12	0.76	84.07	0.10	0.21	2.28
DU2	(d) Uncycled	4.44	4.27	4.88	1.05	82.36	0.15	0.33	2.53
	(e)Porous	2.34	8.56	65.31	0.25	22.21	0.39	0.43	0.50

Trace phosphorus and fluorine content should be related to $LiPF_6$ salt remaining after rinsing. The small amount of silicon detected is likely again due to a combination of silicon carbide paper used for polishing, and as an impurity in the Al alloy itself. Lithium cannot be detected due to the overlap of its low energy x-rays with the baseline peak close to 0 eV.

The porous reactive region in the cycled area of Dural DU1 (**b)** shows significantly elevated carbon, oxygen and fluorine content as was also observed for bare GF and MC Al anodes in Ch. 4.1.3 and 4.2.3 (**Fig. 4-1-15, 4-2-14**). This is again likely due to the presence of electrolyte within the intermetallic structure, as well as the products of solvent electroreduction and salt decomposition in the SEI layer [3]. Cu and Mg are present throughout all cycled Dural material, which suggests that they are indeed inert in the lithiation-delithiation processes but remain at the electrode during the electrochemical and associated phase formation and volume changes. The unreactive alloying elements like copper increase the resistance towards lithiation, resulting in the increased overvoltage and decreased coulombic efficiency seen previously in the CVs and galvanic cycles (**Figs. 4-3-2 to 4-3-6**). This behaviour may also explain the unreactive regions observed by SEM within the cycled area of Dural DU1 (**Fig. 4-3-13 c-d)**. The composition of these flatter regions of the cycled area resembles that of the uncycled area, with slightly more carbon, oxygen and fluorine (**c**). When pushed towards failure, DU2 resembles the composition of the reactive porous regions in DU1 with a few percent of Cu and Mg present (**e**). This composition will be fairly consistent across the entire cycled area of DU2, which supports our assumption that this sample is a fully reactive version of DU1. We again observed dramatically higher F:O and F:Al ratios in terms of percentage composition for DU2 relative to the 4x8 experiment DU1. Considering the $LiPF_6$ salt this fluorine content should predominantly come from the electrolyte. However it is not clear in what form does this elevated fluorine content exist within the homogenous porous structure of DU2. With sustained cycling mechanical stresses accumulate in the electrode, one can expect a constant partial destruction of the SEI at the surface of the structure, which will results in exposure of fresh portions of Al material for

more SEI formation. As was mentioned before, the $LiPF_6$ salt is also expected to thermally degrade over time into LiF and PF_5 if any trace moisture content is present [4].

4.3.4 References

1. Dey, A.N., *Journal of the Electrochemical Society*, **1971**, *118*, 1547-1549.
2. Liu, Y.; Hudak, N.S.; Huber, D.L.; Limmer, S.J.; Sullivan, J.P.; Huang, J.Y., *Nano Lett.* **2011**, *11*, 4188-4194.
3. Schroder, K.W.; Dylla, A.G.; Harris, S.J.; Webb, L.J.; Stevenson, K.J., *ACS Appl. Mater. Interfaces*, **2014,** *6,* 21510-21524.
4. Yang, H.; Zhuang, G., *Journal of Power Sources,* **2006,** *161,* 573-579.

4.4 Aluminum-CNx and Dural-CNx Anodes

Summary

In Ch. 4.1 and Ch. 4.3 we investigated the lithiation-delithiation behaviour of bare Goodfellow Al (GF Al) and Duraluminum (Dural) respectively. These Al materials have differing mechanical properties, through the use of strain-hardening processing for GF Al (half-hard), and precipitation hardening with copper and magnesium alloying in Dural. Here we examine the effects of amorphous carbon nitride (CNx) thin films on lithiation-delithiation behaviour with various CNx-coated anodes prepared on both GF Al and Dural substrates with the native surface oxide removed. The idea was twofold. First, we wanted to see if CNx can change the kinetics and mechanism of lithiation of Al anodes, for instance, by changing the kinetics of electrochemical reactions at the electrode or by modifying the properties of Al substrate, e.g., via nitridization or similar processes. It was also conceivable that some Li would be intercalated in CNx, since carbon (graphite) is a well-known intercalation material. Second, since the formation of LiAl intermetallic phase was shown to be accompanied by pronounced volume changes that are detrimental to the electrode performance and can result in poor reversibility of the lithiation-delithiation processes, we anticipated that CNx could act as a kind of scaffold that would be able to control the volume change and prevent mechanical disintegration of the active material.

Half-hard GF Al was chosen as the substrate for the Al-CNx samples instead of soft McMaster-Carr Al (MC Al). This choice was made due to the strain-hardening of GF Al offering improved structural stability in repeated scanning and cycling of the resulting intermetallic alloy (Ch 4.1 and 4.2). For Al-CNx anodes the first sample AC1 was prepared with 75 nm of CNx deposited on oxide-free half-hard GF Al under parameters of 50 W, 1 Pa and 75% N_2 plasma. The second sample AC2 was similarly prepared and then underwent post-deposition thermal annealing at 150 ^{o}C for 2 hours. The magnetron power of 50 W was chosen to achieve both a reasonable deposition rate and film stability

in solution [1-2]. The lower deposition pressure of 1 Pa was chosen to make the resulting film more dense and less disordered [3-5]. From an earlier preliminary study in our group with Al-CNx samples of different nitrogen contents we determined that an optimum 75% N_2 plasma composition for the CNx film results in the most stable charge/discharge response at high current densities with the best reversibility.

These samples were characterized electrochemically in 4x8 experiments, which began with a cyclic voltammogram (CV) for three scans, followed by four sets of eight galvanic cycles at progressively higher current densities. In the initial CV of non-annealed Al-CNx (AC1) we observed increased SEI formation and overvoltage relative to bare GF Al (half-hard), as well as strong evidence of volume change containment during intermetallic phase formation. The increased SEI formation is likely to be due to formation of a porous intermetallic structure with SEI formed at the walls of the pores. Importantly, SEI formation confirms that these pores are accessible to electrochemical reactions. Annealing of Al-CNx (AC2) showed further increases in SEI formation and volume change containment with a decreased overvoltage relative to AC1. In the galvanic cycles we observed minor differences in the charge-discharge plateau separation, as well as poor initial reversibility of AC1 at lower current densities relative to GF Al (half-hard). This poor initial performance was further exacerbated in the annealed version AC2. The surface analysis of the AC1 sample after electrochemistry revealed a relatively homogenous porous intermetallic alloy structure that was in parts covered by the remnants of the CNx film. The analysis of AC2 revealed a similar structure but with the remaining CNx most likely buried under the growing LiAl phase. An additional sample (AC3) of the same type as AC1 (non-annealed Al-CNx), which showed improved performance over annealed Al-CNx (AC2), was characterized electrochemically in a failure experiment, in which galvanic cycling of the anode begins immediately at a higher current density without initial conditioning through a CV. This cycling was sustained for 180 cycles to observe the anode performance over time, which manifested with multiple plateau jumps and severe coulombic efficiency (CE) degradation relative to bare half-hard GF Al (oxide removed). However surface analysis revealed less systematic cracking

of the intermetallic alloy compared to bare GF Al, with the CNx film further pulverized into smaller pieces.

For Dural-CNx anodes the first sample DC1 was prepared with 75% N_2 plasma similar to the non-annealed Al-CNx sample AC1 but on oxide-free Dural. To test the effect of nitrogen content the second sample DC2 was prepared similar to DC1 but with 25% N_2 plasma. These samples were characterized electrochemically in 4x8 experiments. In the initial CV of DC1 (75% N_2 Dural-CNx) we observed increased SEI formation and comparable overvoltage relative to bare Dural, with some evidence of volume change containment. With lower nitrogen content DC2 (25% N_2 Dural-CNx) showed further increases in SEI formation with similar overvoltage relative to DC1 but decreased ability to contain volume changes. In the galvanic cycles we observed minor differences in the charge-discharge plateau separation, with superior reversibility (higher CE) for DC1 (75% N_2) at lower current densities relative to bare Dural and comparable reversibility at higher current densities. At lower current densities the initial reversibility of DC2 (25% N_2) was poorer but also became comparable at higher current densities. Surface analysis of the DC1 sample after electrochemistry revealed a highly heterogeneous surface with very limited reactivity in which the unreactive areas resembled uncycled Dural-CNx. In DC2 the cycled area was again very heterogeneous but with improved reactivity. Additional samples DC3 and DC4 of the same type as DC1 and DC2 respectively were characterized electrochemically in failure experiments. Cycling was sustained for 300 cycles to observe the anode performance over time, which manifested in DC3 (75% N_2) with multiple plateau jumps and severe CE degradation relative to bare Dural. Both of these trends were worse with decreased nitrogen content in DC4 (25% N_2). For both samples surface analysis revealed a fully reactive intact porous morphology characteristic of the bare Dural anode failure experiment from Ch. 4.3, with no evidence of CNx film remnants present anywhere throughout either cycled area.

4.4.1. Cyclic Voltammograms, Galvanic Cycles, Calculations

Al-CNx anodes

The typical features of CVs with bare Al anodes were described previously in Ch. 4.1.1. Therefore this section will focus only on differences observed in the CV features of Al-CNx anodes relative to bare half-hard GF Al anodes with the oxide removed. First we consider the partial cathodic scans between 1.5V and 0.25V vs. Li^+/Li reference electrode (**Fig. 4-4-1**). For the purposes of comparison the bare GF Al anode GF1 Ch. 4.1 is included. The bolded numbers **1** to **3** denote the GF1, AC1 and AC2 samples respectively (1, bare GF Al; 2, Al-CNx; 3, annealed Al-CNx).

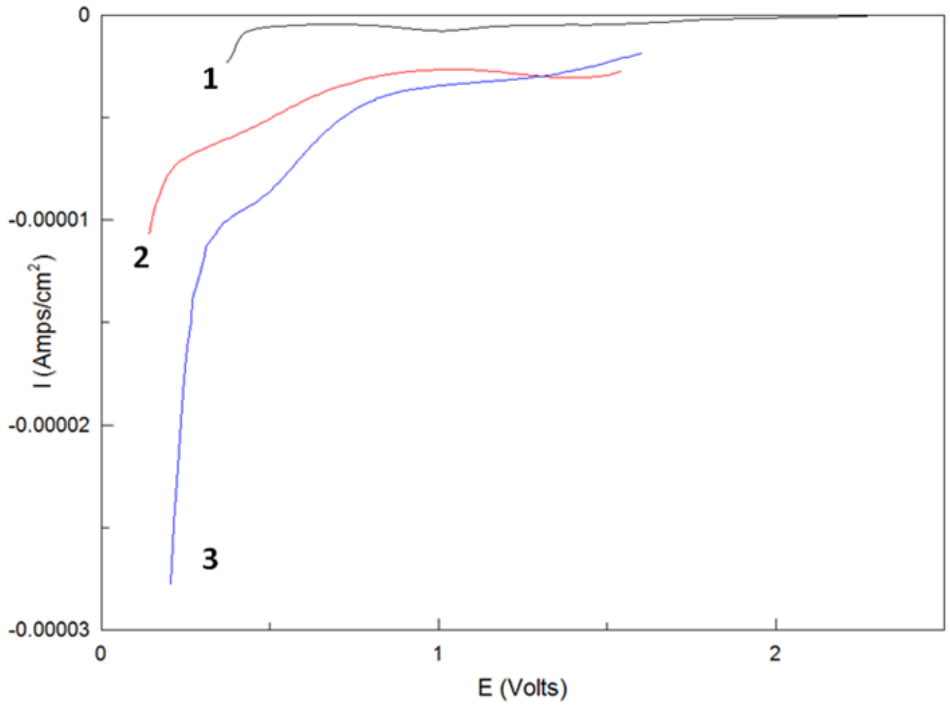

Figure 4-4-1: Initial cyclic voltammograms of non-annealed and annealed 75% N_2 Al-CNx anodes AC1 (2, red) and AC2 (3, blue). Comparative bare half-hard GF Al anode GF1 (1) from Ch. 4.1 is also included in black. Partial cathodic scans from 2V to 0.25V to highlight SEI formation and lithiation onset behaviour.

First of all, we see that the lithiation onset potential is greatly affected by the presence of the CNx film. Addition of the 75% N_2 75 nm sputtered CNx layer (AC1) to the GF Al substrate shifts the onset significantly towards more negative potentials. This feature indicates that formation of the LiAl intermetallic phase is more difficult at the Al-CNx electrode (AC1) compared to bulk GF Al (GF1). At a plasma composition of 75% N_2 the resulting CNx film in AC1 will be considerably less conducting than amorphous graphite and the bare GF Al itself [7]. This alone would shift the potential to more negative potentials. Furthermore, the high nitrogen incorporation will cause significant cross-linking of graphite through nitrogen-containing functional groups, effectively increasing its mechanical stability (hardness). Therefore volumetric expansion to create the new LiAl phase in Al-CNx anode will require more energy and therefore more overvoltage. Thermal annealing of the Al-CNx anode (AC2) shifts the onset to a value intermediate between that of non-annealed Al-CNx (AC1) and bare GF Al (GF1). This indicates a decrease in the overvoltage of LiAl formation for the AC2 anode, suggesting that a mild thermal annealing treatment may improve the conductivity of the CNx film, or decrease its mechanical strength, or both. It is also consistent with the increased lithiation currents observed for AC2 in the next figure (**Fig. 4-4-2**).

Both Al-CNx samples show larger cathodic currents for the SEI formation relative to bare GF Al, which should be related to the fact that SEI layer is now formed not on Al but on CNx (**Fig. 4-4-1**). This effect is further amplified in the annealed Al-CNx sample AC2. Evidence of increased SEI presence on cycled Al-CNx anodes will be presented in the TOF-SIMS depth profiling results of Ch. 4.6. The SEI formation in both Al-CNx samples here in the CV appears broadened with no distinct reduction peaks, which is similar to the effect we observed for increased surface oxide content on GF Al and MC Al substrates in Ch. 4.1 (**Fig. 4-1-2**) and 4.2 (**Fig. 4-2-1**). Additional scanning in the CV will produce larger amounts of additional SEI formation for AC1 (non-annealed Al-CNx) relative to GF1 (bare GF Al), with this formation further increased in AC2 (annealed Al-CNx). The greater amount of additional SEI formation in the Al-CNx samples relative to bare GF Al indicates that a different nanostructure is formed on these substrates with higher porosity. SEI will then form on the inner walls of the pores too. The increase in

the SEI current then suggests that these pores are accessible to electrolyte and to electrochemical reactions. The additional SEI formation may be also due to cracking of the coating during subsequent CV scans, which will be demonstrated in the SEM imaging section 4.4.2. As the CNx coating progressively cracks during LiAl phase formation and dissolution it will expose more fresh Al material for SEI formation. Furthermore the cracking of the coating itself will also partially destroy the SEI layer present on it.

Next we compare the full CV scans of all samples in **Fig. 4-4-2**. Sample AC1 (non-annealed Al-CNx) shows a significantly smaller loop area relative to GF1 (bare GF Al) in the anodic scans. This suggests that the CNx coating is acting to contain the volume changes of LiAl phase formation and dissolution. Comparing the scan of AC2 (annealed Al-CNx) versus AC1 shows a further amplification of this effect. Even though the lithiation currents of the annealed sample are much larger the resulting loop area is still quite small. The annealed CNx coating may have stronger adhesion to the GF Al substrate as well as improved mechanical stability. The larger loop size observed for GF1 is consistent with the steeper slope of the current following the lithiation onset also seen in this figure, and again indicates that there is a larger degree of volume change for intermetallic phase formation in this uncoated bare GF Al sample. Moving on, we observe that both coated samples only show a single broad delithiation peak, which suggests that lithiation-delithiation of Al-CNx anodes predominantly occurs through LiAl alloying/de-alloying, with the CNx film acting as an ionic conducting pathway but not an intercalation material. This is also supported by our TOF-SIMS depth profiling measurements that show very low content of Li containing species in the CNx portion of the cycled Al-CNx anode as compared to the underlying intermetallic phase (see Ch. 4.6.) This delithiation peak potential in both coated samples is shifted significantly positive relative to bare GF Al (GF1). The resulting increased overvoltage would suggest kinetic limitations and increased resistance for the de-alloying process due to the CNx film. However the delithiation onset potentials (non-zero anodic current) for all three samples appear fairly similar around 0.6V.

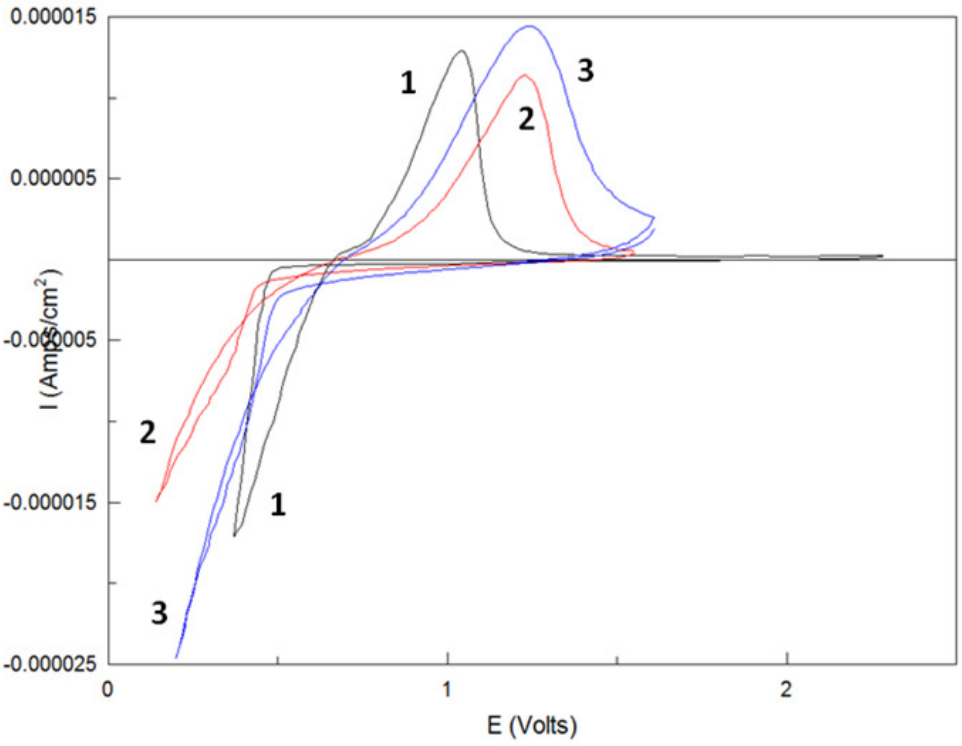

Figure 4-4-2: Initial cyclic voltammograms of non-annealed and annealed 75% N_2 Al-CNx anodes AC1 (2, red) and AC2 (3, blue). Comparative half-hard GF Al anode GF1 (1) from Ch. 4.1 is also included in black.

Shown in **Fig. 4-4-3** are the features of a typical set of galvanic cycles for non-annealed Al-CNx anode AC1 at a current density of 0.25 mA/cm^2 in red color, with the comparative cycle set of the bare half-hard GF Al anode GF1 (oxide removed) in black color. Overall, we observe a similar sequence of events (denoted in the numbers **1** to **5**) within the cycle set as described previously for GF Al anodes in Ch. 4.1, with single long and flat plateaus for both the charge and discharge portions. However, the presence of CNx clearly gives rise to occurrence of additional diffusion-limited processes in the discharge portion, as well as a slight increase in the plateau separation that suggests an increase in the resistance.

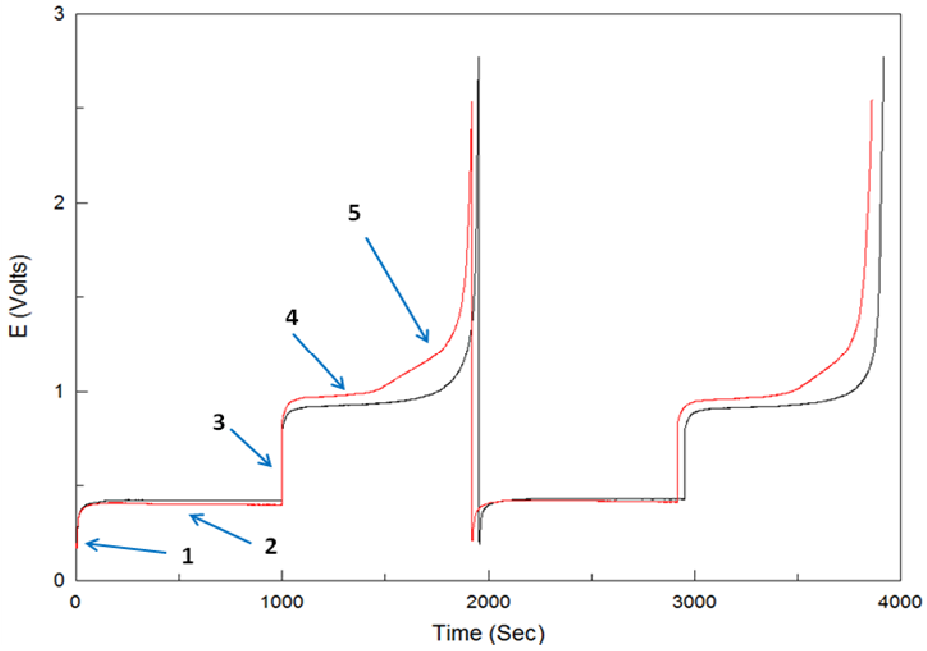

Figure 4-4-3: Typical galvanic cycles for lithiation/delithiation of an Al-CNx anode (red curve). This is sample AC1 in which the CNx film was deposited prior to electrochemical scans. Comparative bare half-hard GF Al anode GF1 (oxide removed) from Ch. 4.1 is also included (black curve). Numbers indicate the features of interest: (1) potential overshot (2) charge plateau (3) IR drop (4) discharge plateau (5) diffusion-controlled discharge tail. Galvanic cycles are shown at a current density of 0.25 mA/cm^2.

Shown in **Fig. 4-4-4** are the set of galvanic cycles of non-annealed and annealed Al-CNx anodes AC1 and AC2 in red and blue colors respectively at a current density of 0.25 mA/cm^2. The comparative cycle set of the bare GF Al anode GF1 (oxide removed) is included in black color. In both Al-CNx anodes we observe pronounced diffusion-limited processes in the discharge cycle, which, however, largely disappear by the 8th cycle. This indicates that while at first CNx is impeding the delithiation process, this effect is temporary. Also, there is a shift in both lithiation plateau potentials during cycling. For example, non-annealed Al-CNx (AC1) had a consistently more negative lithiation onset potential in the CV than bare GF Al (GF1) (**Fig. 4-4-1**), but here in the first cycle AC1 undergoes lithiation near the potential of GF1, and then transitions to even more positive

potential closer to that of annealed Al-CNx (AC2) by the eighth cycle. The AC2 anode had a lithiation onset potential In the CV that was intermediate between that of AC1 and GF1 (**Fig. 4-4-1**), while here in the cycles the charge plateau is notably more positive than both of those samples. Overall these effects together emphasize the evolution of the nanostructure at both Al-CNx anodes. We also observe shifting in the delithiation plateau potentials of AC1 and AC2 with cycling, but these potentials still remain more positive than for GF1. Therefore delithiation is still more difficult in Al-CNx, which is consistent with the more positive peak potentials in the CV (**Fig. 4-4-2**), and suggests that CNx may be reacting to some extent with components of the intermetallic nanostructure. One possible explanation maybe that CNx expands the concentration range of the existence of α-LiAl phase, which features more positive potential than β-LiAl that we mostly observe in our experiments. The α-LiAl phase is a solid solution of Li in Al. It exists only at very low Li loads but perhaps the presence of CNx can affect this behaviour.

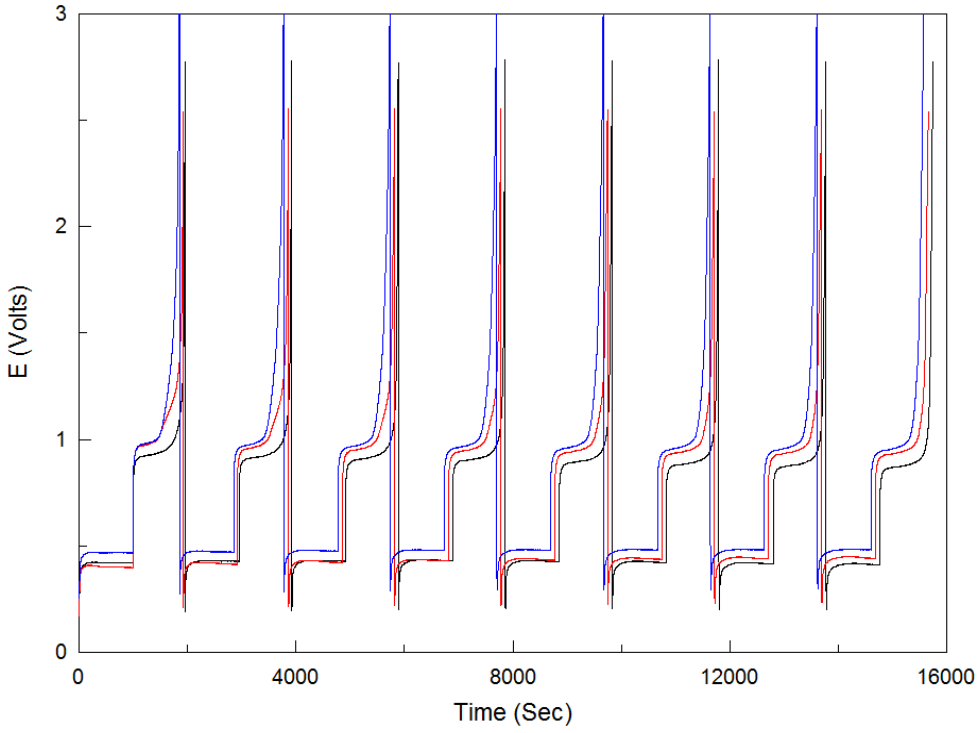

Figure 4-4-4: Galvanic cycles of non-annealed and annealed 75% N_2 Al-CNx anodes AC1 (red) and AC2 (blue) at a current density of 0.25 mA/cm^2. Comparative bare half-hard GF Al anode GF1 from Ch. 4.1 is also included in black.

Shown in **Fig. 4-4-5** are the first (a) and last (b) galvanic cycles for all samples in this set. One can see that the CNx coating of AC1 (non-annealed Al-CNx) decreases the duration of the main discharge plateau due to appearance of the diffusion limited process. Therefore, the coulombic efficiency (CE) also decreases relative to bare half-hard GF Al (GF1) **(Fig. 4-4-5 a)**. This trend is also seen from the initial discharge peak shape of AC2 (**Fig. 4-4-5 a**). By the eighth cycle the differences in CE of all three samples will largely disappear as the discharge peak shapes become comparable **(Fig. 4-4-5 b)**. The evolution of the coulombic efficiencies with the cycle number is shown in **Fig. 4-4-6** for the four current densities used. We observe that the initial CE of both coated samples is again poor relative to GF1 (GF Al, black) but rapidly become comparable over time in the third set **(Fig. 4-4-6 c).** At the highest current density both coated samples perform poorly but the CE of AC1 (non-annealed Al-CNx) now exceeds that of GF1 (bare GF Al) **(Fig. 4-4-6 d)**. Here the AC2 (annealed Al-CNx) sample encountered the charging potential limit early in the seventh cycle, resulting in the remaining two cycles being terminated quickly and therefore omitted from this figure.

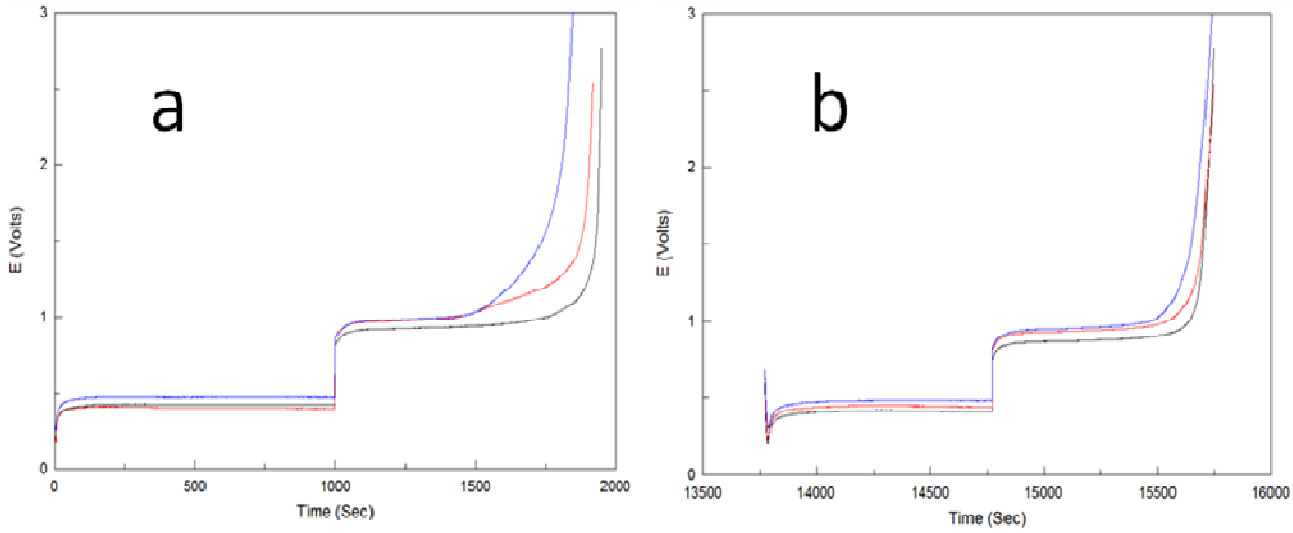

Figure 4-4-5: (a) First and (b) last galvanic cycles of non-annealed and annealed 75% N_2 Al-CNx anodes AC1 (red) and AC2 (blue) at a current density of 0.25 mA/cm^2. Comparative bare half-hard GF Al anode GF1 from Ch. 4.1 is included in black. Cycles in the right figure have been offset to overlap the curves on the same time scale.

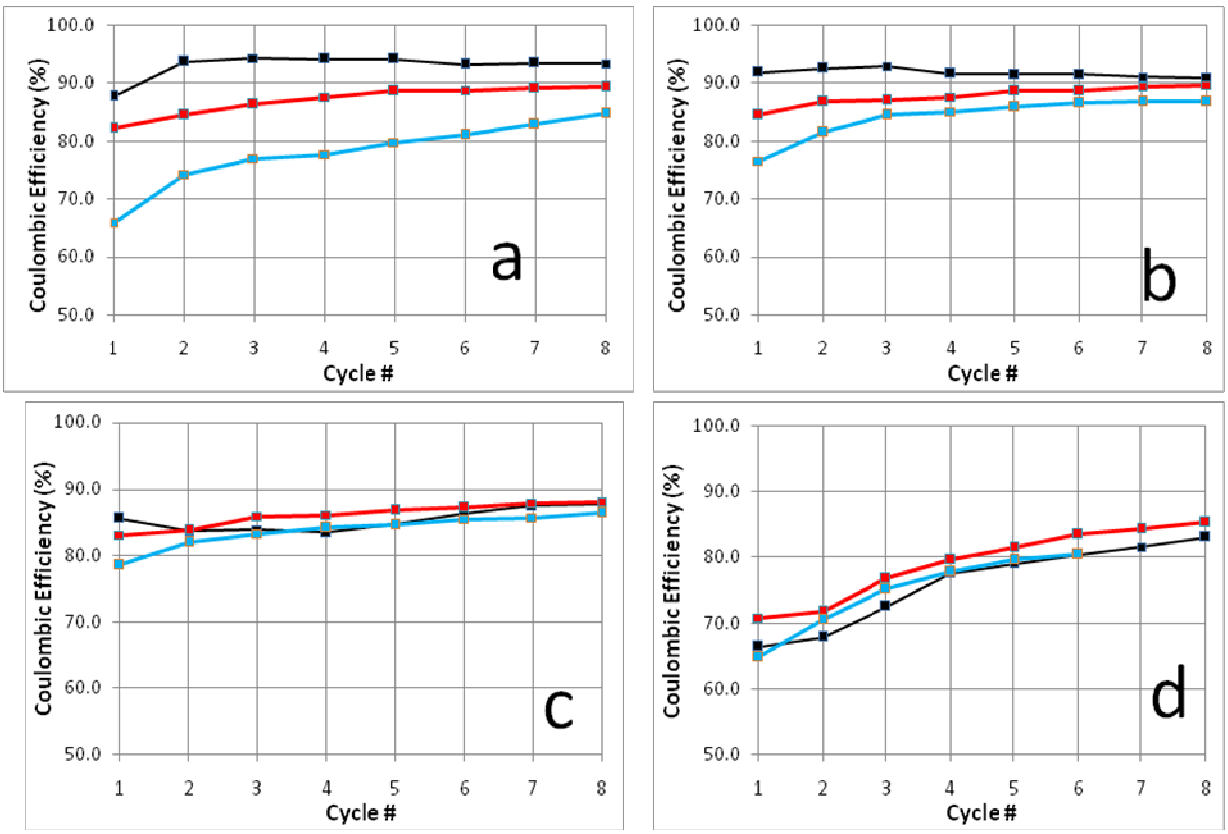

Figure 4-4-6: Coulombic efficiencies of non-annealed and annealed 75% N_2 Al-CNx anodes AC1 (red) and AC2 (blue) at current densities of (a) 0.13 (b) 0.25 (c) 0.5 and (d) 1 mA/cm^2. Comparative bare half-hard GF Al anode GF1 from Ch. 4.1 is included in black.

Overall these results suggest that the reversibility of lithiation-delithiation for Al-CNx is worse initially at lower current densities relative to bare GF Al. Initial formation of the porous nanostructure at the anode surface will be restricted by volume change containment and increased resistivity/kinetic limitations due to the presence of CNx as seen in the CV (**Fig. 4-4-2**). This constraint is further enhanced by the thermal annealing treatment. More overvoltage is then required in Al-CNx for lithiation-delithiation early and the LiAl intermetallic phase that is created is likely to be more compact, which causes the occurrence of diffusion limitations for lithium extraction (**Fig. 4-4-6 a-b**). As the porous structure develops more towards the higher current densities, emphasized by the shifting cycle plateau potentials, less overvoltage is required for volume changes.

Therefore more lithium can be recovered upon delithiation which makes the efficiency of Al-CNx at higher densities approach or surpass that of bare GF Al (**Fig. 4-4-6 c-d**).

To investigate the stability and cycling ability of the Al-CNx anode we performed a half-cell failure experiment on a new sample AC3. The sample was prepared in the same way as "non-annealed Al-CNx" sample AC1 described above. We chose a CNx coating without thermal annealing for AC3 because the reversibility of both non-annealed and annealed Al-CNx anodes appear comparable at higher current densities (**Fig. 4-4-6 c-d**). As in previous half-cell failure experiments in Ch. 4.1 to 4.3, no prior electroformation of the LiAl phase was performed using either a CV or galvanic cycles at low current densities. The cycling was commenced immediately at a high current density of 0.5 mA/cm^2 for a total of 180 cycles. This current density is equivalent to that of the third set of cycles in the 4x8 experiments.

Shown in **Fig. 4-4-7** is the full set of the corresponding galvanic cycles. One can see that the cycling behaviour is quite unstable compared to the similar experiment with bare half-hard GF Al (GF5) (**Fig. 4-1-8**). Here the plateau potential jumps occur with significantly larger amplitude and higher frequency. Before each jump the overvoltages in both charging and discharging plateaus significantly increase so that the charge plateau potential drifts well below 0V vs. Li^+/Li.

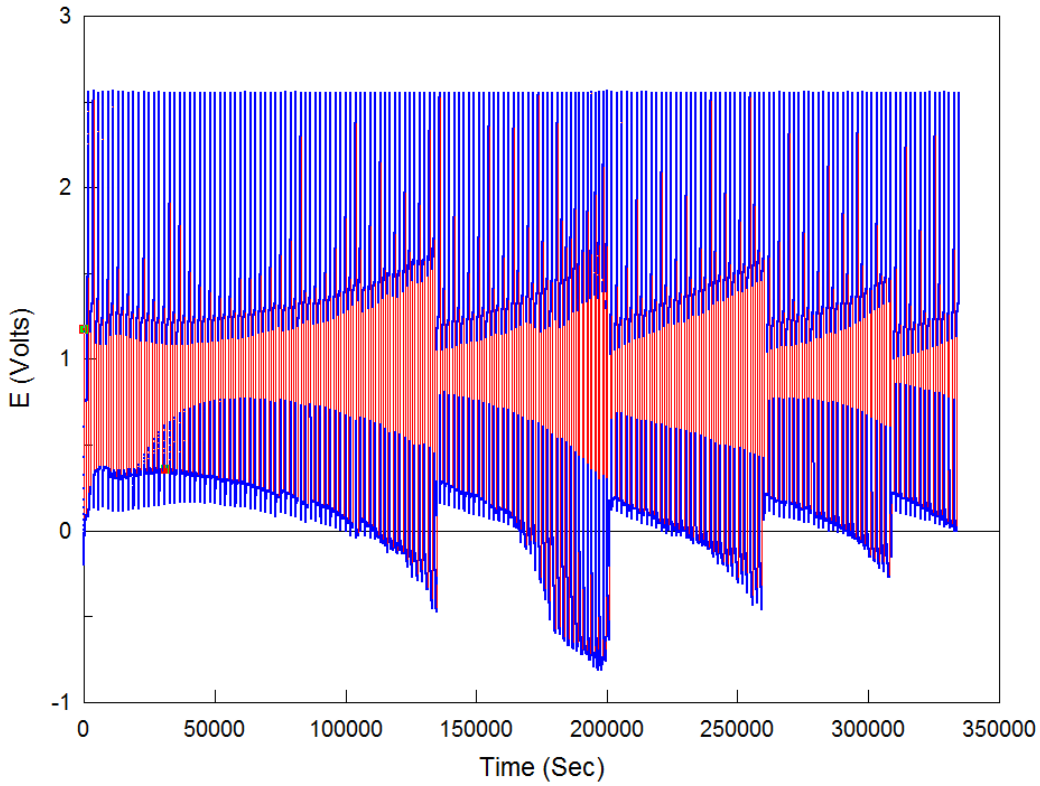

Figure 4-4-7: Full set of galvanic cycles for the AC3 non-annealed 75% N_2 Al-CNx anode subjected to 180 cycles at a current density of 0.5 mA/cm^2 without an initial CV.

Fig. 4-4-8 a-b shows the first two and last two cycles in black and red, respectively. Arrows in the red curve indicate the secondary and tertiary plateaus appearing over time in the discharge portion of the cycle, which were also observed with cycling of bare GF Al earlier in Ch. 4.1 (**Fig. 4-1-9**) and have been attributed to the diffusion-controlled delithiation of the α-LiAl intermetallic phase. The very first cycle shows two discharge plateaus with comparable lengths (**Fig. 4-4-8 a**). The higher plateau at 1.47V is a similar potential to the discharge plateau of 1.41V in the first cycle of the bare GF Al failure anode GF5 (**Fig. 4-1-9**). Therefore this higher plateau should be delithiation from an intermetallic alloy. The lower plateau here around 0.77V may uniquely arise from delithiation from just the CNx itself. If these two discharge plateaus in the first cycle are fitted together we achieve a main CE of 60%. In the second cycle the lower discharge plateau disappears with the upper plateau shifting down to 1.25V and changing its shape

to indicate the removal, to a large extent, the diffusion limitations (**Fig. 4-4-8 a**). Therefore beyond the first cycle of AC3 lithiation-delithiation is considered to occur entirely through intermetallic alloy phase formation and dissolution, as suggested by the shape and parameters of the last cycles in the set (red curve).

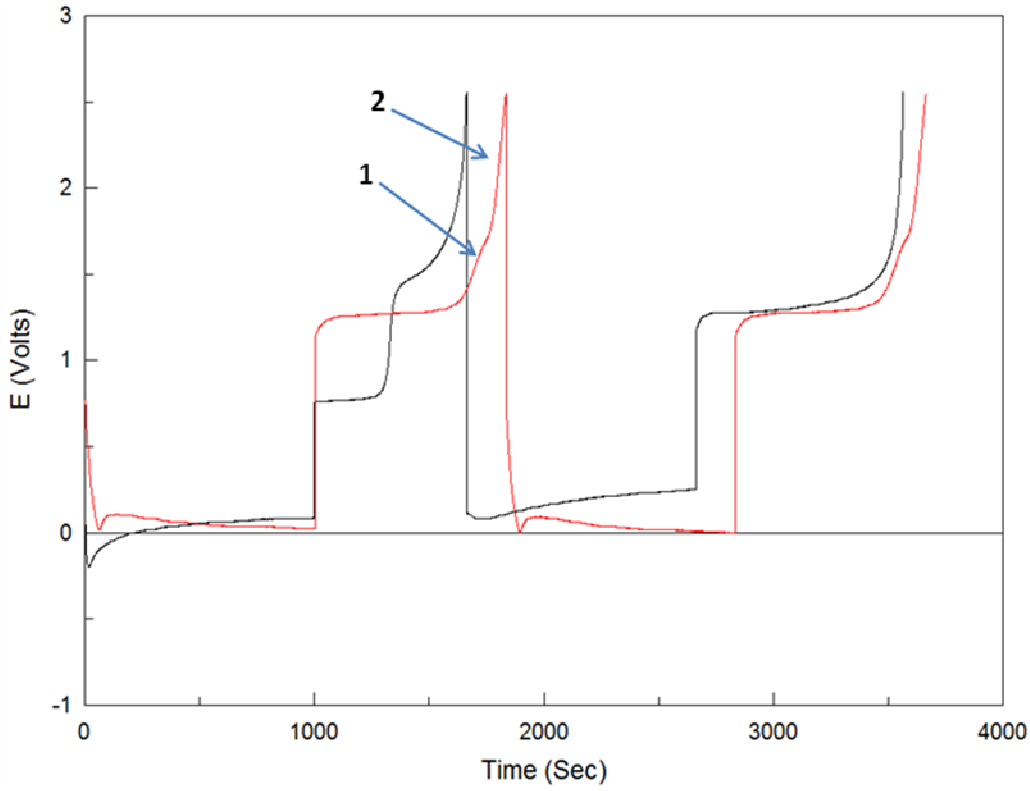

Figure 4-4-8: First two (black) and last two (red) galvanic cycles for the AC3 non-annealed 75% N_2 Al-CNx anode subjected to 180 cycles at a current density of 0.5 mA/cm^2 without an initial CV. Numbers in the red curve denote the secondary and tertiary diffusion-limited plateaus. The red curve has been offset to overlap with the time scale of the black curve.

To further characterize the performance of the sample, the separation between the charge plateau and the main discharge plateau is plotted in **Fig. 4-4-9,** together with the coulombic efficiencies of the main as well as the secondary and tertiary discharge plateaus shown in **Fig. 4-4-10** and **Fig. 4-4-11** respectively for every fifth cycle starting

from the first cycle. Additionally, the figures also show the data for cycles right before and after the potential jumps observed within the cycle set. We did not observe the secondary diffusion plateau until approximately the 15th cycle and the tertiary diffusion plateau until approximately the 5th cycle. For the sake of comparison, the data from bare half-hard GF Al half-cell failure experiment (GF5, oxide-removed) from 4.1 is included in black color in both **Fig. 4-4-9** and **Fig. 4-4-10**, with the new non-annealed Al-CNx AC3 data appearing in red color.

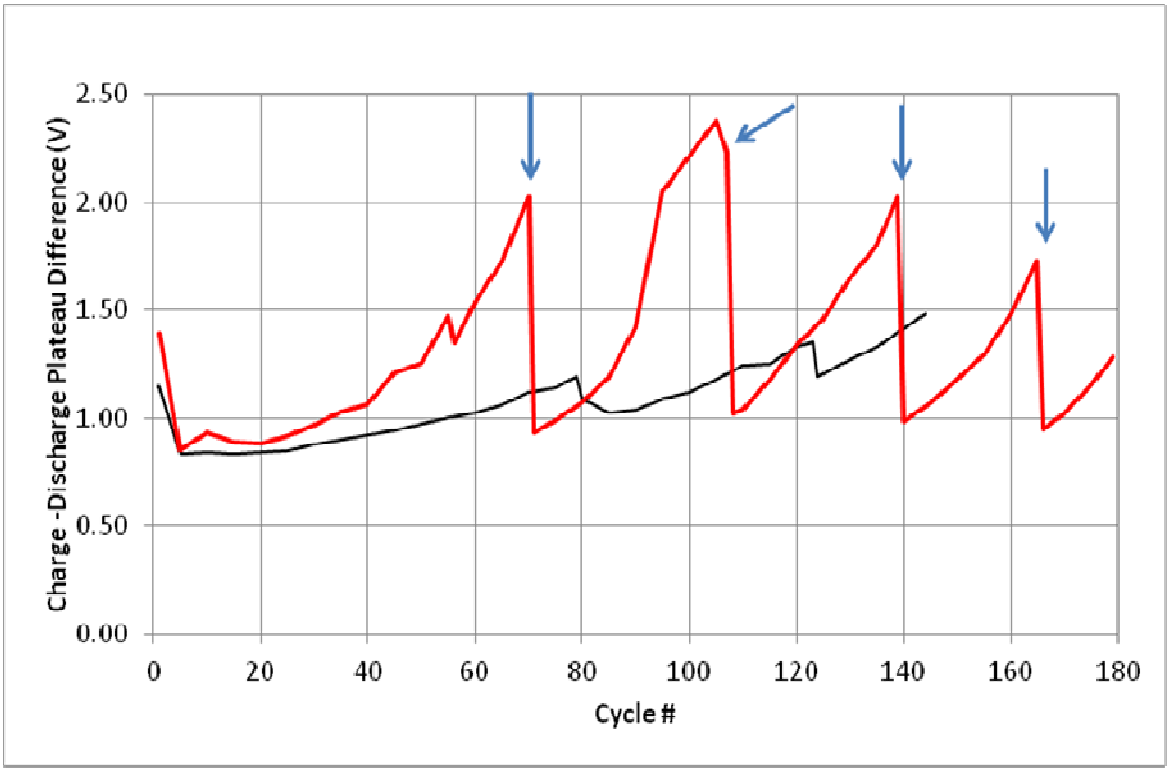

Figure 4-4-9: Charge-Discharge plateau separation (red curve) for the main discharge plateau for AC3 non-annealed 75% N_2 Al-CNx anode subjected to 180 cycles at a current density of 0.5 mA/cm^2 without an initial CV. For comparison, data for bare half-hard GF5 GF Al anode (oxide removed) from Ch. 4.1 is included in black. Plateau jump events in AC3 are indicated with arrows.

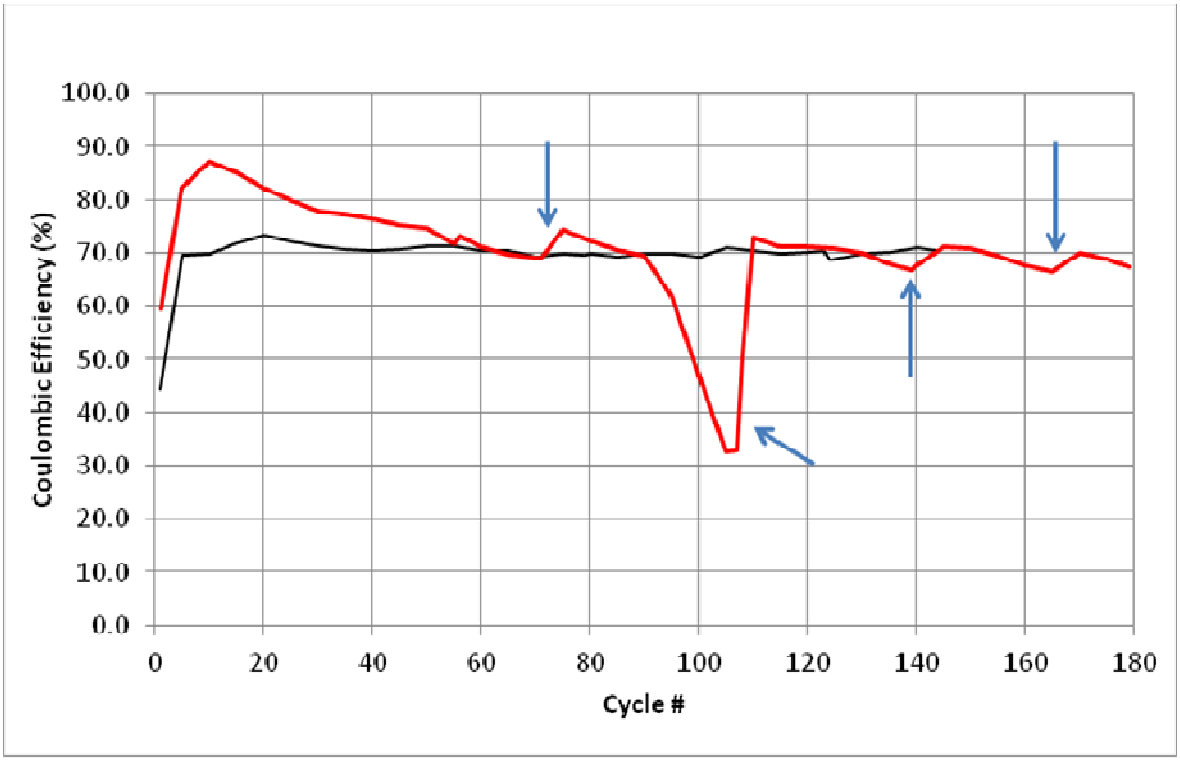

Figure 4-4-10: Coulombic efficiency data for the main discharge plateau (red curve) for AC3 non-annealed 75% N_2 Al-CNx anode subjected to 180 cycles at a current density of 0.5 mA/cm^2 without an initial CV. For comparison, data for bare half-hard GF5 GF Al anode (oxide removed) from Ch. 4.1 is included in black. Plateau jump events in AC3 are indicated with arrows.

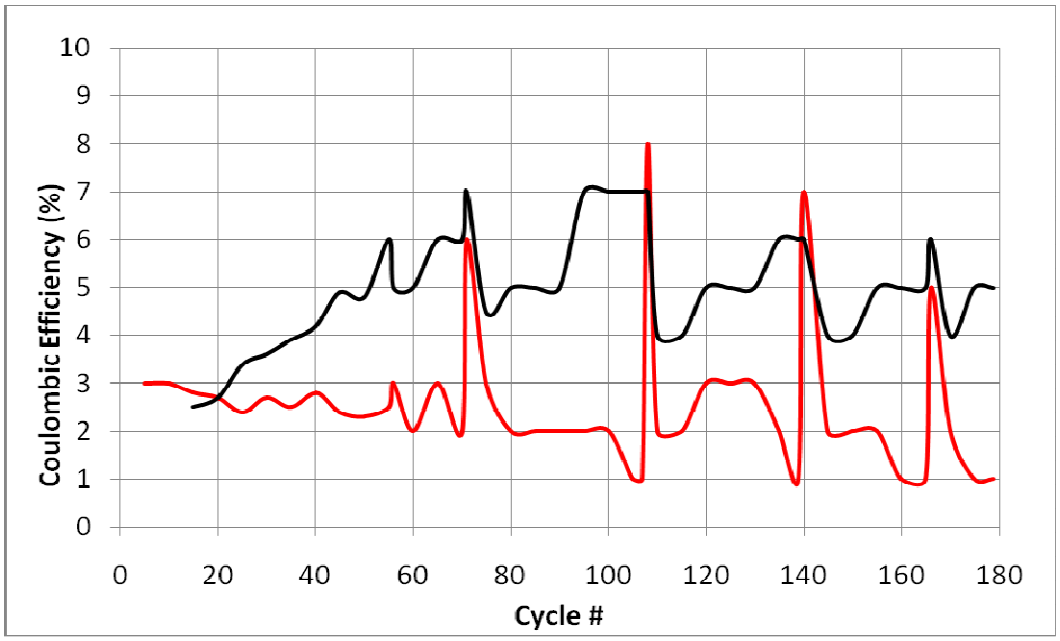

Figure 4-4-11: Coulombic efficiencies for the secondary (black) and tertiary (red) diffusion-limited discharge plateaus for AC3 non-annealed 75% N_2 Al-CNx anode subjected to 180 cycles at a current density of 0.5 mA/cm^2 without an initial CV.

One can see that at first the plateau separation decreases and the coulombic efficiency increases indicating the formation of the LiAl phase and improvement in the kinetics and reversibility of the lithiation-delithiation. Progressing towards the fifth cycle the main CE increases sharply up to 82% with a set minimum of 0.85V for the plateau separation (**Figs. 4-4-9, 4-4-10**). At the fifth cycle the tertiary diffusion-limited plateau appears around 2.15V with a CE of 3% (**Fig. 4-4-11**). Moving from the 5th to the 10th cycle the main CE reaches maximum value for the whole set of 87% with the plateau separation remaining small around 0.93V (**Figs. 4-4-9, 4-4-10**). This value for Al-CNx (AC3) is noticeably higher than the max main CE of 73% observed over the whole set for the bare GF Al failure anode (GF5) (**Fig. 4-4-10**). This suggests that the presence of the CNx coating at first considerably improves the reversibility of lithiation-delithiation under these cycling conditions. At the 15th cycle the secondary diffusion-limited plateau appears at 1.63V with an initial CE of 2.5% (**Fig. 4-4-11**). This process will steadily grow to a maximum CE of 7% by the 100th cycle of AC3 (Al-CNx) and is very similar to the

maximum value of 7% observed for the same experiment in bare GF Al (GF5, **Fig. 4-1-12**). After the 15th cycle the main CE shows a constant steady drop accompanied by a continuous increase in the main plateau separation (**Figs. 4-4-9, 4-4-10**). This indicates unfavourable changes in the structure of the LiAl phase with cycling and is consistent with the behaviour of the other half-cell failure anodes presented in this work (Ch. 4.1 to 4.3). Here we see that the degradation of AC3 (Al-CNx) is significantly worse than for GF5 (bare GF Al). The downward curvature in the charging plateau for AC3 also becomes far more severe as it drifts negative below 0V (**Fig. 4-4-7**). As usual the tertiary plateau potential shifts upward over time and hits the upper potential limit of +2.6V at the 25th cycle (**Fig. 4-4-11**). The degradation observed in the performance of AC3 (non-annealed Al-CNx) will instead be directly related to a combination of increasing secondary diffusion losses and a shortening of the main discharge plateau itself. Taken together, these changes indicate that the lithiation-delithiation of the nanosructure present at the anode surface at this time is getting progressively more and more difficult.

By the 70th cycle the main CE has decreased to 69% with the plateau separation increasing to almost 2V and the secondary CE up to 6% (**Figs. 4-4-9, 4-4-10, 4-4-11**). The CE is now equal to the one observed with uncoated GF Al indicating that the positive initial effect of the CNx coatings has largely disappeared. At the 71st cycle we observe the first jump in the plateau potentials. In the bare GF Al failure experiment (GF5) we did not observe the first plateau jump until the 80th cycle, likely related to the more severe degradation of Al-CNx (AC3) here. To recall, the jump is related to shedding of the irregular disordered portion of the LiAl phase responsible for the kinetic limitations observed in the previous cycles. Immediately following the jump the plateau separation resets to 0.93V with the charge plateau itself becoming flat again (**Fig. 4-4-9**). The change in potentials here are far more drastic than the first jump in GF5. As usual we observe a local maximum of the tertiary CE as the process has a longer duration before being terminated by the upper limit (**Fig. 4-4-11**). However, in the other respects, the overall peak shape and width appeared fairly similar before and after the jump.

After the jump the AC3 system appears to briefly stabilize and improve. From the 71st to the 75th cycle the main CE increases to 74% and the secondary and tertiary CEs decrease to 4.5% and 3% respectively. As in other half-cell failure anodes the effect is only temporary and the same degradation trends soon continue as a new portion of the disordered phase accumulates at the surface. From the 75th to the 95th cycle the main CE has dropped to 61% with the plateau separation up to 2V again (**Figs. 4-4-9, 4-4-10**). From the 95th to the 107th cycle the degradation accelerates, with both charge and discharge portions showing very noisy potential responses (**Fig. 4-4-7**). By the 107th cycle the main CE has plummeted down to only 33% due to the entire discharge peak width drastically narrowing (**Fig. 4-4-10**). However the secondary CE remains noticeable at 7% while the tertiary CE is essentially absent (**Fig. 4-4-11**). The plateau separation is almost 2.3V with the charge plateau itself around -0.8V (**Fig. 4-4-9**). The degradation behaviour observed within this particular cycling interval of AC3 (non-annealed Al-CNx) is more significant than for any other half-cell failure anode experiments in this thesis.

At the 108th cycle we observe the second jump in plateau potentials. Following the jump the plateau separation resets to 1.02V and the charge plateau is flat again (**Fig. 4-4-9**). Here we immediately observe a large main CE increase in the discharge peak of the 108th cycle up to 51%, with the secondary CE remaining significant around 7% (**Figs. 4-4-10, 4-4-11**). From the 108th to the 110th cycle we will again observe a temporary performance improvement similar to the first jump. This time the improvement is much larger with the main CE up to 73% as the secondary and tertiary CEs decrease to 4% and 2% respectively. Onwards from the 110th cycle the degradation of the anode will begin again, but to a far more subtle degree than the trends preceding the second jump. By the 139th cycle the main CE only shows a small decrease to 67% (**Fig. 4-4-10**). However the plateau separation again increases sharply to a value of 2.03V (**Fig. 4-4-9**). At the 140th cycle we observe the third jump in plateau potentials, with the separation resetting to 0.98V (**Fig. 4-4-9**). Again there will be a temporary improvement of the main CE up to 71% by the 145th cycle (**Fig. 4-4-10**). As in the trends preceding the third jump the degradation that follows here will be subtle. A fourth and final jump is observed in this set around 165th cycle, see (**Fig. 4-4-7**). The AC3 anode does continue to steadily fail

slowly at this point with a main CE of 67% by the 180th cycle, with the secondary and tertiary CEs remaining around 5% and 1% respectively. Even though the frequency and severity of jumps is much higher here in the AC3 (non-annealed Al-CNx) anode the final main CE of 67% is comparable to the value of 70% for GF5 (bare GF Al) after 140 cycles. Additionally the maximum secondary CE of 6-7% observed here is again similar to the GF5 set, even though the process appears earlier in AC3.

As in previous failure experiments the plateau jump events are likely due to pulverization of the porous intermetallic structure as mechanical stresses of lithiation/delithiation accumulate in the anode. The presence of the CNx coating results in more regular porous nanostructure developed at the anode surface. This results in improved cycling performance (efficiency) for Al-CNx (AC3) relative to bare GF Al (GF5). Afterwards the failure of the Al-CNx anode is significantly worse both in terms of the plateau separation and the efficiency trends. The excessive plateau separation implies a build-up of resistance in the anode over time. Firstly, a more compact porous structure formed in Al-CNx may make some regions of the surface less accessible towards lithiation-delithiation. Secondly, in Ch. 4.6 we will reveal with TOF-SIMS depth profiling that the film-metal interface of Al-CNx anodes may contain aluminium carbides and/or nitrides. These compounds are known to be insulators which would increase the resistance. Also, their presence may extend the region of solid solution α-LiAl phase. As the porous structure is pulverized here under continuous cycling we would expect the CNx film to also fracture into progressively smaller sections. This will be demonstrated in the SEM imaging section 4.4.2 where the volume change containment by the CNx results in the underlying porous structure experiencing significantly less cracking. However this causes the CNx film to be essentially destroyed. The severe degradation in the main CE between the first and second plateau jumps of Al-CNx (AC3) (**Fig. 4-4-10**) may correspond to just this process. After this point the efficiency rapidly improves to and remains around 70%, similar to that of bare GF Al (GF5). The influence of CNx coatings on capacity loss mechanisms in Al anodes will be further discussed in Ch. 5.

Dural-CNx anodes

Shown in **Fig. 4-4-12** are the partial cathodic scans of 75% N_2 and 25% N_2 plasma Dural-CNx samples DC1 and DC2 between 2V and 0.25V vs. Li^+/Li electrode (**Fig. 4-4-1**). For the purposes of comparison the bare Dural anode DU1 from Ch. 4.3 is also included. The bolded numbers **1** to **3** denote the DU1, DC1 and DC2 samples respectively (1, Dural; 2, 75% N_2 Dural-CNx; 3, 25% N_2 Dural-CNx).

We see that in the first scan the presence of the CNx film has very minimal if any effect on the lithiation onset potential for Dural-CNx, possibly because it is already difficult to lithiate Dural relative to GF Al. However additional scanning in the CV will produce a more positive lithiation onset potential for Dural-CNx relative to Dural, with a further positive shift as the nitrogen content is increased to 75% N_2 (DC1) (**Fig. 4-4-13**). This suggests that after some initial formation of the porous nanostructure in Dural-CNx further lithiation will occur with this structure rather than with previously unreactive Dural because it is energetically more favourable. This effect of CNx on the lithiation onset potential of Dural is quite different from GF Al where the coating resulted in a consistently more negative lithiation onset potential in the CV (**Figs. 4-4-1, 4-4-2**). Both Dural-CNx samples show larger cathodic currents for the SEI formation relative to bare Dural which again suggests that the SEI is formed not only on Dural but on the CNx coating as well. This effect is further amplified in the 25% N_2 sample DC2. The 75% N_2 sample DC1 shows a broad SEI formation similar to bare Dural DU1 with no distinct reduction peaks. However DC2 does appear to contain two peaks in the region of 0.75 to 1.0V. Additional scanning in the CV will produce larger amounts of additional SEI formation for DC1 (75% N_2 Dural-CNx) relative to DU1, with this formation further increased in DC2 (25% N_2 Dural-CNx).

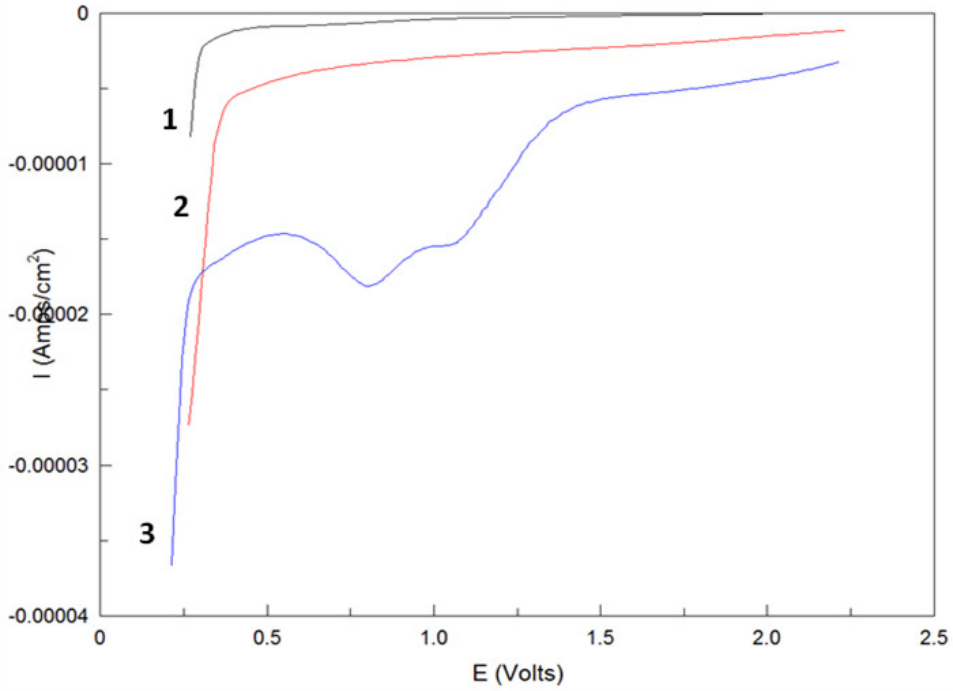

Figure 4-4-12: Initial cyclic voltammograms of non-annealed 75% N_2 and 25% N_2 Dural-CNx anodes DC1 (2, red) and DC2 (3, blue). Comparative bare Dural anode DU1 (1) from Ch. 4.3 is included in black. Partial cathodic scans from 2V to 0.1V to highlight SEI formation and lithiation onset behaviour.

Shown in **Fig. 4-4-13** are full CV scans of the three samples. Sample DC1 (75% N_2 Dural-CNx) shows a smaller loop area relative to DU1 (bare Dural) in the anodic scan, even with a higher lithiation current for the coated sample. However the difference in loop areas here is not nearly as dramatic as was observed in Al-CNx relative to bare GF Al (**Fig. 4-4-2**), and the effect here is further decreased in sample DC2 (25% N_2 Dural-CNx). The minor difference in loop areas for Dural-CNx versus Dural is consistent with the lithiation slopes only appearing slightly more gradual for both coated samples. Together these features suggest that the containment of volume changes of intermetallic phase formation upon applying the CNx coating in Dural is less significant than in GF Al (**Fig. 4-4-2**), and the effect is even more minimal as the nitrogen content is decreased. Dural itself should already be considerably more tougher mechanically against the lattice contractions and expansions of lithiation-delithiation, resulting in the formation of a more compact intermetallic phase. The decreased volume change containment at lower

nitrogen content (DC2) can be understood again on the basis that less incorporation of nitrogen-containing functional groups effectively decreases the cross-linking within the CNx and therefore its mechanical stability (hardness). As in Al-CNx anodes both Dural-CNx anodes show only a single delithiation peak, suggesting again that lithiation-delithiation occurs entirely through intermetallic phase formation and dissolution with the Al content. While both Dural-CNx anodes show an earlier lithiation onset potential the delithiation peak potentials are still shifted positive relative to Dural. The resulting overvoltages are however still smaller for Dural-CNx. This behaviour is unlike Al-CNx, where the inclusion of the 75% N_2 CNx film clearly increased the overvoltage of the GF Al anode system in the CV (**Fig. 4-4-2**). Like the subtle changes in the onset slope and loop areas, this again suggests that a different nanostructure may be formed during lithiation-delithiation of Dural-CNx.

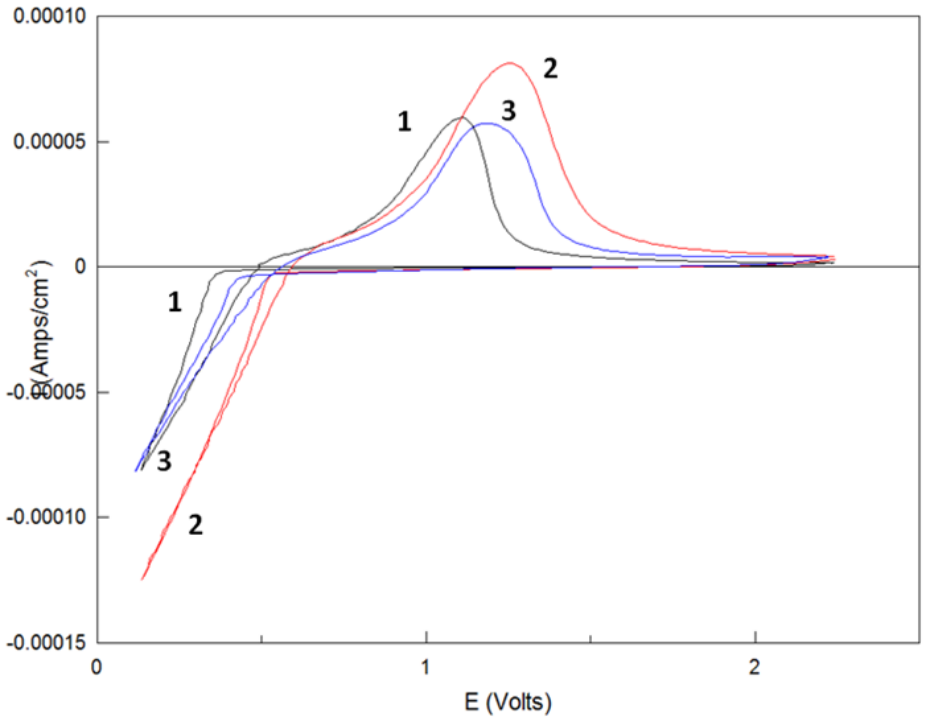

Figure 4-4-13: Initial cyclic voltammograms of non-annealed 75% N_2 and 25% N_2 Dural-CNx anodes DC1 (2, red) and DC2 (3, blue). Comparative bare Dural anode DU1 (1) from Ch. 4.3 is included in black. Full single scans.

Shown in **Fig. 4-4-14** are the features of a typical set of galvanic cycles for 75% N_2 Dural-CNx anode DC1 at a current density of 0.25 mA/cm^2 in red color, with the comparative cycle set of the Dural anode DU1 in black color. Overall we observe a similar sequence of events (denoted in the numbers **1** to **5**) within the cycle set. Similar to bare Dural (DU1) there is increased curvature between the IR jump and establishment of the discharge plateau for DC1, as well as increased curvature in the charge and discharge plateaus themselves. However, now we see that the presence of CNx affects more the lithiation rather than delithiation potential. This may be related to the fact that the lithiation potential of Dural is shifted already to more negative potentials due to slow kinetics at Cu and Mg alloying elements. When the Dural anode is coated with CNx, the reduction will occur on CNx rather than Dural and will require less overpotential.

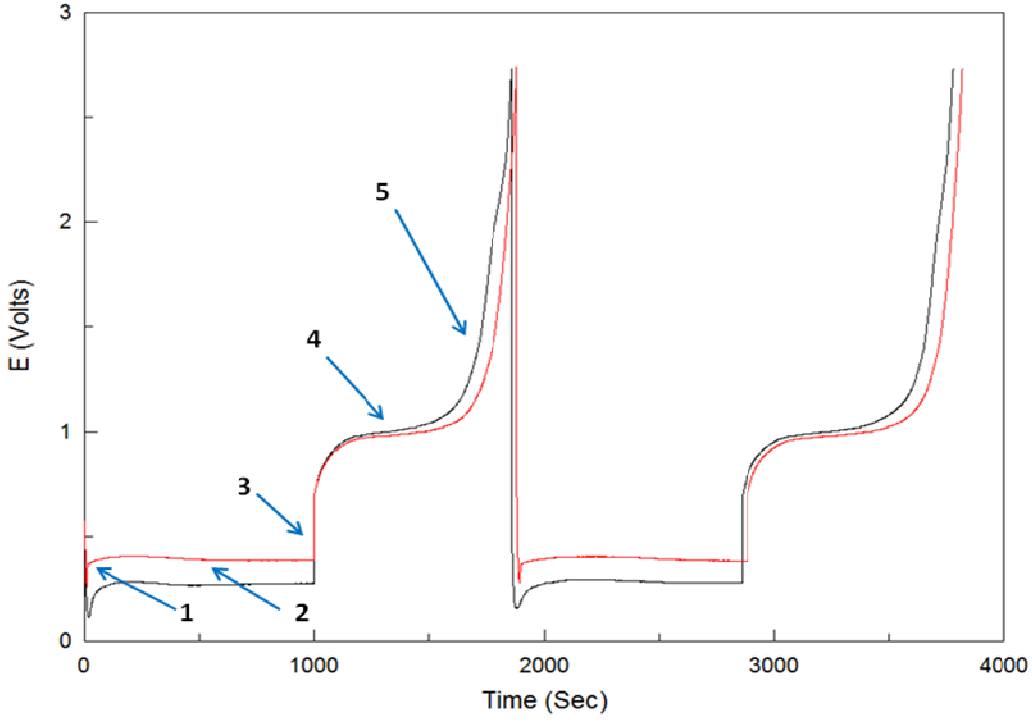

Figure 4-4-14: Typical galvanic cycles for lithiation/delithiation of a Dural-CNx anode (red curve). This is sample DC1 in which the CNx film was deposited at 75% N_2 plasma prior to electrochemical scans. Comparative bare Dural anode DU1 from Ch. 4.3 is also included (black curve). Numbers indicate the features of interest: (1) potential overshot (2) charge plateau (3) IR drop (4) discharge plateau (5) discharge tail. Galvanic cycles are shown at a current density of 0.25 mA/cm^2.

Shown in **Fig. 4-4-15** are the set of galvanic cycles of non-annealed 75% N_2 and 25% N_2 Dural-CNx anodes DC1 and DC2 in red and blue colors respectively at a current density of 0.25 mA/cm^2. The comparative cycle set of the Dural anode DU1 is included in black color. In both Dural-CNx anodes we observe a stable charging/discharging response and again several important features emerge. Again, throughout the set 75% N_2 Dural-CNx (DC1) has a significantly more positive lithiation (charging) potential relative to Dural (DU1), consistent with the more positive lithiation onset potential observed for DC1 in the CV (**Fig. 4-4-13**). With decreased nitrogen content (DC2) the charging potential is shifted between that of DC1 and DU1, similar again to the correlation observed in the CV. Therefore, we confirm that lithiation is relatively easier to perform in Dural-CNx and increased nitrogen content enhances this effect, because the lithiation now occurs at nitrogen-containing species. The delithiation (discharging) potential of both Dural-CNx samples is shifted negative relative to Dural. Therefore delithiation is now also relatively easier to perform in Dural-CNx, which is opposite from the trend in the CV (**Fig. 4-4-13**). This plateau potential in the cycles appears to be unaffected by the nitrogen content. This may be due to a different charge transfer resistance and/or rate determining step. Finally, we note here that while the Dural-CNx samples have a consistently smaller plateau separation than Dural, the values are still notably larger than those observed for the same cycles of the non-annealed 75% N_2 Al-CNx anode AC1 (**Fig. 4-4-4**).

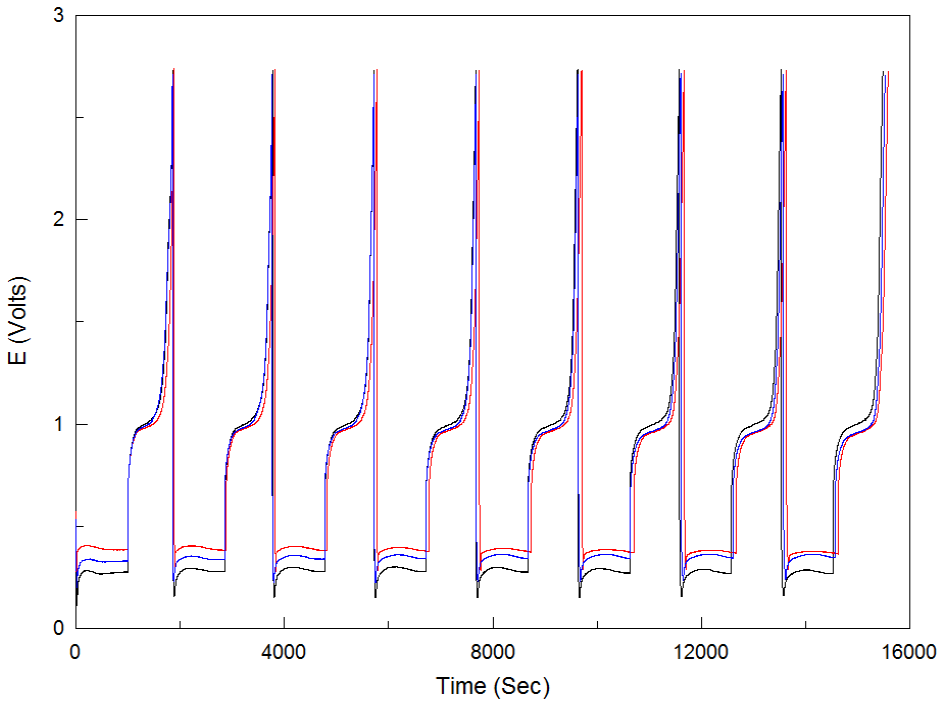

Figure 4-4-15: Galvanic cycles of non-annealed 75% N_2 and 25% N_2 Dural-CNx anodes DC1 (red) and DC2 (blue) at a current density of 0.25 mA/cm^2. Comparative bare Dural anode DU1 (oxide removed) from Ch. 4.3 is included in black.

Shown in **Fig. 4-4-16** are the first (a) and last (b) galvanic cycles for all samples in this set. One can see that with the 75% N_2 CNx coating the DC1 sample actually shows a longer main discharge plateau and improved coulombic efficiency (CE) relative to DU1 (bare Dural) **(Fig. 4-4-16 a)**. However the discharge of DC2 (25% N_2 Dural-CNx) is still significantly impeded, which will bring the initial CE below that for DU1. By the eighth cycle the differences in CE of all three samples will disappear as the discharge peak shapes become nearly identical **(Fig. 4-4-16 b)**. The evolution of the coulombic efficiencies with the cycle number is shown in **Fig. 4-4-17** for the four current densities used. Progressing to the third set the discharge peak shapes of all three samples will be similar throughout and so will the CE trends **(Fig. 4-4-17 c).** This will continue towards the end of the highest current density set where the trends diverge and DU1 (bare Dural) now having a superior performance relative to both coated samples **(Fig. 4-4-17 d)**.

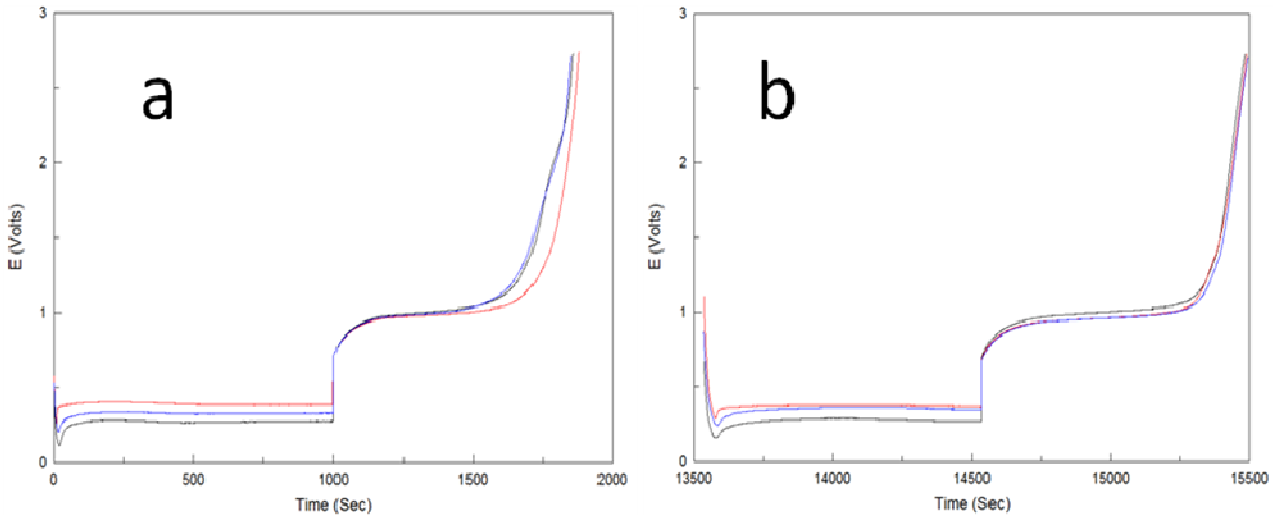

Figure 4-4-16: (a) First and (b) last galvanic cycles of non-annealed 75% N_2 and 25% N_2 Dural-CNx anodes DC1 (red) and DC2 (blue) at a current density of 0.25 mA/cm^2. Comparative bare Dural anode DU1 (oxide removed) from Ch. 4.3 is also included in black. Cycles in the right figure have been offset to overlap the curves on the same time scale.

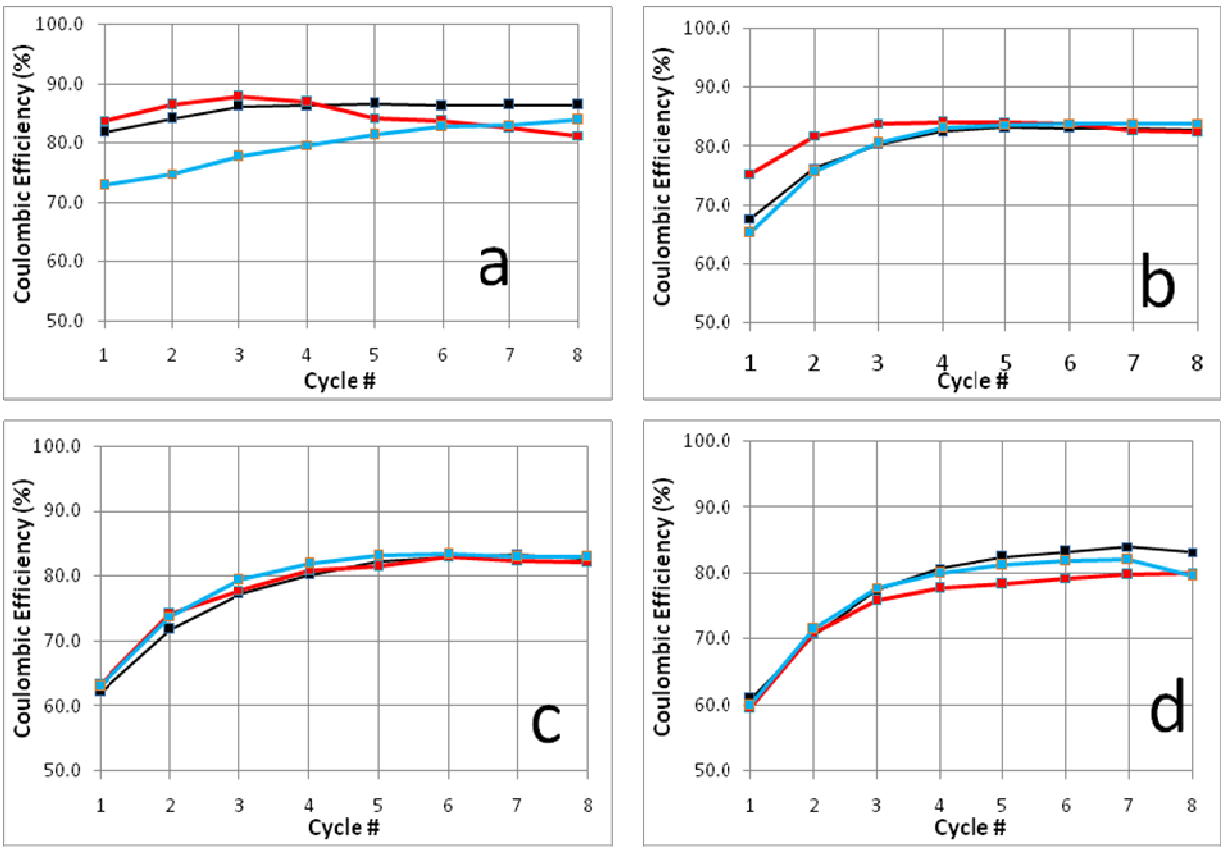

Figure 4-4-17: Coulombic efficiencies of non-annealed 75% N_2 and 25% N_2 Dural-CNx anodes DC1 (red) and DC2 (blue) at current densities of (a) 0.13 (b) 0.25 (c) 0.5 and (d) 1 mA/cm^2. Comparative bare Dural anode DU1 (oxide removed) from Ch. 4.3 is also included in black.

Overall these results suggest that at lower current densities the CNx coating can actually improve the reversibility of lithiation-delithiation in Dural, when comparing 75% N_2 Dural-CNx (DC1) to bare Dural (DU1) (**Fig. 4-4-17 a-b**). In contrast, the presence of the 75% N_2 CNx coating on GF Al noticeably impaired the reversibility at lower current densities (**Fig. 4-4-6 a-b**). Only at the highest current density did non-annealed Al-CNx achieve a consistently higher CE than bare GF Al (**Fig. 4-4-6 d**). The significant positive and negative shifts of charging and discharging plateau potentials for Dural-CNx (DC1) imply that lithiation-delithiation is relatively easier to perform even with very minimal intermetallic phase formation (**Fig. 4-4-15**). The porous structure that is formed with Dural-CNx may possibly be more stable resulting in less diffusion-limited delithiation

behaviour. The superior performance of DC1 (75% N_2) relative to DC2 (25% N_2) at lower current densities should be due to higher incorporation of nitrogen-based functional groups, which creates a film with superior mechanical properties.

To investigate the stability and cycling ability of the Dural-CNx anodes we performed half-cell failure experiments on new samples DC3 and DC4. The samples were prepared in the same way as DC1 (75% N_2) and DC2 (25% N_2) samples respectively used in the 4x8 experiments. We tested both 75% N_2 and 25% N_2 Dural-CNx samples to observe the influence of nitrogen content on the failure mechanism. As in previous half-cell anode failure experiments no prior electroformation of the LiAl phase was performed using either a CV or galvanic cycles at low current densities. The cycling was commenced immediately at a high current density of 0.5 mA/cm^2 for a total of 300 cycles each. This current density is equivalent to that of the third set of cycles in the 4x8 experiments.

Shown in **Fig. 4-4-18** are the full sets of the corresponding galvanic cycles for (a) DC3 (75% N_2) and (b) DC4 (25% N_2) Dural-CNx anodes. Beginning with DC3 we observe that the cycling behaviour is less stable compared to the similar experiment with bare Dural (DU2) (**Fig. 4-3-7**). The plateau potential jumps occur with larger amplitude and higher frequency. Before each jump the overvoltages in both charging and discharging plateaus significantly increase so that the charge plateau potential drifts well below 0V vs. Li^+/Li. With lower nitrogen content in the CNx film the DC4 sample shows even more pronounced degradation with twice the number of plateau potential jumps, even though the amplitude of the jumps is comparable to DC3. **Fig. 4-4-19** shows the first two (a) and last two (b) cycles respectively of both samples. Arrows in the figure indicate the secondary and tertiary plateaus appearing over time in the discharge portion of the cycles for both samples, which were also observed with cycling of bare Dural earlier in Ch. 4.3 (**Fig. 4-3-8**) and have been attributed to the diffusion-controlled delithiation of the α-LiAl intermetallic phase. To further characterize the performance of both samples, the separation between the charge plateau and the main discharge plateau is plotted in **Fig. 4-4-20**, together with the coulombic efficiencies of the main as well as the secondary and tertiary discharge plateaus shown in **Fig. 4-4-21** and **Fig. 4-4-22** respectively for every

fifth cycle starting from the first cycle. Additionally, the figures also show the data for cycles right before and after the potential jumps observed within the cycle set. For DC3 (75% N_2 Dural-CNx) and DC4 (25% N_2 Dural-CNx) we did not observe the secondary diffusion plateau until approximately the 25th and 30th cycles respectively. Additionally the tertiary diffusion plateau for DC3 was not observed until approximately the 5th cycle. Therefore the secondary and tertiary process CEs are absent within those regions of **Fig. 4-4-22**. For the sake of comparison, the data from the bare Dural half-cell failure experiment (DU2, oxide removed) from Ch. 4.3 is included in black color in both **Fig. 4-4-20** and **Fig. 4-4-21**, with the new DC3 (75% N_2) and DC4 (25% N_2) data appearing in red and blue colors respectively.

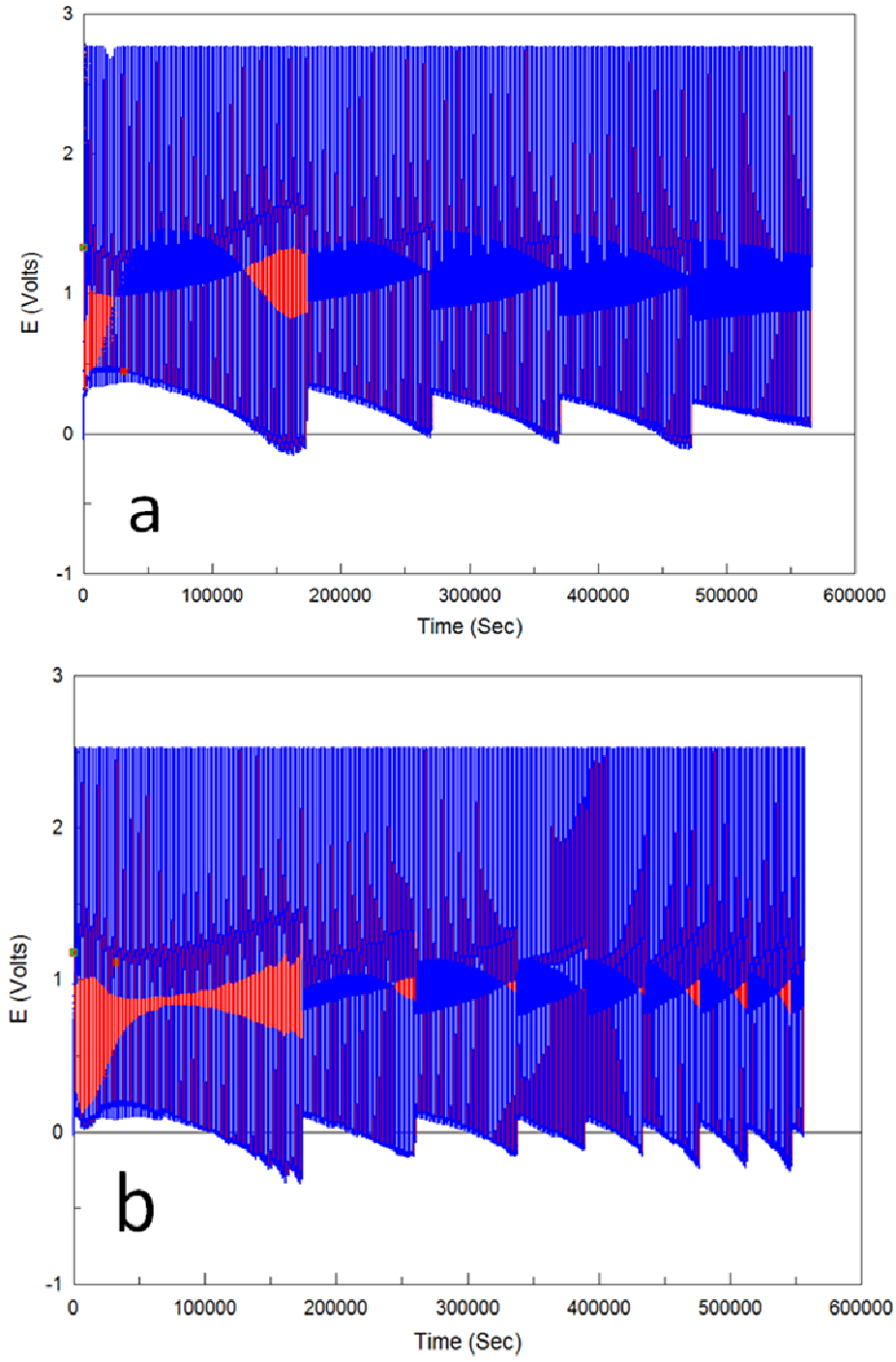

Figure 4-4-18: Full set of galvanic cycles for non-annealed (a) DC3 75% N_2 and (b) DC4 25% N_2 Dural-CNx anodes subjected to 300 cycles each at a current density of 0.5 mA/cm^2 without an initial CV.

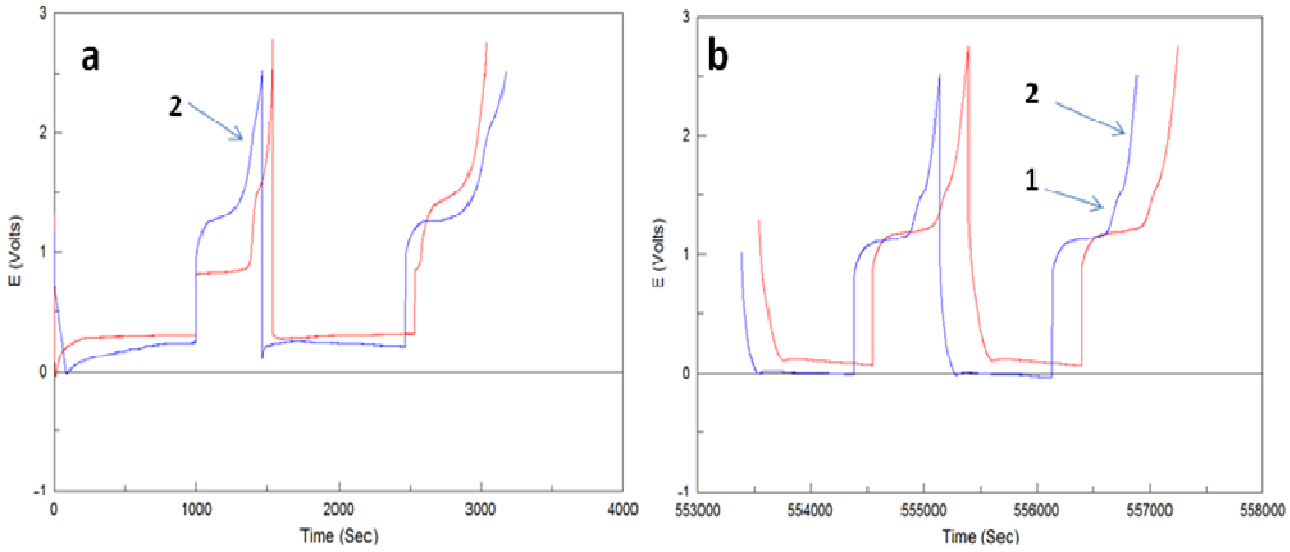

Figure 4-4-19: (a) First two and (b) last two galvanic cycles for non-annealed DC3 75% N_2 (red curve) and DC4 25% N_2 Dural-CNx anodes (blue curve) subjected to 300 cycles each at a current density of 0.5 mA/cm^2 without an initial CV. Numbers in the figures denote the secondary and tertiary diffusion-limited plateaus.

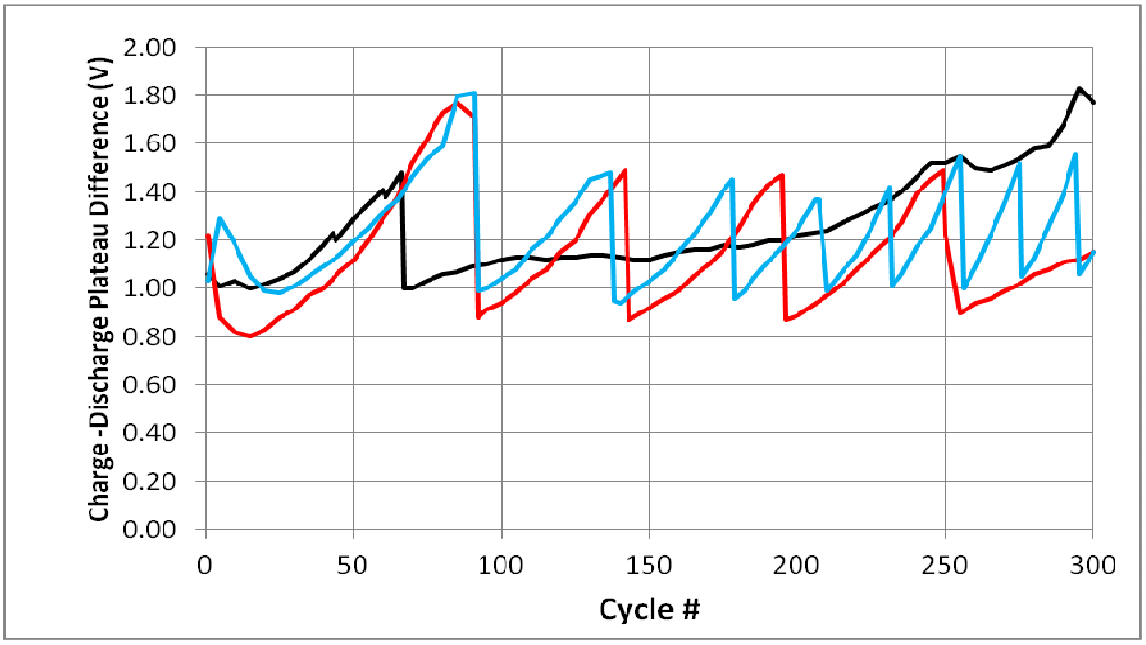

Figure 4-4-20: Charge-Discharge plateau separation for the main discharge plateau for non-annealed DC3 75% N_2 (red curve) and DC4 25% N_2 (blue curve) Dural-CNx anodes subjected to 300 cycles each at a current density of 0.5 mA/cm^2 without an initial CV. For comparison, data for bare DU2 Dural anode (oxide removed) from Ch. 4.3 is included in black.

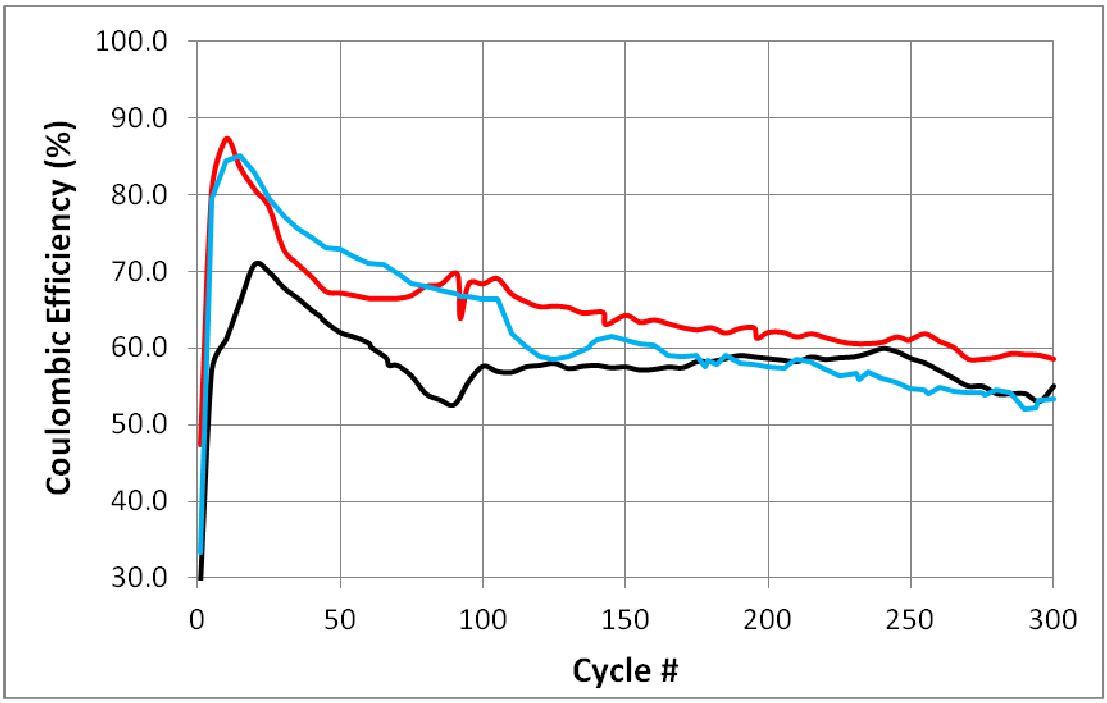

Figure 4-4-21: Coulombic efficiency data for the main discharge plateau for non-annealed DC3 75% N_2 (red curve) and DC4 25% N_2 (blue curve) Dural-CNx anodes subjected to 300 cycles each at a current density of 0.5 mA/cm^2 without an initial CV. For comparison, data for bare DU2 Dural anode (oxide removed) from Ch. 4.3 is included in black.

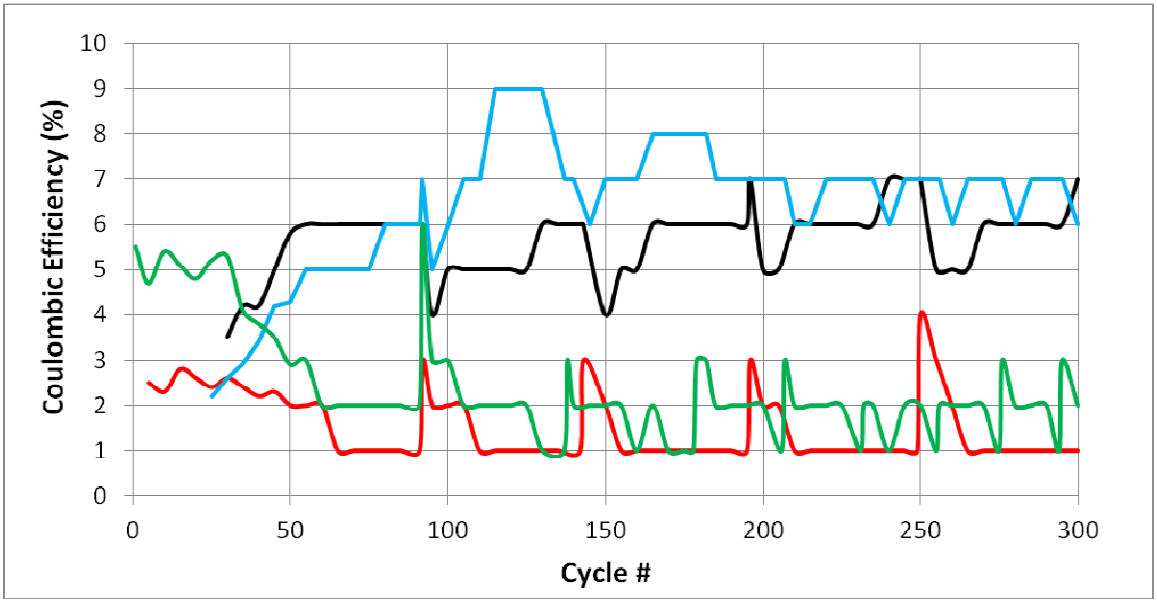

Figure 4-4-22: Coulombic efficiencies for the secondary and tertiary diffusion-limited discharge plateaus for non-annealed DC3 75% N_2 and DC4 25% N_2 Dural-CNx anodes subjected to 300 cycles each at a current density of 0.5 mA/cm^2 without an initial CV. Secondary and tertiary efficiencies of DC3 (75% N_2 Dural-CNx) in black and red colors respectively with DC4 (25% N_2 Dural-CNx) in blue and green colors respectively.

The first two cycles of DC3 (75% N_2 Dural-CNx) show two discharge plateaus (**Fig. 4-4-19 a**). In the first cycle this is dominated by the lower discharge plateau around 0.83V which may again uniquely arise from delithiation from CNx itself. For the second cycle of DC3 the discharge is instead dominated by the intermetallic phase plateau around 1.44V. This initial double discharge plateau behaviour was also observed in the first cycle of the non-annealed Al-CNx failure anode AC3 (**Fig. 4-4-8**). From the third cycle of DC3 (75% N_2 Dural-CNx) onwards we only observe a single discharge plateau beginning around 1.37V, which should constitute lithiation-delithiation from an intermetallic alloy. The tertiary plateau appears at the 5th cycle at a high potential of 2.6V with an initial CE of 2.5% (**Fig. 4-4-22**). As expected this tertiary process will shift upwards over time and be terminated early by the upper limit. Therefore it will remain as

a minor contribution for the entire set outside of the plateau jump cycles. There is a large early increase over time in the main CE consistent with initial SEI and intermetallic phase formation (**Fig. 4-4-21**). It culminates with a maximum main CE for the whole set of 87% at the 10th cycle for DC3 (75% N_2 Dural-CNx), which is higher than the value of 71% observed for DU2 (bare Dural). This improvement in DC3 is directly due to a longer main plateau duration since the tertiary process contributions are minor in both cases. The higher maximum main CE of Dural-CNx versus Dural is consistent with the same behaviour observed in the failure experiments of Al-CNx versus bare GF Al earlier in this chapter (**Fig. 4-4-10**). Within this cycle region the plateau separation for DC3 shows a minimum of 0.8V, which is smaller than the minimum value of 1V for DU2 (**Fig. 4-4-20**). This is consistent with the smaller overvoltage and plateau separation observed for Dural-CNx samples relative to Dural in the 4x8 experiments (**Fig. 4-4-15**). The secondary diffusion-limited plateau appears at the 30th cycle at 1.66V with an initial CE of 3% (**Fig. 4-4-22**).

Approaching the first jump in plateau potentials the main CE shows a steady decrease, together with the increasing contribution of the secondary diffusion process. The tertiary process gradually disappears due to the upper cycle potential limit (**Figs. 4-4-21, 4-4-22**). Here the degradation over time for the main CE of DC3 (75% N_2 Dural-CNx) is larger than in DU2 (bare Dural). Additionally, the change in the plateau separation over time is considerably more severe. Both of these trends are consistent with the faster degradation of the main CE and drifting of plateau potentials observed in non-annealed 75% N_2 Al-CNx versus bare GF Al (**Figs. 4-4-9, 4-4-10**). For DC3 (75% N_2 Dural-CNx) the secondary process CE will only reach a set maximum of 7%, unlike the maximum value of 15% seen in DU2 (bare Dural) (**Fig. 4-4-22**). This is in contrast to Al-CNx and GF Al failure experiments which had comparable maximum of the secondary process CEs over time (**Figs. 4-1-12, 4-4-11**). Immediately after the first plateau jump in the 92nd cycle of DC3, the plateau separation resets and the main CE drops further due to a shorter main plateau (**Figs. 4-4-20, 4-4-21**). As expected, the secondary process CE here remains unchanged and the tertiary process CE increases due to the downward potential shift (**Fig. 4-4-22**). Soon after the plateau jump there is a short and small improvement of the main

CE because the secondary process CE temporarily decreases (**Fig. 4-4-21**). As the DC3 anode continues to degrade again this will create a Christmas tree pattern for the plateau separation over time, which has been observed previously in this work such as in the failure experiment of non-annealed Al-CNx AC3 (**Fig. 4-4-7**). Over the span of 300 cycles there will be four total plateau jumps for DC3 (75% N_2 Dural-CNx) (**Fig. 4-4-18 a**). In comparison, the bare Dural failure anode DU2 only experienced two jumps after 300 cycles (**Fig. 4-3-7**), while the non-annealed Al-CNx failure anode AC3 already had four jumps after just 180 cycles (**Fig. 4-4-7**). The higher jump frequency and faster degradation of the main CE for Dural-CNx versus bare Dural anodes is consistent with the same behaviour observed in the failure experiments of Al-CNx versus bare GF Al anodes. Approaching the 300th cycle of DC3 the main CE will continue to decrease due to a shortening of the main plateau. This further degradation is unrelated to the secondary diffusion process as that CE has not increased beyond 7% (**Fig. 4-4-22**).

For the DC4 (25% N_2 Dural-CNx) anode there is no initial double discharge behaviour (**Fig. 4-4-19 a**). Instead we immediately observe only a single discharge plateau at 1.25V. However this first cycle shows significantly more diffusion-limited behaviour than the first cycle of DC3 (75% N_2). The tertiary diffusion process is already present around 2.14V with an initial efficiency of 5% (**Fig. 4-4-22**). This is consistent with the 4x8 experiments of the 25% N_2 (DC2) and 75% N_2 (DC1) Dural-CNx anodes (**Fig. 4-4-16, 4-4-17**). Like in DC3 this tertiary process in DC4 will soon become minor and only spike at the plateau jump cycles. The main CE of DC4 rapidly increases to a maximum value of 85% at the 15th cycle (**Fig. 4-4-21**). Within this region the plateau separation shows a minimum of 1V, which is larger than the minimum value of 0.8V in DC3 (**Fig. 4-4-20**). This is consistent with the larger overvoltage and plateau separation observed in the 4x8 experiments of 25% N_2 versus 75% N_2 Dural-CNx anodes (**Figs. 4-4-13, 4-4-15**). In DC4 (25% N_2 Dural-CNx) the secondary diffusion-limited plateau appears at the 25th cycle at 1.52V with an initial CE of 2% (**Fig. 4-4-22**).

Approaching the first jump in plateau potentials we observe the typical trends of main CE decreasing, secondary process CE increasing and tertiary process CE decreasing due to

the upper cycle potential limit (**Figs. 4-4-21, 4-4-22**). Both the main CE degradation and the plateau separation change over time in DC4 (25% N_2) here are comparable to DC3 (75% N_2). For DC4 the secondary process CE will reach a set maximum of 9%, then steadily decrease and remain at 7% (**Fig. 4-4-22**). Immediately after the first plateau jump in the 92nd cycle of DC4 the plateau separation resets and the main CE is unchanged (**Figs. 4-4-20, 4-4-21**). As expected the secondary process CE here remains unchanged and the tertiary process CE increases due to the downward potential shift (**Fig. 4-4-22**). Even though the secondary process CE will briefly decrease for a few cycles following the jump, the plateau separation and main CE will continue to degrade without any temporary improvement (**Figs. 4-4-20, 4-4-21**). While the degradation of DC4 (25% N_2) is comparable to DC3 (75% N_2) approaching the first jump, it will now be more severe beyond this point. This again results in a Christmas tree pattern for DC4 with eight plateau jumps across 300 cycles (**Fig. 4-4-18 b**). Even though the jump frequency for DC4 is much higher the amplitude of the jumps over time is still comparable to DC3 (**Fig. 4-4-20**). Approaching the 300th cycle of DC4 the main CE will continue to decrease due to a shortening of the main discharge plateau (**Fig. 4-4-19 b**). This further degradation is unrelated to the secondary diffusion process as that CE has steadily decreased from its maximum of 9% (**Fig. 4-4-22**).

4.4.2 SEM images

Shown in **Fig. 4-4-23** are SEM images of the uncycled areas of the non-annealed (AC1) and annealed (AC2) Al-CNx anodes, as well as the reference bare GF Al anode (GF1) from Ch. 4.1. In both cases the uncycled Al-CNx morphology is dominated by the etching pattern of the Al substrate, with higher magnification revealing the fine grain structure of the overlaying CNx film (**Fig. 4-4-23 b-c**). **Fig. 4-4-24** shows the cycled areas of the same Al-CNx samples at different magnifications after being subjected to the 4x8 experiments. The non-annealed Al-CNx (AC1) shows a homogenous porous alloy morphology (**Fig. 4-4-24 c**), very similar to that observed for bare GF Al in Ch. 4.1.2 (**Fig. 4-1-13 b**). Overlaying this porous structure are relatively flat remnants of a thin film, which upon closer observation strongly resemble the fine grains of CNx in the

uncycled area (**Fig. 4-4-24 a**). The annealed sample AC2 under 4x8 conditions shows the opposite behaviour (**Fig. 4-4-24 b-d**). The remaining CNx is not found at the surface of the porous structure. Instead the CNx film appears to be located inside and below the porous alloy, which suggests that it may be incorporated in the growing LiAl phase, or buried under this phase during its growth. Therefore the annealing treatment appears to offer improved adhesion and stability for the film.

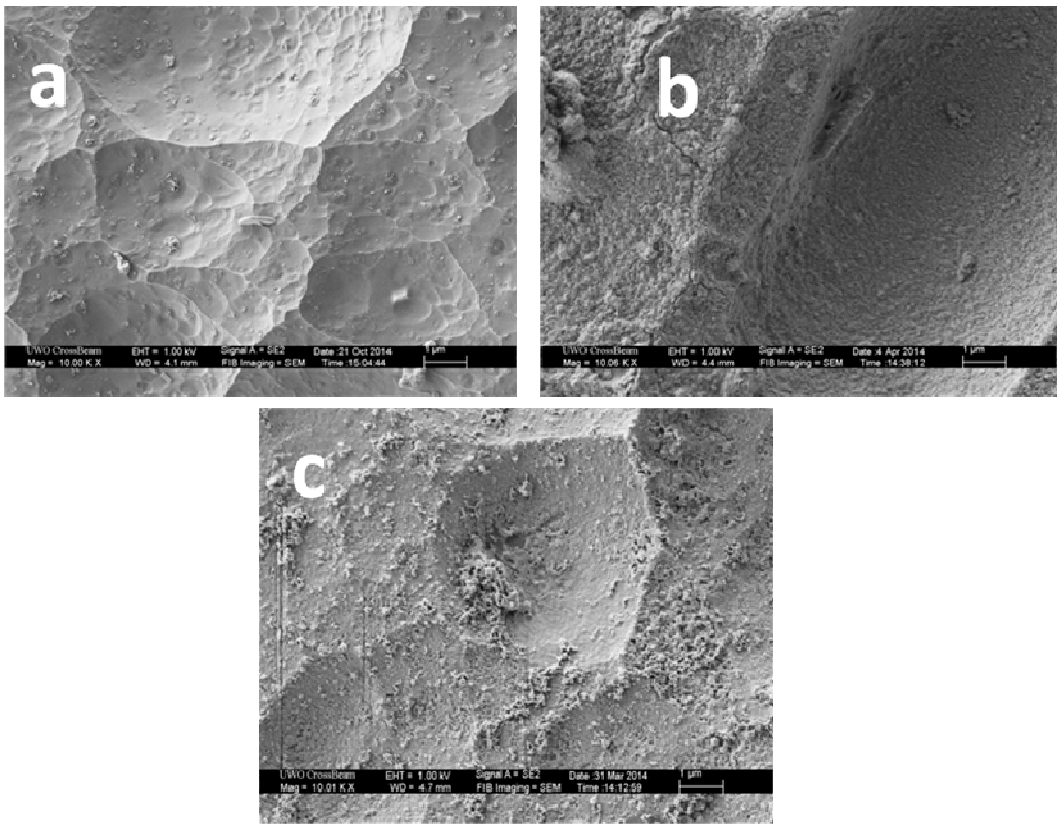

Figure 4-4-23: SEM images of uncycled areas for (a) bare GF Al (GF1), (b) non-annealed (AC1) 75% N_2 Al-CNx, (c) annealed (AC2) 75% N_2 Al-CNx anodes. Magnifications of 10000x.

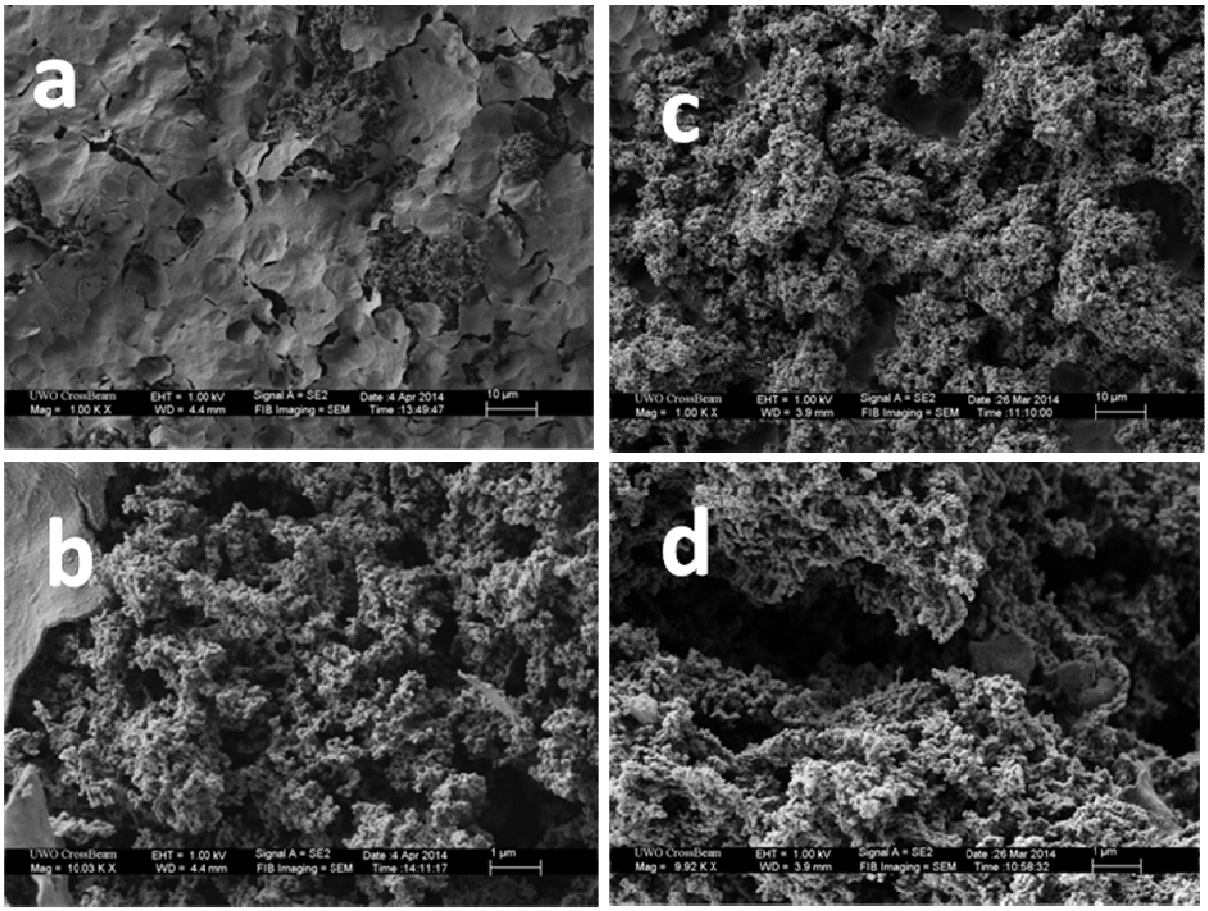

Figure 4-4-24: SEM images of cycled areas for (a-b) non-annealed (AC1) 75% N_2 Al-CNx, (c-d) annealed (AC2) 75% N_2 Al-CNx anodes. Magnifications of (a,c) 1000x (b,d) 10000x.

Fig. 4-4-25 shows the cycled area of the non-annealed Al-CNx failure anode (AC3) at various magnifications, as well as the reference bare GF Al failure anode (GF5) from Ch. 4.1. Pushing the Al-CNx anode towards failure again creates some large scale cracking, observed at the lowest magnification (**Fig. 4-4-25 d**). However both the size of these cracks and their coverage across the entire cycled area appear to be considerably lower than in the analogous bare GF Al anode under failure cycling (GF5) (**Fig. 4-4-25 a**). This suggests containment of the volume changes and improvement of the mechanical stability by the CNx film even after extended cycling. Closer inspection reveals that the remaining

CNx are still found at the surface as blocky patches both on top and wrapped around various portions of the porous intermetallic alloy (**Fig. 4-4-25 e-f**). The highest magnification images reveal quite similar nanostructures developed upon cycling for bare GF Al (oxide removed) (GF5) and non-annealed Al-CNx (AC3), except for some residual CNx still observed in the latter image. Essentially the non-annealed Al-CNx failure anode (AC3) appears to follow the trends developing with the non-annealed Al-CNx anode in 4x8 experiments (AC1) (**Fig. 4-4-24 a-b**), with the residual CNx progressively cracked into smaller pieces. The significant pulverization of the CNx film here may help explain the dramatically worse reversibility and plateau separation trends observed in the galvanic cycles of AC3 between the first and second plateau potential jumps (**Figs. 4-4-9, 4-4-10**).

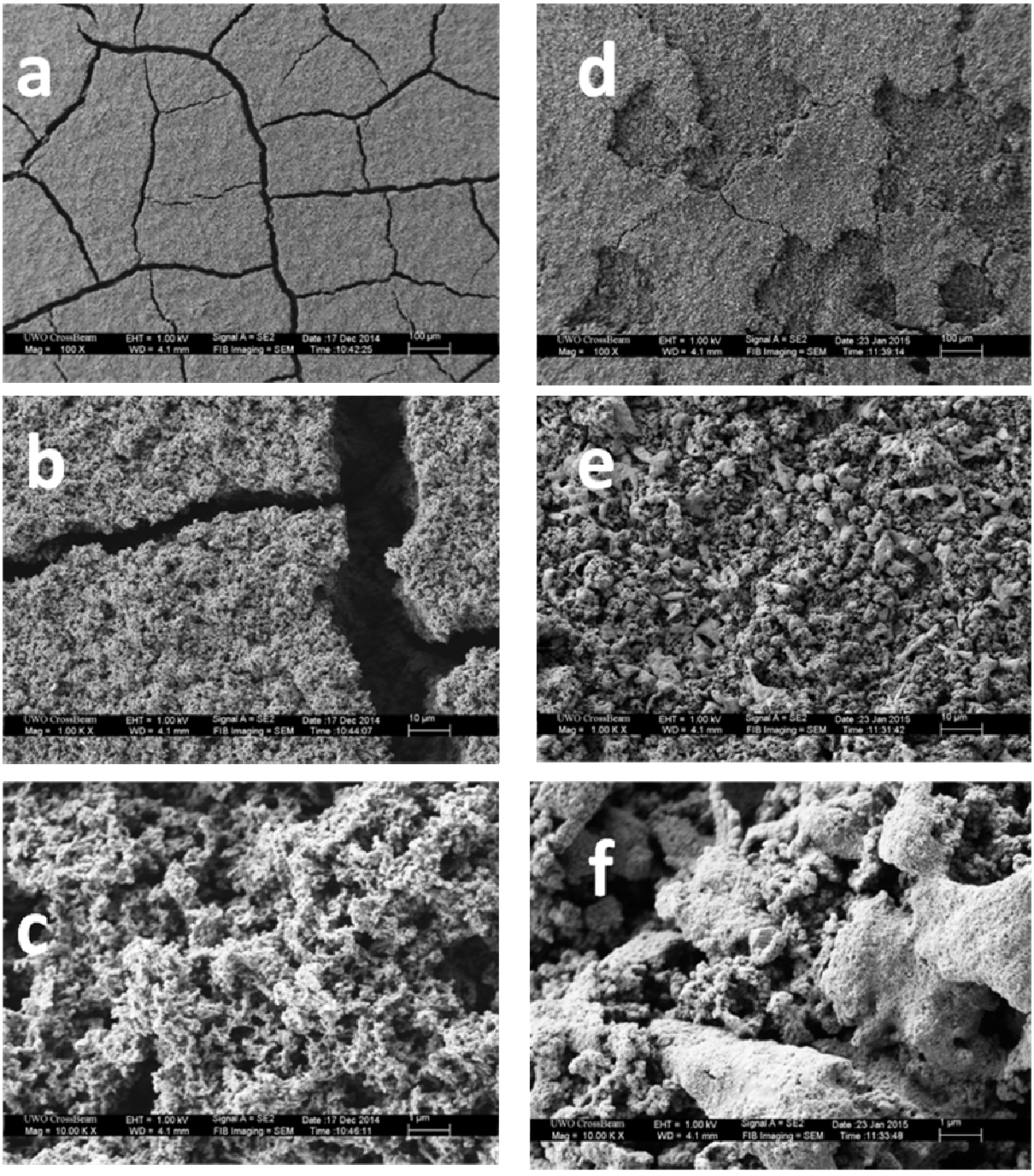

Figure 4-4-25: SEM images of cycled areas for (a-c) bare GF Al (oxide removed) (GF5) (d-f) non-annealed Al-CNx (AC3), subjected to 140 and 180 cycles each respectively at a current density of 0.5 mA/cm2 without an initial CV. Magnifications of (a,d) 100x, (b,e) 1000x, (c,f) 10000x.

Shown in **Fig. 4-4-26** are SEM images of the uncycled areas of the non-annealed 75% N_2 (DC1) and 25% N_2 (DC2) Dural-CNx anodes, as well as the reference bare Dural anode (DU1) from Ch. 4.3. For both CNx coated samples the uncycled morphology is dominated by the rough pitted etching pattern of the Dural substrate (**Fig. 4-4-26 b-c**), with the finer details of the CNx grain structure at higher magnification (**Fig. 4-4-26 d**). **Fig. 4-4-27** shows the cycled areas of the same Dural-CNx samples at different magnifications after being subjected to the 4x8 experiments. The 75% N_2 Dural-CNx sample (DC1) shows a cycled morphology that is quite distinct from that described above for the analogous non-annealed 75% N_2 Al-CNx sample AC1. There is a roughly equal mixture of flat and porous regions (**Fig. 4-4-27 a**), indicating significantly limited lithiation-delithiation reactivity similar to that observed for bare Dural in Ch. 4.3.2. The flat regions of DC1 strongly resemble the uncycled areas (**Fig. 4-4-26 b**). While the CNx remnants in the non-annealed Al-CNx sample (AC1) were overlaid on the porous alloy (**Fig. 4-4-24 a**), here in DC1 they are instead located near the metal substrate. This confirms that the phase formation for Dural-CNx is quite different than with Al-CNx. It may help explain the electrochemical differences observed in the CVs and galvanic cycles for these series of anodes both in the 4x8 and the failure experiments. Therefore, the containment of the volume change in Dural through the use of CNx coatings and the associated changes in conductivity should be different than in GF Al. Cycling Dural-CNx with lower nitrogen content under 4x8 conditions (DC2) produces again a heterogeneous morphology similar to that described above for DC1 (75% N_2). However the porous regions are now much more numerous and occupy more surface area (**Fig. 4-4-27 c**). This suggests increased lithiation-delithiation reactivity of Dural-CNx with decreased nitrogen content in the CNx film, which is unusual given the smaller lithiation-delithiation currents observed for this sample in the CV (**Fig. 4-4-13**). Despite these differences between the two Dural-CNx samples the higher magnification images reveal very similar porous morphology (**Fig. 4-4-27 b,d**). Therefore a similar nanostructure is formed in both cases.

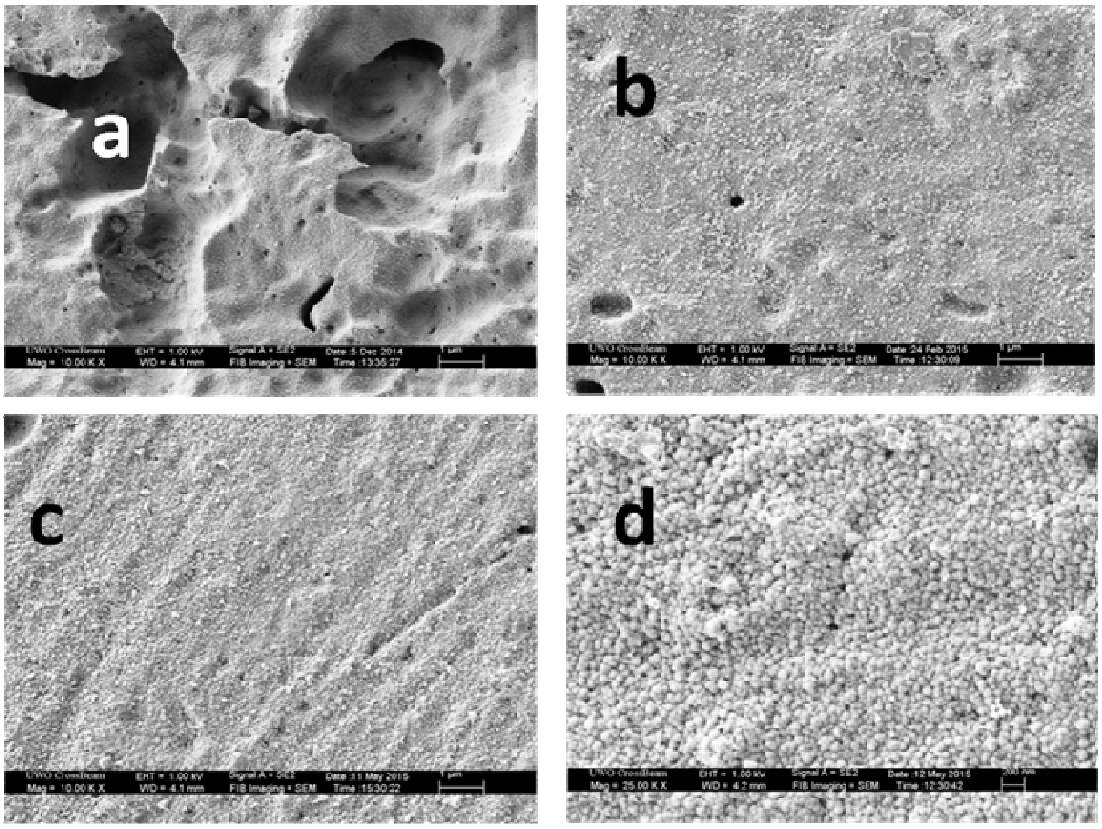

Figure 4-4-26: SEM images of uncycled areas for (a) bare Dural (DU1), (b) non-annealed 75% N_2 (DC1) Dural-CNx, (c) non-annealed 25% N_2 (DC2) Dural-CNx anodes. Magnifications of 10000x. Image (d) shows higher magnification (25000x) of image (b).

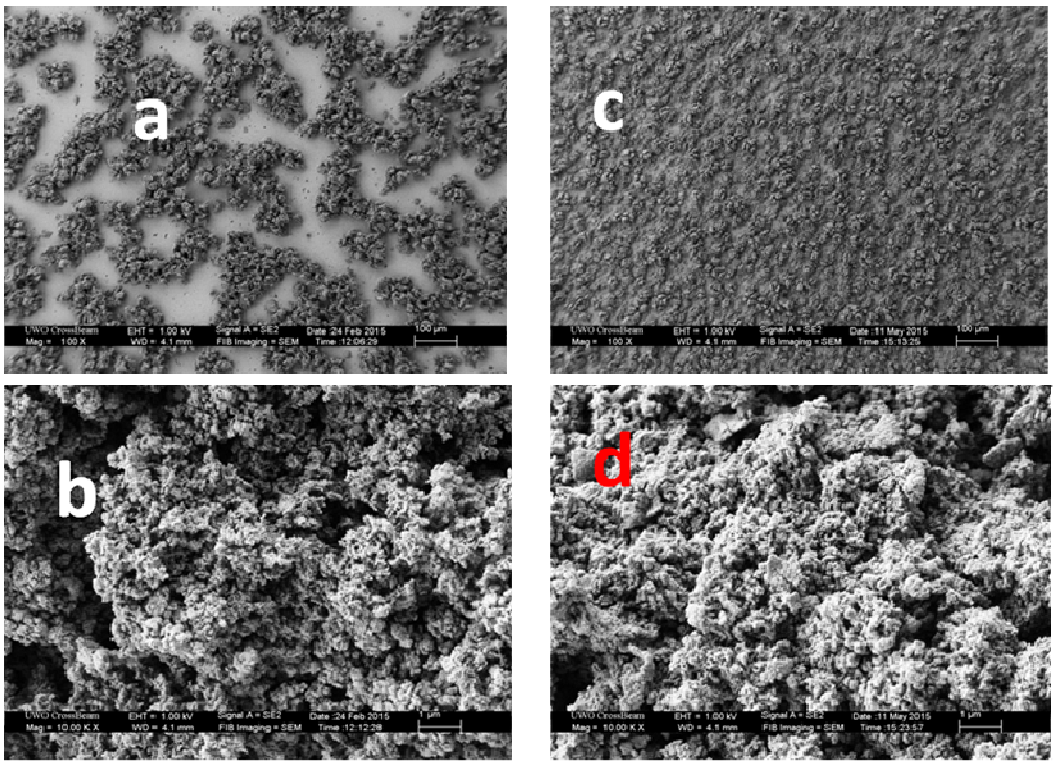

Figure 4-4-27: SEM images of cycled areas for (a-b) non-annealed 75% N_2 (DC1) Dural-CNx, (c-d) non-annealed 25% N_2 (DC2) Dural-CNx anodes. Magnifications of (a,c) 100x, (b,d) 10000x.

Fig. 4-4-28 shows the cycled areas of the non-annealed 75% N_2 (DC3) and 25% N_2 (DC4) Dural-CNx failure anodes. The DC3 sample (**Fig. 4-4-28 a-b**) shows an overall porous cycled morphology that is considerably more homogenous than the 4x8 version (**Fig. 4-4-27 a**). It is very similar to the bare Dural failure anode in Ch. 4.3.2 with full reactivity, large porous cluster size and no cracks present. This should be attributed to longer cycling and repeated formation and pulverization of the LiAl phase for the failure samples. Unlike the non-annealed Al-CNx failure anode (AC3), no residual CNx film seems to appear in this Dural-CNx failure anode. This was confirmed by EDX analysis, with no nitrogen content found anywhere throughout the cycled area of this Dural-CNx failure anode. It suggests that the CNx remaining after prolonged cycling of Dural-CNx is buried underneath several micrometers of intermetallic alloy, possibly near the interface with the Dural substrate. Pushing the Dural-CNx anode with lower nitrogen content

towards failure in DC4 (25% N_2) again produces a homogenous porous morphology very similar to that described above for DC3 (75% N_2) (**Fig. 4-4-28 c-d**). Once again, no residual CNx film is found after prolonged cycling. Therefore, the lower nitrogen content in the CNx film does not appear to affect the resulting morphology for Dural-CNx under these failure conditions. Both Dural-CNx samples do not visibly crack under failure conditions and the nanostructure produced is similar.

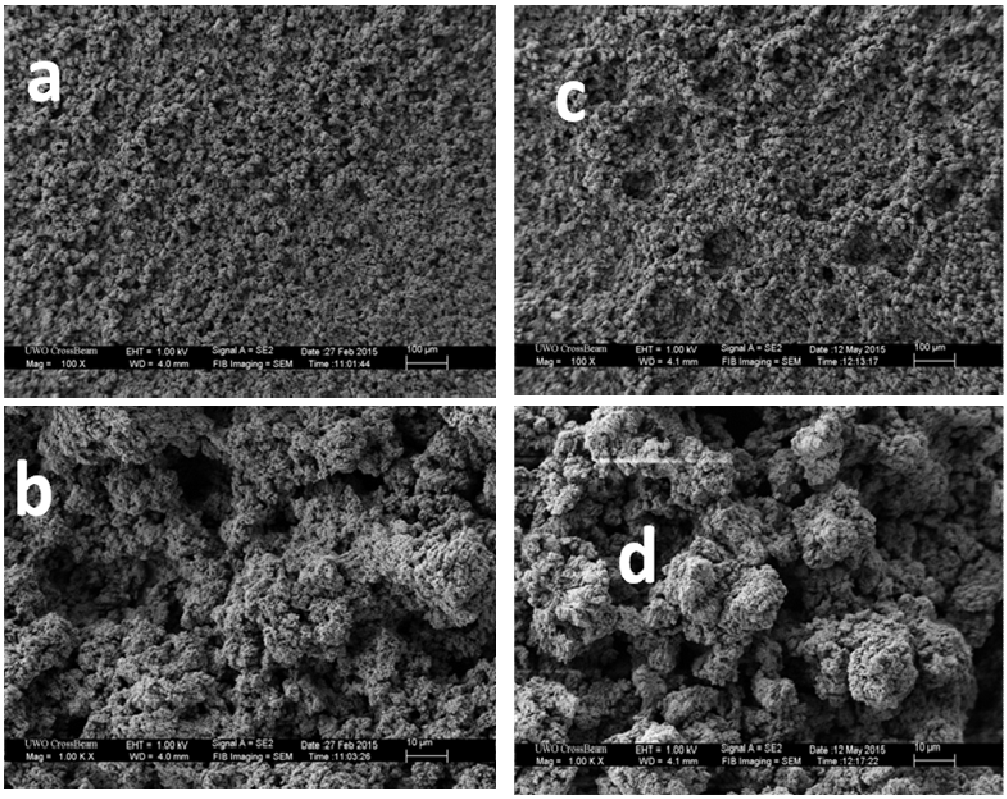

Figure 4-4-28: SEM images of cycled areas for (a-b) 75% N_2 (DC3) Dural-CNx, (c-d) 25% N_2 (DC4) Dural-CNx anodes subjected to 300 cycles each at a current density of 0.5 mA/cm^2 without an initial CV. Magnifications of (a,c) 100x, (b,d) 1000x.

Finally shown in **Fig. 4-4-29** is a comparison of the cycled areas for the non-annealed 75% N_2 Al-CNx (AC3) and the non-annealed 75% N_2 Dural-CNx (DC3) failure anodes presented earlier in separate figures. Here we observe that both porous morphologies are fairly stable. With Dural as the substrate the nanostructure produced is rougher (**Fig. 4-4-**

29 c-d), and with GF Al as the substrate there is more evidence of cracking (**Fig. 4-4-29 a-b**). However, the fine morphology of the LiAl phase formed is quite similar in both cases.

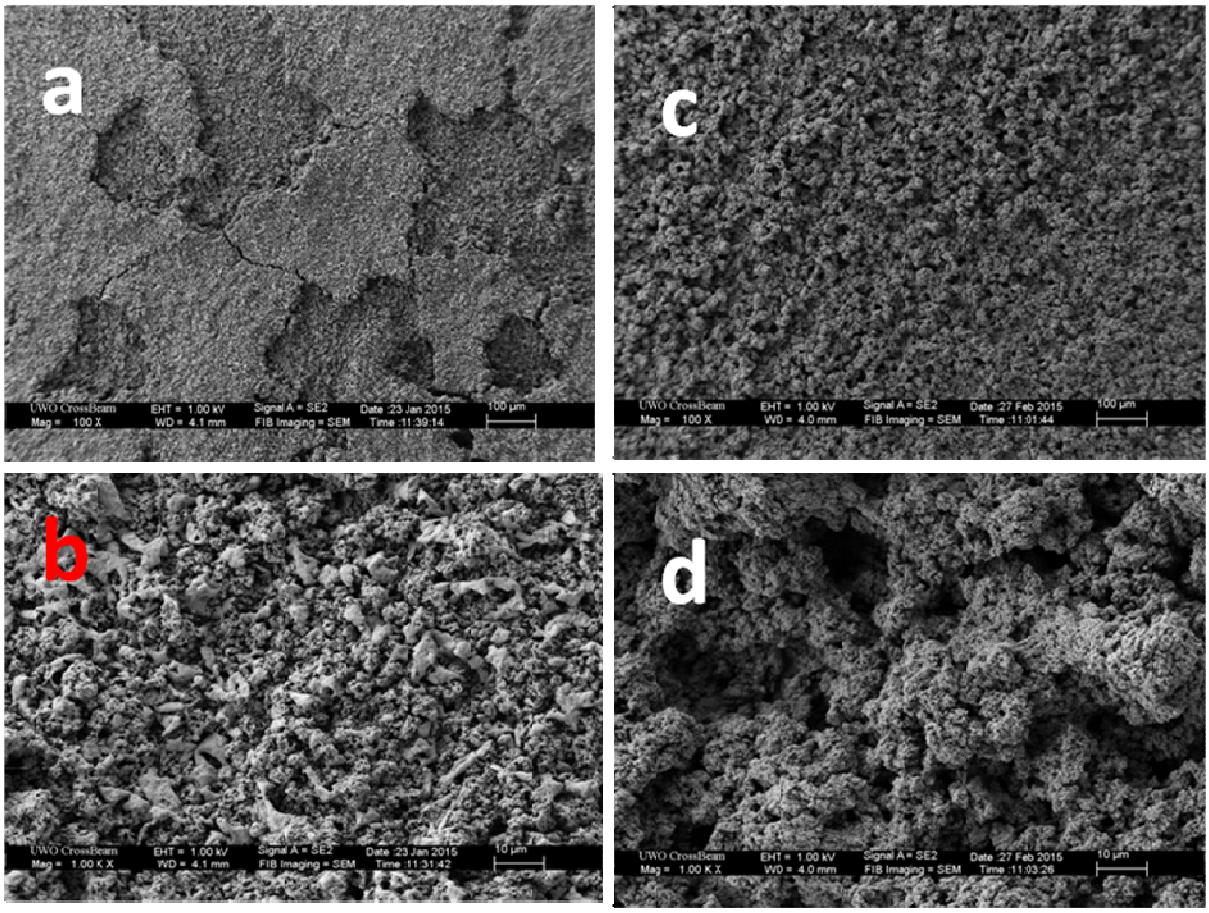

Figure 4-4-29: SEM images of cycled areas for (a-b) 75% N_2 Al-CNx (AC3), (c-d) 75% N_2 Dural-CNx (DC3) anodes subjected to 180 and 300 cycles each respectively at a current density of 0.5 mA/cm^2 without an initial CV. Magnifications of (a,c) 100x, (b,d) 1000x.

4.4.3 EDX Composition Charts

Shown in **Table 4-4-30** is the EDX composition data of the uncycled, cycled porous and cycled flat areas of the non-annealed (AC1) and annealed (AC2) 75% N_2 Al-CNx anodes after being subjected to the 4x8 experiments as well as the non-annealed 75% N_2 Al-CNx anode (AC3) after being subjected to 180 cycles at a current density of 0.5 mA/cm^2. For Al-CNx the predominance of Al with small amounts of nitrogen within the uncycled area indicates an unreactive Al-CNx anode with surface contamination by the electrolyte (**a,d,g**). Carbon and oxygen content should arise from a combination of trace propylene carbonate and residual surface oxide present after the electrode preparation before film deposition. The CNx film will contribute carbon as well as 5 to 10 percent nitrogen. The resulting very low uncycled oxygen content of a few percent is expected given the polished and etched preparation before CNx film deposition. Trace phosphorus and fluorine content should arise from $LiPF_6$ salt remaining after rinsing. The small amount of silicon detected is likely again due to a combination of silicon carbide paper used for polishing, and as an impurity in the Al alloy itself. Lithium content cannot be monitored due to the overlap of its low energy x-rays with the baseline peak close to 0 eV.

Both porous and flat cycled areas of AC1 (non-annealed Al-CNx) show significantly elevated oxygen and fluorine content (**b,c**). This is likely due to the presence of electrolyte within the intermetallic structure, as well as the products of solvent electroreduction and salt decomposition in the SEI layer [8]. Nitrogen content within the porous region is very low at around 1% (**b**), and much higher in the flat area around 9% (**c**). This again suggest that CNx partially impedes the growth of LiAl. The large Al content of 26% observed within the flat region (**c**) is likely due to the 7 kV column voltage which roughly corresponds to a profiling depth of 100 nm. Therefore spectra acquisition of the flat remnants in the non-annealed sample will to some extent also profile the composition of the porous intermetallic structure underneath. The contrast in the nitrogen content between these two cycled areas supports our previous statements as to the location of the CNx film after lithiation-delithiation. For non-annealed Al-CNx

(AC1) the CNx coating rapidly cracks and becomes detached from the Al core with the remnants sitting on top of the intermetallic structure (**Fig. 4-4-24 a**).

Table 4-4-30: EDX composition chart of uncycled and cycled areas of non-annealed (AC1) and annealed (AC2) Al-CNx anodes after being subjected to 4x8 experiments and non-annealed Al-CNx anode after being subjected to 180 cycles at a current density of 0.5 mA/cm^2 (AC3). Spectra were collected at a column voltage of 7 kV for 50 seconds at 1000x magnification.

		Atomic %						
Sample	**Area**	**C**	**N**	**O**	**F**	**Al**	**Si**	**P**
AC1	(a)Uncycled	31.84	10.14	2.05	0.32	55.50	0.13	0.02
	(b)Porous	14.62	1.76	24.99	24.61	33.00	0.10	0.92
	(c) Flat	30.89	9.40	16.02	16.79	26.08	0.15	0.66
AC2	(d) Uncycled	30.68	8.48	2.18	0.24	58.16	0.15	0.11
	(e) Porous	7.15	1.02	18.13	39.35	33.04	0.23	1.08
	(f) Flat	26.58	7.03	5.17	9.11	51.84	0.15	0.14
AC3	(g)Uncycled	27.99	9.47	2.43	0.62	59.09	0.35	0.05
	(h)Porous	3.51		8.49	57.04	28.69	0.75	1.52
	(i)Flat	26.25	12.97	10.19	35.02	12.28	0.95	2.35

The composition of the cycled porous (**e**) and flat (**f**) regions in the annealed sample (AC2) strongly resemble the cycled porous (**b**) and uncycled (**a**) areas of non-annealed AC1. Therefore, the remaining CNx in AC2 is instead located close to the film-metal interface, likely due to increased film adhesion and stability (**Fig. 4-4-24 c-d**). The composition of the cycled porous area of the non-annealed Al-CNx failure anode (AC3) (**h**) resembles the cycled porous area of AC1 (**b**) with no nitrogen content and significantly higher F:O and F:Al ratios. In contrast, the blocky fine-grained patches nearby show a strong nitrogen signal (**i**). This confirms our assessment from the SEM images of AC3 that the CNx film has been pulverized significantly into very small warped pieces (**Fig. 4-4-25 e-f**). Similar to uncoated anode failure experiments from Ch. 4.1 to 4.3, the elevated fluorine content here should predominantly come from the $LiPF_6$ electrolyte. As described in the CV section, the continued lithiation-delithiation of Al-CNx will cause some degree of additional SEI formation beyond the first cycle (**Fig. 4-4-1**). With sustained cycling in AC3 mechanical stresses will accumulate and result in cracking in both the CNx film and the underlying intermetallic structure. This will continuously cause partial destruction of the SEI present in both regions and also expose fresh Al material for more SEI formation. As before the $LiPF_6$ salt is also expected to thermally degrade over time into LiF and PF_5 if any trace moisture content is present [9].

Shown in **Table 4-4-31** is the EDX composition data of the uncycled, cycled porous and cycled flat areas of the non-annealed 75% N_2 (DC1) and 25% N_2 (DC2) Dural-CNx anodes after being subjected to the 4x8 experiments as well as the non-annealed 75% N_2 (DC3) and 25% N_2 (DC4) Dural-CNx anodes after being subjected to 300 cycles each at a current density of 0.5 mA/cm^2. For uncycled areas of Dural-CNx samples the composition will be similar to uncycled Al-CNx but with small amounts of Cu and Mg present (**a,d,g,i).** Overall the EDX data appears to support our hypothesis made previously from the SEM imaging. The composition of the porous regions in DC1 (75% N_2) (**b**) and DC2 (25% N_2) (**e**) is similar to that observed for porous regions in the bare Dural anodes in Ch. 4.3.3, with minimal nitrogen content present. As predicted the flat lowered regions in DC1 (**c**) and DC2 (**f**) show strong nitrogen signals, with a composition resembling partially reactive versions of their uncycled areas (**a,d**). The 4x8 Dural-CNx

sample prepared under 25% N_2 plasma (DC2) has a similar composition to DC1 with predictably less nitrogen content in both the flat and uncycled areas. The composition of Dural-CNx failure samples DC3 (75% N_2) (**h**) and DC4 (25% N_2) (**j**) resemble the cycled porous area of DC1 (75% N_2) with significantly higher fluorine content and a lack of nitrogen content (**b**). This confirms that most of the CNx remaining after extended lithiation-delithiation of Dural-CNx must be buried underneath the intermetallic alloy. This is again distinctly different from the fresh Al-CNx failure anode (AC3) in which the porous intermetallic alloy is overlaid in several areas by nitrogen-rich CNx remnants.

Table 4-4-31: EDX composition chart of uncycled and cycled areas of non-annealed 75% N_2 (DC1) and 25% N_2 (DC2) Dural-CNx anodes after being subjected to 4x8 experiments, and non-annealed 75% N_2 (DC3) and 25% N_2 (DC4) Dural-CNx anodes after being subjected to 300 cycles each at a current density of 0.5 mA/cm^2. Spectra were collected at a column voltage of 7 kV for 50 seconds at 1000x magnification.

		Atomic %								
Sample	**Area**	**C**	**N**	**O**	**F**	**Mg**	**Al**	**Si**	**P**	**Cu**
DC1	(a)Uncycled	31.42	12.13	2.64	0.25	0.65	51.05	0.25	0.04	1.58
	(b)Porous	3.62		18.04	45.72	0.16	25.24	5.75	0.81	0.66
	(c) Flat	27.90	10.61	4.87	6.72	0.57	46.78	1.05	0.05	1.44
DC2	(d)Uncycled	25.71	8.00	3.21	1.16	0.78	58.88	0.16	0.13	1.97
	(e) Porous	9.66	0.64	25.63	36.19	0.34	26.03	0.25	0.48	0.78
	(f) Flat	22.16	5.59	3.89	11.86	0.54	53.81	0.07	0.11	1.99
DC3	(g)Uncycled	30.60	11.92	3.24	0.58	0.59	51.14	0.22		1.71
	(h)Porous	1.97		9.57	65.48	0.14	21.51	0.07	0.79	0.47
DC4	(i)Uncycled	25.01	7.83	2.46	0.86	0.72	60.92	0.27		1.93
	(j) Porous	1.85	0.40	9.18	64.31	0.21	22.51	0.41	0.57	0.57

4.4.4 Conclusions for this chapter

We may conclude that for Dural anodes, similarly to GF Al, CNx films initially improve the reversibility of lithiation-delithiation, when considering the early cycling performance of DC3 (75% N_2 Dural-CNx) and DC4 (25% N_2 Dural-CNx) relative to DU2 (Dural) (**Fig. 4-4-21**). Even when the efficiency of the main discharge plateau begins to degrade for DC3 it still remains better than DU2 for two reasons. Firstly, the presence of the CNx coating notably decreases the appearance of secondary and tertiary diffusion-limited discharge plateaus in Dural, directly increasing the duration of the main discharge plateau (**Fig. 4-4-22**). This is consistent with the decreased diffusion-limited delithiation behaviour observed in the 4x8 experiments for 75% N_2 Dural-CNx (DC1) relative to Dural (DU1) (**Figs. 4-4-16, 4-4-17**) but in contrast to the behaviour observed with Al-CNx samples (**Figs. 4-4-6, 4-4-7**). Secondly, repeated plateau jump events in Dural-CNx allow for multiple temporary improvements in efficiency. Decreasing the nitrogen content in DC4 (25% N_2) produces faster efficiency degradation and higher jump frequency, possibly due to the decreased mechanical stability of the CNx film. The Dural substrate appears to offer increased mechanical toughness against pulverization of the intermetallic alloy. Additionally the CVs and 4x8 experiments of Dural-CNx anodes suggest a phase formation that is quite different from that of Al-CNx anodes. Together these details may help explain the slower degradation observed here for the non-annealed 75% N_2 Dural-CNx anode (DC3) (**Figs. 4-4-20, 4-4-21**) relative to the non-annealed 75% N_2 Al-CNx anode (AC3) described earlier in the chapter (**Figs. 4-4-9, 4-4-10**). Both Dural-CNx and Al CNx showed quite ordered nanoscale morphology However, the coulombic efficiencies for the Dural anodes remained too low and the drift in the charging-discharging potentials too severe for the Dural anodes to have any possible applications in Li ion batteries.

As for Al-CNx anodes, we see that there is significant positive effect of CNx in the beginning, which, however, largely disappears by the 40th-50th cycle. The CNx coated Al anodes still experience unacceptably large potential jumps and decrease in the efficiency. This indicates that CNx coating alone is not able to improve the performance

of Al-based anodes to the point that it they will be suitable for the use in practical Li ion batteries.

4.4.5 References

1. Byers, J.C.; Billon, F.; Debiemme-Chouvy, C.; Deslouis, C.; Pailleret, A.; Semenikhin, O.A. *Acs Applied Materials & Interfaces,* **2012**, *4*, 4579.
2. Peponas, S.; Guedda, M.; Benlahsen, M., *Solid State Communciations,* **2008,** *146*, 78-82.
3. Kaltofen, R.; Sebald, T.; Weise, G., *Thin Solid Films,* **1996,** *290-291,* 112-119.
4. Alibart, F.; Durand Drouhin, O., *Applied Surface Science,* **2008,** *254,* 5564-5568.
5. Durand-Drouhin, O.; Benlahsen, M., *Solid State Communications,* **2004,** *131,* 425-429.
7. Mubumbila, N. ; Tessier, P.Y.; Angleraud, B.; Turban, G., *Surface and Coatings Technology,* **2002,** *151-152,* 175-179.
8. Schroder, K.W.; Dylla, A.G.; Harris, S.J.; Webb, L.J.; Stevenson, K.J., *ACS Appl. Mater. Interfaces*, **2014,** *6,* 21510-21524.
9. Yang, H.; Zhuang, G., *Journal of Power Sources,* **2006,** *161,* 573-579.

4.5 Composite Anodes

Summary

In Ch. 4.1 to 4.4 we investigated the lithiation-delithiation behaviour of a variety of anode systems in which the bulk Al metal substrate was the only source of Al available for intermetallic phase formation. In the literature the optimization of Al anode performance is solely focused on the use of nanostructured anodes such as nanowires and thin films. Here we examine the effects on lithiation-delithiation of thin and therefore soft Al films relative to the crystalline bulk Al substrates. An additional advantage of this approach is that with thin Al films, as opposite to bulk Al anodes, we know the mass of the Al available and thus can determine the specific capacities of our Al anodes, that is, the amount of charge that an electrode can store per unit weight of the active material.

A variety of multilayer structured anodes were prepared on both half-hard Goodfellow Al and half-hard copper substrates with the surface oxide removed, using radiofrequency magnetron sputtering for deposition of Al thin films. Copper was used as substrate because it is known to be non-reactive towards Li intercalation or alloy formation. Half-hard GF Al was chosen as the substrate for the Al-Al and Al-Al-CNx samples instead of soft McMaster-Carr (MC) Al. This choice was made due to the strain-hardening of GF Al offering improved structural stability in repeated scanning and cycling of the resulting intermetallic alloy (Ch 4.1 and 4.2). In addition to the amorphous Al thin film layer these anodes have zero, one or two CNx layers also present. The role of CNx was twofold. First, CNx films deposited on top of Al films were expected to affect the volume changes and kinetics of the reduction of Li ions, as was discussed in the previous chapters. The CNx underlayers were supposed to affect the internal strain buildup in the deposited Al layer and again help to absorb some of the volume changes. Reactions between the components of the CNx layer and LiAl intermetallic phase also could not be excluded.

The first sample ACM1 was prepared with 25 nm of sputter-deposited Al film on oxide-free GF Al using a power of 50 W, 2 Pa pressure and pure Ar plasma. The second sample ACM2 was prepared similarly to ACM1 with an additional deposition step to yield 75 nm CNx film at 50 W, 1 Pa and 75% N_2 plasma. The third sample ACM3 was prepared identically to ACM2 and then underwent post-deposition thermal annealing at 150^{o}C for 2 hours. For both Al and CNx thin film depositions, the magnetron power of 50 W was chosen to achieve both a reasonable deposition rate and film stability in solution [1-2]. The lower deposition pressure of 1 Pa for CNx was chosen to make the resulting film more dense and less disordered [3-5]. As in the Al-CNx anodes presented in Ch. 4.4 we were interested in films with significant nitrogen incorporation, which produce stronger and more adherent films. From preliminary tests with Al-CNx samples of different nitrogen contents we determined that 75% N_2 plasma has the optimal performance. Therefore the same plasma composition was chosen for Al-Al-CNx, Cu-Al-CNx and Cu-CNx-Al-CNx samples.

These samples were characterized electrochemically in 4x8 experiments, which begin with a cyclic voltammogram (CV) for three scans, followed by four sets of eight galvanic cycles at progressively higher current densities. In the initial CV of non-annealed Al-Al (ACM1) we observed increased SEI formation relative to bare half-hard GF Al (GF1), with multiple distinct lithiation and delithiation processes. Addition of CNx to non-annealed (ACM2) and annealed (ACM3) Al-Al-CNx anodes resulted in further increases of SEI formation with some evidence of volume change containment during intermetallic phase formation. In the galvanic cycles we observed multiple distinct charge and discharge plateaus at the lowest current density with accompanying reversibility that was initially very poor relative to bare half-hard GF Al (GF1). As the systems were conditioned at lower current densities, the charge/discharge behaviour transitioned into single plateaus and the performance became comparable to GF Al. Surface analysis of the Al-Al (ACM1) and especially both Al-Al-CNx (ACM2 and ACM3) samples after electrochemistry revealed a unique honeycomb porous morphology distinct from that observed in bare GF Al (GF1) or Al-CNx (AC1, AC2) samples.

For copper-based anodes the first sample CM1 was prepared with 25 nm of Al film deposited on oxide-free Cu at 50 W, 2 Pa and pure Ar plasma. followed by an additional deposition step consisting of 75 nm of non-annealed CNx at 50 W, 1 Pa and 75% N_2 plasma. The second sample CM2 was prepared identically to CM1 and then underwent post-deposition thermal annealing at 150 ^{o}C for 2 hours. The third sample CM3 was prepared identically to CM1 with an additional 75 nm CNx underlayer deposited first between the Cu substrate and the Al film. Finally the fourth sample CM4 was prepared similarly to CM3 with the layer thicknesses changed to 25 nm CNx, 75 nm Al and 50 nm CNx. These samples were also characterized electrochemically in 4x8 experiments. In the initial CVs we observed further increases in SEI formation relative to Al-Al-CNx anodes, with multiple distinct lithiation and delithiation processes depending on the sample. In the galvanic cycles we initially observed multiple charge and discharge plateaus at lower current densities which gradually transitioned to single charge and discharge plateaus at higher current densities. Even with the total duration of both discharge processes considered together the resulting coulombic efficiencies were quite poor relative to Al-Al-CNx, Al-CNx and other anode systems presented previously in this thesis work. These samples also could not withstand cycles at high current densities. Surface analysis after electrochemistry in all cases revealed very rough heterogeneous surfaces as compared to Al-CNx and Al-Al-CNx anode systems with multiple reactive and non-reactive domains.

4.5.1 Cyclic Voltammograms, Galvanic Cycles, Calculations

Al thin film anodes on GF Al substrate

The typical features of CVs with bare Al anodes were described previously in Ch. 4.1.1. Therefore this section will focus only on differences observed in the CV features of Al-Al based anodes relative to bare half-hard GF Al anodes with the oxide removed. First we consider the partial cathodic scans between 2.0V and 0.2V vs. Li^{+}/Li reference electrode (**Fig. 4-5-1**). For the purposes of comparison the bare GF Al anode GF1 (oxide removed) from Ch. 4.1 is included. The bolded numbers **1** to **4** denote the GF1, ACM1, ACM2, and

ACM3 samples respectively (1, bare GF Al; 2, non-annealed Al-Al; 3, non-annealed Al-Al-CNx; 4, annealed Al-Al-CNx).

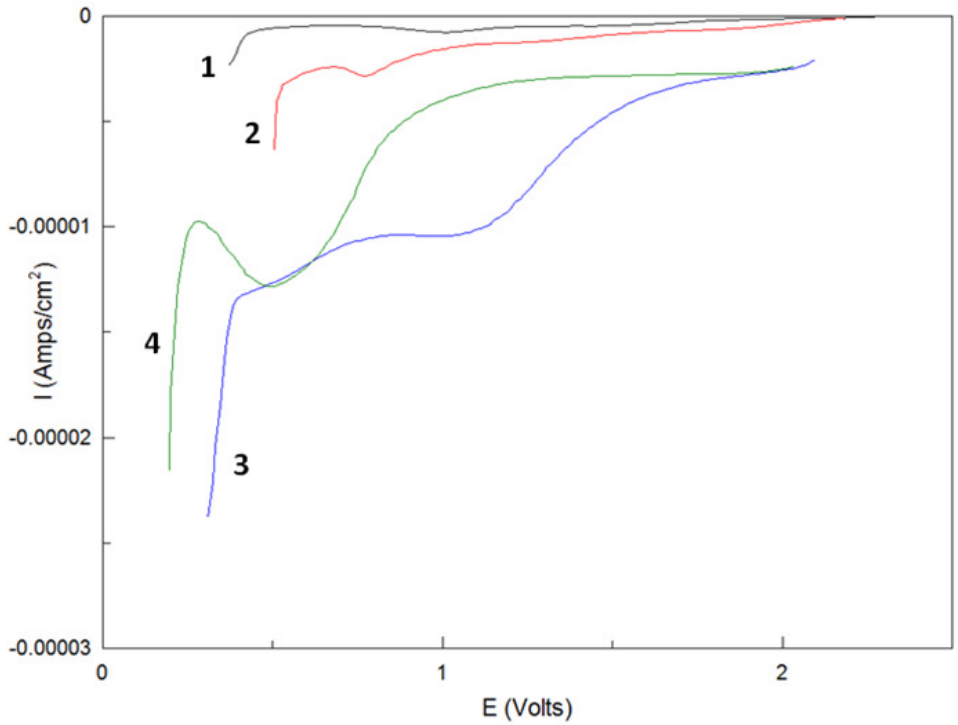

Figure 4-5-1: Initial cyclic voltammograms of non-annealed Al-Al and non-annealed and annealed Al-Al-CNx anodes ACM1 (2, red), ACM2 (3, blue) and ACM3 (4, green). Comparative bare half-hard GF Al anode GF1 (1) from Ch. 4.1 is also included in black. Partial cathodic scans from 2V to 0.2V to highlight SEI formation and lithiation onset behaviour.

First of all, we see that the lithiation onset potential is heavily affected by the structure of the electrode. Addition of a sputtered Al layer (ACM1) shifts the onset towards less negative potentials, which indicates that formation of the LiAl intermetallic phase occurs easier at the thin-film Al electrode as compared to bulk Al. The sputter-deposited thin Al film in ACM1 should be mechanically softer as compared to the GF bulk Al substrate. This should result in the increased ease of three-dimensional volumetric expansion of the LiAl nanostructure and less energy and therefore less overvoltage required for the formation of the new LiAl phase. Addition of CNx on top of Al film (ACM2. ACM3) shifts the onset towards more negative potentials, especially for annealed films. This

indicates an increase in the overvoltage of LiAl formation for CNx coated electrodes. The reasons here may be the additional IR drop at the electrode due to added resistance of CNx films and the limitation of the volumetric expansion by the CNx films.

The Al-Al (ACM1) sample shows larger SEI formation currents relative to bare GF Al (GF1), which could be related to increased surface roughness of the Al thin film layer. Both Al-Al-CNx samples (ACM2, ACM3) show further amplification of this effect. This can be related to difference kinetics and mechanism of the reactions of the solution components on the CNx surface. Furthermore, GF1 as described previously in Ch. 4.1 shows a distinct reduction peak around 1.0V, which is the typical potential range observed for SEI formation on Al nanowires [7]. The Al-Al (ACM1) sample has instead a peak shifted lower around 0.75V. Non-annealed Al-Al-CNx (ACM2) has a local current minima at 1.0V which may be considered a peak. Annealed Al-Al-CNx (ACM3) instead shows a large broad SEI peak around 0.6V. This peak in ACM3 is not related to the lithiation onset potential because the current becomes smaller afterwards, and then does not drop significantly until closer to 0.25V. The peaks present in both Al-Al-CNx samples are in contrast to the broad SEI formation observed in both Al-CNx samples of Ch 4.4 (**Fig. 4-4-1**), as well as a similar broadening effect observed for increased surface oxide content on GF Al and MC Al substrates in Ch. 4.1 and 4.2 (**Figs. 4-1-2, 4-2-1**). Therefore, this behaviour should be related to the presence of the sputter-deposited Al thin film. Additional scanning in the CV will produce larger amounts of additional SEI formation for Al-Al (ACM1) relative to bare GF Al (GF1), with this formation further increased in CNx coated ACM2 and ACM3. This indicates the formation of porous nanostructure with the SEI forming at the inner walls of the nanopores. The accumulation of large amounts of solution components inside the nanostructure was also noted by TOF-SIMS depth profiling (see Ch. 4.6).

Next we compare the full CV scans of all samples in **Fig. 4-5-2**. First we observe that there are multiple lithiation and delithiation processes present, which should be attributed to the differences in kinetics and mechanism of lithiation-delithiation processes on soft sputtered Al thin film and underlying hard crystalline substrate. The non-annealed Al-Al

(ACM1) sample shows a well defined cathodic peak around 0.35V which is consistent with lithiation observed in amorphous Al thin films, thin Al foils and nanowires anodes [7-8]. The lithiation process starts considerably earlier compared to bulk Al (GF1), as has been already mentioned. The main delithiation peak for this sample is also shifted to more negative potentials as compared to bulk Al (GF1) indicating that less overvoltage is required for delithiation. Interestingly, this peak also has a shoulder at more positive potentials, which may indicate delithiation of the underlying bulk Al. The fact that we observe a shoulder only may be related to the fact that this Al-Al sample (ACM1) had a slightly more positive left vertex and thus the lithiation of the underlying substrate was limited. The annealed Al-Al-CNx (ACM3) shows a similar cathodic peak but which is shifted negatively, likely due to the increased resistance caused by the nitrogen-rich CNx layer [9]. However this cathodic peak is not present in non-annealed Al-Al-CNx (ACM2) and lithiation simply continues past the onset potential until it is terminated by the left vertex. This may indicate more disorder and amorphous character in the non-annealed electrode, accompanied by higher resistivity. The increasing cathodic currents observed below 0.3V near the left vertex of ACM2 and ACM3 are likely related to lithiation of bulk Al following lithiation of the Al film. Following two lithiation processes, we also observe two delithiation peaks here. The earlier peak around 1V should be related to delithiation of the Al thin film, whereas the second peak around 1.2V should be the delithiation of the bulk Al. One can see that the annealed Al-Al-CNx anode showed the greatest extent of lithiation-delithiation of the bulk Al substrate. The slight shift in the potential of the 1st delithiation peak in non-annealed Al-Al-CNx sample may again indicate a greater disorder and higher resistivity. The loop areas for both Al-Al-CNx samples (ACM2, ACM3) near the left vertex are very small relative to bare GF Al (GF1). This suggests that the CNx coating is able to contain the volume change of intermetallic phase formation even when it is deposited on a soft Al thin film layer.

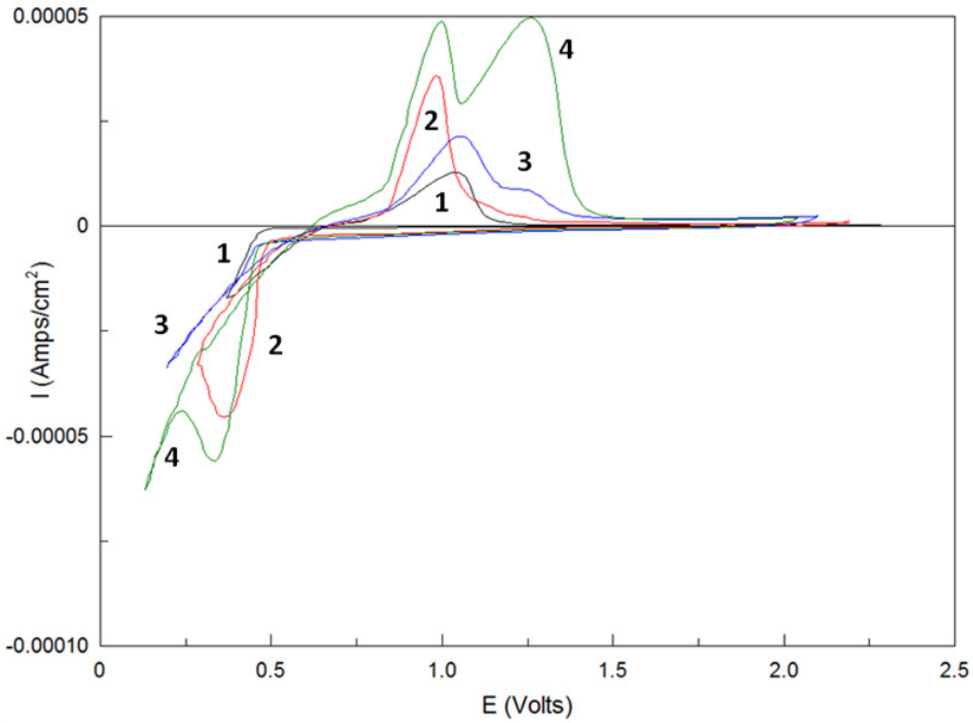

Figure 4-5-2: Initial cyclic voltammograms of non-annealed Al-Al ACM1 (2, red) and non-annealed and annealed Al-Al-CNx anodes ACM2 (3, blue) and ACM3 (4, green). Comparative bare half-hard GF Al anode GF1 (1) from Ch. 4.1 is also included in black.

Shown in **Fig. 4-5-3** in blue color are the features of a typical set of galvanic cycles for non-annealed Al-Al-CNx (ACM2) at the lowest current density of 0.13 mA/cm^2 immediately following the initial CV, with the comparative cycle set of the bare half-hard GF Al anode GF1 (oxide removed) in black color. Overall we observe multiple charge and discharge plateaus consistent with the CV behaviour (**Fig. 4-5-2**). Therefore the diagram has been modified here from previous sub-chapters. The higher potential charge plateau **2** should be Al thin film lithiation followed by the lower potential charge plateau **3** for bulk Al lithiation. Following the IR jump we have Al thin film delithiation **5** followed by bulk Al delithiation **6**. Cycling at this first current density will gradually transition the system into single charge/discharge plateau behaviour indicative of a single composite intermetallic phase. The progression of this double delithiation plateau behaviour and the resulting effects on reversibility will be discussed in the next figures for each sample.

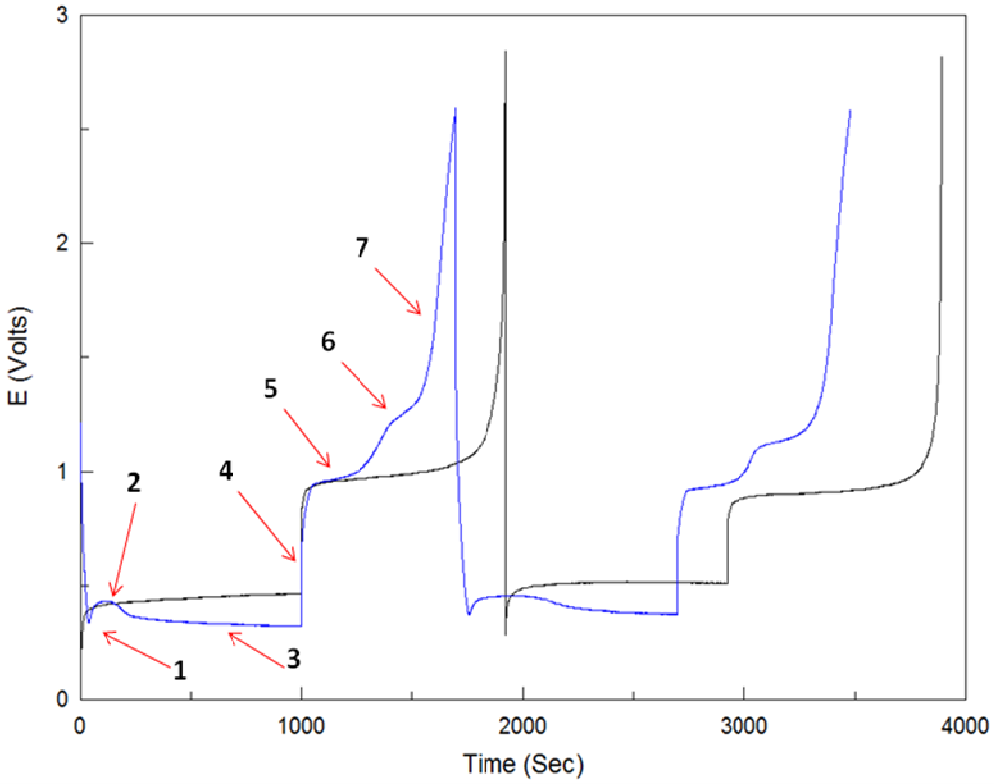

Figure 4-5-3: Typical galvanic cycles for lithiation/delithiation of an Al-Al-CNx anode (blue). This is sample ACM2 in which the Al and CNx films were deposited prior to electrochemical scans. Comparative bare half-hard GF Al anode GF1 (oxide removed) from Ch. 4.1 is also included (black). Numbers indicate the features of interest in ACM2: (1) potential overshot (2) Al film charge plateau (3) bulk Al charge plateau (4) IR drop (5) Al film discharge plateau (6) bulk Al discharge plateau (7) discharge tail. Galvanic cycles are shown at a current density of 0.13 mA/cm^2.

Importantly, the fact that we have well separated plateaus for the charging portion of the galvanic cycles allows us to determine the specific capacities for the processes in question. Usually, we have bulk Al anodes and therefore the mass of Al available for lithiation is unlimited. Here we know the thickness of the sputtered Al layer and thus can determine its mass. From the duration of the first charging plateau we know the associated charge. Using the following data: first plateau duration 185 s; current 0.13 mA/cm^2, thickness 25 nm; density 2.7 g cm^{-3}, we find that the specific capacity for the

first process is 989 mA·h/g. This is very close to the theoretical specific capacity of LiAl formation, which is equal to 993 mA·h/g [7]. Therefore, this result confirms that indeed the first plateau in the charging cycle corresponds to lithiation of sputtered Al layer, with the resulting stoichiometry of the alloy being LiAl. When the whole sputtered layer is converted into LiAl, lithiation of the bulk Al substrate starts. It occurs at more negative potentials because more energy is required for the associated volume changes in the bulk material. Note that while it may appear that the lithiation potential for the bulk Al substrate is more negative in the Al-Al-CNx sample than in bulk GF Al, this difference is due to the resistance of the additional CNx layer.

Shown in **Fig. 4-5-4** are the set of galvanic cycles of Al-Al and non-annealed and annealed Al-Al-CNx anodes ACM1, ACM2, ACM3 in red, blue and green colors respectively at this current density of 0.13 mA/cm^2. The comparative cycle set of the bare GF Al anode GF1 is included in black color. For the Al-Al sample without CNx, ACM1 (red), the double delithiation behaviour transitions into single plateaus fairly quickly by the second cycle. Addition of CNx in ACM2 (blue) slows down this transition significantly with a single discharge response not clearly observed until the seventh cycle. This contrast may be related to the volume change containment offered by the CNx layer. Thermal annealing in ACM3 (green) then appears to speed up the transition relative to ACM2 with a single discharge response observed by the fourth cycle. By the eighth cycle all samples have very close potentials of the charging plateau, whereas the discharge potentials still vary significantly.

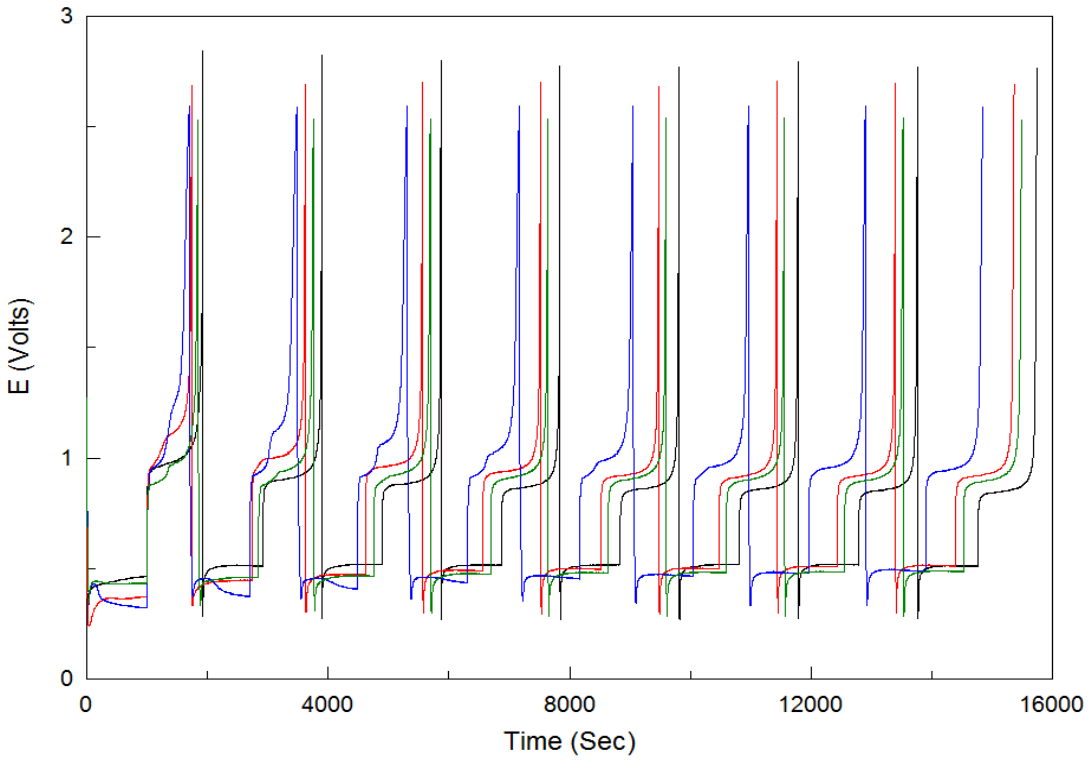

Figure 4-5-4: Galvanic cycles of non-annealed Al-Al and non-annealed and annealed Al-Al-CNx anodes ACM1 (red), ACM2 (blue) and ACM3 (green) at a current density of 0.13 mA/cm^2. Comparative bare half-hard GF Al anode GF1 (oxide removed) from Ch. 4.1 is also included (black)

This is illustrated by **Fig. 4-5-5** that shows the first (a) and last (b) galvanic cycles for all samples in this set. We can see that by the 8th cycle all samples show very similar shapes of the charging and discharging cycles and very close charging potentials; however, the discharging potentials and thus the plateau separation that characterizes the reversibility of the lithiation-delithiation processes are still quite different for the four samples. The lengths of the discharging plateaus that characterize the coulombic efficiency and reversibility of the lithiation-delithiation also remains different. This indicates that although one combined intermetallic phase is formed in all four layered samples as indicated by the appearance of the single discharge plateau, the properties of this combined phase remain quite different depending on the sample. Bare GF Al (GF1) has the lowest plateau separation and the least positive discharge potential thus indicating the highest reversibility. This is also confirmed by the coulombic efficiency data (see also

below). Non-annealed Al-Al-CNx (ACM2) sample showed the worst reversibility and the highest delithiation potential among all samples, both at the beginning and in the 8th cycle, although the difference becomes considerably smaller. Annealing of CNx layer (ACM3) produces major improvements in first few cycles as compared to non-annealed Al-Al-CNx sample (ACM2), but the difference largely disappeared by the 8th cycle.

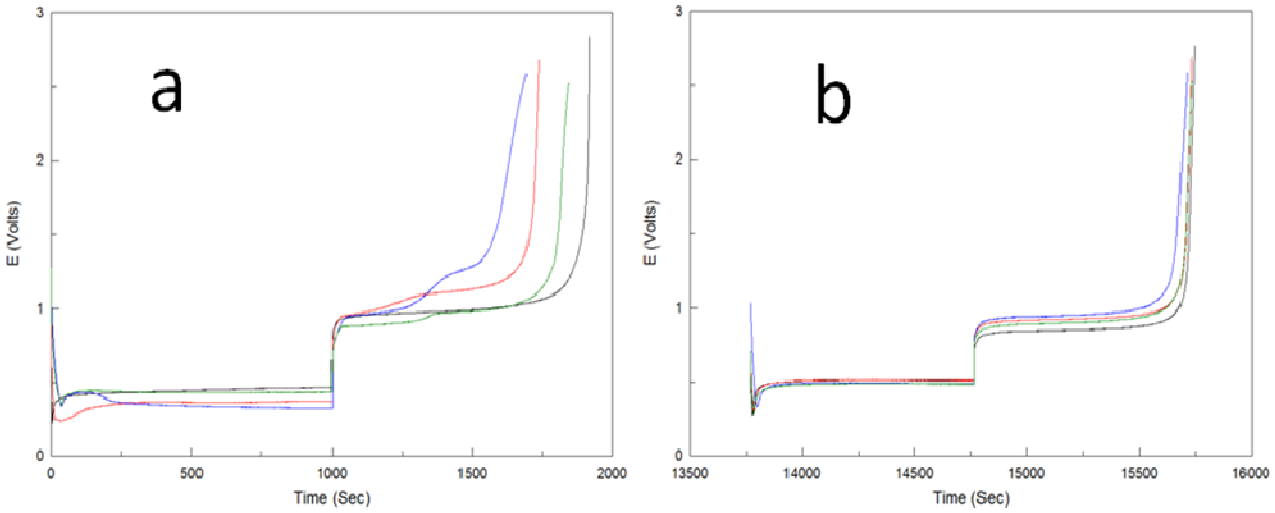

Figure 4-5-5: (a) First and (b) last galvanic cycles of Al-Al and non-annealed and annealed Al-Al-CNx anodes ACM1 (red), ACM2 (blue) and ACM3 (green) at a current density of 0.13 mA/cm^2. Comparative bare half-hard GF Al anode GF1 (oxide removed) from Ch. 4.1 is also included (black). Cycles in the right figure have been offset to overlap the curves on the same time scale.

The double delithiation behaviour present early in the first set of the three coated samples produces a shorter combined discharge plateau length and thus the coulombic efficiency (CE) is lower relative to bare GF Al (GF1), with the greatest severity observed in non-annealed Al-Al-CNx (ACM2) (**Fig. 4-5-5 a**). As the conditioning progresses to a single discharge plateau (**Fig. 4-5-5 b**), the efficiencies become much more comparable (**Fig. 4-5-6 a**). The evolution of the coulombic efficiencies for all samples is further illustrated in **Fig. 4-5-6** for the four current densities used. In the first set both discharge plateaus have been fitted together as one delithiation process for the efficiency calculation. One can see that significant differences exist only during first 8 cycles at the lowest current densities,

in the rest of the experiments the sample performance was very similar. However, one should note that non-annealed Al-Al-CNx sample (blue) continued to suffer from high resistivity causing early termination of its cycling at the highest current density (**Fig. 4-5-6 d**).

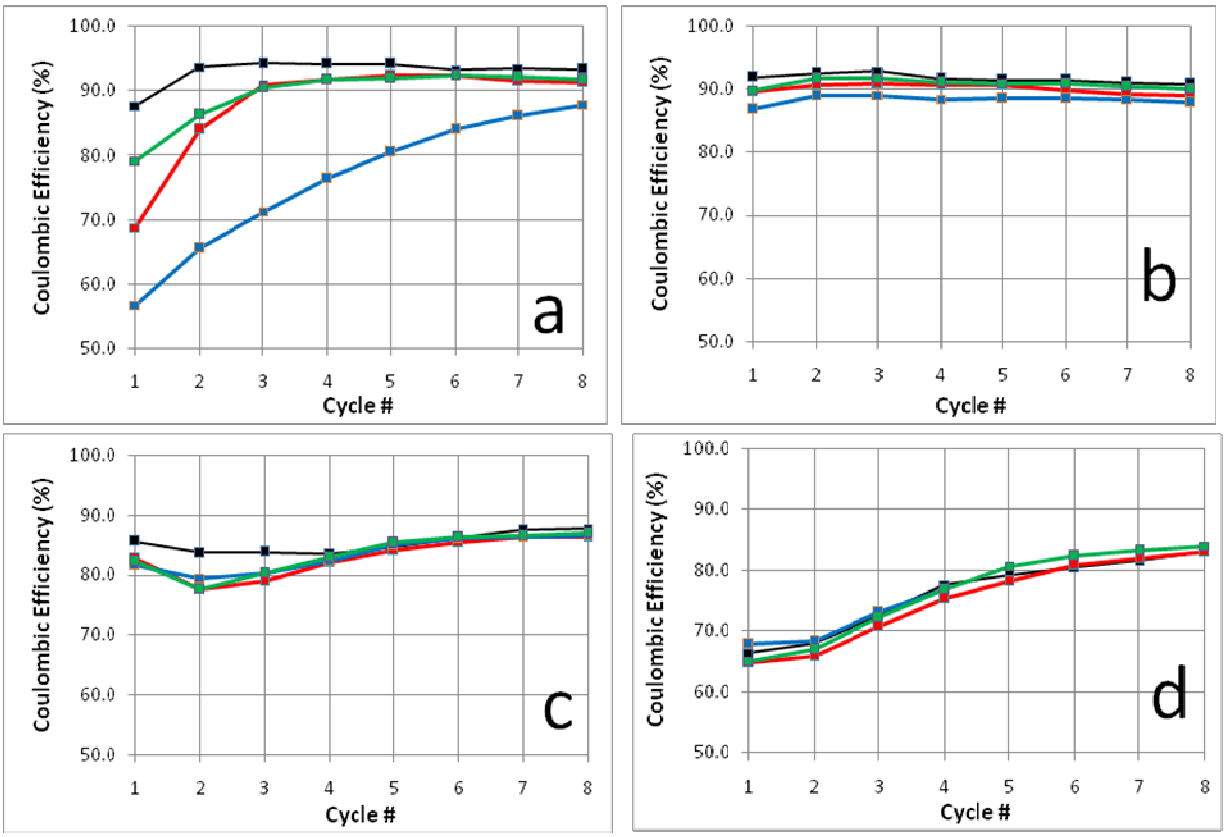

Figure 4-5-6: Coulombic efficiencies of non-annealed Al-Al and non-annealed and annealed Al-Al-CNx anodes ACM1 (red), ACM2 (blue) and ACM3 (green) at current densities of (a) 0.13 (b) 0.25 (c) 0.5 and (d) 1 mA/cm^2. Comparative bare half-hard GF Al anode GF1 from Ch. 4.1 is included in black.

Overall these results suggest that the while the structure and properties of the nanostructured anodes were very different in the first charge-discharge cycles, this difference becomes quite minor as the cycling progresses and a single composite intermetallic phase is gradually formed. When annealed, the presence of the CNx layer

appears to help the initial reversibility during the Al-Al conditioning (**Fig. 4-5-6 a**), but the effect rapidly disappears with cycling. As a result, we did not perform any further experiments on these types of anodes. Considering the fragile mechanical properties of the Al thin film, and its contribution towards the poor reversibility of Al-Al based anode systems, we would expect the resulting trends of coulombic efficiency and plateau separation degradation to be more severe for Al-Al relative to bare GF Al itself. Similarly we would expect Al-Al-CNx anodes to perform worse over time relative to Al-CNx anodes presented in Ch. 4.4. At the same time, using layered Al-Al anodes allowed us to determine the specific capacity and confirm that the main lithiation process is formation of LiAl with theoretical capacity of 993 mA·h/g.

Al thin film anodes on Cu substrate

Since in the above experiments one of the principal processes remained lithiation of the bulk Al substrate, further set of experiments was performed with thin Al layer deposited onto Cu substrate with or without CNx layers. Copper is known to be inert towards Li intercalation or intermetallic phase formation [8]. Shown in **Fig. 4-5-7** is the set of galvanic cycles for non-annealed and annealed 25+75 nm Cu-Al-CNx anodes CM1 and CM2, as well as the non-annealed 75+25+75 nm and 25+75+50 nm Cu-CNx-Al-CNx anodes CM3 and CM4 . One can see that the cycles have quite complex structure that comprise different charging and discharging processes. Shown in **Fig. 4-5-8** are the combined coulombic efficiencies of all the charge-discharge processes for the four copper-based anodes across the four current densities. One can see that all electrodes had quite low reversibility of the charging-discharging processes, with the overall coulombic efficiencies not exceeding 80% except for CM1 in the third set (**Fig. 4-5-8 c**). Overall, these results suggest that anode systems with nanostructures as the only source of Al have significantly poorer reversibility of lithiation-delithiation relative to anodes based on bulk Al. Additionally they do not appear to be able to sustain lithiation-delithiation at relatively high current densities as seen in the failures of the third and fourth sets (**Fig. 4-5-8 c-d**). Even when the contributions of all lithiation-delithiation processes in the copper-based anodes are summed together, the total efficiencies are still poor. In

comparison even the analogous Al-Al-CNx anodes (ACM2, ACM3) that also had the Al thin film layer easily surpassed this value at higher current densities (**Fig. 4-5-6 c-d**). SEM images (see below 4.5.2) showed very rough and disordered structures at the surface of Cu-based anodes upon cycling. The most likely reason for this behaviour is poor mechanical stability and inability to withstand volume changes for thin Al films on foreign substrates. These facts indicate that the presence of bulk Al substrate is essential for the development of Al-based anodes for Li ion batteries.

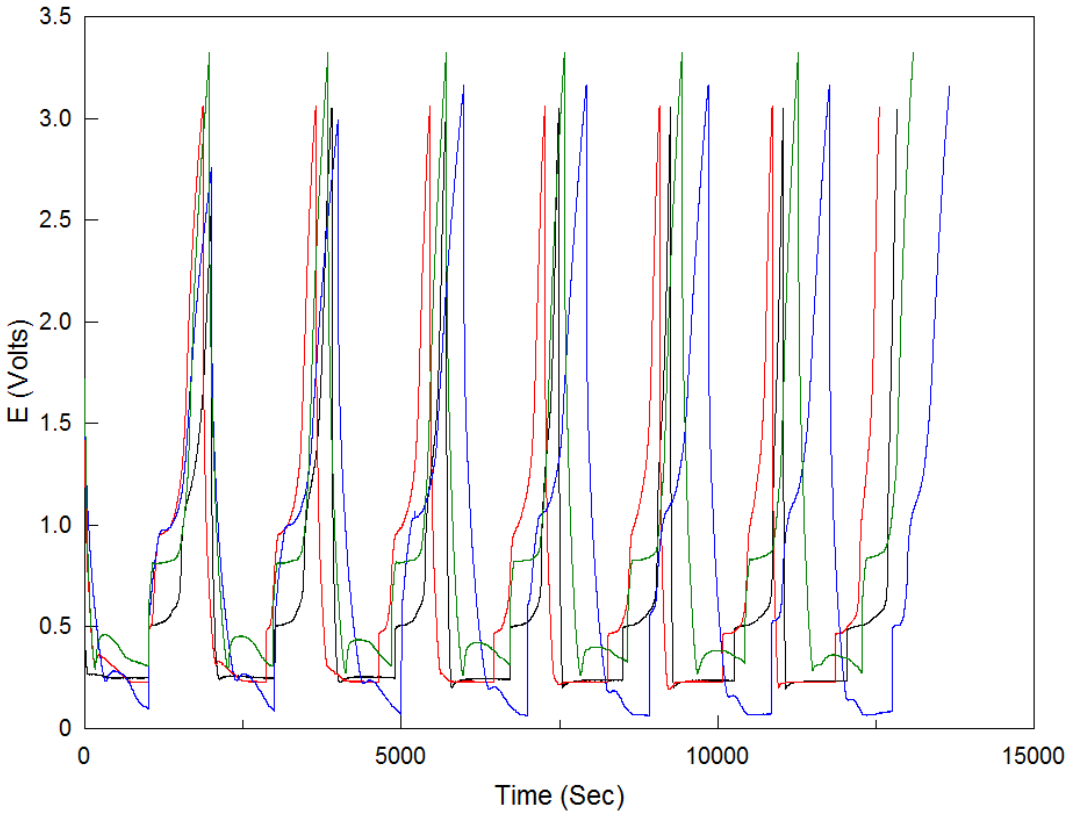

Figure 4-5-7: Galvanic cycles for non-annealed and annealed 75% N_2 25+75 nm Cu-Al-CNx anodes CM1 (black) and CM2 (red), non-annealed 75% N_2 75+25+75 nm and 25+75+50 nm Cu-CNx-Al-CNx anodes CM3 (blue) and CM4 (green), at a current density of 0.13 mA/cm^2.

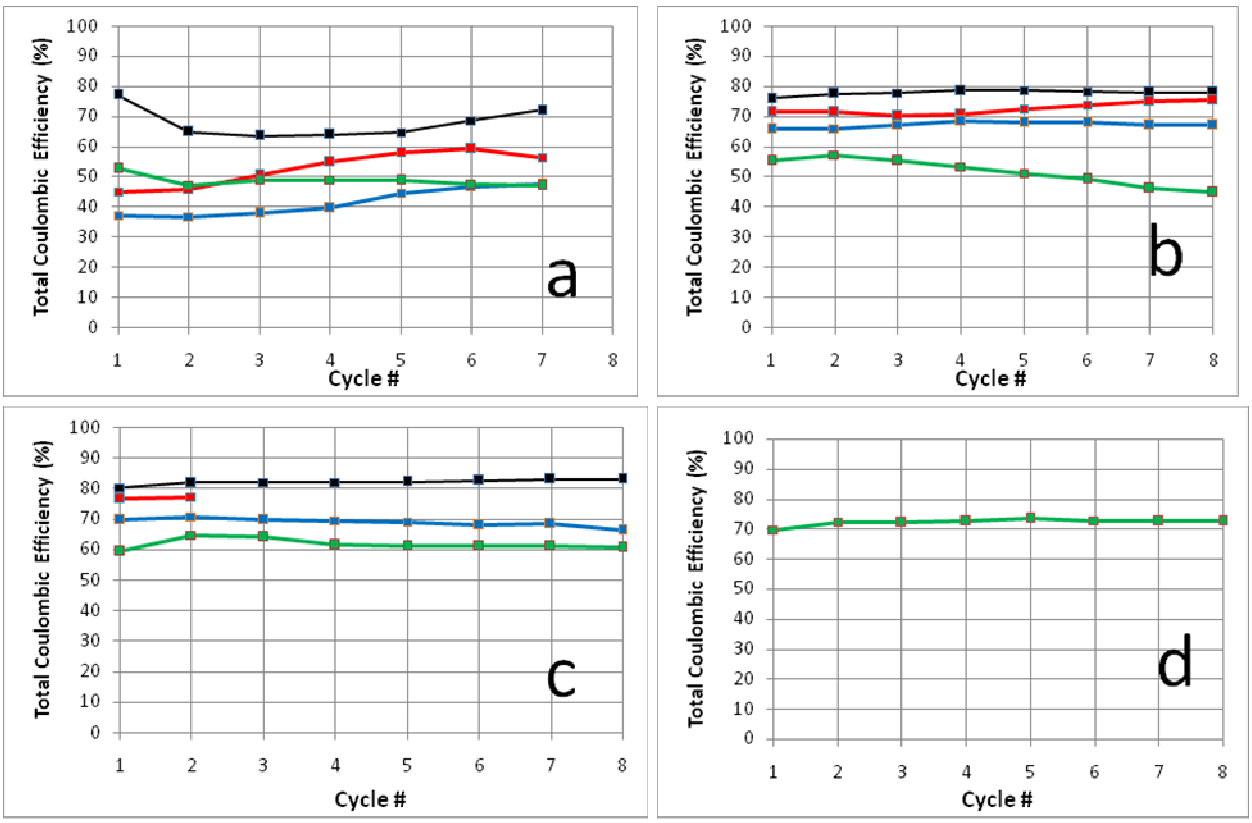

Figure 4-5-8: Coulombic efficiencies of non-annealed and annealed 25+75 nm Cu-Al-CNx anodes CM1 (black) and CM2 (red), non-annealed 75+25+75 nm and 25+75+50 nm Cu-CNx-Al-CNx anodes CM3 (blue) and CM4 (green) at current densities of (a) 0.13 (b) 0.25 (c) 0.5 and (d) 1 mA/cm^2. All lithiation/delithiation processes have been summed together for calculation of the coulombic efficiency.

4.5.2 SEM images

Shown in **Fig. 4-5-9** are SEM images of the uncycled areas of 3 multilayer samples ACM1-ACM3 prepared on Al substrates, as well as the reference bare GF Al (GF1) sample. The uncycled morphology is dominated by the etching pattern of the underlying substrate with higher magnification revealing the fine grain structure of the overlaying amorphous films. **Figs. 4-5-10 - 4-5-12** show the cycled areas of the same samples at different magnifications after being subjected to the 4x8 experiments. One can see that images at the lowest magnification show quite similar and relatively uniform large-scale

morphology (**Fig. 4-5-10**). One can see that, as with bulk Al samples, cycling and especially cycling and annealing removes the CNx film from the surface (**Fig. 4-5-10 c-d**). It is either incorporated in the growing LiAl phase, or is buried under this phase during its growth, or is partially peeled off due to the volume changes. In particular, one can see some preserved CNx in the non-annealed Al-Al-CNx sample (ACM2). Some leftover CNx are also seen in the annealed Al-Al-CNx (ACM3) sample but clearly it has very much reacted.

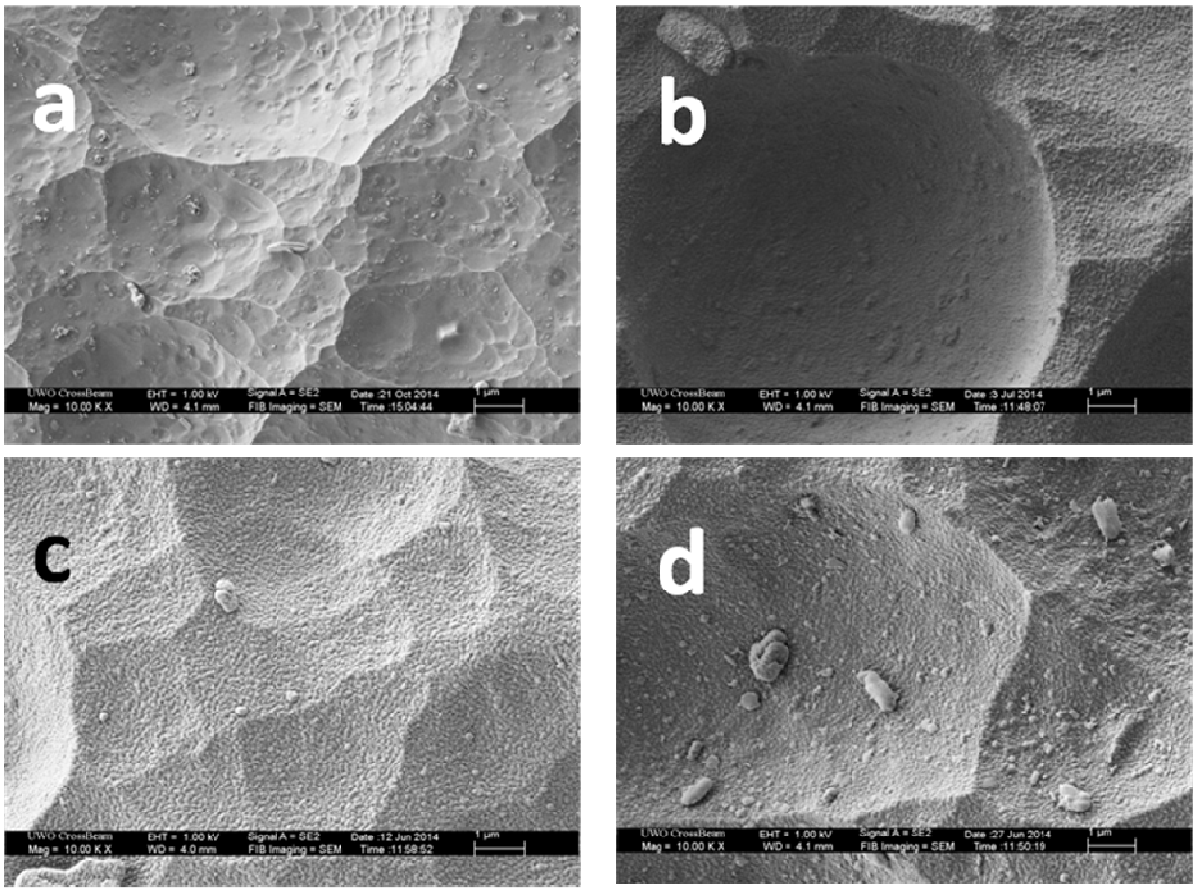

Figure 4-5-9: SEM images of uncycled areas for (a) bare GF Al (oxide removed) (GF1), (b) non-annealed 25 nm Al-Al (ACM1), (c) non-annealed 75% N_2 25+75 nm Al-Al-CNx (ACM2), (d) annealed 75% N_2 25+75 nm Al-Al-CNx (ACM3). Magnifications of 10000x.

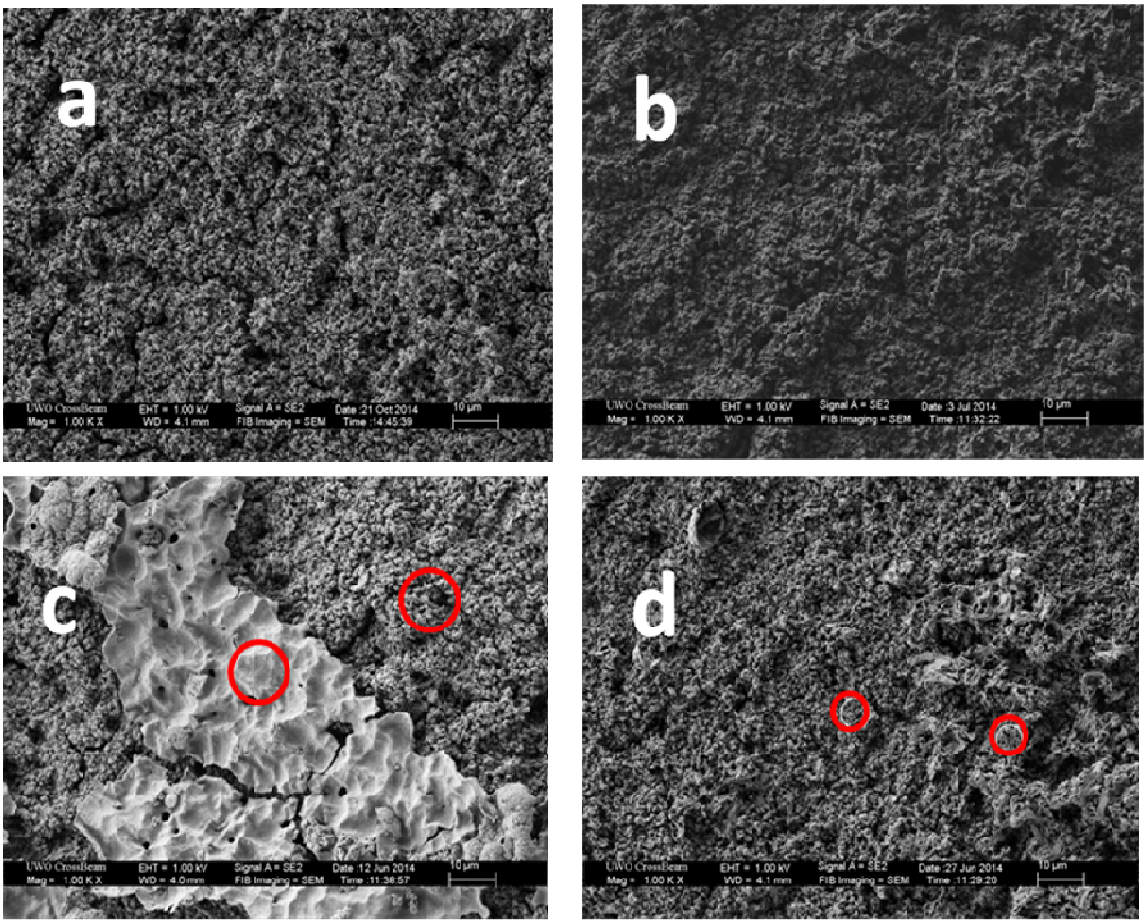

Figure 4-5-10: SEM images of cycled areas from 4x8 experiments for (a) bare GF Al (oxide removed) (GF1), (b) non-annealed 25 nm Al-Al (ACM1), (c) non-annealed 75% N_2 25+75 nm Al-Al-CNx (ACM2), (d) annealed 75% N_2 25+75 nm Al-Al-CNx (ACM3). Magnifications of 1000x. Red circles in figures c-d indicate flat and porous sub-areas.

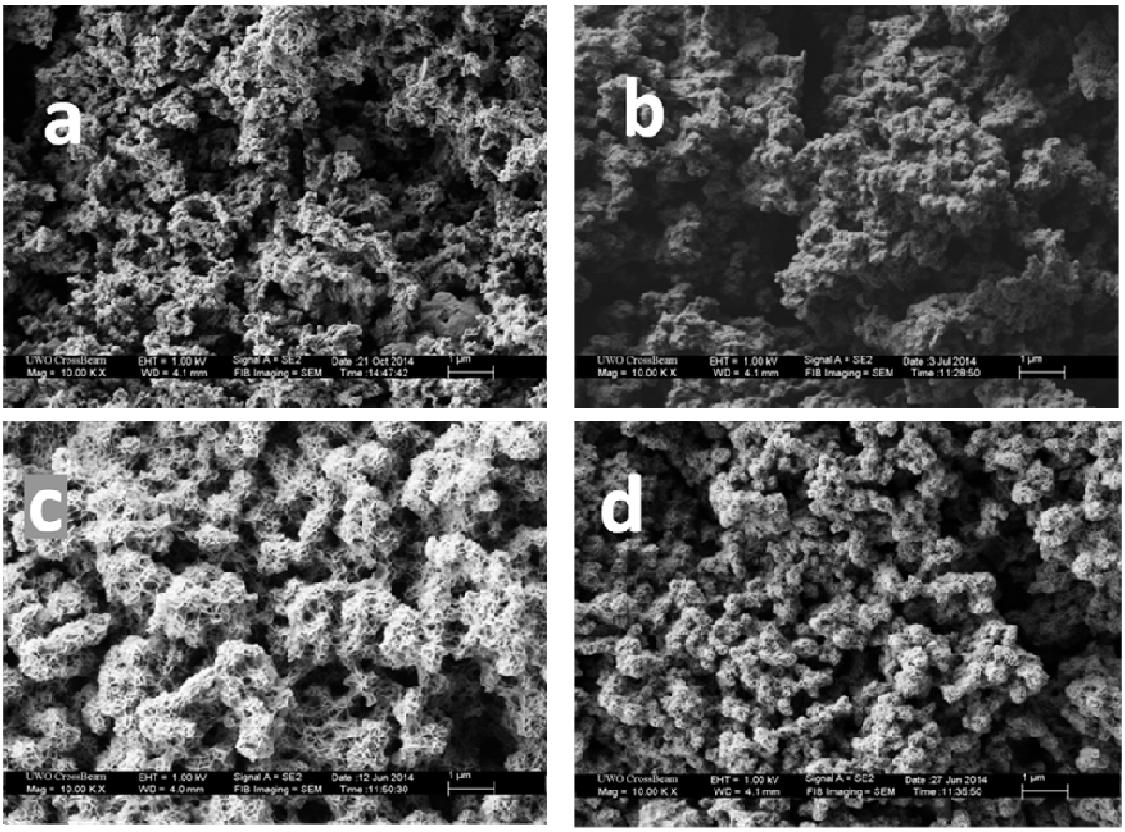

Figure 4-5-11: SEM images of cycled areas from 4x8 experiments for (a) bare GF Al (oxide removed) (GF1), (b) non-annealed 25 nm Al-Al (ACM1), (c) non-annealed 75% N_2 25+75 nm Al-Al-CNx (ACM2), (d) annealed 75% N_2 25+75 nm Al-Al-CNx (ACM3). Magnifications of 10000x.

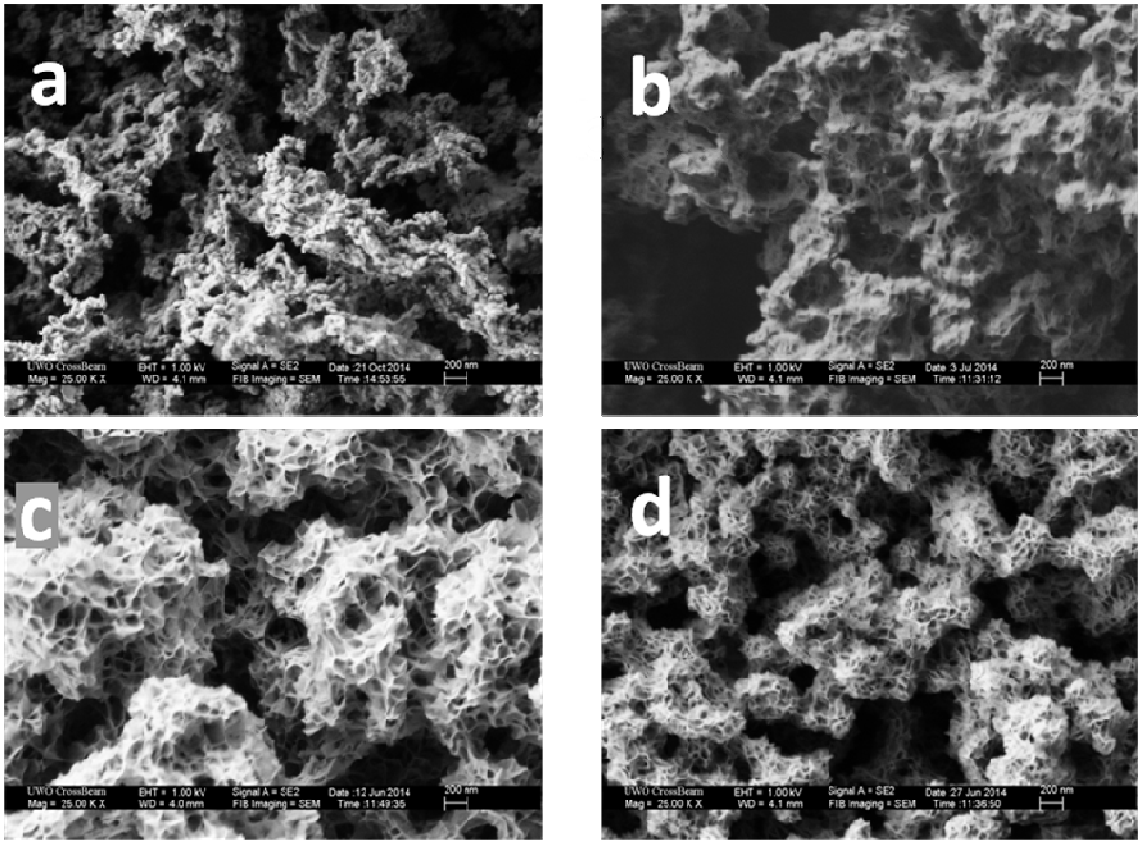

Figure 4-5-12: SEM images of cycled areas from 4x8 experiments for (a) bare GF Al (oxide removed) (GF1), (b) non-annealed 25 nm Al-Al (ACM1), (c) non-annealed 75% N_2 25+75 nm Al-Al-CNx (ACM2), (d) annealed 75% N_2 25+75 nm Al-Al-CNx (ACM3). Magnifications of 25000x.

Fig. 4-5-11 shows the same samples but at higher magnification. Now we start to see the significant differences between the samples. The Al-Al sample (ACM1) is clearly rougher and more heterogeneous than the reference bare GF Al (GF1) sample but shows a similar morphology. At the same time, samples with CNx start to show a quite unique globular-porous morphology with clearly pronounced nanosize pores resembling a honeycomb. Annealing makes the morphology different, with both the pores and the globules being smaller.

Shown in **Fig. 4-5-12** are the same 4 samples but at the highest magnification. One can now clearly see the differences in morphology. The bulk GF Al sample (GF1) shows

relatively open heterogeneous structure which, however, does not have any nanopores. The sputtered Al-Al sample (ACM1) without CNx shows a similar but rougher morphology, with some hints of honeycomb nanopores in some areas of the sample. At the same time, both CNx coated Al-Al-CNx samples show a remarkable morphology that combines a globular pattern with very fine and regular honeycomb-like nanopores. The size of the globules is ca. 1 μm in non-annealed Al-Al-CNx sample (ACM2) and 200-400 nm in the annealed one (ACM3). The size of the nanopores is also different: ca. 50-200 nm in the non-annealed sample and ca. 10-50 nm in the annealed one. These difference should be related to structural and chemical changes that happen with the Al-Al-CNx electrode during annealing. For instance, annealed Al-Al-CNx sample showed a higher initial overvoltage of the LiAl formation in the CV (**Fig. 4-5-1**). This may result in smaller morphological features since the phase growth will be inhibited. The nanoporous structure does not form without CNx, which suggest that this inhibiting effect is essential. Also essential seems to be the availability of soft sputtered Al layer. However, in our later work, we succeeded in obtaining the honeycomb nanostructured anodes without sputtered Al (see Ch. 4.7).

The occurrence of the honeycomb nanoporous morphology should be related to the effects of repeated lithiation-delithiation and the corresponding volume changes. As the electrode charges, new LiAl phase is formed, which has a higher volume than non-lithiated Al. However, upon discharge, the volume should decrease again. In the right conditions, this volume decrease will produce regular voids that can be filled again during the next lithiation cycle without changes in the overall size of the electrode. An additional advantage of the nanoporous morphology is the formation of highly developed interface between the Al electrode and electrolyte, which should increase the available current densities and remove transport limitations. Therefore, such honeycomb nanostructure should withstand well the volume changes and improve the cycling ability and reversibility of the lithiation-delithiation processes at Al anodes, also at high current densities. However, in order to form the honeycomb structure itself, low current densities should be used (called conditioning in the other chapters).

Shown in **Figs. 4-5-13 - 4-5-15** are SEM images of the cycled areas obtained after 4x8 experiments for various samples prepared on the copper substrates. Specifically, the following samples were studied: (a) 75% N_2 25+75 nm Cu-Al-CNx (CM1), (b) 75% N_2 25+75 nm annealed Cu-Al-CNx (CM2), (c) 75% N_2 25+75+50 nm Cu-CNx-Al-CNx (CM4) (d) 75% N_2 75+25+75 nm Cu-CNx-Al-CNx (CM3). **Fig. 4-5-13** shows the sample morphology at the lowest magnification. One can see that the Cu-Al-CNx sample is relatively uniform showing a bit disordered intermetallic phase at this magnification. Annealing seems to passivate the sample and preserve most CNx film on the sample surface. The presence of underlying CNx layer underneath the sputtered Al seem to increase the sample heterogeneity. It looks as the sputtered Al was clearly redistributed during the cycling, with thinner Al and thicker underlying CNx layer (**Fig. 4-5-13 d)** facilitating the redistribution as compared to **Fig. 4-5-13 c**. In particular, the sputtered Al in **Fig. 4-5-13 d** is clearly clustered in few separate aggregates, with the areas between them showing CNx film on the top. In **Fig. 4-5-13 c**, there are relatively fewer areas blocked with CNx, with highly heterogeneous LiAl phase in between, which should have originated from lithiation of sputtered Al.

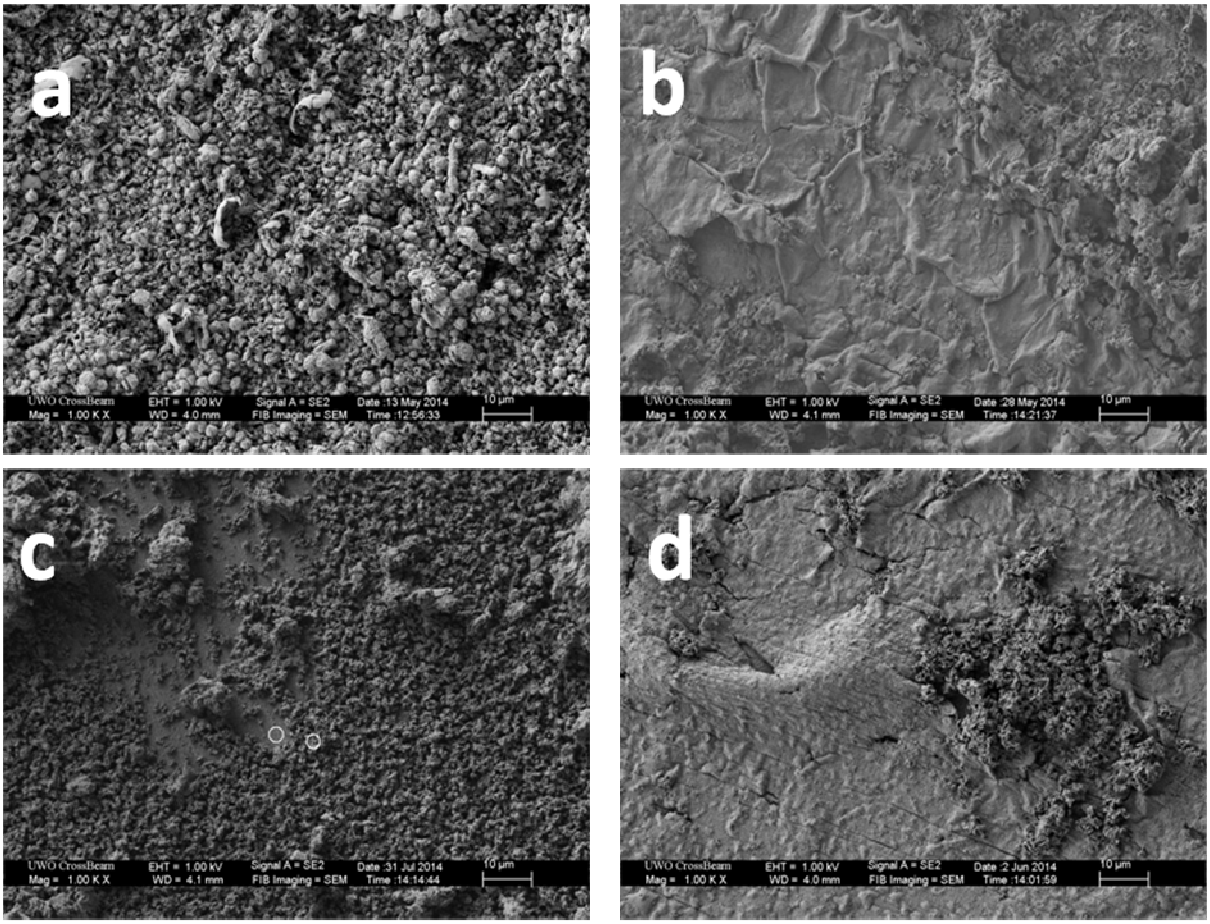

Figure 4-5-13: SEM images of cycled areas from 4x8 experiments for (a) non-annealed 75% N_2 25+75 nm Cu-Al-CNx (CM1), (b) annealed 75% N_2 25+75 nm Cu-Al-CNx (CM2), (c) non-annealed 75% N_2 25+75+50 nm Cu-CNx-Al-CNx (CM4), (d) non-annealed 75% N_2 75+25+75 nm Cu-CNx-Al-CNx (CM3). Magnifications of 1000x.

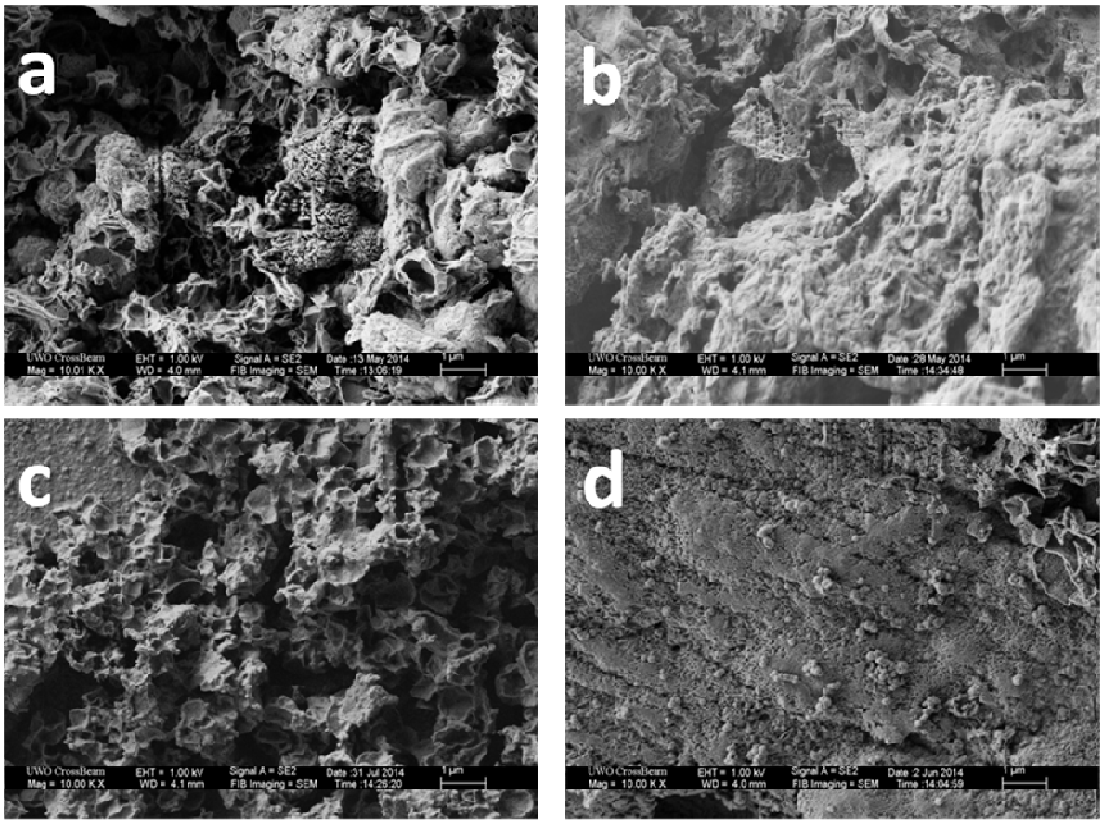

Figure 4-5-14: SEM images of cycled areas for (a) non-annealed 75% N_2 25+75 nm Cu-Al-CNx (CM1), (b) annealed 75% N_2 25+75 nm Cu-Al-CNx (CM2), (c) non-annealed 75% N_2 25+75+50 nm Cu-CNx-Al-CNx (CM4), (d) non-annealed 75% N_2 75+25+75 nm Cu-CNx-Al-CNx (CM3). Magnifications of 10000x.

This is again highlighted in images taken at higher magnifications (**Figs. 4-5-14, 4-5-15**). In particular, **Fig. 4-5-15** shows high resolution images of both passive and heterogeneous areas on the sample surface. The heterogeneous structure is quite similar for the two Cu-CNx-Al-CNx samples with the underlying CNx layers (**Fig. 4-5-15 c-d**). They can be distantly related to the honeycomb structure obtained with samples on Al surface but with much larger voids and much higher degree of disorder. A somewhat similar but even more disordered structure is also seen for non-annealed Cu-Al-CNx sample (CM1) (**Fig. 4-5-15 a**). The degree of disorder is even higher for the annealed Cu-Al-CNx sample (CM2), which did not even permit us to obtain a high resolution image

due to pronounced surface charging. Interestingly, the heterogeneous areas on both samples with underlying CNx layers (CM3, CM4) both showed signs of development of very fine honeycomb nanopores (**Fig. 4-5-15 c-d**), along with relatively intact underlying CNx in the passive areas (**Fig. 4-5-15 e-f)**. This may mean that formation of nanoporous honeycomb structure starts with some kind of structural modification of CNx. Overall, as has been already noted, samples prepared on copper substrate featured very high heterogeneity and disorder and were not investigated further.

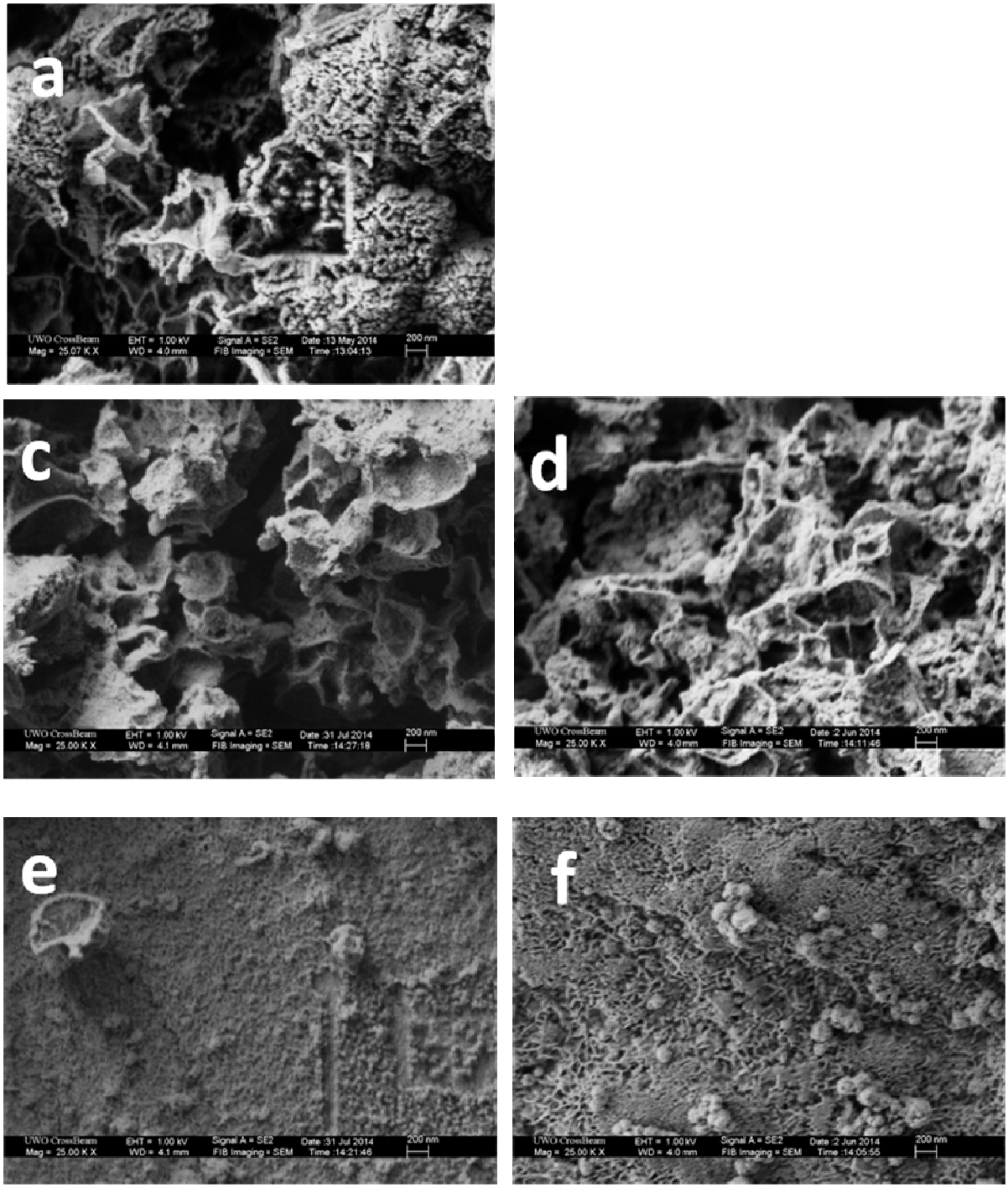

Figure 4-5-15: SEM images of cycled areas from 4x8 experiments for (a) non-annealed 75% N_2 25+75 nm Cu-Al-CNx (CM1), (c,e) non-annealed 75% N_2 25+75+50 nm Cu-CNx-Al-CNx (CM4) two areas, (d,f) non-annealed 75% N_2 75+25+75 nm Cu-CNx-Al-CNx (CM3) two areas. Magnifications of 25000x.

4.5.3 EDX Composition Charts

Shown in **Table 4-5-16** is the EDX composition data in atomic % of the uncycled, cycled porous and cycled flat areas of the non-annealed Al-Al and non-annealed and annealed Al-Al-CNx anodes ACM1, ACM2, ACM3 after being subjected to the 4x8 experiments. The predominance of a strong Al signal within the uncycled areas (**a,c,f**) indicates an unreactive anode with surface contamination by the electrolyte. Carbon and oxygen content should arise from a combination of trace propylene carbonate and residual surface oxide present after the electrode preparation before film deposition. The CNx films will contribute carbon as well and 5 to 15 percent nitrogen depending on total thickness. The very low oxygen content of a few percent is expected given the polished and etched preparation before film deposition. Trace phosphorus and fluorine content should arise from $LiPF_6$ salt remaining after rinsing. The small amount of silicon detected in all samples likely originates from a combination of silicon carbide paper used for polishing, and as an impurity commonly found in Al 1100 alloys. Lithium content cannot be tracked due to the overlap of its low energy x-rays with the baseline peak close to 0 eV.

The cycled porous region of non-annealed Al-Al-CNx (ACM2) (**d**) shows significant carbon, oxygen and fluorine content as was observed for bare GF Al, MC Al, Dural and CNx-coated anodes in Ch. 4.1.3, 4.2.3, 4.3.3 and 4.4.3 respectively. This is again likely due to the presence of electrolyte within the cycled structure, as well as the products of solvent electroreduction and salt decomposition in the SEI layer [10]. Here the oxygen content is considerably higher, possibly due to the increased presence of both electrolyte and SEI layer within the honeycomb. The porous honeycombs of both non-annealed Al-Al (ACM1) (**b**) and annealed Al-Al-CNx (ACM3) (**g**) strongly resemble the composition seen here in ACM2, with a complete absence of nitrogen content. Moving on to the cycled flat region of ACM2 (**e**) there is nitrogen content but the signal is fairly weak compared to such flat regions in Al-CNx anodes. Perhaps the CNx remnants in these multilayer samples are thinner resulting in the 7 kV column voltage mostly profiling the underlying alloy. A similar composition is observed for the twisted flat remnants in the

cycled flat area of the annealed Al-Al-CNx (ACM3) (**h**). These EDX results confirm our assessments from the SEM images and electrochemistry of these three Al-Al based samples. For Al-Al based anodes the modified porous morphology in the form of the disordered honeycomb should be due to conversion of Al thin film into the intermetallic alloy phase during lithiation-delithiation. The CNx film layer however rapidly cracks and remains in various flat or twisted pieces on top of the alloy. Additionally there is no improvement in CNx film stability offered by thermal annealing of Al-Al-CNx as in the single layered Al-CNx anodes (AC1, AC2) in Ch. 4.4.2 (**Fig. 4-4-24**).

Table 4-5-16: EDX composition chart of uncycled, cycled porous and cycled flat areas for non-annealed 25 nm Al-Al (ACM1) and non-annealed (ACM2) and annealed (ACM3) 75% N_2 25+75 nm Al-Al-CNx anodes after being subjected to 4x8 experiments. Spectra data was collected at a column voltage of 7 kV for 50 seconds at 1000x magnification.

		Atomic %						
Sample	**Area**	**C**	**N**	**O**	**F**	**Al**	**Si**	**P**
ACM1	(a)Uncycled	2.74		3.99	0.16	93.01	0.02	0.08
	(b)Porous	5.59		46.42	25.82	21.01	0.16	1.00
ACM2	(c)Uncycled	28.18	9.52	3.47	0.24	58.44	0.09	0.06
	(d)Porous	7.41		44.20	20.00	27.63	0.14	0.63
	(e)Flat	14.59	2.63	27.28	44.70	10.17	0.16	0.47
ACM3	(f)Uncycled	28.90	9.11	3.29	0.32	58.25	0.11	0.02
	(g)Porous	5.87		45.92	25.34	21.72	0.09	1.06
	(h)Flat	16.19	4.29	37.06	24.78	16.70	0.20	0.77

Shown in **Table 4-5-17** is EDX composition data in atomic % for the four copper-based anodes in the uncycled areas as well as the cycled porous and flat sub-areas. The predominance of Cu signal here within the uncycled areas again indicates an unreactive anode with surface contamination by the electrolyte **(a,d,g,j)**.

Table 4-5-17: EDX composition chart of uncycled, cycled porous and cycled flat areas for non-annealed (CM1) and annealed (CM2) 25+75 nm Cu-Al-CNx anodes, non-annealed 75+25+75 nm (CM3) and 25+75+50 nm (CM4) Cu-CNx-Al-CNx anodes after being subjected to 4x8 experiments. Spectra data was collected at a column voltage of 7 kV for 50 seconds at 1000x magnification.

		Atomic %							
Sample	**Area**	**C**	**N**	**O**	**F**	**Al**	**Si**	**P**	**Cu**
CM1	(a)Uncycled	33.37	11.80	3.23		9.28	1.56	0.10	40.67
	(b)Porous	27.03	0.40	66.55	4.71	0.58	0.16	0.57	
	(c)Flat	31.50	3.64	49.18	2.87	4.76	0.29	0.50	7.26
CM2	(d)Uncycled	32.43	10.27	3.03	0.11	12.62	1.51		40.03
	(e)Porous	19.54		60.36	17.31	1.88	0.08	0.72	0.10
	(f)Flat	26.38	3.83	32.71	9.40	3.61	1.80	0.42	21.85
CM3	(g)Uncycled	41.49	17.02	3.47	0.09	7.85	0.88	0.01	29.29
	(h)Porous	21.19	0.37	55.81	19.47	2.05	0.07	0.59	0.44
	(i)Flat	26.41	7.47	31.64	16.41	5.55	0.26	0.14	12.13
CM4	(j)Uncycled	26.30	9.86	2.81	0.79	26.80	0.54		32.90
	(k)Porous	20.34		58.08	20.43	0.14	0.11	0.69	0.21
	(l)Flat	12.80		10.39	4.09	0.51	0.04	0.24	71.93

As expected the higher ratio of CNx to Al content in 75+25+75 nm Cu-CNx-Al-CNx (CM3) relative to non-annealed (CM1) and annealed (CM2) Cu-Al-CNx produces higher C:Al and N:Al ratios within the uncycled area **(g)**, with these trends reversed in the

uncycled area of 25+75+50 nm Cu-CNx-Al-CNx (CM4) prepared with higher thickness of Al film **(j)**. For the composition of the cycled areas we first consider the non-annealed (CM1) and annealed (CM2) Cu-Al-CNx anodes. From the SEM images the porous regions would suggest the existence of intermetallic alloy due to strong C, O and F signals **(b,e)**. However Al content is only detected with a few percent here which is far less than what has been observed in any previous porous morphologies. This may be explained if we assume that we have a very thick and very disordered intermetallic structure filled with components of electrolyte and products of their reactions. If the intermetallic alloy in these regions degraded and peeled off from the copper substrate at higher cycling currents we would expect to see a strong Cu signal which is absent. For both CM1 and CM2 samples the composition of cycled flatter regions shows some resemblance to the uncycled area, but with weaker N, Al and Cu signals **(c,f)**. Perhaps this is due to partial reactivity as seen in the significantly higher oxygen content here. For both Cu-CNx-Al-CNx samples the cycled porous regions again shows very low Al and N signals (**h,k**). The composition of the flat region of CM3 **(i)** suggests partial reactivity similar to the flat regions of CM1 and CM2. However the flat region of CM4 with a thicker Al layer has both negligible Al and N content, which is very unusual (**L**). The very strong Cu signal here suggests that we have here a very thin film on essentially bare Cu substrate. We would expect the thicker Al layer present in CM4 to manifest itself as an appreciable Al signal somewhere in the cycled area.

Overall the electrochemistry and surface analysis results in Ch. 4.5 suggest that nanostructured anodes with amorphous Al thin films grown on a Cu substrate are considerably more fragile than those based on crystalline bulk Al. At higher cycling currents these anodes rapidly degrade both in efficiency as well as the mechanical stability of any intermetallic phases present. The inclusion of single or multiple CNx layers underneath and on top the amorphous Al does not appear to improve this behaviour. The poor performance of Al nanostructure anodes relative to those of Si and SnO_2 is a recurring theme in the literature and will be further discussed in Ch. 5.

4.5.4 References

1. Byers, J.C.; Billon, F.; Debiemme-Chouvy, C.; Deslouis, C.; Pailleret, A.; Semenikhin, O.A. *Acs Applied Materials & Interfaces,* **2012**, *4*, 4579.
2. Peponas, S.; Guedda, M.; Benlahsen, M., *Solid State Communciations,* **2008,** *146*, 78-82.
3. Kaltofen, R.; Sebald, T.; Weise, G., *Thin Solid Films,* **1996,** *290-291,* 112-119.
4. Alibart, F.; Durand Drouhin, O., *Applied Surface Science,* **2008,** *254,* 5564-5568.
5. Durand-Drouhin, O.; Benlahsen, M., *Solid State Communications,* **2004,** *131,* 425-429.
7. Oltean, G.; Tai, C.W.; Edstrom, K.; Nyholm, L., *Journal of Power Sources*, **2014**, *269*, 266-273.
8. Dey, A.N., *Journal of the Electrochemical Society*, **1971**, *118*, 1547-1549.
9. Mubumbila, N. ; Tessier, P.Y.; Angleraud, B.; Turban, G., *Surface and Coatings Technology,* **2002,** *151-152,* 175-179.
10. Schroder, K.W.; Dylla, A.G.; Harris, S.J.; Webb, L.J.; Stevenson, K.J., *ACS Appl. Mater. Interfaces*, **2014,** *6,* 21510-21524.

4.6 TOF-SIMS Secondary Ion Depth Profiles and Surface Profilometry

Time-of-flight secondary ion mass spectrometry (TOF-SIMS) dual-beam depth profiling was performed on several anode samples from Ch. 4.1, 4.2, 4.4 and 4.5 after completion of their 4x8 experiments and removal from the liquid half-cell setup. This specialized analytical technique was described previously in Ch. 2.7. Depth profiling of anode samples was performed in the negative ion mode for both uncycled and cycled areas. Bi_3^+ was used as the analysis beam and Cs^+ as the sputter beam. The slope and roughness of the depth profiles described in this chapter will vary due to multiple factors including SIMS instrumental parameters, heterogeneity of solid-electrolyte interphase (SEI), surface roughness and ion-induced surface damage [2]. Considering all these effects we do not extend our analysis to comparing the relative concentrations of different species on the basis of ion signal. Therefore the work in this chapter is strictly a qualitative treatment and discussion of the depth profiling of these anodic materials after their respective 4x8 liquid half-cell experiments. The secondary ions shown here should be representative of their respective structural components in both cycled and uncycled areas of the samples. As a complimentary technique to TOF-SIMS depth profiling we also performed surface profilometry on these anode samples to determine the step height and roughness of the cycled areas relative to uncycled areas.

4.6.1 Bare half-hard Goodfellow Al (GF Al) anode GF1 (oxide removed) from Ch. 4.1

TOF-SIMS Secondary Ion Depth Profiles of GF1

Shown in **Fig. 4-6-1 a-d** and **Fig. 4-6-2 a-d** are the secondary ion depth profiles for bare half-hard Goodfellow Al (GF Al) anode GF1 (oxide removed) in both uncycled and cycled areas respectively after the 4x8 experiment. For all depth profiles the vertical axis

is the raw ion intensity in counts with the horizontal axis as the total time in seconds that the Cs^+ sputter beam has been active. Intensities on the vertical axis are shown in logarithmic scale to magnify low intensities of some characteristic secondary ions. Depth profiling was performed on the uncycled area until the intensity of characteristic electrolyte species dropped to negligible levels. For GF1 this corresponds to 200 sec of sputter time. For depth profiling of the cycled area we were not certain of the thickness of the intermetallic alloy at the time. Therefore we stopped SIMS profiling of the cycled area after 700 sec, once most ion species plateaued in intensity. After SIMS analysis we did surface profilometry to reveal that the average step height of the cycled area was several micrometers thick. Based on our SIMS instrumental parameters in this work such a depth would have required many hours of profiling, and therefore almost certainly would have not guaranteed a stable primary ion current that entire time. Clearly a much higher sputter time (5-10 sec) per scan would be required to depth profile the entire thickness of the intermetallic alloy. Therefore, our SIMS analysis of the cycled areas refers to the portions of the electrode close to its outer surface. Al oxide and bulk Al regions were defined in the uncycled area of **Fig. 4-6-1 a-d** with vertical dashed lines. These regions were approximated by requiring at least 75% of the maximum intensity of ions characteristic of that layer [3]. For example this would involve AlO^- and Al_2^- ions as species characteristic of Al oxide and Al metal layers respectively. The use of this criterion is fairly simple for the uncycled area of this sample. However the rough porous morphology of cycled electrodes results in significantly more complex secondary ion behaviour. This makes it considerably more difficult to assign discrete layers. Therefore we simply discuss what may be the predominant components corresponding to regions in the cycled profiles.

First we consider the depth profiles of the uncycled area in **Fig. 4-6-1 a-d**. As mentioned previously the term "uncycled" here denotes the area outside the gasket, which should not be exposed to electrolyte. A maximum of Al oxide species is observed in the first 15 sec of sputtering time **(Fig. 4-6-1 b)**, indicating some partial re-growth of the surface oxide after it has been etched away during substrate preparation. This behaviour may also be seen by tracking the $^{18}O^-$ isotope ion **(Fig. 4-6-1 a)**. Care was taken to remove the surface

oxide through a combination of polishing and then etching in alkaline KOH solution. However there was brief exposure of sample to ambient atmosphere during the transfer and preparation steps. Bulk Al below the oxide layer is characterized with Al_2^- and Al_3^- ions, similar to Si_2^- ions used in depth profiling of Si anodes [3]. In comparison the monoatomic Al^- secondary ion was only very weakly detected, and therefore ignored for the purpose of this analysis. These bulk aluminium cluster species rapidly rise in intensity and plateau after approximately 50 sec. We detected secondary ion species characteristic of the $LiPF_6$ salt as Li^-, LiO^-, F^-, PO_2^- and PO_3^- **(Fig. 4-6-1 a,d)** . The F^- ion in particular shows an extremely high intensity in the uncycled area, likely due to its very high negative ionization yield under Cs^+ sputtering [1]. The CO_2H^- and $C_3H_3O_2^-$ secondary ion species **(Fig. 4-6-1 d)** should arise from fragmentation of propylene carbonate solvent as well as the products of its electroreduction in SEI formation [2]. Other CO containing secondary ions could not be definitively identified in the spectra. These various electrolyte species were detected with high intensity initially but show rapid decline once the bulk Al region is reached. Therefore the electrolyte present in this uncycled area should exist mostly as trace surface contamination on top of the unreacted Al electrode. This profiling behaviour shows that the gasket is working properly to isolate this outside area as a reference "uncycled" area in our half-cell experiments. The residual electrolyte should have been introduced into the uncycled area when rinsing the sample after its removal from the cell.

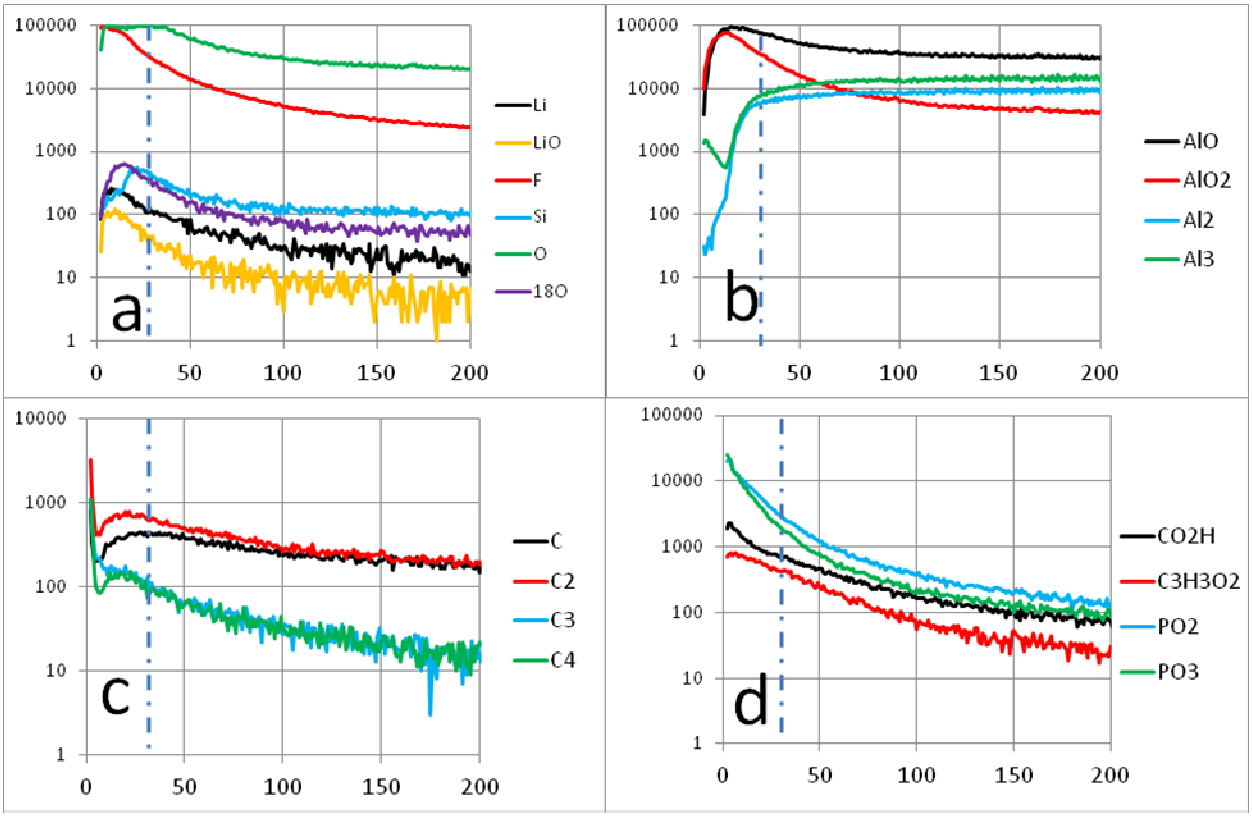

Figure 4-6-1: TOF-SIMS negative secondary ion depth profiles of uncycled area of bare half-hard Goodfellow Al anode GF1 (oxide removed) subjected to 4x8 experiment from Ch. 4.1. Vertical axis is raw ion intensity counts. Horizontal axis is total active time in seconds for Cs^+ sputter beam. Vertical dashed line denotes the approximated boundary between the surface oxide region and the bulk Al.

We detected several low mass carbon-containing species C^- to C_4^- **(Fig. 4-6-1 c)**. C_1^- and C_2^- are typically attributed to adventitious (atmospheric) carbon contamination in the TOF-SIMS analysis chamber. They are observed even in inorganic systems such as sputter cleaned Si single crystal [4]. The faster intensity drop in the bulk Al region of C_3^- and C_4^- vs. C_1^- and C_2^- may suggest that the former pair are also produced by fragmentation of the propylene carbonate solvent. Commercial Al 1100 alloy is typically 99% Al with the most abundant impurities being Fe and Si. Negative Fe containing species such as FeO^- and FeO_2^- were not definitively identified in the spectra. Their

absence may simply be due to the low abundance of this impurity relative to the bulk aluminium present. However silicon is detected as Si^- with a maxima at 20 sec and intensity that persists into the bulk Al region **(Fig. 4-6-1 a)**. The near overlap of this Si^- maxima with Al oxide species may be due to polishing with SiC paper for removal of surface oxide during substrate preparation.

We now turn attention to the cycled area of GF1 in **Fig. 4-6-2 a-d**. As mentioned previously in Ch. 2.3.3 the XRD analysis of cycled Al anodes shows Li_xAl_y crystalline alloy phases [5-9]. Experimentally this typically only contains the lowest order alloy LiAl. Here in TOF-SIMS depth profiling of our Al anode systems we did not detect compound $Li_xAl_y^-$ secondary ion species. However we did simultaneously detect Li^- and Al_y^- species immediately in profiling the sample surface. Furthermore, these ion species persist at high intensities throughout the entire profiling depth of the cycled area. The distribution of these species was relatively uniform throughout the film, except for slight decrease at the surface. The question still remains why do we not see emission of compound intermetallic secondary ions. The alloy may possibly be fragmented into these simple species during the Cs^+ sputtering event. Alternatively perhaps there are intact intermetallic species emitted from the surface that are then fragmented before they reach the detector. We can only state that the behaviour is likely due to some combination of poor sputtering and/or ionization yield of these species. As shown previously the SEM images of GF1 show homogenous porous morphology indicating full reactivity across the entire cycled area **(Fig. 4-1-13 c)**. Therefore both the entire sputter and analysis areas here in TOF-SIMS profiling contain this porous morphology, because these areas are considerably larger than the area observed in SEM images. As a result there must be intermetallic composition present throughout the entire TOF-SIMS profiling depth of each cycled area. This is again consistent with the redox behaviour observed in the CVs **(Fig. 4-1-3)**, and the long flat plateaus in the galvanic cycles **(Fig. 4-1-4)**.

While the uncycled area shows less than 1000 counts of electrolyte species, the cycled area of this GF1 sample contains up to 10000 counts **(Fig. 4-6-2 a,d)**. Additionally these secondary ions persist throughout the entire profiling depth of the cycled area, considered

as intermetallic LiAl alloy. Therefore instead of simple surface contamination in the uncycled region, the electrolyte here is due to the presence of solid-electrolyte interphase (SEI) layer. The formation of the SEI layer was demonstrated previously in the partial cathodic CV scans in **Fig. 4-1-2**. The SEI contains various organic and inorganic components (2). Organic components are generally known to result from partial electroreduction of the solvent, which in our work was propylene carbonate.

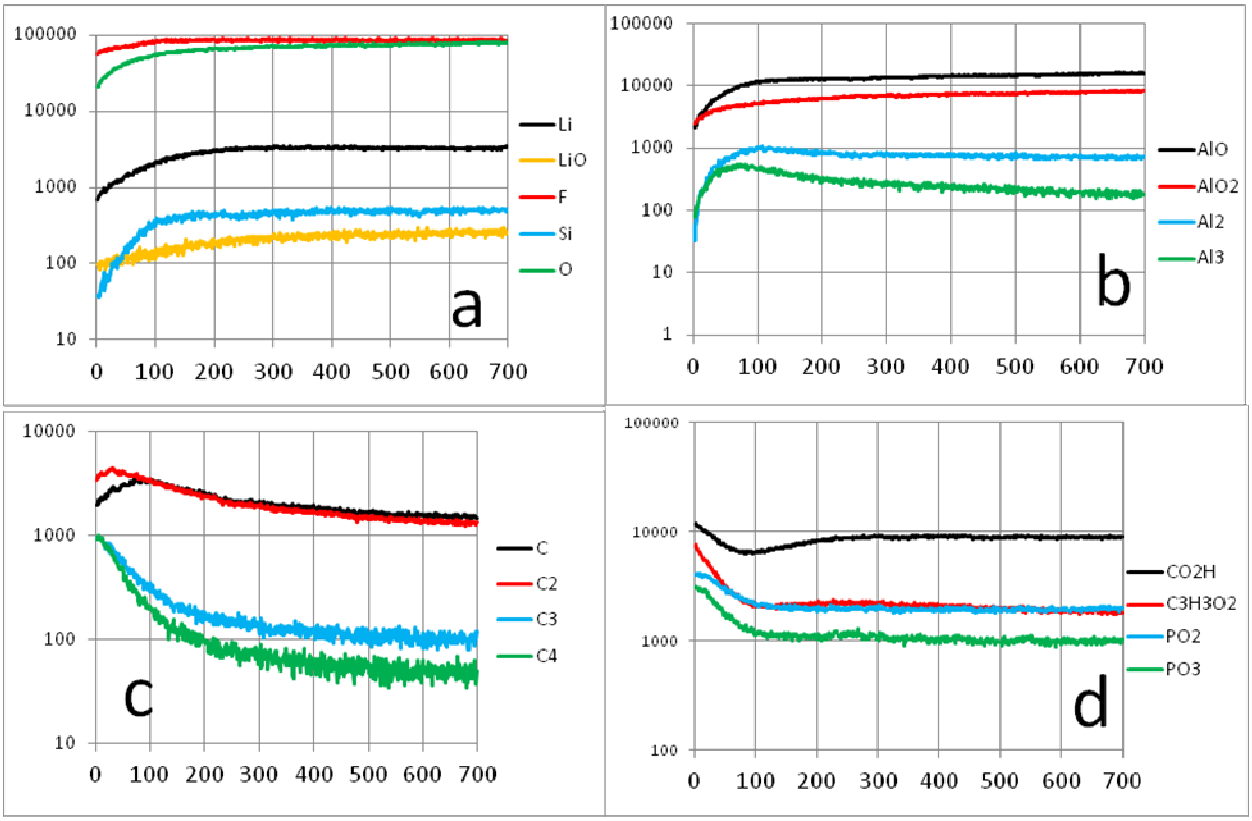

Figure 4-6-2: TOF-SIMS negative secondary ion depth profiles of cycled area for bare half-hard Goodfellow Al anode GF1 (oxide removed) subjected to 4x8 experiment from Ch. 4.1. Vertical axis is raw ion intensity counts. Horizontal axis is total active time in seconds for Cs^+ sputter beam.

This process will be assisted by lithium ions due to their presence at the electrode surface in the electric double layer. Electroreduction will therefore generate various lithium carbonate species as well as alkoxy and carboxyl functionalities in the SEI. The

formation of inorganic products will be due to thermally-driven decomposition of the $LiPF_6$ salt, which will be accelerated if there is trace moisture content present in the electrolyte and/or solvent [2]. This process will generate various Li containing species such as LiF and Li oxides. The organic and inorganic components of SEI formation were monitored through various secondary ions, similar to previous TOF-SIMS studies performed on silicon nanowire anodes [2-3]. Organic carbonate products were tracked as CO_2H^- and $C_3H_3O_2^-$, and inorganic products as Li^-, LiO^-, F^-, PO_2^- and PO_3^-. In our profiling of the GF1 anode we were unable to conclusively identify other CO containing ions in the spectra. Therefore we take those ions to approximate both intact solvent and the products of its electroreduction in the SEI. Similarly for inorganic products of SEI we were unable to identify LiF^-, PF_6^- or higher order species like LiF_2^-. However lithium oxide species still appeared to be present in the cycled area in the form of LiO^-. In the case of LiF_x^- ions these species may preferentially be fragmented here into Li^- and F^- due to a difference in SIMS instrumental parameters. Similarly to Li^-, we see persistent Si^- intensity throughout the entire profiling depth of the alloy (**Fig. 4-6-2 a**). This behaviour suggests that the Si impurity in the 1100 Al metal may be chemically incorporated into the porous structure and therefore electroactive towards lithiation/delithiation [10].

Considering the persistent high intensities of F^-, PO_2^-, PO_3^-, CO_2H^- and $C_3H_3O_2^-$ ions throughout the sample over the whole profiling depth (**Fig. 4-6-2**), these species should be characteristic of SEI formation and composition for cycling of Al anodes in $LiPF_6$ and propylene carbonate. Based on this assumption, the LiAl alloy framework observed should occur simultaneously with the components of the SEI layer. This strongly suggest high porosity of the LiAl intermetallic phase formed during the cycling, with the SEI formed at the internal walls of the nanopores. Most of the SEI species appear more concentrated within the first 120 sec where Al and Li content is still increasing. This suggests that the intermetallic structure is more open towards the surface of the anode. However, the porosity persists throughout all the profiled depth indicating formation of highly developed nanoporous structure as a result of cycling. Nothing like that was observed in non-cycled areas.

Looking at **Fig. 4-6-2 b** we see persistent high AlO_x content throughout the profiling depth in this cycled area, with higher intensities apparent in the intermetallic-rich region after 120 sec. These AlO_x^- profiles also roughly follow the behaviour of the Li^- and Al_y^- ions. Unlike the uncycled area profiles **(Fig. 4-6-1 b)** there is an absence of initial maxima of these oxide species. This absence suggests that the Al oxide may have been reduced during the lithiation (charging) steps of the CV and galvanic cycles for GF1. As previously mentioned this is unlikely for the CV scans **(Fig. 4-1-3)** due to the standard potential of 0.14V vs. Li^+/Li for this process [5]. However for galvanic cycles the highest current density of 1 mA/cm^2 did result in lithiation occurring below 0V vs. Li^+/Li **(Fig. 4-1-4)**. We instead offer two alternative explanations for the persistent high oxygen content observed throughout the TOF-SIMS profiling depth. Firstly the uncycled area of GF1 **(Fig. 4-6-1 b)** only showed a brief initial maxima for AlO_x^- intensity, before Al_y^- sharply rises and dominates in the bulk Al region. Therefore the AlO_x^- species throughout the cycled area should not be formed from oxygen present in the initial residual oxide layer. Additionally, electrochemical preparation of the cells was performed in a glovebox with < 1 ppm O_2 and H_2O content. Therefore the source of oxygen should primarily be from electroreduction of the propylene carbonate solvent (mentioned previously) [2]. There is clearly significant Al content present from the intermetallic alloy as seen in the profiles Al_2^- and Al_3^-. As a result there may be recombination of fragments during the Cs^+ sputtering event, to give high AlO_x^- intensity through the profiled alloy depth. Such behaviour has been observed in SiO_2^- and LiO^- ions for depth profiling of cycled Si anodes [2-3]. Secondly, Al anode systems may suffer a parasitic loss of efficiency due to irreversible lithiation of the surface oxide into a super-hard Li-O-Al layer [6]. This process occurs first before lithiation of the Al core, which was described previously in the onset of lithiation in the CVs **(Fig. 4-1-2)**. The resulting Li-O-Al layer surrounds the underlying LiAl intermetallic phases and opposes the volume changes of lithiation-delithiation. Our TOF-SIMS and SEM results here clearly show a highly porous intermetallic alloy structure that is several micrometers thick. If this structure contains a lithiated oxide layer we should therefore detect persistent intensities of AlO_x^- ions.

Surface Profilometry of GF1

After TOF-SIMS depth profiling we performed surface profilometry on this sample (**Fig. 4-6-3**). The surface profile corresponds to a line scan of the stylus from the gasket area to the cycled area, and across to the opposite gasket area for a total distance of 7 mm. The surface profile shows an average step height of 5 um for this cycled area, which is defined as the difference in the average height of region A2 compared to A1. As expected the profile also shows significant roughness (height variation) which is consistent with the highly porous morphology observed in SEM imaging (**Fig. 4-1-13 c,e**).

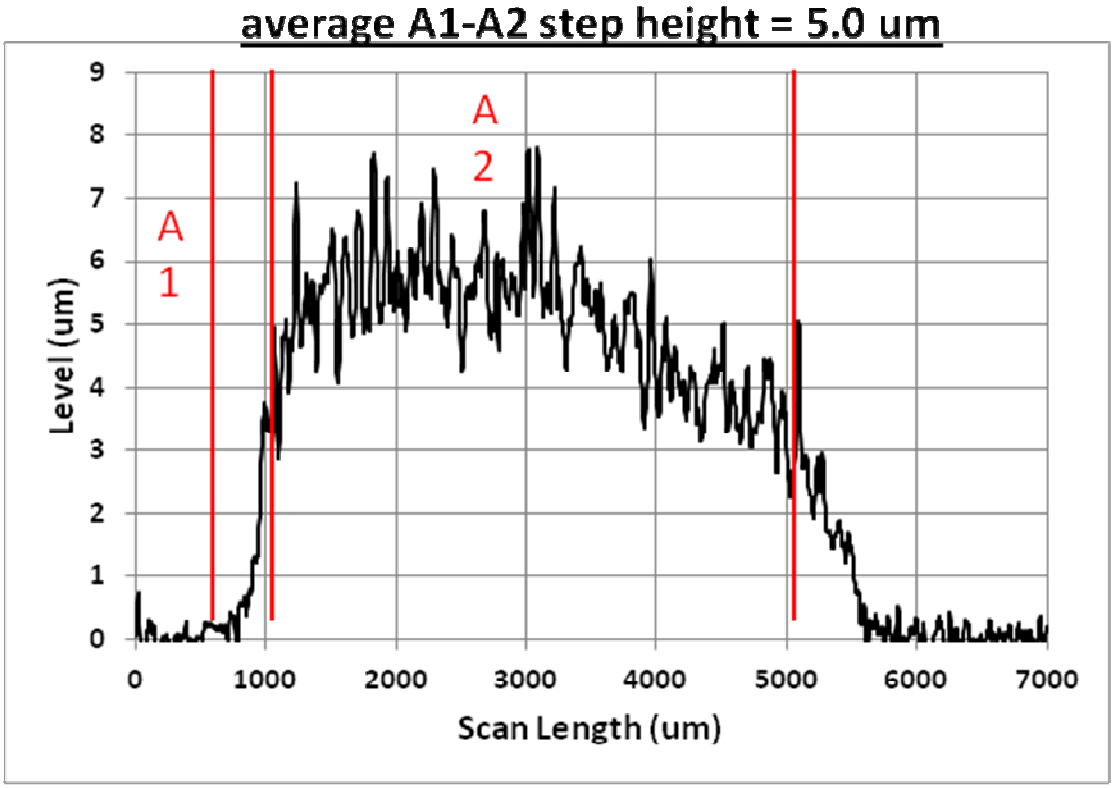

Figure 4-6-3: Surface profile of bare half-hard Goodfellow Al anode GF1 (oxide removed) subjected to 4x8 experiment from Ch. 4.1. Line scan is from gasket area to cycled area to gasket area. Step height is average difference of A1 and A2 areas.

Therefore, to conclude, our TOF SIMS studies of half-hard GF Al anode after a 4x8 experiment suggest the formation of thick Li-containing Al phase with relatively uniform distribution of Li and Al species over the profiling depth. SEI was found to be present throughout the whole profiling depth, which indicated formation of highly porous structure. The average thickness of the Li-containing phase was much greater than the profiled depth and was equal to ca. 5 μm.

4.6.2 Bare soft McMaster-Carr Al (MC Al) anode MC1 (oxide removed) from Ch. 4.2

TOF-SIMS Secondary Ion Depth Profiles of MC1

Shown in **Fig. 4-6-4 a-d** and **Fig. 4-6-5 a-d** are the secondary ion depth profiles for soft McMaster-Carr Al (MC Al) anode MC1 (oxide removed) in both uncycled and cycled areas respectively after the 4x8 experiment. For all depth profiles the vertical axis is the raw ion intensity in counts with the horizontal axis as the total time in seconds that the Cs^+ sputter beam has been active. Intensities on the vertical axis are shown in logarithmic scale to magnify low intensities of some characteristic secondary ions. Depth profiling was performed on the uncycled area until the intensity of characteristic electrolyte species dropped to negligible levels. For MC1 this corresponds to 200 sec of sputter time. For depth profiling of the cycled area we were not certain of the thickness of the intermetallic alloy at the time. Similarly to GF1, we stopped SIMS profiling of the cycled area after 700 sec, once most ion species plateaued in intensity. This was not enough to profile the whole film thickness as revealed by surface profilometry. Al oxide and bulk Al regions were defined in **Fig. 4-6-4 a-d** with vertical dashed lines. These regions were approximated by requiring at least 75% of the maximum intensity of ions characteristic of that layer [3]. For example this would involve AlO^- and Al_2^- ions as species characteristic of Al oxide and Al metal layers respectively. The use of this criterion is fairly simple for the uncycled area of this sample. However the rough porous morphology of cycled electrodes results in significantly more complex secondary ion behaviour.

Therefore we simply discuss what may be the predominant components corresponding to regions in the cycled profiles.

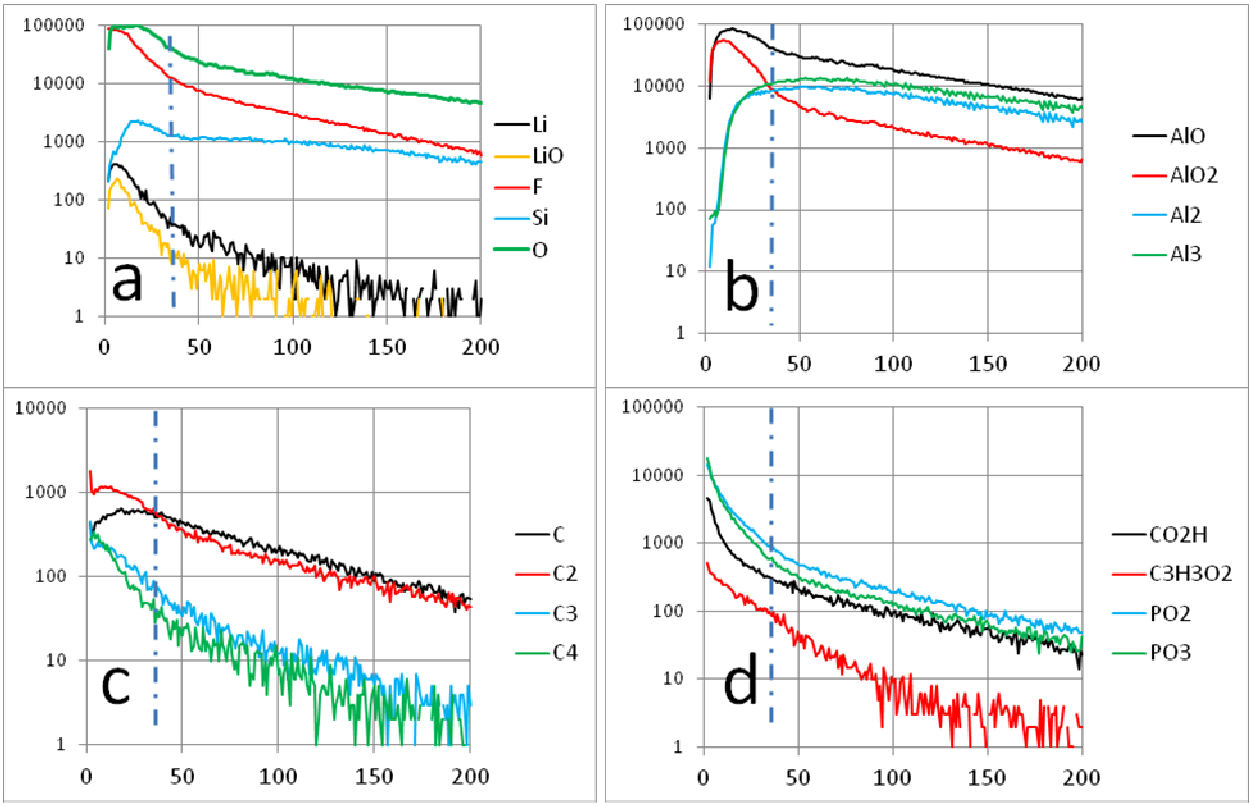

Figure 4-6-4: TOF-SIMS negative secondary ion depth profiles of uncycled area for bare soft McMaster-Carr (MC Al) anode MC1 (oxide removed) after being subjected to a 4x8 experiment from Ch. 4.2. Vertical axis is raw ion intensity counts. Horizontal axis is total active time in seconds for Cs^+ sputter beam. Vertical dashed line denotes the approximated boundary between the surface oxide region and the bulk Al.

First we consider the depth profiles of the uncycled area in **Fig. 4-6-4 a-d**. Overall the SIMS depth profiles in the uncycled area are very similar to those described for the bare GF Al anode GF1 in the previous section (**Fig. 4-6-1**). As mentioned previously the term "uncycled" here denotes the area outside the gasket, which should not be exposed to electrolyte. A maxima of Al oxide species is observed in the first 15 sec of sputtering

time **(Fig. 4-6-4 b)**, indicating some partial re-growth of the surface oxide after substrate preparation. Bulk Al below the oxide layer is characterized with Al_2^- and Al_3^- ions, similar to Si_2^- ions used in depth profiling of Si anodes [2-3]. In comparison the monoatomic Al^- secondary ion was only very weakly detected, and therefore ignored for the purpose of this analysis. These bulk aluminium cluster species rapidly rise in intensity and plateau after approximately 50 sec. We detected secondary ion species characteristic of the $LiPF_6$ salt as Li^-, LiO^-, F^-, PO_2^- and PO_3^- **(Fig. 4-6-4)** . The F^- ion again shows an extremely high intensity in the uncycled area, likely due to its very high negative ionization yield under Cs^+ sputtering [1].

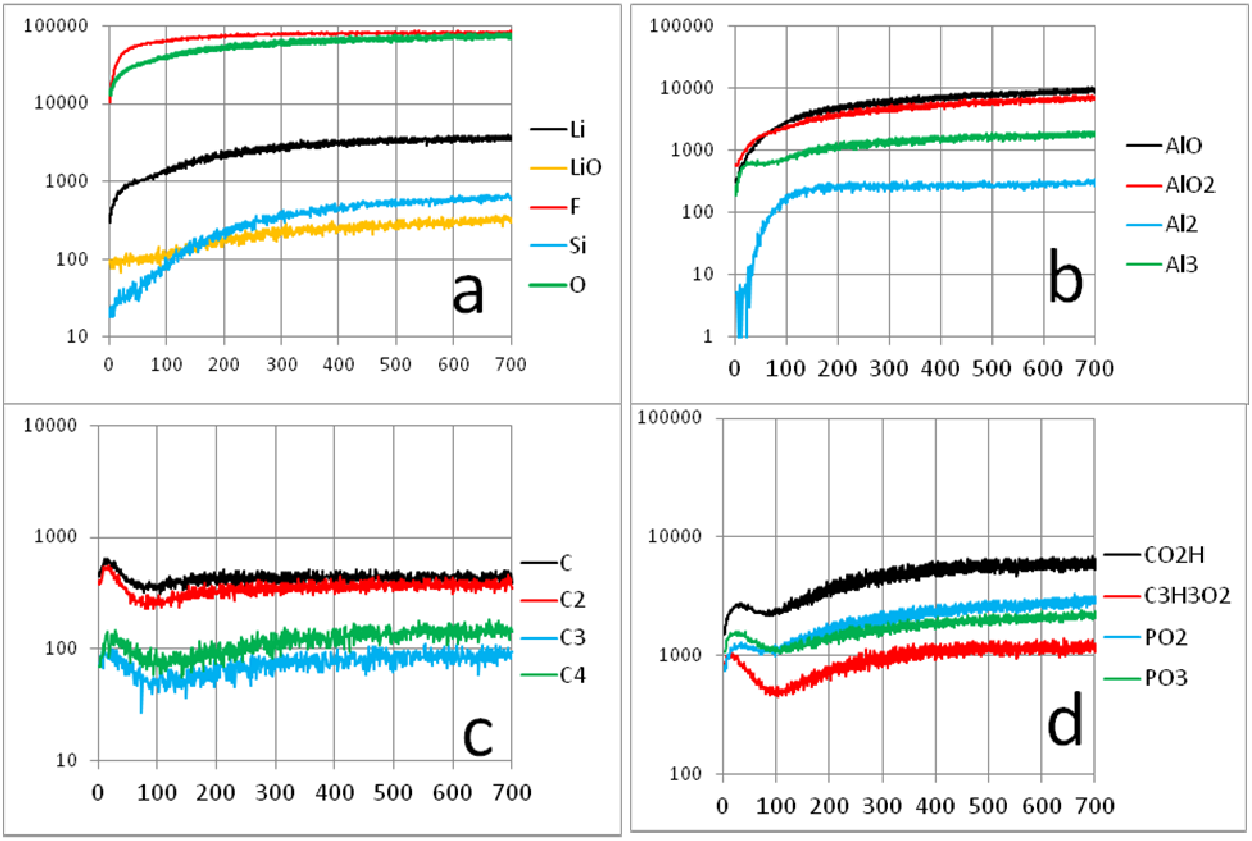

Figure 4-6-5: TOF-SIMS negative secondary ion depth profiles of cycled area for bare soft McMaster-Carr (MC Al) anode MC1 (oxide removed) after being subjected to a 4x8 experiment from Ch. 4.2. Vertical axis is raw ion intensity counts. Horizontal axis is total active time in seconds for Cs^+ sputter beam.

The CO_2H^- and $C_3H_3O_2^-$ secondary ion species **(Fig. 4-6-4 d)** should arise from fragmentation of propylene carbonate solvent as well as the products of its electroreduction in SEI formation [2]. Other CO containing secondary ions could not be definitively identified in the spectra. These various electrolyte species were detected with high intensity initially but show rapid decline once the bulk Al region is reached. Therefore the electrolyte present in this uncycled area should exist mostly as trace surface contamination on top of the unreacted Al electrode. We detected several low mass carbon-containing species e.g. C^- to C_4^-, which should arise from a combination of adventitious (atmospheric) carbon contamination in the TOF-SIMS chamber as well as fragmentation of the propylene carbonate solvent **(Fig. 4-6-4 d)**. Like in GF Al we detected Si^- here with a maxima at 20 sec and intensity that persists into the bulk Al region (**4-6-4 a**). This species arises from a combination of Si impurities in the MC Al material as well as due to polishing with SiC paper for removal of surface oxide during substrate preparation.

We now turn attention to the cycled area of MC1 in **Fig. 4-6-5 a-d** and its similarities to the cycled depth profiles of the GF Al anode GF1 in the previous section (**Fig. 4-6-2**). Like in GF Al we did not detect compound intermetallic $Li_xAl_y^-$ secondary ion species here in MC Al, but instead high concomitant Li^- and Al_y^- intensities throughout the entire profiling depth of the cycled area. Together with the fairly homogenous porous morphology observed across the entire cycled area of MC1 (**Fig. 4-2-12**) there should be intermetallic composition present throughout the TOF-SIMS profiling depth here. This is consistent with the redox behaviour of MC Al observed in the CVs **(Fig. 4-2-2)** and the long flat plateaus in the galvanic cycles **(Fig. 4-2-3)** being similar to GF Al.

While the distribution of Li and Al containing species in cycled MC Al was fairly similar to that observed for cycled GF Al, one can see that there was a considerable gradient in Li content up to sputtering time of ca. 400 sec. Such behaviour was not observed for GF Al (**Fig. 4-6-2**). This is consistent with greater heterogeneity of the intermetallic structure formed on soft MC Al noted in Ch. 4.2.

Again, the cycled area of MC1 (**4-6-5 a,d**) indicated the presence of the electrolyte components that could not be attributed to surface contamination. The organic components of the SEI are tracked with CO_2H^- and $C_3H_3O_2^-$ species. The inorganic components of the SEI are tracked with Li^-, LiO^-, F^-, PO_2^- and PO_3^- species. As in GF Al these secondary ions persist throughout the entire profiling depth of the cycled area, suggesting the formation of highly porous structure with SEI formed at the internal walls of the nanopores throughout the thickness of the intermetallic LiAl alloy. However, unlike GF Al, the concentrations of the electrolyte species seem to increase with the profiling depth. This again indicate the formation of highly heterogeneous structure with possible delamination and cracking of the portions of the active intermetallic phase. This would allow more electrolyte to penetrate inside the LiAl nanostructure.

Looking at **Fig. 4-6-5 b** there is persistent high AlO_x content throughout the profiling depth in this cycled area, with higher intensities apparent later in the profiles. These AlO_x^- profiles also roughly follow the behaviour of the Li^- and Al_y^- ions. This behaviour is similar to what was observed for GF Al. As for GF Al, we offer similar explanations here for MC Al. Firstly the residual surface oxide may have been reduced during the charging (lithiation) steps occurring below 0V vs. Li^+/Li at the highest current density of 1 mA/cm^2 in the 4x8 galvanic cycles. Secondly there may be recombination of Al-containing species from the intermetallic alloy with O-containing species from electroreduction of the propylene carbonate solvent in the SEI [2]. Finally there is the possibility of the residual surface oxide being lithiated irreversibly into a super-hard Li-O-Al layer that surrounds the underlying porous intermetallic structure [6].

Surface Profilometry of sample MC1

After TOF-SIMS depth profiling we performed surface profilometry on this sample (**Fig. 4-6-6**). The surface profile corresponds to a line scan of the stylus from the gasket area to the cycled area, and across to the opposite gasket area for a total distance of 7 mm. The surface profile shows an average step height of 3.4 um for this cycled area, which is defined as the difference in the average height of region A2 compared to A1. This step

height is considerably smaller than was observed for bare GF Al (GF1) under identical (**Fig. 4-6-3**). The profile of MC1 still shows significant roughness (height variation) which is consistent with the highly porous morphology observed in SEM imaging (**Fig. 4-2-12**).

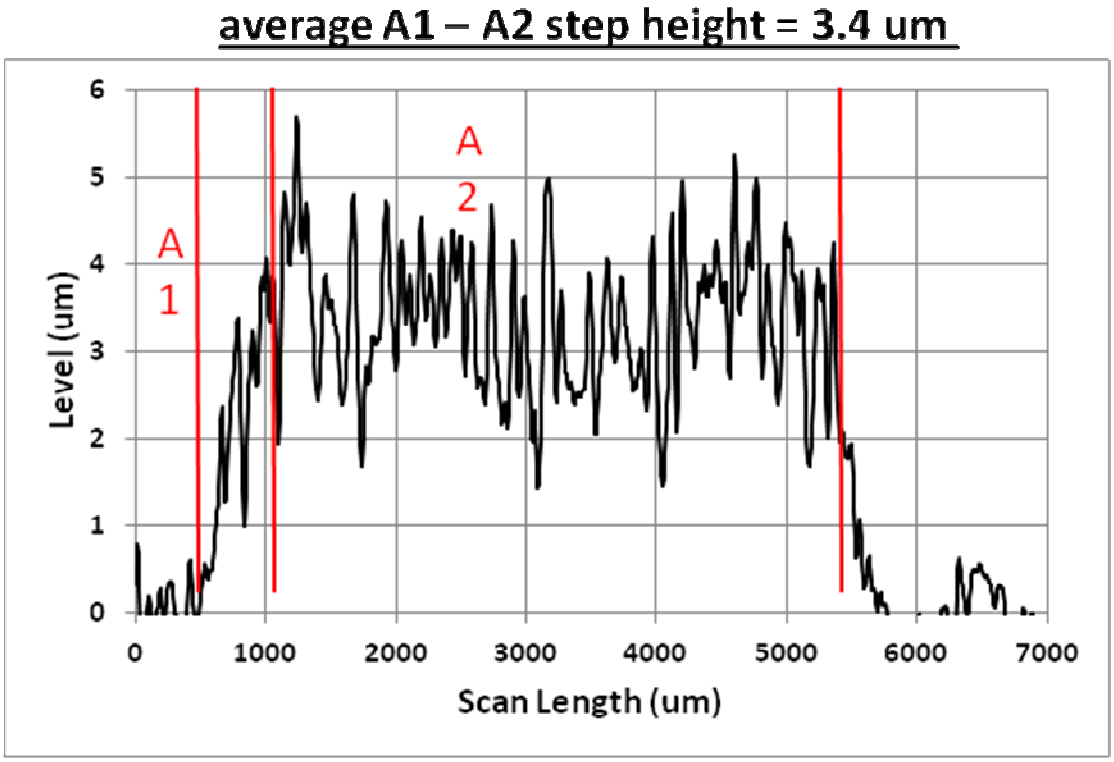

Figure 4-6-6: Surface Profile for bare soft McMaster-Carr (MC Al) anode MC1 (oxide removed) after being subjected to a 4x8 experiment from Ch. 4.2. Line scan is from gasket area to cycled area to gasket area. Step height is average difference of A1 and A2 areas.

To conclude, our TOF SIMS studies of soft MC Al anode after a 4x8 experiment suggest the formation of thick Li-containing Al phase, similarly to what was observed for GF Al. However, the distribution of the Li and Al species as well as the components of SEI over the profiling depth suggests that the nanostructure formed on the surface of MC Al is much more heterogeneous as compared to the one found on GF Al, with more cracks and voids and possible delamination allowing the penetration of the electrolyte components

deep inside he intermetallic phase. This is consistent with SEM results reported in Ch. 4.2.

4.6.3 Non-annealed (AC1) and Annealed (AC2) 75% N_2 75 nm Al-CNx anodes from Ch. 4.4

TOF-SIMS Secondary Ion Depth Profiles of AC1 and AC2

Shown in **Fig. 4-6-7 a-d to Fig. 4-6-10 a-d** are the secondary ion depth profiles for AC1 (non-annealed Al-CNx) and AC2 (annealed Al-CNx) in both uncycled and cycled areas after their 4x8 experiments. For all depth profiles the vertical axis is the raw ion intensity in counts with the horizontal axis as the total time in seconds that the Cs^+ sputter beam has been active. Intensities on the vertical axis are shown in logarithmic scale to magnify low intensities of some characteristic secondary ions. Depth profiling was performed on the uncycled area of these Al-CNx samples until the bulk Al region was reached. For both samples this corresponds to 300 sec of sputter time.

For depth profiling of the cycled areas we were again not certain of the thickness of the intermetallic alloy at the time. Therefore we stopped SIMS profiling of the cycled areas once most ion species plateaued in intensity. For AC1 (non-annealed Al-CNx) and AC2 (annealed Al-CNx) this corresponds to 700 sec and 500 sec respectively. As before, various layers at the sample surface, such as Al oxide, bulk Al, CNx and interfacial layers were defined in **Fig. 4-6-7** and **Fig. 4-6-8** with vertical dashed lines. These regions were approximated by requiring at least 75% of the maximum intensity of ions characteristic of that layer [3]. For example this would involve AlO^- and Al_2^- ions as species characteristic of Al oxide and Al metal layers respectively. No such assignment was performed, as before, in more complex cycled areas.

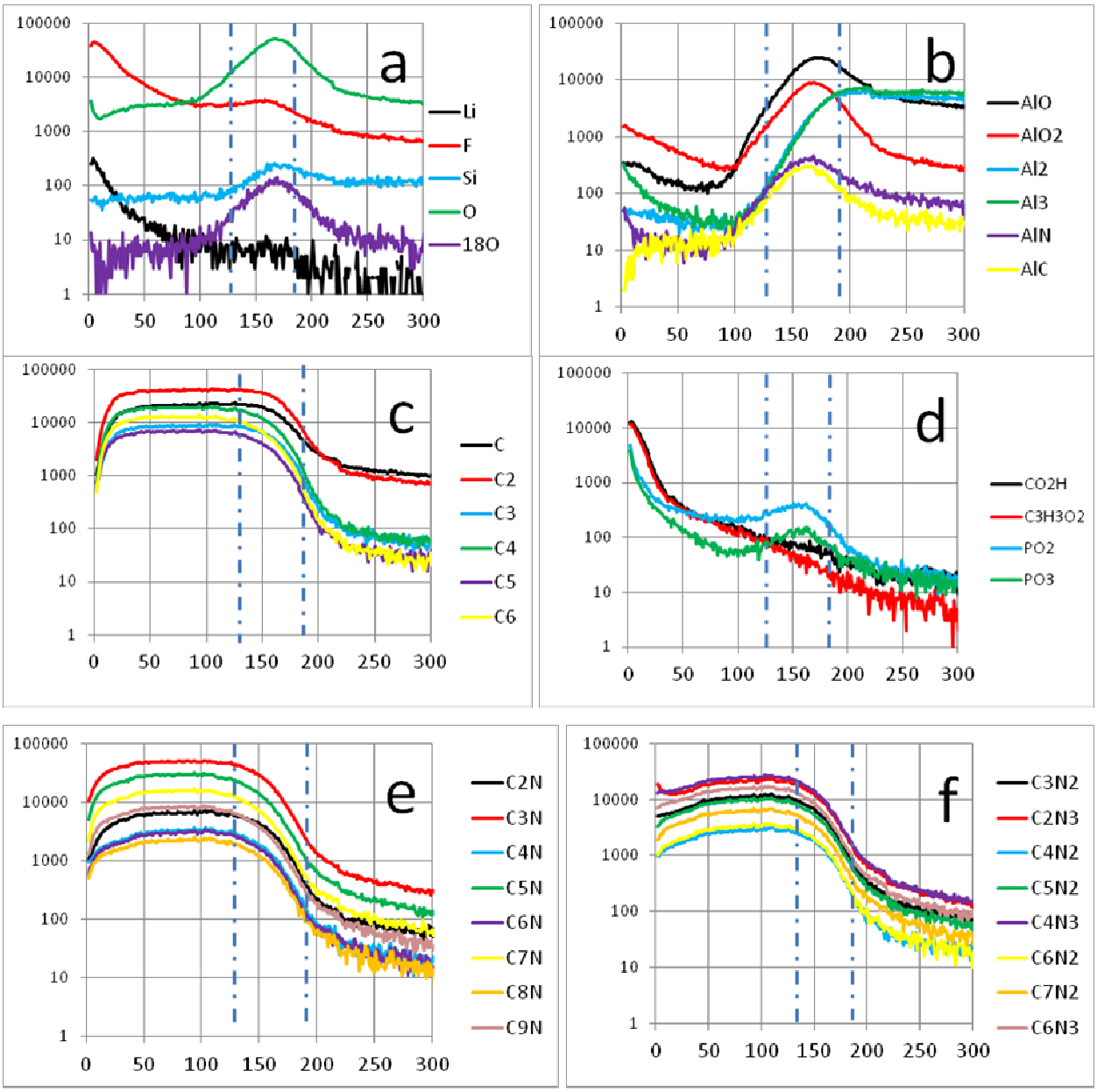

Figure 4-6-7: TOF-SIMS negative secondary ion depth profiles of uncycled area for non-annealed 75% N_2 Al-CNx anode AC1 after being subjected to a 4x8 experiment from Ch. 4.4. Vertical axis is raw ion intensity counts. Horizontal axis is total active time in seconds for Cs^+ sputter beam. Vertical dashed lines denote the approximated regions of CNx film, interfacial layer and bulk Al.

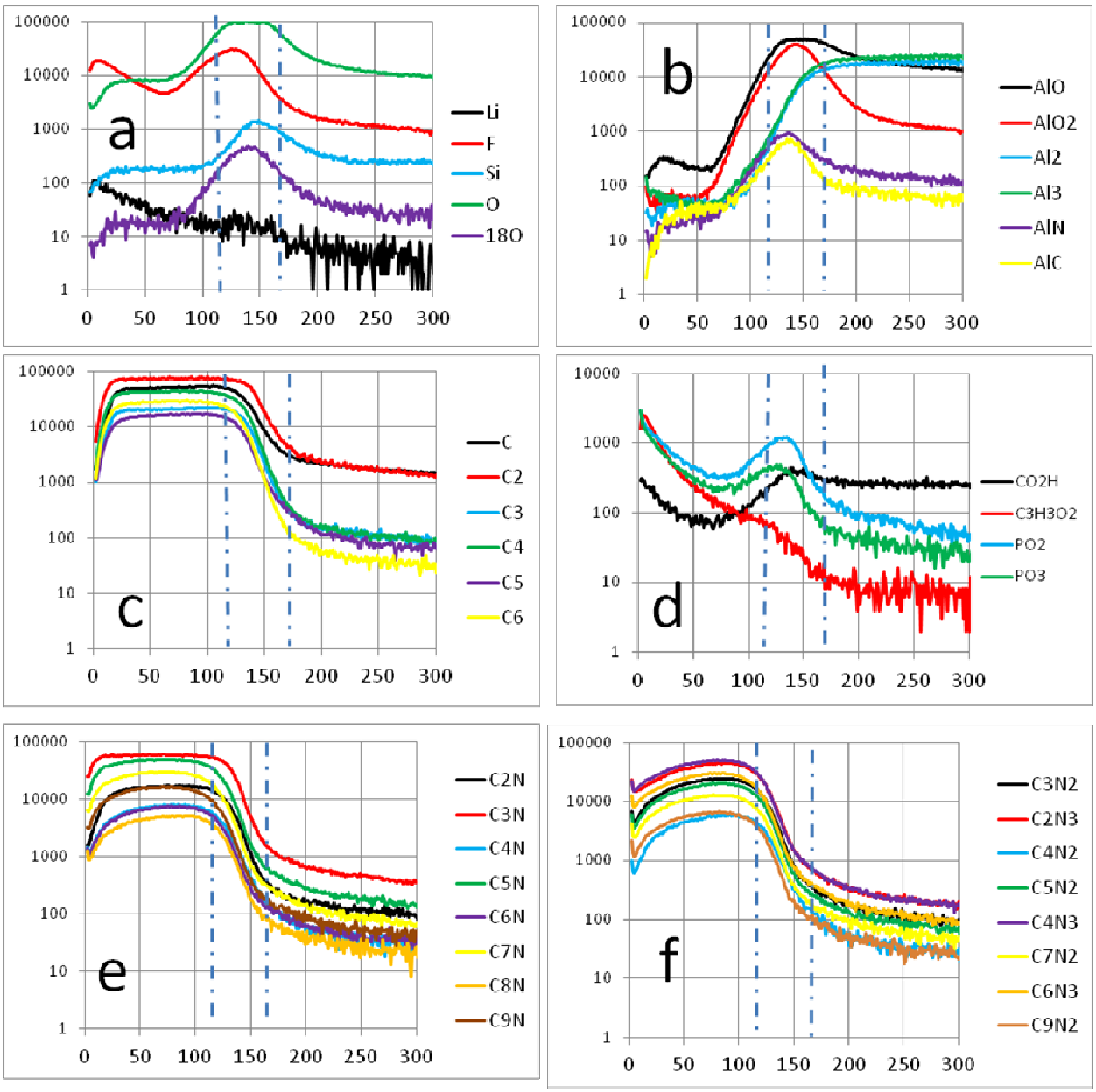

Figure 4-6-8: TOF-SIMS negative secondary ion depth profiles of uncycled area for annealed 75% N_2 Al-CNx anode AC2 after being subjected to a 4x8 experiment from Ch. 4.4. Vertical axis is raw ion intensity counts. Horizontal axis is total active time in seconds for Cs^+ sputter beam. Vertical dashed lines denote the approximated regions of CNx film, interfacial layer and bulk Al.

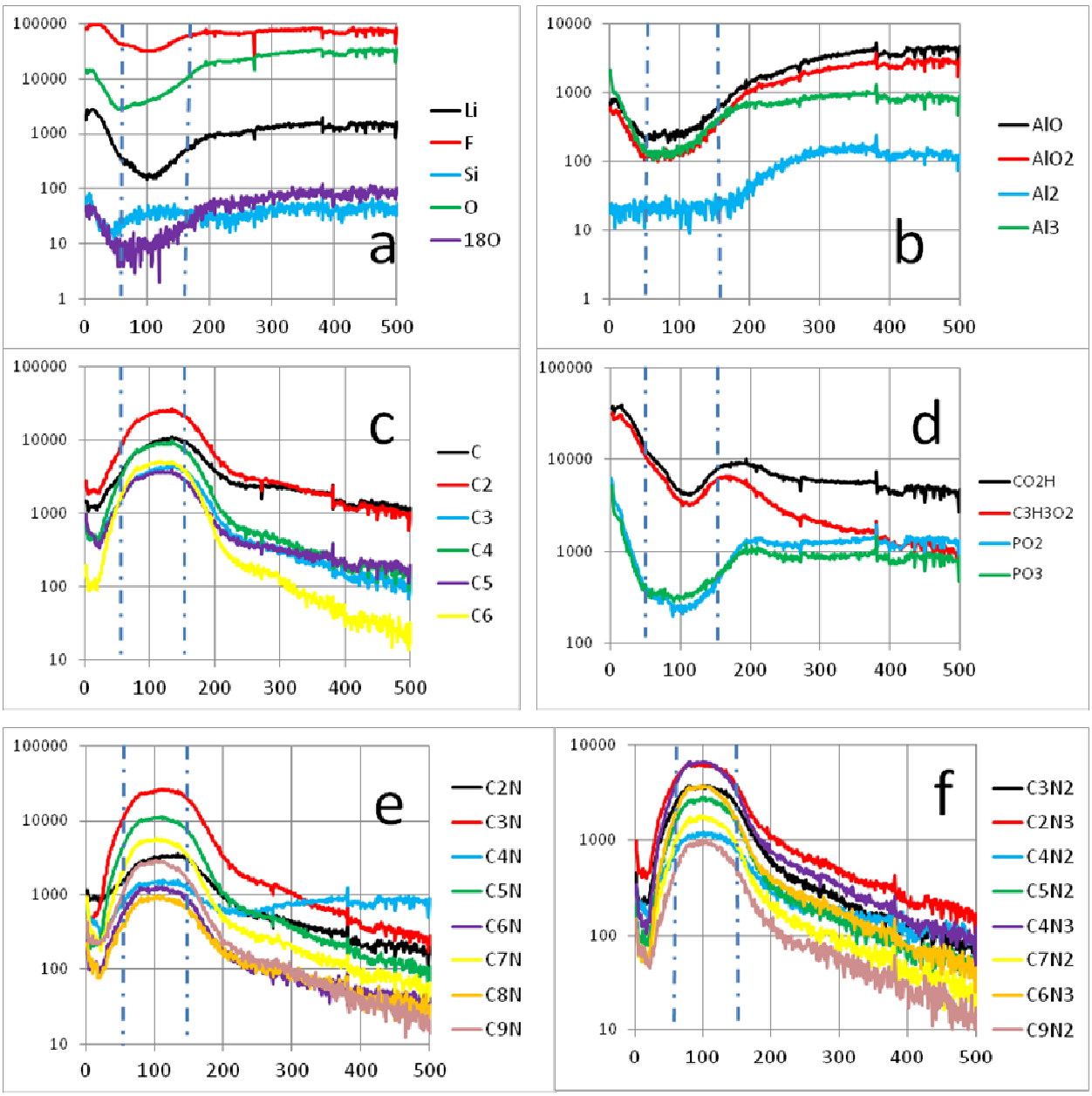

Figure 4-6-9: TOF-SIMS negative secondary ion depth profiles of cycled area for non-annealed 75% N_2 Al-CNx anode AC1 after being subjected to a 4x8 experiment from Ch. 4.4. Vertical axis is raw ion intensity counts. Horizontal axis is total active time in seconds for Cs^+ sputter beam. Vertical dashed lines denote the approximated regions of SEI-rich layer, CNx-rich layer and Intermetallic-rich layer

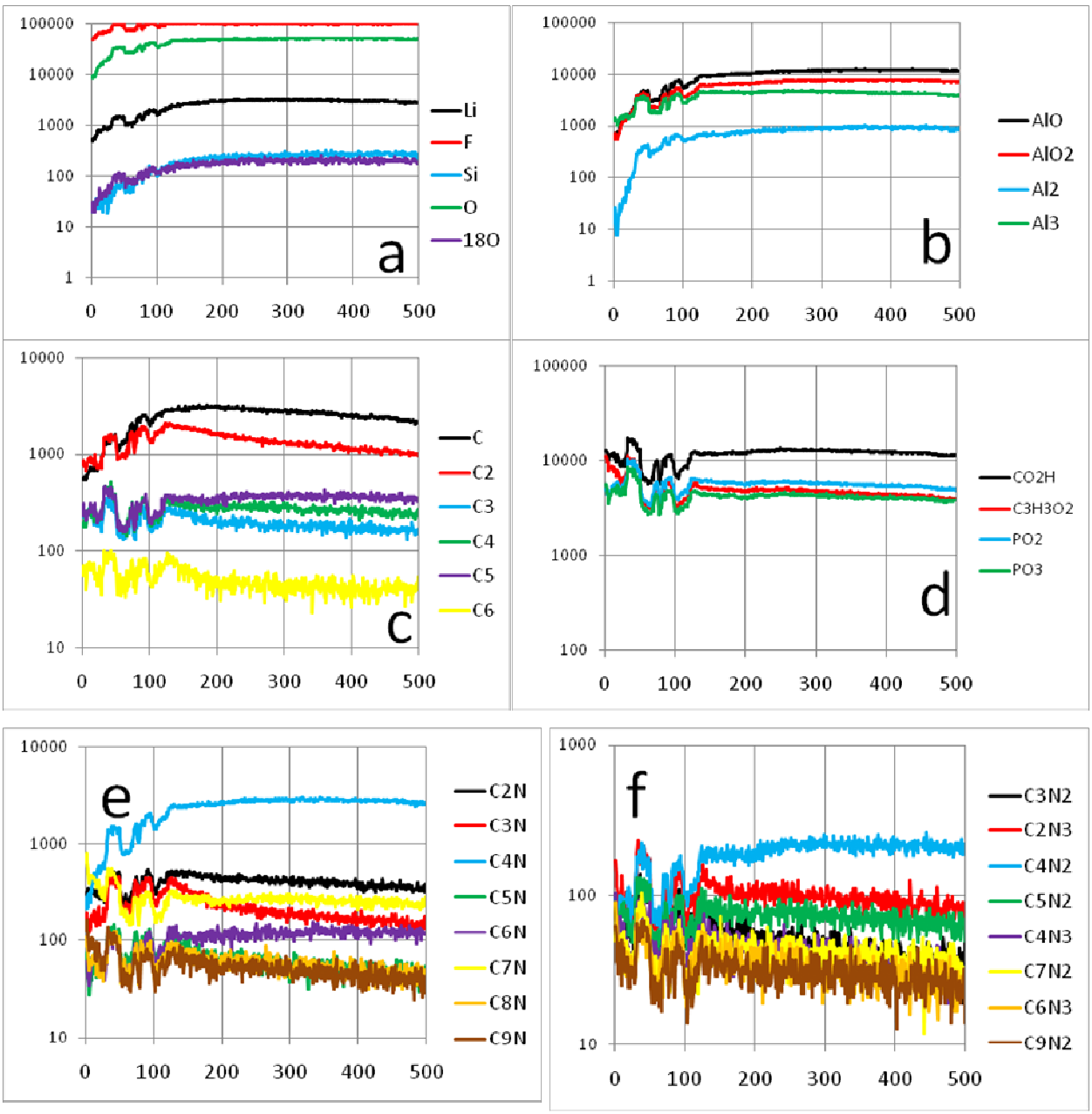

Figure 4-6-10: TOF-SIMS negative secondary ion depth profiles of cycled area for annealed 75% N_2 Al-CNx anode AC2 after being subjected to a 4x8 experiment from Ch. 4.4. Vertical axis is raw ion intensity counts. Horizontal axis is total active time in seconds for Cs^+ sputter beam.

First we consider the depth profile of the uncycled area of AC1 (non-annealed Al-CNx) in **Fig. 4-6-7 a-f**. As mentioned previously the term "uncycled" here denotes the area outside the gasket, which should not be exposed to electrolyte. Al-CNx is a layered structure with a distinct film-metal interfacial layer. Based on our labeling criterion for AC1 the CNx layer is approximately 0-130 sec, interfacial layer 130-190 sec and bulk Al 190+ sec. As in the profiling of bare GF Al (GF1) and MC Al (MC1) samples in the previous sections there are electrolyte species detected here with high intensity that rapidly drop after the first 25 sec. These electrolyte species are Li^-, F^-, PO_2^-, PO_3^-, CO_2H^- and $C_3H_3O_2^-$ (**Fig. 4-6-7 a,d**). As described earlier in Ch. 2.6 carbon nitride thin films are created by nitrogen incorporation into the amorphous graphitic network [11]. This results in various sp, sp^2 and sp^3 nitrogen substituted functional groups. The use of cluster primary ion analysis beams in SIMS results in structurally characteristic species generated from thin films [12]. Therefore we expect characteristic CN containing secondary ions would arise from fragmentation of N-substituted regions. Here in SIMS we see that overall the CNx layer is characterized by C_x^-, C_xN^- and higher order $C_xN_y^-$ species (**Fig. 4-6-7 c,e,f**). For the C_x^- ion series C_5^- and higher were also detected, unlike the profiling of bare Al where they were absent. Therefore these higher mass C_x^- species should be more indicative of CNx and not simply carbon contamination or solvent. For characterizing carbon nitride the C_x^- ion series should arise from fragmentation of both graphitic and N-substituted regions. This is important to consider because even a CNx thin film deposited under a 100% N_2 plasma in magnetron sputtering will at most result in approx. 1:1 C:N stoichiometry [13]. For the C_xN^- ion series C_2N^- and higher were also detected, unlike the lone CN^- species in the bare Al profiling. The $C_xN_y^-$ ($y > 1$) series is of particular interest due to their complete absence in the profiling of bare GF Al (**Figs. 4-6-1, 4-6-2**). Therefore they should be the most analytically useful in TOF-SIMS characterization of CNx thin films. Higher mass $C_xN_y^-$ species are typically not observed intensely with monoatomic primary ion analysis beams like Cs^+ and Ga^+, due to excessive fragmentation of the sample surface structure during the collision cascade [4,14-15]. The $C_xN_y^-$ species shown here in the profiling were the most intense species of this type in the spectra. There were many ions of this type but they all appeared to behave

similarly in the uncycled film. These series of peaks go into m/z of a few hundred since this is a polymeric thin film even though there is no long range order.

Overall these results show that for TOF-SIMS characterization of CNx films it is important to focus on higher order C and CN peaks. This is due to significant overlap (interference) of lower order peaks with adventitious carbon, nitrogen and oxygen species on the sample surface. In this work beginning around C_5^- and C_2N^- respectively we can be confident that these species arise predominantly from the CNx film. Additionally this work shows the importance of utilizing polyatomic primary ions as the analysis beam to achieve strong intensities of characteristic high mass secondary ions. Higher order CNO containing species were not detected when profiling the CNx region. Similarly the intensity of $^{18}O^-$ is much lower in this region which suggests very low oxygen content present in the CNx layer as gaseous occlusions **(Fig. 4-6-7 a)**. This is a very important requirement for application of these materials as anodes in lithium ion batteries. Moisture and gaseous oxygen content under the cycling conditions in this work may cause unwanted electrochemical processes. Similarly this is why aprotic carbonate solvents are used for electrolytes. The proportion of characteristic CNx ion species do not significantly change when profiling through CNx layer. Therefore the proportions of functional groups should be fairly consistent throughout the CNx layer. The plasma parameters for magnetron sputtering deposition were stable throughout the 20 minute deposition time. Based on these observations we can be fairly certain that the CNx film has a homogenous composition within the thickness of 75 nm for the coated samples investigated in this work.

The layered structure results in a distinct interfacial layer located between the CNx film and bulk Al metal **(Fig. 4-6-7 b)**. Considering the maxima of Al oxide species around 170 sec this is likely an interfacial oxide. In a similar fashion to depth profiling of uncycled bare GF Al and MC Al in previous sections there was likely partial oxide re-growth during preparation of the substrate. The local intensity maxima of electrolyte species in this region is possibly a matrix effect which will increase the ionization yields of secondary ions containing electronegative atoms such as O and F [1]. Si was also

detected as an interfacial maxima, likely again due to polishing with SiC paper. As the interfacial layer is traversed, bulk aluminium Al_2^- and Al_3^- species rapidly rise in intensity and plateau at approximately 200 sec. In addition we identified unique interfacial species in the form of AlC^- and AlN^- ions in the same profile region. These ions may possibly arise from fragmentation of aluminium carbides and nitrides respectively. $AlCN^-$ as well as higher order $Al_xN_y^-$ and $Al_xC_y^-$ species were not detected, which may possibly be due to fragmentation of those species into AlC^-/AlN^- and/or low ionization yield.

The presence of an Al-C composite layer at the interface should be beneficial considering the superior cycling capacity and stability of these materials compared to Al or graphite itself [16-17]. Formation of hard aluminium nitrides is known to occur under nitrogen plasma deposition conditions on Al [18]. A practical use of this method is in the automotive industry to improve the low hardness and wear resistance of pure Al. Nitrides of first row transition metals have also shown some promise as an anodic material [19]. However the cycling performance of aluminium nitrides in lithium ion batteries has never been investigated. In our case it appears that the process of magnetron sputtering modifies the Al surface due to chemical reactivity with the bombarding CN-containing species. This is an addition to the expected reactivity of CN species formation occurring inside the plasma. Therefore magnetron sputtering for our deposition conditions is not simply just a physical sputtering phenomenon. In addition to being receptive towards lithium ions the formation of these interfacial species may improve adhesion of CNx to bulk Al. This is important due to the required volume changes of lithiation-delithiation in these anodic materials.

Fig. 4-6-8 a-f shows the depth profile of the uncycled area of the annealed Al-CNx sample AC2. Based on our labeling criterion the CNx layer is approximately 0-110 sec, interfacial layer 110-165 sec and finally bulk Al 165+ sec. Therefore the series of characteristic CN containing ions are shorter in terms of sputtering time relative to the non-annealed sample AC1. This suggests that the CNx film is more compact in the annealed sample **(Fig. 4-6-8 e-f)**. This is likely due to stress relief in the film, which at temperatures up to 200^{o}C predominantly arises from the combination of decreased nitrile

content and the conversion of N-C sp^3 to N=C sp^2 bonding [20]. The intensity proportions of C_x^-, C_xN^- and $C_xN_y^-$ ion series do not change noticeably in the "bulk" of the CNx layer when annealed. However as profiling approaches the interface of this annealed sample the C_xN -series of ions do show different onsets of intensity decay **(Fig. 4-6-8 e)**. C_5N^-, C_7N^- and C_9N^- show the earliest decay, followed by C_4N^-, C_6N^- and C_8N^-, then C_2N- and finally C_3N^-. This is in contrast to the uncycled area of the non-annealed sample where the entire set of C_xN^- ions showed a similar onset of intensity decay (**Fig. 4-6-7 e**). As in the non-annealed sample AC1 the C_x^- and $C_xN_y^-$ series of ions here in AC2 all show a similar onset of intensity decay around the CNx-Al interface **(Fig. 4-6-8 c,f)**. It is not clear how to explain the discrepancy in these interfacial CNx ion trends between the non-annealed and annealed Al-CNx. Clearly the preferred fragmentation pathways for sputtering of these various CNx species must be interrelated. It stands to reason that a low mass CNx species may be formed from fragmentation of both small and large nitrogen-substituted functional groups. Perhaps there is formation of unique CNx-containing interfacial phases in the annealed sample that are not present in the non-annealed sample. The interfacial distribution of AlN^- and AlC^- appears to be broader in the annealed sample (**Fig. 4-6-8 b**), even though the interfacial layers of both non-annealed and annealed samples show comparable thickness according to our labeling scheme. This behaviour suggests increased formation or diffusion of interfacial aluminium nitrides and carbides upon thermal annealing. Taken together, these data suggest that some chemical interactions occur between Al and CNx during annealing. This modification may be beneficial for improving film adhesion to the bulk Al substrate upon lithiation-delithiation.

Shown in **Fig. 4-6-9 a-f** are the depth profiles of the cycled area of the non-annealed Al-CNx sample AC1. In this non-annealed Al-CNx like in cycled bare GF Al (**Fig. 4-6-2**) we detect high Li^-, Al_2^- and Al_3^- intensities immediately. It should be noted that we did not detect any compound intermetallic ions of the type Li-C-N-Al, Li-C-Al or Li-N-Al, or AlN^- and AlC^- in the SIMS analysis of both non-annealed and annealed cycled Al-CNx. Similar to Li_xAl_y intermetallics in cycled bare GF Al, they may be present in the material but not emitted and detected as ions. Similarly, we observe electrolyte species at

high intensities relative to those in the uncycled version. As in the cycled bare GF Al the SEI species appear to be more concentrated near the surface, within the first 50 sec. However, unlike with the previous samples, we observe sharp minima in the intensities of intermetallic, electrolyte and oxide species at ca. 100 s sputtering time **(Fig. 4-6-9 a,b,d)**. Within this same region we also observe sharp maxima in characteristic CNx species **(Fig. 4-6-9 c,e,f)**. According to our labeling criterion this CNx-rich region extends from 50 sec to approximately 150 sec in the profile. This feature in the profiling likely corresponds to the CNx film remnants that were observed near the surface of the intermetallic alloy in the SEM images of non-annealed Al-CNx AC1 **(Fig. 4-4-24 a)**. It also corresponds to the nitrogen content observed in the EDX spectra of flat versus porous regions **(Table 4-4-30)**. The fact that the SEI and Li concentrations go through their minima in CNx film clearly indicate that there is no or very little intercalation of Li into the CNx. Since intercalation of Li ions into graphite is well known, one might expect similar intercalation into CNx as well. However, our SIMS data rule out this possibility. Overall TOF-SIMS depth profiling is still a very useful tool to determine where the CNx film is located after cycling these materials.

Apart from this initial localization of CNx ions described above the depth profiles do not differ significantly from that of cycled GF Al (**Fig. 4-6-2**). After 300 sec most ion species except for decreasing CN ions plateau or show minimal change. Therefore the 200+ sec region can again be considered rich in intermetallic alloy. This is in agreement with the underlying porous morphology of cycled Al-CNx being similar to cycled GF Al after 4x8 cycling experiment (**Figs. 4-1-13 e, 4-4-24 b**). As with GF Al, the concentration of SEI components remains high throughout the film indicating formation of a nanoporous structure.

Shown in **Fig. 4-6-10 a-f** are the depth profiles of the cycled area of the annealed Al-CNx sample AC2. As in the non-annealed version the profiling of Li^-, Al_2^- and Al_3^- suggests the presence of an intermetallic porous framework filled with SEI, consistent with the CV **(Figs. 4-4-1, 4-4-2)**. However, unlike the case with non-cycled Al-CNx sample (AC1), no clear localization of the CNx layer can be made and therefore all characteristic CNx

peaks are detected consistently throughout the profiling depth of the cycled area of the annealed sample **(Fig. 4-6-10 c,e,f)**. All of these species show significantly lower intensities relative to the CNx ion maxima in the cycled area of the non-annealed sample (**Fig. 4-6-9 c,e,f**). The only exception appears to be C_4N^-, possibly due to mass interference with another ion **(Fig. 4-6-10 e)**. C^- and C_2^- are also elevated throughout the profile but not considered significant due to overlap with adventitious carbon. Within this same profiling depth of depressed CNx ions the intermetallic and SEI species conversely show strong intensities **(Fig. 4-6-10 a,b,d)**. Overall these results suggest that cycling of annealed CNx, as opposed to non-annealed CNx, resulted in CNx reacting or otherwise interacting with the LiAl phase so that the CNx films does not exist anymore at the surface of the electrode. SEM data do suggest that while some remnants of the CNx film can be seen in non-annealed sample (**Fig. 4-4-24 a**), they are not found in annealed CNx sample (**Fig. 4-4-24 c**). Another possible explanation is that CNx species become buried under the growing LiAl intermetallic phase and thus were not reached in profiling the annealed Al-CNx sample AC2 (since we did not profile the whole thickness of the sample). Therefore the SIMS profiles of cycled annealed Al-CNx (AC2) appear to support the conclusions made from the SEM morphology and EDX spectra **(Fig. 4-4-24 c-d, Table 4-4-30)**.

As in the non-annealed Al-CNx (AC1) the interfacial AlN^- and AlC^- species were again not observed anywhere in cycled profiling depth of AC2 **(Fig. 4-6-10 b)**. Considering the remaining CNx appears beneath the alloy the interfacial species may remain deep below, near the alloy/Al interface. Again we cannot be certain of this because the sputtering time of 1 sec per scan only resulted in less than 1 um of profiling depth. Even at a low temperature of 150 ^oC the annealing results in much more homogenous behaviour in the cycled profiles of AC2 (**Fig. 4-6-10**). The initial instability seen for all annealed Al-CNx profiles within the first 100 sec may be due to increased roughness near surface. Another possibility is some small initial fluctuations in the analysis and sputter beam currents. Considering the homogenous profile behaviour it does not appear that this cycled area has layers rich in any specific components. Therefore we did not attempt to assign labels corresponding to different regions.

Surface Profilometry of samples AC1 and AC2

After TOF-SIMS depth profiling we performed surface profilometry on these Al-CNx samples **(Fig. 4-6-11 a-b)**. The surface profile of the non-annealed Al-CNx sample AC1 shows an average step height of 5.6 um for this cycled area, which is defined as the difference in the average height of region A2 compared to A1 **(Fig. 4-6-11 a)**. This step height is comparable to that observed previously in cycled bare GF Al **(Fig. 4-6-3)**. However the surface roughness is significantly higher, possibly due to the presence of the highly cracked CNx layer seen in the SEM images **(Fig. 4-4-24 a-b)**.

The increased homogeneity of the annealed Al-CNx sample AC2 upon lithiation-delithiation is demonstrated physically in its surface profile **(Fig. 4-6-11 b)**. The average step height of 5.9 um is comparable to the non-annealed version AC1. However the roughness of the cycled region is considerably smaller. Overall these SEM, SIMS and surface profilometry results suggest that thermal annealing even at lower temperatures may be an effective tool for creating a more homogenous Al-CNx anode nanostructure. This modified anode could then be more resilient against the detrimental effects of volume change in lithiation-delithiation.

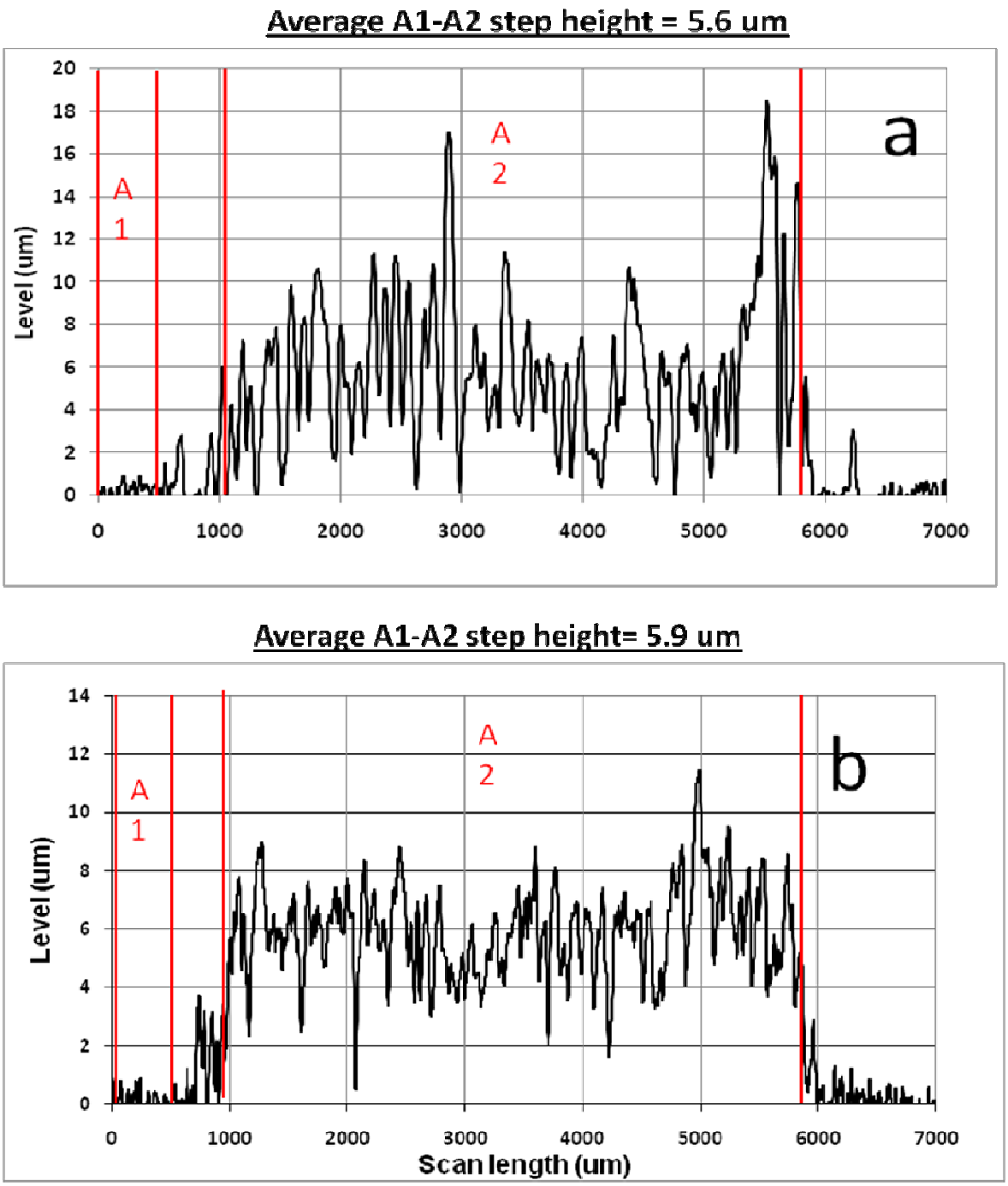

Fig. 4-6-11: Surface Profiles for (a) non-annealed AC1 and (b) annealed AC2 75% N_2 Al-CNx anodes after being subjected to 4x8 experiments in Ch. 4.4. Line scan is from gasket area to cycled area to gasket area. Step height is average difference of A1 and A2 areas.

To conclude, the main outcome of our SIMS study of Al-CNx samples was that SIMS does not show any significant intercalation of Li into CNx phase. Both films showed formation of relatively uniform highly porous Li-Al intermetallic phase. For non-annealed samples, some CNx can be found at the surface of the sample, whereas for annealed samples CNx was either buried under the growing LiAl intermetallic phase or reacted with it during galvanic cycles.

4.6.4 Non-annealed 75% N_2 25+75 nm Al-Al-CNx anode ACM2 from Ch. 4.5

TOF-SIMS Secondary Ion Depth Profiles of ACM2

Shown in **Fig. 4-6-12 a-d** and **Fig. 4-6-13 a-d** are the secondary ion depth profiles for non-annealed 75% N_2 25+75 nm Al-Al-CNx anode ACM2 in both uncycled and cycled areas after the 4x8 experiment. For all depth profiles the vertical axis is the raw ion intensity in counts with the horizontal axis as the total time in seconds that the Cs^+ sputter beam has been active. Intensities on the vertical axis are shown in logarithmic scale to magnify low intensities of some characteristic secondary ions. Depth profiling was performed on the uncycled area of this sample until the bulk Al region was reached. This corresponds to 300 sec of sputter time. For the cycled area we were not certain of the thickness of the intermetallic alloy at the time. Therefore we stopped SIMS profiling of the cycled area once most ion species plateaud in intensity. For ACM2 this corresponds to 400 sec of sputter time. After SIMS analysis we did surface profilometry to reveal that the average step height of the cycled area was several micrometers thick. Bulk Al, Al oxide, thin film Al, CNx and interfacial layers were defined in **Fig. 4-6-12 a-f** with vertical dashed lines. These regions were approximated by requiring at least 75% of the maximum intensity of ions characteristic of that layer [3].

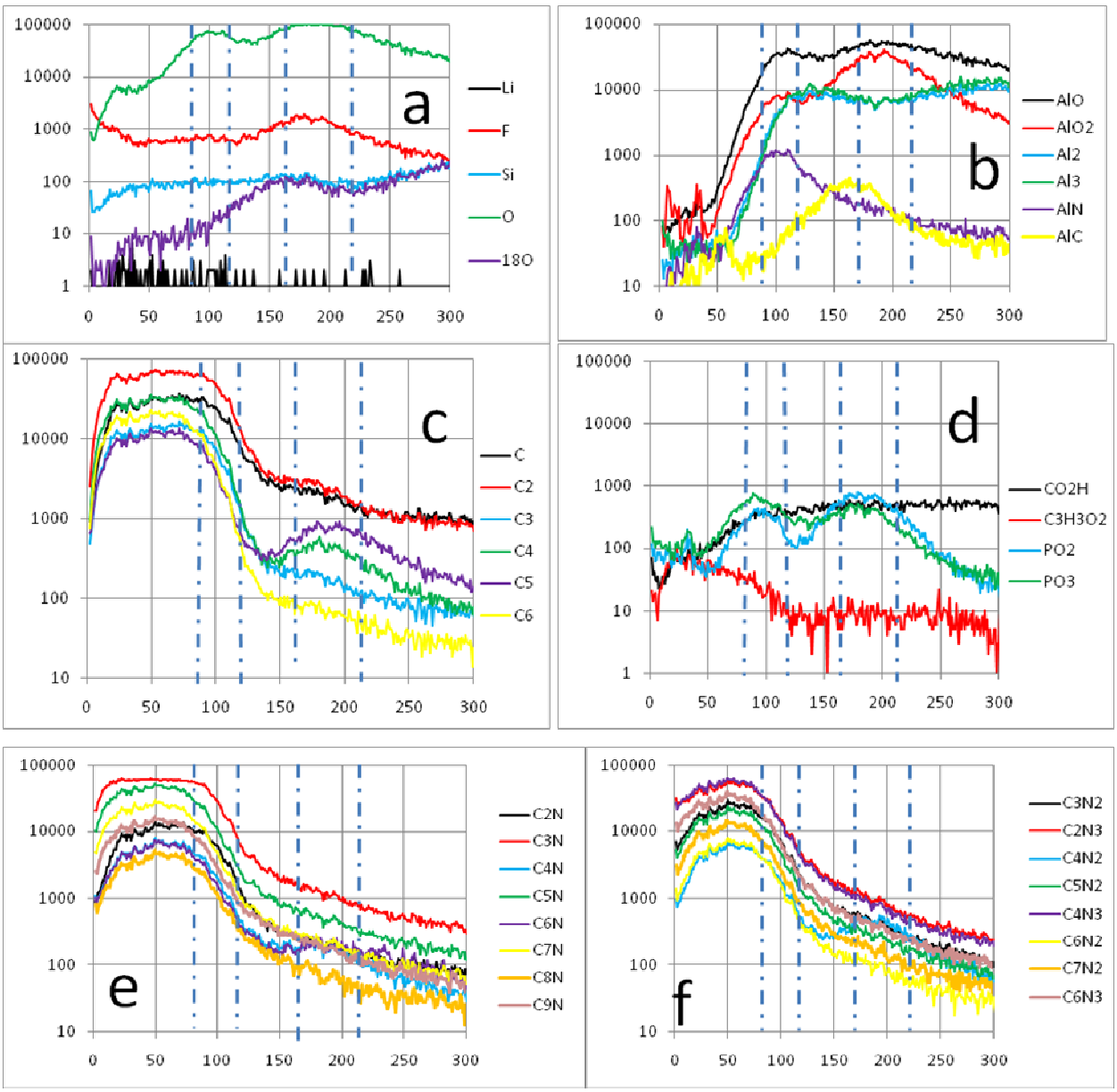

Figure 4-6-12: TOF-SIMS negative secondary ion depth profiles of uncycled area for non-annealed 75% N_2 25+75 nm Al-Al-CNx anode ACM2 after being subjected to a 4x8 experiment in Ch. 4.5. Vertical axis is raw ion intensity counts. Horizontal axis is total active time in seconds for Cs^+ sputter beam. Vertical dashed lines denote the approximated regions of CNx film, first interfacial layer, Al thin film, second interfacial layer and bulk Al respectively.

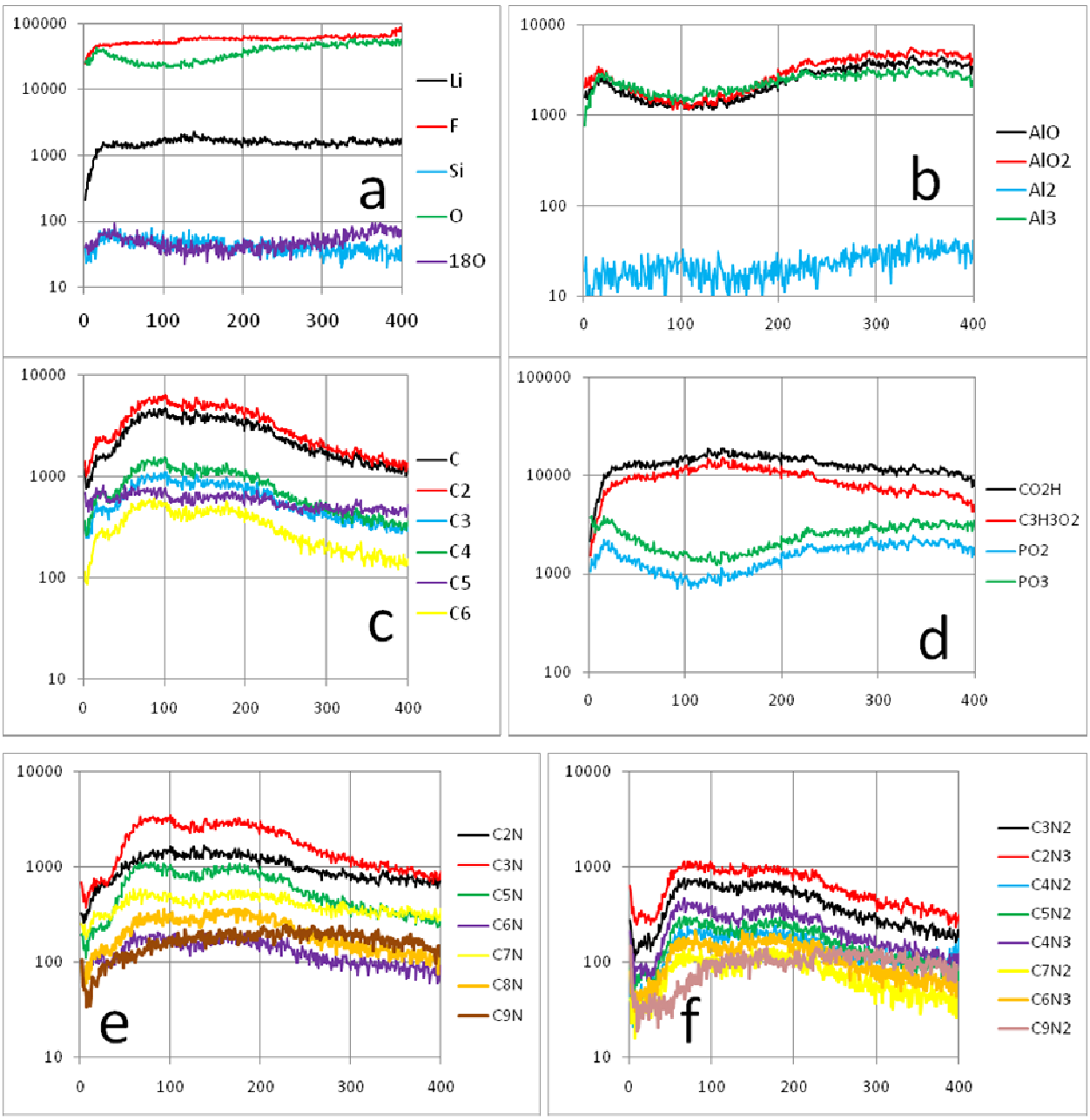

Figure 4-6-13: TOF-SIMS negative secondary ion depth profiles of cycled area for non-annealed 75% N_2 25+75 nm Al-Al-CNx anode ACM2 after being subjected to a 4x8 experiment in Ch. 4.5. Vertical axis is raw ion intensity counts. Horizontal axis is total active time in seconds for Cs^+ sputter beam.

First we consider the depth profile of the uncycled area of non-annealed Al-Al-CNx (ACM2) in **Fig. 4-6-12 a-f**. As expected the Al thin film layer in Al-Al-CNx results in additional discrete profiling regions as compared to Al-CNx (**Fig. 4-6-7**). Therefore in this anode we have both film-film and film-metal interfaces. Based on our labeling criterion the CNx layer is approximately 0-80 sec and first interfacial layer 80-115 sec. This is followed by the thin Al film layer at 115-165 sec, second interfacial layer 165-215 sec and finally bulk Al at 215+ sec. The electrolyte species (Li^-, F^-, PO_2^-, PO_3^-, CO_2H^-, $C_3H_3O_2^-$) present in uncycled Al-Al-CNx (**Fig. 4-6-12 a,d)** do not show an initial sharp intensity drop like in uncycled Al-CNx (**Fig. 4-6-7 a,d**). However the number of counts is still comparable so the electrolyte should still exist here as surface contamination. The discrepancy between these two types of samples may be due to less solvent present within the chosen analysis area of ACM2. As expected the electrolyte species now show local intensity maxima at both interfaces of ACM2, likely again due to matrix effects.

The first interface (CNx-Al film) centered at 100 sec results in a maximum of AlN^- intensity (**Fig. 4-6-12 b)**. This localization of AlN^- here shows that unique interfacial species can be formed from reactivity of two different sputtered layers. The second interface (Al film - bulk Al) centered at 180 sec is dominated by the partial surface oxide present on bulk Al again after substrate preparation (**Fig. 4-6-12 b**). In Al-Al-CNx the interfacial AlC^- species instead shows a maxima near the Al-Al interface. This is unusual given the localization of AlC^- near the CNx-Al interface in the Al-CNx samples (**Fig. 4-6-7 b**). Al oxide species are also detected intensely at the first interface of ACM2 though less than at second interface. This is likely due to the plasma being temporarily turned off after sputtering of the thin Al layer, before sputtering of the CNx layer, in order to allow the turbo pump to cool down between deposition steps. The deposition chamber has very low oxygen content but a pause would allow some brief accumulation after deposition of the thin Al film. Al_2^- and Al_3^- intensities show a plateau after the first interface with a small decrease centered at the second interface (**Fig. 4-6-12 b)**. After passing the second interface into the bulk Al the intensities increase again to higher values relative to those in the Al film. This may be due to increased density in the bulk Al relative to sputtered soft Al film, which should increase the sputter yield of Al containing species. Except for

this discrepancy there were no other apparent differences in profiling of the Al film versus bulk Al.

The proportion of characteristic C_{x-}, C_xN^- and $C_xN_y^-$ species in Al-Al-CNx (**Fig. 4-6-12 c,e,f)** does not significantly change compared to those observed in Al-CNx (**Fig. 4-6-7 c,e,f**). This is expected considering the magnetron sputtering deposition parameters for the CNx layer were identical to that of Al-CNx anodes. However the profile region for CNx in Al-Al-CNx appears considerably shorter than in Al-CNx. According to our labeling above this CNx region is approximately until 80 sec compared to 130 sec in Al-CNx (**Fig. 4-6-7 c,e,f**). At the same time, CNx ion intensities are still considerably higher at the first (CNx-Al film) interface beyond 80 sec (**Fig. 4-6-12 c,e,f**), compared to CNx-bulk Al interface in Al-CNx (**Fig. 4-6-7 c,e,f**). This suggests that there is some penetration or reaction of CN containing species with the Al thin film layer. In particular, some CNx species may be pushed inwards or "implanted" in a deeper layer of the sample during the collision cascade caused by sputtering. In TOF-SIMS depth profiling this is commonly referred to as a "knock-in" effect [2]. These implanted CNx species may be emitted by a sputtering event later in the profiling. Considering the relative softness of the sputtered Al thin film it should be easier to "implant" CN containing species there compared to bulk Al.

The profiles for cycled Al-Al-CNx (**Fig. 4-6-13 a-f)** shows some similarities to cycled Al-CNx (**Fig. 4-6-8 a-f**). In particular, an intermetallic framework filled with SEI layer is clearly seen in the profiles, whereas the interfacial species of AlN^- and AlC^- are not detected. However the profiling trends for cycled Al-Al-CNx are considerably more subtle. First of all, there is a small maxima of CNx intensities (**Fig. 4-6-13 c,e,f**) accompanied by small minima of Al containing ions around 50-200 sec (**Fig. 4-6-13 b**). This is followed by (roughly) plateau behaviour in Al content after 240 sec. Additionally the Al_3^- ion intensity is a hundred times higher than for Al_2^-. This is in sharp contrast to intermetallic content in cycled bare GF Al where Al_2^- and Al_3^- showed similar intensity behaviour (**Fig. 4-6-2 b**). This is consistent with the differences in both the electrochemical behaviour and the morphology of the cycled area as revealed by SEM,

which shows the occurrence of a unique highly porous honeycomb nanostructure in Al-Al-CNx (**Fig. 4-5-12 c**). Taken together with the SIMS data, this suggests that the honeycomb structure may constitute an outer intermetallic phase. This outer phase may be of lower density with its own distinct composition and arises predominantly from lithiation-delithiation of the sputtered Al thin film. It also has more voids as indicated by the profiles of the SEI components in this area. The chemical environment of this outer layer may create a matrix effect which strongly promotes the formation of Al_3^- over Al_2^-. However, importantly, the Li^- content remains remarkably uniform throughout the film (**Fig. 4-6-13 a)** except a narrow area at the sample surface where this signal shows a sharp increase initially over the period of ca. 30 sec. This is likely related to the fact that SIMS profiling was performed after electrochemical discharge of the anode. Therefore, it is no wonder that the Li concentration near the surface should be depleted. What is also important is that the concentration gradient for Li containing species at the surface is the steepest in the Al-Al-CNx sample, thus suggesting the high reversibility of the lithiation-delithiation processes and high rate of diffusion in the porous honeycomb nanostructure found in Al-Al-CNx.

Surface Profilometry of sample ACM2

After TOF-SIMS depth profiling we performed surface profilometry on this non-annealed Al-Al-CNx sample (**Fig. 4-6-14**). The surface profile of the non-annealed sample ACM2 shows an average step height of 7.7 um for this cycled area, which is defined as the difference in the average height of region A2 compared to A1. This step height as well as the surface roughness are considerably larger than that observed previously in cycled Al-CNx (**Fig. 4-6-11 a**). This should be related to the formation of the more porous and less dense honeycomb nanostructure at the surface of Al-Al-CNx.

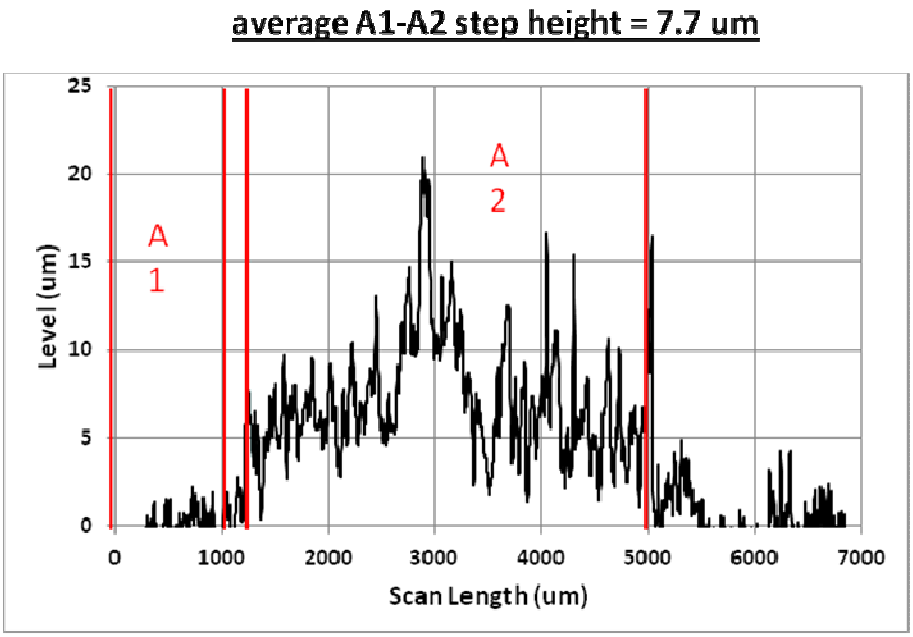

Figure 4-6-14: Surface Profile for non-annealed 75% N_2 25+75 nm Al-Al-CNx anode ACM2 after being subjected to 4x8 experiment in Ch. 4.5. Line scan is from gasket area to cycled area to gasket area. Step height is average difference of A1 and A2 areas.

To conclude, SIMS profiling allowed us to obtain important information regarding distribution of various species inside the cycled and non-cycled Al anodes of various structure. It was confirmed that a nanoporous LiAl nanostructure is formed upon repeated electrochemical lithiation-delithiation of Al anodes. The best nanostructure would seem to be formed with Al-Al-CNx sample, which correlates well with the electrochemical and SEM data. No significant intercalation of Li into CNx phase was observed.

4.6.5 References

1. Gnaser, H., *Physical Review B*, **2001,** *63*, 045415.
2. Schroder, K.W.; Dylla, A.G.; Harris, S.J.; Webb, L.J.; Stevenson, K.J., *ACS Appl. Mater. Interfaces*, **2014,** *6,* 21510-21524.

3. Pereira-Nabais, C.; Swiatowska, J.; Chagnes, M., *Appl. Surf. Sci.* **2013,** *266,* 5-16.
4. Huang, L.; Hung, Y.; Chang, S., *IEEE Transactions on Magnetics,* **1997,** *33,* 4551-4559.
5. Oltean, G.; Tai, C.W.; Edstrom, K.; Nyholm, L., *Journal of Power Sources*, **2014**, *269*, 266-273.
6. Liu, Y.; Hudak, N.S.; Huber, D.L.; Limmer, S.J.; Sullivan, J.P.; Huang, J.Y., *Nano Lett.* **2011**, *11*, 4188-4194.
7. Hudak, N.S.; Huber, D.L., *ECS Transactions,* **2011,** *33(24),* 1-13.
8. Liu, D.X.; Co, A.C., *J. Am. Chem. Soc.,* **2016**, *138*, 231-238
9. Hamon, Y.; Brousse, T.; Jousse, F.; Topart, P.; Buvat, P.; Schleich, D.M., *Journal of Power Sources*, **2001,** *97-98*, 185-187.
10. Park, C.M.; Kim, J.H.; Sohn, H.J., *Chem. Soc. Rev.,* **2010**, *39*, 3115-3141.
11. Rodil, S.E.; Muhl, S., *Diamond and Related Materials,* **2004,** *13,* 1521-1531.
12. Seah, M.P.; Green, F.M.; Gilmore, I.S., *J. Phys. Chem. C,* **2010,** *114,* 5351-5359.
13. Byers, J.C.; Billon, F.; Debiemme-Chouvy, C.; Deslouis, C.; Pailleret, A.; Semenikhin, O.A. *Acs Applied Materials & Interfaces,* **2012**, *4*, 4579.
14. Lopez, S.; Dunlop, H.M.; Benmalek, M., *Surface and Interface Analysis,* **1997,** *25,* 827-835.
15. Neuhaeuser, M.; Hilgers, H., *Diamond and Related Materials,* **2000,** *9,* 1500-1505.
16. Park, J.H.; Hudaya, C.; Kim, A.Y.; Rhee, D.K.; Yeo, S.J.; Choi, W.; Yoo, P.J.; Lee, J.K., *Chem. Commun.,* **2014**, *50*, 2837.
17. Huang, Y.; Lin, X.; Pan, Q.; Li, Q.; Zhang, X.; Yan, Z.; Wu, X.; He, Z.; Wang, H., *Electrochimica Acta*, **2016,** *193*, 253-260.
18. Visuttipitukul, P.; Aizawa, T., *Materials Transactions,* **2003,** *44,* 2695-2700.
19. Nitta, N.; Yushin, G., *Part. Part. Syst. Charact.* **2014**, *31*, 317-336.
20. Lejeune, M.; Benlahsen, M., *Diamond and Related Materials,* **2008,** *17,* 29-35.

4.7 Testing of Electrodes in Prototype Battery Design

Summary

A series of coated and uncoated Goodfellow Al (GF Al) anodes were tested in a 2 electrode battery prototype utilizing a polyethylene oxide (PEO) based solid polymer electrolyte (SPE) and a conductive $LiFePO_4$ cathode. The half-hard GF Al material was chosen as the substrate for anodes in battery samples instead of soft McMaster-Carr Al (MC Al). This choice was made due to the strain-hardening of GF Al offering improved structural stability in repeated scanning and cycling of the resulting intermetallic alloy (Ch 4.1 and 4.2). The preparation of battery components and assembly for cell testing has been previously described in the experimental details of Ch. 3. Galvanic cycling on the battery system was performed in sets with steadily increasing current density and a large number of cycles to allow uniform and controlled growth of the porous structure. Cycling was then continued in all cases until battery failure was observed, indicated by an extreme charge/discharge potential response and zero or near zero coulombic efficiency (CE). Physically this may correspond to massive cracking and pulverization of the battery active materials and specifically the intermetallic alloy structure present at the anode, which results in irreversible loss of capacity, damage to the solid polymer electrolyte, changes of the internal resistance, etc.

Battery testing with a bare polished and etched GF Al anode (BAT1) produced a very stable charging/discharging response with high coulombic efficiency across a range of current densities. The internal resistance of the battery decreased over time as well as with increasing current density, and faster changes were observed at the lowest current density. These features indicated growth of the porous structure at the anode with the fastest growth occurring early. Most importantly there were no plateau jump events observed until current densities approaching those of the half cell failure experiments. However, this sample still failed when certain current density limit was exceeded. Performing similar battery testing with a non-annealed 75% N_2 Al-CNx anode (BAT2)

resulted in decreased resistance relative to sample BAT1 and comparable coulombic efficiency with stable operation at even higher current densities, due to the CNx film acting as an additional scaffold to constrain growth of the porous structure. However, the secondary diffusion-limited plateau began to strongly manifest in the discharge portion of the BAT2 sample cycles as the current densities approached those of the half-cell experiments in previous chapters, and eventual failure also followed. Attempts to further improve the performance of battery testing based on Al-CNx anodes by thermally annealing the anode prior to testing (BAT3), or reducing the nitrogen content in the CNx coating (BAT4) resulted in a deterioration in the performance. In both cases battery failure in the form of steep increase in the internal resistance and complete loss of reversibility was observed at lower current densities relative to systems with bare GF Al (BAT1) or non-annealed 75% N_2 Al-CNx (BAT2) anodes.

In this series of experiments, the duration of one cycle was kept constant at each current density. As a result, the total charge that was applied to the battery per cycle was incrementally increasing with each set of increasing current. This resulted in continuing growth of the LiAl nanostructure at high current densities. Our data revealed that the structure of the LiAl phase grown at high current densities is very heterogeneous and lead to damage of the SPE layer, breaking off of the portions of the nanostructure and eventual failure of the battery. Therefore, in the last experiment (BAT5) with non-annealed 75% N_2 Al-CNx anode, we made sure to apply the same total charge both at low and high current densities. This meant that each cycle set had decreased charge/discharge time limits as the current density was increased. With this approach we observed dramatically improved performance in terms of a stable charge/discharge response and high coulombic efficiency at current densities surpassing both the previous battery experiments and the half cell failure experiments. This result suggests that in order to have high performance, the anodes should have the active LiAl nanostructure electroformed at low rather than high current densities.

Surface analysis of the BAT1 anode after cycling revealed a fully reactive highly porous morphology. There was an absence of any systematic cracking that we would typically

observe for anode failure. Instead the porous structure was overlaid by heterogeneous fibrous or disc-shaped features which were confirmed by EDX analysis as also containing traces of SPE and cathodic materials. The presence of these contaminants may have occurred due to the uncontrolled heterogeneous growth of the porous structure at high current densities between the strands of the SPE, leading to greatly increased local current densities at this portions of the nanostructure and local degradation of the SPE and the cathode. In Al-CNx anodes of battery samples with constant charge/discharge times (BAT2 - BAT4) we likewise observed a relatively fully reactive highly porous morphology with the same overlaying features. Here we were unable to identify morphological features or nitrogen content related to CNx film remaining after lithiation-delithiation in the BAT2 anode. However careful SEM and EDX analysis of BAT3 and BAT4 anodes did reveal certain areas which contained traces of CNx dispersed inside the porous LiAl structure. Overall the surface analysis here suggested that the growth of the LiAl phase causes most of the CNx to be buried underneath the porous structure.

The proportional charge/discharge times of the final battery experiment (BAT5) resulted in a significantly smoother and regular morphology that mostly contained a unique and very regular honeycomb morphology with nanometer-size regular pores found throughout the material. It is likely that the reversibility and good performance of this material is related to the presence of such pores that can accommodate the volume change upon lithiation without changing the overall dimensions of the anode and therefore without associated damage to the SPE and the battery assembly. Additionally, in contrast with all other samples, this proportional conditioning approach resulted in some areas where relatively intact SPE and CNx films can be located on the anode surface. No morphological features and copper content indicative of cathodic material contamination was found for this sample. This suggested improved structural stability of SPE and cathodic materials relative to BAT2, BAT3, BAT4 experiments. To investigate the initial lithiation-delithiation reactivity of a non-annealed 75% N_2 Al-CNx anode in battery testing, an additional experiment (BAT6) was performed with very limited cycling. This revealed a highly heterogeneous anode surface with limited reactivity and significant intact CNx film still remaining. In this case the intermetallic alloy formed and broke

through the coating only at few active sites with the remaining CNx film located at a lower elevation surrounding these active regions.

4.7.1: Galvanic Cycles and Calculations

Shown in **Fig. 4-7-1** are typical galvanic cycles measured in a battery prototype utilizing a GF Al anode, $LiFePO_4$ cathode as well as a PEO-TiO_2 solid polymer electrolyte at a current density of 0.13 mA/cm^2. One can see that the battery prototype can readily withstand 100 charging-discharging cycles without noticeable changes.

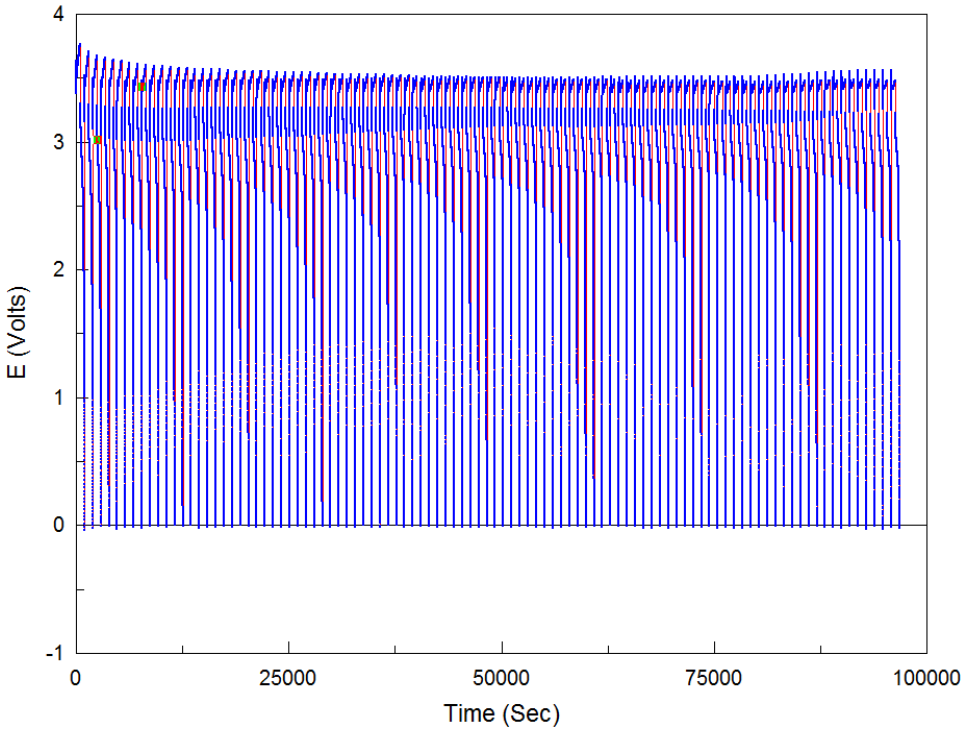

Figure 4-7-1: Battery galvanic cycles with a PEO-TiO_2 solid polymer electrolyte, $LiFePO_4$ cathode and a GF Al anode at current density of 0.13 mA/cm^2 for 100 cycles.

Shown in **Fig. 4-7-2** are the characteristic features of these galvanic cycles to which we will frequently refer in our presentation and discussion of the battery results. The battery

galvanic cycles show the charging and discharging regions, the IR drop due to the solid polymer electrolyte resistance, the coulombic efficiency and the charging/discharging voltages. These features are generally similar to the features observed in the 4x8 liquid-cell experiments, but now the cell voltage rather than potential of one electrode, anode, is measured. Therefore, the features appear "reversed" since the cell voltage is measured between the cathode and the anode.

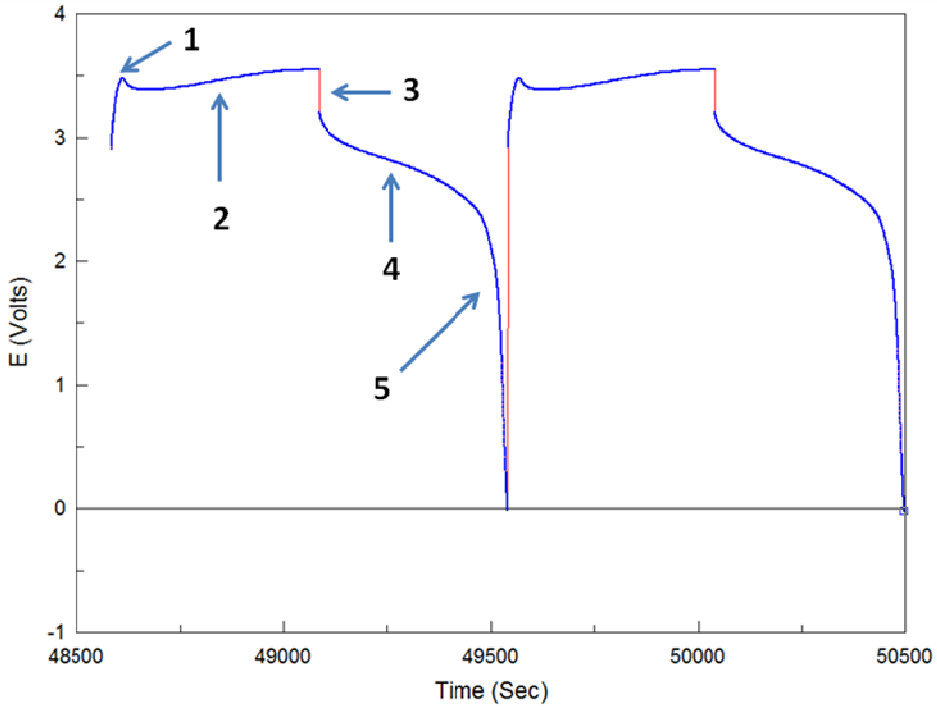

Figure 4-7-2: Characteristic features of galvanic cycles for lithiation-delithiation in a battery prototype setup with a solid polymer electrolyte, $LiFePO_4$ cathode and a GF Al anode at a current density of 0.065 mA/cm^2. Numbers indicate the features of interest: (1) potential overshot (2) anode lithiation and cathode delithiation plateau (3) IR drop (4) anode delithiation and cathode lithiation plateau (5) discharge tail.

As described in **Ch. 3.15.2** after applying the current density that charges the prototype, the cell potential sharply rises and a small overshoot of the potential is observed at the beginning of each charging region, which indicates the start of the charging process (**1**). This local potential maximum is followed by a single long plateau which we term the

"charging plateau" **(2)** involving lithiation of the anode and delithiation of the cathode. Similar to the half cell experiments this charging portion will typically continue until it is terminated by a time constraint. Then the opposite current density is applied and we observe the instantaneous IR drop **(3)**. After the IR drop there is soon another single long plateau which we term the "main discharging plateau" **(4)** involving delithiation of the anode and lithiation of the cathode. Fitting the linear portion of the main discharging plateau and dividing by the total charging time allows for calculation of the coulombic efficiency (CE) used to describe the reversibility of lithiation-delithiation in the battery system. As we leave the main discharging plateau region the potential will begin to decrease again. As the potential further decreases there may be one or multiple additional changes of inflection corresponding to additional electrochemical processes of a very short duration (**5**). As in the half-cell results presented in Ch. 4.1 to 4.4 these additional 'secondary' or 'tertiary' discharge processes will typically appear at higher current densities **(5)**. The battery cycle terminates when the cell potential reaches a lower preset limiting value, which in all battery tests was 0V vs. Li^+/Li.

In theory both charge and discharge plateaus of the cycle are dependent on lithiation-delithiation processes occurring at both electrodes simultaneously. However in practice we made the $LiFePO_4$ cathode provide an excess of lithium. Its composition is not expected to change significantly in regards to lithium content throughout a cycle. Therefore the cycle features for the battery prototype are dominated by lithiation-delithiation processes occurring at the anode. Unlike the half-cell experiments described in previous sub-chapters we note the charging and discharging plateaus here in battery testing are clearly not flat. There may be considerable upward potential drift within the charging plateau and downward potential drift in the discharging plateau. As the current density is increased this potential drifting may further increase and the significance of this feature will be explained in the results below. While not shown here in this sample figure each battery system will eventually reach a current density where signs of systematic failure appear in the cycling. In that case the charge/discharge plateau drifting will become extreme due to an excessive IR drop and the CE will rapidly decrease to zero.

To describe how the cycle features relate to electroformation of LiAl phase in the battery system, we consider the first full set of eight galvanic cycles (**Fig. 4-7-3**) of the first sample BAT1 utilizing a bare polished and etched GF Al anode at a current density of 0.033 mA/cm^2 with charge/discharge times of 500 seconds each. The very first battery cycle of the BAT1 sample entirely involves formation of a new intermetallic LiAl phase. The plateau voltage is higher than for the subsequent cycles indicating higher overvoltage for the formation of new phase on a foreign substrate. There is very minimal potential overshot and the charging plateau is flat. In the next cycles there is a progressively higher potential overshot followed by a decrease in the voltage leading to a short flat portion, which is in turn followed by a gradual increase in the voltage. This indicates that we first charge the LiAl phase formed during previous cycles and then continue to progressively form new intermetallic phase formation with each additional cycle in the porous structure created during delithiation of the previous cycles. The overshot is present because formation of a new phase usually requires higher overvoltage. Charging of the already formed phase occurs at lower potentials, and then the voltage increases again when new portion of the phase is formed.

During these scans, the electrode undergoes a major change from a bare Al to surface coated with developed nanostructured LiAl intermetallic phase. Therefore, we observe major changes in all the parameters: the output voltage, the coulombic efficiency (CE) and the internal resistance (R) of the cell. The evolutions of the coulombic efficiency and resistance (R) are shown in **Fig. 4-7-4** and **Fig. 4-7-5** respectively at the four current densities used. The R values in Ω cm^2 of **Fig. 4-7-5** were obtained by dividing the potential difference of the IR drop for each cycle by the current density. For both of these plots the horizontal axis is the cumulative number of cycles for all sets together with individual sets at current densities of 0.033, 0.065, 0.13 and 0.32 mA/cm^2 indicated in black, red, blue and green curves respectively.

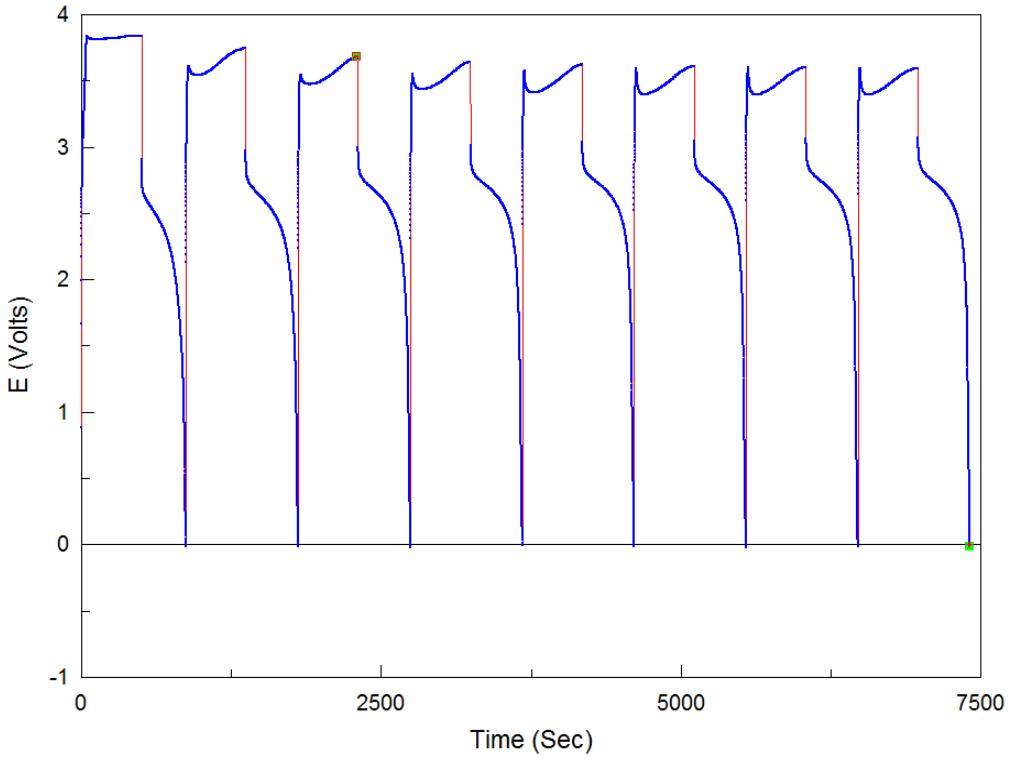

Figure 4-7-3: Full set of battery galvanic cycles of sample BAT1 with a solid polymer electrolyte, $LiFePO_4$ cathode and a bare polish + etch GF Al anode at a current density of 0.033 mA/cm^2 for 8 cycles with charge/discharge times of 500 seconds each.

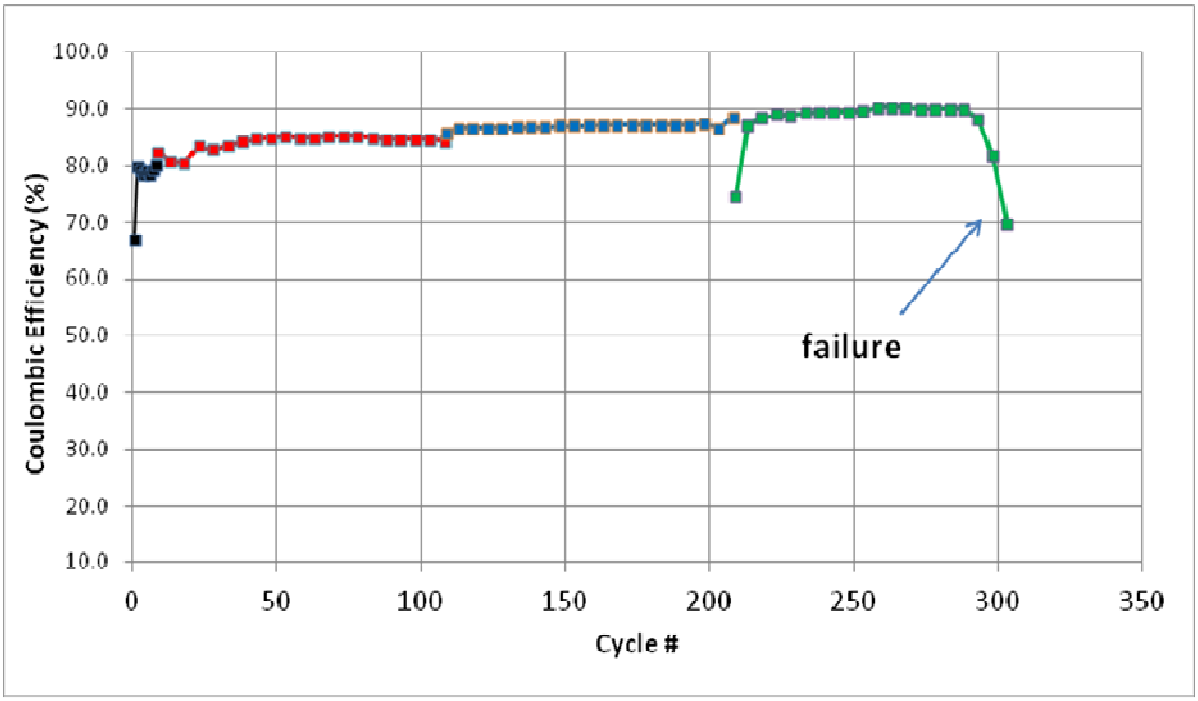

Figure 4-7-4: Coulombic efficiency for the main discharge plateau in battery galvanic cycles of sample BAT1 with a solid polymer electrolyte, $LiFePO_4$ cathode and a bare polish + etch GF Al anode at current densities of 0.033 (black), 0.065 (red), 0.13 (blue) and 0.32 (green) mA/cm^2. Horizontal axis shows the cumulative number of cycles of all sets together. The arrow in the green curve indicates the onset of battery failure.

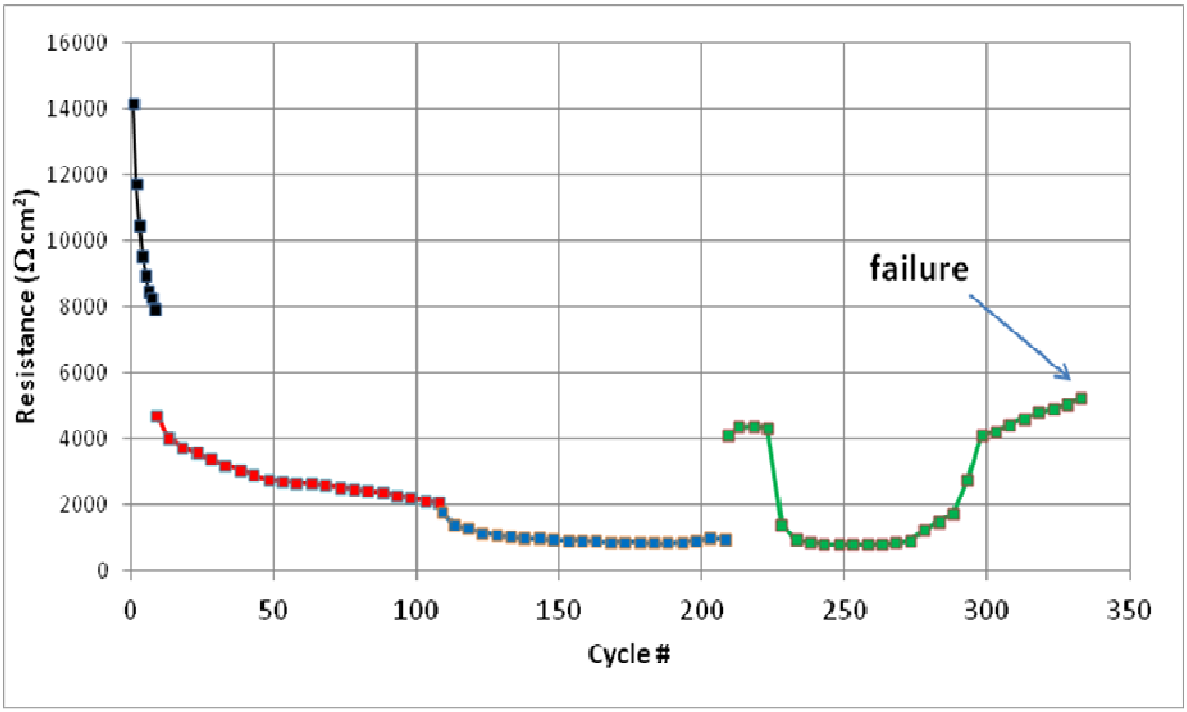

Figure 4-7-5: Resistance calculated from the IR drop for battery galvanic cycles of sample BAT1 with a solid polymer electrolyte, $LiFePO_4$ cathode and a bare polish + etch GF Al anode at current densities of 0.033 (black), 0.065 (red), 0.13 (blue) and 0.32 (green) mA/cm^2. Horizontal axis shows the cumulative number of cycles of all sets together. The arrow in the green curve indicates the onset of battery failure.

One can see that the growth of the intermetallic phase during the first set of cycles is indeed accompanied by a rapid and very substantial decrease in the resistance, as well as an improvement in the coulombic efficiency. These facts are related to (a) the change in the surface area of the intermetallic phase in contact with the electrolyte as compared to the bare Al, and (b) changes in the kinetics and reversibility of the electrochemical lithiation-delithiation on nanostructured LiAl and bare Al substrates. The latter is in particular evidenced by the change in the CE values that cannot be explained by the changes in the surface area.

The trends described in the first set of BAT1 will continue to lesser degrees at higher current densities. This indicates that the electroformation and structural changes related to

the LiAl intermetallic phase continue in these conditions too. Shown in **Fig. 4-7-6** are galvanic cycles from the (a) beginning and (b) middle of the sets at current densities of 0.065 (red) and 0.13 (blue) mA/cm^2. Sample cycles from the end of the respective sets are not shown because the difference in features from the middle cycles (**Fig. 4-7-6 b**) is very minimal. We note there is a marked decrease of resistivity (R) as the intermetallic nanostructure continues to be formed at the higher current densities of 0.065 and 0.13 mA/cm^2 (**Fig. 4-7-5**). Furthermore, unlike the half-cell experiments described in previous chapters, **Fig. 4-7-6** suggests that the IR drop and the accompanying charge-discharge plateau separation do not increase with increasing current density for battery cycles. This indicates more efficient growth and better quality of the nanostructure formed in battery prototypes with SPE. Also worth noting is that the plateau separation decreases almost exclusively due to an increase in the discharge voltage; the charging voltage stays roughly the same. This indicates improvements in the delithiation kinetics as the nanostructure is formed.

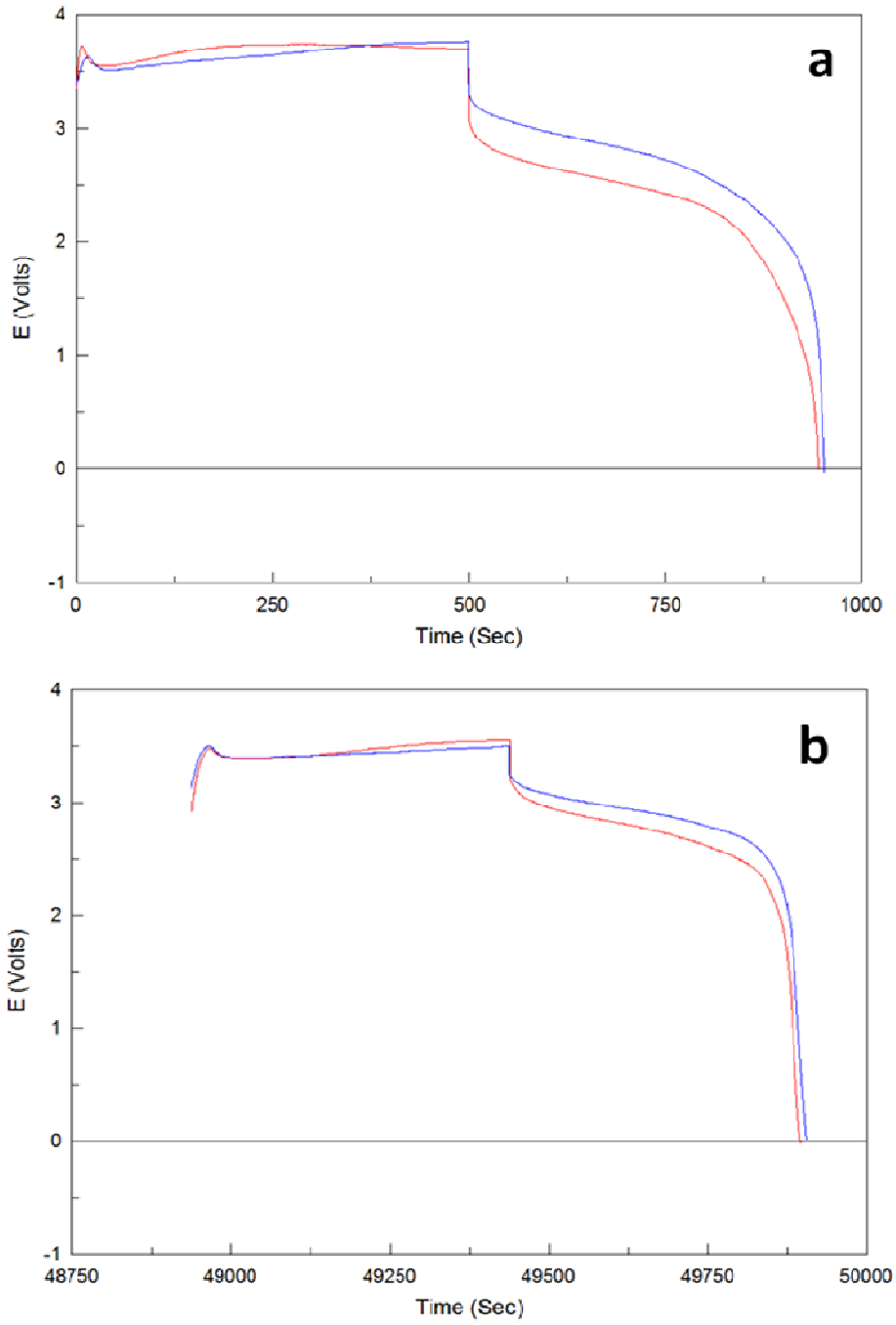

Figure 4-7-6: (a) Initial and (b) middle battery galvanic cycles of sample BAT1 with a solid polymer electrolyte, $LiFePO_4$ cathode and a bare polish + etch GF Al anode at current densities of 0.065 (red) and 0.13 (blue) mA/cm^2. For both current densities cycling was performed for 100 cycles each with charge/discharge times of 500 seconds. Cycles have been offset in figure b to overlap the curves on the same time scale.

The changes in the CE and R trends are more gradual during the second and third sets (**Figs. 4-7-4, 4-7-5**). The CE of the second set (red) is improved over the first set (black) because there is relatively less phase formation remaining at this point (**Fig. 4-7-4**). The CE of the third set (blue) is then further improved over the second set (red) as the phase formation is relatively more complete by now. The resistance also continues to decrease indicating further albeit more subtle improvements in the delithiation kinetics. Eventually we reach the fourth and the highest current density set at 0.32 mA/cm^2. Here multiple signs of battery failure appeared in the cycles of BAT1 with rapidly increasing IR drop, extreme drifting of charge/discharge plateau potentials and CE dropping to zero. We do not show sample cycles for this final set. Instead we show CE and R values in the respective plots (green curves) and indicate the onset of failure with an arrow (**Figs. 4-7-4, 4-7-5**).

Overall lithiation-delithiation in this solid electrolyte based battery prototype with a GF Al anode produces a very stable charging/discharging response with good CE at lower current densities. There is a small increase of charge/discharge plateau potential drifting with increasing current density and the internal resistance shows minimal change beyond the early cycles. Increasing the current density does slightly alter the discharge peak shape but the secondary diffusion-limited discharge process does not appear (**Fig. 4-7-6**). Most importantly there is a complete absence of any plateau potential jump events in both charging and discharging portions of the cycle for BAT1. This stable battery operation with Al anodes is made possible for two reasons. First is conditioning of the battery for a large number of cycles at lower current densities. This allows a regular nanostructure to gradually form close to equilibrium conditions. Secondly there is the mechanically rigid solid polymer electrolyte (SPE) which likely acts as a scaffold to restrain the phase growth, further aided by the inclusion of TiO_2 nanoparticles. However, approaching the current densities of the half-cell failure experiments in the fourth set here, the BAT1 battery system fails rapidly (**Fig. 4-7-4**), even with 100 cycles of conditioning in the two previous sets. The reason may be uncontrolled LiAl phase growth at this highest current density, which is more heterogeneous and dendrite-like (**Fig. 4-7-28 a**). This results in

damage of the SPE and possibly formation of a short circuit due to direct contact of anodic and cathodic active materials.

As a next step we tested if applying a non-annealed 75% N_2 75 nm CNx coating to the GF Al anode would produce a stable battery charging/discharging response at these higher current densities, with the CNx film acting as an additional scaffold to contain phase growth. Shown in **Fig. 4-7-7** is the first full set of eight battery galvanic cycles of the second sample BAT2 utilizing a non-annealed 75% N_2 75 nm Al-CNx anode at a current density of 0.033 mA/cm^2 with charge/discharge times of 500 seconds each. With an Al-CNx anode the features of the battery results and their evolution will be largely similar to the previous sample with bare GF Al anode (BAT1). However there are some notable differences beginning with **Fig. 4-7-7**. The first cycle again shows formation of entirely new intermetallic LiAl phase as indicated by the slow potential increase and an elevated charge plateau together with an excessively large IR drop. A visibly long flat charge plateau appears by the end of the first set of BAT2 with very minimal upward potential drifting. This is in contrast to the charge portion shape by the end of the first set of BAT1 (**Fig. 4-7-3**). The continued appearance of a relatively flat charge plateau here in BAT2 suggests that the CNx coating is able to partially suppress the intermetallic phase formation relative to the same cycling conditions with bare GF Al anode. This containment of volume change by the CNx coating was observed previously in the 4x8 half-cell results of non-annealed Al-CNx versus bare GF Al anodes in Ch. 4.4. As a result of the impeded phase formation during early cycling of BAT2 both the resistance (**Fig. 4-7-9**) and coulombic efficiency (**Fig. 4-7-8**) for this sample are initially much worse as compared to BAT1 but improve rapidly.

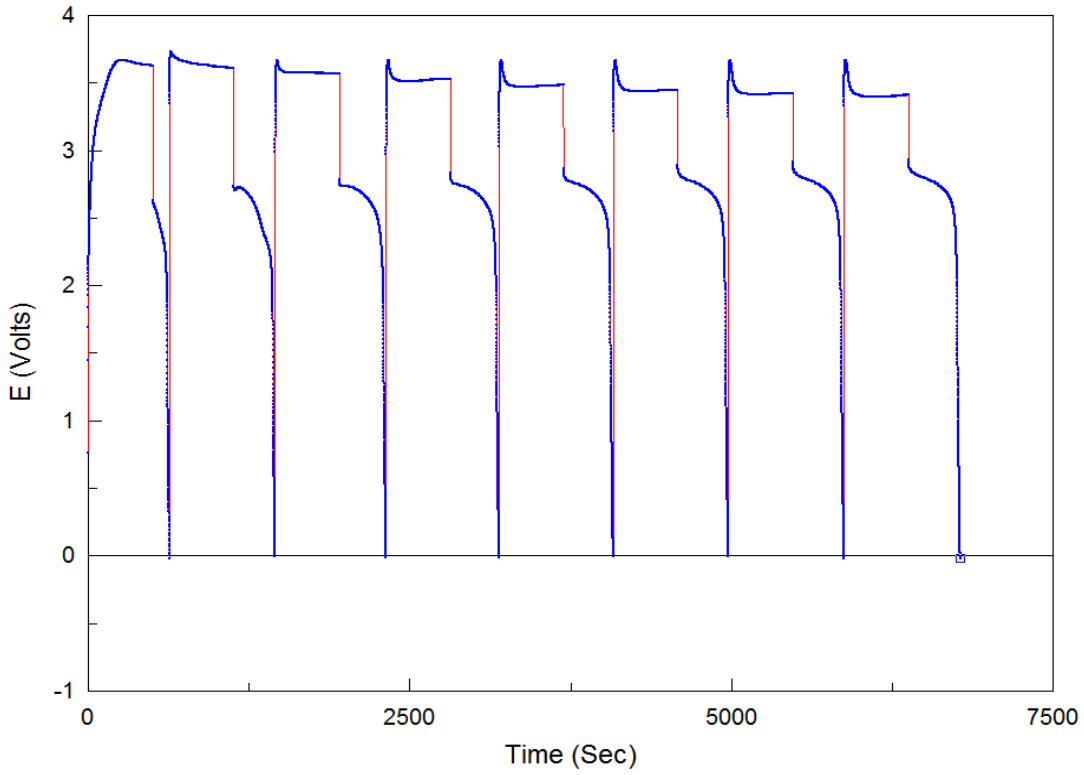

Figure 4-7-7: Full set of battery galvanic cycles of sample BAT2 with a solid polymer electrolyte, $LiFePO_4$ cathode and a non-annealed 75% N_2 75 nm Al-CNx anode at a current density of 0.033 mA/cm^2 for 8 cycles with charge/discharge times of 500 seconds each.

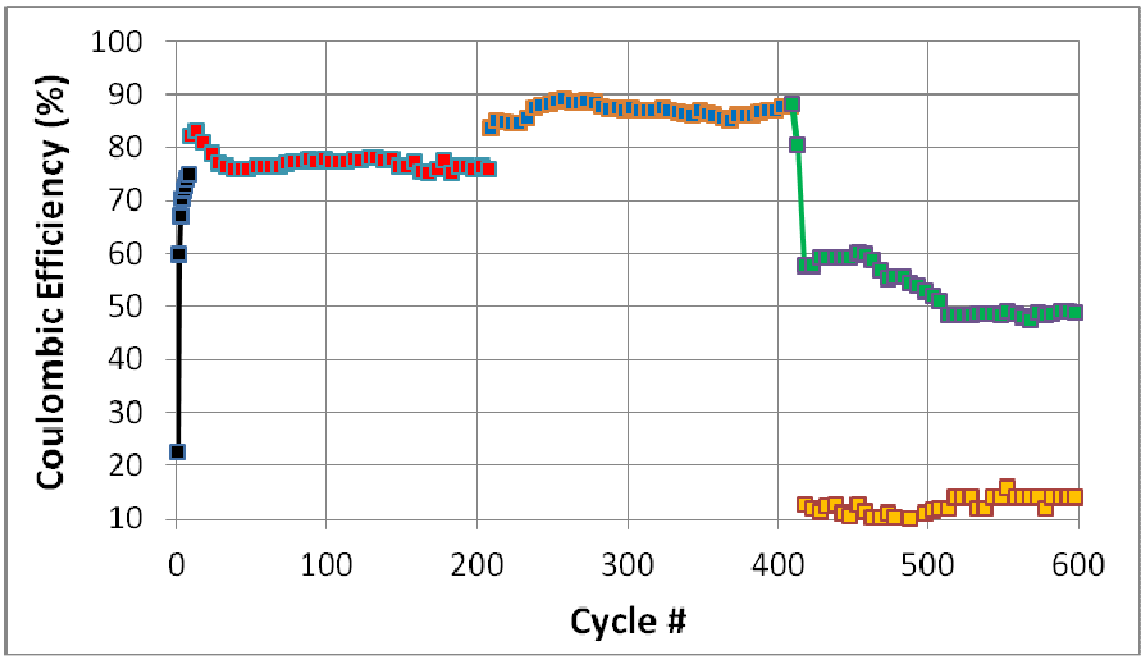

Figure 4-7-8: Coulombic efficiency for the main discharge plateau in battery galvanic cycles of sample BAT2 with a solid polymer electrolyte, $LiFePO_4$ cathode and a non-annealed 75% N_2 75 nm Al-CNx anode at current densities of 0.033 (black), 0.065 (red), 0.13 (blue) and 0.32 (green) mA/cm^2. Yellow curve shows coulombic efficiency of secondary diffusion-limited discharge plateau at 0.32 mA/cm^2. Horizontal axis shows the cumulative number of cycles of all sets together.

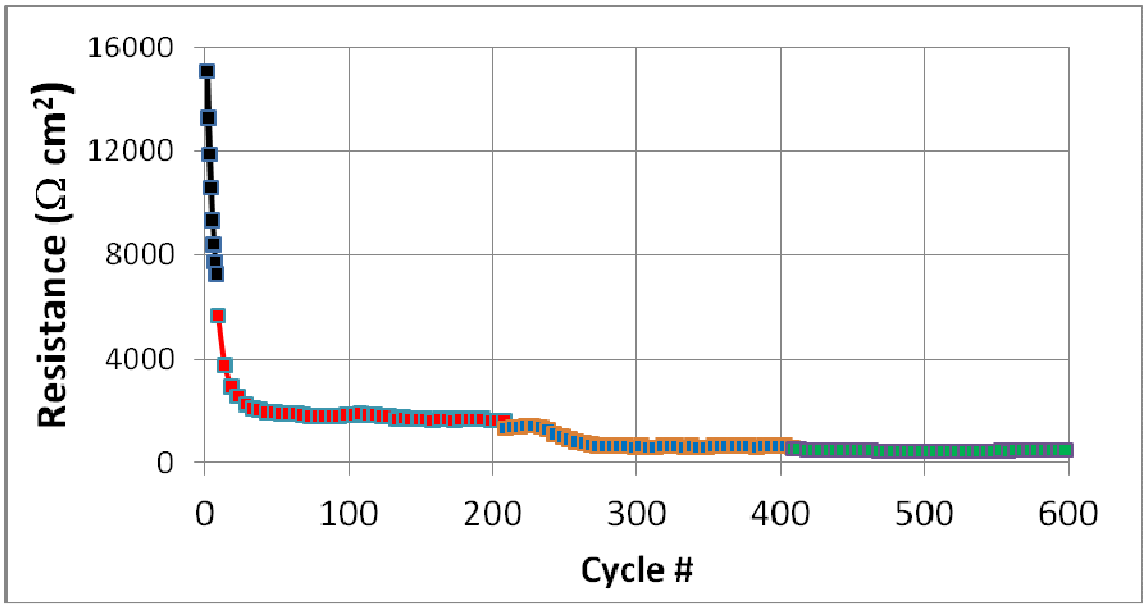

Figure 4-7-9: Resistance calculated from the IR drop for battery galvanic cycles of sample BAT2 with a solid polymer electrolyte, $LiFePO_4$ cathode and a non-annealed 75% N_2 75 nm Al-CNx anode at current densities of 0.033 (black), 0.065 (red), 0.13 (blue) and 0.32 (green) mA/cm^2. Horizontal axis shows the cumulative number of cycles of all sets together.

Shown in **Fig. 4-7-10** are galvanic cycles from the (a) beginning and (b) middle of the sets at current densities of 0.065 (red), 0.13 (blue) and 0.32 (green) mA/cm^2. As usual intermetallic phase growth continues at all current densities in progressively smaller amounts as seen in the decreasing resistance (**Fig. 4-7-9**) and increasing CE (**Fig. 4-7-8**) between the initial (a) and middle cycles (b). We note that there is some subtle variation in the R and CE trends of BAT2 after the initial cycles at higher current densities (red, blue, green). This behaviour may possibly be related to degradation of the CNx film as intermetallic phase growth continues, because CNx contributes towards the reversibility and kinetics of lithiation-delithiation at the Al-CNx anode.

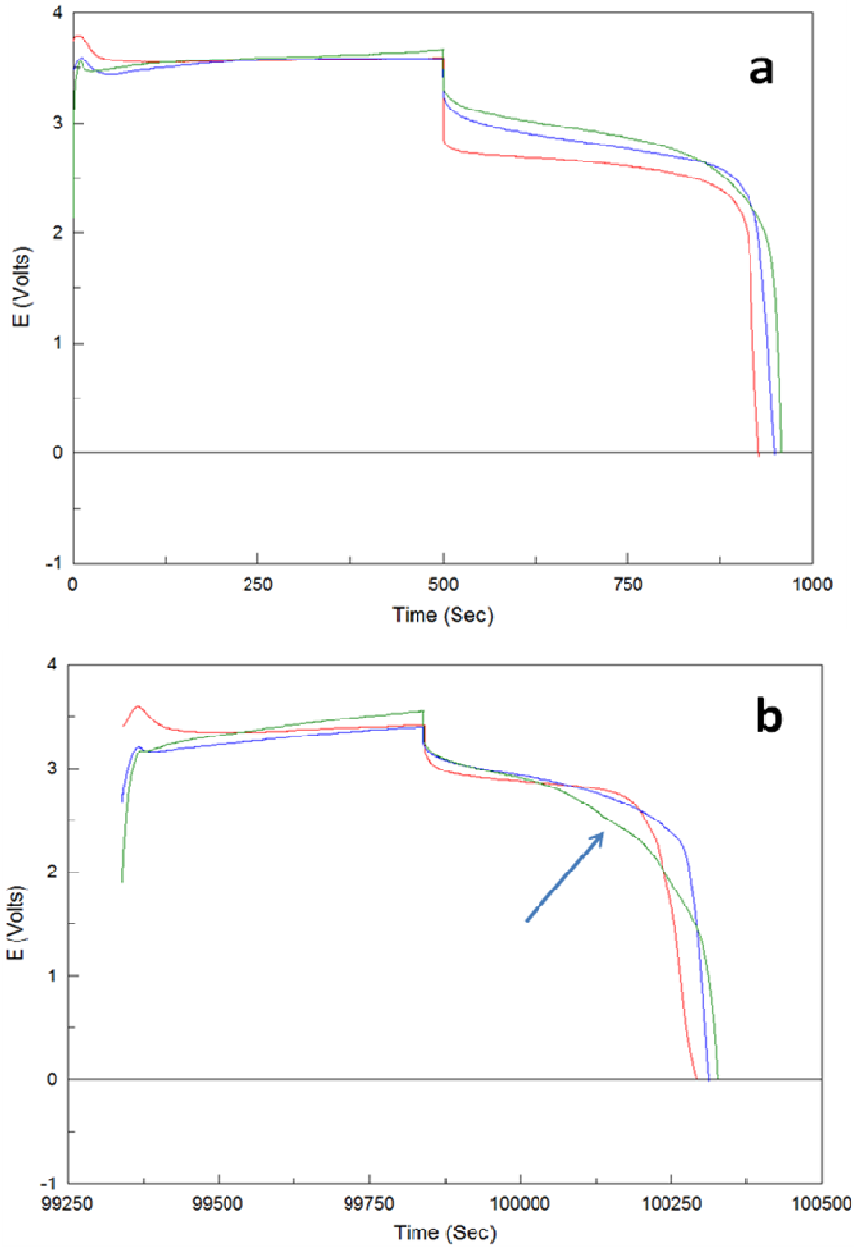

Figure 4-7-10: (a) Initial and (b) middle battery galvanic cycles of sample BAT2 with a solid polymer electrolyte, $LiFePO_4$ cathode and a non-annealed 75% N_2 75 nm Al-CNx anode at current densities of 0.065 (red), 0.13 (blue) and 0.32 (green) mA/cm^2. For all current densities cycling was performed for 200 cycles each with charge/discharge times of 500 seconds. Cycles have been offset in figure b to overlap the curves on the same time scale. Arrow in green curve of figure b indicates appearance of secondary diffusion-limited discharge plateau.

When we reach the highest current density of 0.32 mA/cm^2 (green) here in BAT2, at first there are no signs of battery failure (**Fig. 4-7-10 a**). However, even though the charge/discharge response is stable the secondary diffusion-limited discharge plateau rapidly grows in appearance by the middle of the set (indicated by arrow in green curve of **Fig. 4-7-10 b**). This secondary process that grows over time to a CE of 16% restricts the CE of the main discharge plateau at 0.32 mA/cm^2 (green) down to just 50% (**Fig. 4-7-8**). At the same time, the internal resistance R remains low until the end of the set (**Fig. 4-7-9**).

Overall battery testing with a non-annealed Al-CNx anode produces a quite stable charging/discharging response with good CE at lower current densities. Here there is a consistent increase of charge/discharge plateau potential drifting with increasing current density. Both the R and CE trends differ slightly from that of the bare GF Al sample BAT1 (**Figs. 4-7-4, 4-7-5**), possibly due to structural changes occurring in the CNx film during phase growth at the anode surface. Once again there is a complete absence of any plateau potential jumps in both charging and discharging portions of BAT2 cycles. At the higher current density of the fourth set (0.32 mA/cm^2) the BAT1 system had a rapid deterioration leading to complete failure by the 130th cycle (**Figs. 4-7-4, 4-7-5**). Here the fourth set of BAT2 still has a very stable charge/discharge response for all 200 cycles even though the diffusion-limited discharge has become significant (**Figs. 4-7-8, 4-7-9**) and the CE dropped significantly below acceptable levels. The presence of the CNx coating must be the key reason for the improvements here of BAT2 over BAT1. These results are distinct from the half-cell failure experiments of Al-CNx anodes relative to bare GF Al anodes in Ch. 4.4, where Al-CNx did offer a higher maximum reversibility of lithiation-delithiation but the overall degradation in performance was significantly worse (**Figs. 4-4-9, 4-4-10**). This effect should be attributed to the presence of solid polymer electrolyte (SPE) and the additional mechanical and volumetric constraints of the SPE-based battery cell architecture in controlling the volume change. Therefore the CNx film and the rigid solid polymer electrolyte can effectively act together as two scaffolds to control the phase growth at the anode. In contrast, for a liquid-based half cell the CNx coating will rapidly crack into pieces and disappear from the electrode surface.

We then attempted to further improve the strong performance of BAT2 by modifying the Al-CNx anode either through post-deposition thermal annealing (sample BAT3) or by applying CNx film with lower nitrogen content (sample BAT4). In particular, we expected that thermal annealing treatment would offer improved mechanical properties of the CNx film and further restrict growth of the porous structure at higher current densities.

Shown in **Fig. 4-7-11** is the first full set of eight battery galvanic cycles of the third sample BAT3 utilizing an annealed 75% N_2 75 nm Al-CNx anode at a current density of 0.033 mA/cm^2 with charge/discharge times of 500 seconds each. With an annealed Al-CNx anode one observes several important differences compared to battery cycling with the previous non-annealed Al-CNx anode (BAT2). Initially in the first set there is an unstable charging potential response observed with two discharge plateaus. However, further cycles showed improved internal resistance and coulombic efficiency (**Figs. 4-7-12, 4-7-13**), although we sometimes observed some random changes in these properties. According to our half-cell results in Ch. 4.4.2, thermal annealing improves the mechanical stability (hardness) of the CNx film on the anode (**Fig. 4-4-24 c**), leading to enhanced containment of volume change in the CV (**Fig. 4-4-2**). The behaviour observed in this experiment is generally consistent with this picture. The annealed CNx films may be more rigid and prone to sudden cracks and ruptures, which caused the random jumps in CE and R.

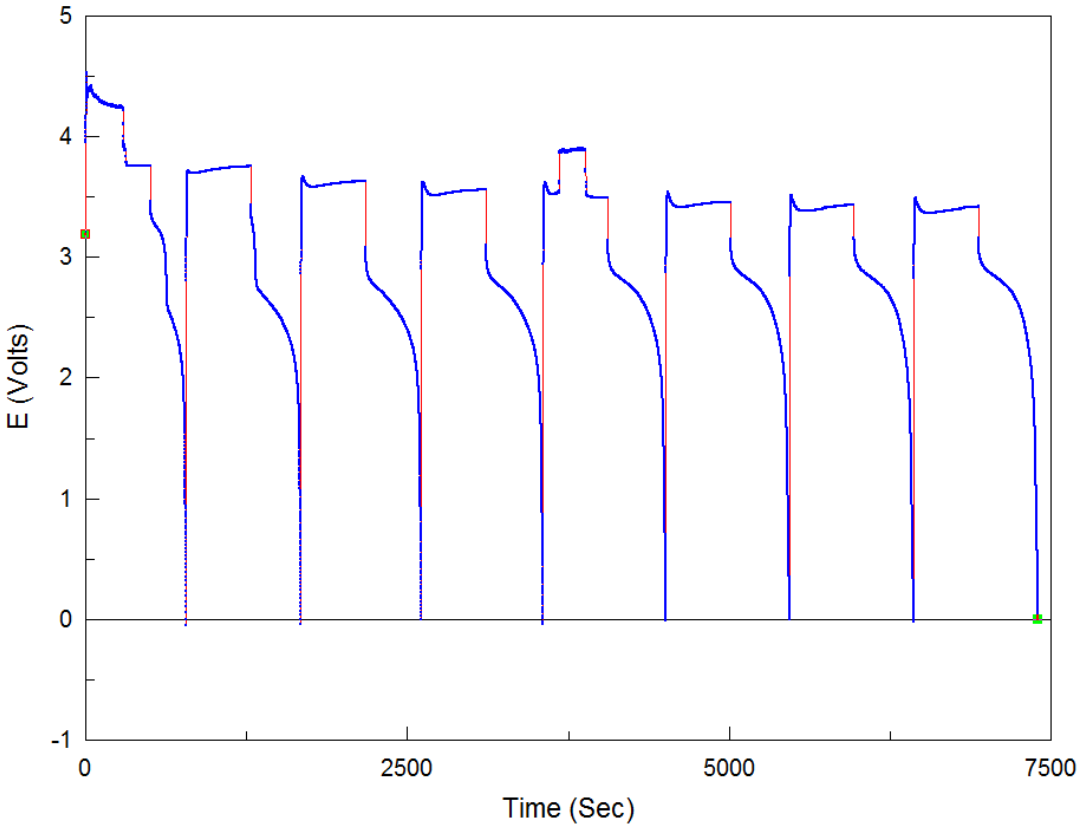

Figure 4-7-11: Full set of battery galvanic cycles of sample BAT3 with a solid polymer electrolyte, $LiFePO_4$ cathode and an annealed 75% N_2 75 nm Al-CNx anode at a current density of 0.033 mA/cm^2 for 8 cycles with charge/discharge times of 500 seconds each.

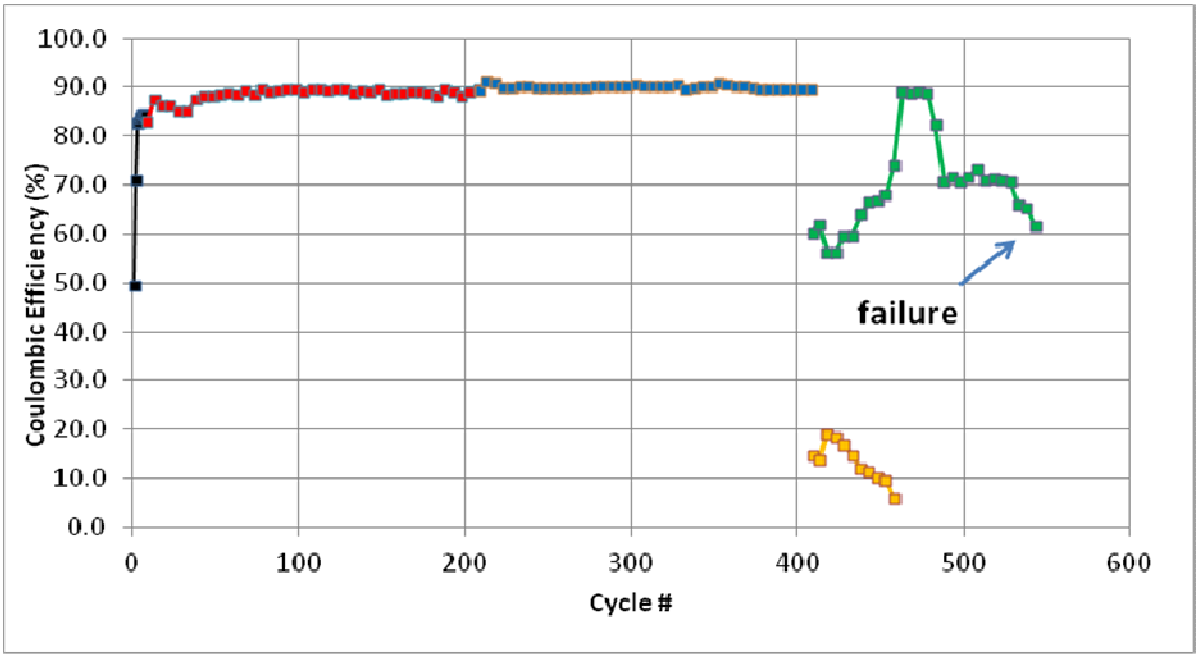

Figure 4-7-12: Coulombic efficiency for the main discharge plateau in battery galvanic cycles of sample BAT3 with a solid polymer electrolyte, $LiFePO_4$ cathode and an annealed 75% N_2 75 nm Al-CNx anode at current densities of 0.033 (black), 0.065 (red), 0.13 (blue) and 0.32 (green) mA/cm^2. Yellow curve shows coulombic efficiency of secondary diffusion-limited discharge plateau at 0.32 mA/cm^2. Horizontal axis shows the cumulative number of cycles of all sets together. The arrow in the green curve indicates the onset of battery failure.

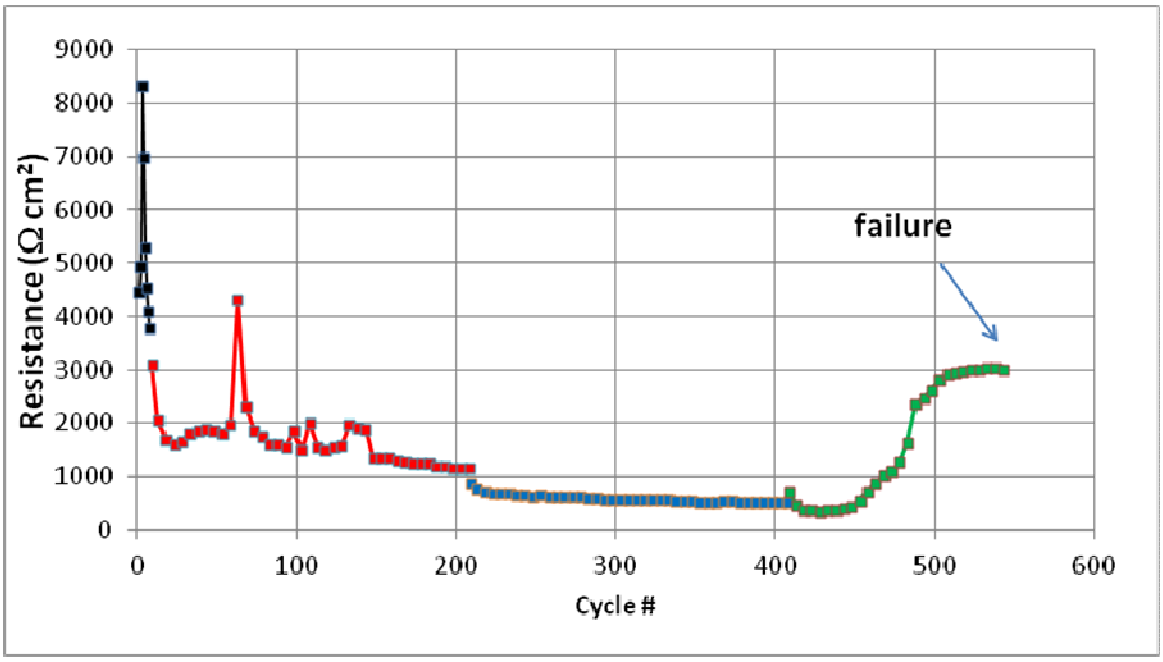

Figure 4-7-13: Resistance calculated from the IR drop for battery galvanic cycles of sample BAT3 with a solid polymer electrolyte, $LiFePO_4$ cathode and an annealed 75% N_2 75 nm Al-CNx anode at current densities of 0.033 (black), 0.065 (red), 0.13 (blue) and 0.32 (green) mA/cm^2. Horizontal axis shows the cumulative number of cycles of all sets together. The arrow in the green curve indicates the onset of battery failure.

Shown in **Fig. 4-7-14** are galvanic cycles from the (a) beginning and (b) middle of the sets at current densities of 0.065 (red) and 0.13 (blue) mA/cm^2. At higher current densities for BAT3 the single discharge plateau behaviour remains with decreasing resistance (**Fig. 4-7-13**) and increasing coulombic efficiency (**Fig. 4-7-12**) characteristic of continued intermetallic phase growth. However, signs of an unstable charge/discharge response remain with multiple plateau potential jumps seen in the middle cycles at 0.065 mA/cm^2 (**Fig. 4-7-14 b**) and the resistance trend (**Fig. 4-7-13**). At the same time, the shape and the parameters of the potential traces by the middle of the third set of cycles (blue) clearly improved in all respects, such as plateau separation, etc. This indicates the formation of mature LiAl nanostructure.

At the highest current set of 0.32 mA/cm^2 for BAT3 the secondary diffusion-limited discharge plateau is immediately apparent at a CE of 15% (yellow curve), which restricts the CE of the main discharge plateau to 60% (green curve) (**Fig. 4-7-12**). The appearance of this secondary process at this higher current density is consistent with the discharge behaviour observed for the sample with non-annealed Al-CNx anode (BAT2) (**Figs. 4-7-8, 4-7-10 b**). For BAT3 the secondary process will disappear by the 55th cycle of the fourth set (yellow), increasing the CE of the main discharge plateau (green) to 89% (**Fig. 4-7-12**). However the onset of battery failure will soon follow beginning from the 75th cycle and accelerating beyond the 125th cycle (indicated with arrow).

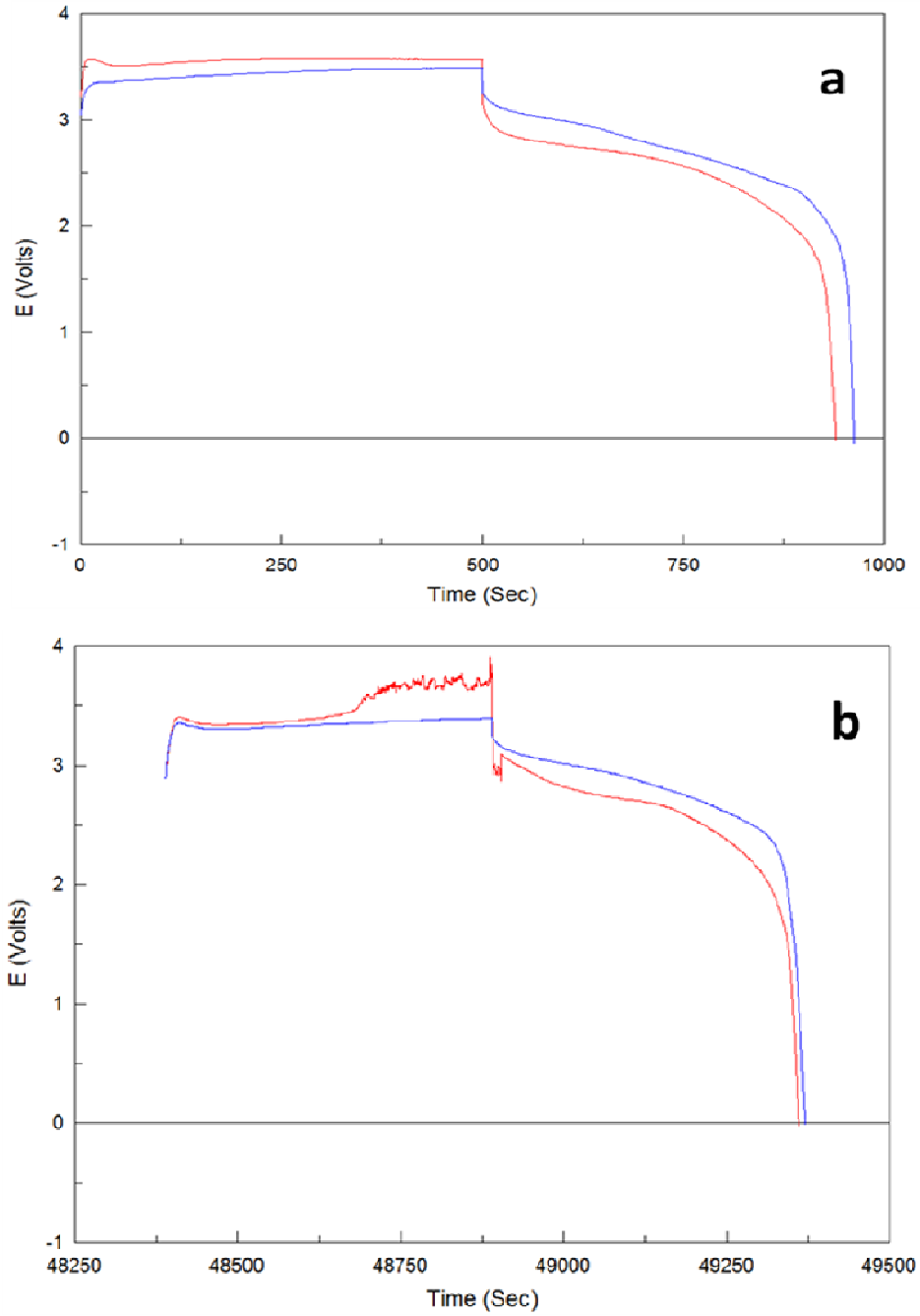

Figure 4-7-14: (a) Initial and (b) middle battery galvanic cycles of sample BAT3 with a solid polymer electrolyte, $LiFePO_4$ cathode and an annealed 75% N_2 75 nm Al-CNx anode at current densities of 0.065 (red) and 0.13 (blue) mA/cm^2. For both current densities cycling was performed for 200 cycles each with charge/discharge times of 500 seconds. Cycles have been offset in figure b to overlap the curves on the same time scale.

Overall we observe a worse battery performance with thermal annealing of the Al-CNx anode prior to application of the solid polymer electrolyte layer and cell assembly. Even at lower current densities there is a relatively unstable charging/discharging response with multiple plateau potential jumps (**Figs. 4-7-11, 4-7-14 b**). The annealed version is still strongly diffusion-limited at the current density of the fourth set (0.32 mA/cm^2) with the appearance of the secondary process (**Fig. 4-7-12**). Battery failure then occurs with an extreme IR drop and severe loss of CE at a current density where the non-annealed Al-CNx anode version (BAT2) still had stable performance for 200 cycles (**Figs. 4-7-8, 4-7-9**). In the surface analysis of annealed Al-CNx anodes cycled under liquid half-cell conditions (Ch. 4.4.2) we observed increased adhesion and stability of the CNx film (**Fig. 4-4-24 c-d**). As discussed in the non-annealed Al-CNx battery sample (BAT2) the solid-state battery cell architecture here should help in allowing the CNx coating to constrain the growth of the porous structure at the anode. The addition of thermal annealing of the Al-CNx anode might make the CNx coating too mechanically rigid. This would be problematic because it may result in the coating excessively constraining the intermetallic phase formation, possibly causing cracking (pulverization) of the porous structure. As in the solid polymer electrolyte layer a certain degree of elasticity is required in the CNx coating. Another consideration is that the thermal annealing treatment applied to the anode also includes the GF Al substrate itself which may soften its mechanical properties and therefore impair reversibility. The relation between softened mechanical properties in bulk Al materials and poor cycling performance was documented previously in Ch. 4.2 with McMaster-Carr Al (MC Al) anodes.

Even worse performance was obtained using a non-annealed 25% 75 nm Al-CNx anode BAT4, which did produce initially a more stable charge/discharge response at lower current densities, but failure was even more immediate at the highest current density. Shown in **Fig. 4-7-15** is the first full set of eight galvanic cycles of a battery with the BAT4 anode at a current density of 0.033 mA/cm^2 with charge/discharge times of 500 seconds each. Overall the cycle features again suggest a significant restriction of initial intermetallic phase growth by the CNx film at the anode surface. The effect is severe enough such that a visible potential overshot is not observed until the fourth cycle.

Furthermore, the charging voltage in the first cycles is very high and only gradually decreases with cycling. Another notable feature is the main discharge plateau that actually does not appear in the discharge portion of the first cycle. Even in the second cycle the main discharge plateau is only barely seen. The overall discharge peak of the first few cycles is instead almost entirely dominated by the tertiary diffusion-limited discharge plateau at a potential close to 1V. Taken together, these cycle features suggest that the initial intermetallic phase formation is very much impeded when the nitrogen content in the CNx film is decreased.

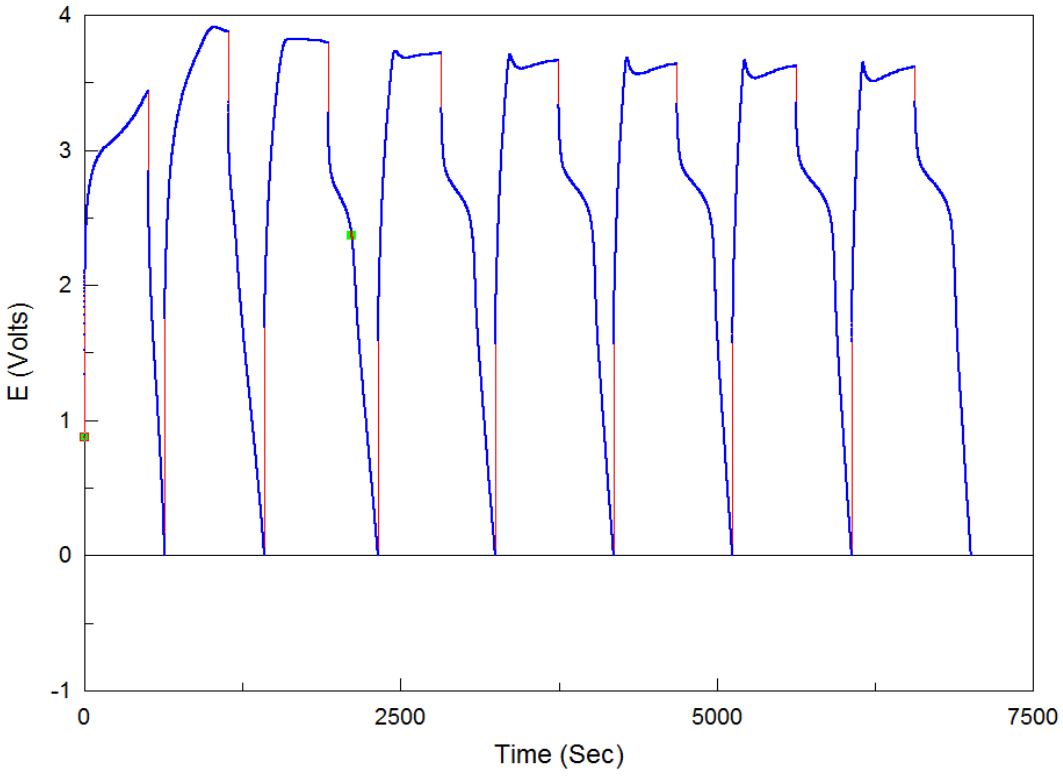

Figure 4-7-15: Battery galvanic cycles of sample BAT4 with a solid polymer electrolyte, $LiFePO_4$ cathode and a non-annealed 25% N_2 75 nm Al-CNx anode at a current density of 0.033 mA/cm^2 for 8 cycles with charge/discharge times of 500 seconds each.

However the remaining cycles in this set start to show noticeable potential overshots in the charging portion followed by significant upward drifting in the charge plateau potential. In comparison the latter cycles of the first set of sample BAT2 with 75% N_2 Al-CNx anode showed charging portions that remained relatively flat (**Fig. 4-7-7**). This contrast suggests that the intermetallic phase formation is actually less restricted with decreased nitrogen content in the CNx film of the anode for sample BAT4. Increased nitrogen content in the plasma during CNx deposition will lead to increased incorporation of nitrogen-containing functional groups in the film. This results in further cross-linking of the CNx structure effectively increasing its mechanical stability (hardness). The decreased volume change containment here in BAT4 is consistent with half-cell results of 25% N_2 versus 75% N_2 Dural-CNx in **Ch. 4.4** (**Fig. 4-4-13**). As the phase growth progresses in the first set of BAT4 we see the typical trends of decreasing resistance (**Fig. 4-7-17**) and increasing coulombic efficiency (**Fig. 4-7-16**).

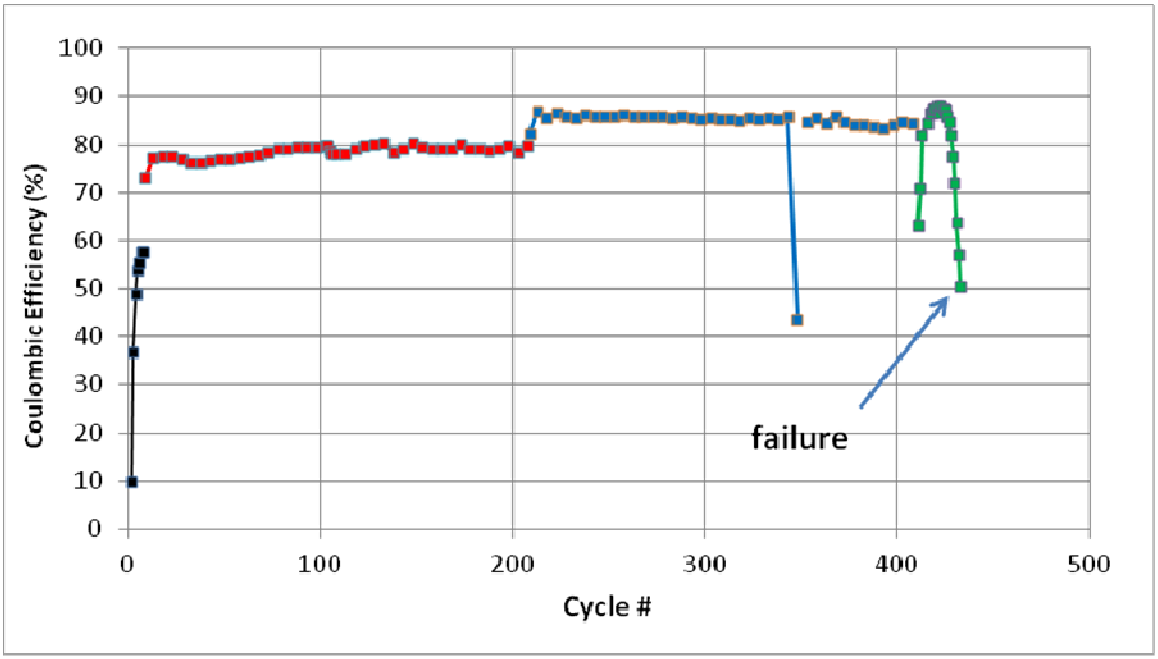

Figure 4-7-16: Coulombic efficiency for the main discharge plateau in battery galvanic cycles of sample BAT4 with a solid polymer electrolyte, $LiFePO_4$ cathode and a non-annealed 25% N_2 75 nm Al-CNx anode at current densities of 0.033 (black), 0.065 (red), 0.13 (blue) and 0.32 (green) mA/cm^2. Horizontal axis is the cumulative number of cycles of all sets together. The arrow in the green curve indicates the onset of battery failure.

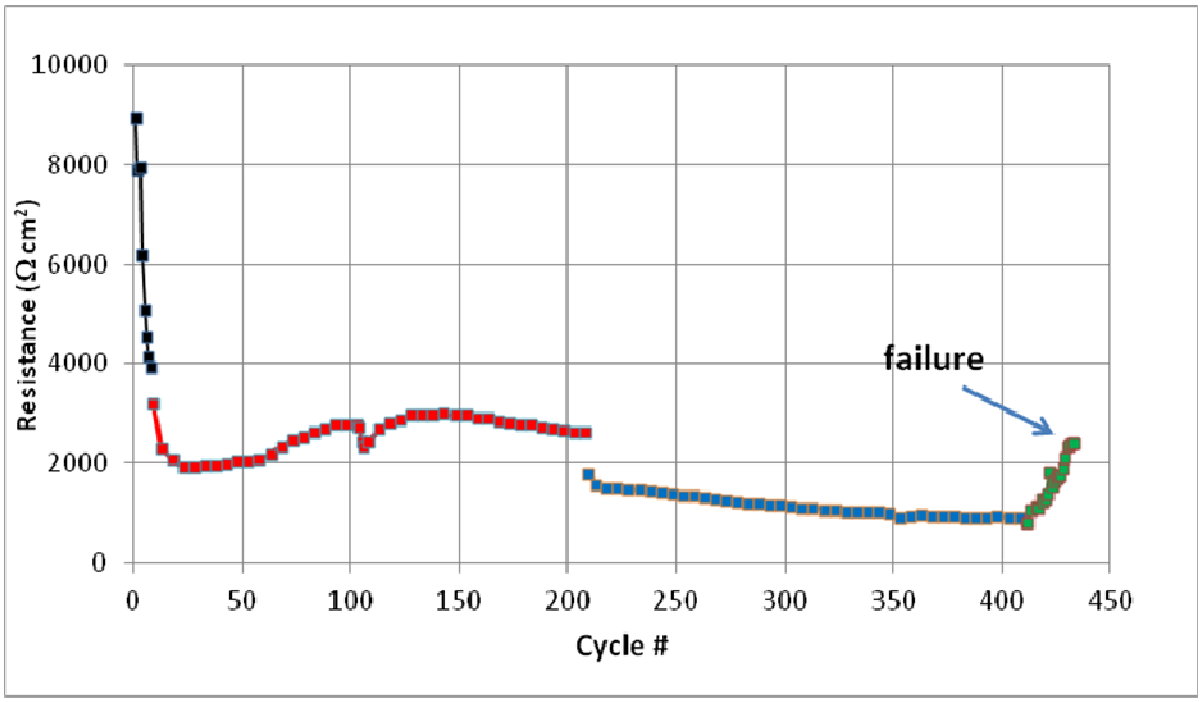

Figure 4-7-17: Resistance calculated from the IR drop for battery galvanic cycles of sample BAT4 with a solid polymer electrolyte, $LiFePO_4$ cathode and a non-annealed 25% N_2 75 nm Al-CNx anode at current densities of 0.033 (black), 0.065 (red), 0.13 (blue) and 0.32 (green) mA/cm^2. Horizontal axis shows the cumulative number of cycles of all sets together. The arrow in the green curve indicates the onset of battery failure.

Shown in **Figs. 4-7-16 – 4-7-18** are the evolution of the coulombic efficiency and the internal resistance with cycling, as well as typical galvanic cycles from (a) the beginning and (b) the middle of the sets at higher current densities of 0.065 (red) and 0.13 (blue) mA/cm^2. Intermetallic phase growth continues but at a progressively smaller rate. The tertiary diffusion-limited discharge plateau remains in the second set (red), restricting the CE of the main discharge plateau, but disappears by the third set (blue). The charge/discharge response remains relatively stable here for BAT4, except for some brief intermittent failure observed around cycle 140 of the third set, seen in the CE plot (blue curve) (**Fig. 4-7-16**). As described for the BAT2 and BAT3 battery samples, there are some minor variations in the R and CE values at higher current densities in BAT4 beyond the early cycles, suggesting that structural changes occur in the CNx film as intermetallic phase growth continues. At the highest current density set of 0.32 mA/cm^2 we observed a very rapid onset of battery failure. Additionally, no secondary diffusion-limited plateau was observed too, likely due to the rapid failure. Here the CE of the main discharge plateau improved from an initial value of 63% up to 88% by the 15th cycle, followed by a very fast decline (**Fig. 4-7-16**).

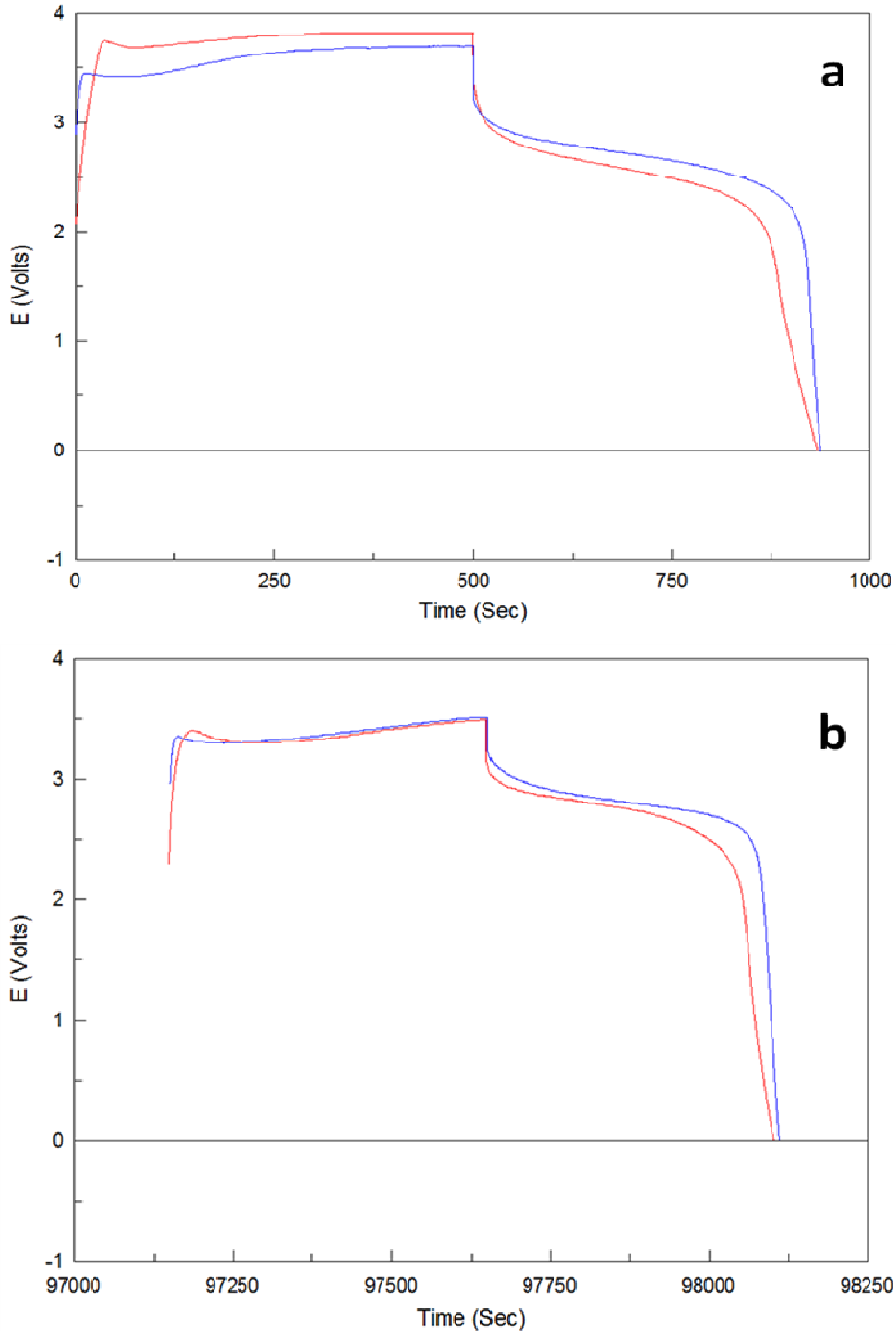

Figure 4-7-18: (a) Initial and (b) middle battery galvanic cycles of sample BAT4 with a solid polymer electrolyte, $LiFePO_4$ cathode and a non-annealed 25% N_2 75 nm Al-CNx anode at current densities of 0.065 (red) and 0.13 (blue) mA/cm^2. For both current densities cycling was performed for 200 cycles each with charge/discharge times of 500 seconds. Cycles have been offset in figure b to overlap the curves on the same time scale.

In general we observe comparable battery performance at lower current densities with lower nitrogen content in the CNx film. The charge/discharge response is reasonably stable and the CE of the main discharge plateau exceeds 80%. However the performance at the higher current density of the fourth set (green) (**Fig. 4-7-16**) is significantly worse than the non-annealed 75% N_2 version (BAT2) (**Fig. 4-7-8**), with the onset of failure occurring after just 15 cycles. The battery sample with a bare GF Al anode (BAT1) did not show onset of failure at the highest set (green) until approximately 75 cycles (**Fig. 4-7-4**). Therefore the use of a lower nitrogen content CNx film here in BAT4 does not result in any improvement in the reversibility of lithiation-delithiation compared to bare GF Al anode without CNx coating. The poor performance of battery samples with 25% N_2 versus 75% N_2 Al-CNx anodes is consistent with half-cell results of 25% N_2 versus 75% N_2 Dural-CNx anodes described previously in Ch. 4.4. In those tests we observed significantly faster performance degradation upon decreasing the nitrogen content in the CNx film, with increased frequency of plateau potential jumps and faster deterioration of coulombic efficiency (**Figs. 4-4-20, 4-4-21**). As in the half-cell tests, the positive effect of nitrogen-rich 75% N_2 Al-CNx anodes is likely related to greater incorporation of nitrogen-based functional groups in the CNx film. This allows for more cross-linking within the CNx structure effectively increasing the hardness of the film. Therefore the 75% N_2 CNx film has an improved ability to act as a scaffold to control the intermetallic phase growth through containment of volume changes, particularly at higher current densities. Apparently, the 25% film is too soft. Additionally, the increased nitrogen incorporation may improve film adhesion through increased interfacial reactivity with the GF Al substrate.

Throughout these series of battery experiments the charging/discharging time was kept unchanged at 500 seconds. Therefore the total charge (Q) being applied to both the anode and the cathode per cycle was consistently increasing set over set, which resulted in continuing formation of the new portions of the LiAl intermetallic phase at progressively higher current densities. We were concerned that by doing this we may be accelerating the battery failure through more heterogeneous or dendritic growth of this porous structure at high current densities. This uncontrolled growth as also evidenced by SEM

data (Ch. 4.7.2) may have caused damage to the SPE, leading to a short circuit through direct contact of anodic and cathodic active materials, or loss of contact. The failure would then manifest in the form of extreme IR jumps and complete loss of CE. Therefore we performed another battery experiment with a non-annealed 75% N_2 Al-CNx anode BAT5, similar to BAT2, but with the progressively decreasing cycle durations at high current densities to keep the total applied charge constant. In contrast, the cycle duration at low current densities was increased, to increase the amount of LiAl phase formed in these conditions. The anode and battery cell preparation was identical to the second sample (BAT2) described earlier in this chapter.

Shown in **Fig. 4-7-19** are the first two full sets of eight galvanic cycles of the BAT5 prototype utilizing a non-annealed 75% N_2 75 nm Al-CNx anode at current densities of 0.016 (black) and 0.033 (red) mA/cm^2 with charge/discharge times of 1000 seconds each. **Fig. 4-7-20** shows the coulombic efficiency of the main discharge plateau, with the resistance (R) calculated from the IR jump represented in **Fig. 4-7-21** for the eight current densities used in this experiment, cumulatively in a series numbered **1** to **8**.

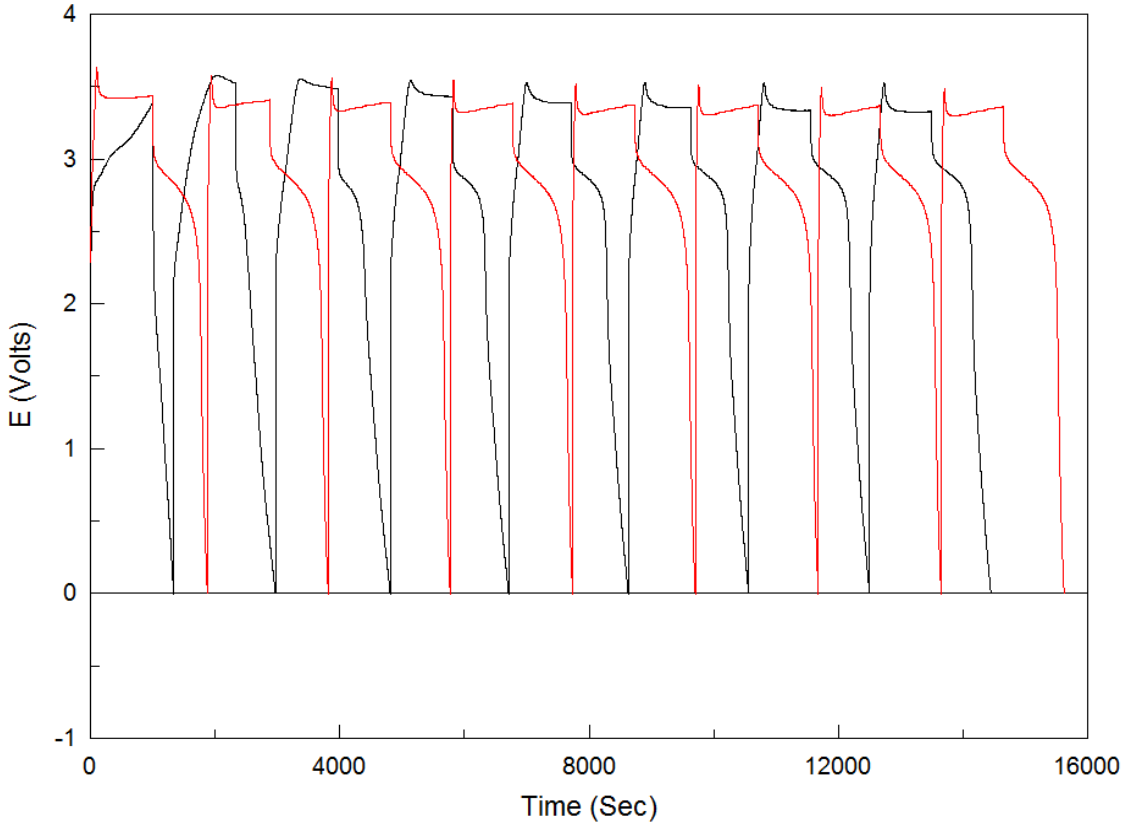

Figure 4-7-19: Battery galvanic cycles of sample BAT5 with a solid polymer electrolyte, $LiFePO_4$ cathode and a non-annealed 75% N_2 75 nm Al-CNx anode at current densities of 0.016 (black) and 0.033 (red) mA/cm^2 for 8 cycles each and charge/discharge times of 1000 seconds.

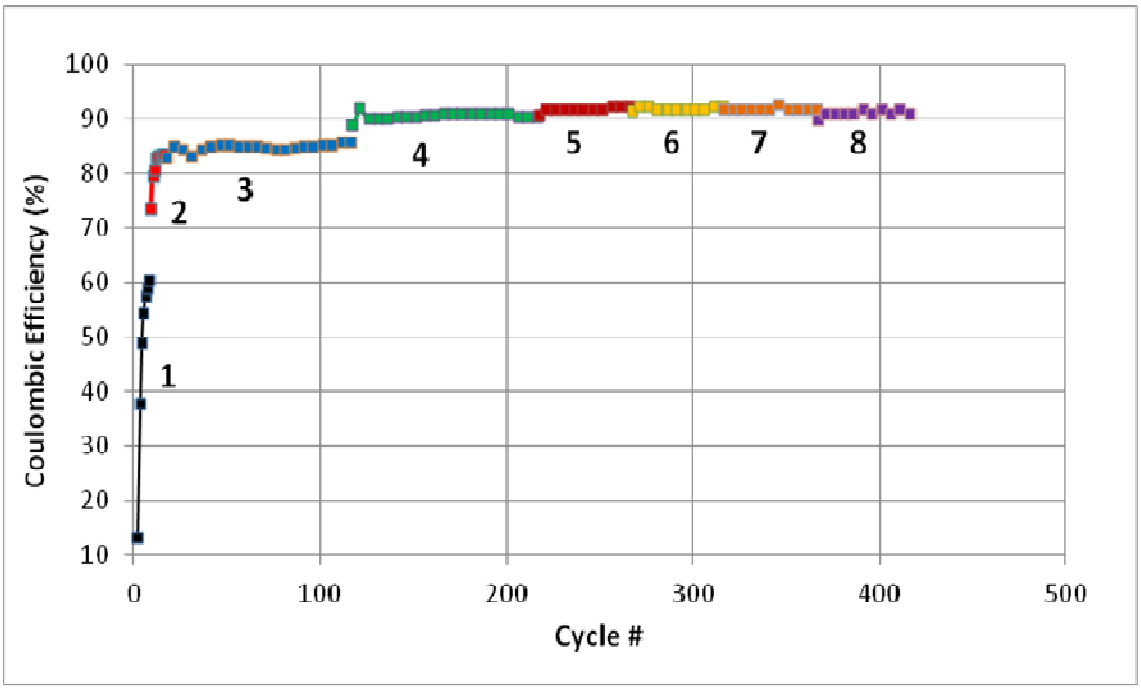

Figure 4-7-20: Coulombic efficiency for the main discharge plateau in battery galvanic cycles of sample BAT5 with a solid polymer electrolyte, $LiFePO_4$ cathode and a non-annealed 75% N_2 75 nm Al-CNx anode at current densities of 0.016 (1, black), 0.033 (2, red), 0.065 (3, blue), 0.13 (4, green), 0.32 (5, brown), 0.46 (6, yellow), 0.59 (7, orange), 0.65 (8, purple) mA/cm^2. Horizontal axis is the cumulative number of cycles of all sets together.

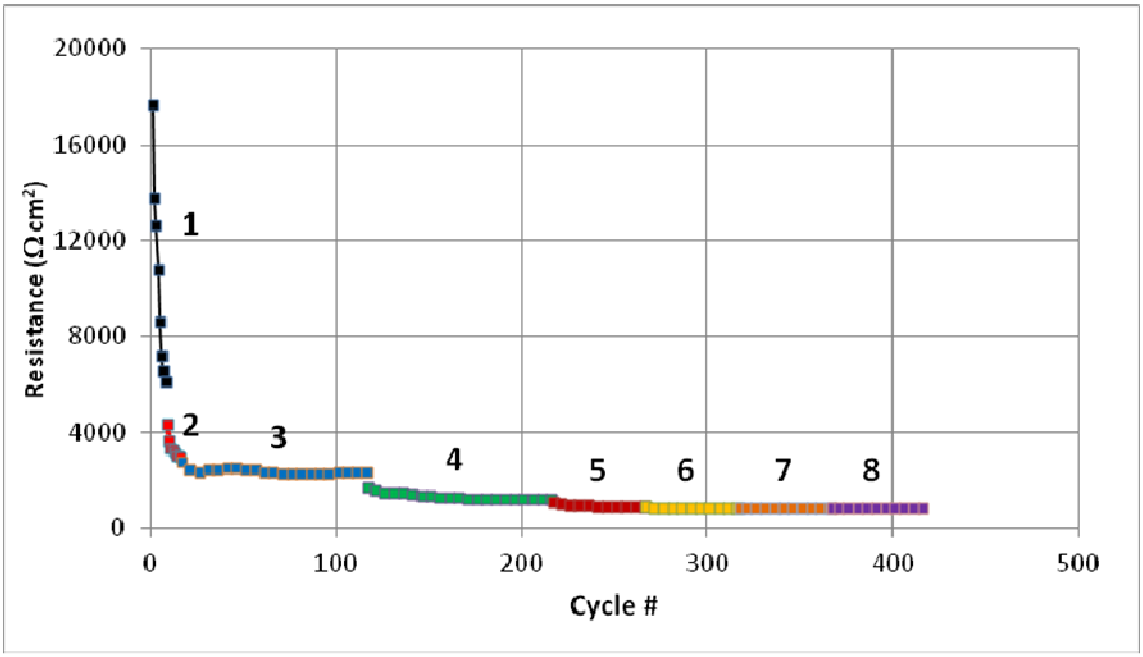

Figure 4-7-21: Resistance calculated from the IR drop for battery galvanic cycles of sample BAT5 with a solid polymer electrolyte, $LiFePO_4$ cathode and a non-annealed 75% N_2 75 nm Al-CNx anode at current densities of 0.016 (1, black), 0.033 (2, red), 0.065 (3, blue), 0.13 (4, green), 0.32 (5, brown), 0.46 (6, yellow), 0.59 (7, orange), 0.65 (8, purple) mA/cm^2. Horizontal axis is the total number of cycles of all sets together.

At the lowest current density (black curve) we observe the typical cycling behaviour characteristic of initial growth of the new intermetallic phase at the anode surface similar to that described in previous samples (**Fig. 4-7-19**). The rapid increase in the surface area of the growing phase as well improvement of the lithiation-delithiation kinetics causes a steep drop in the resistance after a few cycles (**Fig. 4-7-21**) and a large increase in the CE of the main discharge plateau (**Fig. 4-7-20**). Here in the BAT5 sample the CE is initially very poor in the first set (black curve) and is accompanied by the dominant appearance of the tertiary diffusion-limited discharge plateau (**Fig. 4-7-19**). Progressing to the second set (red curve) (**Fig. 4-7-19**) we see clear evidence of electroactive intermetallic phase formed during the previous cycles in the form of more pronounced charge plateau, lower resistance (**Fig. 4-7-21**), and further improved CE (**Fig. 4-7-20**). The improved CE of the

main discharge plateau in the second set is directly related to the steadily diminishing tertiary discharge process.

Shown in **Fig. 4-7-22** are galvanic cycles from the (a) beginning and (b) middle of the next two sets at current densities of 0.065 (blue) and 0.13 (green) mA/cm^2, in which the charge/discharge times have now been cut to 500 sec each compared to the 1000 sec in the previous two sets. The number of cycles was increased to 100 for these two sets to ensure proper conditioning of the porous structure at the anode before further increases in current density. Here in the blue curve of **Fig. 4-7-22** the tertiary discharge process is even more minor so the CE of the main discharge plateau improves again (**Fig. 4-7-20**). By the fourth set (green curve) this tertiary process disappears altogether (**Fig. 4-7-22**). The internal resistance also continues to decrease (**Fig. 4-7-21**).

Shown in **Fig. 4-7-23** are galvanic cycles from the (a) beginning and (b) middle of the last four sets at current densities of 0.32 (black), 0.46 (red), 0.59 (blue) and 0.65 (green) mA/cm^2. The charge/discharge times were decreased in the order of 250 (black), 200 (red), 150 (blue) and 100 (green) seconds respectively. A minimum of 50 cycles each was performed to ensure sufficient conditioning before progressing to the next current density.

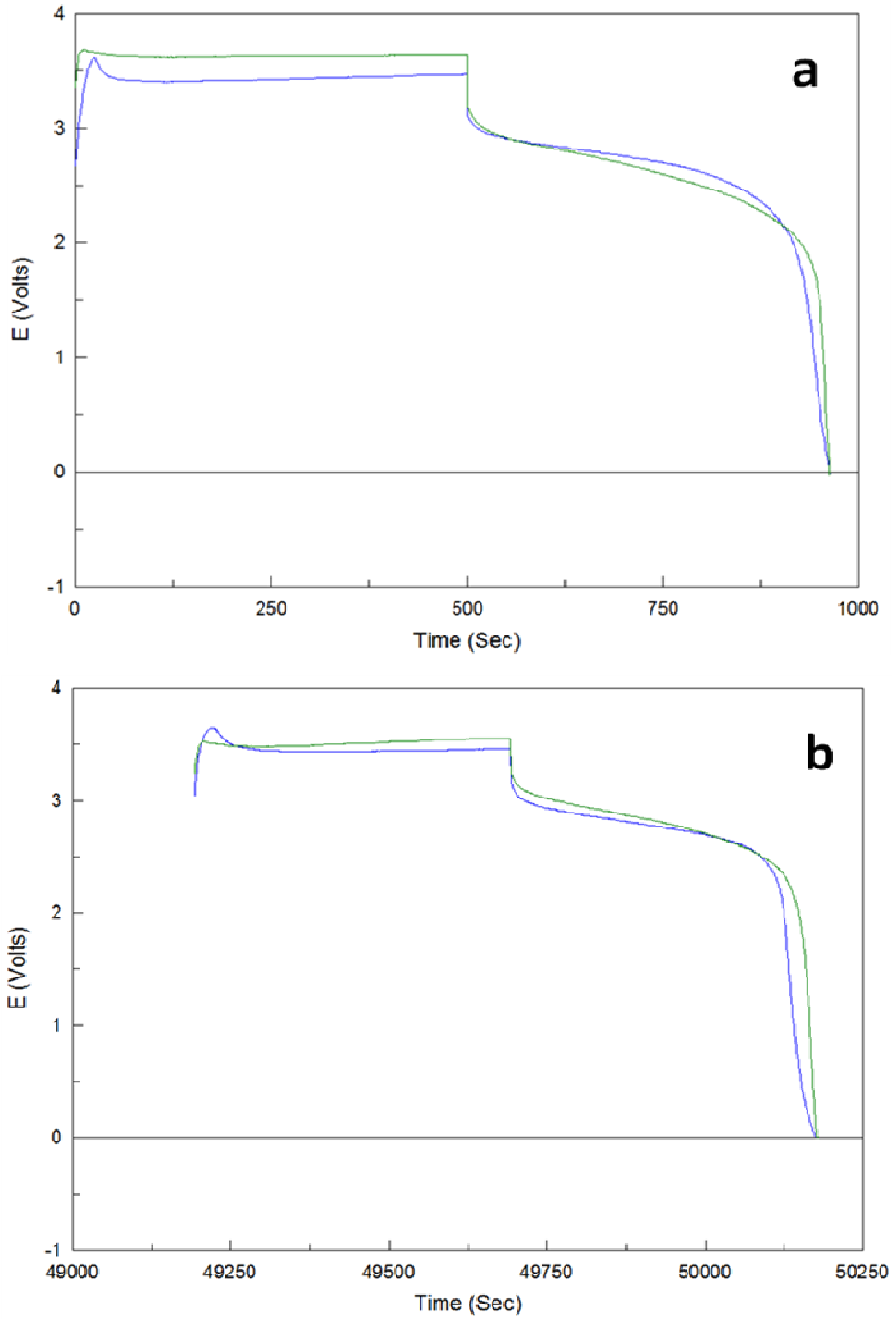

Fig. 4-7-22: (a) Initial and (b) middle battery galvanic cycles of sample BAT5 with a solid polymer electrolyte, $LiFePO_4$ cathode and a non-annealed 75% N_2 75 nm Al-CNx anode at current densities of 0.065 (blue) and 0.13 (green) mA/cm^2. For both current densities cycling was performed for 100 cycles each with charge/discharge times of 500 seconds. Cycles have been offset in figure b to overlap the curves on the same time scale.

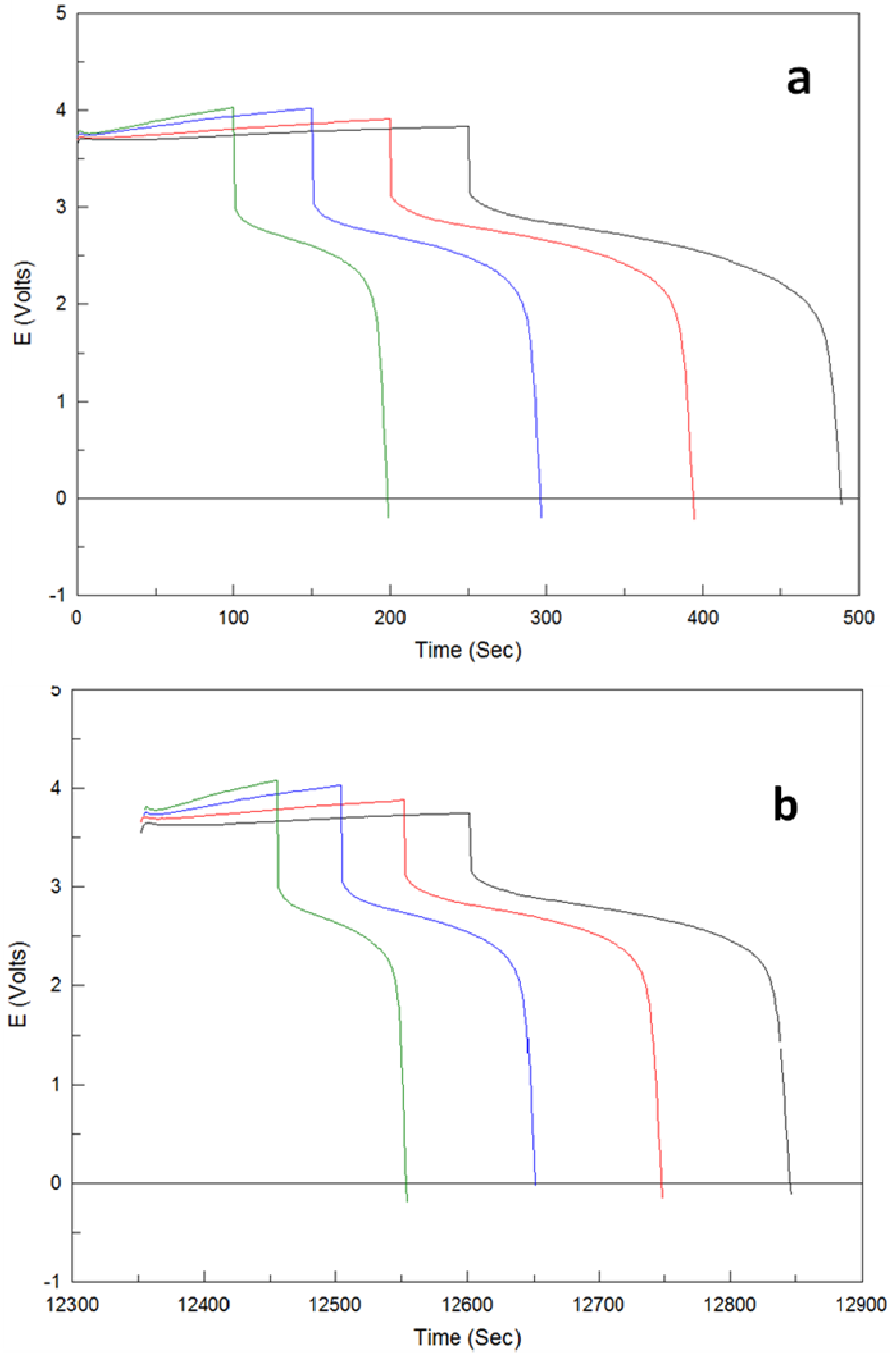

Fig. 4-7-23: (a) Initial and (b) middle battery galvanic cycles of sample BAT5 with a solid polymer electrolyte, $LiFePO_4$ cathode and a non-annealed 75% N_2 75 nm Al-CNx anode at current densities of 0.32 (black), 0.46 (red), 0.59 (blue) and 0.65 (green) mA/cm^2. Charge/discharge times of 250, 200, 150 and 100 seconds each respectively. Cycles have been offset in figure b to overlap the curves on the same time scale.

We note a few interesting features here in these latter cycle sets of BAT5, all indicative of stable and improved performance at high current densities. Firstly it would appear that the IR drop progressively increases with current density going from 0.32 mA/cm^2 (black) to 0.65 mA/cm^2 (green) (**Fig. 4-7-23**). When dividing by the current density the resistance will actually keep further decreasing until the 0.46 mA/cm^2 set (red), where it will approximately remain constant even when the current density is further increased to 0.59 mA/cm^2 (blue) and 0.65 mA/cm^2 (green) (**Fig. 4-7-21**). Secondly we note that even at these higher current density sets the secondary diffusion-limited discharge process does not appear after the main discharge plateau. In the experiment with constant charge/discharge times and an identical non-annealed 75% N_2 Al-CNx anode (BAT2) this secondary process was readily apparent by the 0.32 mA/cm^2 set (**Figs. 4-7-8, 4-7-10 b**). Therefore, the CE of the main discharge plateau for BAT5 rises above 90%, which is the highest reversibility observed in any battery prototype tested in this chapter (**Fig. 4-7-21**).

The absence of additional phase formation at higher current densities is consistent with the CE and R trends that show minimal change in the last three sets (**Figs. 4-7-20, 4-7-21**). It is also consistent with the data at the lower current densities where the cycle features (**Fig. 4-7-19**), CE (**Fig. 4-7-20**) and R (**Fig. 4-7-21**) trends suggest that most of the new phase growth occurs during that time. Overall, the restriction of intermetallic phase growth by proportionally decreasing the charge/discharge times, coupled with the volume change containment and improved conductivity offered by the combined SPE and CNx layers, results in a stable charge/discharge response at current densities that significantly surpass the previous battery experiments. There are no plateau potential jump events, degradation of coulombic efficiency or sharply elevated resistance that would be characteristic of battery failure. The improved regularity of BAT5 due to limited and controlled growth of the porous structure is also demonstrated by the SEM and EDX results. A summary of the average coulombic efficiencies of the main discharge plateau of the five battery samples presented in this chapter is shown in **Table 4-7-24**.

Table 4-7-24: The average coulombic efficiency of the main discharge plateau for battery tests with a solid polymer electrolyte, $LiFePO_4$ cathode and different anode materials. The anodes are bare GF Al oxide removed (BAT1), non-annealed 75% N_2 75 nm Al-CNx (BAT2, BAT5), annealed 75% N_2 75 nm Al-CNx (BAT3), non-annealed 25% N_2 75 nm Al-CNx (BAT4).

Current Density (mA/cm^2)	BAT1	BAT2	BAT3	BAT4	BAT5
0.016	-	-	-	-	47.4
0.033	77.7	64.1	77.9	45.7	81.3
0.065	84.1	76.4	88.5	78.5	84.9
0.13	87.0	86.8	90.2	84.3	90.7
0.32	Failed	54.1	Failed	Failed	92.0
0.46	-	-	-	-	92.1
0.59	-	-	-	-	92.2
0.65	-	-	-	-	91.2

4.7.2 SEM Images

Shown in **Fig. 4-7-26** are SEM images at low magnification (100x) of the center area of the five battery anodes: bare GF Al (BAT1), non-annealed 75% N_2 Al-CNx (BAT2), annealed 75% N_2 Al-CNx (BAT3), non-annealed 25% N_2 Al-CNx (BAT4) and non-annealed 75% N_2 Al-CNx (BAT5) after galvanic cycling and separation from the solid polymer electrolyte (SPE) and cathode. From these low magnification images we observe that the first four anodes with constant charge/discharge times for each cycle set (**Fig. 4-7-26 a-d**) show a fairly heterogeneous morphology, with relatively large morphological features (10 μm and more) and some debris present at the surface. However, the coverage is 100% suggesting relatively uniform reactivity across the anode surface. The fifth Al-CNx anode with proportionally decreased charge/discharge times (**Fig. 4-7-26 e**) showed a much finer structural feature and much smoother morphology; however, one can also see certain heterogeneity and in particular the presence of certain sub-regions that appear as lighter spots in the image.

Fig. 4-7-27 shows the center area of the same battery anodes at higher magnification of 1000x. Here for the first four anodes we see the features of the porous structure emerge with varied roughness (**Fig. 4-7-27 a-d**). For the last anode (**Fig. 4-7-27 e**) we observe that the lighter region shown previously in **Fig. 4-7-26 e** is actually an overlaying film on the right, while the region on the left contains the fine porous structure. No evidence of systematic cracking of the intermetallic structure or pulverization that may cause battery failure appears in these first two sets of SEM images. Surveying across the entire area of each anode surface also did not reveal such cracking features. There was some local variation in morphology such as small hills or pits, but closer inspection still revealed a porous structure in all cases.

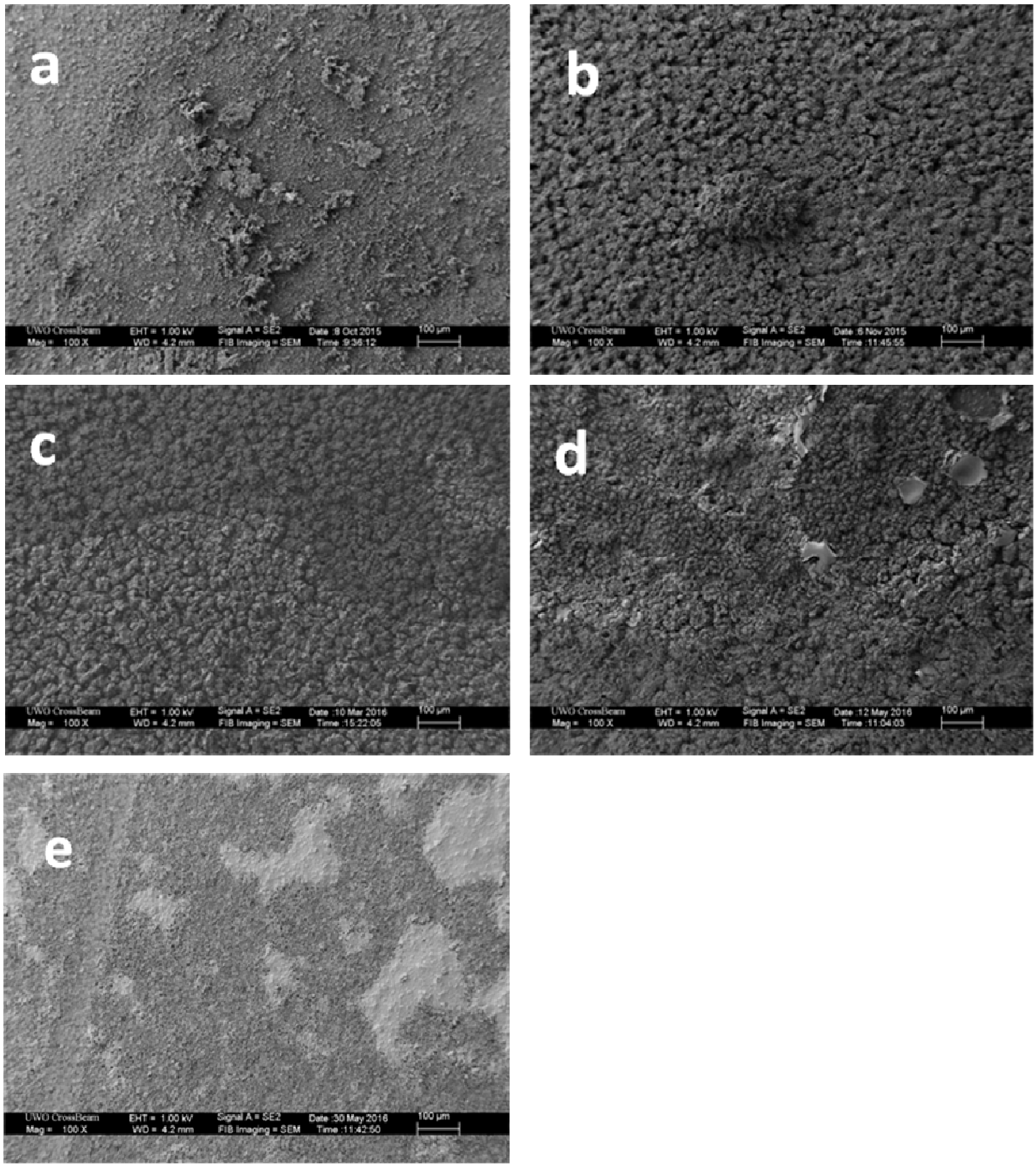

Figure 4-7-26: SEM images of center area for battery anodes (a) bare GF Al (BAT1), (b) non-annealed 75% N_2 Al-CNx (BAT2), (c) annealed 75% N_2 Al-CNx (BAT3), (d) non-annealed 25% N_2 Al-CNx (BAT4), (e) non-annealed 75% N_2 Al-CNx (BAT5) after galvanic cycling followed by separation from the solid polymer electrolyte and cathode. Magnification of 100x.

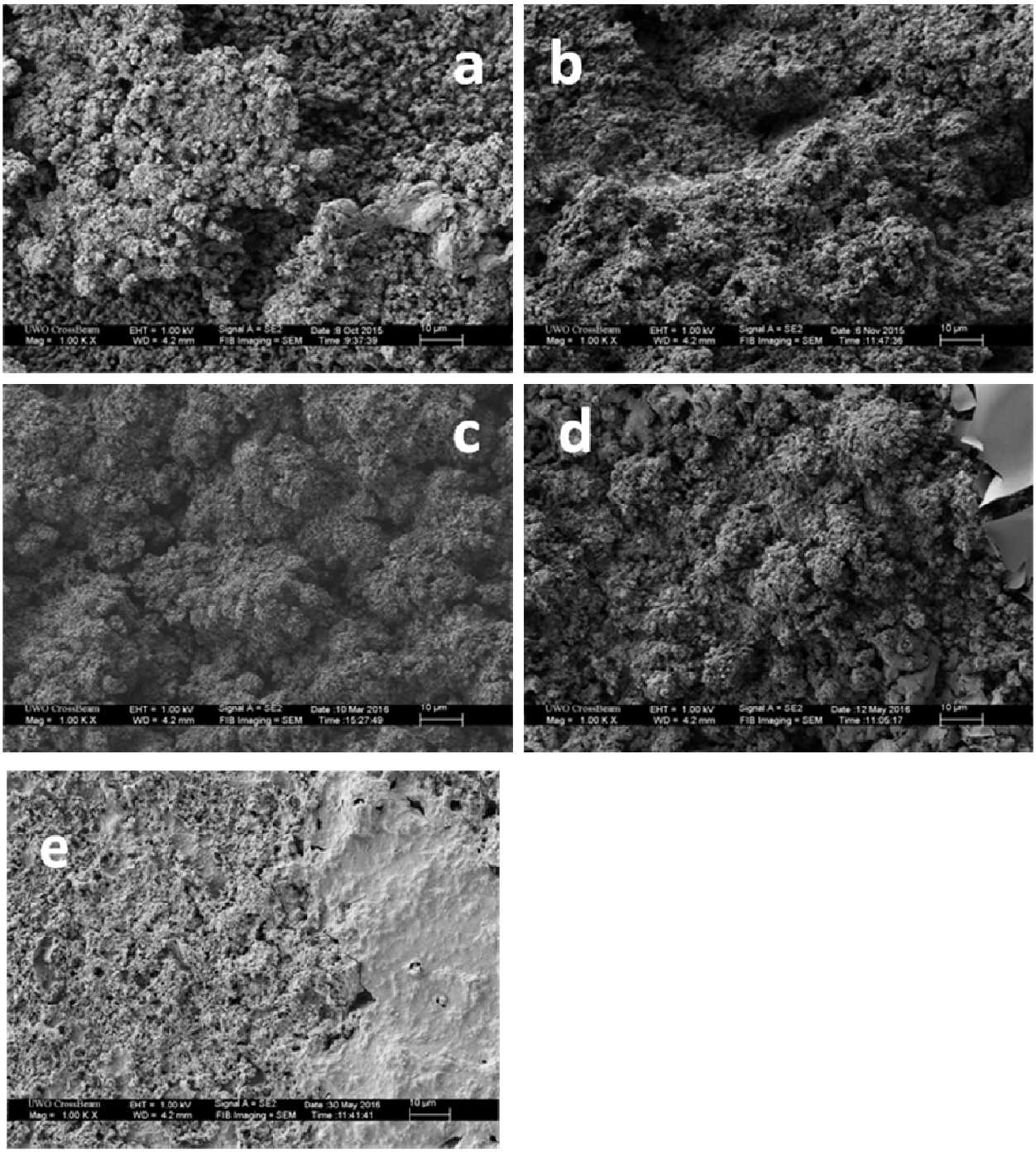

Figure 4-7-27: SEM images of center area for battery anodes (a) bare GF Al (BAT1), (b) non-annealed 75% N_2 Al-CNx (BAT2), (c) annealed 75% N_2 Al-CNx (BAT3), (d) non-annealed 25% N_2 Al-CNx (BAT4), (e) non-annealed 75% N_2 Al-CNx (BAT5) after galvanic cycling followed by separation from the solid polymer electrolyte and cathode. Magnification of 1000x.

Fig. 4-7-28 shows the center area of the battery anodes at a yet higher magnification of 10000x. In general we were not able to obtain SEM images beyond this magnification due to excessive surface charging. Here at this highest magnification we immediately observe several important details. In the first three anodes (**Fig. 4-7-28 a-c**) we can see that the rough porous structure observed in the lower magnification images actually has a very specific heterogeneous morphology consisting of fibrous or disc-shaped pieces. This is especially pronounced in bare GF Al sample (BAT1) of **Fig. 4-7-28 a.** The presence of CNx coatings (**Fig. 4-7-28 b-c)** partially suppressed this feature but it is still evident in some areas of the images. In the fourth anode (BAT4) these features are not observed (**Fig. 4-7-28 d**) and the structure generally resembles that found in bare Al anodes in liquid half-cell experiments. On the contrary, the image of **Fig. 4-7-28 e** (BAT5) clearly shows the "honeycomb" fine porous structure that was noted before in some Al-based anodes, especially, those containing CNx films and thin sputtered Al layers (Ch. 4.5.2) and was attributed to formation of fine porous nanostructure by controlling the volume change. Obviously, the same situation is observed here. Unlike other samples. the BAT5 sample was cycled with decreasing the cycle duration at high current densities so that to maintain the lithiation charge constant. Therefore, after the initial conditioning and formation of LiAl phase at low current densities, no further LiAl growth was permitted and the sample was restricted to lithiation-delithiation of the LiAl phase already formed previously resulting in the fine honeycomb morphology.

Following the same argument, the disc-shaped features found in **Fig. 4-7-28 a-c** should be related to uncontrolled growth of LiAl phase at high current densities right before anode failure. They cannot comprise CNx film remnants because they are observed in **Fig. 4-7-28 a** (BAT1, bare GF Al anode), and they are also observed in the "Al edge" areas (no CNx present originally). They may be envisioned as "blown-up" honeycomb pores evident in **Fig. 4-7-28 e** and noted in other samples before as a result of excessive and not contained volume change. Alternatively, since they were never observed in liquid-cell experiments, they may be formed as a result of penetration of the growing LiAl phase into the voids between the fibers of the solid polymer electrolyte.

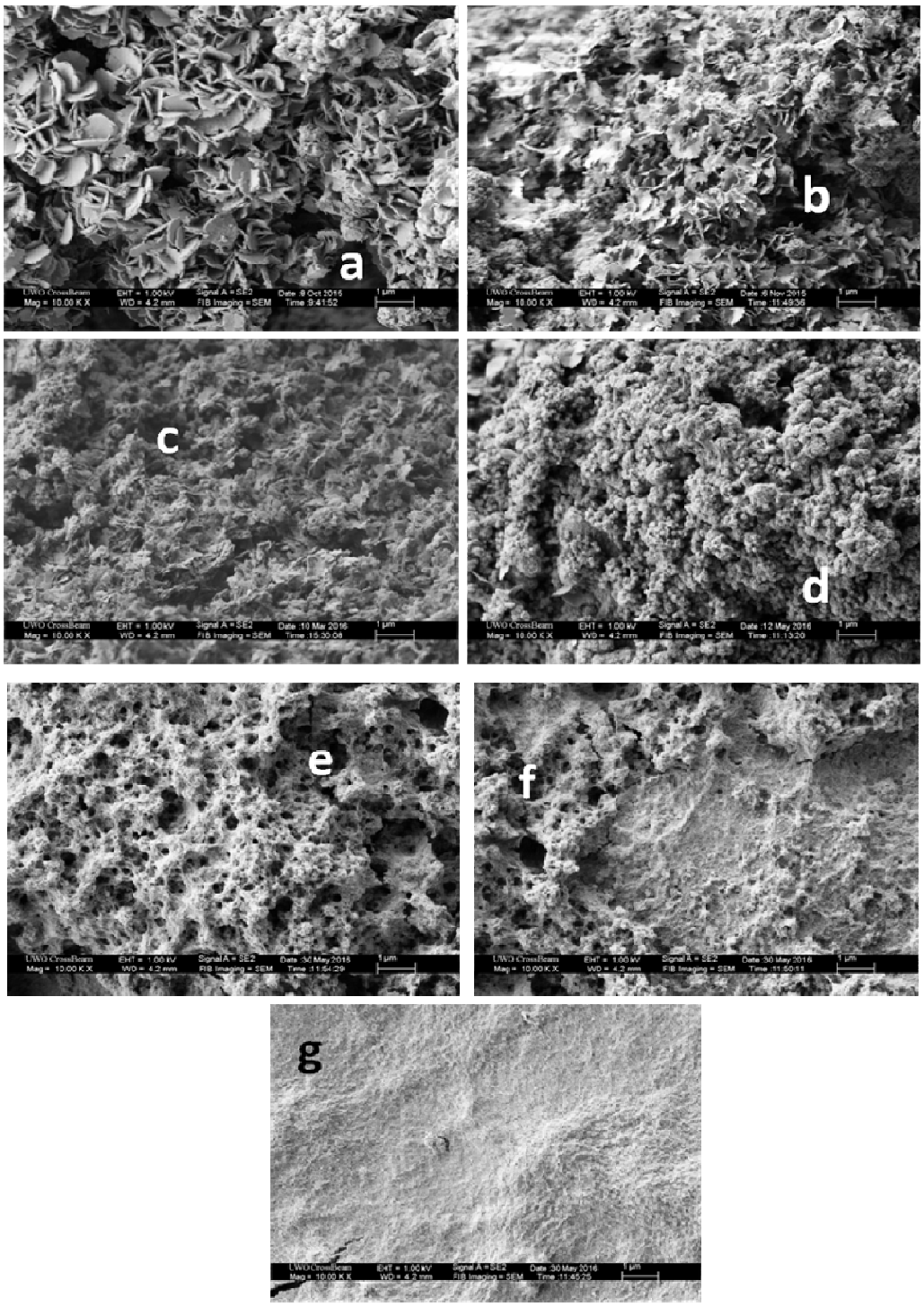

Figure 4-7-28: SEM images of center area for battery anodes (a) bare GF Al (BAT1), (b) non-annealed 75% N_2 Al-CNx (BAT2), (c) annealed 75% N_2 Al-CNx (BAT3), (d) non-annealed 25% N_2 Al-CNx (BAT4), (e-g) non-annealed 75% N_2 Al-CNx (BAT5) after galvanic cycling followed by separation from the solid polymer electrolyte and cathode. Magnification of 10000x.

A question still remains as to where the CNx is located after lithiation-delithiation in battery tests with Al-CNx anodes. For the three Al-CNx anodes with constant charge/discharge times (BAT2 - BAT4) SEM imaging of the CNx (center) areas did not reveal any fine morphological features that may correspond to cracked CNx film remaining after cycling. This suggests that any CNx film remaining after battery cycling must be located deeper, possibly buried within or beneath the porous structure close to the bulk Al. This is distinct from both 4x8 and failure experiments of Al-CNx anodes in a liquid half-cell (Ch. 4.4) where CNx film remnants were readily identified on top of the porous structure after cycling (**Fig. 4-4-24 a**).

It was also revealed using EDX analysis that the flatter and lighter regions found in SEM image of non-annealed 75% N_2 Al-CNx (BAT5) sample of **Fig. 4-7-27 e** and also shown in higher magnification in **Fig. 4-7-28 g** are also in fact not CNx films that were somehow preserved at the electrode surface. Rather, it was found that these overlaying film features of image **Fig. 4-7-28 g** should correspond to intact SPE remaining on the anode after separation. Interestingly, this feature was not observed in other prototype samples. This indicates the important role that is played by SPE film in controlling the LiAl phase growth and conditioning the surface of the anode to form the advantageous honeycomb structure. In fact, the LiAl growth should happen inside the voids of the solid polymer electrolyte, the latter acting as a scaffold containing excessive phase growth. However, the growth should be performed at low current density; otherwise the rate of growth becomes too high for the SPE to contain and more heterogeneous and disorder morphologies are formed, eventually leading to uncontrolled growth and failure of the anode.

To investigate how the Al-CNx anode morphology would appear with very limited lithiation-delithiation reactivity we prepared another battery sample BAT6, identical to BAT2 and BAT5. In this sample galvanic cycling was only performed at a low current density of 0.016 mA/cm^2 for 8 cycles, after which the anode was separated with the same procedure as previous battery samples and then subjected to surface analysis. Shown in **Fig. 4-7-29** are SEM images of the BAT6 anode after cycling within the CNx **(a)** and Al

edge **(b)** areas. The CNx area reveals a highly heterogeneous morphology with significant amounts of intact CNx film still remaining on unreactive Al **(a)**. It appears that the intermetallic alloy just starts to form and break through the coating. The CNx film that remains at a higher elevation then surrounds these porous alloy regions. In the Al edge area outside of the CNx area we also see limited reactivity **(b)**. Here most of the surface will be dominated by unreactive Al substrate and its typical etching pattern at a lower elevation relative to the isolated porous regions containing intermetallic alloy. However, even now, one can see that the reacted LiAl phase starts to show the characteristic honeycomb morphology. This fact highlights the importance of both CNx and SPE scaffolds in forming the honeycomb structure. The CNx film is likely to control the phase formation at very early stages. Then its gets buried under the growing LiAl phase, which is now controlled not by CNx but by SPE layer. This is confirmed by the results of liquid cell experiments of Ch 4.4 which demonstrated that CNx at first shows a very positive effect on the reversibility and coulombic efficiency; however, without SPE, this effect mostly disappears after 20-30 charge-discharge cycles (**Figs. 4-4-9, 4-4-10**).

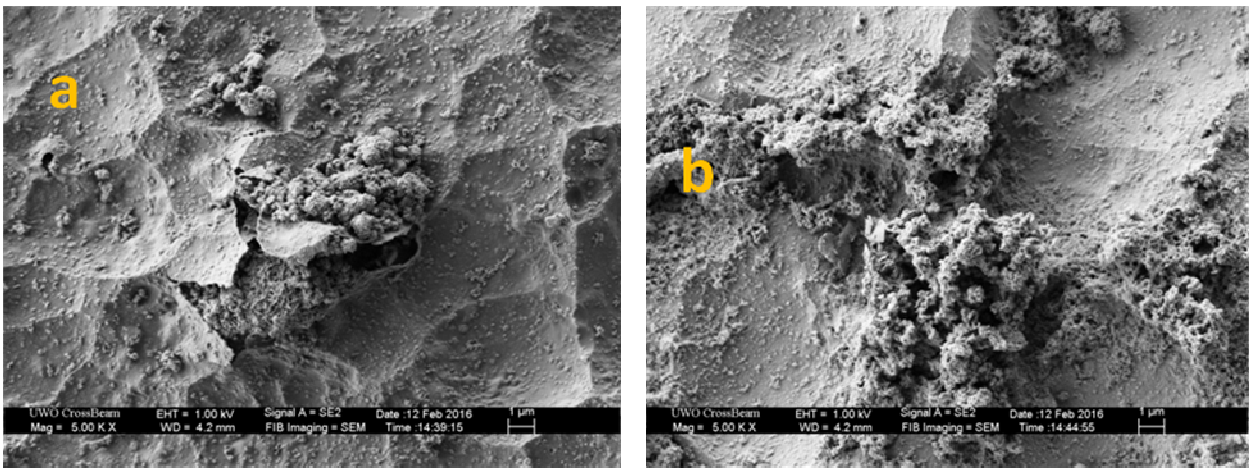

Figure 4-7-29: SEM images of (a) Center area (b) Al edge area of non-annealed 75% N_2 Al-CNx battery anode (BAT6) after limited galvanic cycling at a current density of 0.016 mA/cm^2 for 8 cycles followed by separation from the solid polymer electrolyte and cathode. Magnification of 5000x.

4.7.3 EDX Composition Chart

Due to contamination of the anode surface from SPE and cathode material remnants upon separation of the anode EDX analysis would likely be of limited usefulness. However we still attempted EDX analysis on the Al-CNx anodes separated from battery samples BAT2 - BAT6 in an effort to determine the location of the CNx film after cycling near the center of the anode surface. For comparison EDX analysis was also performed in the cycled Al area near the edge of the anode where there was no CNx film present originally.

Shown in **Table 4-7-30** is an EDX composition chart in atomic % for the various cycled areas of these anodes. The labels "CNx area" and "Al edge area" denote the areas where the CNx film was present or absent respectively before testing. As expected all porous regions considered as reactive have noticeable contamination from SPE and cathode materials. This is observed in the copper and titanium signals as well as the significantly elevated oxygen content approaching or exceeding 50%. Flat regions considered as unreactive or of limited reactivity have a smaller proportion of these elements. Carbon content will come from a possible combination of CNx film remnants, propylene carbonate, polyethylene oxide (PEO) as well as carbon black and polyvinylidene fluoride (PVDF) binder materials from the cathode. Phosphorous and fluorine content will arise from the $LiPF_6$ salt in the SPE remaining after separation. C, O, F and P signals could also arise from the products of SEI layer present on or within the anode. The small amount of silicon detected should be due to a combination of silicon carbide paper used for polishing of electrode substrates, and as an impurity in the GF Al metal substrate itself. Lithium content cannot be tracked due to the overlap of its low energy x-rays with the baseline peak close to 0 eV.

Table 4-7-30: EDX composition chart of cycled center (CNx) and Al edge (Al) areas for battery anodes after being subjected to battery testing experiments and then separated from the cell assembly. Spectra data was collected at a column voltage of 7 kV for 50 seconds at 1000x magnification.

		Atomic %								
Anode	**Cycled Area**	**C**	**N**	**O**	**F**	**Al**	**Si**	**P**	**Ti**	**Cu**
BAT2	(a) CNx, porous	7.52		51.60	2.13	15.69	0.38	0.38	7.84	14.47
	(b) Al, porous	5.54		54.74	0.38	8.07	1.39	0.31	10.77	18.80
BAT6 *single cycle set	(c) CNx, porous	11.06	0.34	48.37	8.29	20.54	0.14	0.92	8.47	1.87
	(d) CNx, flat	25.72	8.56	7.92	1.19	54.43	0.10	0.08	1.87	0.12
	(e) Al, porous	2.25		50.40	5.36	13.78	2.88	2.08	17.11	6.14
	(f) Al, flat hole	0.78		3.25	0.78	93.66	0.17	0.18	0.89	0.29
BAT3	(g) CNx, porous	7.32		55.89	0.50	11.76	0.08	0.18	3.55	20.72
	(h) CNx, flat hole	15.78	1.41	18.09	0.96	51.72	0.22	0.51	7.23	4.08
	(i) Al, porous	2.77		61.50	3.35	24.67	0.14	0.28	2.84	4.45
BAT4	(j) CNx, porous	6.39		49.40	4.97	8.42	0.02	0.30	10.87	19.64
	(k) CNx, flat hole	31.05	4.10	37.39	8.41	14.52	0.05	1.23	3.51	3.25
	(l) Al, porous	3.56		45.74	2.87	9.41	0.02	0.06	10.00	28.34
	(m) Al, flat hole	2.27		43.02	4.88	40.49	0.03	0.33	6.78	2.21
BAT5	(n) CNx, porous	1.74		64.79	1.14	23.54	0.02	0.24	7.94	0.60
	(o) CNx, flat hole	23.39	11.15	16.10	0.18	48.11	0.13	0.13		0.81
	(p) CNx, flat film	1.49		65.82	1.18	22.74	0.06	0.27	7.88	0.56
	(q) Al, porous	1.98		56.57	0.99	32.51	0.03	0.26	7.40	0.27
	(r) Al, flat hole	4.90		6.87	0.10	84.52	0.05	0.07	3.49	0.01

In the non-annealed 75% N_2 Al-CNx anode of sample BAT2 we were unable to detect nitrogen anywhere throughout the area where the film was present originally **(a)**. Attempting a variety of column voltages and acquisition times did not yield a different result. Overall the composition of this porous "CNx area" resembles that of the porous "Al edge area" outside **(b)**. The absence of nitrogen content here confirms our assessment from the SEM images that any CNx film remaining after cycling in this fully reactive region must be located much deeper within or buried beneath the intermetallic alloy. Moving onto the non-annealed 75% N_2 Al-CNx anode of BAT6 the compositions here confirm the limited reactivity both in the CNx and Al edge areas seen in the SEM images. For the CNx area the porous composition **(c)** resembles that of BAT2 **(a)**. In contrast the flat regions suspected to be intact CNx film show a strong nitrogen signal of 8.5% **(d)**. Moving to the Al edge area of BAT6 the porous region in **(e)** is similar to **(c)** while the flat region in **(f)** appears to be mostly unreactive Al substrate. In the annealed 75% N_2 (BAT3) and non-annealed 25% N_2 (BAT4) Al-CNx anodes we were initially unable to locate nitrogen anywhere in the CNx areas **(g,j)**, with the composition obtained being similar to the respective Al edge porous areas **(i,l)**. However further investigation of the CNx areas in the BAT3 and BAT4 anodes did reveal a few holes that could only be located using the higher 7 kV column voltage used in EDX analysis. Acquiring spectra here did reveal small nitrogen signals of 1.4% (**h**) and 4.1% (**k**) respectively, as well as significantly higher carbon signals indicative of CNx. Together with the higher Al content and lower O content suggests that these holes are spots of limited lithiation-delithiation reactivity, compared to the more unreactive flat regions in the CNx area of BAT6 **(d)**.

The SEM imaging of the non-annealed 75% N_2 Al-CNx anode with proportional charge/discharge times (BAT5) suggested that the large overlaying film portions observed within the CNx area may consist of intact CNx remaining after lithiation-delithiation (**Figs. 4-7-27 e, 4-7-28 g**). The EDX analysis here ("CNx flat film") did not reveal any nitrogen signal regardless of the column voltage used (**p**). Instead the composition of these film regions resembled the porous regions ("porous") located nearby that were not overlapped by this film (**n**). This suggests that the overlaying film

features are instead intact solid polymer electrolyte remaining after separation of the anode. CNx remaining after lithiation-delithiation was located in the "flat hole" regions (**o**) between the porous honeycomb regions away from these overlaying film features. Within these flat hole regions the Al signal is also very strong with much lower oxygen signal, suggesting very limited lithiation-delithiation reactivity. These regions of partial/limited reactivity were also observed in the Al edge area of BAT5 (**r**). Overall the larger proportion of "flat hole" regions (relative to porous) within the CNx and Al edge sub-areas in BAT5, suggests that the proportional conditioning approach essentially results in significantly less reactivity of the anode surface resulting in significantly less formation of the porous structure relative to BAT2 - BAT4. This may help explain why it was more difficult to locate these "flat hole" areas with nitrogen signal within the CNx areas of those BAT2 - BAT4 samples compared to BAT5. We also note here that unlike the other samples the copper content was very low throughout the entire BAT5 anode regardless of where EDX analysis was performed (**n-r**). This can be explained by the fact that this sample actually was the only one that did not fail before examination. It is also consistent with what we visually observed when separating away the cathode after cycling of BAT5. The entire conductive bound assembly of the cathode was still intact and uniform in the BAT5 sample after separation, unlike samples BAT2 - BAT4 where it was significantly more disordered and heterogeneous. The contrast in morphological features and copper content suggests that that samples BAT2 - BAT4 may have failed at higher current densities due to pulverization of cathode active materials or short-circuiting through the SPE layer. In either case, high local currents would be observed right before failure that were likely to disturb and break down the SPE layer resulting in electrical and mechanical contact between the anode and cathode materials. Therefore the proportional conditioning approach used in BAT5 also appears to be beneficial towards structural stability of the cathode materials.

Chapter 5

5 Discussion

5.1. Mechanism of lithiation-delithiation and formation of the porous nanostructure in bulk Al anodes

5.1.1. Structural changes at the surface of Al anodes upon lithiation-delithiation

We will first describe the mechanism of lithiation-delithiation and formation of the porous structure in the context of a 4x8 experiment with a bare Goodfellow (GF Al) anode. Lithiation initially occurs with nucleation of α-LiAl intermetallic phase at surface sites of the bulk crystalline (metal) Al that has a high density of mobile dislocations [2]. At first, α-LiAl phase is formed that is considered a substitutional solid solution of Li in an FCC lattice of Al. The lattice constant for α-LiAl (4.01 Å) is practically the same as for Al itself. It has the same FCC structure. The only difference is that we have now Li, not Al, in the corners of the unit cell. As lithiation continues, additional sites of α-LiAl will be nucleated on the surface of bulk Al. At the same time, the increased lithium concentration at the previous sites of α-LiAl will cause crystallization of α-LiAl to the β-LiAl phase, which has an accompanying lattice expansion from 4.01 to 6.37 Å [2]. This is the origin of the volume change in this material. The β-LiAl phase is stable at room temperature and has the crystal structure of NaTl, also known as Zintl phase (diamond-like lattice for Al with Li positioned in the voids of the lattice) [10]. Therefore the initial lithiation of bulk Al can be considered as formation of isolated regions of intermetallic alloy. Our SEM data suggests that this is indeed the case at early stages of lithiation during the first few cycles of lithiation-delithiation.

Electrochemically, when sufficient amount of β-LiAl phase is formed, the electrochemical cell potential will exhibit a flat charging plateau according to the Nernst equation. The potential will stay stable with further formation of β-LiAl because the activity of an individual phase does not change with its amount. Usually, the Gibbs phase rule is invoked in the literature and it is stated that the independency of the potential during the charging is due to the presence of two phases (the number of the thermodynamic degrees of freedom in this case is zero). However, strictly speaking, this is not necessary because of all phases that may be present at the electrode surface, only one will be potential determining (the one with the highest exchange current).

Upon switching to the discharge current initial delithiation will solely occur from these isolated porous intermetallic alloy regions at or near the anode surface. This process will leave them essentially as isolated Al regions that are depleted of lithium. Importantly, delithiation should be accompanied by a decrease in the phase volume so that these Al regions will have to develop voids or pores. The delithiation will occur through the same system of α and β-LiAl phases producing a discharge plateau [2]. Volume changes occurring in the first lithiation and delithiation steps will destroy some SEI layer that was formed both on unreacted bulk Al regions and these reactive porous regions [1]. Before the second lithiation occurs additional SEI layer will form where there is exposed Al material (in either form) after the first delithiation.

The second lithiation that follows forms more intermetallic alloy again inside the previously depleted porous Al regions from the first cycle. It will also form new nucleation sites at new portions of unreactive Al sites that did not undergo alloying previously. With increased nucleation of intermetallic alloy at the surface sites in the second lithiation some lithium will penetrate further into the bulk of the anode. This will progress as a diffusion-driven front of α-LiAl (a diffusing solid solution) through movement of dislocations. In other words the diffusion front of α-LiAl will be surrounded by a high density of mobile dislocations. This reaction front was visualized by in-situ TEM measurements both initially at the surface and later towards the bulk of anode materials and has been described as the "medusa zone" [3]. For SnO_2 nanowire

anodes the dislocation density of the medusa zone during lithiation-delithiation has been estimated to be ~ $10^{17}/m^2$. This is more than two orders of magnitude greater than what is naturally observed in heavily strain-hardened face-centered cubic metals themselves such as bulk Al. The second delithiation will occur both from surface sites of α and β-LiAl as well as to some degree from lithium that has been incorporated into the α-LiAl solid solution further in the bulk of the anode [2]. It will be again accompanied by negative volume change leaving behind more pores and/or voids.

Eventually, continued lithiation-delithiation will cause saturation of all surface sites of the original bulk Al, resulting in the entire anode surface becoming covered in a porous structure either consisting of intermetallic alloy or Al that has been depleted of lithium. Therefore there will not be any more unreacted Al near the surface. As these processes continue, more lithium will react and diffuse to progressively deeper portions of the anode bulk causing more crystallization of α-LiAl to β-LiAl there. Overall, the porous structure will become thicker by growing into progressively deeper regions of bulk Al. In the end we produce a thick (**Fig. 4-6-3**), highly porous (**Fig. 4-1-13 c,e**) structure filled with SEI layer (**Fig. 4-6-2**) compared to the original bulk GF Al (**Fig. 4-1-13 a**).

It is important to realize that as soon as all electrode surface becomes covered with the new phase, any subsequent charging cycle will start with lithiation of the previously formed and depleted intermetallic phase. Only if the charge applied to the electrode exceeds the capacity of the phase formed previously, new portions of the LiAl phase will be formed, resulting in further volume change. However, if the charge does not exceed the capacity, the volume changes associated with lithiation-delithiation will be confined exclusively within the pores or voids of the intermetallic nanostructure and result in no change in the overall dimensions of the anode. This condition will be fulfilled if the efficiency of extraction of Li during the delithiation cycle is high, and if no or very little Li diffuses into the bulk Al during the charging step. These conditions seem to be easy to fulfill if sufficient amount of ordered and reactive intermetallic phase is formed, which is structurally and mechanically stable and readily supports electrochemical reactions both on its surface and inside the pores/voids. If such a phase is formed, it can be cycled

without changing the overall dimensions of the anode and thus without any damage to electrolyte or the battery assembly, short-circuiting, etc., the problem that precludes the adoption of Al anodes in practical Li ion batteries today. Finding the conditions to form such a phase is one of the goals of this thesis.

The importance of proper electroformation and growth of the porous intermetallic phase is highlighted by our half-cell failure experiments. In this case the anode is immediately subject to a high current density. Therefore the porous structure formation and growth is rapid with immediate extreme volume changes compared to the 4x8 experiments. For a brief time (around 20 cycles) the system behaves as expected with a rapid decrease in plateau separation (resistance) and increase in coulombic efficiency (**Figs. 4-1-10, 4-1-11**). However, beyond that point, signs of failure appear quickly, in particular with the plateau separation rapidly increasing outside of acceptable tolerances. The reason for anode failure is likely pulverization (cracking) of the porous structure that had a higher degree of disorder. This highlights the need to use low current densities to form more stable and regular intermetallic phase on the surface of Al anode for it to be able to withstand prolonged cycling and high charging-discharging rates.

To visualize the progression of the formation of the porous structure let us consider the internal resistance (R) associated with lithiation-delithiation that is calculated from the charge-discharge plateau separation of a galvanic cycle divided by the current density. Shown in **Fig. 5-1-1** is the internal resistance (Ω cm^2) of the GF Al anode GF1 (oxide removed) at the four current densities of the 4x8 experiment from **Ch. 4.1**. In particular at the first set (black curve) we observe a steady marked drop in resistance with each cycle. In the second (red) and third (blue) sets the initial resistance further decreases and the change over time is more gradual.

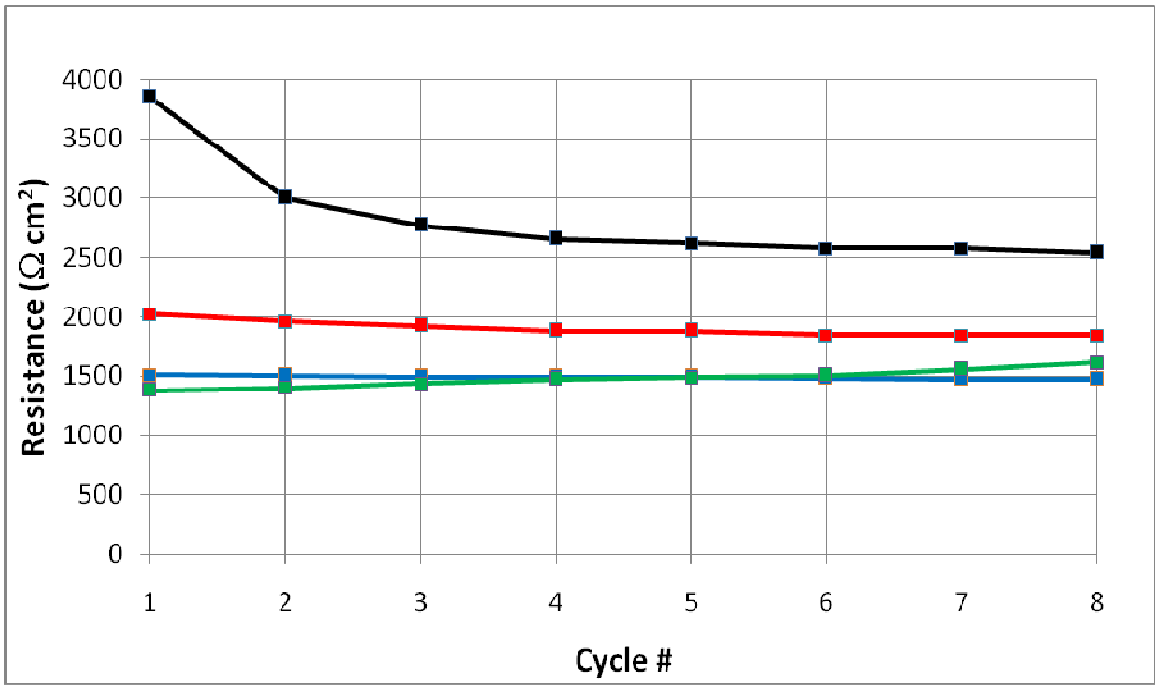

Figure 5-1-1: Internal resistance calculated from the charge-discharge plateau separation of galvanic cycles for bare GF Al anode GF1 (oxide removed) from **Ch. 4.1** at current densities of 0.13 (black), 0.25 (red), 0.5 (blue) and 1 (green) mA/cm^2.

This trend can be understood by considering the following equation (Eq. 1):

$$R = \rho \frac{d}{A}, \qquad (1)$$

where $\boldsymbol{\rho}$ is the specific resistivity, $\boldsymbol{d}$ is the distance between electrodes and $\boldsymbol{A}$ is the contact surface area. If we assume that $\boldsymbol{\rho}$ and $\boldsymbol{d}$ remain constant we must conclude that a decrease in resistance must be attributed to an increase in the contact area $\boldsymbol{A}$. As growth of the porous structure occurs across the original Al anode surface this effectively increases the contact area of this structure which decreases resistance. Therefore the resistance based on the charge-discharge plateau separation allows us to track the formation of the porous structure in the context of the lithiation-delithiation mechanism described previously. The rate of change in coverage (contact area $\boldsymbol{A}$) of the structure is

likely fastest in the first set (black), resulting in the fastest decrease of R (**Fig. 5-1-1**). In the second set (red) the formation continues so the initial R is even lower in the first cycle. However the relative change in area is less during this second set, producing a smaller decrease over time in R. In the third set (blue) R is again initially decreased but the decrease over time is very minimal, because the porous structure has likely covered most of the original Al anode area. This is further supported by the initial R of the fourth set (green) appearing only slightly smaller. In this fourth set the porous structure should now cover the entire original anode surface. As a result there is no further change in contact area. Additional growth will now only occur vertically using previously unreacted bulk Al material located below the porous structure. This process will noticeably increase the internal stresses in the anode. Furthermore there are kinetic (diffusion) limitations to consider for lithium transport that start manifesting themselves at this highest current density, to be discussed in detail later. Together these two effects cause the resistance to now increase over time in the fourth set.

Before we continue it is worth briefly discussing the role of increased oxide content in formation of the porous structure. In the literature in-situ TEM studies have revealed that the surface oxide in Al nanowire anodes is lithiated into a Li-O-Al layer [6]. This process is irreversible and occurs first at more positive potentials than the lithiation onset for LiAl formation. In the electrochemistry this irreversible lithiation of the oxide is typically associated with initially poor reversibility (coulombic efficiency) as well as increased SEI formation. Both of these electrochemical features are consistent with what we observed in our data in both GF Al and MC Al systems with increased oxide content. In the initial CVs the effect of oxide is readily apparent in increased cathodic currents for SEI formation (**Figs. 4-1-2, 4-2-1**). In the 4x8 galvanic cycles at lower current densities there is initially a detrimental effect on coulombic efficiency that gradually becomes minimal and eventually disappears at the cycles at higher current densities (**Figs. 4-1-7, 4-2-6**). Therefore the native oxide is initially detrimental for reversibility of both bulk GF Al and MC Al anode systems, likely because it is irreversibly lithiated, but this effect quickly disappears as cycling continues. In terms of porous structure formation and growth we did observe increased heterogeneity for both anode systems with increased oxide content

(**Figs. 4-1-13 f, 4-2-12 f**), as well as evidence of limited reactivity (**Fig. 4-1-13 d**). Overall we conclude that it is best for the native oxide to be removed from bulk Al anodes through a combination of polishing and etching treatment, as well as minimizing oxide re-growth prior to and during cycling experiments.

5.1.2. Mechanical Stresses of Lithiation-Delithiation and Volume Changes

To better understand the limitations of the Al anodes that are associated with continuous pronounced volume changes during their lithiation-delithiation, we consider both the contribution of mechanical instabilities within the active material, and also the mass transport limitations of lithium in the intermetallic phases. First we consider the internal stresses that arise during lithiation/delithiation. We focus our discussion of these stresses and their effects in the context of a crystalline structure of bulk Al, and the formation and growth of intermetallic phases within it.

Lithiation-delithiation and the associated lithium-metal alloy formation and dissolution occurs through movement of dislocations and a change in the lattice dimensions (lattice parameters) [2]. To accommodate such changes, a so-called “medusa zone” is formed during lithiation near the lithiation front that contains an extremely high density of mobile dislocations and produces a dislocation-induced stress (DIS) [4], which is the driving force for the structural change and expansion. In the initial stages of lithiation-delithiation, the lithium incorporation is largely confined to the anode surface. Therefore, initially, the DIS is at maximum near the surface of the anode. As lithiation/delithiation continues lithium will accumulate to progressively deeper levels in the anode bulk. Therefore, the intermetallic alloy formation will also progress towards the bulk of the anode. Since lithium transport occurs through the movement of dislocations, the DIS will also progress further into the bulk of the anode. This will relatively decrease the DIS near the surface and increase it towards the bulk of the anode. Eventually a steady state should be reached in which the DIS near the surface and in the bulk is similar.

The processes of lithiation-delithiation will also create steep Li-concentration gradients within the host material [5]. Therefore at any instant, adjacent regions within the same active material may have different crystal phases (structures) and different molar volumes. Furthermore, these different co-existing phases would possess different elastic properties. The interaction and contact between such regions within a continuum leads to mismatch induced stress development through further generation of dislocations. These differences depend on transport limitations that are associated with Li diffusivity and current density. Therefore they are expected to be more severe at higher charge/discharge current densities.

The accumulation of these internal stresses during repeated lithiation-delithiation events has profound effects both physically and in terms of the electrochemical results. Physically the strain response can be described as elastic-plastic deformation occurring through the formation and propagation of cracks or voids within the active material [5]. After reactive saturation of surface sites the active material in our Al anode system would be considered primarily as the porous structure consisting of intermetallic alloy or Al that has been depleted of lithium. Localized cracking between adjacent regions of the porous structure will cause loss of electrical contact at the site of the crack. If cracking surrounds an entire portion of the porous structure that portion may lose complete electrical contact and be rendered inactive. This will usually be accompanied by the loss of mechanical contact as well. Overall this form of degradation has been termed 'pulverization' of active materials in the literature [6]. We readily observe such systematic cracking in the porous structure of our bulk GF Al and MC Al anodes when they are continuously cycled at a relatively high current density in a liquid half-cell environment **(Figs. 4-1-14, 4-2-13)**.

Electrochemically, in the continuing lithiation-delithiation of Al anodes, we observed increasing charge-discharge plateau separation over time (**Fig. 4-3-9**). Additionally we observed increasing drifting of charge/discharge plateau potentials within the same cycle, i.e. increased overvoltage. Both of these effects should be related to the accumulation of internal stresses that will then influence the thermodynamics of the electrochemical processes [7-9]. Lithiation-delithiation in the form of repeated alloying-dealloying phase

formation and dissolution produces internal stresses in the material. There are elastic and plastic energies associated with the elastic-plastic strain accommodation of the material towards these stresses. The elastic-plastic accommodation energy is an energy barrier against lithiation/delithiation. It increases the free energy of the material and decreases (makes more negative) the lithiation equilibrium (Nernstian) potential. The decrease of lithiation equilibrium (plateau) potential $\Delta E_{lithiation}$ can be determined from eq. 2 [9].

$$\Delta E_{lithiation} = E_o - E_{ce} = \frac{\Delta G^{elastic}_{lithiation} + \Delta G^{plastic}_{lithiation}}{nF} \quad (2)$$

where E_o is the theoretical (accommodation-free) equilibrium potential, E_{ce} is the lithiation equilibrium potential after consideration of the accommodation process during Li ion insertion, $\Delta G_{elastic\text{-}lithiation}$ and $\Delta G_{plastic\text{-}lithiation}$ are elastic and plastic accommodation energies during lithiation process, n is the number of electrons passed per atom of host material reacted and F is Faraday's constant. The volume changes during the Li ion extraction will also be accommodated by the elastic-plastic process [7-9]. Here the accommodation energy during Li ion extraction will increase the electrode potential (make it more positive, that is, increase the overvoltage). The potential increase during the delithiation process $\Delta E_{delithiation}$ can be determined from eq. 3 [9].

$$\Delta E_{delithiation} = E_{de} - E_o = \frac{\Delta G^{elastic}_{delithiation} + \Delta G^{plastic}_{delithiation}}{nF} \quad (3)$$

where E_{de} is the delithiation equilibrium potential after consideration of the accommodation process, $\Delta G_{elastic\text{-}delithiation}$ and $\Delta G_{plastic\text{-}delithiation}$ are elastic and plastic accommodation energies during delithiation process. Therefore the strain accommodation of internal stresses through elastic-plastic deformation consumes energy, which decreases the energy available for the phase transformations associated with lithiation-delithiation and increases the overvoltages with respect to stress-free material. In other words, the energy accommodation during elastic-plastic deformation of the electrode materials

decreases the lithiation equilibrium potential and increases the delithiation equilibrium potential, both with respect to the equilibrium potential under stress free conditions. Continuous cycling of Al anodes in the failure experiments produced an increase in the charge-discharge plateau separation. This should be attributed to accumulation of internal stresses according to this mechanism. As the stresses accumulate to a point when they exceed the mechanical strength of the material, mechanical fracture happens that is accompanied by sudden jumps in plateau potentials which decreased the separation (**Fig. 4-3-9**). This should relieve internal stresses and reduce the overvoltage and thus the plateau separations. Therefore it would be reasonable to assume that the jumps in the plateau potential observed in the continuous cycling indicate such mechanical fracturing events. Physically, they may correspond to cracking, or total pulverization of a portion of the active material. Overall, due to repeated fracturing events, the potential response that is observed over time during failure experiments has a serrated appearance (**Fig. 4-3-9**).

In the liquid half cell environment the entire electroactive area of the anode is directly exposed to the bulk electrolyte solution. As a result there is no external mechanical force which is being applied to the exposed area of the Al anode. This is an important feature to consider for several reasons. Firstly, the growth of the porous structure can progress indefinitely in terms of thickness because there is no external force suppressing the volume changes associated with its formation (there is no limit in the supply of Al from the bulk Al anodes). Secondly the absence of such an external compression force will allow less accumulation of internal stress before fracture and thus change the lithiation-delithiation potentials. Thirdly, the absence of such force may allow cracks that form to propagate uncontrollably in the porous structure, as well more heterogeneous dendritic growth to occur. In the extreme case this could result in a portion of the porous structure becoming separated and lost into the electrolyte.

Moreover, as the intermetallic structure develops and get thicker, transport limitations may occur. They are sometimes referred to as lithium trapping in the literature [13-14]. Such transport limitations will manifest themselves as additional overvoltages associated with concentration gradients inside the LiAl phase and will result in further shifts in the

delithiation potentials potential in addition to potential shifts described by eqs. 2 and 3. In particular, for bulk Al this was represented in the form of secondary and tertiary discharge plateaus that appeared at high current densities after the main discharge plateau, and then steadily increased in duration with cycling (**Figs. 4-1-12, 4-2-11, 4-3-11**). However the cumulative contribution of these diffusion-limited processes in our experiments typically did not exceed 10% (except in Dural), and the effect was only severe close to the plateau jump events. Physically the phenomenon of lithium trapping in our bulk Al system can arise in two ways. Firstly there may be cases when lithium cannot be extracted because its transport is diffusionally hindered and there is insufficient concentration gradient or diffusivity (low diffusion coefficient) to get it out. Secondly there is lithium that may be present in a portion of the porous structure that has broken off during cracking and is therefore rendered inactive for delithiation because it has lost electrical contact with the metal support. The latter cause is equivalent to pulverization, while the former will be relatively minor if the proper porous nanostructure is produced through an optimum combination of materials, protective coatings and conditioning at low current densities.

In light of the situation described above we will employ multiple (concurrent) strategies to mitigate the mechanical degradation (pulverization) of the porous structure. Most importantly there is the consideration of mechanical properties of the bulk anode materials, which will be discussed in detail in Ch. 5.2, as well as how these properties affect the serrated potential response characteristic of anode failure. Obviously, a stronger material will better resist the accumulation of internal stresses and fracture. Secondly, we will explore the ways to contain the volume changes and associated stresses by applying various coatings and architectures that would act as scaffolds and exert a compressive force to contain phase growth and fracture. Such strategies are presented in Ch. 5.3. In particular we discuss the advantage of using of mechanically rigid yet elastic solid polymer electrolytes as an additional scaffold in solid-state battery prototype architecture. We will also highlight the need to use low current densities at the early stages of formation of the LiAl nanostructure since low growing rates should produce less stress accumulation and therefore more ordered, stable and rigid structure.

5.1.3 References

1. Schroder, K.W.; Dylla, A.G.; Harris, S.J.; Webb, L.J.; Stevenson, K.J., *ACS Appl. Mater. Interfaces*, **2014,** *6,* 21510-21524.
2. Liu, D.X.; Co, A.C., *J. Am. Chem. Soc.,* **2016**, *138*, 231-238.
3. Liu, X.H.; Huang, J.Y., *Energy Environ. Sci.,* **2011,** *4,* 3844.
4. Zhu, J.; Zhou, J.; Chen, B.; Liu, Z.; Liu, T., *J. Solid State Electrochem.,* **2016**, *20*, 37-46.
5. Mukhopadhyay, A.; Sheldon, B.W., *Progress in Materials Science*, **2014,** *63*, 58-116.
6. Liu, Y.; Hudak, N.S.; Huber, D.L.; Limmer, S.J.; Sullivan, J.P.; Huang, J.Y., *Nano Lett.* **2011**, *11*, 4188-4194.
7. Sethuraman, V.A.; Srinivasan, V., *Journal of the Electrochemical Society,* **2010,** *157(11),* A1253-A1261.
8. Sheldon, B.W.; Soni, S.K., *Electrochemical and Solid State Letters,* **2012,** *15(1),* A9-A11.
9. Zhu, Y.; Wang, C., *Journal of Power Sources,* **2011,** *196*, 1442-1448.
10. McAlister A.J., *Bulleting of Alloy Phase Diagrams,* **1982,** *3*, 177-183.
13. Owen, J.R.; Maskell, W.C.; Steele, B.C.H., *Solid State Ionics*, **1984,** *13*, 329-334.
14. Oltean, G.; Tai, C.W.; Edstrom, K.; Nyholm, L., *Journal of Power Sources*, **2014**, *269*, 266-273.

5.2 Role of Mechanical Properties of Aluminium Alloy

Before we examine the role of mechanical properties in the lithiation-delithiation of bulk Al anodes we clarify some terminology that will be used in this section. Applied stress that produces a strain response in a material before the yield point results in elastic deformation. This is considered a reversible deformation. Conversely applied stress that produces a strain response in a material at or beyond the yield point results in plastic deformation. This is considered an irreversible deformation, with severe plastic deformation causing the formation and propagation of cracks and eventually fracture. Substitutional alloys are the structures in which the alloying atoms or ions substitute the ones originally found in atomic positions of the host crystalline lattice. There are also interstitial alloys whereby the alloying elements go into interstices, or voids existing between atoms or ions in the original crystal. During the process of plastic deformation there is movement of mobile dislocations and diffusion of alloying atoms through vacancies. When mobile dislocations are relatively free to move during plastic deformation and are not obstructed, this produces homogenous plastic deformation in the material. No or little internal stress is accumulated in this process. However when there is a dynamical interaction of the mobile dislocations and the diffusing solute atoms, or dislocations with other dislocations, the dislocations may become immobilized or "pinned". This causes what is termed "jerky flow" of dislocations, producing localized (inhomogenous) bands of plastic deformation in the material. This phenomenon is referred to as the Portevin-LeChatelier (PLC) effect and is visualized in a serrated stress-strain curve [1-4]. The stress-strain curve has a "serrated" appearance with periodic discontinuous drops in stress separated by portions of smooth deformation (**Fig. 5-2-1**).

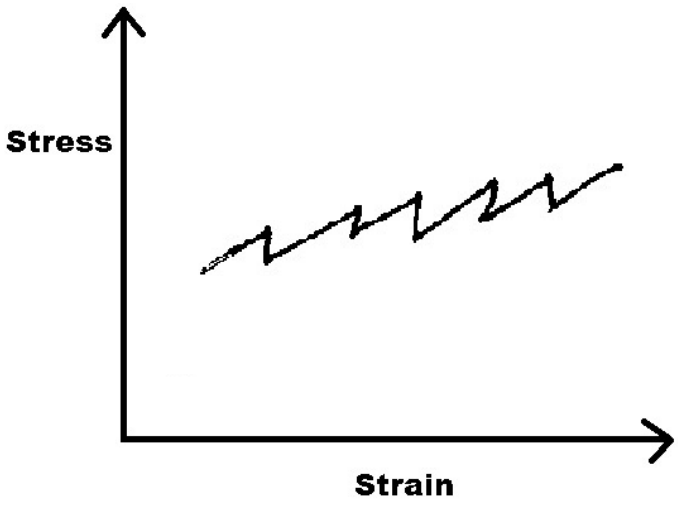

Figure 5-2-1: Serrated stress-strain curve for a material characteristic of jerky flow of mobile dislocations

The onset of the PLC effect starts at a so-called "critical strain" which is the minimum strain needed for the onset of the serrations in the stress-strain curve. The critical strain to create these serrations will depend on multiple factors [1-4]. In particular these would be the host and solute elements, whether the solute is present as a substitutional or interstitial alloy in the host, the concentration of the solute element in the host, and whether the material has undergone treatment that affects dislocations such as strain-hardening and thermal annealing.

Lithiation-delithiation of Al anodes occurs through generation and movement of dislocations [5-6]. At low concentrations of Li this occurs in a substitutional solid solution of Li in an FCC lattice of Al, referred to as the α-LiAl intermetallic phase [6-7]. Diffusion of Li in this solid solution occurs through movement and generation of dislocations. Solid solutions of LiAl (α-LiAl) are known to consistently exhibit the PLC effect when the Li concentration increases sufficiently to promote some short range ordering of Li in the alloy [3], i.e. when the Li concentration increases sufficiently to promote localized regions of crystallized β-LiAl intermetallic phase formation [6-8]. Therefore this effect implies an interaction between Li solute atoms and dislocations of

the Al lattice during the strain response of deformation that occurs in lithiation-delithiation. Mobile dislocations may become trapped (pinned) both by diffusing Li solute atoms (solid solution of α-LiAl) and by the short-range order present in localized regions of crystallized β-LiAl formation, as well as other dislocations when the size of β-crystalline domains become large enough. In fact, trapping of dislocations is the physical mechanism behind cold or work hardening of materials.

The Al anodes in this thesis work are bulk materials. Therefore the processing methods used to manufacture the material must be considered, because these methods will determine the mechanical properties, and the properties will be determined by the distribution and mobility of dislocations. There are many processing methods available for bulk Al materials which can produce a wide variety of mechanical properties. The mechanical properties can be modified through cold-working (strain-hardening) or thermal annealing (softening) treatment of the bulk Al material itself. Alternatively the properties can be modified by introducing alloying elements in the molten state followed by quenching and ageing. Since the mechanical properties determine the distribution and mobility of dislocations they will greatly determine the strain response of the bulk Al material towards the internal stresses that are produced in lithiation-delithiation. In particular this would concern the strain response of the material towards the stresses that are produced by formation of an α-LiAl solid solution, and then later crystallization to β-LiAl with increasing Li concentration. If the mechanical properties of a bulk Al material produce jerky flow (PLC effect) during repeated lithiation-delithiation processes this would be visualized by a serrated stress-strain curve (**Fig. 5-2-1**). As described previously in Ch. 5.1 the elastic-plastic strain response of the material towards lithiation-delithiation stresses will affect the Nernstian equilibrium potentials of the respective processes [9-11], because energy that is used to accommodate strain is lost for the purposes of insertion/extraction of Li. Therefore a serrated strain response during lithiation-delithiation should produced a similar response in the respective plateau potentials over time. This would be visualized as instantaneous (discontinuous) jumps in plateau potentials during galvanic cycling. In addition there could be smaller more localized changes of potential within a plateau region. Physically an increased PLC effect should

manifest as more severe localized cracking in the porous structure i.e. inhomogenous plastic deformation.

In the comparison of Goodfellow Al (GF Al) versus McMaster-Carr (MC Al) we need to consider the effect of cold-working (strain hardening) and thermal annealing (softening) processing methods applied to these materials during manufacture. Strain-hardening is a form of cold-working for Al materials. It both multiplies the number of dislocations in the material and "entangles" them relative to the original unworked material [4]. In other words there is a dislocation-dislocation interaction which impedes their mobility because a significant portion of dislocations are now considered immobile (forest dislocations). Plastic deformation occurs through movement of mobile dislocations. Therefore strain-hardening has the effect of decreasing the relative ease of plastic deformation and thus the strain at a given stress. The dislocations in the Al effectively trap each other, preventing movement. If strain-hardening impedes the mobility of dislocations within the host, and diffusion of Li solute atoms during lithiation occurs through movement of dislocations, then the relative degree of lithiation occurring through intermetallic phase formation will be lower for GF Al. Therefore, indicators of volume change and degree of phase formation (alloying) in the electrochemistry should decrease. In the 4x8 experiment of GF Al the initial CV shows a smaller loop size, more gradual slope following lithiation onset as well as a decreased overvoltage relative to MC Al (**Fig. 4-2-2**). Similarly In the 4x8 galvanic cycles we clearly see a decreased plateau separation for GF Al when comparing cycles from both materials at the same cycle number and current density (**Fig. 4-2-3**), which can be related to less pronounced changes in volume and the associated energy (Eq. 2).

For MC Al the process of thermal annealing decreases the number of dislocations as the material progresses towards its equilibrium state through the redistribution of atoms [1]. It is also typically characterized by grain growth in which the microstructure starts to coarsen resulting in softening of the material. Overall, thermal annealing has the effect of increasing the relative ease of plastic deformation. While this processing method annihilates a significant portion of dislocations that were present, there remains a

relatively higher number of mobile dislocations than in strain-hardened GF Al, and they can travel farther due to the coarser grain boundaries. Therefore for lithiation-delithiation this should offer a greater capability for the volume change due to intermetallic phase formation. As a result the 4x8 experiment of MC Al has an initial CV with larger loop size, steeper slope following lithiation onset and increased overvoltage (**Fig. 4-2-2**). Similarly the 4x8 galvanic cycles have a larger plateau separation (**Fig. 4-2-3**). The increased capability for volume change and intermetallic phase formation in MC Al has a drawback. It initially decreases the reversibility (coulombic efficiency, CE), likely for two main reasons (**Fig. 4-2-6**). Firstly a larger volume change upon delithiation may partially destroy part of the porous structure that was created during lithiation, trapping Li inside. In Al nanowires this has been observed as void formation that only occurs after the delithiation scan [12]. Secondly larger volume changes in MC Al may cause additional destruction of the SEI layer that was present. Since Li that is used for SEI formation during lithiation is irreversibly lost the Li that is recovered upon delithiation will be less (lower CE).

In the half-cell failure tests of GF Al (GF5) versus MC Al (MC3) we observed that MC Al produced a significantly more unstable lithiation-delithiation potential response over time as well as severe degradation in CE (**Figs. 4-2-7 to 4-2-10**). First let us consider the effect here of the native surface oxide which was present in MC Al (MC3) but was removed in GF Al (GF5) prior to cell assembly and testing. As described in Ch. 5.1 the native oxide is initially detrimental for CE, likely because it is irreversibly lithiated to a Li-O-Al layer [12], but quickly becomes irrelevant. At the higher current density of 0.5 mA/cm^2 used in half-cell failure tests the oxide should be fully lithiated within a few cycles, which helps explain the decreasing CE trend observed very early in MC Al (**Fig. 4-2-10**). After that point the CE of MC Al rapidly improves over time similar to GF Al, and actually reaches a higher maximum value. The pronounced failure that follows for MC Al should be primarily due to the softened mechanical properties. The greater capability for volume change and phase formation in MC Al allows for a short time a higher CE than in GF Al. However it is these same properties that are ultimately

detrimental for the mechanical stability of the porous structure, that has less pronounced dislocation trapping and thus is less resistant to fracturing, cracking and ultimate failure.

The cycle sets of both GF Al (GF5) and MC Al (MC3) show discontinuities in lithiation-delithiation potentials, i.e. plateau potential jumps (**Figs. 4-1-8, 4-2-7**). The amplitude of these discontinuities is larger in MC Al because the potentials shift more drastically over time prior to the jumps. Therefore both materials should exhibit serrations in their stress-strain behaviour (jerky flow, PLC effect) during repeated lithiation-delithiation events at a relatively high current density, and this behaviour is more severe in MC Al than GF Al. In strain-hardened GF Al the absolute number of dislocations within the material is much higher than in MC Al. However a large portion of these dislocations are immobile because of dislocation-dislocation interactions [4]. Therefore the relative number of mobile dislocations available to interact with Li atoms and become immobilized (pinned) by them is less in GF Al. This should decrease the frequency and magnitude of serrations in the strain-stress curve, which is what we observe in the charge/discharge potential response over time for GF Al (**Fig. 4-1-8**). The thermal annealing processing that creates MC Al will annihilate a significant portion of the dislocations that were present in the original Al 1100 material [1]. However the relative number of mobile dislocations in MC Al is higher than in GF Al. Together with the coarser grain boundaries (larger grains) produced by the annealing method these mobile dislocations are more free to move to interact with diffusing Li atoms and become pinned by them. This should increase the frequency and magnitude of serrations in the stress-strain curve, which is what we observe in the charge/discharge potential response over time for MC Al (**Fig. 4-2-7**).

Physically the increased serrated yielding response of MC Al (MC3) should be producing many localized bands of plastic deformation (cracking) in the porous structure. This is observed in the SEM images of MC Al after the half-cell failure test was complete (**Fig. 4-2-13**). There are numerous small cracks positioned laterally and vertically between portions of the porous structure, which could help to release portions of the porous structure into the liquid electrolyte. This cracking behaviour produces the multilayered porous structure seen in MC Al. In the SEM of GF Al after the half-cell failure test there

is also evidence of localized bands of plastic deformation (PLC effect) (**Fig. 4-1-14**). This is seen in the long cracks of GF Al (**Fig. 4-1-14 a**), that are considerably wider than any cracking observed in MC Al (**Fig. 4-2-13 a**). However when looking at lower magnification the portion of the cycled area that appears free of mechanical degradation is significantly larger in GF Al (**Fig. 4-1-14 b**) than in MC Al (**Fig. 4-2-13 b**). Furthermore there is no cracking in GF Al that causes peeling of portions of the porous structure away into the liquid electrolyte and therefore no multilayered structure. Overall the comparison of GF Al versus MC Al half-cell failure tests suggests that softened mechanical properties in the bulk MC Al produces a more serrated strain response under repeated lithiation-delithiation events at a relatively high current density. This strain response then manifests itself as increased drifting in lithiation/delithiation potentials (overvoltage), increased plateau separation as well as plateau potential jumps due to severe plastic deformation of the porous structure. Therefore, softened mechanical properties can be considered as detrimental towards the cycle stability and cycle lifetime of bulk Al anodes in lithium-ion batteries. Similar tendencies have been demonstrated by even softer thin sputtered Al films described in Ch. 4.5. In view of this discussion, it is not surprising that numerous attempts in the literature to achieve high performance of Li based anode using traditional approaches involving various nanoparticles, nanowires and thin films, were unsuccessful. Such objects are just too soft to resist fracturing and pulverization. Also, nanosize objects cannot have the same degree of dislocation hardening because moving dislocations will be trapped at the grain boundaries and not able to accumulate.

In Dural (Al 2024) the mechanical properties are modified instead by introducing Cu and Mg as alloying elements in the molten state. During quenching and aging these alloying elements will primarily precipitate at the grain boundaries. This process is referred to as "precipitation hardening" and the end result is that plastic deformation is significantly more difficult to perform relative to any Al 1100 material. First let us consider the results of the 4x8 experiment of Dural relative to GF Al and MC Al (**Ch. 4.3**). Copper is considered inert towards lithiation and therefore cannot undergo Li-Cu alloy formation like in Li-Al [13]. However the process of Li-Mg alloying can occur at room temperature

[13]. With copper being inert towards lithiation and precipitating at the grain boundaries of Dural we would expect its presence would result in slower kinetics of the lithiation process. This behaviour is seen in the notably larger CV overvoltage and galvanic cycle plateau separation of Dural relative to GF Al and MC Al (**Figs. 4-3-2 to 4-3-4**). Dural also features notable diffusion limitations of delithiation (see below). This directly decreases the coulombic efficiency of the main discharge plateau (**Fig. 4-3-5**). Physically the detrimental effect of copper is seen in the limited reactivity of the Dural surface after the 4x8 experiment from the SEM imaging (**Fig. 4-3-13 c-d**). Even at low magnification there are visible regions in the cycled area with minimal if any coverage by porous material.

The presence of precipitates (Cu, Mg) has an influence on the appearance/disappearance of serrations in the stress-strain curve of Al materials. Specifically the PLC effect (jerky flow) is well documented in very dilute (a few at. %) solid solutions of Mg [2] as well as Cu [14] in Al. These effects are ascribed to a strong misfit interaction between Cu and Mg solute atoms and mobile dislocations in Al. When Dural undergoes lithiation it is now further alloyed, this time with Li. Therefore we would expect the detrimental PLC effect to increase because now the mobile dislocations can be pinned by Cu, Mg and Li solute atoms. This is revealed in the half-cell failure test of Dural (DU2) which shows the first jump in plateau potentials appearing earlier than both GF Al (GF5) and MC Al (MC3), with an amplitude that is much larger than GF Al and comparable to MC Al (**Figs. 4-3-7, 4-3-9**). The more pronounced PLC effect around this cycle region of the Dural half-cell failure test likely explains the higher coulombic efficiencies of the diffusion-limited discharge plateaus (**Fig. 4-3-11**). As described previously in Ch. 5.1 we associate these 'secondary' and 'tertiary' plateaus following the main discharge plateau with the phenomenon of 'lithium trapping'. The severe diffusion-limited discharge behaviour of Dural in the half-cell failure test is consistent with similar behaviour observed in the 4x8 experiment (**Figs. 4-3-5, 4-3-6**). If Li transport within Dural is impaired by dislocation pinning and interactions with Cu + Mg atoms then this effectively decreases the amount of Li that can be recovered during delithiation. It is this

poor Li transport that directly decreases the CE of the main discharge plateau for Dural under these half-cell failure conditions relative to GF Al and MC Al (**Fig. 4-3-10**).

Given the relatively stronger PLC effect present early in Dural we expected that additional plateau potential jumps would soon follow in higher frequency and greater amplitude than GF Al (GF5) and also possibly MC Al (MC3). However no abrupt change in potentials or CE is observed until approaching the 250th cycle (**Figs. 4-3-7, 4-3-9, 4-3-10**). This region of cycling stability implies that no further significant plastic deformation (homogenous or inhomogenous) occurred between the first plateau jump and much later in the cycling of Dural. The reason may be the improved mechanical toughness of Dural itself which makes fracture due to plastic deformation considerably more difficult than Al 1100 materials. This assertion is supported by the SEM imaging of Dural which shows a fully reactive highly porous surface that is otherwise relatively intact (**Fig. 4-3-14 d-e**) compared to the cycled morphologies of GF Al (**Fig. 4-1-14**) and MC Al (**Fig. 4-2-13**). Even considering this region of mechanical stability in the cycling of Dural the CE still remained poor below 60% (**Fig. 4-3-10**). As mentioned this poor CE was primarily due to more diffusion-limited discharge behaviour because of slower kinetics and diffusivity due to the presence of alloying elements. Overall we can conclude that the improved mechanical toughness of Dural results in significantly decreased plastic deformation (cracking, fracture, etc.) in response to the internal stresses of lithiation-delithiation. This offers a relatively more stable charging/discharging response relative to GF Al and MC Al when cycling continuously at a high current density. However the alloying elements (Cu and Mg) that are responsible for this mechanical stability simply present too many disadvantages. Specifically, these drawbacks are poorer lithiation-delithiation kinetics, diffusivity and reversibility, which makes Dural an unsuitable anode material for Li ion batteries relative to strain-hardened bulk Al 1100 materials such as GF Al.

5.2.1 References

1. Van Den Beukel, A., *Acta Metall.,* **1980**, *28*, 965-969.
2. Mulford, R.A.; Kocks, U.F., *Acta Metall.,* **1979,** *27,* 1125-1134.
3. Evans, J.T., *Scripta Metallurgica*, **1987,** *21*, 1435-1438.
4. Van Den Beukel, A.; Kocks, U.F., *Acta Metall.,* **1982,** *30,* 1027-1034.
5. Zhu, J.; Zhou, J.; Chen, B.; Liu, Z.; Liu, T., *J. Solid State Electrochem.,* **2016**, *20*, 37-46.
6. Liu, D.X.; Co, A.C., *J. Am. Chem. Soc.,* **2016**, *138*, 231-238.
7. Owen, J.R.; Maskell, W.C.; Steele, B.C.H., *Solid State Ionics*, **1984,** *13*, 329-334.
8. Kishio, K.; Brittain, J.O., *J. Phys. Chem. Solids.,* **1979,** *40,* 933-940.
9. Sethuraman, V.A.; Srinivasan, V., *Journal of the Electrochemical Society,* **2010,** *157(11),* A1253-A1261.
10. Sheldon, B.W.; Soni, S.K., *Electrochemical and Solid State Letters,* **2012,** *15(1),* A9-A11.
11. Zhu, Y.; Wang, C., *Journal of Power Sources,* **2011,** *196*, 1442-1448.
12. Liu, Y.; Hudak, N.S.; Huber, D.L.; Limmer, S.J.; Sullivan, J.P.; Huang, J.Y., *Nano Lett.* **2011**, *11*, 4188-4194.
13. Dey, A.N., *Journal of the Electrochemical Society*, **1971**, *118*, 1547-1549.
14. E.O. Hall, *Yield Point Phenomena in Metals and Alloys*, Macmillan and Co, London, 1970.

5.3 Role of CNx and SPE Protective Coatings on Aluminium

In Ch. 5.1 we discussed that one of the possible ways to contain the volume changes and associated stresses is by applying various coatings that would act as scaffolds and exert a compressive force to contain phase growth and fracture. In this section, we discuss the use of vacuum deposited carbon nitride (CNx) as well as solid polymer electrolyte (SPE) for this purpose. But let us first consider how the deposition of CNx film can modify the bulk Al surface. The compositing of aluminium with carbon is ideally performed through methods that allow for Al-C hybridization at the nanoscale. This has been performed through gas-phased chemical-vapor deposition (CVD) methods [3], but more recently a facile synthesis method has emerged involving ultrasonication and heat treatment of Al powders and carbon precursors [5]. Methods such as these that allow for nanoscale hybridization are believed to result in formation of Al carbides at the nanoscale interface of Al and sp^2 (graphitic) carbon. This interfacial reactivity improves both conductivity and stability (capacity retention) of the composite anode during the repeated volume changes of continuous cycling. Nitrogen doping of sp^2 carbon composited with Si and Sn nanostructured anodes has been shown to offer two benefits [4]. Firstly there is higher theoretical capacity relative to anodes composited with only graphitic materials because of the higher electronegativity of nitrogen relative to carbon. Specifically some N-containing functional groups have a strong interaction with the metal and metal oxide, possibly through the formation of unique interfacial species, but this has not been 100% proven. This behaviour improves adhesion between the active material (metal and metal oxide) and the buffering component (carbon). Secondly significant levels of N-doping can offer a high proportion of pyridinic and pyrrolic functional groups, which may improve lithium penetration into the carbon structure.

Our radiofrequency magnetron sputtering (RFMS) method of CNx deposition on Al can be considered as a physical vapor deposition (PVD) method of production of nitrogen-doped carbon plasma species. However, our substrate is bulk Al metal instead of nanostructured Al such as Al nanoparticles or nanowires that are used in the literature. Therefore RFMS deposition limits us only to planar interfacial reactivity at the Al

surface, but at the surface there should still be nanoscale hybridization of Al and N/C containing species. This hybridization should at least provide a planar distribution of Al carbide and nitride species. In TOF-SIMS depth profiling of uncycled areas of non-annealed and annealed Al-CNx we observed intensity maxima of AlC^- and AlN^- ions at the film-metal interface, suggesting the formation of Al carbides and/or nitrides (**Figs. 4-6-7 b, 4-6-8 b**). We also observed interfacial maxima of AlO_x^- ions in both samples. These oxide ion maxima indicate that the surface oxide that was re-grown on GF Al initially after substrate preparation was not reduced by the process of CNx film deposition. This interfacial oxide presence may not be detrimental for lithiation/delithiation due to the improved binding of N-containing functional groups mentioned above [4]. We expect this beneficial binding effect would be significant given the high nitrogen content of the plasma (75% N_2) which produces significant incorporation of N-containing functional groups in amorphous sp^2 carbon. Overall our TOF-SIMS depth profiling results suggest that for our Al-CNx anode system the CNx layer should to some extent alter the Al electrode surface, through planar interfacial reactivity during the sputter deposition event with the highly reactive bombarding species that are formed in the plasma. This reactivity would then promote some CNx film adhesion to the Al substrate during the volumetric changes of intermetallic alloy formation and dissolution.

The compositing of carbon (graphite, nanotubes, etc.) with metal-alloying anode materials such as Si and Sn generally serves two purposes [1-5]. Firstly the low volumetric expansion of graphitic carbon offers a buffering component against cracking and pulverization of the metal-alloying active material upon intermetallic phase formation. Additionally the carbon content improves conductivity through continuous electrical contact between Si or Sn particles while preventing their aggregation in the nanoscale architecture, and also facilitating ion transport to these particles. While the second consideration obviously does not apply to our situation (bulk Al anodes have higher conductivity than any carbon material), the first one is relevant to containing the volume change.

When considering the electrochemistry of lithiation-delithiation in the coated versus uncoated bulk Al anodes of this thesis work there are multiple possible effects of the CNx layer. Firstly the CNx layer may alter the electrical and ionic conductivity of the anode. These effects were well documented in Ch. 4.4. Secondly the CNx layer itself may be lithiated and therefore contribute to the capacity of the anode system. This is unlikely to be true for two reasons, beginning with the electrochemistry. In the initial CVs of Al-CNx and Dural-CNx anodes we did not observe additional reduction peaks between the lithiation onset potential for intermetallic alloy formation and the left vertex (**Figs. 4-4-2, 4-4-13**). Similarly we did not observe additional oxidation peaks outside the broad peak around +1V characteristic of intermetallic alloy dissolution. In the 4x8 galvanic cycles of Al-CNx and Dural-CNx anodes we also did not observe any additional lithiation-delithiation processes that may uniquely arise from just CNx itself (**Figs. 4-4-3 to 4-4-5, 4-4-14 to 4-4-16**). The half-cell failure experiments of these two types of coated anodes did initially reveal pronounced double discharge plateaus in the first one or two cycles (**Fig. 4-4-8, 4-4-19**). However even in these experiments the discharge behaviour quickly transitioned to a single plateau by the second or third cycle, and remained so for the rest of the set.

The most conclusive evidence can be found in the TOF-SIMS depth profiling results of cycled non-annealed Al-CNx in **Ch. 4.6**. In particular, profile regions with intensity maxima of CNx containing ions corresponding to residual CNx film (**Fig. 4-6-9 c,e,f**), simultaneously showed a minima of Li^- ions (**Fig. 4-6-9 a**). Overall we conclude that lithiation-delithiation of CNx itself is relatively insignificant in this work. The CNx film instead serves two purposes in our work. Firstly it acts as an ionic conducting pathway to the Al core. Secondly and more importantly it acts as a scaffold to contain the volume changes of intermetallic LiAl phase formation and dissolution, and therefore to control growth of the porous intermetallic structure that are responsible for the charge-discharge processes in Al anodes.

In 4x8 experiments of both non-annealed and annealed Al-CNx the initial CVs show smaller nucleation loops and a more gradual slope of lithiation below the onset potential

(**Fig. 4-4-2**). Both of these features suggest containment of volume changes by CNx associated with formation of the porous LiAl structure. In Si and Sn anodes carbon coatings have been shown to buffer against volume change by significantly reducing the density of mobile dislocations at the medusa zone during nucleation and growth of intermetallic phases [2]. This is important because lithiation-delithiation of metal-alloying electrodes such as Al occurs through movement and generation of dislocations within the host matrix [6]. Therefore we expect a similar mechanism may occur in our Al-CNx system. Surface analysis of the non-annealed Al-CNx anode revealed that the CNx coating cracks and becomes separated from the underlying bulk Al core, with the remnants sitting instead on top of the porous structure (**Fig. 4-4-24 a**). Conversely in the annealed Al-CNx anode the remaining CNx is located close to the film-metal interface, buried beneath the porous structure (**Fig. 4-4-24 c**). This suggests that there is likely increased film-metal interfacial reactivity during the annealing process. In combination with the stress relief within the annealed film, this benefit should increase CNx adhesion and stability during lithiation-delithiation of Al. Therefore, the annealed CNx film should be more effective in controlling growth of the porous structure. The effect of CNx coated on Dural is quite different from the situation described above for CNx coatings on GF Al. In the initial CV of the 4x8 experiments we only observed minor differences in the size of nucleation loops relative to Dural (**Fig. 4-4-13**). This suggests that the containment of volume changes of intermetallic phase formation by CNx is relatively minor with a Dural substrate compared to GF Al. The volume change capability for Dural-CNx could already be significantly constrained by the hardness of Dural itself as described in Ch. 5.2.

In the half-cell failure test we expected the presence of the CNx layer would decrease the accumulation of internal stresses in the bulk Al anode, as the surface sites are gradually saturated and the porous structure continues to grow with continuous cycling. This would then decrease the strain response in terms of formation and propagation of cracks in the porous structure, leading to a more stable charge/discharge response and CE trend relative to bare GF Al itself. During early cycling of Al-CNx (AC3) this indeed appeared to be true with a higher maximum CE observed (**Fig. 4-4-10**), but the effect was transient and largely disappeared after 40-50 cycles, followed by large plateau jumps (**Fig. 4-4-9**)

and decrease in CE. The poor performance was likely due to the CNx coating being rapidly destroyed as was revealed by surface analysis afterwards (**Fig. 4-4-25 e-f**). While the CNx film appeared severely degraded the underlying porous structure actually showed significantly less systematic cracking (**Fig. 4-4-25 d-e**) relative to the half-cell failure test of GF Al (**Fig. 4-4-25 a-b**). Therefore the CNx film to some degree was effective in minimizing the lithiation-delithiation induced strain. We did not test annealed Al-CNx anodes under half-cell failure conditions. Considering the improved adhesion and stability observed in the SEM images from the 4x8 experiment (**Fig. 4-4-24 c**) we would expect less degradation of CE and a more stable charge/discharge response relative to non-annealed Al-CNx.

Ultimately, trying to achieve any prolonged benefit from using carbon coatings such as CNx on bulk Al anodes is likely futile in a liquid half-cell environment. Here the CNx exposed to the liquid electrolyte rapidly cracks into pieces within a few cycles. Then those remnants can separate from the anode and be lost into the electrolyte, similar to portions of the porous intermetallic structure during the stress relief events of systematic cracking in the half-cell failure tests. When this occurs, the CNx benefits of constraining the volume changes of intermetallic phase formation are lost, as well as any benefits towards the conductivity or reversibility of the anode system. To fully realize the benefits of CNx coatings on bulk Al anodes requires the solid-state battery prototype design in tandem with a mechanically rigid solid polymer electrolyte, which would act as a second scaffold to both keep the CNx from separation and control the volume change by exerting external compression force.

In the solid-state battery prototype there are multiple mechanical constraints present (**Fig. 3-1**). Firstly, there is the solid polymer electrolyte (SPE) which acts as a mechanically strong yet elastic scaffold. Secondly, the total volume of the cell is kept constant by the cell design. Therefore there is a limitation on how much porous structure can be formed at the Al anode. Additionally the large relief of internal stresses within the anode through systematic cracking and release of active materials should not be possible in the solid-state battery prototype. The dramatic plateau potential jump events observed in the half-

cell failure tests (**Fig. 4-3-9**) were not observed in the battery tests. In the battery test failures at higher current densities the charge/discharge plateau drifting and IR drop simply kept increasing until there was a complete loss of coulombic efficiency (**Figs. 4-7-4, 4-7-5, 4-7-12, 4-7-13, 4-7-16, 4-7-17**). This indicates that the battery architecture was successful in preventing the pulverization and detachment of the active material. The eventual failure that we did observe with battery tests was likely due to uncontrolled heterogeneous and dendritic growth of the porous structure between the strands of SPE at the highest current densities. This uncontrolled growth could not only damage the SPE but also allow direct contact with cathodic materials leading to the formation of a short circuit in the cell. In the surface analysis of battery anodes cycled with constant charge/discharge times at elevated current densities (samples BAT1 to BAT4 in Ch. 4.7) we consistently observed overlaying features on the porous anode morphology, characteristic of dendritic growth of the porous structure and damage of SPE/cathodic components (**Figs. 4-7-28 a-c**).

The mechanical constraints present in the solid-state battery cell prototype are also beneficial for the CNx film on the bulk Al anode. Even if the CNx film significantly cracks during anode charge/discharge the remaining pieces will still be localized near the anode instead of being lost into a liquid electrolyte as in the half-cell. Therefore the CNx can act as a secondary scaffold in addition to the SPE layer. The battery test with very limited cycling of the Al-CNx anode (BAT6) suggests that CNx constrains the phase formation during the initial stages (**Fig. 4-7-29 a**). However if growth of the porous structure is not carefully controlled during battery conditioning due to the use of constant charge/discharge times then the porous structure rapidly breaks through and grows over any remaining CNx. In this case the CNx rapidly becomes buried underneath the thick porous structure. Therefore its effectiveness of acting as an additional scaffold is quickly lost, and at that point the constraining of continued phase growth (porous structure) solely relies on the SPE layer. This situation is likely what occurred in the battery test with non-annealed 75% N_2 Al-CNx anode (BAT2). The performance was improved over the test with bare GF Al anode (BAT1), producing a stable charge/discharge response (**Fig. 4-7-9**) and good coulombic efficiency (**Fig. 4-7-8**) at a higher current density where BAT1

rapidly failed (**Figs. 4-7-4, 4-7-5**). However the porous structure growth still got out of control at the highest current density, with the CNx becoming buried and evidence still appearing for damage of SPE and cathodic materials (**Fig. 4-7-28 b**). Overall the results are a vast improvement but at the same time they highlight the need to limit the current density used to electroform the intermetallic structure. If the charge/discharge times exceeds the capacity of the intermetallic structure formed at low current densities, uncontrolled growth at high current densities follows that results in rapid cell failure.

Therefore, in the final battery experiment (BAT5) we first used the already established approach of conditioning at lower current densities with a high number of cycles. This allowed for equilibrium growth of the nanostructure that was controlled and uniform. Then we proportionally limited the charge/discharge times so that not to exceed the capacity of the formed nanostructure and to avoid the continued growth at higher current densities. The result was a honeycomb morphology in the nanostructure (**Fig. 4-7-28 e**). Here the volume change was contained within the pores, effectively decreasing the accumulation of strain on the anode side and keeping the overall anode dimensions constant. There was no destruction of the SPE layer, with large portions of intact SPE instead remaining on the anode after separation from the cell assembly (**Figs. 4-7-27 e, 4-7-28 g**). We were even able to detect some areas on the anode surface that still contained relatively intact CNx film (**Fig. 4-7-28 f**). This CNx could then maintain its effectiveness as an additional scaffold while improving the electrical/ionic conductivity for lithiation-delithiation. The combined battery conditioning approach in BAT5 also offered another benefit. It eliminated the presence of diffusion-limited discharge plateaus and related processes (**Fig. 4-7-23**), that plagued the battery performance with Al-CNx anodes (**e.g. Fig. 4-7-10 b**), in which the nanostructure growth was not controlled at higher current densities. Therefore this conditioning approach also decreased the effect of lithium trapping likely due to the shorter diffusion length in the nanopores of the honeycomb, resulting in greatly improved coulombic efficiency (**Fig. 4-7-20**).

5.3.1 References

1. Chen, Z.; Qian, J., *Electrochimica Acta,* **2009,** *54,* 4118-4122.
2. Liu, X.H.; Huang, J.Y., *Energy Environ. Sci.,* **2011,** *4,* 3844.
3. Park, J.H.; Hudaya, C.; Kim, A.Y.; Rhee, D.K.; Yeo, S.J.; Choi, W.; Yoo, P.J.; Lee, J.K., *Chem. Commun.,* **2014**, *50*, 2837.
4. Li, Z.; Wu, G.; Deng, S., *Chemical Engineering Journal,* **2016,** *283,* 1435-1442.
5. Huang, Y.; Lin, X.; Pan, Q.; Li, Q.; Zhang, X.; Yan, Z.; Wu, X.; He, Z.; Wang, H., *Electrochimica Acta*, **2016,** *193*, 253-260.
6. Liu, D.X.; Co, A.C., *J. Am. Chem. Soc.,* **2016**, *138*, 231-238.

Chapter 6

6 Conclusions and Future Work

Overall, in this work, we were able to demonstrate that the problems that have been plaguing Al anodes and precluding their use in Li ion batteries despite obvious advantages do not appear to be insurmountable. We were able to prepare battery prototypes with Al anodes, $LiFePO_4$ cathodes and solid polymer electrolyte that showed sustained performance for more than 400 cycles over wide range of charge-discharge rates without any failure or capacity fading. The key advances that allowed us to achieve this goal can be formulated as following:

1. We were the first who noted and studied in detail the effect of the mechanical properties of the Al material on the formation of the LiAl intermetallic phase and the ensuing performance of the anode.
2. We were the first to suggest the use of electrochemical approach to formation of the LiAl nanostructure directly on the bulk anode surface, as opposed to usual approaches tested in the literature that involved various kinds of nanoparticles, nanowires, as well as thin evaporated or sputtered films.
3. We were the first to suggest using CNx and/or SPE scaffold to ensure high stability and activity of the LiAl intermetallic phase formed. A unique honeycomb structure was discovered that showed very high performance in a wide range of current densities.
4. Yet another key was the use of solid polymer electrolyte as additional scaffold ensuring excellent performance of the battery prototypes.

Further work will concentrate on two directions:

(1) Further improvement of the procedures to grow the nanostructure, optimization of the growth conditions, etc. The goal is to be able to grow even thicker layers to improve the capacity. One concern here would be the possible re-appearance of the diffusion limitations. The failure mechanism also needs to be investigated in more detail.

(2) Studies and optimization of the cell design and in particular the properties of the solid polymer electrolyte. A parallel project in our group has been underway in our group and we were able, using different SPE formulation, to achieve even better performance than was demonstrated in this work. This work will be continued.

Curriculum Vitae

Name:	Mike Nieradko
Post-secondary Education and Degree:	The University of Western Ontario London, Ontario 2012-2016 PhD (Physical Chemistry) The University of Western Ontario London, Ontario 2006-2008 MSc (Physical Chemistry) The University of Western Ontario London, Ontario 2001-2005 BSc (Honors Chemistry)
Related Work Experience:	Teaching Assistant The University of Western Ontario 2006-2008, 2012-2016
Publications:	1) **M. Nieradko**, N.W. Ghonaim, L. Xi, H.Y. Nie, J. Francis, O. Grizzi, K. Yeung, and W.M. Lau, "Primary ion fluence dependence in time-of-flight SIMS of a self-assembled monolayer of octadecylphosphonic acid molecules on mica - discussion of static limit", Can. J. Chem. 85, 1075-1082 (2007). 2) N.W. Ghonaim, **M. Nieradko**, L. Xi, H.-Y. Nie, J.T. Francis, O. Grizzi, K.K.C. Yeung, and W.M. Lau, "Primary ion fluence dependence in time-of-flight SIMS of self assembled monolayer of alkyl thiol molecules on Au (111) – discussion of static limit", Appl. Surf. Sci. **255**, 1029-1032 (2008).